UNIVERSITY OF CATANIA

DOCTORAL THESIS

Upgrade of harbor rubble mound breakwaters in the context of climate change

Author:
Martina STAGNITTI

Supervisors:
Prof. Enrico FOTI
University of Catania
Prof. Javier LÓPEZ LARA
University of Cantabria
Prof. Rosaria E. MUSUMECI
University of Catania

A thesis submitted in fulfillment of the requirements
for the degree of Doctor of Philosophy

in

Assessment and mitigation of urban and territorial risks - XXXIV cycle
Department of Civil Engineering and Architecture

November 2021

Dedicated to my parents

Abstract

Upgrade of harbor rubble mound breakwaters in the context of climate change

Despite the importance of upgrading aging harbor rubble mound breakwaters under the effects of climate change, to the author's best knowledge a comprehensive methodology for the design of upgrading solutions able to deal with the uncertainties linked to the current state of existing structures, the intrinsic variability of external loading, and the empirical nature of the design formulas has not been proposed yet. In this context, the present work aims to contribute to the definition of a methodology for the assessment of the performances of upgrading solutions of existing harbor rubble mound breakwaters, also considering the effects of climate change. First, a novel easy-to-use method for the assessment of the current state of existing structures is presented, which is based on the diachronic analysis of field aerial and UAV data. The obtained information are useful for the selection of the most appropriate upgrading concepts for the considered breakwater, as demonstrated by the results of the application to the case study of the Catania harbor breakwater. Then, a general framework of the variation of past and future sea level and wave climate due to climate change in the Italian seas is provided, which allows the definition of the external loading to be used for the probabilistic design of the upgrading options. Results on the behavior of upgraded rubble mound structures under wave attack, acquired through the composite modeling of the upgraded Catania harbor breakwater, are also presented. Two-dimensional experiments have been performed, considering six different upgraded configurations. Both traditional and novel techniques have been employed for the analysis of the armor layer damage dynamics. Furthermore, the mean overtopping discharge has been measured to compare the hydraulic performances of the tested structures. A deeper investigation of the overtopping phenomena, at both laboratory and prototype scale, has been conducted, through two-dimensional numerical simulations based on the solution of the VARANS equations. The outcomes of the composite modeling have allowed us the definition of site-specific empirical formulas for the design of upgrading solutions. A probabilistic method for the assessment of the performances of upgrading solutions under both present and future climate, based on a Monte Carlo simulation technique, is described, together with the outcomes of the application to the case of the Catania harbor breakwater. Finally, some general findings have been derived from the analysis of the considered case study, concerning the armor layer damage dynamics, the importance of using specific design formulas and the necessity of maintenance interventions for existing harbor breakwaters.

Acknowledgements

Contents

List of Abbreviations

CFD	Computational Fluid Dynamic
CFSR	Climate Forecast System Reanalysis
ECMWF	European Centre for Medium-Range Weather Forecasts
EES	Equivalent Exponential Storm model
EMD	Empirical Mode Decomposition
FFT	Fast Fourier Transform
GEV	Generalized Extreme Value
GIS	Geographic Information System
GPD	Generalized Pareto Distribution
LNG	Liquefied Natural Gas
MME	Methods of Moments Estimation
MSL	Mean Sea Level
NASA	American National Aeronautics and Space Administration
NCEP	National Centers for Environmental Prediction
NOAA	American National Oceanic and Atmospheric Administration
NSS	Not Sufficient Support
OLS	Operational Limit State
POT	Peaks Over Threshold
PSMSL	Permanent Service for Mean Sea Level
RANS	Reynolds Averaged Navier-Stokes
RCP	Representative Concentration Pathway
RLR	Revised Local Reference
SfM	Structure from Motion
SLR	Sea Level Rise
SLS	Serviceability Limit State
SRES	Special Report on Emissions Scenarios
SS	Sufficient Support
STD	STandardDeviation
UAV	Unmanned Aerial Vehicle
ULS	Ultimate Limit State
VARANS	Volume-Averaged Reynolds Averaged Navier-Stokes

List of Symbols

Latin

A	Slope of the linear regression model	
a	Multiplicative parameter of the power law	
a_E	Coefficient of the EurOtop (2018) formula	—
a_r	Coefficient of the Zanuttigh and van der Meer (2008) formula	—
$A_{e,i}$	Eroded area of the $i - th$ cross section	m^2
$APSD$	Areal power spectral density	m^4
B	Intercept of the linear regression model	
B_s	Width of the tested section	m
b	Exponent of the power law	—
b_{ds}	Empirical coefficient of the relationship between d_s and H_{s0}	h/m
b_E	Coefficient of the EurOtop (2018) formula	—
b_r	Coefficient of the Zanuttigh and van der Meer (2008) formula	—
b_{SS}	Empirical coefficient of the relationship between H_{s0} and h_{SS}	—
b_{Tm}	Empirical coefficient of the relationship between H_{s0} and T_m	—
b_{Tp}	Empirical coefficient of the relationship between H_{s0} and T_p	—
CB	95% confidence bounds	
CB_{lo}	Lower 95% confidence bound	
CB_{up}	Upper 95% confidence bound	
CV	Relative error for the estimation of P_f	—
c_F	Coefficient of the of the Forchheimer's relationship	—
c_{Hs}	Empirical coefficient of the relationship between H_{s0} and H_s	—
D_m	Mean wave direction	°
D_{n50}	Median nominal diameter of the armor units	m
d_f	Degrees of freedom of the t-distribution	—
d_s	Wave storm duration	h
ERI	Economic Repercussion Index	—

e_{Hs}	Percentage difference between input and output H_s	%
e_{Tp}	Percentage difference between input and output T_p	%
FoC	Factor of change	—
f	Frequency of wave spectra	Hz
f_{SS}	Annual wave storm frequency of occurrence	events/years
f_c	Experimental coefficient of the van der Meer (1988c) formula	—
f_R	Probability density function of R	—
f_S	Probability density function of S	—
$f_{x,c}$	Spectrum centroid frequency along x	m^{-1}
$f_{y,c}$	Spectrum centroid frequency along y	m^{-1}
G	Armor units gradation factor	—
g	Gravitational acceleration	m/s^2
Hyp_0	Null hypothesis of the Students't-test	m
H_{max}	Maximum wave height	m
H_s	Significant wave height	m
$\overline{H}_s$	Mean H_s characteristic of the site	m
H_{s0}	Deep-water significant wave height	m
$H_{s,d}$	Design significant wave height	m
HD	Macro-roughness maximum wave height along y	m
HH	Symmetrically normalized root mean square error	—
h	Water depth	m
h_{at}	Contribution of astronomical tide to water level	m
h_{SS}	Contribution of storm surge to water level	m
h_{wall}	Height of the wave wall with respect to the toe of the structure	m
I_s	Interarrival time of wave storms	h
k	Turbulent kinetic energy	m^2/s^2
k_d	Design wave number	m^{-1}
k_r	Reflection coefficient	m^{-1}
L	Structure lifetime	years
M_f	Statistical moment evaluated for the future period	
$M_{m,c}$	Statistical moment evaluated for the modeled control period	
$M_{m,f}$	Statistical moment evaluated for the modeled future period	
m	Coefficient of a generic overtopping formula	—
m_{-1}	Moment of the wave spectrum of order -1	$m^2 \cdot s$
m_0	Moment of the wave spectrum of order 0	m^2
N	Number of observations	—
N_f	Number of life cycles with at least one failure	—

N_L	Geometric model scale weight of prototype and model unit	–
N_{moved}	Number of displaced units	–
N_{od}	Damage parameter of Hedar (1960)	–
N_w	Number of incident waves	–
N_{wa}	Stability number (Hudson et al., 1979)	–
N_r	Number of life cycles generated for the Monte Carlo simulation	–
$N_{\gamma a}$	Ratio between specific weight of prototype and model unit	–
$N_{\gamma a/\gamma w-1}$	Ratio between buoyant density of prototype and model unit	–
NBI	Normalized bias	–
NBI_θ	Normalized bias for circular quantities	–
$NRMSE_\theta$	Normalized root mean square error for circular quantities	–
n_{cs}	Number of cross sections	–
n_s	Sample size	–
n_{ss}	Number of generated sea storm in a life cycle	–
n_V	Volumetric porosity	–
$\bar{O}$	Average of the observed values	
O_i	$i-th$ observed value	
$OIER$	Operational Index of Economic Repercussion	–
P_f	Probability of failure	–
$P_{f,i}$	Probability of failure related to the $i-ith$ failure mode	–
$P_{f,L}$	Probability of failure during lifetime L	–
$P_{f,l}$	Lower bounds of the total probability of failure	–
$P_{f,Lmax}$	Maximum acceptable probability of failure during life time	–
$P_{f,total}$	Total probability of failure	–
$P_{f,u}$	Upper bounds of the total probability of failure	–
Pos	Position of a generic breakwater cross section	–
p_i	Pressure field in Einstein notation	Pa
$\bar{p}_i$	Mean pressure in Einstein notation	Pa
p'_i	Turbulent pressure in Einstein notation	Pa
q	Mean overtopping discharge per meter	$m^3/s \cdot m$
$q*$	Non-dimensional mean overtopping discharge per meter	–
R	Resistance function	–
R^2	Coefficient of determination	–
R_d	Design resistance	–

R_c	Structure freeboard	m
R_n	Nominal resistance	−
r	Correlation coefficient	−
$r_{f,OLS}$	Required minimum operationality	−
S	Solicitations function	−
$\bar{S}$	Average of the simulated values	
S_d	Design solicitation	−
$S_{d,c}$	Calculated damage parameter of Broderick and Ahrens (1982)	−
$S_{d,m}$	Measured damage parameter of Broderick and Ahrens (1982)	−
S_i	$i - th$ simulated value	
S_n	Nominal solicitation	−
SE	Standard error	
$SERI$	Social and Environmental Repercussion Index	−
SPI	Storm power index	m^2/h
SSH	Sea surface height	m
SST	Sea surface temperature	°C
s	Dispalcement of the breakwater "shoreline"	m
s_{max}^+	Maximum advancement of the breakwater "shoreline"	m
s_{max}^-	Maximum retreat of the breakwater "shoreline"	m
s_{mean}	Mean variance of the breakwater "shoreline"	m
T_e	Wave energy period	s
T_m	Mean wave period	s
$\bar{T}_m$	Mean T_m characteristic of the site	s
T_{m0}	Deep-water mean wave period	s
$T_{m-1,0}$	Spectral wave period	s
T_p	Peak wave period	s
$\bar{T}_p$	Mean T_p characteristic of the site	s
T_r	Return period	years
u_i	Velocity field in Einstein notation	m/s
$\bar{u}_i$	Mean velocity in Einstein notation	m/s
u_i'	Turbulent velocity in Einstein notation	m/s
WP	Wave power	W/m
X_i	Generic stochastic variable	
Z	Reliability function	−

Greek

α	Sea side slope angle	°
α_{sc}	Scale parameter of the probability distribution	−
α_F	Coefficient of the Forchheimer's relationship	−

β	Reliability index	$-$
β_F	Coefficient of the Forchheimer's relationship	$-$
β_{OLS}	Required minimum reliability index	$-$
Δ	Relative buoyant density of the armor units	$-$
$\Delta d_{s,k}$	Duration of the $k-th$ segment of the sea storm profile	h
$\Delta H_{s,k}$	Wave height of the $k-th$ segment of the sea storm profile	h
Δq_{SLR}	Increase of q due to SLR	%
Δq_{E-}	Decrease of q due to the upgrade of the structure	%
ϵ	Rate of dissipation of turbulent kinetic energy	m^2/s^3
ϵ_i	Error term of the linear regression model	
ζ_{lc}	Location parameter of the probability distribution	$-$
γ	Global safety factor	$-$
γ_f	Friction factor of the armored slope	$-$
θ_{Oi}	$i-th$ circular observed value	radiant
θ_{Si}	$i-th$ circular simulated value	radiant
κ_{sh}	Shape parameter of the probability distribution	$-$
λ	Mean annual frequency of wave storms from POT analysis	events/year
λ_M	Macro-roughness mean wavelength	m
λ_m	Micro-roughness mean wavelength	m
μ	Mean of the Normal distribution	
ν	Kinematic viscosity of the fluid	m^2/s
$\xi_{m-1,0}$	Iribarren number	$-$
ρ	Density of the generic fluid	kg/m^3
ρ_{qs}	Density of the quarry stone units	kg/m^3
ρ_w	Water density	kg/m^3
ρ_s	Armor block density	kg/m^3
σ	Standard deviation of Normal distribution	
σ_{fc}	Standard deviation of f_c	$-$
σ_o	Standard deviation of the observed values	
σ_{Pf}	Standard deviation of the probability of failure	$-$
$\sigma_{Pf,L}$	Standard deviation of the probability of failure during lifetime	$-$
σ_s	Standard deviation of the simulated values	
τ_{ij}	Mean viscous stress tensor	N/m^2
Φ	Cumulative normal distribution which links P_f and β	$-$

Subscripts

$ERA5$	Wave characteristic from ERA5 data-set	
exp	Referred to the results of physical modeling	
m	Annual mean value of the wave climate descriptor	

NOAA	Wave characteristic from NOAA data-set
num	Referred to the results of numerical modeling
RON	Wave characteristic from RON data-set
99	Annual 99th percentile value of the the wave climate descriptor

List of Figures

List of Tables

Chapter 1

Introduction

1.1 Statement of the problem

Coastal zones are highly populated, because of the huge number of economic activities linked to the presence of harbors, industries and communication infrastructures. In particular, more than 40% of the European population lives in areas close to the sea (European Environment Agency, 2015). In addition, countless marine ecosystems composed of many kinds of unique species live in coastal zones. Therefore, the economic, social, and environmental relevance of coastal regions leads to the need to protect them, through the implementation of defense plans. Such plans should provide both structural and not structural interventions able to mitigate coastal risk, and at the same time to improve coastal resilience, also to cope with the effects of climate change.

In this context, the defense of ports from the action of sea storms deserves special attention, because of their fundamental role in worldwide economy as hubs of the global trading network (Izaguirre et al., 2021; Camus et al., 2019). Indeed, the most prosperous and advanced past populations grew around ports, which were essential for the exchange of goods and cultures, but also for the reinforcement of military hegemony. The layout of historical ports was progressively modified over time, through the construction of new infrastructure or the adaptation of existing ones, in order to ensure an adequate response to the growing necessity of developing societies. Nowadays, existing harbors still need interventions of maintenance and upgrade, in view of the always increasing demand of port services and of the implementation of long-term strategy for the sustainable development of the so-called "green ports" (Pavlic et al., 2014).

The maintenance and upgrade of harbor defense structures represents a challenge, particularly in the presence of the effects of climate (Hughes, 2014; Toimil et al., 2020). Indeed, mean sea level rise (Lambeck et al., 2011; Church et al., 2013; Galassi and Spada, 2014), increase of extreme storm surge height and frequency of occurrence (Lowe and Gregory, 2005; Vousdoukas et al., 2016), inter-annual variability of wave characteristics (Chini et al., 2010; Hemer et al., 2013a; Camus et al.,

2017; Morim et al., 2019), and reduction of extreme sea levels return period (Vousdoukas et al., 2018) directly influence the hydraulic performances of harbor breakwaters. In particular, increased wave run-up heights and overtopping rates are expected in many worldwide coastal areas under the effects of climate change(Chini and Stansby, 2012; Isobe, 2013; Arns et al., 2017), with the consequent decrease in port operability (Sanchez-Arcilla et al., 2016; Camus et al., 2019; Izaguirre et al., 2021). In addition, the effects of climate change produce increasing uncertainties in the definition of the design conditions, because the assumption of stationary forcing is no more valid (Milly et al., 2008; Mudersbach and Jensen, 2010; Chini and Stansby, 2012; Davies et al., 2017).

Historical harbor defense structures are usually non-conventional breakwaters, which have been repeatedly modified over the years and often converted into rubble mound structures (Lara et al., 2019). In most cases, the structural interventions implemented during the breakwater lifetime have not been properly documented, and hence the actual layering is unknown. The use of common upgrading concepts, such as the heightening of the wave wall, the addition of extra armor units or the construction of a submerged or emerged barrier at the toe of the structure (Burcharth et al., 2014; Foti et al., 2020), clearly enhances, or at least maintains, the non-conventional nature of existing rubble mound breakwaters. Due to the deviation of the existing and upgraded structures from their original design in terms of geometry and porosity, the traditional damage progression models (Hudson, 1959; van der Meer, 1988a; van der Meer, 1988c; Gent et al., 2004) and overtopping formulas (van der Meer, 1995; van der Meer and Bruce, 2014) developed for newly built breakwaters may not be capable of describing the interaction between waves and structures. However, neither formulas nor models specific for the design of upgrading solutions for existing breakwaters have been proposed yet. Moreover, the available numerical models have not been sufficiently calibrated to simulate all the common upgrading concepts, particularly concerning the stability of the armor layer (Burcharth et al., 2014; Lara et al., 2019). The available state of art on the upgrade of rubble mound breakwaters mainly consist in design exercises using only desk study tools (Burcharth et al., 2014), in the suggestion of experience-based or theoretical methods for the identification of the possible restoration and adaptation solutions for existing breakwaters (Croeneveld et al., 1985; Foti et al., 2020) or in not systematic investigations on specific practical case studies that did not provide generally valid outcomes (Reis et al., 2011; Santos-Ferreira et al., 2015; Main et al., 2016).

In the context characterized by the necessity to deal with the effects of climate change, the non-conventionality of existing structures, the design of upgrading solutions for historical rubble mound breakwaters is complicated by the following questions: i) uncertainties in the assessment of the design conditions in the presence of climate change; ii) lack of knowledge about the layering of the existing breakwater, which is known only punctually at best; iii) absence of systematic investigations on

the behavior of upgraded rubble mound structures and consequently of specific design formulas and models. Therefore, further research is required for the definition of a practical methodology for the design of upgrading solutions for rubble mound breakwaters, which should be able to take into account the peculiarities of existing structures, but also the variability of external loading due to the effects of climate change. The first aspect requires the performance of physical and numerical modeling of upgraded structures (Lara et al., 2019), whereas the second matter could be solved following a probabilistic approach, which enables to include the stochastic nature of external forcing and of the structure characteristics, and the uncertainties of the employed equations in the design calculations (Burcharth, 1987).

The present work aims to contribute to the development of practical tools for the design of upgrading solutions of existing rubble mound breakwaters, which could be easily employed for the adaptation of existing defense structures to the effects of climate change. More specifically, the study focuses on the definition of a reliable methodology for the choice of the best upgrading options for existing rubble breakwaters, based on the combined analysis of the results of field surveys, the elaborations of climate data and the outcomes of physical and numerical modeling of upgraded structures. The selection of the optimal upgrading options is then performed following a probabilistic approach, which allows the comparison between different possible configurations in terms of probability of failure.

1.2 Objectives

The main objective of the present thesis is to define methods for the design of upgrading solutions for harbor rubble mound breakwaters, which are able to include the peculiarities of existing structures, but also the variability of climate forcing due to climate change.

Indeed, as stated in section 1.1, there is a lack of specific formulas and models for the design of upgrading solutions, which at present can be performed only using state of art formulations for newly built rubble mound breakwaters, not calibrated to simulate the response of the common upgrading concepts (Burcharth et al., 2014; Lara et al., 2019). In addition, the effects of climate change makes the principle of stationary forcing no more valid for the definition of the hydrodynamic design conditions, whose intrinsic assumption is that what happened in the past will occur in the future. Indeed, the traditional stationary approach cannot deal with the significant variability of wave climate and mean sea level caused by global warming (Chini and Stansby, 2012; Davies et al., 2017; Milly et al., 2008; Mudersbach and Jensen, 2010; Chini and Stansby, 2012).

In order to address the gaps of the state of art on upgrading harbor rubble mound breakwaters, the following specific objectives are set for the present work:

1. **Contributing to the development of a methodology for the assessment of the state of deterioration of harbor rubble mound breakwaters.** Existing rubble

mound structures are usually significantly different from their original design, because of the reshaping action of past sea storms. Various damage modes could have affected the segments of a certain breakwater, thus leading to a geometrically non-homogeneous structure. A simple methodology for the quantitative assessment of the damage suffered by existing breakwaters is proposed, which is based on the diachronic analysis of aerial georeferenced data.

2. **Providing a general framework of the variation of present and future sea level and wave climate due to climate change in the Italian seas.** In view of the impacts of global warming, modifications of the present wave characteristics (e.g. significant wave height, peak wave period) and sea level are expected in the future. Since wave climate and mean sea level determine the magnitude of the external forces acting on coastal defense structure, such modifications should be quantified, and included in the design process. The present work focuses on the wave climate and sea level conditions of the Italian seas, for which only specific investigations related to certain regions or waves descriptors are available.

3. **Acquiring experimental and numerical data on the behavior of upgraded rubble mound structures and construct models for their interpretation.** State of art formulations for the design of rubble mound breakwaters were mainly derived from experimental results of physical model tests on newly built structures. The definition of new formulas or the calibration of existing ones, using both physical and numerical modeling, should be performed for the most common upgrading concepts, in order to provide specific design tools. In this context, the present work gives a contribution to through the analysis of a systematic investigation on a selected case study.

4. **Defining a detailed procedure for the evaluation of the probability of failure of upgraded structures, also considering the effects of climate change.** The probabilistic design seems the only feasible approach for taking into account all the uncertainties which affect the definition of the hydrodynamic conditions, and also the description of the response of upgraded structures to external loads. Guidance on how to include all the involved stochastic input variables into the probabilistic calculations is necessary. Moreover, some considerations for the selection of the most suitable design formulas and mathematical algorithms for the evaluation of the probability of failure are needed.

1.3   Methodology

The definition of a practical methodology for supporting the design of upgrading solutions for harbor rubble mound breakwaters has been performed through the achievement of the specific objectives described in section 1.2.

The methodology for the assessment of the state of deterioration of harbor rubble mound breakwaters is based on the diachronic analysis of georeferenced data concerning the structure of interest, such as orthophotos of 3D point cloud, combined with original design information. The required georeferenced data are acquired through aerial survey, which nowadays can be performed at low cost and in short times using Unmanned Aerial Vehicles (UAVs). The analysis of such data allows the evaluation of the current state of rubble mound breakwaters in terms of advancement or retreat of the "shoreline", and variation of the armor layer slope both in time and space. The possibility to efficiently employ the proposed methodology, which could be useful for a systematic monitoring of harbor breakwaters and the quantification of the damage produced by sea storms, has been demonstrated through the application to the case study of the Catania harbor breakwater.

As regards the assessment of the climate variability due to climate change, a general framework of the modifications of the present and future hydrodynamic conditions in the Italian seas is provided through the combination of literature data on mean sea level and new elaborations of wave climate time series. As regards the mean sea level, results of both historical trend analysis and future climate projections have been collected and critically discussed. Also the wave climate has been investigated in terms of historical long-term tendencies and future projections, under RCP4.5 and RCP8.5 scenarios. The long-term trend analysis has been carried out for eight representative Italian coastal sites, using both measured (i.e. RON) and modeled (i.e. NOAA and ERA5) data, from which descriptors of the annual mean and extreme wave climate have been extracted. The quantification of the trends has been performed in terms of slope of the linear regression model fitted to the time series through the least square method, whereas their statistical significance has been assessed through the application of the Student's t test. As regards the future wave climate, the factor of change method (Peres and Cancelliere, 2018; Fatichi et al., 2011; Kilsby et al., 2007) has been employed for the evaluation of the expected variation of the statistics of maximum sea storm significant wave height, duration of sea storms, peak wave period and mean wave period.

The case study of the Catania harbor breakwater has been chosen for the acquisition of data on the response of six different upgrading options, which include the rising of the wave wall and also the addition of extra armor units equal or smaller than the existing ones over the structure crest and slope. The composite (or hybrid) modeling has been employed to study the behavior of the upgraded structures, in order to overcome the intrinsic limits of the simple physical and numerical modeling (Oumeraci, 1999; Guanche et al., 2015; Di Lauro et al., 2019; Kamphuis, 2020). The results of two-dimensional model scale experiments on damage dynamics and overtopping have been combined with the outcomes of numerical simulations based on the solution of Volume-Averaged Reynolds Averaged Navier-Stokes (VARANS) equations using the software IH2VOF (Lara et al., 2011b; Lara et al., 2011a). Besides the creation of a huge data-set on armor stability and mean overtopping discharge

for upgraded rubble mound breakwaters, the definition of new site-specific formulas for the description of damage progression and overtopping phenomenon have been carried out.

A probabilistic approach has been employed for the comparison in terms of probability of failure between different upgrading solutions of the Catania harbor breakwater. Level III calculations, based on the performance of Monte Carlo simulations (Jonkman et al., 2015), have been implemented for the evaluation of the probability of failure due to the collapse of the armor layer and of the probability of losing port operability due to huge overtopping discharges (Puertos del Estado, 2010). The results of the previous phases of analysis of the hydrodynamic conditions and composite modeling have been used respectively for the characterization of the present and future input wave load, and for the definition of the reliability functions. It is worth to point out that a simplified approach based on empirical site-specific analysis has been adopted for the evaluation of the wave characteristics at the breakwater site.

1.4   Limits

The present work is affected by some limits, specific for each objective described in section 1.2, whose effects on the validity of the obtained results have been minimized.

As regards the assessment of the current state of existing breakwaters, the difficulties in finding the required georeferenced data should be noted. The existing orthophotos can not date back to before the middle of the XX century, when the aerial photogrammetry started to be widely employed, whereas 3D point clouds acquired by UAVs are relatively recent. In addition, information about the original design and the subsequent modifications of historical harbor defense structure is usually not available (e.g. design layouts and cross sections). The proposed methodology is able to provide sufficient information regarding the state of deterioration of the breakwater, even if only data concerning the emerged part of the structure are used. However, the study of the entire slope of the breakwater requires data from submerged surveys, which could be not available. Surely, when bathymetric LIDAR technologies (Irish and White, 1998) for both emerged and submerged surveys will become more affordable, the proposed technique could be further improved. It should be noted that in the present work the analysis of possible local breakage mechanisms of the armor units, which can be performed using data acquired during visual inspections, has not been considered. Finally, the intrinsic dynamic nature of the breakwater "shoreline" has been taken into account in the assessment of its advancement or retreat, through the definition of a range of uncertainty linked to the tidal level and to the continuous movement of the free surface due to waves and winds.

Concerning the study of the present and future hydrodynamic conditions in the Italian seas, the omnidirectional annual analysis of wave climate is presented, which ignores possible peculiarities of the various angular sectors and also the seasonality of marine events. Moreover, in Italy there is a lack of long measured time series of high-quality met-ocean data. Indeed, the Italian National Sea Wave Measurement Network (RON), which represented one of the Italian most advanced system for the monitoring of the directional wave motion, was cast off, and now wave monitoring is performed only by some of the Italian Regions without following a national standard. In the present work, the absence of long measured time series of wave data has been overcome by using longer modeled time series, validated against observed data. Finally, the future projections of both wave climate and sea level are affected by intrinsic uncertainties coming from different sources (Morim et al., 2018), which in someway have been limited by the application of the factor of change method, instead of the analysis of the raw data.

The performed physical modeling of upgraded rubble mound breakwaters is subjected to some limitations, which are typical of all experimental investigations. Indeed, it is known that the dynamic similarity conditions between model and prototype cannot be all satisfied, thus determining an incomplete similarity which cause the so-called scale effects. Despite the impossibility to eliminate such effects, in the present work the small scale (i.e. 1:70) physical model tests have been carried out trying to minimize them following state of art suggestions (Frostick et al., 2011), in order to obtain reliable results for the intended purpose. In this regard, the numerical modeling represents a tool for the quantification of the significance of the scale effects, because it allows to work at full scale. Both physical and numerical tests have been conducted in a two-dimensional wave tank, thus neglecting the effects of oblique wave attack. However, the simulation of orthogonal wave motion to the structure is in favor of safety. Moreover, a schematic reproduction of the bathymetry has been employed in both physical and numerical experiments, which could only slightly influence the solicitation conditions of the tested structure.

The specific limits of the performed simulations of upgraded rubble mound breakwaters under wave attack are typical of numerical modeling, and essentially linked to the required computational power and to the necessity to introduce some simplification for the formulation of the problem. In particular, the resolution of the VARANS equations is based on a macroscopic approach, which provides the volume-averaged description of the porous media properties and interactions with the fluid (Liu et al., 1999). Such an approach is not able to capture the interaction between the single units of the armor layer and the incident wave motions, and hence only analyses concerning the overtopping phenomenon and the dynamic pressure can be performed. Furthermore, the volume-averaged approach requires the empirical calibration of several porosity parameters, which can be carried out only if a sufficient number of experimental results are available. Finally, the numerical simulation of the overtopping phenomenon is affected by higher uncertainty for

low mean overtopping rates, for which the characteristics of individual waves have a stronger impact.

Probabilistic calculations for the evaluation of the probability of failure of upgraded rubble mound breakwaters are affected by some limits. First, in the present work the interaction between different failure mode has not been considered, focusing only on two of the main failure mechanisms of rubble mound structures, i.e. the collapse of the armor layer due to the displacement of the blocks, which represents an ultimate limit state, and the excessive mean overtopping discharge, which represents a serviceability limit state. Moreover, the calculation of the input wave load at the breakwater site has been derived from the deep-water condition using a simplified approach, based on the definition of empirical site-specific relationships between wave climate descriptors. However, the above mentioned limitations do not invalidate the proposed procedure for probabilistic design of upgraded structure, which could be improved by further studies. It should be noted that level III probabilistic calculations do not take into account the cost of the studied designs, which could be included using a level IV approach. In this regard, it is worth to point out that the performance of Monte Carlo simulations implies a certain computational cost, which have been contained through optimization of calculation time and accuracy of the outcomes.

A general limit of the present work is the fact that only a case study has been considered. Further studies on historical harbor breakwaters could integrate the obtained results, considering different existing structures in terms of state of deterioration and component materials. In addition, in the present work only two upgrading concepts and their combination have been studied, i.e. the rising of the wave wall and the addition of an extra armor layer made up of units having a similar shape to the existing ones, and equal or smaller weight. Therefore, the use of additional armor blocks completely different from the existing ones should be investigated.

Although the aforementioned limitations, in the opinion of the author the present work still provides a useful contribute to the definition of methods and tools for the design of upgrading solutions for harbor rubble mound breakwaters.

1.5 Phases of the work

In Chapter 2 the literature review of the state of art on upgrading existing rubble mound breakwater is presented. The chapter is divided into three sections, each one of which is dedicated respectively to methodologies for design of rubble mound breakwaters, possible approaches for upgrading existing coastal defense structures, and effects of climate change on coastal areas.

Chapter 3 describes the proposed methodology for the design of upgrading solutions for harbor rubble mound breakwaters. In addition, the emblematic case study of the Catania harbor breakwater, which has been selected for the application of the proposed methodology, is presented.

Chapter 4 provides the description of a methodology for the assessment of the current state of existing rubble mound breakwaters, based on the analysis of georeferenced data acquired during the structure lifetime, together with information about its original design. The results of the application of such a methodology to the case study of the Catania harbor breakwater are also presented.

In Chapter 5 the analysis of the long-term variations of sea level and wave climate conditions in the Italian seas is described. First, the collection of literature data on sea level rise is presented, considering both historical trends and future projections. Then, the outcomes of the detection of long-term tendencies on historical wave data representative of Italian coastal sites are discussed. Finally, the results of wave climate projections under RCP4.5 and RCP8.5 for the same coastal sites are elaborated and made usable for the probabilistic calculations.

Chapter 6 describes the methodology for the composite modeling of upgraded structure and presents the results of the application to the case study of the Catania harbor breakwater. The experiments conducted in the Laboratory of Hydraulics of the University of Catania allowed the investigation of the damage progression through traditional and novel technique, and also the analysis of the mean overtopping discharge for six upgrading options. Instead, the numerical modeling has been used to further explore the overtopping phenomenon.

Chapter 7 provides the description of the methodology for the probabilistic design of upgrading solutions for rubble mound breakwaters through level III calculations, based on the results described on the previous chapters. In particular, the probability of collapse of the armor layer and of excessive mean overtopping discharge have been studied, considering the emblematic case of the Catania harbor breakwater.

Finally, Chapter 8 presents the conclusions of the work, and discusses some suggestions for future investigations.

Chapter 2

State of art of upgrading rubble mound breakwaters

2.1 Overview

Breakwaters have been realized all over the world as harbor defense structures, having peculiar structural and hydraulic features depending on the nature of the places and on the performances that they have to guarantee.

The design of breakwaters is a very difficult task, because of the huge number of heterogeneous variables which are involved during the interaction between waves and structure, whose physical laws are often not well known. The complexity of the design of breakwaters is enhanced by the fact that these variables are generally not completely understood and measured or exhibit a stochastic behavior. In particular, rubble mound breakwaters show a more flexible behavior than other typology of breakwaters (e.g. vertical breakwaters), which make the comprehension of the response mechanisms of this kind of structures even more challenging. Therefore, a design approach which allows to take into account all the uncertainties related to the interaction between wave load and structure is essential for the realization of breakwaters able to reliably fulfill all the project requirement during their lifetime.

Nowadays the above mentioned difficulties are exacerbated by the need for repair or rehabilitation interventions of the huge number of aging rubble mound breakwaters, which are mainly non-conventional structures whose current composition is usually unknown. The repair interventions aims to simply restore the original design performances, or more often to upgrade them to fulfill new requirements due to social and economic growth, and to properly withstand the external forcing modified by the effects of climate change.

The need to upgrade existing rubble mound breakwater in the presence of the effects of climate change highlights the interest in developing a novel design methodology, necessarily based on probabilistic approaches to take into account at best all the involved sources of uncertainty.

In the following, a brief review of the current state of art concerning the reliability-based design of breakwaters, the methodologies for the upgrade of existing coastal

structures and the effects of climate change on coastal areas is presented, with special regard to harbor rubble mound breakwaters.

2.2   Probabilistic design of rubble mound breakwaters

2.2.1   Overview on probabilistic design approach

The purpose of harbor breakwaters is to provide shelter from waves, in order to guarantee safe maneuvering and berthing of vessels. In particular, rubble mound breakwaters protect the harbor basin thanks to the reduction of the incident wave energy, through the reflection of the waves towards the open sea and turbulent dissipation, though some overtopping and wave penetration are usually accepted (Burcharth, 1993b). Different kinds of rubble mound breakwaters can be identified, on the basis of their structural characteristics (Vicinanza et al., 2019). First, submerged or emerged breakwaters can be distinguished, depending on whether the crest of the structure is under or above mean sea level. In addition, multilayer rubble mound breakwaters with or without superstructure can be designed. Finally, considering the shape of the structure, the following three typologies exist: i) multilayer rubble mound breakwaters with bermed front; ii) reshaping rubble mound breakwaters (i.e. berm breakwater); iii) multilayer rubble mound breakwaters with S-shaped front.

Even if the theoretical basis of the probabilistic design of harbor breakwaters date back to second half of the twentieth century (CIAD project group, 1985; van der Meer, 1988b; Burcharth, 1993a), only recently it has been included in national codes and regulations (US Army Corps of Engineers, 2002; Ports and Harbours Bureau et al., 2009; Puertos del Estado, 2010). Indeed, the recent diffusion of relatively cheap and high-performing computers has allowed the execution of complex probabilistic calculations in acceptable times and with contained costs, thus encouraging further research on methods and techniques to deal with the variability of the variables involved in the design process and with the interactions between failure mechanisms. Indeed, the probabilistic design allows to take into account the stochastic nature of most of the variables involved in the interaction between structure and wave load, and also the uncertainties on the definition of the physical laws which lead these phenomena (Burcharth, 1987).

In particular, the following main source of uncertainty can be taken into account if the design of harbor breakwaters is performed through a probabilistic approach (Burcharth, 1993a): i) the experimental formulas which describe the considered failure modes; ii) the environmental parameters; iii) the structural parameters. As regards the equations which describe the failure modes, they can add significant uncertainties to the reliability based design process. Indeed, such formulas usually derive from curve fitting of experimental scattered cloud data, with coefficients of variation of 15-20% or even larger. The uncertainty related to the environmental parameters is due to measurement errors and variability and errors of different and

imperfect calculations methods (e.g. wave hindcast models, algorithms for time series analysis). In addition, uncertainties coming from short-term randomness of the variables and the use of theoretical distribution as a representative of the unknown long-term must be considered. Finally, further uncertainty is caused by the extrapolation from short samples of data-sets to events of low probability of occurrence distribution and by statistical vagaries of the elements. The uncertainties related to material parameters (e.g. density) and geometrical parameters (e.g. slope angle and size of structural elements) are generally much smaller than the uncertainties related to the environmental parameters and to the design formulas.

Malliouri (2020) proposed the following procedure for the implementation of the probabilistic design of a generic coastal defense structure. First, the identification of the design requirements, in terms of ensured protection and lifetime, and the evaluation of the hydraulic boundary conditions must be carried out. Then, a preliminary design can be performed, following a traditional deterministic approach. The results of the preliminary design represent the input variables for the probabilistic calculations. Indeed, the probability of failure of the pre-designed structure is evaluated and compared to the design requirements. If the probability of failure is greater than the fixed threshold, the structure is under-designed and needs to be modified to improve its performances. The modified design is the new object of the probabilistic calculations, and the process goes on in an iterative way until the design requirements are reached. On the contrary, if the probability of failure is equal or smaller than the fixed threshold, two cases can occur: i) the structure is over-designed and needs to be modified in order to reduce costs; ii) the structure is optimally designed. As in the case of too high probability of failure, the existence of case i) or ii) can be verified by means of an iterative process. Therefore, the evaluation of the designed structures in terms of probability of failure enables optimization, thus avoiding over or under-design (Kim and Suh, 2006).

The definition of the design requirements is performed by fixing the acceptable probability that the structure reaches a certain limit state. Following the definition of the British Standards Institution (BSI) (1991), two limit states can be considered:

- the ultimate limit state (ULS), which represents the failure of the structure, i.e. a condition in which the breakwater no longer substantially fulfills its function of providing protection to a harbor or land area or if the cost of damage repair, including interference with commercial operations, is unacceptable;

- the serviceability limit state (SLS), which exists when damage to the breakwater of considerable magnitude has occurred, but it is still possible to carry on most normal operations inside the harbor.

In addition, the operational limit state (OLS) can be taken into account, which occurs when the exploitation of the port area is temporarily reduced or suspended because of causes external to the structure without any structural damage (Puertos del Estado, 2010).

The acceptable probability of failure or the acceptable degree of damage during the life of the breakwater should be decided at the beginning of the design process, on the basis of the functions for which it is designed, according to the indications of standards and codes, the experience of existing structures and economic evaluations. In the following, the expression probability of failure is used to generally indicate the reaching of the desired limit state (i.e. ULS, SLS or OLS).

The correct identification of the events which can potentially lead to the ULS, SLS or OLS can be performed only by carrying out a risk analysis, i.e. the analysis of all the possible failure mechanisms and their interaction, specific for each type of breakwater (e.g. rubble mound, caisson, composite), and often for the single case study. According to the procedure proposed by CIAD project group (1985), the risk analysis of a generic breakwater consists on the following steps:

1. edit a detailed description of the structural system, which can give the necessary information to identify all the breakwater components;

2. separately assume the failure of each component of the structure, in order to analyze the breakwater behavior and all the possible consequences;

3. identify the initiating events potentially responsible of the failure of the components;

4. construct a fault tree to represent all the possible accident sequences, from initiating event via single components failure to total failure of the structure;

5. quantitatively evaluate the reliability of the structure by combining the probabilities of component failures and initiating events, according to the logical sequences defined in the fault tree.

In order to implement steps 1, 2, 3 and 4, it is worth to consider the breakwater as a system composed of single components, which can either function or fail. Depending on the interactions between these components, failure of one component can cause failure of another element and even of the total system (US Army Corps of Engineers, 2002). As a consequence, the detailed description of the relationships between the failure of the breakwater and of its single elements must be carried out, together with the identification of the external events which can lead to the various failure modes. The so-called fault tree is the usually employed tool to simply represent the complex interactions between the breakwater components and external events that can potentially trigger a failure mode. Failure mechanisms summarized by the fault tree can be related in series or parallel (US Army Corps of Engineers, 2002; Jonkman et al., 2015), as schematically showed in Figure 2.1. Therefore, the evaluation of the upper and lower bounds of the probability of failure of a complex system should be carried out by decomposing the overall system into elementary series and parallel systems.

Series system
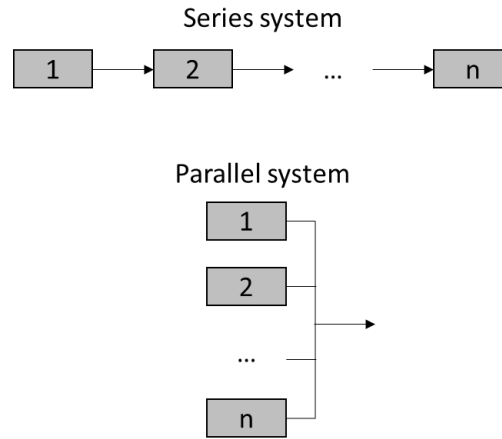
Parallel system

FIGURE 2.1 Schemes of a series system and a parallel system. Adapted from US Army Corps of Engineers (2002).

Failure of a generic series system occurs if any of the elements of the system fails. Therefore, the upper (*u*) and lower (*l*) bounds of the total probability of failure of a system composed of *n* elements can be evaluated as follows:

$$P_{f,u} = 1 - \prod_{i=1}^{n}(1 - P_{fi}) \tag{2.1}$$

$$P_{f,l} = max[P_{fi}] \tag{2.2}$$

where P_{fi} is the probability of failure related to the $i - th$ element of the series system. The upper and lower bounds respectively correspond to no correlation and full correlation between the failure modes.

Instead, a parallel system fails only if all its components fail. Therefore, the upper (*u*) and lower (*l*) bounds of the total probability of failure of a system composed of *n* elements can be calculated as follows:

$$P_{f,u} = min[P_{fi}] \tag{2.3}$$

$$P_{f,l} = \prod_{i=1}^{n} P_{fi} \tag{2.4}$$

where P_{fi} is the probability of failure related to the $i - th$ element of the series system. The upper and lower bounds respectively correspond to full correlation and no correlation between the failure modes.

The failure modes contained in a generic fault tree can be correlated through common parameters contained in the correspondent limit state equations (e.g. significant wave height, mean wave period, mean sea level), but also by physical interactions (US Army Corps of Engineers, 2002). The latter can be included through the evaluation of the joint probability of occurrence of the considered failure mechanisms, as described for a general simple case by Castillo et al. (2004) and for vertical

type breakwaters by Puertos del Estado (2010).

For the case of multilayer rubble mound breakwaters with superstructure, which are the focus of the present work, a great variety of failure modes can occur, whose reciprocal interactions are often complex and hardly comprehensible. Indeed, rubble mound breakwaters show a more flexible behavior than other typology of breakwaters (e.g. vertical breakwaters), which make the comprehension of the response mechanisms of this kind of structures even more challenging. Figure 2.2, adapted from Burcharth and Liu (1995), summarizes the main failure modes typical of rubble mounds breakwaters. Failure can occur because of the erosion of the armor layer, both on the sea and rear side. Besides the armor hydraulic instability, the breakage of the armor units can take place, due to wave induced stresses, cracking processes resulting from thermal stress and fatigue of concrete. In addition, toe berm erosion as well as scour at the toe could can led to the failure of the whole structure. Slip failure can affect various part of the breakwater, i.e. toe berm, core, filter and armor layer. Moreover, settlement of the core and of the subsoil can occur, as well as instability of the filter layer. The impact of the wave load can also induce the breakage or the sliding of the wave wall. Finally, huge overtopping discharges can cause the failure to satisfy the design requirements of protection.

Due to the great variety of failure modes which can affect rubble mound breakwaters, the fault tree of a rubble mound breakwater results particularly intricate. For instance, Figure 2.3 shows a simplified fault tree, where the breakwater failure corresponds to excessive wave transmission. The probability to reach not acceptable levels of wave transmission (i.e. probability of failure) depends on the probability of occurrence of the single failure mechanisms and on their mutual relationships. However, due to the complexity of the quantification of physical mutual interactions between failure modes of rubble mound breakwaters, they are often neglected in the probabilistic calculations.
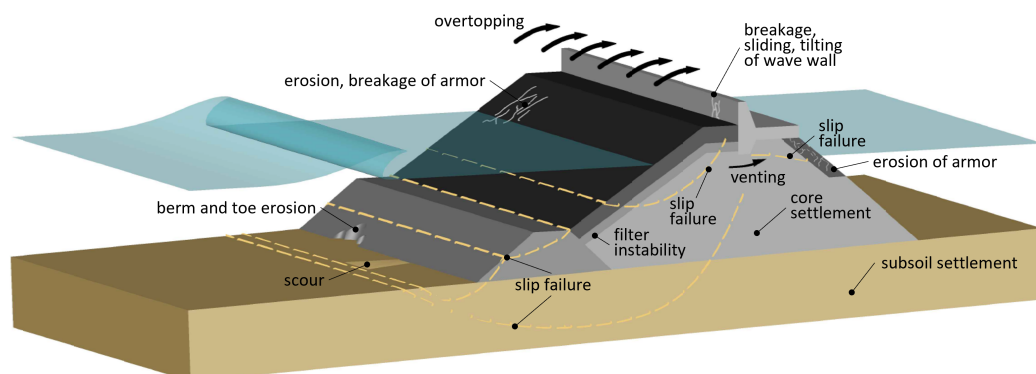
FIGURE 2.2 Failure modes of rubble mound breakwaters. Adapted from Burcharth and Liu (1995).
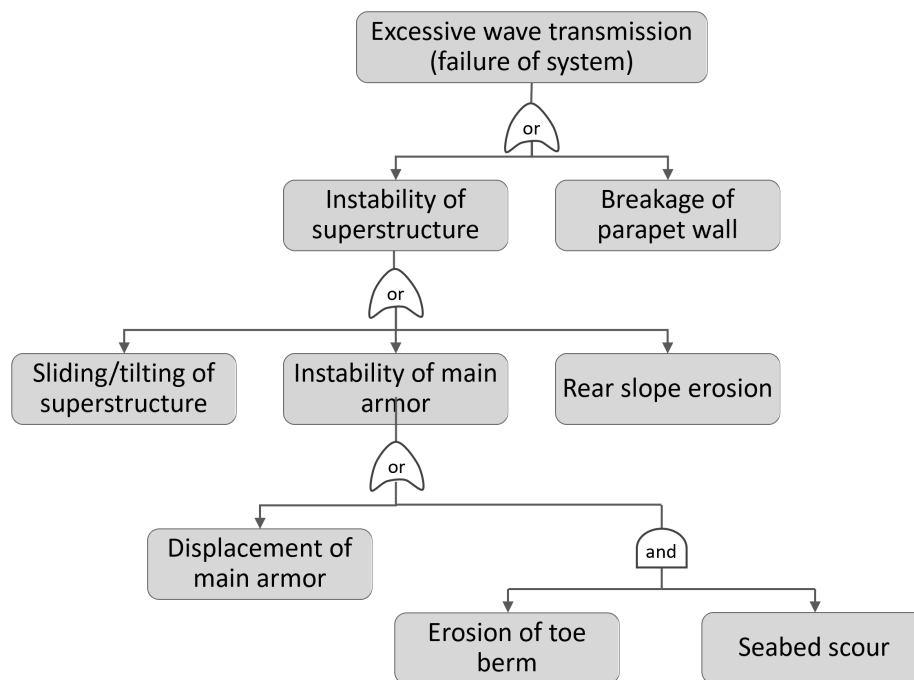
FIGURE 2.3 Example of simplified fault tree for rubble mound breakwaters. Adapted from US Army Corps of Engineers (2002).

2.2.2 Probability of failure due to a single failure mode

The evaluation of the probability of failure of the structure referred to a single failure mode can be performed by means of the definition of the correspondent limit state equation, usually referred to as reliability function, in the following form (US Army Corps of Engineers, 2002; Jonkman et al., 2015):

$$Z = R - S \tag{2.5}$$

where R represents the resistance of the structure to external solicitations S. The reliability function can be derived from state of art or case-specific equations describing the studied failure mode (e.g. stability of the armor layer, mean overtopping discharge, toe berm stability, etc).

In general, if $Z < 0$ (i.e. $R < S$), the selected limit state is overcome by the structure, and hence the probability of failure (P_f) corresponds to the probability that the reliability function assumes negative values (i. e. $P(Z < 0)$). Once the probability of failure has been calculated, the reliability of the structure referred to the selected failure mode can be evaluated as the complement to unity of P_f. In this regard, it should be noted that in many cases the probability of failure is expressed as function of the reliability index β:

$$P_f = \Phi(-\beta) \tag{2.6}$$

TABLE 2.1 Relationship between the failure probability P_f and the reliability index β. Source: Jonkman et al. (2015).

P_f	10^{-1}	10^{-2}	10^{-3}	10^{-4}	10^{-5}	10^{-6}	10^{-7}
β	1.28	2.32	3.09	3.72	4.27	4.75	5.20

where Φ is a cumulative normal distribution. The relationship between P_f and β is illustrated in Table 2.1.

The components R and S contained in equation 2.5 depend on several stochastic variables, following relationships not always well known:

$$R = R(X_1, X_2, X_3, ..., X_m) = R(\underline{X_1}) \tag{2.7}$$

$$S = S(X_{m+1}, X_{m+2}, X_{m+3}, ..., X_n) = R(\underline{X_2}) \tag{2.8}$$

and, as consequence, Z is a complicated function of all these variables:

$$Z = Z(X_1, X_2, X_3, ..., X_n) = Z(\underline{X_1}, \underline{X_2}) = Z(\underline{X}) \tag{2.9}$$

Therefore, the probability of failure of a certain system for a selected failure mode can be calculated by solving the following equation:

$$P_f = \int_{Z<0} f_{\underline{X}} d\underline{x} \tag{2.10}$$

where $f_{\underline{X}}$ are the n-dimensional probability density functions of the stochastic variables $\underline{X}$.

For instance, Figure 2.4 shows the representation of a linear reliability function Z in the $S - R$ plane in case of S and R probability density functions are well known and independent. In this simple situation, the probability of failure is easily evaluated as follows:

$$P_f = \int \int \int_{Z<0} ... \int f_R(x_1, x_2, ...x_m) f_S(x_{m+1}, x_{m+2}, ...x_n) dx_1 dx_2 ...dx_n \tag{2.11}$$

where f_R and f_S are respectively the probability density function of R and S. In other words, the probability of failure of the structure is equal to the volume of the joint probability density function in the unsafe region.

Considering a more general case, the evaluation of failure probability can be carried out using five different categories of methods (CIAD project group, 1985; Jonkman et al., 2015):

- Level 0 methods, which are based on the deterministic calculation of the probability of failure, usually considering deterministic or nominal values of the
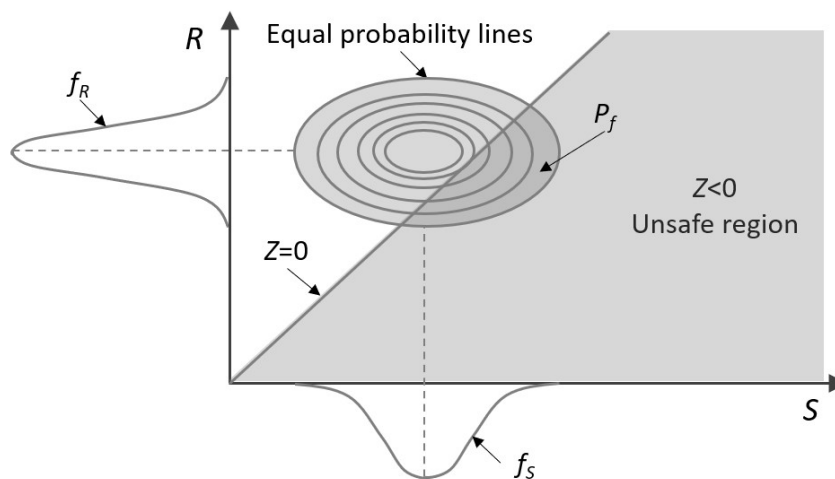
FIGURE 2.4 Linear reliability function Z in $S - R$ plane with probability functions f_R and f_S. The probability of failure of the system corresponds to the volume of the joint probability density function in the unsafe region. Adapted from Jonkman et al. (2015).

involved variables and one global safety factor γ. The comparison between resistance and forcing of the system is performed according to an equation with the following format:

$$R_n > \gamma S_n \tag{2.12}$$

where the subscript n indicate that nominal values are considered.

- Level I methods (semi-probabilistic approach), which consider the stochastic nature of the parameters involved in the design processes by using one characteristic value for load and one for resistance, the so-called design values. In particular, the characteristic value of R corresponds to a low percentile, whereas the characteristic value of S corresponds to a high percentile. The calculation of these percentiles is carried out by means of partial factors resulting from probabilistic calculation of level II. The comparison between resistance and forcing is performed according to the following equation:

$$R_d > S_d \tag{2.13}$$

where the subscript d indicate that design values are considered, i.e. $R_d = \gamma_R R$ and $S_d = \gamma_S S$.

- Level II methods (probabilistic with approximations), in which normal probability distribution are assumed for both strengths and loads and the reliability function is linearized at a specific point to determine the actual probability of failure. On the basis of the applied linearization process, three different approach can be considered: i) the first order mean value approach, which consists on the linearization of the reliability function about the expected mean

value of the involved parameters using Taylor-series expansion; ii) the first or-
der design-point approach, which consists on the linearization of the reliability
function about the point of failure envelope ($Z = 0$) having the highest joint
probability density, using an iterative procedure in the case of nonlinear fail-
ure envelopes; iii) the approximate full-distribution approach, which is similar
to (ii), but the exact probability distributions are approximated by equivalent
normal distribution in the vicinity of the design point.

- Level III methods (fully probabilistic), in which the probability of failure is
  evaluated by using the exact joint probability distribution functions of the
  variables, thus modeling the correlation between them. In very few cases the
  problem of the evaluation of the probability of failure can be solved by means
  of analytical formulations. Instead, it is usually necessary to apply numerical
  integration or to perform Monte Carlo simulations.

- Level IV methods (risk-based), which also takes into account the consequences
  of failure in terms of cost and the risk, defined as the consequence multiplied
  the probability of failure, which is used as a measure of the reliability.

Since the present work focuses on the evaluation of failure probability of rubble
mound breakwaters without quantifying the consequences, level IV methods will
not be further discussed. Furthermore, it is worth to point out that before using the
above-mentioned methods, they have to be calibrated so that consistent reliability
levels are obtained. In particular, level I methods can be calibrated using level II
methods and level II methods can be calibrated using level III methods (Jonkman
et al., 2015).

It should be noted that the deterministic approach does not allow to evaluate
the probability of failure of the system, but only to predict if the failure may occur
or not with the assigned values of the variables involved in the reliability function
(i.e. state equation) and the global safety factor. As regards the application of level
I methods, the aim is to ensure a certain reliability of the structure, depending on
the partial coefficients used. However, the stochastic nature of the parameters in-
volved in the design processes is considered in a very simplified way, which enables
to create standards to be applied for the principal categories of breakwater projects.
Therefore, it is clear that if level 0 or level I method are employed, design optimiza-
tion is not possible (US Army Corps of Engineers, 2002).

Level II and III methods can be used to overcome the shortcomings of determin-
istic and semi-probabilistic approaches. Nevertheless, the implementation of such
methods is affected by difficulties related to the lack of insight in the correlation be-
tween different failure modes of structure. Indeed, if the probability of failure of a
single mechanism can be calculated in a relatively simple way, the exact probability
of failure of the whole system is still a challenge. As already stated, failure modes
can be correlated through common parameters contained in the limit state equations,

but also by physical interaction (US Army Corps of Engineers, 2002). However, information about the interactions between failure modes are usually insufficient and further research is needed (Castillo et al., 2004; Plate, 1995; Burcharth, 1992; Burcharth and Liu, 1995).

2.2.3 Existing regulations and guidelines for the design of breakwaters

Since the possibility of employing probabilistic methods for the design of breakwaters (i.e. level II and III) in a cost and time effective way is relatively recent, most of the main existing national regulations and guidelines suggests the use of deterministic (i.e. level 0) or semi-probabilistic (i.e. level I) methods. The description of the indications given by the most significant standards and manuals for the design of breakwaters regarding the methodologies for the assessment of the reliability of these structures is presented in the following and summarized in Table 2.2.

TABLE 2.2 Methods for the assessment of breakwaters reliability suggested by: the British Standards Institution (BSI) (1991), UK91; PIANC (1992), PIANC92; the Italian guidelines for the design of maritime dikes (Consiglio Superiore dei Lavori Pubblici, 1996), ITA96; the Coastal Engineering Manual (US Army Corps of Engineers, 2002), CEM02; The Rock Manual (CIRIA et al., 2007), TRM07; the Spanish recommendation for maritime works (Puertos del Estado, 2010) ROM10; the EurOtop Manual (EurOtop, 2018), ETM18; the Technical Standards and commentaries on Port and Harbour Facilities in Japan (Ports and Harbours Bureau et al., 2009), JAP09.

Method	Description	Proposed	Suggested
Level 0	Deterministic calculation of the probability of failure considering deterministic or nominal values of the variables involved and one global safety factor.	• UK91 • ITA96 • ETM18 • TRM07 • ROM10	
Level I	The stochastic nature of the parameters involved in the design processes is considered by using one characteristic value for load and one for resistance, defined as design values.	• PIANC92 • CEM02 • ETM18 • ROM10 • JAP09	• UK91 • ITA96 • TRM07
Level II	Normal probability distributions are assumed for both strengths and loads, and the reliability function is linearized at a specific point to determine the actual probability of failure.	• CEM02 • ROM10 • JAP09	• UK91 • TRM07 • ETM18
Level III	The probability of failure is evaluated by using the exact joint probability distribution functions of the variables, thus modeling the correlation between them. It is usually necessary to apply numerical integration or to perform Monte Carlo simulations.	• CEM02 • ROM10 • JAP09	• UK91 • TRM07 • ETM18

The British Standards BS 6349-7 (1991)

The British Standards BS 6349-7 (British Standards Institution (BSI), 1991) highlight the necessity to carry out a risk analysis in order to obtain the best assessment of probability of failure of the breakwater. In particular, once the service lifetime of the breakwater is chosen on the basis of the requirements that the structure must fulfill, the risk can be evaluated as the product between the probability of failure during the structure lifetime and its consequences. Such kind of analysis requires the inventory of all possible failure modes and thus the construction of a fault tree which can represent the relationships between the failure of each component of the structure.

However, the method proposed for the evaluation of the reliability of the breakwater is deterministic and based on the evaluation of the return period of the design wave as a function of service lifetime and acceptable probability of failure of the breakwater. Level II and III methods are only mentioned as under development.

PIANC partial safety factors method (1992)

Burcharth (1992) developed a partial safety factors method (i.e. level I method) for the design of rubble mound breakwaters, whose detailed explanation is given by PIANC (1992). The description of such a method for vertical breakwaters is presented by Burcharth and Sørensen (1999) and PIANC (2003).

Four kind of partial safety factors were calibrated through a reliability analysis of level II: i) a load partial safety factor to be applied to the mean value of the permanent load equal to 1; ii) a partial safety factor to be used to the combination of the mean values of the resistance variables; iii) a load partial safety factor to be applied to the design significant wave height, which is a function of the structure service lifetime and the acceptable probability of failure; iv) a partial safety factor to be used with the mean value of undrained shear strength of clay materials in the subsoil. The magnitude of these partial safety factors reflects both the uncertainty and the relative importance in the reliability function of the related variable.

For calibration of the PIANC safety factors, wave data from four quite different geographical locations (i.e. Bilbao, Sines, Tripoli and Fallonica) were selected and fitted to a Weibull distribution. The wave data from Bilbao, Sines and Tripoli correspond to deep water waves, whereas the wave data from Fallonica correspond to shallow water waves. The uncertainties related to quality of the measured wave data were modeled by a multiplicative stochastic variable F_{H_s} normally distributed with mean value 1 and standard deviation between 0.05 and 0.02 depending on the reliability of the data-set (e.g. buoy measurements, hindcast numerical models). As regards the design lifetime, periods of 20, 50 or 100 years were considered, whereas the acceptable values of failure probability were 0.01, 0.05, 0.10, 0.20 and 0.40. The partial safety factors were evaluated for two typologies of structure: rubble mound

breakwaters and vertical-wall caisson structures. In the first case, failure modes related to armor stability, toe berm breakage, run-up and scour were considered for different kinds of armor blocks. In the latter case, failure modes related to foundation (sand or clay subsoil), sliding, overturning, scour and toe berm were studied.

Even though the PIANC partial coefficient system represents an advanced level I method for the design of breakwaters for a specific failure probability level, it is applicable only to the failure modes selected for the study, and hence it is scarcely flexible to situations which differ from the reference ones.

Italian guidelines for the design of maritime dikes (1996)

The Italian guidelines for the design of maritime dikes (Consiglio Superiore dei Lavori Pubblici, 1996) suggest a methodology very close to the one presented in the British Standards BS 6349-7 (British Standards Institution (BSI), 1991). Indeed, a deterministic approach for the evaluation of the reliability of the breakwater is described, considering the structure lifetime and the maximum acceptable probability of failure as functions of the typology of breakwater and the requirements it must satisfy. Then, the return period of the design wave height is calculated, and the verification of the deterministic state equations is carried out.

However, the design of rubble mound breakwaters requires a special attention, because not negligible damages are often accepted for this kind of structures. Hence, a more complex risk analysis is needed to assess the probability of failure of a rubble mound breakwater and to this aim the Italian guidelines suggests the PIANC partial safety factors method PIANC (1992).

Coastal Engineering Manual (2002)

An important international reference for the solution of most coastal engineering problems is represented by the Coastal Engineering Manual (US Army Corps of Engineers, 2002), which summarizes in a single source the state of the art of coastal engineering until 2002, replacing the Shore Protection Manual (Coastal Engineering Research Center (US), 1984) and several other US Army Corps of Engineers manuals.

In particular, part VI of the Coastal Engineering Manual (US Army Corps of Engineers, 2002) provides a comprehensive description of definitions and procedures needed in the planning and design processes for coastal projects, stressing the necessity to move from a deterministic to a risk-based approach for the following reasons:

1. forcing, represented by wave characteristics, winds, water levels and currents both over short and long term, has a stochastic behavior;

2. the deterministic analysis of the interaction between structures and external loads masks the existing uncertainties and can be misleading;

3. damage and thus functional performances of a coastal project evolve incrementally;

4. because of the above factors, benefits and risks cannot be fully represented in deterministic terms;

5. in addition to the uncertainties associated directly with the coastal project considered, significant possibilities for changing adjacent areas can be introduced.

Reliability-based design of coastal structures is also presented in the part VI of the Coastal Engineering Manual (US Army Corps of Engineers, 2002). The construction of the reliability function for a single failure mode is explained and both level II and III methods for its solution are presented. Furthermore, a possible way to evaluate the probability of failure of the whole structure is described , taking into account the series or parallel-type links between the different failure modes. In particular, the upper and lower bound of the probability of failure are evaluated considering the extreme conditions of no and full correlation between the elements of the fault tree, by means of the decomposition of the latter in simpler series or parallel subsystems. The methodology presented should be improved by a better understanding of the relationships between the different failure modes of a structure. Furthermore, in order to carry out an optimization of a design, the probability of failure must be used together with economic considerations. Finally, the PIANC advanced partial safety factor method PIANC (1992) is described in detail and tables containing the value of the safety factors for the different failure modes of rubble mound breakwaters and vertical-wall caisson structures.

The Rock Manual (2007)

The Rock Manual (CIRIA et al., 2007) is a reference guideline for the use of rock in hydraulic engineering, born from the collaboration between France, Netherlands and United Kingdom. It represents an extensive summary of good practices on the design, the construction and the maintenance of rock structures for rivers, coasts and seas, and it has incorporated all the significant advances in knowledge that have occurred over the $10 \div 15$ years before 2007.

As regards the design approach for rock structures, the following reasons why deterministic methods have been traditionally applied are discussed: i) limited existing data regarding progressive failure mechanisms; ii) the structural response models (e.g. design equations) are largely deterministic because they have been developed from failure criteria; iii) the past tendency to prefer a robust design based on safety factors in contrast to an optimized one. Furthermore, such a kind of approach is based on the unrealistic hypothesis that the structure remains safely intact, providing the same level of protection until the end of its design lifetime. Indeed, as structures ages, the probability of failure and the uncertainties in its response to external load usually increase.

The risk-based design approach proposed to consider the above mentioned uncertainties consists in assessing the sensitivity of failure relative to a single mode to

the variation of different parameters involved in the reliability function, thus constructing fragility curves, which graphically express how the probability of failure changes with the selected parameter. Therefore, the method proposed can be considered as an advanced level 0 method, which allows a simplified evaluation of the probability of failure relative to a single mode.

Level I, II and III approaches for the evaluation of the reliability of breakwaters are considered as alternative to the deterministic method with sensitivity analysis proposed and the following brief indication are given: i) for level I approaches, it is recommended the PIANC safety partial factors method PIANC (1992); ii) for level II approaches, the first order design-point method is mentioned, although not recommended because of problems in the convergence of most computer routines; iii) for level III approaches, a fully integration method based on Monte Carlo simulations is suggested.

No further information is given regarding the evaluation of the probability of failure of the whole structure based on the relationships between the elements which constitute its failure fault tree.

Technical Standards and commentaries on Port and Harbour Facilities in Japan (2009)

The Technical Standards and commentaries on Port and Harbour Facilities in Japan (Ports and Harbours Bureau et al., 2009) are applied to the construction, improvement and maintenance of port and harbor facilities in Japan. These technical standards propose a performance-based design system where: i) the objective is the reason why the structure considered is needed; ii) the performance requirements represent the performance that the structure must satisfy to achieve the objective; iii) the performance criteria are the technical explanation of a set of rules for the verification of the performance requirements; iv) the performance verification is the act to verify that the performance criteria are satisfied. Whereas objectives, performance requirements and performance criteria are ruled, no particular method for performance verification is mandatory.

The technical standards suggest the use of reliability-based design methods, since they are able to take into account the actions on the structure, the requirements for services and the uncertainty of the performances. However, other reliable methods such as numerical analysis methods, model test methods, and in situ test methods should be considered in specific situations.

As regards the reliability-based methods, level I, II and III approaches are described, although the level I one is adopted considering agreement with the upper-level standards, and also simplicity and convenience in practical design work. Nevertheless, this does not restrict the use of the level II and level III approaches, that rather are suggested if high control of the probability of failure is desired. For level II approaches, the partial safety factor relative to a generic variable is calculated as a

function of its probability distribution (i.e. normal or log-normal) and a target reliability index, whose evaluation is based on the average safety level of conventional design criteria. Furthermore, the calculation of the target reliability index using a method based on the investment effect necessary for avoiding the risk of human loss, and hence on the minimization of the life cycle cost, is not rejected.

The necessity to consider a set of failure modes and their mutual links for the evaluation of the whole structure failure probability is also underlined and formulas for the evaluation of the system failure probability are proposed.

ROM 1.0-09: Recommendations for the Project Design and Construction of Breakwaters

The Spanish ROM 1.0-09 (Puertos del Estado, 2010) are part of the second generation of documents of the ROM Program, which appeared after the publication of the ROM 0.0 (Puertos del Estado, 2002). These guidelines provide a characterization of project design factors of breakwaters to be considered, with special emphasis on climate, atmospheric and marine agents, whose actions can have a significant impact on maritime structures. Here, the methodological framework for coastal defense structures described in the ROM 0.0 (Puertos del Estado, 2002) is discussed in more detail. In particular, verification procedures related to failure and operational stoppage modes of breakwaters with semi-probabilistic approaches (i.e. level I) are presented and procedures to simplify the practical use of probabilistic methods (i.e. level II and III) are developed.

In order to facilitate the probabilistic description of the involved variables in breakwaters design, their stochastic nature is considered spatially uniform and stationary in time. In particular, the probabilistic characterization of climate agents in terms of short-term, medium-term, and long-term time scales is described. The verification of breakwater projects requires the selection of the climate agents that act simultaneously and the identification of their values, taking into account their compatibility on the basis of the correspondent probability density functions, if possible evaluated from measurements performed at the site.

The design of breakwaters is based on three fundamental general criteria: i) the structure is spatially divided into homogeneous subsets and the works are organized in distinct temporal phases; ii) the desired performances of each subset in the various phases are selected; iii) the overall requirements in terms of structure safety and serviceability are defined.

Each subset is characterized by specific geometry, material, soil structure, topography, external solicitations and required hydraulic and structural performances. Generally, five subsets of a breakwater can be identified:

1. junction of the breakwater with the soil;

2. main alignment that controls and protects against the prevailing wave action;

3. secondary alignments that link the different subsets of the breakwater;

4. transition or subset between two alignments or types;

5. head or upper part of the breakwater.

The project phases are fundamentally three: i) construction; ii) serviceability; iii) repairs, maintenance, and dismantling. As regards the serviceability phase, i.e. lifetime of the breakwater, it corresponds to a period less than 5 year for provisional structures and greater than 5 years for definitive ones, depending on the Economic Repercussion Index (*ERI*) of the maritime structure, as described in Table 2.3.

The safety and serviceability requirements that every subsets of the breakwater should fulfill during each design phase are defined by a maximum accepted joint probability of failure or operational stoppage. In the case of ULS or SLS, these limit probabilities (and the correspondent reliability index) are fixed as function of the social and environmental repercussion index (*SERI*) relative to the considered structure, following the indication in Table 2.4. In the case of operationality during the serviceability phase, the required minimum operationality $r_{f,OLS}$ and the correspondent reliability index $\beta_{f,OLS}$ are evaluated based on the operational index of economic repercussion (*OIER*), following the indication of Table 2.5. It is worth to point out that the values *ERI*, *SERI* and *OIER* are determined as function of the type of protected area, according to the reference tables contained in the guidelines.

For each project phase, the satisfaction of the project requirement relative to a limit state (i.e. ULS or SLS) can be evaluated using the following expression, although the set of failure or stoppage modes are mutually exclusive:

$$\sum_{i=1}^{n_{fm}} P_{f,i} \geq P_{f,total} \tag{2.14}$$

where $P_{f,i}$ is the probability of failure of the $i-th$ failure mode, n_{fm} is the number of failure modes and $P_{f,total}$ is the overall probability of failure referred to a limit state. Only if two or more modes occur with the same agent values, they can be considered to have the same individual failure or stoppage probability, thus adding their joint probability once.

TABLE 2.3 Minimum useful life in the serviceability project design phase for permanent structures as a function of *ERI*. Source: Puertos del Estado (2010)

ERI	Useful life in years
5	15
6÷20	25
> 20	50

TABLE 2.4 Maximum joint probability in the serviceability phase or the useful life of the breakwater for ULS and serviceability limit states SLS. Source: Puertos del Estado (2010)

SERI	P_f		β	
	ULS	SLS	ULS	SLS
<5	0.20	0.20	0.84	0.84
5-19	0.10	0.10	1.28	1.28
20-29	0.01	0.07	2.32	1.50
≥ 30	0.0001	0.07	3.71	1.50

TABLE 2.5 Minimum operationality during the serviceability phase of the breakwater. Source: Puertos del Estado (2010)

OIER	$r_{f,OLS}$	β_{OLS}
<5	0.84	0.84
5-19	1.28	1.28
20-29	2.32	1.50
≥ 30	3.71	1.50

The verification of the expression 2.14 needs the definition of a complete sets of failure or stoppage modes and the evaluation of their failure probability. In particular, after the analysis of mutually exclusive occurrence of the modes and the discussion of their statistical dependence, a fault tree of the set of failure or stoppage modes can be draft, considering both parallel and series links. For verification purpose, the failure modes are classified as: i) modes that can be verified by deterministic methods imposed by other regulations; ii) non-principal modes, characterized by the possibility to significantly improve the reliability of the subset by slightly increasing the total cost of the structure; iii) principal modes, which are failure and stoppage mode for which the reliability can be hardly improved. The contribution to the joint probability of failure of the first two categories during the structure lifetime is negligible. Therefore, the joint probability of failure is evaluated considering only the principal modes and it can be distributed by using a method that evaluates the total annual cost for the set of subsets of the structure and the construction processes. First assumptions regarding the probability distribution that satisfy the joint probability requirement are chosen. Then, the section of the subset is designed according to this probability distribution. Finally, the total cost of the investment is calculated as the sum of the expected cost of yearly damage produced by each of the principal modes, and the equivalent annual cost of the investment.

Regarding the verification of a single failure mode in the structure or subset, a limit state equation must be solved applying one of the following methods:

- deterministic (i.e. level 0), which neglect the variability of the variables involved in the design process and simply applying global safety factors;

TABLE 2.6 Indications for the choice of the appropriate method for the solution of the state equation of a failure or stoppage mode based on ERI and SERI indexes. Source: Puertos del Estado (2010)

ERI	SERI			
	<5	5÷19	20÷29	>30
5	Level 0	Level I	Level I and II or III	Level I and II or III
6÷20	Level I	Level I	Level I and II or III	Level I and II or III
> 20	Level I and II or III	Level I and II or III	Level I and II or III	Level I and II or III

- semi-probabilistic (i.e. level I), which consider characteristic values of the variables involved in the design process by means of partial safety factors determined on the basis of probabilistic calculations;

- probabilistic (i.e. level II and III), which determine the values of the variables involved in the design process by using their respective probability distribution to be used in numerical simulation able to perform a great number of experiments (e.g. Monte Carlo simulations).

Level 0 methods should be applied only for the verification of those failure and stoppage modes that do not contribute to the joint probability of failure of the structure. As regards principal failure and stoppage mode, the selection of the most appropriate method for the solution of the state equation is based on economic, social and environmental requirements, expressed by the *ERI* and *SERI* indexes, as shown in Table 2.6. When a multiple verification procedure (a level I method along with a level II or III method) is indicated, the state equation is verified if the two considered procedures show that the reliability, functionality or operationality required are fulfilled. Since level I methods must be included in these cases, and also since they are easy to use, it is suggested to use them for the pre-dimensioning of the structure.

In conclusion, the main innovations introduced by the Spanish ROM 1.0-09 compared to the previous breakwater design guidelines are: i) the detailed description of the methodology for the characterization of the set of climate agents and other project factors; ii) the detailed description of the methodology for the calculation of the joint probability of failure of the whole structure; iii) the definition of the situations in which each of the four verification approaches (i.e. level 0, I, II and III) should be used.

EurOtop Manual (2018)

The EurOtop Manual (EurOtop, 2018) gives guidance on analysis of wave overtopping for flood defenses attacked by wave action, referring to three principal types structures: i) sloping sea dikes and embankment seawalls; ii) armored rubble slopes

and mounds; iii) vertical, battered or steep walls. It replaces all the previous version of the manual and also the sections regarding the hydraulic performances of rock defense structures in The Rock Manual (CIRIA et al., 2007). In parallel with the manual, an Artificial Neural Network (i.e. the EurOtop ANN) based on the extended CLASH database is provided to predict mean overtopping discharge for each kind of structure geometries, given by a number of hydraulic and geometrical parameters as input.

Regarding the models for overtopping prediction, four categories of sources of uncertainties can be identified: i) fundamental or statistical uncertainties conditioned by random processes of Nature and which cannot be diminished; ii) data uncertainty, related to measurement errors, non-homogeneity of data, errors during data handling, non-representative reproduction of measurement due to inadequate temporal and spatial resolution; iii) model uncertainty, which leads to an inadequate reproduction of physical processes in Nature; iv) human errors during production, abrasion, maintenance of the structure as well as other human mistakes which are not covered by the model. The problem of the uncertainties related to human errors is not further developed in the manual. The uncertainties of the input parameters can be described using the statistical distributions or relative variation of these parameters. Finally, the model uncertainty is taken into account using the same approach than for parameters uncertainties using a multiplicative approach. Indeed, the standard form of the empirical models for overtopping prediction proposed in the EurOtop Manual (EurOtop, 2018) is the following:

$$q = m * f(x_i) \tag{2.15}$$

where q is the mean overtopping rate, $f(x_i)$ is the model function of the variables x_i and m is the model factor. The model factor m is assumed to be normally distributed with a mean value of 1.0 and a coefficient of variation specifically derived for the model. It is also possible that m is one of the coefficients in a formula, which is assumed to be a stochastic variable, and that the uncertainty is given by the standard deviation of this coefficient.

Therefore, three different approaches are presented to deal with the uncertainties related to the parameters of the wave overtopping models:

1. the mean value approach, which consist in using the formulas as given with the mean value of the stochastic model parameters (i.e. level 0). This method should be applied to predict or compare with test data, also considering a graphical representation of the 5%-exceedance lines or 95%-confidence band, thus including some probabilistic considerations;

2. design or assessment approach, which is an easy semi-probabilistic approach derived from the mean value approach (i.e. level I). The uncertainty of the prediction is included by giving to every involved stochastic parameter a value equal to its mean increased by its standard deviation;

3. probabilistic approach, which consider the stochastic parameters with their given standard deviation and assuming a normal or log-normal distribution (i.e. level II or III).

If no information on statistical distributions is available for water levels or sea state parameters, they can be considered as normally distributed and the following assumptions regarding their coefficients of variation (defined as the ratio between standard deviation and mean of the stochastic variables) could be taken (Schüttrumpf et al., 2007): i) the significant wave height has a coefficient of variation equal to 5.0%; ii) the peak wave period has a coefficient of variation equal to 5.0%; iii) the design water level at the toe has a coefficient of variation equal to 3.0%. Other parameters are independent of their mean values so that standard deviations (prototype measures) can be used for the water depth, the crest height and the height of the berm and the friction factor.

However, the only presented example of a probabilistic approach of level II application is the case of wave overtopping over smooth slopes. Monte Carlo simulations were performed to obtain the uncertainty in the resulting mean overtopping discharges, which is combined with the already proposed model uncertainties for the parameters of the formula. Therefore, EurOtop (2018) does not examine in depth the problem of the uncertainty related to the stochastic nature of the variable involved in the overtopping processes, focusing only on the model uncertainty. Furthermore, since the manual refers only to the hydraulic performances of defense structures, failure modes not linked to excessive overtopping discharges are not analyzed.

2.2.4 Examples of implementation of probabilistic designs

In the following, some examples of application of level II and level III methods for the evaluation of the probability of failure of rubble mound breakwaters are described. As regards the use of probabilistic methods with approximation (i.e. level II), CIAD project group (1985) describes the application to an existing design, for which realistic data are available, but considering probability distribution functions of the involved variables fancied in a realistic way. The probability of failure is evaluated with reference to excessive wave penetration into harbor, which is assumed to occur when in one cross section the crest wall settles to 0.5 m below design level. First, the main mechanisms which could lead to the failure event are identified (e.g. too large deformation of breakwater, failure of the crest element, instability of crest element, etc). Then, the level II combined probabilities are calculated considering the approximate full-distribution approach (AFDA), together with the upper and lower bound of total probability of failure for periods of 1, 10 and 25 years, highlighting the reasonable increase of the latter with time.

van der Meer (1988b) describes the application of level II AFDA probabilistic design for the case of a fictitious rock armor layer. In particular, useful design curves

are proposed, which show the variation of failure probability to changing damage level for lifetimes of 20, 50 and 100 years. Plate (1995) provides an inventory of all the failure mechanisms that could have affected the crested rubble mound breakwater at Ennore (India), during both construction and lifetime of the structure, together with the related fault tree. The probability of occurrence of the top event of such a fault tree is not calculated, due to the lack of both governing equations (i.e. reliability functions) and data. Therefore, the quantification of the yearly probability of failure is performed using level II AFDA approach for: i) instability of a rock armor slope; ii) instability of an armor layer with Accropode units; iii) slip circle of a rock armor layer; iv) horizontal displacement of the crest element. In general, the results show that the significant wave height, which represents the external load, and the model uncertainty are the main contributors to the total uncertainty in the reliability functions.

With reference to the application of level III techniques for the probabilistic design of rubble mound breakwaters, Castillo et al. (2004) proposed a dual design method, based on an iterative process which consists in three steps to repeat until convergence: i) preliminary optimal design using given safety factors; ii) calculation of failure probabilities or bounds of all failure mode through Monte Carlo simulation; iii) adjustment of the safety factors bounds. The application of such a method is presented for the case of a generic rubble mound structure with cubic armor units, considering the failure due to excessive overtopping, armor instability and crownwall sliding, only due to common agents. The presented probabilistic calculations must be considered an incomplete estimate, because of the absence of appropriate information regarding the interaction between failure modes, which requires further experimental research.

Kim and Suh (2010) present the results of calculation of the probability of failure of Tetrapods armor layers of 12 trade harbor breakwaters and 8 coastal harbor breakwater in Korea. Hudson (1958) and van der Meer (1988c) formulas are employed, considering lifetime of 50 years and using both level II AFDA approach and level III Monte Carlo simulation. A linear relationship between the safety factor (i.e. the ratio between resistance and load) and the probability of failure is observed for the studied structures.

Maciñeira et al. (2017) describe the design process of the secondary breakwater in the harbor basin of the Port of La Coruña (Spain), which was based on the indication of Puertos del Estado (2010). The level III calculations concerned the probability of failure due to: i) armor instability ii) berm erosion; iii) wave wall sliding, overturning and plastic failure; iv) excessive overtopping; v) slip circles of soil and core of the structure. In particular, for a lifetime of 50 years the individual probability of failure related to each failure mechanisms was calculated, together with the total probability of failure related to a parallel system (i.e. each failure mode was considered as independent of the other ones). Given the characteristics and peculiarities of the site, it was decided to verify the design by means of small scale physical model

test. A reliability-based methodology for the design of the rock armors weight based on level III probabilistic analysis is also proposed by Tabarestani et al. (2020). The results of the application on the case study of the Noshahr Port breakwater (Iran) show that the most critical parameters affecting the reliability of armor weight are wave height and dimensionless damage level. Therefore, the upgrade of the knowledge of such parameters would enhance the quality of the probabilistic estimation. In this regard, Malliouri et al. (2021) proposed a wave propagation statistical model for the calculation of the failure probability based on the long-term wave climate near the coastal structure using wave observations or measurements in deeper waters, also considering the evaluation of the joint probability density functions of the wave climate characteristics (i.e. significant wave height, mean wave period and mean wave direction). The application to the fictitious rubble mound breakwater in the Port of Malaga (Spain) is also presented. The sea side armor failure, the toe instability, and the rear side armor failure due to overtopping are the considered failure modes, whose physical dependence was neglected. Level III calculations are performed by means of Monte Carlo simulation and direct integration method, which give similar results. In addition, the definition of the so-called unconditional failure probability is given, through the derivation of a relation between an event-based extreme value analysis and an analysis on sea-state conditions within storm events. Also Cho (2021) proposes an upgrade of the quality of level III estimation of the probability of failure of the armor layer of a rubble mound breakwater, through a new non-Gaussian wave slope distribution. Indeed, the traditionally employed Gaussian distribution produces over-estimated failure probability of armor block and the non-negligible occurrence probability of the negative wave slope. Such shortcomings are totally overcome by the proposed non-Gaussian distribution, which is derived from the Longuet–Higgins joint distribution of wave amplitude and period by means of the random variable transformation technique.

The above mentioned research works consider only the present climate for the evaluation of the probability of failure of rubble mound breakwaters. Instead, Galiatsatou and Prinos (2012) describe reliability-based optimization of a fictitious rubble mound breakwater armored with Tetrapods in the marine area of Le Havre (France), taking into account the effects of climate change on coastal areas. Three main failure modes are considered, namely the instability of the armor layer, the excessive wave overtopping and the erosion of the toe of the structure, and level III Monte Carlo simulation is used for the evaluation of the probability of failure of different possible geometries during lifetime of 100 years. The optimal designs are defined as the more cost-effective among the solutions that fulfill the design requirements. The comparison between optimized configurations for present and future climate conditions highlight a general increase of the weight of armor units and of the crest height. In addition, it is observed that the deterministic approach (i.e. level 0) seems to lead to over-sizing of the Tetrapod units and to under-sizing of the crest height.

A novel application of level III probabilistic methods is given by Lara et al. (2019), who developed a reliability based methodology not for the design of new coastal structures, but for assessing how the hydraulic performances of historical ones has evolved during lifetime. Level III calculations (i.e. Monte Carlo simulations) are used to carry out a high-resolution time-dependent analysis considering the case of non-conventional designs located in shallow-water locations. Due to the absence of specific formulas, computational fluid dynamics (CFD) numerical models are employed for the definition of reliability function related to the considered failure modes, i.e. excess of mean overtopping discharge, excess of maximum overtopping volume and sliding of the crown-wall.

2.2.5 Knowledge gaps

The following research gaps can be identified in the existing literature regarding the probabilistic design of rubble mound breakwaters:

1. few information about physical interactions between failure modes are available, and hence further experimental investigations are needed;

2. the existing experimental formulas for the description of single failure modes are often affected by a strong level of uncertainties of the parameters, and hence case-specific physical model tests should be conducted to increase their applicability or to define new empirical laws;

3. a better knowledge and statistical description of wave loading parameters is needed, above all in shallow water conditions;

4. few studies include the effects of climate change into the probabilistic calculations;

5. to the best knowledge of the author, no investigations regarding the probabilistic design of upgrading solutions for existing rubble mound breakwaters have been conducted.

As discussed in section 1.2, the present research work aims to give a contribution to fill such gaps, especially with regards to the need for: i) more case-specific experimental formulas for the description of failure modes; ii) the inclusion of the effects of climate change on coastal areas for the evaluation of the probability of failure; iii) the application of the probabilistic design for the upgrade of existing rubble mound breakwaters.

2.3 Upgrade of existing coastal defense structures

2.3.1 Aging of harbor rubble mound breakwaters

Aging of coastal and harbor defense structures is a worldwide problem, which nowadays goes along with the need of upgrading for protection against the effects

of climate change on coastal areas (Hughes, 2014; Toimil et al., 2020). Special attention must be paid to harbor breakwaters, because the impossibility to fulfill the design requirements would have significant economical and social impacts, above all if national interest and strategic ports are considered.

Great part of the historical coastal and harbor defense structures is in shallow-waters and consists of non-conventional breakwaters, which have been repeatedly modified over the years and usually converted into rubble mound structures (Lara et al., 2019). Therefore, traditional empirical design formulas defined for new structures may be not able to properly characterize the hydraulic behavior of both damaged and restored breakwaters, whose actual composition in terms of material and layers geometry is often unknown, because of the lack of documents and reports regarding the modifications implemented during their lifetime.

In order to give an idea of the process of modification and upgrade undergone by most of the historical structures during their lifetime, a brief description of the history of some Italian harbor breakwaters is here presented. Indeed, Italy boasts a huge number of historical harbor breakwaters, which have been modified during their lifetime to repair damages caused by wave load or to increase the hydraulic performances to allow the growth of the port. In the following, the story of historical harbor breakwaters of relevant Italian commercial and touristic ports is briefly described, from the oldest to the newest one, on the basis of information derived from port master plans, archaeological reports, and news articles.

The Port of Civitavecchia is one of the most ancient Italian harbors, which still plays a relevant role, being the second European and the first Italian cruise port. The harbor basin is mainly protected by the "Cristoforo Colombo" breakwater, whose length is about 2 km. The origins of the structure date back to the II century, when the emperor Traiano ordered the construction of the port of Civitavecchia. The original detached breakwater was incorporated into a longer rubble mound structure connected to the shore, which was progressively extended during the years. The present breakwater is characterized by a not uniform structure. Indeed, after the first part made of Antifer blocks, Tetrapods armored segments alternate with vertical wall stretches. The extension of the breakwater of 400 m was planned, in order to increase the safety of navigation close to the harbor entrance.

The Port of Salerno is another important Italian harbor, whose origins date back to the XIII century. The construction of the eastern outer breakwater of the Port of Salerno started in 1861, but it appears as an extension of the "Manfredi" pier built in 1262. The current structure is about 1.5 km long and armored with cubic blocks.

Also the commercial and touristic Port of Catania has ancient origins. The birth of the breakwater of "Levante" dates back to the beginning of the XVII century. It consisted in a vertical wall made up of 330 t cyclopean blocks constructed over a rubble mound structure. During XIX century, the original breakwater was lengthened up to 258 m. However, after several failures occurred during the construction between 1930 to 1933, the structure was rehabilitated as a rubble mound breakwater

armored with cubic blocks, and it has been progressively extended until the present length of 2.25 km. Since the breakwater of "Levante" appeared severely damaged by extreme sea storms occurred during its lifetime, a rehabilitation intervention was planned, whose definitive design is ongoing.

The origin of the Port of Napoli, which plays a relevant role for commercial and also touristic traffics, dates back to the Ancient Greece period. However, the "San Vincenzo" breakwater was constructed in 1836 for the protection of the military port commissioned by king Ferdinando II. The current structure, which is longer than 2 km, is made of Antifer units with hole in the first part, and of Tetrapods in the last segment.

The Port of Livorno, in which significant commercial and also touristic traffics take place, is mainly protected by a detached rubble mound breakwater, whose building started in 1858 and finished before the Unification of Italy in 1861. The curvilinear structure was armored with cubic blocks obtained from the shaping of natural rocks, instead of concrete units. In 1910, the construction of the straight extension towards North-West (the so called "Meloria" breakwater) started, and several subsequent modifications were made. Currently, the external armor layer of the about 2 km long harbor breakwater is made up of cubes and quarry stones on the crest, and of Tetrapods on the sea side slope. From the last maintenance works completed during the '80s, the structure was significantly damaged by extreme sea storms. Therefore, the armor layer restoration with Tetrapods has been planned, in order to improve the hydraulic performances of the breakwater.

The outer breakwater of the commercial New Port of Crotone is a rubble mound structure almost 1.7 km long, and armored with cubic blocks. The design of the New Port of Crotone started in 1868, but only at the end of the Second World War the outer breakwater was completed.

The commercial and touristic Port of Monopoli is mainly protected by the "Tramontana" breakwater, whose construction started in the first years of the XX century. During the '70s, the existing structure was consolidated, and in 2006 the extension until about 1 km was completed. At present, the outer layer of the breakwater is made of cubic and Antifer blocks.

Finally, the Port of Palermo, which is one of the most important harbor of the Mediterranean sea for dimensions and passenger traffic, is mainly protect by an outer breakwater dated back to the first decade of the XX century, which is connected to the North pier constructed in the years 1570-1590. All the harbor structures suffered significant damages during the Second World War. Moreover, the extreme sea storm happened on 25th October 1973 destroyed great part of the outer breakwater and caused severe effects on the whole harbor area. At present, the outer breakwater is a rubble mound structure armored with cubes in the first 800 m, and a vertical wall structure in the last 600 m.

The above described examples of historical harbor rubble mound breakwaters highlight the complexity and non-conventionality of such structures. In this regard,

an easy-to-use methodology for the analysis of modifications and deterioration processes suffered by existing structure may facilitate their characterization. In addition, the necessity to implement maintenance interventions to ensure the fulfillment of the design requirements despite of the aging of the structure is evident, together with the need for upgrading solutions to withstand the possible increase of external loads due to the effects of climate change. Since total costs for improving the performances of harbor breakwaters might be beyond the reasonable technical limits (Isobe, 2013), a reliable methodology for the design of upgrading solutions for historical rubble mound breakwaters is needed.

2.3.2 Methodological approaches for upgrading rubble mound breakwaters

Despite the practical relevance of the matter concerning the upgrade of aging coastal and harbor breakwaters, few research has been carried out, which mainly consists in design exercises using only desk study tools (Burcharth et al., 2014) and in the definition of experience-based or theoretical methods for the selection of the most suitable upgrading options on the basis of the characteristics of the existing breakwater (Croeneveld et al., 1985; Foti et al., 2020). Moreover, some investigations on implemented upgrading projects are available, that however only describe design procedures, neither defining specific formulas for the design of upgrading options nor testing the adequacy of the traditional equations for newly built structures (Reis et al., 2011; Santos-Ferreira et al., 2015; Main et al., 2016).

Considering the available state of art, a summary of the main phases for the selection of the best upgrading options for a certain existing harbor breakwater is here presented. The choice of the most suitable upgrading solutions for existing rubble mound breakwaters must be addressed considering several factors (Croeneveld et al., 1985; Burcharth et al., 2014; Foti et al., 2020). First, a field survey is required to assess the magnitude of the damage and identify its possible causes, in order to avoid the failure of the restored breakwater for the same reasons. Then, the required structure performances and acceptable risk of failure must be fixed, on the basis of the structure function (e.g. coastal or harbor defense) and economic relevance. Furthermore, the geometric characteristics of the breakwater and the local topography must be considered, together with specific environmental restrictions which could influence the design. Finally, the available materials, equipment and financial resources play a fundamental role for the evaluation of the economic and technical feasibility of different upgrading options.

On the basis of the above mentioned factors, four main repair methods are usually contemplated for the upgrade of damaged rubble mound breakwaters (Croeneveld et al., 1985): i) addition of units of the same type of the existing ones, eventually reinforced or slightly greater to increase their weight; ii) replacement of the entire armor layer, removing all the original units; iii) reconstruction of the rubble

mound structure, replacing not only the original armor layer, but also the under-layers; iv) provision of a submerged toe berm or detached breakwater to reduce the wave impact on the existing structure. If the adaptation of existing rubble mound breakwaters to the effects of climate change is considered, the above-mentioned upgrading strategies can be applied with some tricks to face the increased external forcing. For instance, the overtopping rates can be reduced by heightening the existing wave wall or by the construction of a new one. Furthermore, besides the addition of a submerged toe berm or detached breakwater, if the construction of an extra or totally new armor layer is considered, the rise of the structure crest level to reduce the overtopping discharges or the reduction of the seaside slope to limit wave run-up and increase the armor layer stability can be designed, as showed in Figure 2.5 (Burcharth et al., 2014; Foti et al., 2020).

The selection of the blocks for the armor layer restoration is a difficult issue, because there is a lack of in-depth investigations on the interaction between the existing units and the additional ones. In this regard, Carver (1989) provided an inventory of existing US Army Corps of Engineers (USACE) projects that have used dissimilar armor blocks for repair and rehabilitation of rubble mound coastal breakwaters. The results of the survey showed that in 1989 only the 24% of the considered districts had experienced the use armor units different from the existing ones for the armor layer restoration, thus highlighting the necessity to perform further systematic experimental studies for the evaluation of the interfacing and stability response of different armor blocks. Currently, the only guidance for the choice of shape and size of the additional armor units comes from traditional formulations for new constructions, prototype experience, engineering judgment, inferences from model tests of similar structures, or site-specific model tests. The use of additional armor units heavier than the existing ones could be considered if the present structure appears undersized with respect to the design wave action, in the absence of technical or practical limitations (Croeneveld et al., 1985). Instead, to the best of the author's knowledge, the use of additional armor units smaller (i.e. lighter) than the existing ones, which could be contemplated to fill the voids of the damaged breakwater with limited movements of the present blocks, has not been investigated yet. Certainly, in this case the structural response of the whole armor layer to the design wave load must be evaluated by means of physical model tests. The same applies to the use of units with different interlocking level than the existing ones, for which special attention on the regularization of the laying surface and on the transition zones should be paid.

As regards the available numerical models, they have not been sufficiently calibrated to simulate all the common restoration concepts, particularly concerning the stability of the armor layer (Burcharth et al., 2014; Lara et al., 2019). As a consequence, physical modeling represents the most reliable approach not only to describe the response of existing or upgraded rubble mound structures and their possible failure modes, but also to calibrate existing or new numerical models.

(a)

Extra layer on armour slope and crest

Existing structure

(b)

Flatter extra layer on armour slope

Existing structure

(c)

Additional submerged breakwater

Existing structure
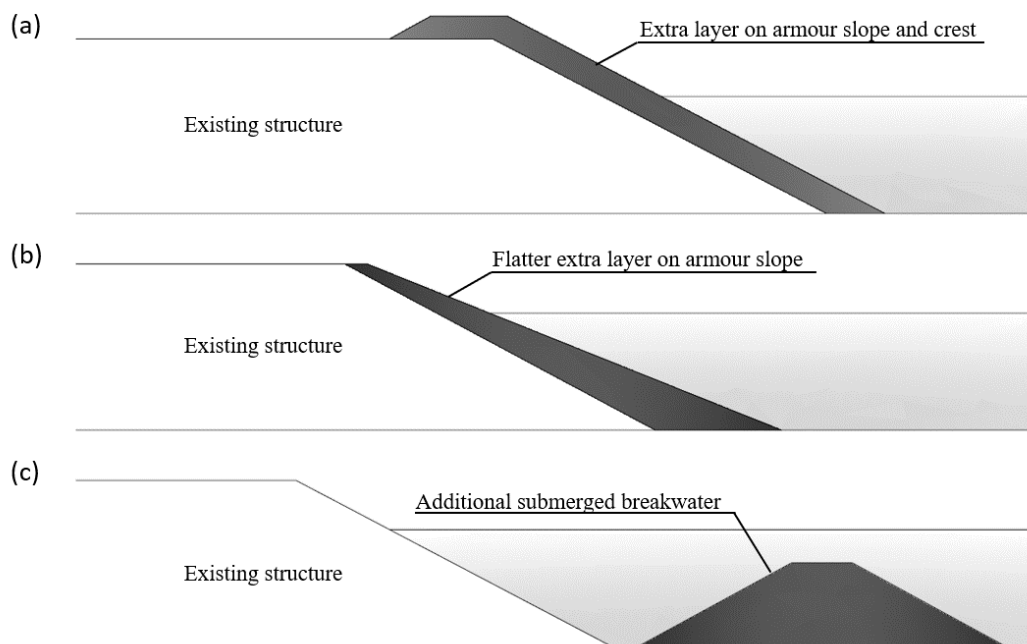
FIGURE 2.5 Examples of concepts for upgrading rubble-mound breakwaters: a) extra armor layer to increase height and stability of the existing structure; b) extra flatter armor layer to limit the impact of the wave motion and increase the structure stability; c) additional submerged breakwater to limit the impact of the wave motion on the existing structure. Source: Foti et al. (2020).

2.3.3 Examples of performed restorations of rubble mound breakwaters

The need for upgrading historical damaged rubble mound breakwaters is a worldwide problem. In the '70s and '80s several restoration projects for damaged rubble mound breakwaters using armor units both equal and different from the existing ones were documented in the USA (Carver, 1989).

Among the most recent rubble mound breakwaters upgrades, the rehabilitation of Sines west breakwater in Portugal deserves to be mentioned(Reis et al., 2011). Between 1978 and 1979, when the construction of the breakwater was nearly complete, extreme sea storms caused failure of almost the entire 42 t Dolosse armor layer and superstructure. Subsequent to the failure, which was most probably a consequence of a combination of different factors (i.e. shortcomings in the selection of design waves, deficiency in project management, differences between the constructed breakwater and the design specifications, low structural strength of Dolosse, physical removal by wave action of the toe stones, incompleteness of the construction), studies were undertaken by several hydraulic laboratories. The scope of such investigations was to analyze the stability and, in some cases, the overtopping of different solutions for the rehabilitation of the Sines west breakwater using Antifer cubes, also considering the reactivation of berths 1, 2 and 3. The final restoration, which implies the reactivation of berth 1, was designed on the basis of the experience gained with the previous rehabilitation works, also using the same materials, and it was tested

in laboratory for the analysis of stability and overtopping for each of the proposed solutions.

The north breakwater of Nazaré Harbor, which is another Portuguese rubble mound breakwater originally made of Tetrapod units, was severely damaged during the winter of 2013-2014 and its head and first section were completely destroyed (Santos-Ferreira et al., 2015). Since the main damage observed in the northern breakwater was probably caused by the increased significant wave height, the rehabilitation solution was designed considering a higher design wave height and Antifer blocks were chosen for their greater robustness and weight with reference to the Tetrapods.

The Coffs Harbor Northern Breakwater in Australia was subjected to excessive rates of overtopping discharge, which represent a risk to human life, vessels and infrastructure and hence the upgrading project was developed (Main et al., 2016). The feasibility study was elaborated by the Australian Department of Industry (Lands) and GHD (one of the world's leading professional services companies operating in the global market sectors of water, energy and resources, environment, property and buildings, and transportation). Given the unique set of constraints and opportunities presented by the Northern Breakwater and surrounds, balanced technical, social, environmental and economic outcomes were achieved not only by means of innovative technical design solutions, but also by means of innovative and transparent approaches to engaging the community, local industry, gaining environmental approvals and support from other stakeholders. The preferred option was a composite armored berm upgrade, which consists of a layer of three legged concrete armor units called Hanbar, to be constructed on top of a newly built rock berm extending from the seaward side of the existing structure at mean sea level. Furthermore, the widening and the rising of the crest of the breakwater along the eastern portion of the structure was plannes. Having undertaken a comprehensive options development and evaluation exercise, Lands was able to proceed directly to physical modeling, with confidence that the preferred option represented the solution that offered the best value for money. UNSW's Water Research Laboratory (WRL) undertook the 3D physical modeling, which provided a more accurate simulation of wave processes in the nearshore area and verified the results from the Neural Network tool for assessment of overtopping. The findings of the physical modeling exercise were used to develop the detailed design and included a number of refinements during testing. Finally, a revised breakwater upgrade design was developed to minimize the environmental impacts of the upgrade works.

2.3.4   Knowledge gaps

The following research gaps can be identified in the existing literature regarding the upgrade of existing rubble mound breakwaters:

1. absence of an easy-to-use methodology for the characterization of the current state of existing structures;

2. lack of systematic investigations on the behavior of differently upgraded rubble mound breakwaters;

3. lack of specific design formulas for the design of upgrading solutions;

4. absence of studies for the validation of traditional design formula for newly built breakwater for the case of upgraded structure.

As discussed in section 1.2, the present research work aims to give a contribution to fill such gaps.

2.4 Effects of climate change on coastal areas

2.4.1 Overview on climate change

A statistically important modification of the mean state of the climate or its variability, which last for an extended period, is defined climate change. The variation in climate patterns may be caused by natural processes, but also by anthropogenic activities that transform the composition of the atmosphere or of the land-use (IPCC, 2014).

The first direct effect of global warming is the shifting of weather patterns, with consequent unpredictability of precipitation and increase of the frequency and/or the magnitude of extreme weather events, such as heavy downpours (Simmons et al., 2010), floods, heat waves (Christidis et al., 2011; Duffy and Tebaldi, 2012), drought (Sheffield et al., 2012), hurricanes and changes in other storms (Bender et al., 2010; Lin et al., 2012; Marsooli et al., 2019). Therefore, it is no more reasonable to assume that what happened in the past will occur in the future, following a fixed probability density function. In other terms, the assumption of stationary forcing is no more valid for the evaluation of future natural loads (Chini and Stansby, 2012; Davies et al., 2017; Mudersbach and Jensen, 2010; Rueda et al., 2016; Toimil et al., 2020; Westra et al., 2010).

As regards the open sea and the coastal zone, climate change appears through several impacts. For instance, the absorption of some of anthropic excess emissions acted by the ocean causes its acidification, which poses a serious threat to underwater life (Hoegh-Guldberg et al., 2017; Sunday et al., 2017). Moreover, global warming generates the rise of the mean sea level, due to melting ice and thermal ocean expansion (Church et al., 2013), increased storm surge events (Chini and Stansby, 2012; Chini et al., 2010; Lowe and Gregory, 2005; Hemer et al., 2013b; Vousdoukas et al., 2016) and changes of the frequency and the direction of extreme wind and wave events (Vousdoukas et al., 2018; González-Alemán et al., 2019; Romero and Emanuel, 2013). As a consequence, extreme wave run-up and overtopping of coastal

structures is likely to rise, thus causing the increment of wave penetration into harbors and more intense beach erosion (Nicholls et al., 2007; Sanchez-Arcilla et al., 2016; IPCC, 2019).

The generation of future projections is based on the definition of emission scenarios to force the climate models. Before the Intergovernmental Panel on Climate Change (IPCC) Fourth Assessment Report (IPCC, 2007), the most widely used and referred-to family of emissions scenarios were the SRES scenarios, defined by the Special Report on Emissions Scenarios (Nakicenovic et al., 2000). Each of the 40 SRES scenarios was included into one of four groups (A1, A2, B1, B2) depending on the subject matter (e.g. population changes, energy sources, economic development, etc.). SRES scenarios were defined under the hypothesis that political or legislative actions have no effect on their development. Moreover, each SRES scenario was based only on socio-economic futures, requiring the sequential performance of the corresponding emission, radiative forcing, and climate model scenarios. Any change in one of the previous scenarios made it necessary to restart the whole sequence.

In order to facilitate future assessment of climate change and its effects, the IPCC request the scientific communities to develop a set of new scenarios as a basis for long-term and near-term modeling experiments (IPCC, 2007). The research community answered with the definition of four different scenarios containing greenhouse gas emission, concentration, and land-use trajectories consistent with current scenario literature, allowing subsequent analysis by both Climate Models (CMs) and Integrated Assessment Models (IAMs). These four scenarios, referred to as representative concentration pathways (RCPs) and whose main features are described in Table 2.7, together span the range of year 2100 radiative forcing values from 2.6 to 8.5 W/m^2 (Van Vuuren et al., 2011), being the radiative forcing a direct measure of the change the Earth's energy balance due to natural and anthropogenic processes. RCP2.6 and RCP8.5 are respectively the best and the worst scenario, since the first one represents a mitigation scenario characterized by a great emission reduction, while the latter corresponds to the pathway with the highest greenhouse gas emissions. In particular, the cumulative total anthropogenic CO_2 emissions from 1870 are expected to reach 3000 GtCO_2 for RCP2.6 and 7600 GtCO_2 for RCP8.5 in 2100 (IPCC, 2014). As regards the change in mean temperature, a rise of 1.8 °C for RCP2.6 and 4.7 °C for RCP8.5 with respect to the period 1861-1880 is forecast for the year 2100 (IPCC, 2014).

Recently, the IPCC has defined a set of five new emissions scenarios, in order to explore the climate response to a broader range of greenhouse gas, land use and air pollutant futures (IPCC, 2021). This set of scenarios drives climate model projections of changes in the climate system, accounting for solar activity and background forcing from volcanoes. Results over the XXI century have been produced for the near-term (2021–2040), mid-term (2041–2060) and long-term (2081–2100) relative to the historical period 1850–1900.

The evaluation of the effects of climate change on marine environment can be

TABLE 2.7 Characterization of IPCC representative concentration pathways (RCPs). Source: Foti et al. (2020)

	RCP2.6	RCP4.5	RCP6	RCP8.5
Radiative forcing pathway	Peak and decline	Stabilization without overshoot	Stabilization without overshoot	Rising
Maximum radiative forcing by 2100 [W/m^2]	2.6	4.5	6.0	8.5
Maximum CO_{2eq} concentration by 2100 [ppm]	490	650	850	1370
Greenhouse gas emission baseline	Very low	Very low	Medium	High baseline
Mitigation policy	None	Medium–low	High	None

undertaken following two approaches: i) the analysis of long historical time series of climate descriptors, in order to detect potential decreasing or increasing trends (Kundzewicz and Robson, 2000); ii) the production of global and regional projections under fixed greenhouse-gas emission forcing scenarios using different types of climate models (Flato et al., 2014). It is important to point out that both approaches are affected by uncertainties. In the case of long-term trend analysis, two main source of uncertainty can be identified, namely the quality of data and the statistical methods employed. Instead, when climate projections are considered, the intrinsic uncertainties of the numerical models and of climate change scenarios affect the reliability of the results.

2.4.2 Trend analysis of historical climate data

In order to detect the effects of climate change on past and present climate, long-term trend analyses must be carried out using records not shorter than 30 years (Kundzewicz and Robson, 2000). A huge number of studies have been performed to detect possible sea level rise rates and substantial tendencies on mean wave climate and storminess, both at global and local scales.

As regards sea level at global scale, Spada and Galassi (2012) provided the review of existing studies based on the analysis of tide gauges data, highlighting the scatter which characterizes the published estimates. Moreover, a novel methodology for the evaluation of mean sea level rise was proposed, which takes into account the glacial isostatic adjustment, and a global sea level rise rate equal to 1.5±0.1 mm/year was found for the period 1880-2012. Similarly, Jevrejeva et al. (2014) elaborated the sea level data from 1277 tide gauges acquired during the period 1807-2009, applying the averaging virtual station method over 14 ocean basins which cover the entire globe. A mean sea global level rise rate of 1.9±0.3 mm/year was calculated and the correspondence with the results from satellite altimeter data analysis was demonstrated.

Considering the regional scale, Marcos and Tsimplis (2007) calculated the following meteorologically corrected sea level rise rate, also including the glacial isostatic adjustment, for the period 1960-2000: 1.1 ± 0.6 mm/year for North-West Atlantic Ocean, 1.3 ± 0.8 mm/year for East Atlantic Ocean, 1.3 ± 1.0 mm/year for the North Sea, 0.9 ± 0.4 mm/year for The Mediterranean Sea. Vecchio et al. (2019) performed a long-term trend in sea level data of nine tide gauges placed in the Mediterranean Sea covering the period 1888-2008, by applying the empirical mode decomposition (EMD) method for the decomposition of the signal in modes that provide a description of the intrinsic timescales present in the time series. The results of the analysis showed that a minimum rate of 0.17 ± 0.02 mm/year and a maximum rate of 2.78 ± 0.04 mm/year characterized the sea level rise during the considered period. Finally, Cazenave et al. (2002) performed a long term trend analysis of tide gauge data for both the Mediterranean Sea and the Black Sea, finding a mean sea level rise rate of respectively 0.41 ± 0.87 mm/years and 2.2 ± 2.5 mm/years for sea level time series longer than 22 years.

Many research on global inter-annual variation of mean and high percentiles of significant wave height and wind speed have been conducted (Caires and Swail, 2004; Stopa et al., 2013; Timmermans et al., 2020; Young and Ribal, 2019). Reguero et al. (2019) found that the global wave power, which is the transport of the energy transferred from the wind to the sea surface, has long-term correlations and statistical dependency with sea surface temperatures and shows a global increasing trend of 0.4% per year. However, global analysis often does not gather local peculiarities, thus several site-specific studies must be conducted. The long-term variation of mean wave climate and storminess parameters was studied for portions of the Atlantic Ocean (Bromirski et al., 2013; Osinowo et al., 2016; Yamaguchi and Hatada, 2002; Wang et al., 2016), the Indian Ocean (Gupta et al., 2015; Hithin et al., 2015; Kumar et al., 2018; Naseef and Kumar, 2020; Patra and Bhaskaran, 2016; Shanas and Kumar, 2015), and the Black Sea (Arkhipkin et al., 2014; Divinsky and Kosyan, 2020).

Concerning the Mediterranean Sea, Lionello and Sanna (2005) found a statistically significant decreasing trend of the monthly average significant wave height generated by the WAM model forced by the ERA-40 wind fields for the period 1958-2001, demonstrating the strong influence of the regional orographic conformation of the basin and fetch in the significant wave height variability regimes. Cid et al. (2016) studied the variation of intensity, duration and frequency of southern Europe extreme surge levels from GOS database for the period 1948-2013, and found that most of the Mediterranean regions do not show significant trends in extreme storm surges, with the exception of the Alboran Sea, gulfs of Gabes and Sirte, northern Adriatic and the easternmost Mediterranean.

Only few detailed investigations have been carried out for the Italian seas. By using a data-set generated by the wave model WAM forced by the ERA-40 wind field for the period 1958-1999 in 27 selected sites near the Italian coast, Martucci et al. (2010) identified a negative trend in the annual and winter-averaged significant

wave height, in accordance with Lionello and Sanna (2005), and highlighted the overall absence of a significant trend in the annual-averaged mean duration of sea states over thresholds. Pomaro et al. (2017) analyzed a 37-year long directional wave time series recorded from 1979 to 2016 at the CNR-ISMAR oceanographic research tower, in the Northern Adriatic Sea, and detected an evident decreasing tendency of the wave activity in terms of intensity of the events (i.e. 99th percentile of significant wave height), and a general increase in terms of frequency (i.e. rate of events over the threshold of sea storms, linked to the lower percentiles of significant wave height). Finally, Caloiero et al. (2019) transposed the ERA-Interim wave data by ECMWF relative to the period 1979-2017 at 50 representative nodes along the Calabrian coast and found that the annual mean significant wave height shows important positive trends along the central and the southern zones of the Ionian coast, whereas the energy wave period exhibits an increasing tendency in most of the considered sites.

2.4.3 Future climate projections

The studies on the effects of climate change on marine climate based on future projections focus on: i) sea level rise; ii) changes in storm surge levels; iii) changes in wind wave climate; iv) rise of intensity and frequency of occurrence of extreme weather events.

As already mentioned, one of the most significant consequence of the increase of the global mean temperature is sea level rise (SLR). Church et al. (2013) found that it is almost certain that global sea level will continue to rise during the XXI century and beyond. In particular, with respect to the year 2000, it is expected an increase of mean global sea level of about 45mc for RCP2.6 and of about 75 cm for RCP8.5, taking into account the uncertainties of these projections. While the main contributing factors to global sea level are thermal expansion of the ocean and melting of the ice sheets, ice caps and glaciers, on a local scale changes in salinity, atmospheric pressure, ocean circulations and land movements may lead to different patterns and magnitudes of sea level rise than the global average. For this reason, coastal management needs local scenarios elaborated from global sea level rise but taking into account all relevant processes for a given spatial scale (Vellinga et al., 2011). Furthermore, the global models do not resolve the coastal shallow regions because of their coarse horizontal and vertical resolution (Malanotte-Rizzoli, 2018).

For instance, the Mediterranean Sea, which is a mid-latitude, semi-enclosed and deep sea, is characterized by a peculiar dynamic regime governed by the Strait of Gibraltar, and hence a regional model is needed. Galassi and Spada (2014) developed a regional model for sea level analysis in the Mediterranean Sea. Using published estimates for terrestrial ice melt and ocean response components of future sea level change (e.g. ocean circulation contributions and thermosteric and halosteric effects resulting from regional, high-resolution coupled models) and glacial isostatic

adjustment modeling, they found that the minimum and maximum spatially averaged projected sea level rise by 2040–2050 in the Mediterranean Sea will be respectively 26 cm and 98 cm. Lambeck et al. (2011) provided sea level rise estimates by 2100 for forty representative sites along the Italian coast, by adding the global averaged contribute of vertical tectonic movements to the projections of a lower and a higher impact scenario, which respectively correspond to a base sea level rise of 18 cm and 140 cm. Finally, Vecchio et al. (2019) evaluated the sea level rise by 2050 and 2100, with respect to 2005, for nine sites in the Mediterranean Sea, considering both the vertical land motion and sea level natural variability contribution. An increase of sea level by 2100 between 26 cm and 60 cm and between 48 cm and 82 cm was found, respectively for RCP2.6 and RCP8.5 future scenarios.

However, sea level rise is not the only effect of global warming which interests coastal areas. Indeed, the inter-annual variability of the wave motion strongly impacts on coastal processes, in some cases more than the projected SLR (Hemer et al., 2013b). Vousdoukas et al. (2016) elaborated projections of extreme storm surge levels along the European coastline, for the baseline period 1970–2000 and the periods 2010–2040 (short term future scenario) and 2070-2100 (long term future scenario) for RCP4.5 and RCP8.5. For instance, for the Mediterranean Sea in 2100 under RCP8.5, the results showed a 29 year reduction in the return period of the present 100-year event along the West zone, whereas the present 100-year event was projected to occur every 95.3 years in the East zone. Instead, Lowe and Gregory (2005) used a high resolution global atmospheric model, a regional model and a storm-surge model in order to simulate two 30 year time-slices, i.e. present day (1961–1990) and future (2071–2100) for the UK. The simulations showed that the height of a storm surge with a 50 years return period, taking into account not only changes in storminess, but also a rise in global sea-level and vertical land movements, will increase along most of the UK coastline, with the largest increases predicted to occur off the southeast coast.

As regards the wave climate, for the northern hemisphere, the outcomes from coupled atmosphere-ocean general circulation models (GCMs) show a general decrease in annual and seasonal mean significant wave height and period for the time slice 2070-2100 (Camus et al., 2017; Hemer et al., 2013b; Morim et al., 2019). In particular, the results from the first community-derived multi-model ensemble of global wave climate projections for the time slice 2070-2100 indicated that, with respect to the present period 1979-2009, the annual mean significant wave height will decrease over 25.8% of the global ocean. Instead, the increase of the annual mean significant wave height is expected over 7.1% of the global ocean, predominantly in the Southern Ocean. In addition, an increase in annual mean wave period over 30.2% of the global ocean and associated rotation of the annual mean wave direction was predicted (Hemer et al., 2013b). The decreasing tendency of annual mean and extreme significant wave height in the northern hemisphere is confirmed for the

Mediterranean Sea by Lionello et al. (2008), who analyzed wind-wave fields generated by the WAM model, and for the North Atlantic Ocean, the Mediterranean Sea and western North Sea by Morim et al. (2019), who compared 91 published global and regional scale wave climate projection studies in terms of resulting projections and related sources of uncertainty. On the contrary, Chini et al. (2010) found that the effect of SLR on wind waves off the coastline of East Anglia is expected to cause the increase of the significant wave height. Indeed, it was shown that for near-shore points, an expected sea level rise of 3.5 mm/year, 7.0 mm/year and 19 mm/year could increase the 100-years return wave height computed without sea level rise respectively by 2%, 4% and 12% in 2090. As regards offshore extreme wave heights, they are not modified by SLR, which is not significant compared to the offshore water depths.

Storm surge and wind waves produced by extreme weather events and high tides influence extreme sea level. Vousdoukas et al. (2018) found a global projected intensification in frequency of occurrence of extreme sea levels, which are determined by the combination of mean sea level rise and water levels driven by tides, waves, and storm surges. For instance, for the Mediterranean Sea, in 2100 the 100-year extreme sea level is expected to occur every 0.2-7.0 years. The reduction of the return period of extreme sea levels will likely exceed the design condition of existing coastal defense structures, and hence a higher coastal risk is expected. The upgrade of existing coastal protection would imply increasing elevations by an average of at least 25 cm by 2050 and by more than 50 cm by 2100. In addition, local required increments can be in the order of $1 \div 2$ m. Therefore, considerable economic, environmental, and societal costs must be borne in order to implement interventions of adaptation to climate change along the 620,000 km of global coastline.

Another consequence of climate change, which will strongly affects coastal zones and relative infrastructures, is the rise of intensity and frequency of occurrence of extreme weather events that were rare or non-existing in the past, such as Medicanes (i.e. Mediterranean hurricane) and hurricanes. Medicanes are intense extra-tropical cyclones that acquire tropical characteristics, associated with extreme winds and rainfall. For instance, on 27th-28th September 2018 the so-called Medicane Zorbas took place in the Ionian Sea. Zorbas was one of the greatest ever recorded hurricane in the Mediterranean Sea, with measured maximum significant wave height equal to 4.1±0.1 m (Scicchitano et al., 2021). Even though Zorbas did not follow the track towards Sicilian coasts predicted by numerical models turning toward, it produced substantial damages to many ports and towns in the provinces of Catania, Syracuse and Ragusa (Eastern Sicily), highlighting the inadequacy of existing coastal defense structures. The assessment of Medicane risk is hard to perform since the rareness of this kind of events makes the evaluation of climatological patterns and long-term changes difficult. However, fewer but more violent Medicanes are projected at the end of the century compared to present considering the effect of climate change, with a greater frequency of occurrence in the cold season and in the western

and central basins of the Mediterranean (Romero and Emanuel, 2013). In particular, González-Alemán et al. (2019) found that the frequency of Medicanes formation will be reduced by 34% in the late XXI century under RCP4.5 scenario. Nevertheless, this lower frequency of Medicanes will contrasts with their longer duration and higher intensity (i.e. stronger winds and increased precipitations). Moreover, there is a substantial shift in the Medicanes location, with a higher density in the Ionian Sea and in proximity of South Italy's eastern coasts, and a reduction accompanied by an eastward shift in the western Mediterranean in proximity of the Balearic Islands.

Finally, it is worth to point out that future climate projections are always affected by uncertainties coming from different sources, not quantifiable by individual studies (Morim et al., 2018). The first one, called inter-scenario uncertainty, is associated to the usage of different future greenhouse-gas emission forcing scenarios. Moreover, the inter-model uncertainty, which is linked to the different representations of atmospheric and oceanic processes given by the climate models, must be considered. Also, the intra-model uncertainty must be taken into account, since perturbed model physics configurations or initialization states can lead to different outputs using the same climate model under the same forcing scenario. Other causes of uncertainty are caused by the atmospheric down-scaling (i.e. use of different statistical or dynamical approaches) and the wind-wave modeling (i.e. use of different inputs data for the same spectral wave model, employment of different spectral wave models, selection between dynamical and statistical modeling, usage of different statistical methods).

2.4.4   Expected impacts of climate change on coastal structures

The effects of climate change on coastal areas influence the performances of coastal defense structures and harbor operability.

Arns et al. (2017) underlined that coastal regions bounded by shallow continental shelf areas are sensitive to several common non-linear feed-backs induced by sea level rise, which can affect wave heights, tide characteristics and surge magnitudes. Simulations suggest that wave height and wave run-up (influenced by the predicted decrease in wave breaking away from the coast) are much more sensitive to sea level rise than tides or surge. The change in design height of a coastal defense can be more than doubled relative to sea level rise alone if these non-linearities are considered in risk assessments. Likewise, Isobe (2013) noticed that the crown height of coastal defense structures should be raised not only because of sea level rise but also because of the increase in wave run-up height and overtopping. Chini and Stansby (2012) carried out the estimation of extreme value of coastal wave overtopping discharge of a sea wall located at Walcott (eastern coast of the UK), applying a methodology based on state of the art modeling of wave overtopping and on the joint probability analysis of extreme water level and wave height, taking into account the non-stationary features of the involved natural processes. The results of the study showed that changes in water level would influence the future projected

overtopping discharge and the frequency of occurrence of a given rate more than changes in significant wave height. For instance, for all the projected climatic scenarios, assuming no improvement in the sea defense, a 100-year return period event would occur at least once in 2 years in 2100, for sea level rise rates higher than 7 mm/year. With regards to caisson breakwaters, Takagi et al. (2011) analyzed the case study of the caisson breakwaters located at the Shibushi Port (Japan), by using SWAN numerical model for the simulation of present and future wave motion, and a reliability based approach for the calculation of the caisson sliding distance. It was found that the combination of sea level rise and increase in wave height due to a potential amplification in typhoon intensity could lead to a more than 5 times increase of the caisson sliding distance with respect to the present scenario.

The importance of evaluating port operation due to wave agitation including the potential effects of climate change emerges because of their fundamental role in local, regional, and global economic growth and development. In particular, potential future consequences of sea level rise and changes in wave height and direction in ports are more frequent docks flooding, greater basin agitation, increased port siltation and the worsening of the structural and hydraulic performances of breakwaters (Sanchez-Arcilla et al., 2016). Therefore, harbors under climate change will have to minimize decreases in port operability due to new climate patterns that are adverse o simply different from the design conditions. Izaguirre et al. (2021) carried out a multi-hazard risk analysis in global port operation, including changes in waves, storm surges, wind, precipitation, temperature, tropical cyclones and sea level rise under RCP8.5 future climate scenario. By 2100 it is expected a general increase of the number of extremely high hazard for ports, mainly along the coasts of the Arabian Peninsula, southern China, the Philippines, Japan and the Bay of Bengal. As regards harbors in the Mediterranean sea, which at present are mainly at very low risk, a general tendency towards a very high level is expected, due to the forecast increase in magnitude of overtopping phenomenon. Camus et al. (2019) presented a probabilistic assessment of port operation under climate change for the Port of Candás (northwest Spain), using a stochastic generator for the synthetic simulation of multivariate forcing conditions at the entrance of the harbor and a metamodel to transfer these marine conditions inside the port. Since time structure dependence was not modeled, the methodology proposed is not useful for the analysis of non-operability persistence. The simulations results pointed out that higher non-operability hours, as well as a higher uncertainty, are expected for higher sea level rise scenarios. Furthermore, a linear trend of the mean hours of non-operability along the XXI century was found.

2.4.5 Knowledge gaps

The analysis of existing literature regarding the effects of climate change on coastal areas highlighted the presence a huge number of investigations focused on both the study of the past climate and the production of future projections. The results

of trend analysis and climate projections of sea levels and and wave characteristics are not always coherent for a certain area, because of the use of different methods, reference periods and input data. Therefore, the combination of outcomes coming from different investigations is not always feasible.

As discussed in section 1.2, the present research work aims to give a contribution to the creation of an overall framework of the variation of present and future sea level and wave characteristics due to the effects of climate change in the Italian seas.

Chapter 3

A probabilistic approach for upgrading existing harbor breakwaters

3.1 Overview

The design of upgrading solutions for harbor rubble mound breakwaters is affected by several uncertainties, which are mainly due to the lack of knowledge about the current state of existing structures, the difficulties in the definition of the external loading, and also the empirical nature of the formulas which describe the interaction between wave motion and coastal structures. In addition, despite the importance of the issue regarding the upgrade of existing rubble mound breakwaters, to the author's best knowledge a comprehensive methodology has not been defined yet.

Therefore, in the present work a probabilistic methodology for the adaptation of existing rubble mound structures was developed, which is able to deal with the above mentioned sources of uncertainty. Such a methodology is based on the following steps: i) the characterization of the actual state of existing breakwaters through the diachronic analysis of field data (i.e orthophotos and 3D point clouds) for the selection of the possible upgrading options; ii) the statistical definition of the local hydrodynamic conditions, taking into account the effects of climate change; iii) the composite modeling (i.e. combination of physical and numerical modeling) of the possible upgrading solutions; iv) the probabilistic assessment of the performances of the selected upgrading options, and the identification of the main sources of uncertainty in the probabilistic calculations.

The proposed methodology has been applied to the emblematic case study of the Catania Harbor breakwater, which allowed to find some general outcomes useful for the design of upgrading solutions for rubble mound breakwaters.

3.2   Proposed methodology for the design of upgrading solutions

The design of upgrading solutions for historical rubble mound harbor breakwater requires the application of a specific methodology, which should take into account all the uncertainties related to the characterization of the structure and of the external load, and also to the physical description of the wave-structure interaction processes. In particular, the following sources of uncertainty affect the design of upgrading solutions for existing rubble mound breakwaters:

1. lack of knowledge about the current state of existing breakwaters, in terms of both layering and degradation level;

2. difficulties in the estimate of the design hydrodynamic conditions due to the stochastic features of the involved variables, especially in the presence of the effects of climate change;

3. empirical nature of the state of art equations that describe the interaction between structure and wave load.

It is worth to point out that the uncertainties related to the estimate of the external hydrodynamic loads and to the description of the wave-structure interaction are typical also of the design of new rubble mound breakwaters. However, as stated in section 2.3, the uncertainty level for the design of upgraded structures is even higher, due to the absence of systematic investigations on the behavior of upgraded rubble mound structures and consequently of specific design formulas and models. Indeed, the reliability of the traditional design equations for the upgrade of existing rubble mound breakwaters has not been assessed yet .

To the author's best knowledge, a methodology for the characterization of the existing structure, the definition of external wave load also considering the effects of climate change, the analysis of the of different upgrading options, and the probabilistic assessment of their performances does not exist. Therefore, in the present work, a comprehensive methodology for upgrading historical harbor rubble mound breakwaters allows to deal with the three mentioned sources of uncertainty, thanks to a probabilistic approach.

First of all, the assessment of the current state of the considered existing structure must be performed, in order to obtain information as accurate as possible concerning the layering of the breakwater and its deterioration level, which is fundamental for the preliminary definition of the possible upgrading options. The second step consists in the definition of the hydrodynamic conditions for the design of the selected upgrading solutions, which can be obtained by applying statistical techniques. Then, the preliminary design of the upgrading solutions can be performed through the deterministic application of the state of art equations for new rubble mound breakwaters. The lack of specific design formulas for upgraded structures

can be overcome through the so-called composite (or hybrid) modeling, which is based on the integration and combination of physical and numerical models for the analysis of complex hydraulic problems, thus taking advantage of the strengths and weaknesses of each individual approach (Oumeraci, 1999; Guanche et al., 2015; Di Lauro et al., 2019; Kamphuis, 2020). Therefore, the performances of existing empirical formulas and numerical models and new design equations can be assessed through the analysis of combined results of physical and numerical tests. The outcomes of the above described phases (i.e. the preliminary design of the upgraded breakwater, the characteristic of the wave load and the appropriate equations for the description of the wave-structure interaction) represents the input data for the probabilistic design, which, as described in section 2.2, is based on the evaluation of the probability of failure of the structure.

In the following, a brief description of the adopted methods for the implementation of the proposed methodology for upgrading existing harbor rubble mound breakwaters is presented.

3.2.1 Characterization of aging rubble mound breakwaters

The design of upgrading solutions cannot disregard the actual state of the existing rubble mound breakwaters, in terms of material and geometry of its constitutive layers, but also of structural deterioration state. However, the layering of the existing breakwaters is often only punctually known, due to the absence of detailed historical reports and documentations and also to the practical difficulties in performing specific and extensive surveys. Indeed, historical breakwaters are usually non-conventional breakwaters, which have been repeatedly modified during their lifetime. Therefore, detailed information about the real composition of historical breakwaters is often not available.

Nevertheless, the actual state of degradation of rubble mound breakwaters can be usually evaluated by means of the diachronic analysis of georeferenced field data in a GIS environment, which allows one the observation of the modifications suffered by the emerged structure due to sea storms occurred during the considered period. For this purpose, georeferenced orthophotos acquired through traditional aerial survey or by means of Unmanned Aerial Vehicle (UAV) over the structure lifetime can be employed, which can be eventually compared with available design layouts.

Furthermore, the latest UAV technologies allow the elaboration of 3D models of the emerged structure, and of the entire breakwater in combination with underwater surveys. From the analysis of such data, the study of the armor layer slope is possible, to quantify differences from the original design but also of spatial variability along the entire breakwater. In this context, the definition of a monitoring plan based on UAV surveys appears as useful tool for the optimal maintenance of existing harbor rubble mound breakwaters.

3.2.2   Statistical definition of hydrodynamic conditions

The traditional approaches for the design of coastal defense structure are based on the definition of design mean sea level and wave characteristics, through the application of statistical techniques under the hypothesis of stationarity of the natural processes. In particular, the so-called design wave height correspondent to a certain return period is calculated, which is the main representative of the external load acting on coastal structure.

However, due to the stochastic nature of the variables involved in the natural processes of interest, i.e. wave motion generation and propagation, approaches aimed to the definition of the probability density functions of such variables instead of specific values relative to certain return periods appears more suitable, above all for the inclusion into the calculations of the probabilistic design. This is even more true if the effects of climate change are considered, which cause the increment of the uncertainty level in the definition of the hydrodynamic conditions.

In such a context, the preliminary trend analysis of historical time series of sea level and wave descriptors relative to the site of interest can be useful for the comprehension of the processes that caused the actual deterioration state of the breakwater, but also to get an insight into the possible future climate pathways.

To this aim, the results of climate models can be used for the estimation of future sea level and wave climate under different greenhouse gas emission scenarios, even with great caution. Indeed, as already described in section 2.4, future climate projections are affected by high uncertainty. In order to limit the impact of such an uncertainty on the design of coastal defense structures, the time series provided by the climate models can be used not as direct input for the probabilistic calculations, but for the modification of the measured data relative to the present climate through, the evaluation of the so-called factors of change (Peres and Cancelliere, 2018; Fatichi et al., 2011; Kilsby et al., 2007). Given a certain variable of interest, the factor of change technique consists in the assessment of the differences between the statistical moments of the modeled present and future time series, for the calculation of corrective factors to be applies to the measured present statistical moments. Afterward, the probability density function of the hydrodynamic conditions descriptors can be evaluated through the method of moments estimators (MME), and then used as input of the probabilistic calculations for the design of the structure.

In the present work, the described approach has been applied for the Italian Seas, with reference to the wave climate. Instead, as regards the mean sea level, the results of existing studies have been considered and critically analyzed.

3.2.3   Composite modeling of upgraded structures

The traditional design of coastal defense structures is based on the use of state of art empirical formulas for the definition of geometry and materials able to withstand the design external load. However, when dealing with particularly complex

or unconventional structures, as in the case of upgraded rubble mound breakwaters, physical model tests should be performed. Due to the development in recent years of increasingly accurate and computationally cost-effective numerical models, the latter are often used as a complementary tool to improve the comprehension of the complex processes that govern the interaction between waves and structure, thus giving further indication for its design. The integration and combination of physical and numerical models to analyze complex hydraulic problems is known in the literature as composite modeling (Oumeraci, 1999; Di Lauro et al., 2019; Kamphuis, 2020) or hybrid modeling (Guanche et al., 2015). Such an approach allows to overcome the lack of specific formulations for upgraded structures and also the intrinsic limits of physical modeling (e.g. scale effects, too invasive measurement instruments, difficulties in the repeatability of the tests).

In the present work, the analysis of the response of upgraded structures to the wave action has been carried out by combining two-dimensional model scale experiments with numerical simulations based on the VARANS equations. The case study of the Catania harbor breakwater has been considered for the investigation on the behavior of upgrading solutions, based on the heightening of the wave wall and on the addition of extra armor units equal or smaller than the existing ones, placed over the existing structure according to different paths.

The experiments have been conducted following the indication of Frostick et al. (2011) for the construction of the physical model and the definition of the test program. The analysis of the damage suffered by the armor layer under increasing wave load has been carried out, considering both traditional and novel techniques for the monitoring of the armor units displacements. The results have been compared with state of art formulas and a specific damage progression formula for the Catania harbor breakwater has been defined. In particular, the modifications of the armor layer surface roughness due to wave attack were studied through a Structure from Motion (SfM) based technique, whose applicability to the prototype scale has been also investigated. Finally, the overtopping phenomena has been analyzed, focusing on the comparative analysis of the possible upgrading solutions.

The numerical model IH2VOF has been properly calibrated using the experimental data on reflection and overtopping phenomena. Then, simulations for the comparison between mean overtopping dishcarge at laboratory and prototype scale have been carried out. Moreover, several simulations for the construction of a considerable data-set on mean overtopping discharge have been run, in order to define specific empirical formulas for the Catania harbor breakwater.

3.2.4 Evaluation of the probability of failure upgraded structures

Rubble mound breakwaters can experience different failure modes, which can be linked to the armor layer and toe berm stability, the overtopping volumes, the resistance of the wave wall or the soil solidity (see Figure 2.2). The comparison between

the probability of failure of different upgrading solutions could be a useful tool for the selection of the most appropriate options for the considered structure.

As described in section 2.2, the evaluation of the probability of failure, i.e. of reaching a certain limit state, can be assessed in terms of probability that the reliability function of the selected failure mode assumes non-positive values. Such a reliability function can be derived from state of art equation or case-specific formulas adapted on experimental or numerical data-sets. In the present work, a level III method based on Monte Carlo simulation have been selected for the calculation of the probability of failure of upgraded structures. A huge number of realizations of the structure life cycle is simulated, through the random draw of input variables contained in the considered reliability functions, namely sea levels and wave characteristics, geometry and material parameters and empirical coefficients. Such random values are generated from their probability density functions, which have been previously defined through statistical techniques or, in some cases, empirical evidences. Moreover, the dependency between variables, which is typical of the hydrodynamic descriptors, is modeled through the definition of site-specific empirical law. Then, the probability of failure related to each considered mechanisms is calculated as the ratio between the number of life cycle which experienced at least one failure and the total number of realizations.

The probabilistic assessment of the performances of different upgrading solutions for the Catania harbor breakwater has been carried out, considering the ULS due to the collapse of the outer armor layer, and the SLS due to excessive mean overtopping discharge, assuming that the two failure modes are related in a series system. The indications of Puertos del Estado (2010) have been followed for the definition of the acceptable probability of failure for both ULS ans SLS, whereas the limits proposed by CIRIA et al. (2007) and EurOtop (2018) for armor layer damage and mean overtopping discharge respectively have been employed. Reliability functions derived from both state of art and site-specific formulas adapted to the results of the composite modeling have been employed (see section 3.2.3), in order to assess the effect of using specific design formulations. In addition, both present and projected future climate coming from the analysis described in section 3.2.2, has been used for the generation of random sea levels and wave characteristics, in order to investigate on the effects of climate change on the probability of failure of the upgraded Catania harbor breakwater.

3.3   The case study of the Catania harbor breakwater

The proposed methodology for the design of upgrading solutions for aging rubble mound structures has been applied to the emblematic case study of the Catania harbor breakwater. In the following, the history of the Catania harbor breakwater is briefly described. Moreover, the main problems which nowadays affect the port

activities are presented, together with the possible upgrading solutions defined in cooperation with the local Port Authority.

3.3.1   History of the Catania harbor breakwater

The Port of Catania is situated on the East coast of Sicily, in a barycentric position between the Suez Channel and the Strait of Gibraltar, and between the European and the North-African ports (see Figure 3.1). Such a strategic position makes the Port of Catania one of the Italian commercial ports of national interest. At present, the harbor basin is mainly protected by the 2.25 km long outer breakwater, known as "Levante" breakwater, whose structure has been modified several times during its lifetime.

The first information about its existence dates back to the XVII century. Indeed, after the extreme sea storm of 1601, which destroyed the first port of Catania, the new harbor defense structure began to be built exactly at the location presently occupied by the Catania harbor breakwater (see Figure 3.2a). As a result of continuous failures of the breakwater, in the XVIII century the Bourbon government funded the construction of a composite defense structure, which consisted in a vertical wall made up of 330 t cyclopean blocks constructed over a rubble mound structure (Franco, 1994; Oumeraci, 1994; Takahashi, 2002).

During the XIX century, the breakwater was lengthened up to 258 m (see Figure 3.2b). However, the composite breakwater failed during construction between 1930 to 1931, because of the lack of horizontal connectivity between adjacent layers. Since no specific measures for the upgrade of the monolithic behavior of the structure were implemented, in 1933 the breakwater failed again (Franco, 1994; Oumeraci,
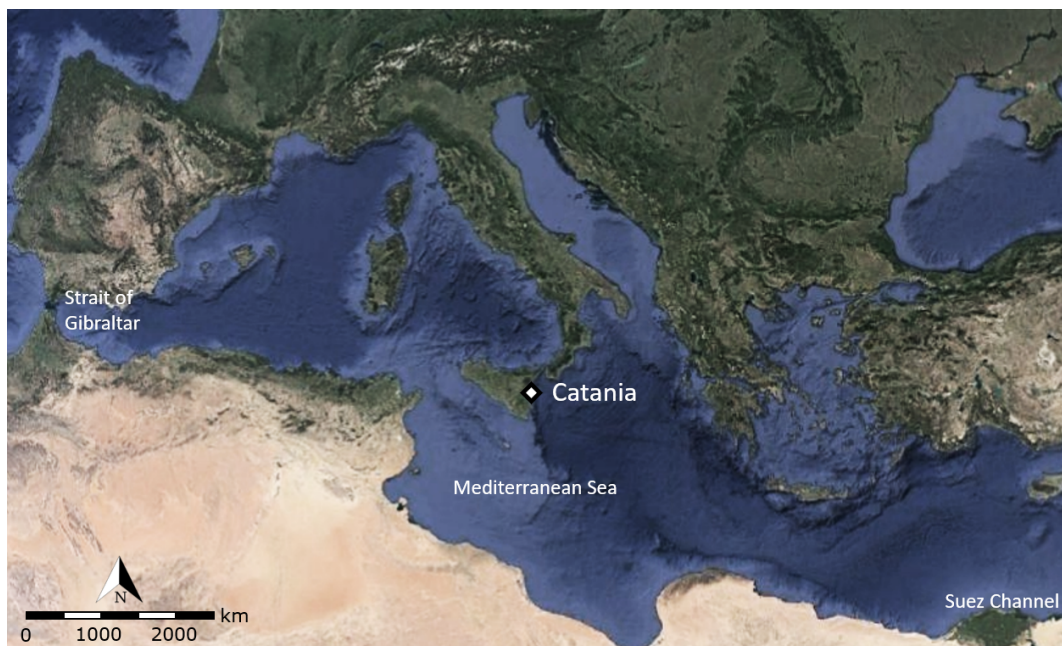
FIGURE 3.1 Location of the Port of Catania (adapted from Google Earth).

(a)

(b)
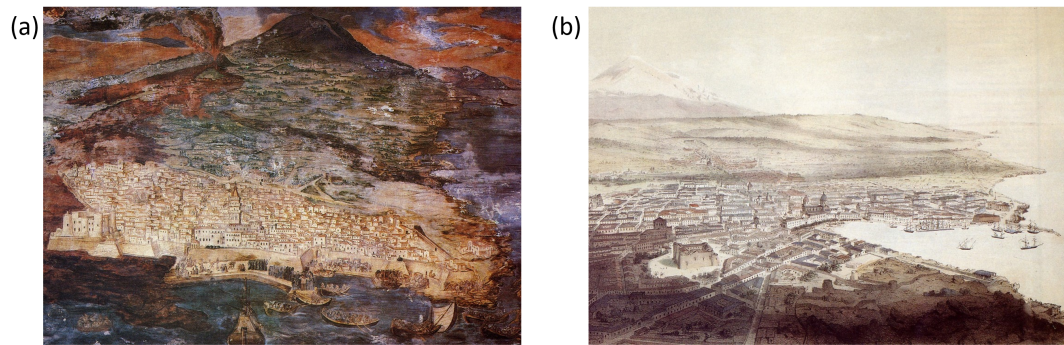
FIGURE 3.2 Historical representation of the Port of Catania in (a) 1669 and (b) 1849 (courtesy of Riccardo Lentini).

FIGURE 3.3 Satellite view of the present Port of Catania (adapted from Google Earth).

1994; Allsop et al., 1997; Takahashi, 2002). The structure was subsequently rehabilitated as a rubble mound breakwater with 62 t cubic armor units, and it has been progressively extended until the present 2.25 km length, whose last 300.00 m were built in the years 2000, together with the temporary head (see Figure 3.3).

3.3.2   Actual state and functionality problems of the Catania harbor breakwater

Currently, the Catania harbor breakwater appears severely damaged by extreme sea storms, and the armor layer made up of 62 t cubic concrete units shows evidence of degradation and structural failures both under and above the mean sea level.

FIGURE 3.4 Overtopping discharge over the Catania harbor breakwater caused by the extreme marine event occurred in February 2019. Source: newspaper *La Sicilia* of 5th July 2021.

A strong reduction of the seaside slope and significant narrowing of the cross sections is observed, because of armor blocks off-shore slip. Nowadays, extreme marine events occurred during the Catania harbor breakwater lifetime not only cause structural deterioration, but also produce significant overtopping discharges that result in severe limitation to the port activities (Figure 3.4). In particular, significant damage to equipment and prefabricated buildings located in the vicinity of the harbor breakwater have been provoked. Moreover, the violent flows produced by the overtopping discharges have flooded the service areas, thus generating evident pavement potholes.

As mentioned, the Port of Catania plays a fundamental role for the maritime trades between North Africa and Europe. However, the growing demand of port services can be satisfied only if the weakness of the actual harbor layout are overcome. In this context, a good strategy for the development of the potentialities of the port cannot be separated from the rehabilitation and upgrade of the harbor breakwater.

3.3.3 Upgrading of the Catania harbor breakwater

Among the possible upgrading options for the Catania harbor breakwater, the addition of extra armor blocks should be considered, because of the deterioration state of the actual armor layer. Moreover, the wave wall should be risen to further improve the hydraulic performances of the structure. However, the design of upgrading solutions involves four main difficult tasks: i) choice of the height of the wave wall; ii) choice of size and shape of the additional armor units; iii) evaluation of the necessity to regularize the existing armor layer before adding the extra units; iv) evaluation of the necessity to provide a toe berm. In the following, a total of six upgrading

options are compared, highlighting their weakness and strengths in the light of the above mentioned issues.

The analysis of the effects of the wave wall height on the reduction of the overtopping discharge can give useful indications for the choice of the most appropriate solutions. Therefore, the simple raising up to +8.50 m and +9.50 m above MSL of the wave wall without addition of extra armor units (respectively configuration E and EM, see Figure 3.5) has been considered in the present work.

In the absence of guidelines and indications, the local Port Authority proposed the so called configuration AS, which consists in the addition of 30 t Antifer blocks over the existing armor layer, following the 1:2 design slope (see Figure 3.6a). A quarry stone toe berm is designed to support the extra armor layer, whereas the wave wall crest is raised up to +8.50 m above MSL to reduce the overtopping discharge. Since some of the 62 t existing cubes have been already displaced by past sea storms, the choice of half weighting blocks could appear questionable. However, the use of smaller units allows to fill the voids of the existing armor layer, thus avoiding technically and economically expensive operations for its reshape. It is worth to point out that the geometric irregularities of the existing armor layer make impossible the uniform distribution of the additional armor units according to a regular design slope. Therefore, the additional armor layer can have different thickness in the same cross section, and also along the entire breakwater. The physical consequence of the non-uniform placements of the armor blocks is the impossibility to predict a homogeneous response of the structure to the external wave load. Another critical issue is represented by the toe berm. Indeed, it is designed to ensure a coherent cross section along the entire breakwater, and this not always ensures support to the additional armor units. For instance, the toe berm gives support to the extra armor layer in the case represented in Figure 3.7a, but not in the case showed in Figure 3.7b.

A variant to configuration AS consists in placing a homogeneous double layer of 30 t Antifer blocks over the existing structure (configuration AD, see Figure 3.6b), in order to guarantee a more uniform behavior of the breakwater. However, the problems related to the likely too low weight of the additional units and to the possible inadequate toe berm remain.
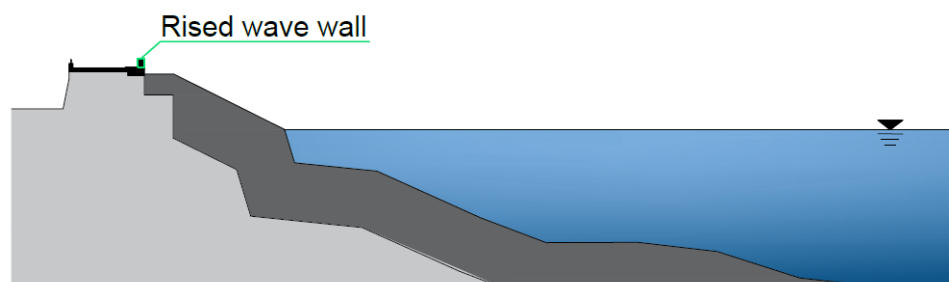
FIGURE 3.5 Upgrading concepts considered for the Catania harbor breakwater: rising of the wave wall.
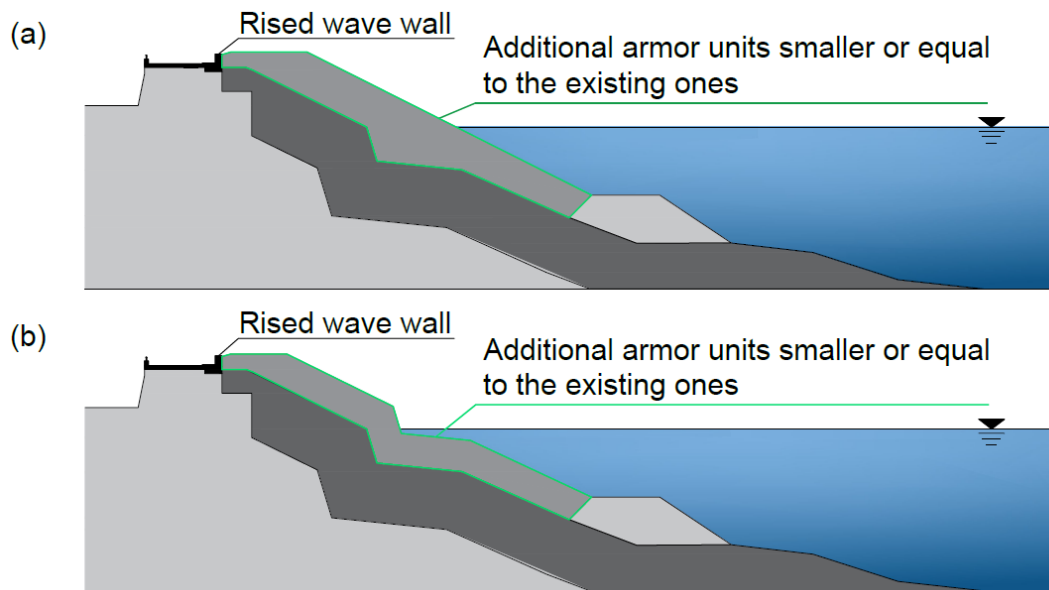
FIGURE 3.6 Upgrading concepts considered for the Catania harbor breakwater: (a) rising of the wave wall and addition of an extra armor layer over the existing one according to a regular design slope; (b) rising of the wave wall and addition of an extra armor layer over the existing one according to a uniform placement method.
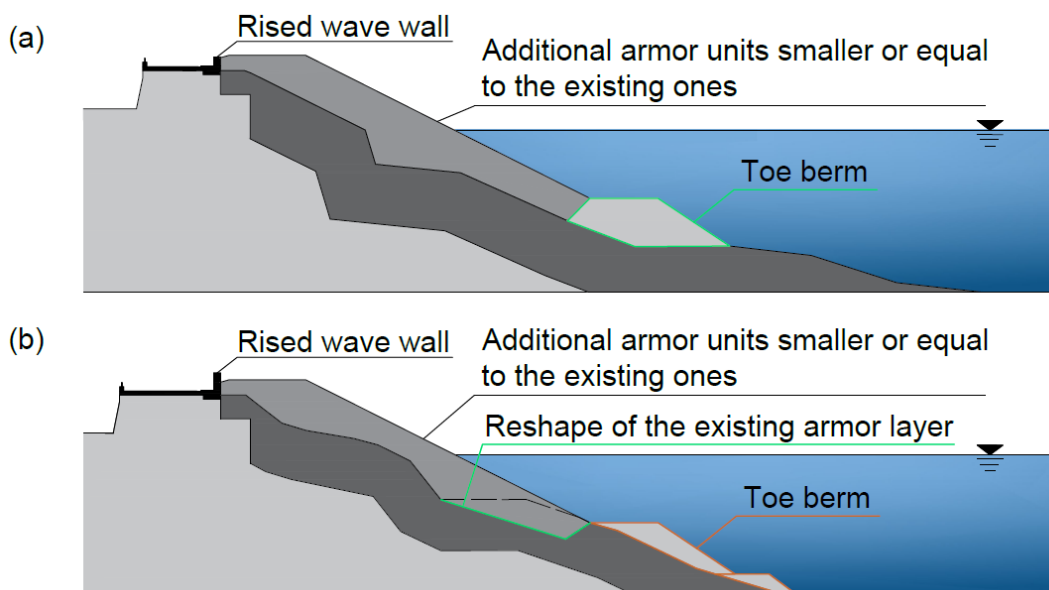
FIGURE 3.7 Upgrading concepts considered for the Catania harbor breakwater: (a) rising of the wave wall and addition of an extra armor layer supported by a toe berm; (b) rising of the wave wall and addition of an extra armor layer, after the regularization of the existing one to ensure a proper toe support and an almost uniform placement of the units.

Configuration CM allows to overcome the issue related to the weight of additional units and to their homogeneous placement, by considering a single layer of cubic blocks equal to the existing ones over the damaged structure (see Figure 3.6b). Nevertheless, a proper support at the toe of the additional units may be not always guaranteed.

Finally, configuration CS solves the issue related to the weight of additional units, their uniform placement and support at the toe. Indeed, such a solutions involves the preliminary regularization of the existing armor layer, by moving the existing blocks where necessary. Then, the 62 t cubic blocks equal to the existing ones are almost uniformly placed over the regularized surface, according to the design section with a 1:2 slope of configuration AS. The support at the toe of the extra armor layer is ensured by the quarry stone toe berm where possible (see Figure 3.7a), otherwise by the properly reshaped existing armor layer (see Figure 3.7b). The wave wall crest is raised up to +9.50 m above MSL to further reduce the overtopping rates.

Chapter 4

Assessment of the current state of rubble mound breakwaters

4.1 Overview

The displacement of the armor blocks due to the wave action causes the reshape and even the damage of the armor layer of rubble mound breakwaters, which can be assessed in terms of both "shoreline" advancement or retreat and mean armor layer slope variation compared to the design one. Traditional monitoring of the emerged part of rubble mound breakwaters based on visual inspections and topographic techniques have some weaknesses, mainly linked to physical restrictions, long time, and high costs for the accurate measurement of highly irregular armor layer surfaces (Drummond et al., 2015; González-Jorge et al., 2016; Henriques et al., 2017). In addition, the sparse data coverage of in situ topographic surveys can lead to significant interpolation errors, and hence to low-resolution reconstructions of the armor layer surface (Drummond et al., 2015).

In the present chapter, the proposed methodology for the evaluation of the state of deterioration of existing harbor rubble mound breakwaters is described, whose outcomes could help to address the choice of the most adequate upgrading solutions. Such a methodology allows the study of the emerged structure time evolution by using georeferenced data (i.e. ortophotos and 3D point clouds) acquired during its lifetime, together with information about the original design if available, thus avoiding the performance of complex topographic surveys.

The assessment of the current state of the Catania harbor breakwater has been carried out by applying the proposed methodology. The ortophoto and the 3D point cloud coming from an Unmanned Aerial Vehicle (UAV) survey performed in 2020 and the orthophoto provided by the Sicilian Regional Territorial Information System for the years 2000, 2007, 2012 have been employed. The diachronic analysis of the breakwater "shoreline" highlighted that during the years 2000-2020 the Catania harbor breakwater was subjected to a general reshaping process, in some cases implying the removal of armor blocks. In addition, the analysis of the deviation of the emerged armor slope from the design one has showed a reduction of the mean sea side slope of about 28%, also pointing out the existence of different damage modes.

Some visual inspections have been performed, which however did not give detailed information about the overall evolution of the Catania harbor breakwater. Indeed, visual inspections are useful for localized studies concerning the integrity of the armor units, which are out of the scopes of the work.

The results of the assessment of the current state of the Catania harbor breakwater have given useful indications for the preliminary analysis of the possible upgrading solutions. In particular, since some of the existing 62 t cubes had been removed by past extreme sea storms, the use of units lighter than the existing cubes for the armor layer restoration must be carefully evaluated. Moreover, the uniform response of the upgraded structure can be ensured only by taking into account the peculiarities of each segment of the breakwater.

4.2   Methodology for the assessment of the current state of rubble mound breakwaters

4.2.1   Time displacement of the breakwater "shoreline"

The analysis of the modifications of the breakwater "shoreline" during its lifetime can be a useful tool for the comprehension of the armor units dynamics due to wave action. Georeferenced data, such as orthophoto and point clouds, referring to different years of the structure lifetime are needed, in order to monitor the advancement or retreat of the breakwater "shoreline". The actual UAV technologies facilitate the acquisition of such kind of data, ensuring sufficient accuracy for the scope, without calibration or validation procedures, and at relatively low cost (Drummond et al., 2015; González-Jorge et al., 2016; Henriques et al., 2017).

The identification of the breakwater "shoreline" from a generic ortophoto can be performed through any commercial or open source GIS software. Due to the usually limited length of rubble mound breakwaters, the "shoreline" can be manually drawn as a vectorial layer. Alternatively, the extrapolation of the breakwater "shoreline" from a generic point cloud can be carried out by automatic image analysis by detecting the boundary of the studied object. Indeed, the manual tracing of a vectorial layer over a point cloud is technically to onerous, above all if a good accuracy is required.

It is worth to underline that point clouds are hardly available over the breakwater lifetime, being the UAV technology rather recent. Therefore, the analysis of the "shoreline" variation of historic rubble mound breakwaters can be usually performed using orthophoto. However, a monitoring plan based on UAV survey could be defined for future analysis of the breakwater state (Fortes et al., 2020; González-Jorge et al., 2016).

As showed in Figure 4.1, the time analysis of the "shoreline" movements is generally carried out with respect to a reference period line, which can be the design one if available. Therefore, for each considered year the variance of the "shoreline"
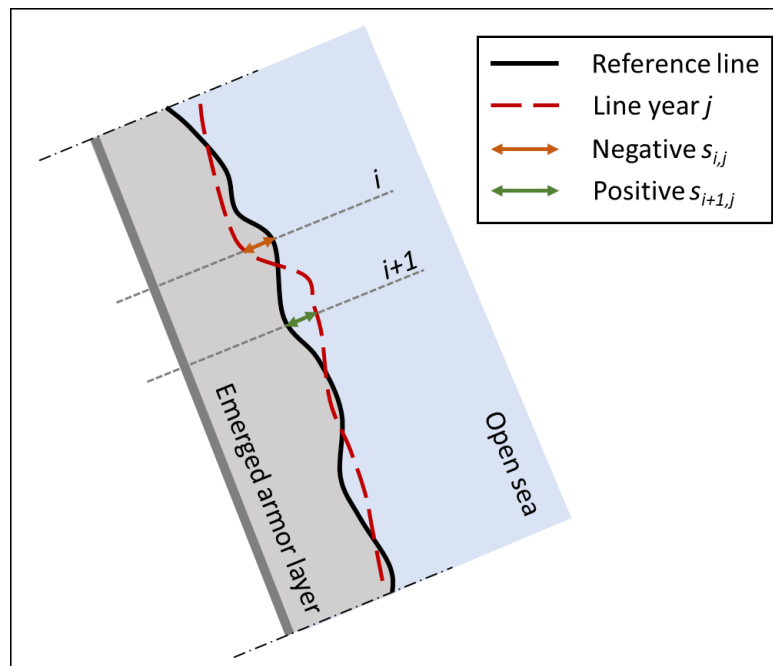
FIGURE 4.1 Sketch of the calculation of breakwater "shoreline" displacement according to the proposed methodology.

from the reference one is evaluated for a certain number of sections, according to the following equation:

$$s_{i,j} = Pos_{i,j} - Pos_{i,0} \qquad (4.1)$$

where $s_{i,j}$ is the displacement of the $i - th$ cross section of breakwater referred to the $j - th$ year, and $Pos_{i,j}$ and $Pos_{i,0}$ are the positions of the $i - th$ cross section respectively in the $j - th$ and reference year. If $s_{i,j}$ is positive, the advancement of the breakwater "shoreline" has occurred in the $i - th$ cross section, otherwise the retreat has taken place (see Figure 4.1).

It is important to point out that the reliability of such a kind of measurement is influenced by the quality of the employed data. In addition, the dynamics nature of the "shoreline" must be taken into account, together with the effects of tides.

The measured positive or negative displacements (i.e. respectively advancement and retreat) must be compared to the armor units dimension, in order to correctly interpret the blocks dynamics and also to quantify the structure damage level. The "shoreline" advancement is indicative of a damage mechanism which causes the armor layer sliding towards the open sea, with a flattening of the sea side slope. Instead, the "shoreline" retreat corresponds to the removal of the emerged units from their initial position.

4.2.2 Time variation of the mean armor slope

The mean sea side slope of a generic rubble mound breakwater can be calculated for specific cross sections from point cloud data, coming from both aerial or underwater
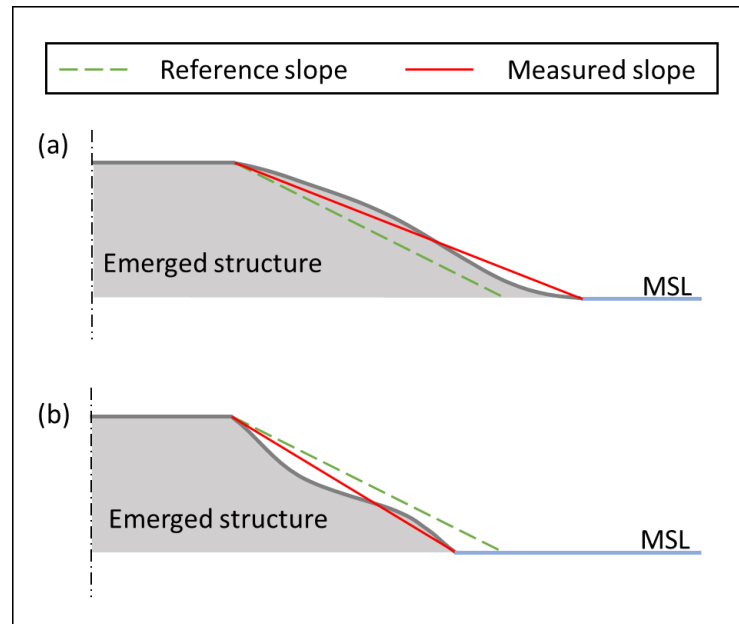
FIGURE 4.2 Sketch of the possible variation of the mean sea side slope of the emerged part of a rubble mound breakwater: (a) reduction of the slope; (b) increase of the slope.

surveys, respectively for the emerged and submerged structure. As stated in section 4.2.1, point clouds are usually not available for different years of the breakwater lifetime, and hence the only reference for possible comparisons with the current state is the design slope if available.

The extrapolation of the mean armor layer slope from point clouds can be performed following a simple procedure, which can be implemented through photogrammetric softwares in combination with common programming and numeric computing platforms. In particular, in the present work, the programming and numeric computing platform *MATLAB* has been chosen, for its simple programming language and the availability of useful functions for the elaboration of point clouds and meshes. First, an appropriate down-sampling of the data is performed, in order to optimize the following computations in terms of both quality of the results and processing time. The choice of the down-sampling level should be empirically defined, by means of the comparison of results coming from differently down-sampled point clouds. Then, the 3D reconstruction of the armor layer is created, thanks to a triangulation-based linear interpolation technique for the calculation of meshes, to be applied to a uniform square grid. It should be noted that a grid step equal to 10% of the armor units diameter seems appropriate to represent the considered rubble mound structure. The generated mesh is properly referenced, by setting the origin of the heights in correspondence of the mean sea level. Finally, the breakwater cross sections of interest are extracted from the previously calculated mesh, and the mean armor layer slope is easily estimated from the linear approximation of the cross profiles. Figure 4.2 schematically shows the possible variations of the mean armor layer slope with respect to a reference slope. The slope reduction means that some blocks have slid towards the open sea. Instead, the slope increase can be explained as a

consequence of armor units removal, which produce the steepening of the armor layer.

It is worth to point out that a comprehensive analysis of the armor slope requires the availability of both aerial and underwater data collected in the same periods. Otherwise, only partial evaluation can be carried out, focusing only on the emerged or submerged structure. Unfortunately, underwater detailed survey of the armor layer are rare and costly.

4.3 Field data on the Catania harbor breakwater

Prior authorization of the local Port Authority, in February 2020 an UAV survey was performed over the Catania harbor breakwater, in order to collect data regarding the actual state of the structure in terms of armor "shoreline" and emerged slope.

The employed drone was a DJI Phantom 4 advanced, which is a 1.4 kg quadcopter, whose uprated camera is equipped with a 1-inch 20-megapixel sensor. The flight autonomy system includes five vision sensors, dual-band satellite positioning (GPS and GLONASS), ultrasonic rangefinders, and redundant sensors.

The elaboration through the Structure from Motion (SfM) technique of the frames acquired by the drone produced a dense 3D point cloud (resolution equal to 1940 points/m^2) and an ortophoto (resolution equal to 34.5 pixel/m) of the area of interest, both in WGS84/UTM zone 33N (EPSG: 32633) geographic coordinates. The point cloud consists of 299,677,460 points, and corresponds to the whole harbor breakwater, also including docks (see Figure 4.3a). Since the present analysis focuses on the sea side armor layer, the study region has been isolated, thus defining an area made of 192,557,211 points (see Figure 4.3b).

The data acquired from UAV survey have allowed to evaluate the current state of the breakwater, but not its time evolution. Therefore, the orthophoto provided by the Sicilian Regional Territorial Information System have been also employed. In particular, the following orthophoto are available:

FIGURE 4.3 Point cloud of the Catania harbor breakwater produced from UAV survey of February 2020 (coordinate system WGS84/UTM zone 33N, EPSG: 32633, resolution equal to 1940 points/m^2): a) whole point cloud (299,677,460 points); b) point cloud of the region of interest (192,557,211 points).
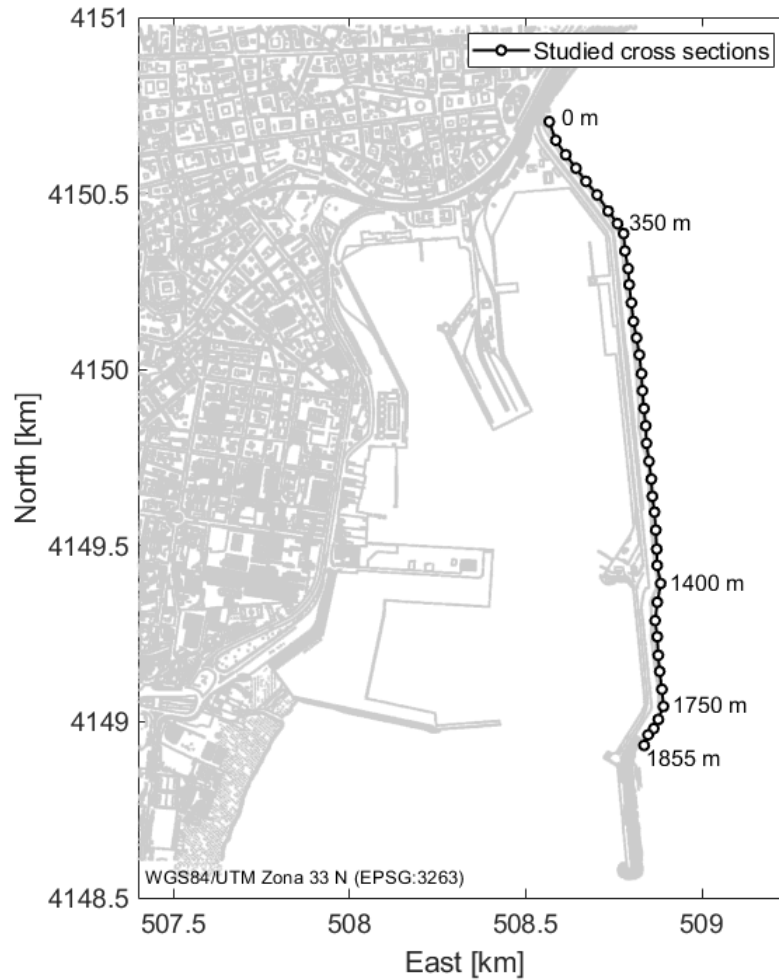
FIGURE 4.4 Layout of the Port of Catania and indication of the cross sections of the harbor breakwater considered in the present work. The progressive distance of some reference cross section is also displayed.

- year 2000, in coordinate system WGS84/UTM zone 33N (EPSG:32633), with resolution equal to 1.0 pixel/m;

- year 2007, in coordinate system WGS84/UTM zone 33N (EPSG:32633), with resolution equal to 4.0 pixel/m;

- year 2012, in coordinate system WGS84/UTM zone 33N (EPSG:32633), with resolution equal to 4.0 pixel/m.

The procedures described in sections 4.2.1 and 4.2.2 have been applied for the evaluation of the current state of the Catania harbor breakwater, considering 40 cross sections spaced of 50 m, as indicated in Figure 4.4. Since the portion of the Catania harbor breakwater beyond the progressive distance 1855 km was added in the period 2000-2007, this last segment has not been analyzed. It is worth to point out that the analysis of the mean armor layer slope could be performed only for the emerged

structure, due to the unavailability of underwater data. Some visual inspections have been also performed, which however did not give further information about the time evolution of the Catania harbor breakwater. Indeed, such a kind of field survey is useful for localized studies concerning the structural integrity of the armor blocks, which have not been investigated in the present work.

4.4 Current state of the Catania harbor breakwater

4.4.1 Diachronic analysis of the breakwater "shoreline"

The variation of the Catania harbor breakwater "shoreline" has been evaluated for the years 2007, 2012 and 2020 with respect to the reference year 2000, considering the 40 cross sections showed in Figure 4.4 for the calculation of advancements and retreats. Attempts have been made to find the design layout of the breakwater, but unfortunately it could not be obtained. Therefore, a comparison between the actual structure and the design one could not be performed.

The bar plots in Figure 4.5 show the advancements (i.e. positive displacements) and retreats (i.e. negative displacements) of the breakwater "shoreline" for years 2007, 2012 and 2020 with respect to year 2000. The error bars indicate the uncertainty due to the effects of the astronomical and meteorological tides, which can produce a maximum excursion equal to 0.46 m, and hence a maximum error in the estimation of s equal to the double of such value (i.e. 0.92 m).

Most of the "shoreline" variations occurred during the period 2000-2007 (see Figure 4.5a) corresponds to displacements lower than the armor units dimension. Therefore, a reshaping process without blocks removal likely happened for about 78% of the considered cross sections. In addition, for the central segment between 400 m and 1550 m a general retreat of the "shoreline" is observed. On the contrary, the most onshore and offshore parts of the structure suffered a general advancement of the "shoreline".

Figure 4.5b shows that also in 2012 great part of the "shoreline" displacements (again about 78%) with respect to year 2000 is less than the median nominal diameter (D_{n50}) of the armor blocks, and hence the reshaping process without blocks removal hypothesized for the period 2000-2007 likely continued until 2012. In this case, a clear spatial distribution of retreat and advancements cannot be identified. The comparison between Figure 4.5a and Figure 4.5b highlights that the generic cross section could have experienced retreat during the period 2000-2007, but a final total advancement in 2012, and vice versa. In addition, even if the displacements of the cross section with respect to year 2000 are of the same sign in both 2007 and 2012, the latter could be lower than the first one, thus implying that the armor units movements did not maintain the same direction during the whole period 2000-2012. Therefore, a time invariant scheme of the direction of the armor blocks displacements cannot be identified.

The displacements of the breakwater "shoreline" registered in 2020 with respect to year 2000 are again lower than the armor blocks dimension for about 80% of the considered cross sections, as showed in Figure 4.5c. A clear spatial distribution of retreat and advancements as well as time invariant scheme of the direction of the armor blocks displacements is not observed.

Table 4.1 summarizes the results of the analysis on the variation of the breakwater "shoreline" with respect to year 2000. As expected, the mean "shoreline" displacements (s_{mean}) is less than the armor units dimension for the three considered period (i.e. 2000-2007, 2000-2012 and 2000-2020). Furthermore, during the years 2000-2007 a mean overall advancement of the "shoreline" occurred, whereas in 2012 and 2020
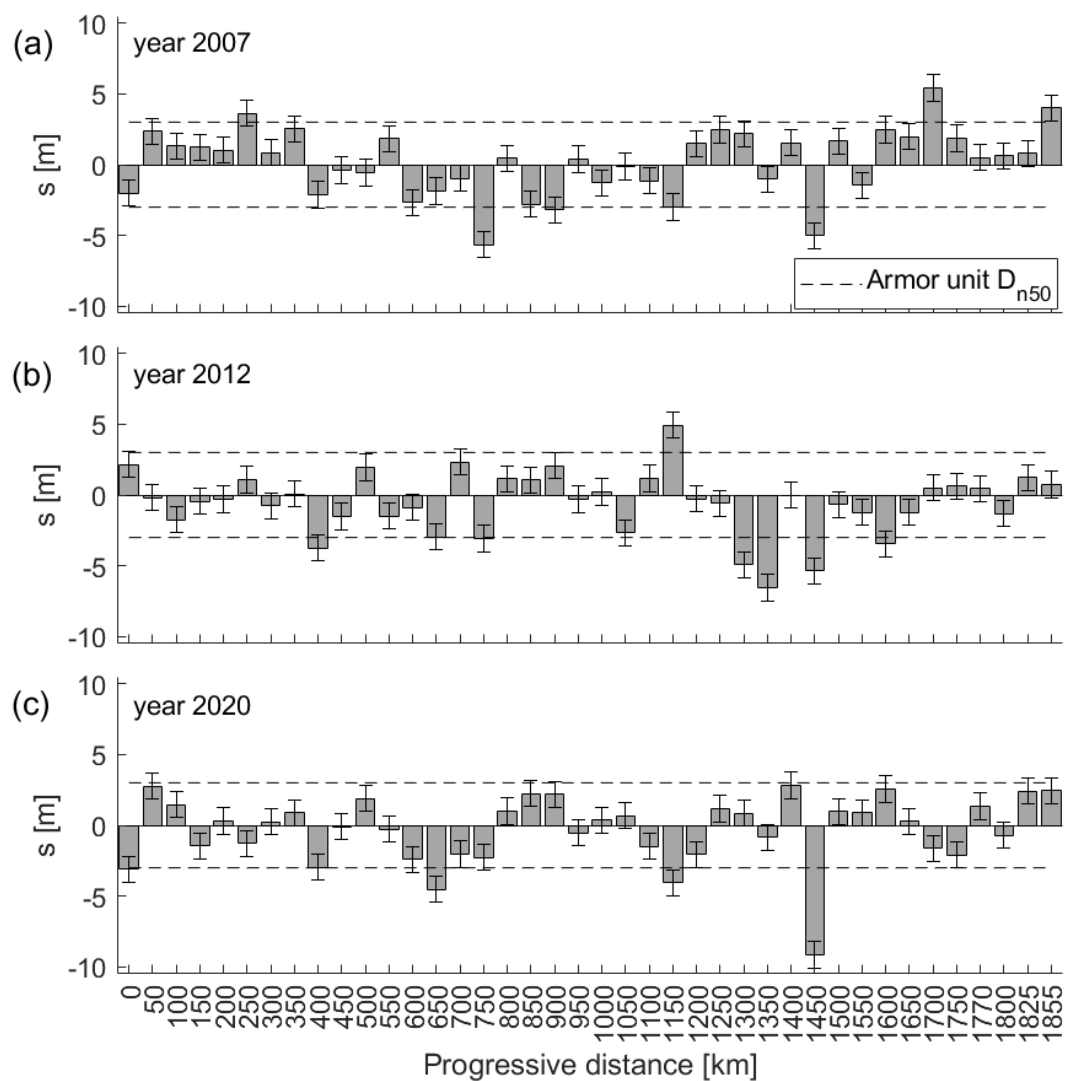
FIGURE 4.5 Variation in time of the Catania harbor breakwater "shoreline" with respect to year 2000: (a) year 2007; (b) year 2012; (c) year 2020. Positive and negative displacements respectively correspond to advancements and retreats. The error bars represent the uncertainty of the measurement due to the combination of astronomical and meteorological tides.

TABLE 4.1 Mean variance (s_{mean}), maximum advancement (s_{max}^+) and maximum retreat (s_{max}^-) of the "shoreline" of the Catania harbor breakwater with respect to the reference year 2000. The value ± 0.46 represents the uncertainty of the measurement due to the combination of astronomical and meteorological tides.

Year	s_{mean} [m]	s_{max}^+ [m]	s_{max}^- [m]
2007	0.19 ± 0.46	5.42 ± 0.46	-5.65 ± 0.46
2012	-0.60 ± 0.46	4.93 ± 0.46	-6.56 ± 0.46
2020	-0.33 ± 0.46	2.83 ± 0.46	-9.15 ± 0.46

a mean overall retreat was registered. Such a result is in agreement with the previously highlighted impossibility to detect a time invariant scheme of the direction of the armor blocks displacements. As regards the maximum advancement of the breakwater "shoreline" (s_{max}^+), it is always greater than the armor blocks D_{n50}, if the range of uncertainty due to he combination of astronomical and meteorological tides (i.e. $\pm 0.92m$) is considered. In particular, for the years 2007 and 2013 s_{max}^+ is about $1.5 \div 2.0$ times the D_{n50} of the armor units, whereas for the year 2020 s_{max}^+ is about $0.8 \div 1.1$ times the D_{n50}. The maximum retreat of the breakwater "shoreline" (s_{max}^-) is similar to s_{max}^+ for the years 2007 and 2012. Instead, for the year 2020 s_{max}^- is about $2.9 \div 3.2$ times the D_{n50} of the armor blocks.

To conclude, during the years 2000-2020 the Catania harbor breakwater was subjected to a reshaping process, which caused a mean "shoreline" retreat equal to 0.33 ± 0.92 m. Significant damage to the armor layer (i.e. retreat greater than D_{n50}) occurred in some cross sections (e.g. progressive distance 1150 m and 1450 m), with removal of armor units. Therefore, the existing 62 t armor blocks in some cases were not able to withstand extreme sea storms occurred during the considered period. In this context, it is worth to point out that the impossibility to find the design breakwater layout or orthophoto previous to year 2000 forbade the quantification of the effective damage suffered by the structure during its entire lifetime.

4.4.2 Deviation of the emerged armor slope from the original design

The analysis of the sea side slope of the armor layer of the Catania harbor breakwater has been carried out considering only the emerged structure. Indeed, as stated in section 4.3, only the point cloud derived from an UAV survey performed in 2020 is available. Such a point cloud has been randomly down-sampled in order to obtain the 5% of the points, which has been demonstrated to ensure accurate results and significant reductions of the computational time. Then, the mesh of the emerged structure has been calculated, with a grid size of 0.30×0.30 m. Figure 4.6 shows the above mentioned mesh, giving an overall view of the entire breakwater and a detail of one of its portions. The evaluation of the mean slope of the armor layer has been performed for the 40 cross sections displayed in Figure 4.6a, which have been also studied in terms of variations of the breakwater "shoreline" (see section 4.4.1).
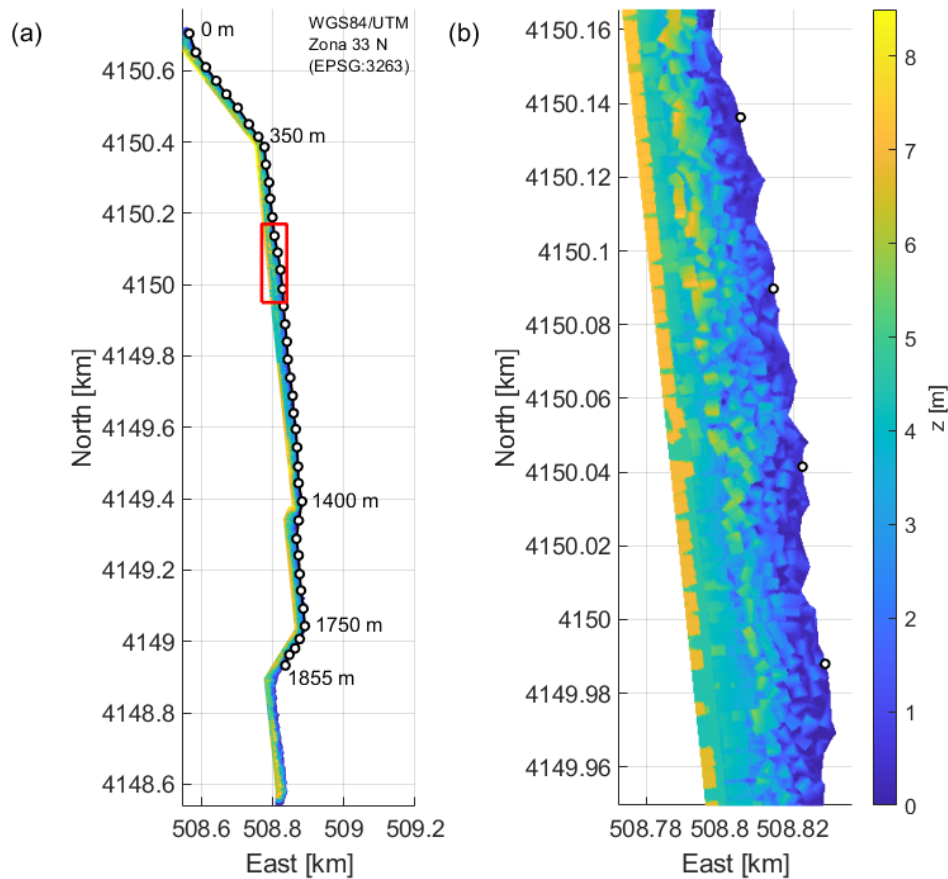
FIGURE 4.6 Mesh of the emerged Catania harbor breakwater (grid size 0.30x0.30 m): (a) whole breakwater and indication of the cross sections considered in the present work (the progressive distance of some reference cross section is also displayed); (b) close-up view of the red framed zone in (a).

The data referring to year 2020 are the only available ones, and hence the evaluated mean armor layer slope could not be compared to previous measurements. However, the schematic design cross section of the reinforced Catania harbor breakwater after the failure occurred in 1933 has been found in Takahashi (2002), where the emerged armor layer presents a 1:3 slope. It is recalled that the upgrade project of the Catania harbor breakwater involves a 1:2 slope of the whole armor layer (see section 3.3.3).

Figure 4.7 shows the mean armor layer slope evaluated for the 40 studied cross sections (see Figure 4.6). The measured mean armor layer slopes range between 0.11 and 0.36, but 70% of the cross sections presents mean slope lower than 0.28. Therefore, for great part of the breakwater a significant reduction with respect to the 1:3 (Takahashi, 2002) slope is observed.

The detailed analysis of the 40 studied cross sections highlighted that various modes of deviation from the 1:3 slope (Takahashi, 2002) can be identified. For instance, Figure 4.8 shows three cross sections characterized not only by different
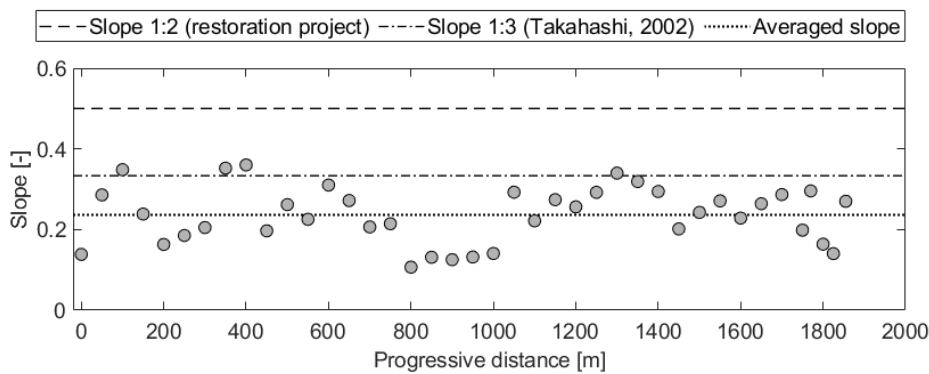
FIGURE 4.7 Mean armor layer slope of the Catania harbor breakwater derived from the elaboration of the point cloud acquired in February 2020 through UAV survey. The slopes calculated for 40 cross sections and the breakwater averaged slope are compared with the 1:3 design slope (Takahashi, 2002) and the 1:2 slope of the restoration project.
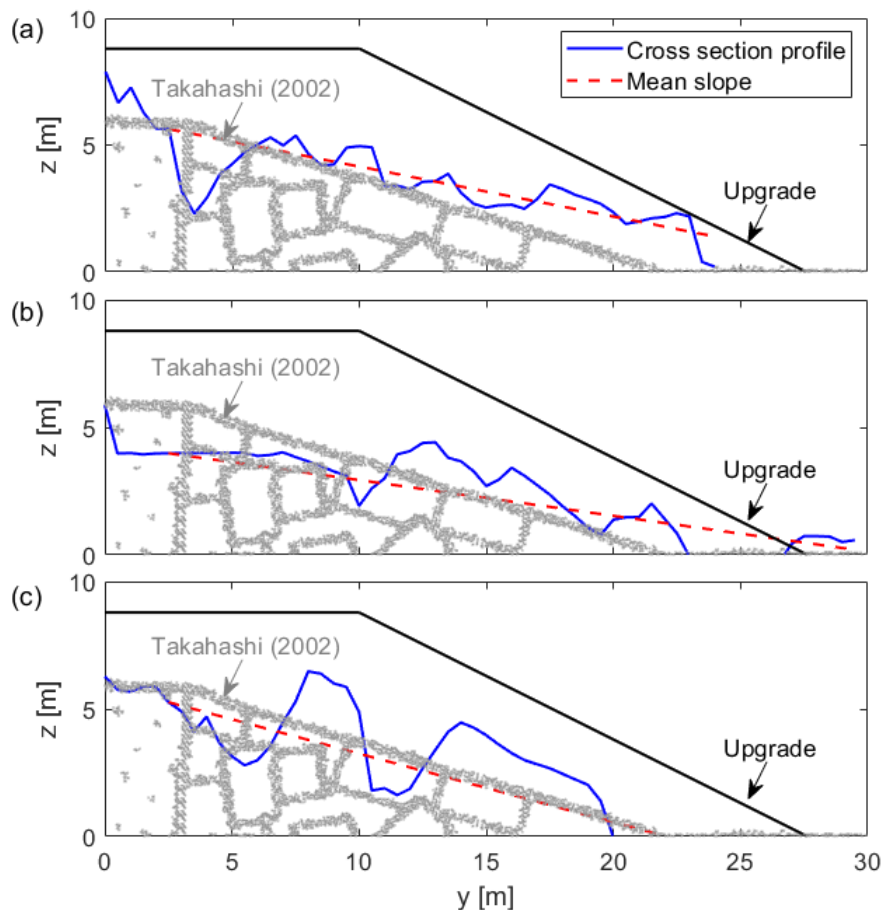
FIGURE 4.8 Cross sections of the emerged part of the Catania harbor breakwater derived from the elaboration of the point cloud acquired in February 2020 through UAV survey. Progressive distance:(a) 450 m; (b) 1000 m; (c) 1855 m.

mean slopes, but also by peculiar modes of deviation from the reference slope. The cross section at progressive distance 450 m (see Figure 4.8a) presents a mean sea side slope equal to 0.20, and the flattening of the armor layer is due to the displacement of the blocks in the lower part of the emerged armor layer. Instead, the cross section

at progressive distance 1000 m (see Figure 4.8b) reached a mean sea side slope equal to 0.14 because the units in the upper part of the structure slid towards the open sea. Finally, the cross section at progressive distance 1855 m (see Figure 4.8c) is characterized by the presence of evident voids along the profile, but a mean sea side slope close to 1:3 (Takahashi, 2002) is maintained.

Therefore, the analysis of the deviation of the emerged armor slope from the design one (Takahashi, 2002) brought out two main results. First, sea storms occurred during the Catania harbor breakwater lifetime produced on average a reduction of the mean sea side slope of about 28%. Secondly, the existence of different modes of deviation from the 1:3 slope (Takahashi, 2002) implies that any upgrade design for the Catania harbor breakwater should take into account the peculiarities of each of its parts, to ensure a uniform response of the upgraded structure.

Chapter 5

Long-term variation of hydrodynamic conditions in the Italian seas

5.1 Overview

The design of coastal defense structures requires information concerning not only the present hydrodynamic conditions of the site of interest, but also the expected future variations under the effects of climate change. Indeed, the design lifetime of a generic coastal defense structure is always at least 50 years, which is a sufficiently long period to observe the impacts of global warming. Among such impacts, sea level rise (SLR) and variation of wave motion characteristics are particularly interesting for the design of new harbor breakwaters or of upgrading solutions for existing ones.

Many studies on global and regional SLR have been conducted, which analyze past sea level data (e.g. tide gauges time series and historical satellite acquisitions) to detect possible trends, or provide modeled projections based on future scenarios. The same holds for the variation of wave climate characteristics, and the modification of extreme marine events in terms of frequency of occurrence and intensity.

The Mediterranean Sea is a mid-latitude, semi-enclosed and deep sea, whose dynamic regime is governed by the Strait of Gibraltar. Therefore, the hydrodynamic of such a basin cannot be adequately described by global scale models, but regional studies are needed. Some investigations on sea level and wave climate historical variations and future projections have been carried out, also focusing on specific areas of the basin (Lionello and Sanna, 2005; Martucci et al., 2010; Lambeck et al., 2011; Galassi and Spada, 2014; Pomaro et al., 2018; Caloiero et al., 2019; Vecchio et al., 2019). In the present chapter, the effects of climate change o the wave climate of the Italian Seas are investigated in detail. First, a review of existing studies on SLR has been conducted, considering the results of historical trend analysis, and also predictions coming from numerical climate models. Moreover, a long-term trend analysis of mean and extreme wave climate has been carried out, based on both measured and modeled historical time series relative to eight representative sites

along the Italian coast. The outcomes of such an analysis have been also compared to existing studies. Finally, the factor of change method (Kilsby et al., 2007; Fatichi et al., 2011; Peres and Cancelliere, 2018) has been applied for the statistical characterization of future extreme wave climate of the same eight Italian sites, based on the wave projections for the European coast provided by Copernicus Climate Change Service (2019), which refer to two future scenarios (i.e. period 2041-2100) corresponding to RCP4.5 and RCP8.5. The evaluation of the statistics of future extreme wave load is useful for the inclusion of the projected future modifications of hydrodynamic loads into the probabilistic design of new or upgraded coastal defense structures, which will be discussed in Chapter 7.

5.2 Sea level rise along the Italian coasts: literature review

5.2.1 Long-term trend analysis of sea level data

The detection of historical sea level trends is a useful tool for the comprehension of velocity and magnitude of past and present variations. It is important to underline that historical sea level change rates do not necessarily correspond to the expected future ones (Galassi and Spada, 2014). However, the integration of the results coming from historical trend analysis and numerical climate modeling allows the construction of an overall framework of sea level evolution. As regard the Italian Seas, few studies concerning the long-term trend detection in sea level data have been carried out. To this aim, it is worth to point out that the evaluation of sea level past long-term trends can be performed only if sufficiently long time series are available.

Cazenave et al. (2002) performed the analysis of monthly Revised Local Reference (RLR) gauge records from the Permanent Service for Mean Sea Level (PSMSL) in the Mediterranean Sea, in order to compare the results with the shorter trends detected from six years of satellite altimeter data. Nine of the considered coastal sites are located in Italy, namely Cagliari, Catania, Civitavecchia, Genova, Napoli, Palermo, Trieste, Venezia Arsenale and Venezia S.Stefano (see Figure 5.1). For each station, the monthly time series have been low-pass filtered, through the Fourier expansion of the original data set with a cutoff at the 2-year period for the removal of the seasonal signal. Then, the slope of the linear trend was evaluated by simply applying linear regression. It is important to underline that the period covered by individual records varies from station to station, from a minimum of 12 years (in Catania) to a maximum of 109 years (in Genova).

Also, Vecchio et al. (2019) carried out long-term analysis of monthly RLR gauge records longer than 60 years collected in the period 1888-2008 by the PSMSL. Three of the nine considered stations belongs to Italy, namely Trieste, Genova and Venezia Punta della Salute (see Figure 5.1). The methodology for the detection of long-term trends in sea level data was based on the Empirical Mode Decomposition (EMD),

FIGURE 5.1 Location of the Italian sites considered for sea level long-term trend analysis by Cazenave et al. (2002) and Vecchio et al. (2019).

which consists in decomposing the analyzed signal in modes that provide a description of the intrinsic timescales present in the time series. In addition the comparison between trends detected by EMD technique and the rates calculated by traditional linear regression was performed, obtaining that the first ones are comparable or slightly higher than the latter ones.

Figure 5.2 shows the comparison between the sea level long-term trends detected by Cazenave et al. (2002) and Vecchio et al. (2019). A general rising tendency of sea level is observed, in the range 0.30÷2.78 mm/year, with the only exception of the site of Catania, whose shorter length of the sea level data time series produced a strong uncertainty of the result, and hence a reduction of its reliability. For the sites of Trieste and Genova, Cazenave et al. (2002) evaluated a SLR rate about 50% smaller than Vecchio et al. (2019). Finally, for the site of Venezia different tidal gauge stations have been chosen, and SLR rate between 0.60 mm/year and 2.78 mm/years are observed. The differences between the results may be due to the analyzed time span, the employed pre-processing techniques, and also the selected approach for the trend detection.

5.2.2 Future projections of sea level rise

Coastal regions usually host a high number of socio-economic activities as well as of marine habitats, which are seriously threatened by possible effects of climate change.
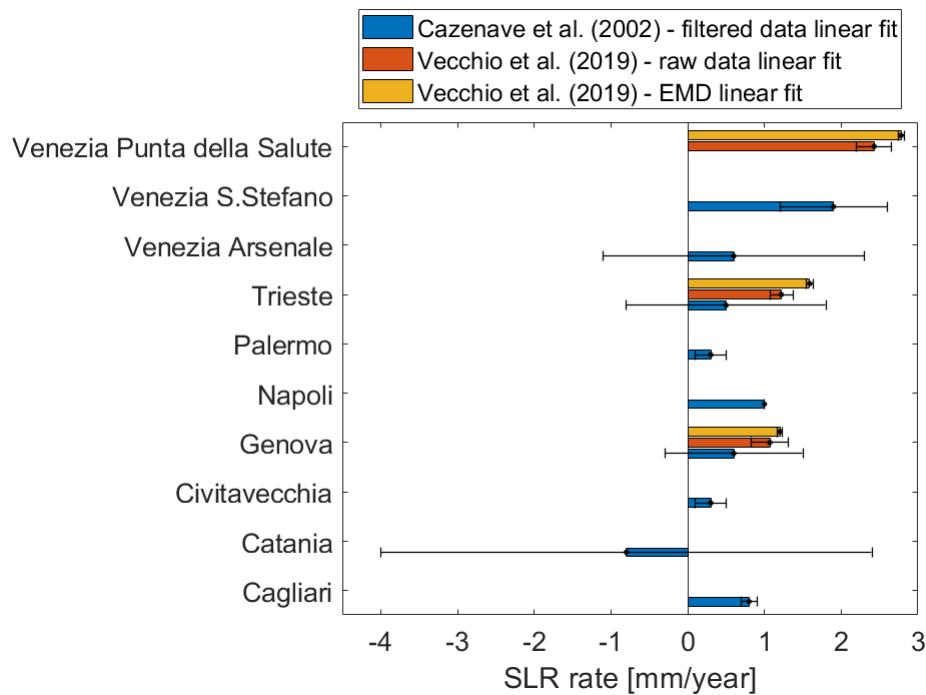
FIGURE 5.2 Comparison of literature long-term sea level trends detected from monthly Revised Local Reference (RLR) gauge records in the Italian Seas from the Permanent Service for Mean Sea Level (PSMSL).

Therefore, several investigations on the effects of global warming on coastal areas have been carried out, aiming to estimating future sea level variation, giving useful indications for coastal planning. As discussed in section 2.4.3, the Mediterranean Sea is a mid-latitude, semi-enclosed and deep sea, whose dynamics regime is governed by the Strait of Gibraltar. Therefore, the hydrodynamic conditions of such a basin can be adequately described only by regional scale models. In the following, the most significant studies on future sea level rise in the Mediterranean sea are briefly discussed, focusing on the Italian Seas.

Galassi and Spada (2014) proposed the estimation of sea level rise in the Mediterranean Sea by 2050, based on the numerical modeling of the following components: i) terrestrial ice melt; ii) glacial isostatic adjustment; iii) ocean response. Among the eight different combinations of the above mentioned contributions to sea level rise, the ones corresponding to a low-end scenario and to a high-end one were further investigated by the authors.

Figure 5.3 shows the six Italian sites considered by Galassi and Spada (2014), whereas Figure 5.4 summarizes the results of the corresponding sea level rise estimation by 2050. A certain homogeneity characterizes the sea level rise estimates. Indeed, both the low-end and high-end sea level rise values vary in relatively narrow ranges (i.e. about 4.0 cm width) among the studied sites, i.e. 7.0÷11.3 cm and 20.4÷25.0 cm respectively. In addition, the difference between low-end and high-end SLR by 2050 is about 13.0 cm.

FIGURE 5.3 Location of the Italian sites considered for sea level rise projections by Galassi and Spada (2014), Lambeck et al. (2011) and Vecchio et al. (2019).

Lambeck et al. (2011) provided projections of sea level rise along 33 Italian coastal plains for the year 2100, by adding the tectonic and isostatic local component to two published estimations of global sea level rise: i) the low-end scenario SLR projection equal to 18.0 cm, which was evaluated by IPCC (2007) considering the contribution due to increased ice flow from Greenland and Antarctica; ii) the high-end scenario SLR projection equal to 140.0 cm, which was calculated by Rahmstorf (2007) by applying an empirical relationship between SLR and global mean surface temperature. It should be noted that the spatial variability typical of the non-uniform response of sea level to climate change was neglected.

Among the 33 Italian coastal plains studied by Lambeck et al. (2011), 12 representative sites were selected, which are showed in Figure 5.3. Figure 5.5 summarizes the outcomes of the evaluation of SLR by 2100, according to the two considered scenarios. The isostatic and tectonic contribute is negative for most of the sites, which means that subsidence processes are expected to produce land down-lift of 4.5 cm on average. The only exceptions to such a general trend are Catania and Gioia Tauro, where no tectonic movements were predicted, and Metaponto, where a land uplift of about 1.8 cm was estimated.

Vecchio et al. (2019) considered the contribution of vertical land motion, which was added to the global RCP2.6 and RCP8.5 SLR projections for the years 2050 and 2100 provided by Church et al. (2013). Such projections were corrected by substituting the glacial ice melt contribution with the natural sea level variability estimated
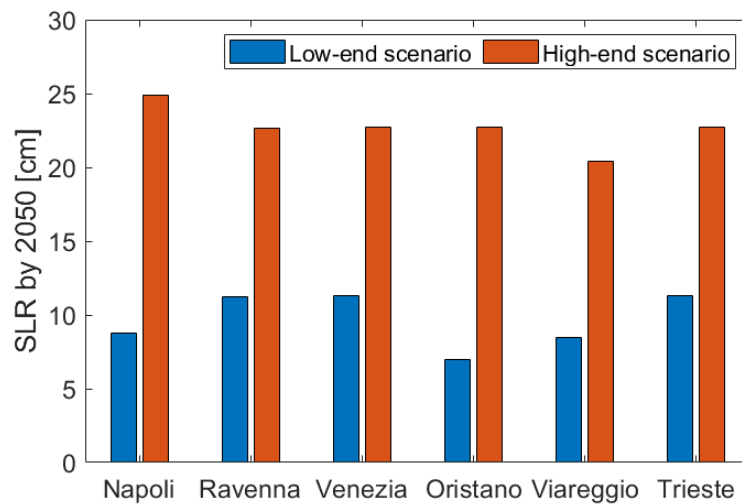
FIGURE 5.4 Sea level rise projections by 2050 estimated by Galassi and Spada (2014) for some Italian coastal sites.
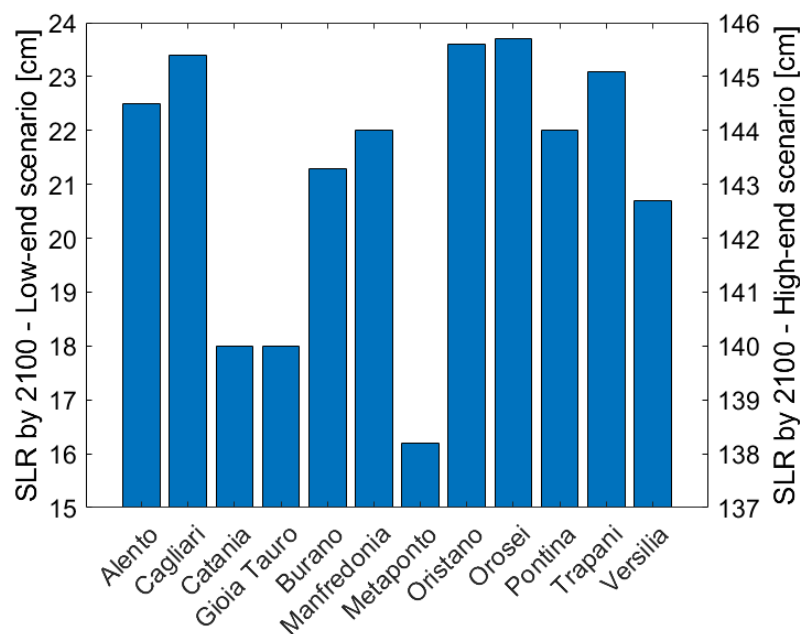
FIGURE 5.5 Sea level rise projections by 2100 estimated by Lambeck et al. (2011) for some Italian coastal sites.

from the EMD analysis of tidal gauge data. Among the nine studied coastal sites, the three Italian ones are here considered (see Figure 5.3).

As regards the SLR by 2050, Figure 5.6a shows that both the low-end and high-end scenarios provides SLR values higher on average than the estimations of Galassi and Spada (2014). In particular, for the site of Trieste the minimum and maximum SLR by 2050 are respectively 3.0 cm and 11.0 cm higher than the ones calculated by Galassi and Spada (2014), whereas for the site of Venezia the low-end and high-end scenario SLR estimations are respectively 17.0 cm and 38.0 cm greater than the ones
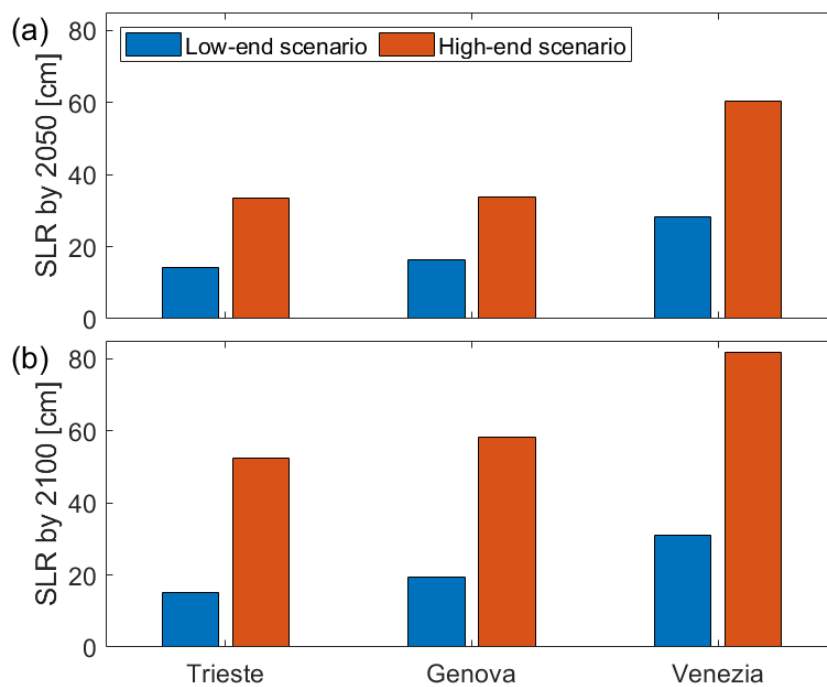
FIGURE 5.6 Sea level rise projections (a) by 2050 and (b) by 2100 estimated by Vecchio et al. (2019) for some Italian coastal sites.

calculated by Galassi and Spada (2014). Instead, Figure 5.6b shows that the SLR values by 2100 are comparable to the ones of Lambeck et al. (2011) only for the low-end scenario. Indeed, the projected SLR under the high-end scenario calculated by Lambeck et al. (2011) is higher than 142 cm for all the considered sites, whereas the one provided by Vecchio et al. (2019) ranges between 50 cm and 80 cm.

In conclusion, the comparison of existing studies on sea level rise in the Italian Seas highlighted significant differences between the produced estimations, in some cases of the order of one meter. Such a diversity is due to the typical sources of uncertainty of climate modeling, which are the usage of various future greenhouse-gas emission forcing scenarios, the diverse representations of atmospheric and oceanic processes given by the climate models, differently perturbed model physics configurations or perturbed initialization states and atmospheric down-scaling methods (Morim et al., 2018). However, a general increase of sea level is expected, of about 20.0 cm by 2100 for the less severe future scenario.

5.3 Trend analysis of wave climate in the Italian seas

5.3.1 Historical Italian wave climate data-sets

Historical wave climate trend analysis has been carried out around Italy, using both measured and reanalysis data, in order to identify significant variations possibly linked to the effects of climate change. In Italy, the National Sea Wave Measurement
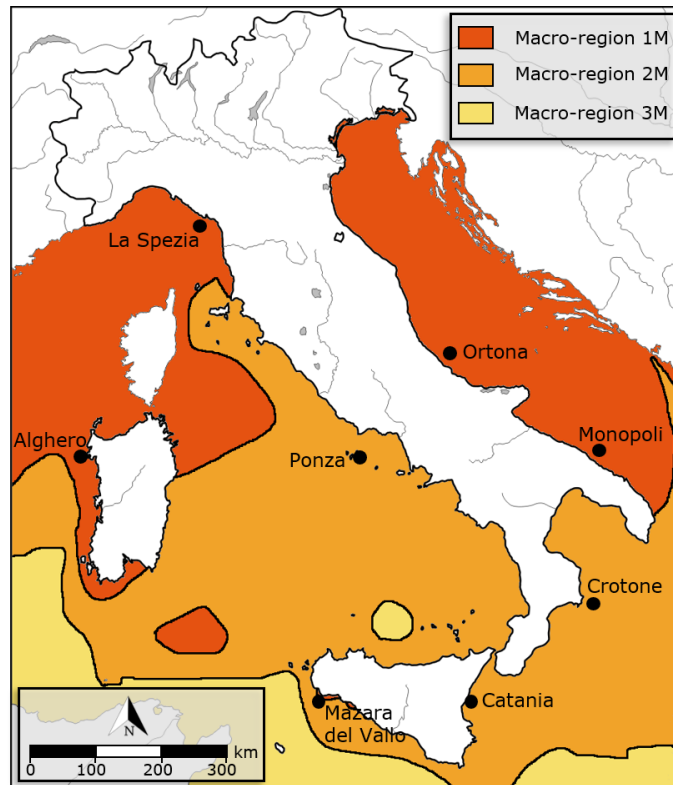
FIGURE 5.7 Location of the eight study sites for the analysis of buoy and modelled wave climate data, considering the definition of homogeneous climatic marine macro-regions proposed by CMCC (2017).

Network (RON) provided wave climate data from 1989 to 2014, i.e. for a period of only 26 years. Therefore, the selection of the study locations has been driven by both the representativeness of the sites and the length of the available time series. In addition, data have been treated considering the homogeneous climatic marine macro-regions defined by CMCC (2017). Three macro-regions were identified from the cluster analysis of sea surface temperature (SST) and sea surface height (SSH) data for the period 1987-2010: i) 1M, characterized by SST around 18.2°C and SSH around -0.07 m, which includes the Adriatic Sea, the Ligurian Sea and the North Sardinia Sea; ii) 2M, whose SST and SSH are respectively around 19.6°C and -0.03 m, which includes the Ionian Sea and the Tyrrhenian Sea; iii) 3M, where SST is around 20.3°C and SSH around 0.05 m, which includes the southernmost part of the Mediterranean Sea, away from the Italian coast and then not covered by RON. Among all the RON measurement stations in macro-regions 1M and 2M, the ones with the longer time series have been chosen: Alghero, La Spezia, Monopoli and Ortona for macro-region 1M, Catania, Crotone, Mazara del Vallo and Ponza for macro-region 2M (see Figure 5.7). The eight chosen buoys were active for 26 years, as opposed to the most recent ones which have only 16 or 13 years long records.

As regards the modeled data, for the same eight sites, the results of two numerical models have been considered: i) the outputs of WAVEWATCH III 30-year Hindcast Phase 1, developed by the American National Oceanic and Atmospheric Administration (NOAA) for the years 1979-2009; ii) ERA5 hourly estimates of variables on pressure levels for the period 1979-2019, which is the latest climate reanalysis produced by the European Centre for Medium-Range Weather Forecasts (ECMWF). It is worth to point out that the advantage of using modeled time series is due to the greater time period that they cover. However, the consistency between measured and modeled data must be assessed in terms of both single events and time tendencies of the wave parameters.

In the following, a brief description of the measured and modeled data-sets is given, focusing on temporal coverage, available parameters and spatial and temporal resolution.

The Italian National Sea Wave Measurement Network (RON) was the national source of wave climate data from 1989 to 2014, i.e. for a period of only 26 years (APAT, 2004). Initially planned and managed by the Italian Ministry of Public Works, with the supervision and assistance of a commission of oceanographers and maritime engineers, the RON was entrusted to the National Hydrological and Marine Service (SIMN) in 1994. In 2002, the network was transferred to the Agency for Environmental Protection and Technical Service (APAT).

The RON was active from July 1989 to December 2014. During this period, several structural upgrades were implemented. At the beginning, the RON was composed by eight pitch-roll Datawell WAVEC directional buoys located offshore of Alghero, Catania, Crotone, La Spezia, Mazara del Vallo, Monopoli, Ortona and Ponza. A data center on the ground received and elaborated the data sent by the corresponding buoy via radio. Since 1998 other stations were added and structural upgrading was implemented, leading to the final configuration of the network composed of 14 Triaxis buoy in 2002. In particular, in 1999 two translation type WAVERIDER Datawell directional buoys were added at Ancona and Cetraro, whereas in 2002 the last four stations were installed at Capo Comino Siniscola, Civitavecchia, Palermo and Punta della Maestra. Unfortunately, the RON was dismissed in December 2014 and now only some Regions perform a regular wave monitoring. Furthermore, the RON time series are affected by missing data caused by malfunctioning of both the measure and transmission system.

Freely available RON data-set consists of three-hourly series of significant wave height ($H_{s,RON}$), peak wave period ($T_{p,RON}$), mean wave period ($T_{m,RON}$) and mean wave direction ($D_{m,RON}$, 0° means coming from North and 90° means coming from East) for the period 1989-2001. Furthermore, for limited time intervals, when storm peak wave heights exceeded the threshold assigned for each station, wave measurements were taken every half-hour and spectral analysis was performed. Instead, from 2002 to 2014, the buoys measured and analyzed the wave data every thirty minutes. Therefore, in the present work, $H_{s,RON}$, $T_{p,RON}$, $T_{m,RON}$ and $D_{m,RON}$ time

series from 1989 to 2014 were employed.

The NOAA data derive from the results of the third generation wind wave model WAVEWATCH III (Tolman, 2009), which was run in order to obtain the global wave climate characterization for the period 1979–2009, requiring ice and winds fields (including the air-sea temperature difference) as input (Chawla et al., 2012). In particular, WAVEWATCH III 30-year Hindcast Phase 1 used the global wind fields at 10 m height from the mean sea level (1/2° resolution at 1 hour intervals) provided by the National Centers for Environmental Prediction (NCEP) Climate Forecast System Reanalysis (CFSR). Hourly air-sea temperature difference with 1/2° spatial resolution were also supplied by the CFSR. Finally, the daily 1/2° resolution ice fields were obtained from measured passive microwave using the American National Aeraonautics and Space Administration (NASA) Team algorithm. The output field parameters are three-hourly series of wind velocity (U-component of input wind and V-component of input wind according to the oceanographic convention), significant height of combined wind waves and swell ($H_{s,NOAA}$), wave peak period ($T_{p,NOAA}$) and mean wave direction at the peak period ($D_{m,NOAA}$, 0° means coming from North and 90° means coming from East). Moreover, there are 2050 output points (buoy locations and virtual locations) where spectral information is saved. For the present analysis, time series of $H_{s,NOAA}$, $T_{p,NOAA}$ and $D_{m,NOAA}$ covering the period 1979–2009 are used.

Finally, ECMWF produced the ERA5 hourly estimates of variables on pressure levels (Hersbach et al., 2019), which provides hourly data on many atmospheric, land-surface and sea-state parameters together with estimates of uncertainty, on regular latitude-longitude grids at 0.25° x 0.25° resolution from 1979 to present day. Like every reanalysis data-set, ERA5 comes from the combination of model data with observations from across the world into a globally complete and consistent data-set using the laws of physics. With respect to the previous ERA-Interim, ERA5 presents several improvements, such as a model input appropriate for climate, the hourly output resolution, a higher spatial resolution and uncertainty estimates. The present study employs hourly time series of significant height of combined wind waves and swell ($H_{s,ERA5}$), peak wave period ($T_{p,ERA5}$), mean wave period ($T_{m,ERA5}$) and mean wave direction ($D_{m,ERA5}$, 0° means coming from North and 90° means coming from East) from 1979 to 2019.

Figure 5.8 highlights the presence of missing data in RON data-set, probably caused by signal transmission problems and malfunctioning of the buoys. In contrast, the NOAA and ERA5 time series are characterized by the absence of missing data, since they result from numerical simulations over continuous time periods.

Table 5.1 shows the geographical coordinates, the covered time period and the rate of missing data of each studied site, with reference to RON, NOAA and ERA5 data-sets. Instead, Table 5.2 summarizes the characteristics of the local wave climate during the covered period, in terms of range of mean wave direction and mean significant wave height ($\overline{H}_s$), peak wave period ($\overline{T}_p$) and mean wave period ($\overline{T}_m$).
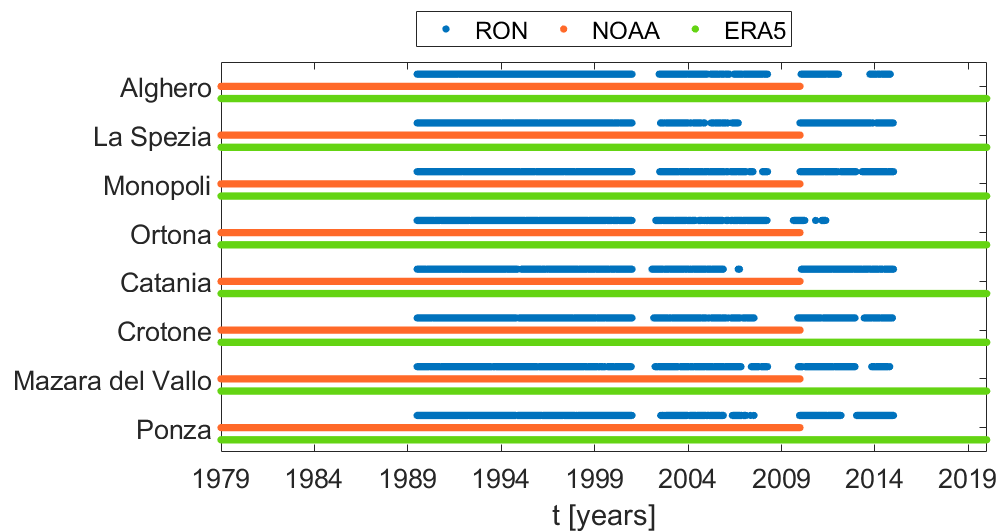
FIGURE 5.8 Temporal availability of wave climate data-sets relative to the eight selected Italian coastal sites during the period 1979-2019.

TABLE 5.1 Characteristics of the RON, NOAA and ERA5 wave climate data-sets in terms of geographical location, covered period and rate of missing data.

Location	Data-set	Coordinates		Period	Missing data
Alghero	RON	40°32′54″N;	08°06′24″E	1989-2014	26.3%
	NOAA	40°30′00"N;	08°00′00″E	1979-2009	0.0%
	ERA5	40°30′00"N;	08°00′00″E	1979-2019	0.0%
La Spezia	RON	43°55′12″N;	09°49′06″E	1989-2014	28.1%
	NOAA	44°00′00″N;	09°50′00"E	1979-2009	0.0%
	ERA5	44°00′00"N;	10°00′00″E	1979-2019	0.0%
Monopoli	RON	40°58′06″N;	17°22′36″E	1989-2014	22.0%
	NOAA	41°00′00″N;	17°30′00″E	1979-2009	0.0%
	ERA5	41°00′00"N;	17°30′00″E	1979-2019	0.0%
Ortona	RON	42°24′24″N;	14°32′12″E	1989-2014	36.3%
	NOAA	42°30′00"N;	14°30′00″E	1979-2009	0.0%
	ERA5	42°30′00"N;	14°30′00″E	1979-2019	0.0%
Catania	RON	37°26′18″N;	15°08′48″E	1989-2014	28.0%
	NOAA	37°30′00"N;	15°10′00"E	1979-2009	0.0%
	ERA5	37°30′00"N;	15°30′00″E	1979-2019	0.0%
Crotone	RON	39°01′06″N;	17°13′18″E	1989-2014	22.3%
	NOAA	39°00′00"N;	17°20′00"E	1979-2009	0.0%
	ERA5	39°00′00″N;	17°30′00″E	1979-2019	0.0%
Mazara del Vallo	RON	37°31′00″N;	12°32′00″E	1989-2014	26.3%
	NOAA	37°30′00"N;	12°30′00″E	1979-2009	0.0%
	ERA5	37°30′00"N;	12°30′00″E	1979-2019	0.0%
Ponza	RON	40°52′00″N;	12°57′00″E	1989-2014	27.7%
	NOAA	40°50′00″N;	13°00′00″E	1979-2009	0.0%
	ERA5	41°00′00"N;	13°00′00″E	1979-2019	0.0%

TABLE 5.2 Characteristics of the RON, NOAA and ERA5 wave climate data-sets in terms of mean wave climate during the considered period.

Location	Data-set	D_m range [°]	$\bar{H}_s$ [m]	$\bar{T}_p$ [s]	$\bar{T}_m$ [s]
Alghero	RON	170-335	1.24	6.65	4.66
	NOAA		1.15	5.51	-
	ERA5		1.10	6.13	5.17
La Spezia	RON	135-260	0.80	6.08	3.99
	NOAA		0.52	5.03	-
	ERA5		0.57	5.44	4.47
Monopoli	RON	310-130	0.70	5.88	3.67
	NOAA		0.58	3.61	-
	ERA5		0.61	4.21	3.62
Ortona	RON	320-130	0.65	5.51	3.72
	NOAA		0.45	3.74	-
	ERA5		0.53	4.19	3.65
Catania	RON	30-150	0.63	6.77	3.85
	NOAA		0.38	4.45	-
	ERA5		0.60	5.16	4.35
Crotone	RON	350-220	0.75	5.66	3.81
	NOAA		0.74	4.48	-
	ERA5		0.85	4.92	4.19
Mazara	RON	100-320	1.01	6.21	4.29
del Vallo	NOAA		1.00	5.36	-
	ERA5		0.97	5.63	4.78
Ponza	RON	70-320	0.89	5.50	3.98
	NOAA		0.75	4.35	-
	ERA5		0.74	4.99	4.31

5.3.2   Characterization of long-term wave climate

In coastal engineering, the identification of possible long-term trends on wave climate characteristics is of practical interest only if parameters which influence coastal erosion and flooding, the design of coastal structure and renewable energy production are considered. Therefore, the following wave climate descriptors have been chosen for the long-term wave climate trend analysis: the significant wave height (H_s), the peak wave period (T_p), the wave power (WP), the wave storm frequency of occurrence (f_{SS}) and duration (d_s), the temporal distance between two consecutive wave storms (I_s) and the storm power index (SPI). Time series of the above mentioned wave climate descriptors should cover at least 30 years, if possible effects of climate change are to be detected (Kundzewicz and Robson, 2000). The present study focuses on an omni-directional analysis of the annual wave climate, i.e. for each of the eight sites all the above mentioned descriptors have been calculated considering events coming from all the directions within the corresponding angular sector (see Table 5.2). Such a kind of analysis represents a first attempt to provide a description of wave climate annual trends in the Italian Seas, whose results may be improved by further investigations considering directional wave events.

The significant wave height H_s and the peak wave period T_p were selected because they strongly influence all coastal processes. Indeed, such wave climate parameters are traditionally used for the evaluation of coastal erosion phenomena and for the structural and hydraulic design of coastal defense structures (US Army Corps of Engineers, 2002; CIRIA et al., 2007).

The wave power WP, which is a function of wave height and period, is useful for the estimation of the wave energy, on which is a key-parameter not only for the wave impact on beaches and coastal structures, but also for the potential to produce renewable energy by means of WECs (Reguero et al., 2015; Divinsky and Kosyan, 2020; Sheng and Li, 2017). It is defined as follows (Divinsky and Kosyan, 2020):

$$WP = \frac{\rho_w g^2}{64\pi} H_s^2 T_e \tag{5.1}$$

where ρ_w is the water density (usually set to 1020 kg/m^3), g is the gravitational acceleration (9.81 m/s^2), H_s is the significant wave height and T_e is the wave energy period, which is equal to 0.90 times the peak wave period T_p.

Finally, wave storms characteristics such as frequency of occurrence (f_{SS}), duration (d_s), interarrival time (I_s) and intensity may have a significant influence on coastal morphodynamics (Dissanayake et al., 2015) and wave-structure interaction (Lira-Loarca et al., 2020). In the Mediterranean Sea, the methodology adopted for counting wave storms that occur during the period of analysis consists in identifying all the events whose significant wave height exceeds a limit equal to 1.5 m and does not assumes values smaller than this threshold for more than 12 h (Boccotti, 2004). The quantification of the storm intensity has been carried out using the storm power index SPI, which has been calculated dividing the storm wave profile into n sub-segments of which each kth element has a duration $\Delta d_{s,k}$ and storm wave height $\Delta H_{s,k}$ (Dissanayake et al., 2015):

$$SPI = \sum_{k=1}^{n} (\Delta d_{s,k} * \Delta H_{s,k}^2) \tag{5.2}$$

A wave climate trend analysis requires not only the selection of the time dependent variables for the description of the characteristics of the wave motion, but also the definition of the temporal aggregation technique. In the present work, the evaluation of the annual mean and 99th percentile values of H_s, T_p, WP, d_s, I_s and SPI has been performed. As regards the wave storm frequency of occurrence f_{SS}, it has been evaluated in terms of annual number of events that have taken place at the considered site. The choice to consider mean and 99th percentile values of the wave climate parameters allows one to investigate both the mean and extreme wave climate.

For each of the above mentioned time-series, a linear regression model has been calculated in the following format, using the least squares method:

$$y_i = At_i + B + \epsilon_i \tag{5.3}$$

where y_i is the value of the time dependent variable corresponding to the time instant t_i, A and B are the slope and the intercept of the linear regression model, respectively, and ϵ_i is the error term relative to the $i-th$ observation. It is important to recall that a linear regression model is appropriate if the residuals (i.e. all the ϵ_i) are normally distributed.

Therefore, the increasing or decreasing tendency of a time dependent variable can be expressed in terms of slope of the correspondent linear regression model. However, it is necessary to assess the significance of the trends (i.e. to statistically measure how much the slope of the linear regression model differs from zero), and to this aim the Student's t-test has been performed. In general, it consists in a statistical hypothesis test in which the test statistics follows a Student's t distribution when the following null hypothesis is supported (Andrade and Estévez-Pérez, 2014):

$$Hyp_0: \quad A = 0 \tag{5.4}$$

where A is the slope of the linear regression model.

First of all, the evaluation of the $t-value$ relative to the slope of the linear regression model has been performed from the following equation:

$$t-value = \frac{A}{SE} \tag{5.5}$$

where A is the slope of the linear regression model and SE is the corresponding standard error. If the $t-value$ is equal to 0, the null hypothesis is completely fulfilled. Instead, as the difference between the tested condition and the null hypothesis increases, the absolute value of the $t-value$ increases.

Once the $t-value$ has been calculated, the Student's t-distribution corresponding to the sample considered can be obtained if its degrees of freedom df are known. In particular, the degrees of freedom of the t-distribution are linked to the sample size and are calculated as follows:

$$df = n_s - 2 \tag{5.6}$$

where n_s is the sample size relative to the linear regression model.

Therefore, the probability for observing a deviation from the null hypothesis associated to the previously calculated $t-value$ can be estimated, considering the case in which A can be either positive or negative (i.e. a two-tailed test). If this probability, called $p-value$, is less than the fixed significance level, the null hypothesis can be rejected and then the trend has the chosen statistical significance. In the present work, a significance level scale derived from IPCC (2010) and reported in Table 5.3 has been considered.

TABLE 5.3 Definition of the significance level of detected trends derived from IPCC (2010).

Trend significance level	Definition
90-100%	Very likely (V)
66-90%	Likely (L)
33-66%	About as likely as not (N)
0-33%	Unlikely (U)

5.3.3 Performances of numerical models in reproducing measured data

As stated in section 5.3.2, the detection of possible effects of climate change on wave climate trends requires the study of sufficient long time series, at least 30 years long according to Kundzewicz and Robson (2000). Since the measured RON data covers no more than 26 years, the possibility to use longer modeled time series has been considered. Therefore, the performances of numerical models in reproducing single wave events and trends have been assessed, according to the procedures described in the following subsections.

Modeled data to reproduce measured events

For each of the eight sites of interest, the comparison between measured RON data and NOAA and ERA5 ones has been considered in terms of significant wave height H_s, mean wave direction D_m, peak wave period T_p and mean wave period T_m. The agreement between RON and NOAA data has been analyzed for the overlapping period 1989-2009, while the correspondence between RON and ERA5 data has been studied for the overlapping period 1989-2014 (see Figure 5.8).

Scatter plots of the measured data against the modeled ones can give an optical representation of the rate of correspondence between them. If the scatter plot presents a dense point cloud symmetrically distributed along the bisector, modeled data are very similar to measured ones. However, a qualitative estimation of the agreement between measured and modeled data is not enough to state if the model performances are good or not.

Therefore, the quantification of the differences between measured and modeled data has been carried out, in accordance with the recommendations of Mentaschi et al. (2013) and Mentaschi et al. (2015).The statistical indicators employed for significant wave height H_s, peak wave period T_p and mean wave period T_m time-series (i.e. scalar integrated quantities) are:

- the normalized bias (NBI), which gives indications about the average component of the error and it assumes a value close to zero for good simulations. It is defined by the following equation:

$$NBI = \frac{\bar{S} - \bar{O}}{\bar{O}} \tag{5.7}$$

where $\bar{S}$ and $\bar{O}$ are the average simulation and observation values respectively;

- the correlation coefficient (r), which provides a representation of the scatter component of the error and a value closer to one indicates a simulation that is less affected by random error. It is calculated as follows:

$$r = \frac{1}{N} \frac{\sum_{i=1}^{N}(S_i - \bar{S})(O_i - \bar{O})}{\sigma_S \sigma_O} \tag{5.8}$$

where S_i is the $i-th$ simulated data, O_i is the $i-th$ observation, σ_S and σ_O are the standard deviations of the simulated and observed data respectively and N is the number of observations available for the analysis;

- the symmetrically normalized root mean square error (HH) introduced by Hanna and Heinold (1985), which combines information about the average and scatter components of the error and it is not biased towards simulations that underestimate the average. It is expressed as follows:

$$HH = \sqrt{\frac{\sum_{i=1}^{N}(S_i - O_i)^2}{\sum_{i=1}^{N} S_i O_i}} \tag{5.9}$$

As regards the mean wave direction D_m, which is a circular quantity, the following normalized statistical indicators have been calculated:

- the bias normalized with respect to a 2π radiant angle (NBI_θ):

$$NBI_\theta = \frac{\sum_{i=1}^{N} mod_{-\pi,\pi}(\theta_{Si} - \theta_{Oi})}{2\pi N} \tag{5.10}$$

where θ_{Si} is the $i-th$ circular simulated data, θ_{Oi} is the $i-th$ circular observation, N is the number of observations available for the analysis and the operator $mod_{-\pi,\pi}$ indicates that if $(\theta_{Si} - \theta_{Oi}) > \pi$ a 2π angle is subtracted from the difference, whereas if $(\theta_{Si} - \theta_{Oi}) < -\pi$ a 2π angle is added to the difference;

- the root mean square error normalized with respect to a 2π radiant angle ($NRMSE_\theta$):

$$NRMSE_\theta = \frac{\sqrt{\sum_{i=1}^{N}[mod_{-\pi,\pi}(\theta_{Si} - \theta_{Oi})]^2/N}}{2\pi} \tag{5.11}$$

Once the above described statistical error indicators relative to H_s, T_p, T_m and D_m time-series have been calculated for the eight sites of interest (see Figure 5.7), an overall evaluation of NOAA and ERA5 capability to reproduce the measured data can be performed. Indeed, such kind of analysis is useful to highlight possible tendencies of the two models to overestimate or underestimate the RON data, thus giving the possibility to investigate the causes.

Modeled data to reproduce measured trends

The possibility to perform a reliable trend analysis of wave climate characteristics using modeled data has been investigated. In particular, the point is if a longer modeled time series can substitute the corresponding shorter and discontinuous RON measured one, despite the not exact correspondence between the two data-sets.

Such a problem has been solved by performing for each of the global annual mean and 99th percentile time-series the comparison between the slope of the linear regression model evaluated from the RON data and the ones calculated from NOAA and ERA5 data, considering the overlapping period 1990-2000. It is worth to point out that the period 1990-2000 has been selected not only because it is covered by all the three data-sets, but also because of the absence of missing data in RON time-series that could influence the evaluation of the linear regression models (Figure 5.8).

The arithmetic calculation of the difference between the two slopes cannot provide a measurement of the statistical significance of their dissimilarity, because the standard errors of the slopes are not taken into account. The already described Student's t-test can be used to asses if the difference between the slopes of two linear regression models is statistically significant. When the comparison between the slopes of two regression models is considered, the null hypothesis can be expressed as follows:

$$Hyp_0: \quad A_1 = A_2 \quad i.e. \quad A_1 - A_2 = 0 \tag{5.12}$$

where A_1 and A_2 are respectively the slope of the first and of the second linear regression model whose comparison is analyzed. It is noted that the Student's t-test described in the previous section represents the special case where $A_1 = A$ and $A_2 = 0$.

The evaluation of the $t - value$ relative to the two slopes is performed using the following equation:

$$t - value = \frac{A_1 - A_2}{\sqrt{SE_1^2 + SE_2^2}} \tag{5.13}$$

where A_1 and A_2 are respectively the slope of the first and of the second linear regression model whose comparison is analyzed and SE_1 and SE_2 are the correspondent standard errors.

In the case of the comparison between the slopes of two linear regression models, the degrees of freedom of the t-distribution are calculated as follows:

$$df = n_{s1} - n_{s2} - 4 \tag{5.14}$$

where n_{s1} and n_{s2} are the sample sizes relative to the first and the second linear regression model respectively.

Therefore, the $p-value$ can be estimated, considering the case in which the difference between A_1 and A_2 can be either positive or negative (i.e. a two-tailed test). If the $p-value$ is greater than the common significance level of 0.05, the null hypothesis cannot be rejected and then the difference between the slope of the two linear regression models is not statistically significant. In this case, the modeled time series can be used instead of the measured one to carry out the long-term trend analysis.

5.3.4   Historical trends in Italian wave climate

The procedure followed to carry out wave climate trend analysis relative to each one of the eight Italian sites (see Figure 5.7) is summarized in Figure 5.9. First of all, RON measured time series have been compared to the correspondent NOAA and ERA5 ones, in order to quantify the capability of modeled data to reproduce measured events. Therefore, following the indications of Mentaschi et al. (2015) and Mentaschi et al. (2013), the evaluation of statistical error indicators has been performed for H_s, T_p, T_m and D_m time series, considering the overlapping periods 1989-2009 and 1989-2014 respectively for the comparison between RON and NOAA and between RON and ERA5.

Then, the time series of the wave climate parameters described in section 5.3.2 have been calculated from the raw measured and modeled data. Annual trend analysis related to the overlapping period 1990-2000, which is free of missing data, has been carried out for all the time series of the three data-sets, using the linear regression model technique. Therefore, for each considered variable, the significance of the differences between RON trends and NOAA and ERA5 ones has been quantified by means of the Student's t-test, as discussed in section 5.3.3. The possibility to replace measured RON time-series with the longer modeled ones for for long-term trend analysis has been related to the results of both the error indicators analysis and the Student's t-test on linear regression model slopes.

In the following, the results of the above described analysis are presented. In addition, the results of the long-term trend analysis carried out for the studied sites are discussed considering the existing research, in order to reconstruct an overall representative frame of the historical wave climate variation along the Italian seas.

Comparison between measured and modeled events

Scatter plots for the comparison between RON and NOAA and ERA5 data allow one a qualitative investigation of the correspondence between measured and modeled data. For instance, Figure 5.10 shows that for the site of Mazara del Vallo, both NOAA and ERA5 models reproduce quite well the measured significant wave height, since the two point clouds are symmetrically distributed along the bisector. In contrast, for the site of La Spezia both NOAA and ERA5 the scatter plots relative to the significant wave height (Figure 5.11) indicate that the two models underestimate the measured data.
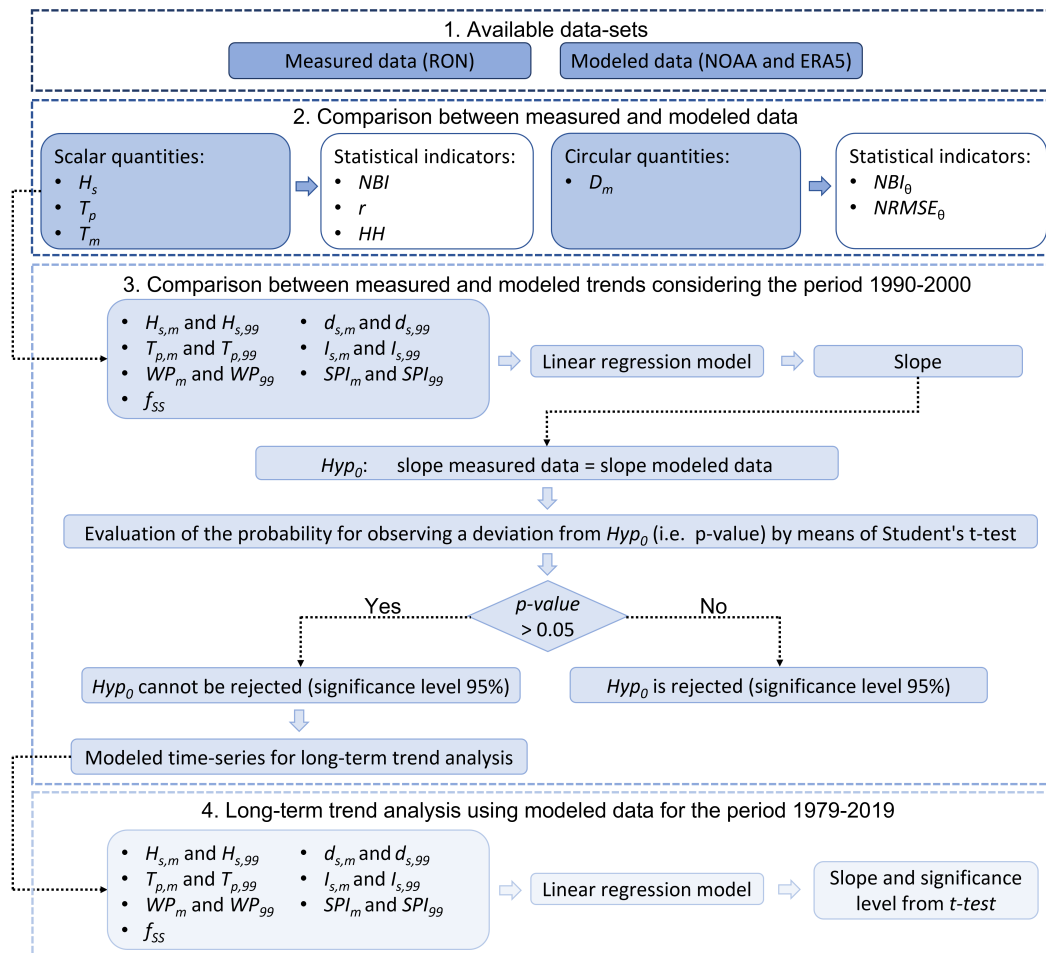
FIGURE 5.9 Block diagram of the methodology applied for long-term trend analysis of wave climate for each of the eight Italian coastal sites considered in the present study.
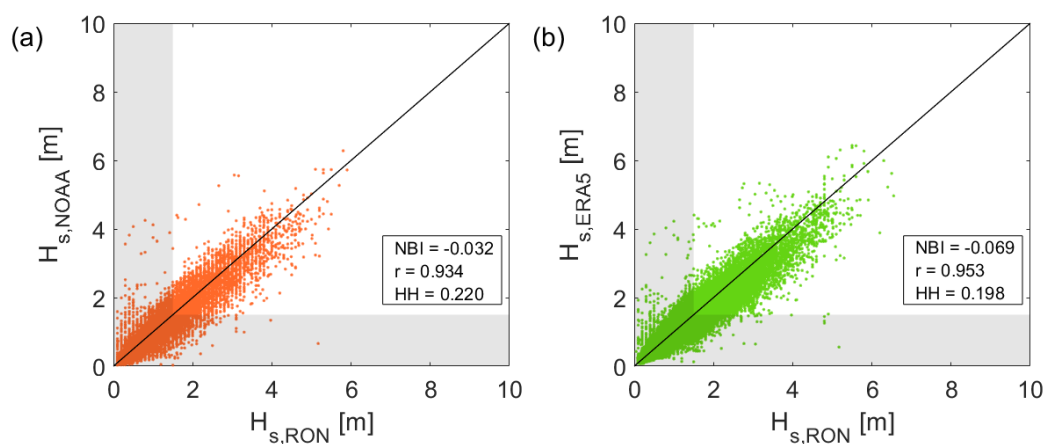
FIGURE 5.10 Scatter plot of the comparison between measured and modeled significant wave height (H_s) for Mazara del Vallo: (a) comparison between RON and NOAA data; (b) comparison between RON and ERA5 data. The gray areas represent the threshold of 1.5 m used for the detection of wave storms.

However, such a first analysis permits only the qualitative distinction between good and bad model performances and the identification of possible model tendencies to under or overestimate the measured data. The outcomes of the statistical analysis carried out in order to quantify the agreement between measured and modeled data are presented in Table 5.4 and in Table 5.5. Regarding the significant wave height and the peak wave period, it can be observed that both NOAA and ERA5 data-sets are affected by a negative *NBI*, which indicates that the two models underestimate the measured data. In particular, the maximum absolute value assumed by *NBI* is 0.383 and 0.296 for NOAA and ERA5 H_s respectively. As regards T_p, the maximum absolute value assumed by *NBI* is 0.362 and 0.277 for NOAA and ERA5 respectively. Obviously, this result can be deduced also from the comparison between the RON time averaged values of significant wave height ($\overline{H}_s$) and peak wave period ($\overline{T}_p$) and the NOAA and ERA5 ones. The only exception is ERA5 overestimation of RON significant wave height for the Crotone buoy. The general underestimation of significant wave height and peak wave period can be explained by the fact that the Mediterranean wave conditions, characterized by the prevalence of the wind wave component and the presence of large fraction of fetch-limited sea winds, differ from swell dominated oceanic ones, for which the two models have been optimized (Mentaschi et al., 2015).

Instead, with regard to the mean wave period, ERA5 data-sets slightly overestimate the measured values, with the exception of Monopoli and Ortona buoys, as shown by both *NBI* values and the comparison between the time averaged mean wave periods ($\overline{T}_m$) of RON and ERA5 data-sets. In any case, the absolute value of *NBI* is always less than 0.100.

The correlation coefficient r calculated for H_s modeled time series indicates that both NOAA and ERA5 are slightly influenced by random errors. In contrast, for T_p
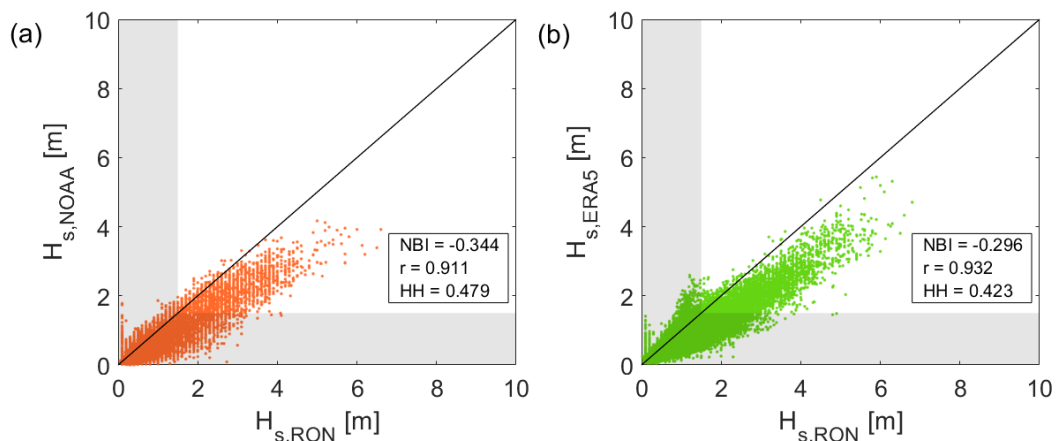
FIGURE 5.11 Scatter plot of the comparison between measured and modeled significant wave height (H_s) for La Spezia: (a) comparison between RON and NOAA data; (b) comparison between RON and ERA5 data. The gray areas represent the threshold of 1.5 m used for the detection of wave storm.

TABLE 5.4 Statistical error indicators evaluated for the assessment of the performances of NOAA and ERA5 data-sets in reproducing RON measured H_s and T_p.

Location	Data-set	H_s			T_p		
		NBI	*r*	*HH*	*NBI*	*r*	*HH*
Alghero	NOAA	-0.104	0.961	0.227	-0.173	0.582	0.400
	ERA5	-0.148	0.974	0.241	-0.084	0.549	0.385
La Spezia	NOAA	-0.344	0.911	0.479	-0.173	0.423	0.516
	ERA5	-0.296	0.932	0.423	-0.100	0.410	0.500
Monopoli	NOAA	-0.176	0.877	0.366	-0.362	0.143	0.917
	ERA5	-0.154	0.899	0.321	-0.277	0.136	0.864
Orotna	NOAA	-0.307	0.858	0.531	-0.253	0.261	0.707
	ERA5	-0.200	0.925	0.352	-0.216	0.196	0.799
Catania	NOAA	-0.383	0.862	0.549	-0.304	0.118	1.008
	ERA5	-0.031	0.867	0.344	-0.216	0.096	0.970
Crotone	NOAA	-0.009	0.919	0.264	-0.202	0.286	0.639
	ERA5	0.104	0.907	0.298	-0.130	0.306	0.614
Mazara del Vallo	NOAA	-0.032	0.934	0.220	-0.135	0.482	0.399
	ERA5	-0.069	0.953	0.198	-0.094	0.477	0.398
Ponza	NOAA	-0.157	0.914	0.316	-0.205	0.463	0.449
	ERA5	-0.187	0.952	0.279	-0.091	0.465	0.398

TABLE 5.5 Statistical error indicators evaluated for the assessment of the performances of NOAA and ERA5 data-sets in reproducing RON measured T_m and D_m.

Location	Data-set	T_m			D_m	
		NBI	*r*	*HH*	*NBI$_\theta$*	*NRMSE$_\theta$*
Alghero	NOAA	-	-	-	0.018	0.115
	ERA5	0.075	0.822	0.204	0.011	0.111
La Spezia	NOAA	-	-	-	0.001	0.155
	ERA5	0.089	0.764	0.226	-0.006	0.136
Monopoli	NOAA	-	-	-	0.016	0.141
	ERA5	-0.042	0.593	0.240	0.009	0.137
Orotna	NOAA	-	-	-	0.044	0.165
	ERA5	-0.041	0.692	0.229	0.018	0.159
Catania	NOAA	-	-	-	0.038	0.154
	ERA5	0.095	0.602	0.293	0.017	0.172
Crotone	NOAA	-	-	-	0.012	0.163
	ERA5	0.069	0.786	0.203	0.005	0.167
Mazara del Vallo	NOAA	-	-	-	0.024	0.129
	ERA5	0.093	0.791	0.194	0.034	0.109
Ponza	NOAA	-	-	-	0.009	0.124
	ERA5	0.057	0.798	0.185	0.010	0.113

modeled time series, r assumes values never greater than 0.6, revealing that random errors significantly affect the simulations. For T_m ERA5 time series the correlation coefficient is also generally low, with a mean value equal to 0.700.

The symmetrically normalized root mean square HH relative to the modeled time series of H_s, T_p and T_m shows a dependency on the averaged mean significant wave height measured by the buoys $\overline{H}_{s,RON}$. In particular, two different decreasing power laws have been fitted for NOAA and ERA5 data in the following form:

$$HH_P = a\overline{H}_{s,RON}^b \qquad (5.15)$$

where the subscript P indicates the considered wave parameter (i.e. H_s, T_p or T_m) and a and b are the coefficients of the power law, assuming different values for NOAA and ERA5 data (see Figure 5.12a-c and Table 5.6).

Considering the significant wave height H_s, Figure 5.12a shows that the two models simulate the significant wave height worse for those locations characterized by higher $\overline{H}_{s,RON}$, being ERA5 performances better than NOAA ones. A similar behavior is observed for T_p, but in this case HH assumes similar values for both NOAA and ERA5 for the same $\overline{H}_{s,RON}$ (Figure 5.12b). Regarding T_m, HH exhibits a decreasing power law dependency on $\overline{H}_{s,RON}$, but in a limited range of values (0.293÷0.185), as shown in Figure 5.12c.

Table 5.5 shows that NOAA and ERA5 mean wave direction time series are affected by a NBI_θ less than 0.050 and $NRMSE_\theta$ less than 0.180 for all the eight locations considered in the present study. Furthermore, it is possible to observe a
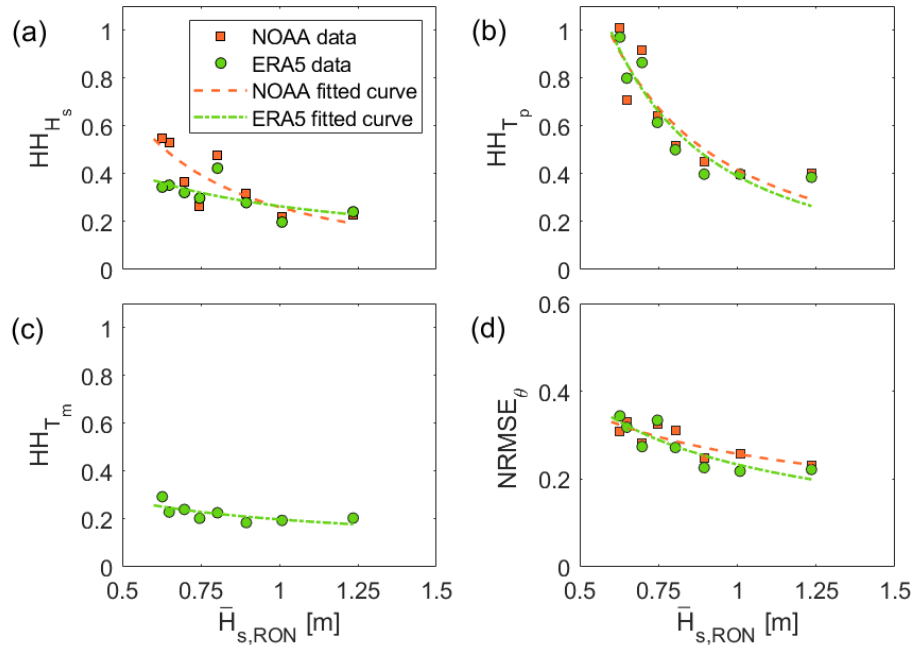
FIGURE 5.12 Influence of $\overline{H}_{s,RON}$ on NOAA and ERA5 models performances in terms of: (a) HH_{H_s}; (b) HH_{T_p}; (c) HH_{T_m}; (d) $NRMSE_{\theta,D_m}$.

TABLE 5.6 Estimate and 95% confidence bounds (CB_{lo} and CB_{up}) of the coefficients of the power laws representing HH_{H_s}, HH_{T_p}, HH_{T_m} and $NRMSE_\theta$ as functions of $\overline{H}_{s,RON}$, and corresponding R^2.

Parameter	Data-set	*a*			*b*			R^2
		Estimate	CB_{lo}	CB_{up}	Estimate	CB_{lo}	CB_{up}	
H_s	NOAA	0.260	0.152	0.369	-1.447	-2.620	-0.273	0.654
	ERA5	0.265	0.194	0.335	-0.670	-1.480	0.140	0.440
T_p	NOAA	0.417	0.271	0.564	-1.670	-2.641	-0.700	0.790
	ERA5	0.390	0.275	0.504	-1.830	-2.631	-1.029	0.871
T_m	NOAA	-	-	-	-	-	-	-
	ERA5	0.198	0.166	0.231	-0.508	-1.014	-0.001	0.503
D_m	NOAA	0.129	0.115	0.143	-0.488	-0.820	-0.156	0.702
	ERA5	0.117	0.099	0.134	-0.745	-1.190	-0.299	0.754

decreasing power law dependency of $NRMSE_\theta$ on $\overline{H}_{s,RON}$ in the following form:

$$NRMSE_\theta = a\overline{H}_{s,RON}^{b} \qquad (5.16)$$

where *a* and *b* are the parameter of the power law, assuming different values for NOAA and ERA5 data (see Figure 5.12d and Table 5.6).

Therefore, both NOAA and ERA5 provide quite good simulations of D_m and the agreement between measured and modeled data slightly improve for those sites characterized by higher $\overline{H}_{s,RON}$.

Finally, the overall analysis of the statistic indicators calculated for NOAA and ERA5 H_s time series lead to the the conclusion that in general ERA5 simulations of H_s seems better than NOAA ones. As regards T_p and D_m, the statistical parameters show that the two models present similar performances.

Comparison between measured and modeled trends

Due to the need to investigate the possibility to use the longer modeled time series instead of the measured ones for wave climate long-term trend analysis, the comparison between the slopes of the linear regression models evaluated from RON, NOAA and ERA5 annual mean and 99th percentile time-series (see section 5.3.2) has been performed for each of the eight studied sites, considering the overlapping period 1990-2000. It is worth to point out that the required normality of the residuals distribution is verified for each of the evaluated linear regression models.

For instance, Figure 5.13 shows the comparison between RON, NOAA and ERA5 $H_{s,m}$, $H_{s,99}$ and f_{SS} for the site of Catania. However, as stated in section 5.3.3, the quantification of the statistical significance of the difference between the slopes is needed. Therefore, Table 5.7 and Table 5.8 summarize the results of the Student's t test applied respectively to the annual mean time-series of H_s, T_p, WP, d_s, I_s and SPI, the annual 99th percentile time-series of the same parameters and f_{SS}. Since the $p - value$ relative to each of the considered time series is greater than 0.05 for
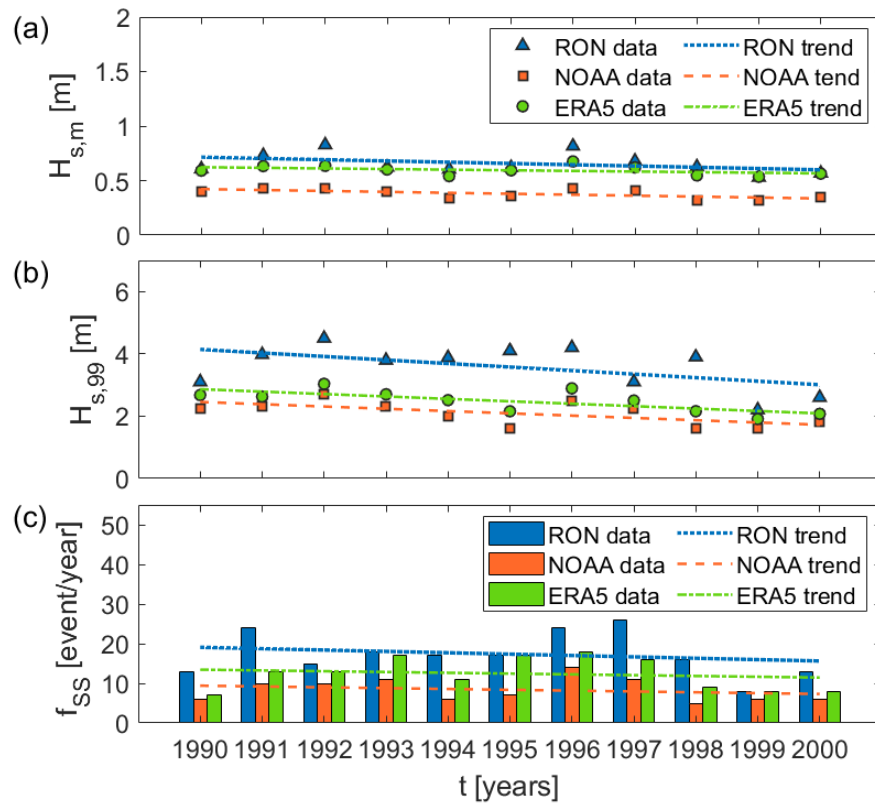
FIGURE 5.13 Comparison between RON, NOAA and ERA5 annual time series for the period 1990-2000 relative to the site of Catania: (a) annual mean significant wave height; (b) annual 99th percentile of significant wave height; (c) wave storm frequency of occurrence.

both NOAA and ERA5 data, there are not significant differences between the slopes evaluated from the measured data and the ones calculated from the modeled data.

Given the impossibility to identify the best performances on the basis of the calculated $p-values$, which are in general far greater than the significance level (i.e. 0.05), the results of the traditional model validation and the length of the time series have been considered for the selection of the data-set for long-term trend analysis. Therefore, the ERA5 modeled data have been chosen because they better simulate measured H_s, also covering a longer time period (i.e. 41 years) compared to the available data-sets.

Long-term trend analysis from ERA5 data-set

Long-term annual wave climate trend analysis has been carried out for the eight sites of interest using the ERA5 data-set. Following the methodology described in section 5.3.2, the tendency of a certain time-dependent variable is expressed in terms of slope of the corresponding linear regression model evaluated using the least squares method, making sure that the required normality of the residuals distribution is verified.

TABLE 5.7 Results of the Student's t-test for the comparison between the slopes of the linear regression models evaluated for RON time-series of $H_{s,m}$, $T_{p,m}$, WP_m, $d_{s,m}$, $I_{s,m}$ and SPI_m and the slopes of the linear regression models evaluated for NOAA and ERA5 time-series of the same variables for the period 1990-2000.

Location	Data-set	$p-value$					
		$H_{s,m}$	$T_{p,m}$	WP_m	$d_{s,m}$	$I_{s,m}$	SPI_m
Alghero	NOAA	0.73	0.73	0.48	0.27	0.17	0.28
	ERA5	0.57	0.83	0.47	0.78	0.19	0.40
La Spezia	NOAA	0.42	0.66	0.77	0.42	0.45	0.81
	ERA5	0.63	0.34	0.84	0.66	0.92	0.94
Monopoli	NOAA	0.70	0.15	0.61	0.12	0.67	0.56
	ERA5	0.91	0.09	0.52	0.84	0.16	0.50
Ortona	NOAA	0.50	0.94	0.96	0.73	0.41	0.83
	ERA5	0.62	0.94	0.98	0.82	0.14	0.78
Catania	NOAA	0.76	0.98	0.45	0.38	0.58	0.74
	ERA5	0.55	0.44	0.46	0.63	0.77	0.79
Crotone	NOAA	0.26	0.88	0.42	0.64	0.87	0.66
	ERA5	0.27	0.97	0.34	0.60	0.50	0.73
Mazara del Vallo	NOAA	0.25	0.90	0.32	0.75	0.17	0.59
	ERA5	0.55	0.93	0.45	0.91	0.06	0.95
Ponza	NOAA	1.00	0.92	0.43	0.52	0.13	0.48
	ERA5	0.62	0.35	0.39	0.45	0.46	0.66

TABLE 5.8 Results of the Student's t-test for the comparison between the slopes of the linear regression models evaluated from RON time-series of $H_{s,99}$, $T_{p,99}$, WP_{99}, f_{SS}, $d_{s,99}$, $I_{s,99}$ and SPI_{99} and the slopes of the linear regression models evaluated from NOAA and ERA5 time-series of the same variables for the period 1990-2000.

Location	Data-set	$p-value$						
		$H_{s,99}$	$T_{p,99}$	WP_{99}	f_{SS}	$d_{s,99}$	$I_{s,99}$	SPI_{99}
Alghero	NOAA	0.89	0.93	0.96	0.23	0.12	0.99	0.32
	ERA5	0.65	0.74	0.92	0.36	0.28	0.51	0.35
La Spezia	NOAA	0.52	0.32	0.54	0.85	0.91	0.25	0.88
	ERA5	0.47	0.48	0.52	0.78	1.00	0.19	0.90
Monopoli	NOAA	0.40	0.71	0.47	0.67	0.86	0.88	0.58
	ERA5	0.39	0.81	0.44	0.37	0.73	0.85	0.18
Ortona	NOAA	0.72	0.15	0.87	0.96	0.26	0.80	0.57
	ERA5	0.87	0.39	0.82	0.55	0.38	0.62	0.71
Catania	NOAA	0.57	0.49	0.40	0.82	0.90	0.69	0.73
	ERA5	0.60	0.49	0.50	0.83	0.89	0.98	0.76
Crotone	NOAA	0.65	0.39	0.65	0.94	0.64	0.68	0.71
	ERA5	0.44	0.49	0.56	0.67	0.71	0.67	0.77
Mazara del Vallo	NOAA	0.39	0.74	0.20	0.45	0.49	0.80	0.10
	ERA5	0.34	0.37	0.21	0.28	0.42	0.41	0.18
Ponza	NOAA	0.39	0.67	0.25	0.15	0.87	0.55	0.73
	ERA5	0.50	0.16	0.28	0.29	0.71	0.29	0.78

In the following, the description of the results of long-term wave climate analysis for the period 1979-2019 are presented, considering the eight sites representative of macro-regions 1M and 2M. The calculated slopes, whose unit of measure is the one of the considered parameter per year, have been converted in %/year with respect to the mean of the time-series, allowing the comparison between trends of different time-dependent variables. In addition, the significance level of the detected trends is defined according to Table 5.3.

As regards the annual mean significant wave height ($H_{s,m}$), positive tendencies between +0.01%/year and +0.15%/year have been found for all the eight considered sites (see Figure 5.14a), in accordance with the results of Caloiero et al. (2019) for the Calabrian coast and of Pomaro et al. (2017) for the Adriatic Sea. However, for La Spezia, Monopoli (macro-region 1M) and Ponza (macro-region 2M) the statistical
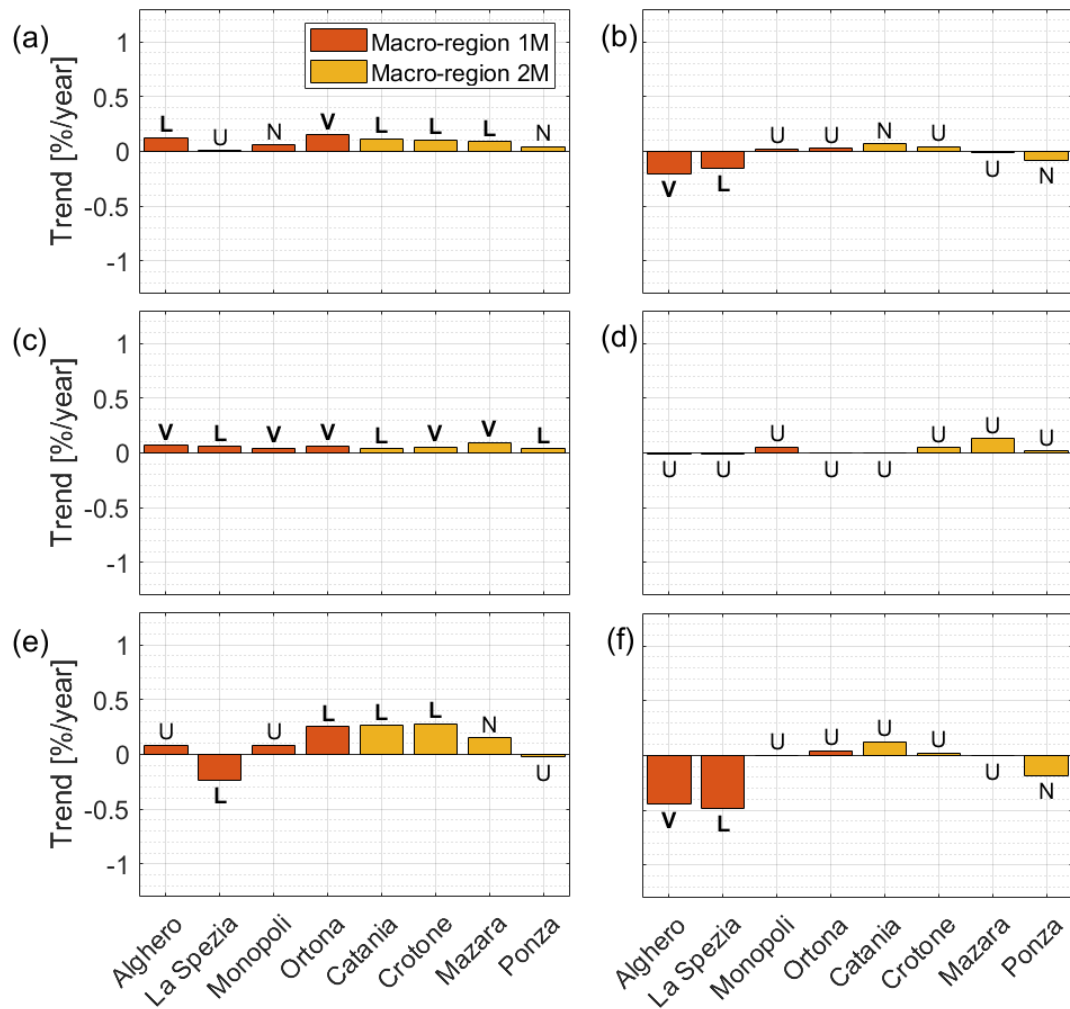
FIGURE 5.14 Long-term trends evaluated during the period 1979-2019 from ERA5 data-set: (a) annual mean significant wave height ($H_{s,m}$); (b) annual 99th percentile of significant wave height ($H_{s,99}$); (c) annual mean peak wave period ($T_{p,m}$); (d) annual 99th percentile of peak wave period ($T_{p,99}$); (e) annual mean wave power (WP_m); (f) annual 99th percentile of wave power (WP_{99}). The significance level of the detected trends is also indicated: V= very likely; L= likely; N= about as likely as not; U= unlikely.

significance of trends is less than 66% (i.e. about as likely as not or unlikely, see Table 5.3). A different behavior was found for the annual 99th percentile of significant wave height ($H_{s,99}$), for which both positive and negative trends have been detected, the first between +0.02%/year and +0.07%/year, the latter between -0.20%/year and -0.01%/year (see Figure 5.14b). Nevertheless, only the negative trends of Alghero and La Spezia (macro-region 1M) have a statistical significance greater than 66% (see 5.3) and are respectively equal to -0.20%/year and -0.15%/year. Therefore, it can be deduced that to an increasing trend of annual mean values of a certain time dependent variable does not necessarily correspond a similar tendency for the extreme ones and vice versa, as found by Pomaro et al. (2017).

The annual mean peak wave period ($T_{p,m}$) shows significant positive tendencies for all the eight considered sites, with value between +0.04%/year and +0.09%/year and in accordance with the increasing trend found by Caloiero et al. (2019) for the energy wave period characteristic of the Calabrian wave climate (see Figure 5.14c). Instead, the annual 99th percentile of peak wave period ($T_{p,99}$), similarly to $H_{s,99}$, does not show a clear increasing or decreasing general tendency. Furthermore, the only significant trends (see Table 5.3) are the ones of Crotone (+0.05%/year) and Mazara del Vallo (+0.13%/year), both in macro-region 2M (see Figure 5.14d).

With reference to the annual mean wave power (WP_m), the general trend is consistent with the results of Reguero et al. (2019) for the global annual mean wave power, and between +0.08%/year and 0.28%/year. The only exceptions are represented by La Spezia (macro-region 1M) and Ponza (macro-region 2M), for which the value of the slope is respectively -0.24%/year and -0.02%/year (see Figure 5.14e). The significance level of the trend is greater than 66% (see Table 5.3) only for La Spezia, Ortona (macro-region 1M), Catania and Crotone (macro-region 2M). For the annual 99th percentile of wave power (WP_{99}), both positive and negative trends have been found, but only for Alghero and La Spezia (macro-region 1M) the significance level is greater than 66% (see Table 5.3), with values of the slope respectively equal to -0.44%/year and -0.48%/year (see Figure 5.14f).

Considering the wave storm frequency of occurrence (f_{SS}), there is not a coherent behavior over time, since both in macro-region 1M and 2M increasing as well as decreasing tendencies have been detected (see Figure 5.15). However, the only significant negative trend has been found for La Spezia (macro-region 1M) and it is equal to -0.41%/year. The other significant slopes are all positive and equal to +0.17%/year for Alghero (macro-region 1M), +0.35%/year for Crotone and +0.22%/year for Ponza (macro-region 2M).

The mean wave storm duration $d_{s,m}$, for which both increasing and decreasing trends have been found (Figure 5.16a), shows a significant positive variation in time only for Ortona in macro-region 1M (+0.54%/year) and Crotone and Mazara del Vallo in macro-region 2M (+0.30%/year and +0.28%/year respectively). A perfect correspondence between trends of $d_{s,m}$ and of the annual 99th percentile of wave storm duration $d_{s,99}$ is observed: a positive/negative trend in $d_{s,m}$ corresponds to
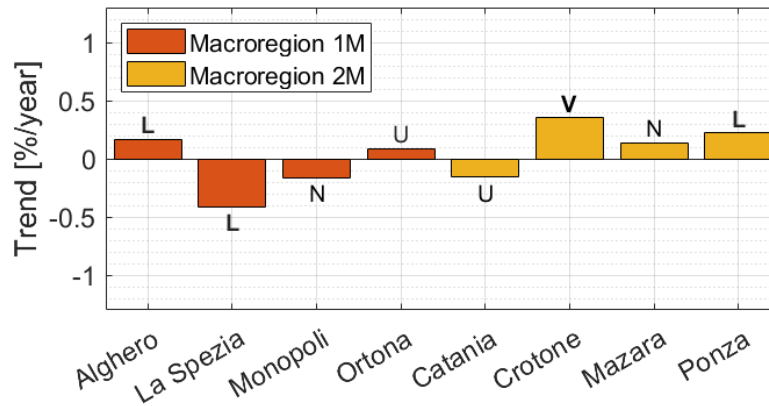
FIGURE 5.15 Long-term trends evaluated during the period 1979-2019 from ERA5 data-set: annual wave storm frequency of occurrence (f_{SS}). The significance level of the detected trends is also indicated: V= very likely; L= likely; N= about as likely as not; U= unlikely.

a positive/negative trend in $d_{s,99}$ (see Figure 5.16b). Furthermore, the significance level of trends is greater than 66% (see Table 5.3) again for the sites of Ortona in macro-region 1M (+0.66%/year) and Crotone and Mazara del Vallo in macro-region 2M (+0.61%/year and +1.03%/year respectively).

In the same way as $d_{s,m}$ and $d_{s,99}$, the annual mean and 99th percentile of the distance between two consecutive wave storms (respectively $I_{s,m}$ and $I_{s,99}$), do not show a coherent behavior within the two considered macro-regions (see Figure 5.16c-d). In particular, $I_{s,m}$ is significantly decreasing for Alghero (-0.29%/year) in macro-region 1M and Crotone (-0.41%/year), Mazara del Vallo (-0.26%/year) and Ponza (-0.23%/year) in macro-region 2M. On the contrary, $I_{s,m}$ shows a significant positive trend only for La Spezia (+0.46%/year) in macro-region 1M. As regards $I_{s,99}$, significant tendencies were found only in macro-region 2M, for Catania (+0.34%/year) and Crotone (-0.84%/year).

Finally, also the annual mean and 99th percentile of the storm power index (respectively SPI_m and SPI_{99}) presents both increasing and decreasing trends in macro-region 1M, as well as in macro-region 2M (see Figure 5.16e-f). For SPI_m, the only significant slopes were found for Ortona (+0.45%/year) in macro-region 1M, and Ponza (-0.29%/year) in macro-region 2M, whereas for SPI_{99} only Ortona shows a negative trend equal to -0.59%/year.

The above described results of the long-term trend analysis highlight the absence of a clear coherent behavior of all the wave climate descriptors within the same macro-region (i.e. 1M or 2M), with the exception of the annual mean significant wave height and peak wave period. Indeed, for such mean wave climate descriptors a general increasing trend has been detected, regardless of the characteristic sea surface temperature SST and height SSH (i.e. belongs in macro-region), and also the orographic features of the considered sites.

A deeper investigation on the the long-term variation of the wave climate in the Italian seas has been performed considering the correlation coefficients between the
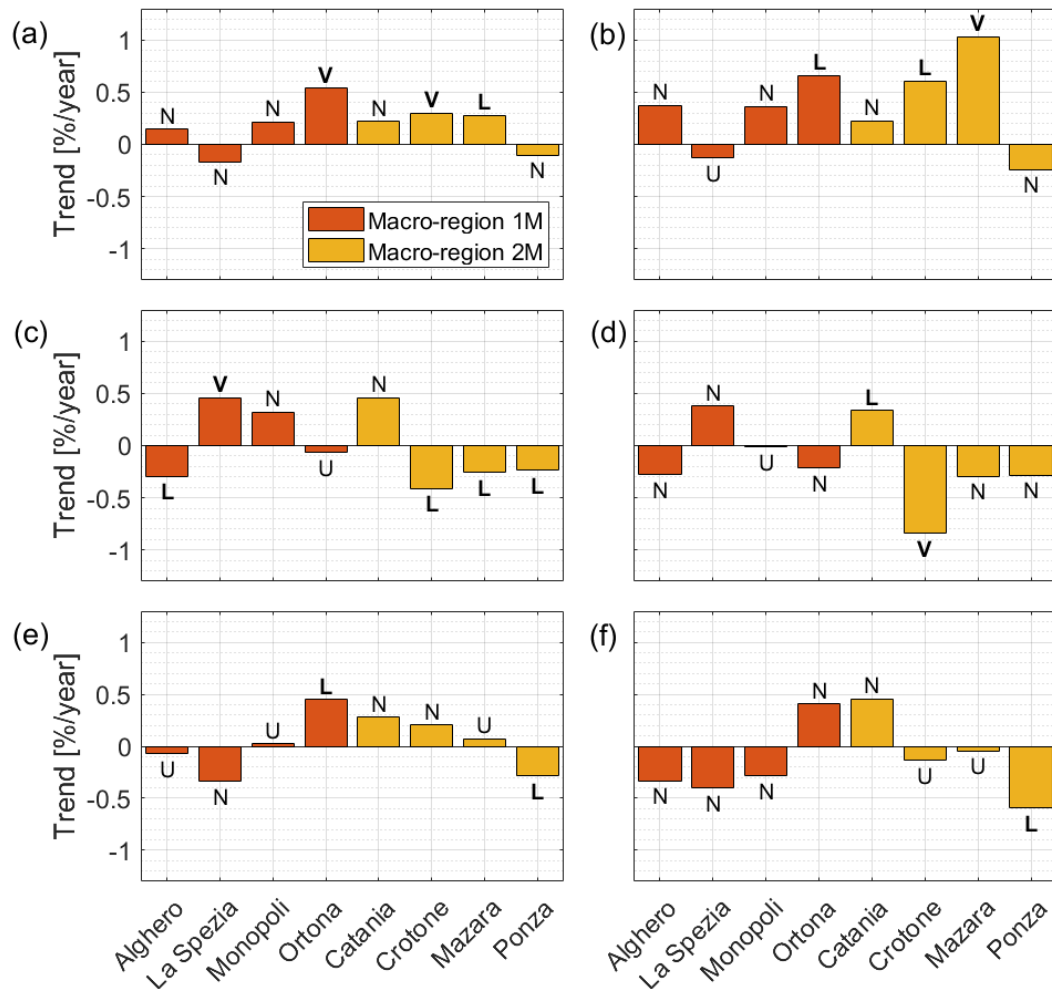
FIGURE 5.16 Long-term trends evaluated during the period 1979-2019 from ERA5 data-set: (a) annual mean wave storm duration ($d_{s,m}$); (b) annual 99th percentile of wave storm duration ($d_{s,99}$); (c) annual time distance between two consecutive wave storms ($I_{s,m}$); (d) annual 99th percentile of time distance between two consecutive wave storms ($I_{s,99}$); (e) annual mean storm power index (SPI_m); (f) annual 99th percentile of storm power index (SPI_{99}). The significance level of the detected trends is also indicated: V= very likely; L= likely; N= about as likely as not; U= unlikely.

detected long-term trends. First of all, the mean and extreme wave climate have been considered separately, as presented in Table 5.9 and Table 5.10. Then, the correspondences between mean and extreme analogue parameters have been studied, as shown in Table 5.11. A threshold correlation coefficient equal to 0.800 has been fixed for the identification of the strongest correlations in absolute terms. The sign of the correlation coefficient gives information about the type of proportionality between the considered variables, which can be direct (i.e. positive) or indirect (i.e. negative).

The following strong correspondence between trends have been identified for the mean wave climate (see Table 5.9): i) $H_{s,m}$ and WP_m; ii) $H_{s,m}$ and $d_{s,m}$; iii) $H_{s,m}$ and SPI_m; iv) WP_m and $d_{s,m}$; v) WP_m and SPI_m; vi) $d_{s,m}$ and SPI_m; vii) f_{SS} and $I_{s,m}$. A linear regression model has been calculated for each of the above mentioned couples of variables, using the least square method (see Figure 5.17 and Figure 5.18a). The

TABLE 5.9 Estimate of the correlation coefficients between the long-term trends of the mean wave climate parameters, detected for each of the studied sites. The correlation coefficients greater than 0.80 are highlighted in bold. Since the matrix of the correlation coefficients between the long-term trends is symmetrical, only half of it is presented.

	$H_{s,m}$	$T_{p,m}$	WP_m	$d_{s,m}$	$I_{s,m}$	SPI_m	f_{SS}
$H_{s,m}$	-						
$T_{p,m}$	0.220	-					
WP_m	**0.858**	0.017	-				
$d_{s,m}$	**0.855**	0.272	**0.868**	-			
$I_{s,m}$	-0.410	-0.416	-0.332	-0.263	-		
$SPI_{s,m}$	**0.840**	0.064	**0.914**	**0.947**	-0.093	-	
f_{SS}	0.522	0.189	0.542	0.372	**-0.948**	0.267	-

TABLE 5.10 Estimate of the correlation coefficients between the long-term trends of the extreme wave climate parameters, detected for each of the studied sites. The correlation coefficients greater than 0.80 are highlighted in bold. Since the matrix of the correlation coefficients between the long-term trends is symmetrical, only half of it is presented.

	$H_{s,99}$	$T_{p,99}$	WP_{99}	$d_{s,99}$	$I_{s,99}$	SPI_{99}	f_{SS}
$H_{s,99}$	-						
$T_{p,99}$	0.331	-					
WP_{99}	**0.974**	0.396	-				
$d_{s,99}$	0.417	0.658	0.502	-			
$I_{s,99}$	-0.132	-0.390	-0.204	-0.469	-		
$SPI_{s,99}$	0.673	-0.056	0.682	0.493	0.159	-	
f_{SS}	0.116	0.301	0.247	0.406	**-0.925**	-0.058	-

TABLE 5.11 Estimate of the correlation coefficients between the long-term trends of the mean and extreme wave climate parameters, detected for each of the studied sites. The correlation coefficients greater than 0.80 are highlighted in bold.

$H_{s,m}$-$H_{s,99}$	$T_{p,m}$-$T_{p,99}$	WP_m-WP_{99}	$d_{s,m}$-$d_{s,99}$	$I_{s,m}$-$I_{s,99}$	SPI_m-SPI_{99}
0.345	0.555	**0.810**	**0.816**	**0.919**	**0.897**

coefficients of the linear regression models and the corresponding R^2 are presented in Table 5.12.

The long-term trends of mean wave power (WP_m), which is function of squared $H_{s,m}$ and $T_{p,m}$, reasonably shows a stronger positive correlation with the trends of $H_{s,m}$ than of $T_{p,m}$ (see Table 5.12 and Figure 5.17a). Also the annual mean wave storm duration ($d_{s,m}$) is strongly positively correlated to $H_{s,m}$ (see Table 5.12 and Figure 5.17b). Such a results seems reasonable, since the wave storm duration is defined as the time interval during which the significant wave height exceeds the fixed threshold for trend detection (i.e. 1.5 m in the present work). The storm power index (SPI_m) obviously presents a strong positive correlation to $H_{s,m}$ (see Table 5.12 and Figure 5.17c), since it is function of squared $H_{s,m}$. Since WP_m, $d_{s,m}$ and SPI_m are positively correlated to $H_{s,m}$, positive correlation coefficients greater than 0.800 have been estimated also for the couples WP_m - $d_{s,m}$, WP_m - SPI_m and $d_{s,m}$ - SPI_m (see Table 5.12 and Figure 5.17d-f). The annual wave storm frequency f_{SS} is obviously inversely
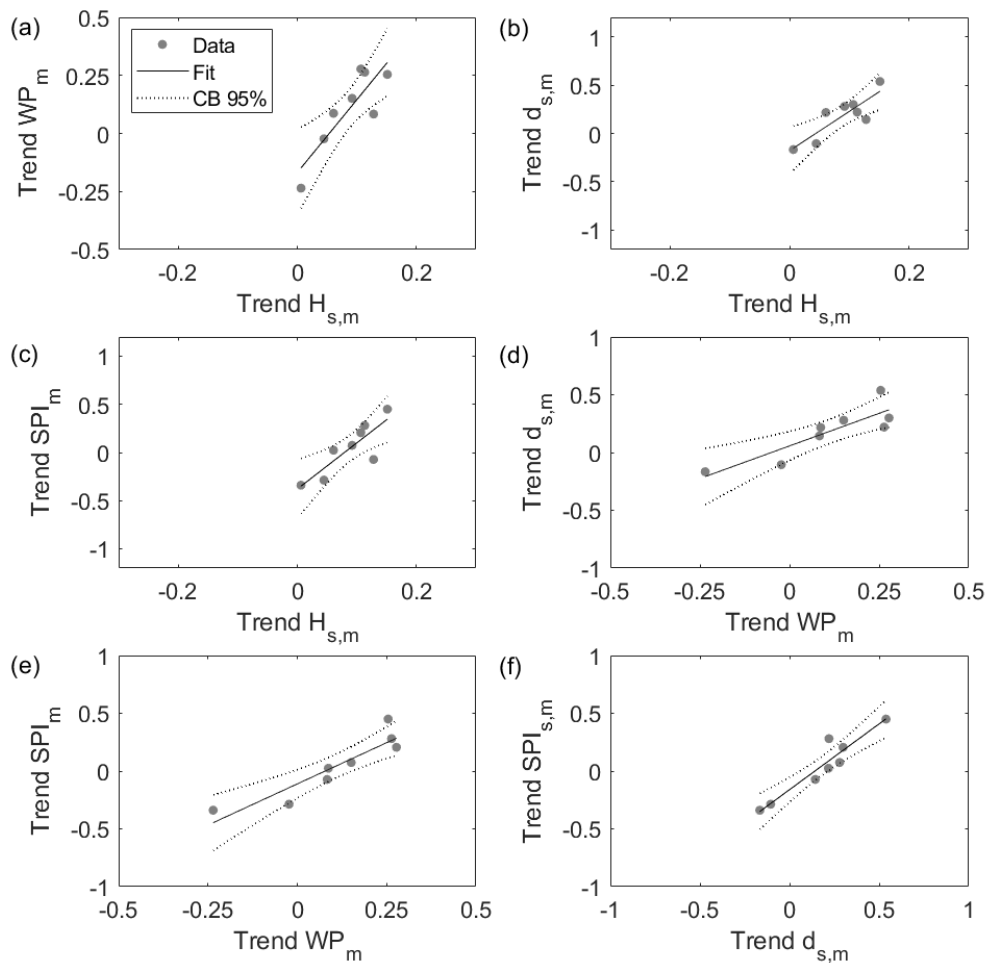
FIGURE 5.17 Linear regression model calculated for the correlated long-term trends of the following wave climate descriptors: (a) $H_{s,m}$ and WP_m; (b) $H_{s,m}$ and $d_{s,m}$; (c) $H_{s,m}$ and SPI_m; (d) WP_m and $d_{s,m}$; (e) WP_m and SPI_m; (f) $d_{s,m}$. Note that the axis limits varies to allow a better graphical representation of the regression models.

proportional to the annual mean time distance between consecutive wave storms $I_{s,m}$ (see Table 5.12 and Figure 5.18a). Indeed, if the number of wave storms that occur in one year decreases, it is expected that the time distance between consecutive events increases.

The extreme wave climate is characterized by an intrinsic randomness that makes it challenging to find comprehensive laws to describe the behavior of extreme. Therefore, only two significant correspondence were found (see Table 5.10): i) $H_{s,99}$ and WP_{99}; ii) f_{SS} and $I_{s,m99}$. A linear regression model has been calculated for each of the above mentioned couples of variables, using the least square method (see Figure 5.18b-c). The coefficients of the linear regression models and the corresponding R^2 are presented in Table 5.12.

As expected, a strong positive correlation is observed between the annual 99th percentile of the significant wave height $H_{s,99}$ and the wave power WP_{99} (see Table 5.12 and Figure 5.18c). Furthermore, an exact correspondence between $H_{s,99}$ and WP_{99} trends in terms of sign and magnitude has been found. With reference to
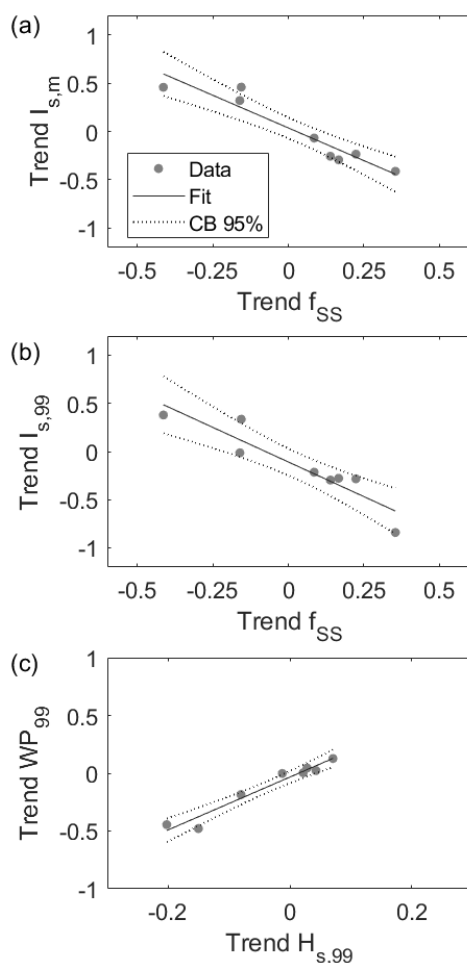
FIGURE 5.18 Linear regression model calculated for the correlated long-term trends of the following wave climate descriptors: a) f_{SS} and $I_{s,m}$; b) f_{SS} and $I_{s,99}$; c) $H_{s,99}$ and WP_{99}. Note that the axis limits varies to allow a better graphical representation of the regression models.

TABLE 5.12 Coefficients and R^2 of the linear regression models which represents the correlation between the long-term trends of the wave climate descriptors considered in the present study.

Independent variable	Dependent variable	A	B	R^2
$H_{s,m}$	WP_m	3.14	-0.17	0.736
$H_{s,m}$	$d_{s,m}$	4.06	-0.18	0.731
$H_{s,m}$	SPI_m	4.80	-0.38	0.706
WP_m	$d_{s,m}$	1.13	0.06	0.754
WP_m	SPI_m	1.43	-0.11	0.835
$d_{s,m}$	SPI_m	1.14	-0.16	0.896
f_{SS}	$I_{s,m}$	-1.35	0.04	0.898
$H_{s,99}$	WP_{99}	2.28	-0.03	0.948
f_{SS}	$I_{s,99}$	-1.44	-0.11	0.856
WP_m	WP_{99}	1.08	-0.23	0.656
$d_{s,m}$	$d_{s,99}$	1.51	0.09	0.665
$I_{s,m}$	$I_{s,99}$	1.00	-0.15	0.845
SPI_m	SPI_{99}	1.24	-0.17	0.805
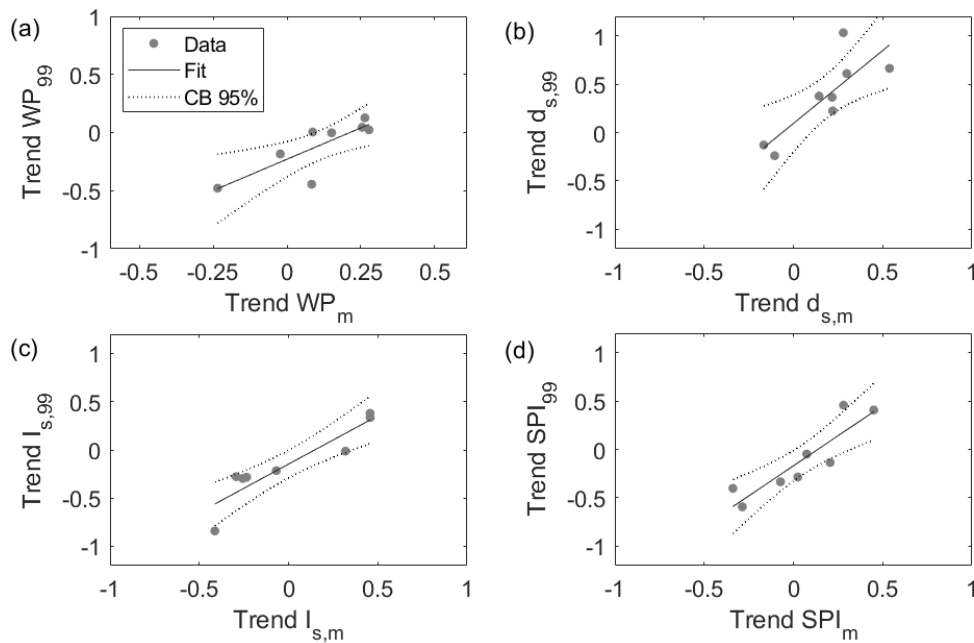
FIGURE 5.19 Linear regression model calculated for the correlated long-term trends of the following wave climate descriptors: (a) WP_{99} and WP_m; (b) $d_{s,m}$ and $d_{s,99}$; (c) $I_{s,m}$ and $I_{s,99}$; (d) SPI_m and SPI_{99}. Note that the axis limits varies to allow a better graphical representation of the regression models.

the annual wave storm frequency f_{SS}, it is inversely correlated to the annual 99th percentile of the time distance between consecutive wave storms $I_{s,99}$, in the same way as $I_{s,m}$ (see Table 5.12 and Figure 5.18b).

Finally, the correspondence between the trends of analogue mean and extreme wave climate parameters has been analyzed, as shown in Table 5.10. The following strong positive correlation have been found: i) WP_m and WP_{99}; ii) $d_{s,m}$ and $d_{s,99}$; iii) $I_{s,m}$ and $I_{s,99}$; iv) SPI_m and SPI_{99}. A linear regression model has been calculated for each of the above mentioned couples of variables, using the least square method (see Figure 5.19). The coefficients of the linear regression models and the corresponding R^2 are presented in Table 5.12.

As already stated, the trends measured for the mean and extreme values of the same variable relative to a certain site are not always correlated Pomaro et al., 2017. Indeed, for the significant wave height and the peak wave period it is not possible to identify a relationship between the long-term trends of the annual mean and 99th percentile values. As a consequence, the study of the annual extreme wave climate cannot be derived from the analysis of the annual mean characteristics.

5.4 Analysis of Italian future wave climate projections

5.4.1 Projected future wave data

The lifetime of harbor defense structure is usually long enough to experience the effects of climate change on coastal areas. Therefore, the projected modifications in

wave climate should be considered for the design of both new and upgraded harbor breakwaters, which should be performed following a probabilistic approach able to take into account the uncertainties of the involved variables. In the present work, the analysis of Italian future wave climate has been carried out for the eight sites showed in Figure 5.7: Alghero, La Spezia, Monopoli and Ortona in macro-region 1M, Catania, Crotone, Mazara del Vallo and Ponza in macro-region 2M.

The ocean surface wave projections for the European coast provided by Copernicus Climate Change Service (2019), which are the only freely available ones, have been employed, considering the current climate for the years 1976-2005, and two future scenarios that correspond to RCP4.5 and RCP8.5 for the period 2041-2100. The ocean surface wave fields were calculated using the ECMWF's Wave Model (SAW) forced by surface wind from a member of the EURO-CORDEX climate model ensemble (i.e. the HIRHAM5 regional climate model downscaled from the global climate model EC-EARTH), also accounting for ice coverage in polar latitudes. In order to assess the impact of climate change on the ocean's surface wave field, the SAW model was run for three different climate scenarios: i) the current climate (HIST); ii) the future climate RCP4.5, which corresponds to an optimistic emission scenario where emissions start declining beyond 2040; iii) the future climate RCP8.5, where emissions continue to rise throughout the century (i.e. business-as-usual scenario). Given that the projections of these climate scenarios are based on a single combination of the regional and global climate models, the uncertainty associated with this data-set is unavoidably underestimated.

The data-set is made of hourly time series of significant wave height (H_s), peak wave period (T_p), mean wave period (T_m), mean wave direction (D_m) and wave spectral directional width for the European coastline along the 20 m bathymetric contour with 30 km spatial resolution. For the present analysis, time series of H_s, T_p, T_m and D_m have been used. Table 5.13 shows the geographical coordinates and the covered time period of each site of the Copernicus Climate Change Service (2019) data-set. Instead, Table 5.14 summarizes the characteristics of the wave climate during the covered period, in terms of range of mean wave direction and averaged significant wave height ($\overline{H}_s$), peak wave period ($\overline{T}_p$) and mean wave period ($\overline{T}_m$).

5.4.2   Statistical characterization of future extreme wave climate

Future climate projections are affected by several uncertainties coming from different sources, namely the usage of various future greenhouse-gas emission forcing scenarios, the diverse representations of atmospheric and oceanic processes given by the climate models, differently perturbed model physics configurations or initialization states, atmospheric down-scaling methods and wind-wave modeling (Morim et al., 2018). Therefore, the characterization of future wave climate has been derived not from the direct analysis of the raw data, but from the application of the factor of

TABLE 5.13 Characteristics of the Copernicus Climate Change Service (2019) wave climate data-set in terms of geographical location and covered period.

Location	Coordinates		Scenario	Period
Alghero	40°36′00″N;	08°12′00″E	HIST	1976-2005
			RCP4.5	2041-2100
			RCP8.5	2041-2100
La Spezia	44°00′00″N;	09°48′00″E	HIST	1976-2005
			RCP4.5	2041-2100
			RCP8.5	2041-2100
Monopoli	40°54′00″N;	17°30′00″E	HIST	1976-2005
			RCP4.5	2041-2100
			RCP8.5	2041-2100
Ortona	42°24′00″N;	14°30′00″E	HIST	1976-2005
			RCP4.5	2041-2100
			RCP8.5	2041-2100
Catania	37°30′00″N;	15°12′00″E	HIST	1976-2005
			RCP4.5	2041-2100
			RCP8.5	2041-2100
Crotone	39°00′00″N;	17°12′00″E	HIST	1976-2005
			RCP4.5	2041-2100
			RCP8.5	2041-2100
Mazara del Vallo	37°36′00″N;	12°30′00″E	HIST	1976-2005
			RCP4.5	2041-2100
			RCP8.5	2041-2100
Ponza	41°12′00″N;	13°00′00″E	HIST	1976-2005
			RCP4.5	2041-2100
			RCP8.5	2041-2100

change (*FoC*) method, which allows the estimation of the expected future modifications of the statistics of the considered descriptors (Kilsby et al., 2007; Fatichi et al., 2011; Peres and Cancelliere, 2018).

Such a method consists in the evaluation of the difference between statistics of climate variables computed for the future period (i.e. RCP4.5 or RCP8.5) and for the present control period (i.e. HIST), by applying the following formula:

$$FoC = \frac{M_{m,f}}{M_{m,c}} \tag{5.17}$$

where *FoC* is the factor of change and $M_{m,f}$ and $M_{m,c}$ are the generic statistical moments evaluated respectively for the modeled future and control period.

Once the *FoC* is calculated, the future value of the considered statistical moment M_f can be evaluated by multiplication by the observed (i.e. measured) moment in the control period $M_{obs,c}$:

$$M_f = FoC \times M_{obs,c} \tag{5.18}$$

The results of the application of the factor of change method can be used for the

TABLE 5.14 Characteristics of the Copernicus Climate Change Service (2019) wave climate data-set in terms of mean wave climate during the considered period.

Location	Scenario	D_m range [°]	$\bar{H}_s$ [m]	$\bar{T}_p$ [s]	$\bar{T}_m$ [s]
Alghero	HIST	170-335	1.26	–	4.74
	RCP4.5		1.19	–	4.64
	RCP8.5		1.24	–	4.70
La Spezia	HIST	135-260	0.85	–	4.24
	RCP4.5		0.80	–	4.15
	RCP8.5		0.82	–	4.20
Monopoli	HIST	310-130	0.60	–	3.08
	RCP4.5		0.59	–	3.05
	RCP8.5		0.59	–	3.06
Ortona	HIST	320-130	0.60	–	3.11
	RCP4.5		0.59	–	3.10
	RCP8.5		0.61	–	3.13
Catania	HIST	30-150	0.53	–	3.43
	RCP4.5		0.54	–	3.47
	RCP8.5		0.53	–	3.45
Crotone	HIST	350-220	0.73	–	3.50
	RCP4.5		0.72	–	3.48
	RCP8.5		0.73	–	3.49
Mazara del Vallo	HIST	100-320	1.09	–	4.30
	RCP4.5		1.07	–	4.22
	RCP8.5		1.10	–	4.30
Ponza	HIST	70-320	0.87	–	3.87
	RCP4.5		0.85	–	3.81
	RCP8.5		0.86	–	3.85

quantification off the expected future variations of the climate descriptor of interest (e.g. significant wave height, peak wave period). In addition, the future statistical moments of the studied variable evaluated by applying the factor of change method can be used for the adaptation of the future probability density function through the method of moments estimation (MME). As will be discussed in Chapter 7, such a method can be employed for the definition of the future probability distribution of extreme significant wave height, which fundamental for the probabilistic design of new or upgraded harbor breakwaters.

Figure 5.20 summarizes the procedure followed for the evaluation of the future statistical characteristics of the Italian wave climate for each of the eight considered site (see Figure 5.7).The extreme wave climate has been considered, because of its usefulness in the design of coastal defense structures. In particular, the following descriptors of extreme wave climate have been selected:

- the maximum wave storm significant wave height, derived from extreme value analysis based on the application of the peaks over thresholds (POT) method;

- the duration of wave storms;
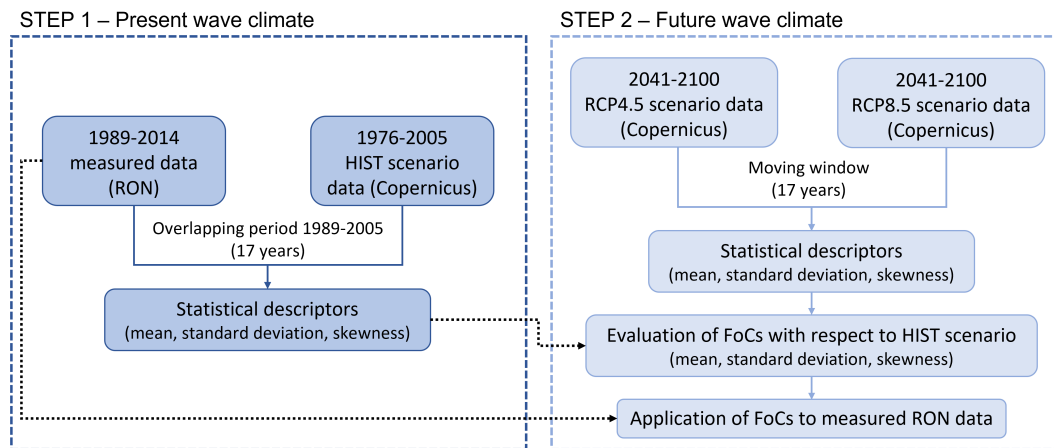
FIGURE 5.20 Block diagram of the methodology applied for the evaluation of the future characteristics of the extreme Italian wave climate for each of the eight considered site.

- the peak wave period corresponding to the maximum wave storm significant wave height;

- the mean wave period corresponding to the maximum wave storm significant wave height.

It is important to point out that the methodology adopted for counting wave storms that occur during the period of analysis consists in identifying all the events whose significant wave height exceeds a limit equal to 1.5 m and does not assumes values smaller than this threshold for more than 12 h (Boccotti, 2004). In addition, the data on mean wave direction have allowed the selection of the wave storms belonging to the angular sector of each site, thus excluding possible unlikely events due to the spatial resolution of the modeled data.

First of all, the control period has been studied considering RON measured data (see section 5.3.1) and the data of the modeled HIST scenario, for the overlapping 17 years 1989-2005. Due to the limited length of the period, the hypothesis of stationary forcing could be employed. For each of the above mentioned descriptors of extreme wave climate, the evaluated statistical moments have been mean, standard deviation (STD) and skewness, which are necessary for the calculation of the parameters of the typical extreme value probability density functions, such as Generalized Extreme Value (GEV) and Weibull.

The evaluation of mean, STD and skewness of extreme wave climate descriptors has been carried out also for the future scenarios RCP4.5 and RCP8.5, considering a moving time window of 17 years (i.e. the same length of the control period). The evaluation of the *FoC*s and their application to the observed RON data has been performed for each moving time window, in order to obtain all the necessary input data for the adaptation of the probability density functions through the MME method, always under the assumption of stationary forcing.

The results of such a kind of analysis are useful for the evaluation of the expected future wave climate variability. In addition, they can be employed for the MME estimation of the probability density functions of the considered wave climate descriptors, which allow to introduce the effects of climate change in the probabilistic calculations for the design of coastal defense structures.

Figure 5.21 schematically shows the physical meaning of a factor of change equal, greater or smaller than one, depending on the considered statistical moment. If *FoC* is equal to unity, the future probability density function maintains the same mean, standard deviation or skewness of the present one (i.e. no change are expected for the future scenario). As regards the mean, if *FoC* is greater or smaller than one, the future probability density function is shifted respectively towards higher or lower values of the considered variable. Since the standard deviation is a measure of the variability of a random variable, *FoC* greater than one implies a wider future probability density function, on the contrary a narrower one is expected. Finally, the skewness represents the symmetry of the probability density function. A negative skewness is typical of left-tailed distributions, whereas a positive skewness is typical of right-tailed distributions. Therefore, *FoC* of the skewness greater or smaller than one represents a deformation of the probability density function respectively to the left and to the right.
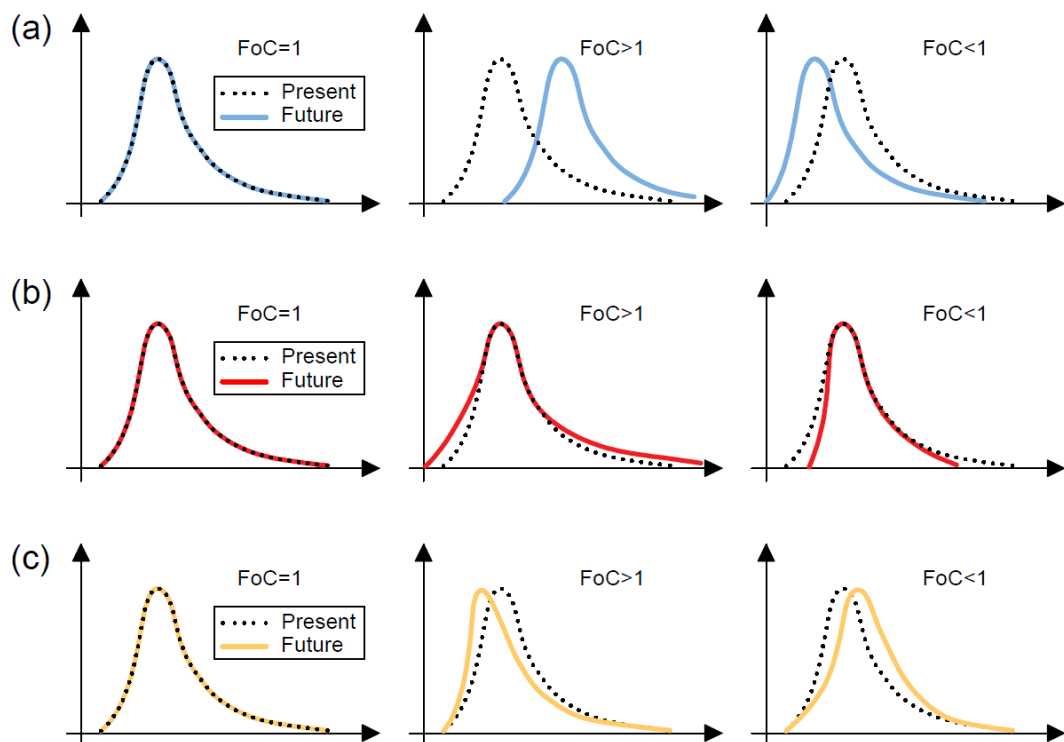
FIGURE 5.21 Simplified sketch of the physical meaning of the factors of change for a generic probability density function: (a) factor of change of the mean; (b) factor of change of the standard deviation; (c) factor of change of the skewness.

5.4.3 Statistics of the future Italian extreme wave climate

The evaluation of the factors of change relative to the mean, standard deviation and skewness of extreme wave climate descriptors has been carried out for the eight sites showed in Figure 5.7, following the methodology described in section 5.4.2.

First, the statistics of the control period 1989-2005 have been evaluated for the observed RON data and for the modeled HIST scenario ones. As showed in Table 5.15, Table 5.16, Table 5.17 and Table 5.18, the modeled wave motion statistics are quite similar to the observed ones for almost all the studied descriptors. As regards the maximum significant wave height of wave storms (see Table 5.15), the modeled means and standard deviations differs on average by about ±0.10 m from the observed ones, whereas the modeled and observed skewness diverge on average by about ±0.35. Instead, the wave storm duration (see Table 5.16) is characterized by a significant deviation of the modeled means and standard deviations from the measured ones, respectively equal on average to ±4.40 h and ±5.28 h. The difference between the modeled and observed skewness of the wave storm duration is on average ±0.89. Concerning the wave storm peak wave period (see Table 5.17), there is a good accordance between measured and modeled statistics, being the differences between means, standard deviations and skewness values respectively equal to ±0.26 s, ±0.09 s and ± 0.21 on average. Finally, also the modeled mean wave period of wave storms (see Table 5.18) is quite similar to the observed one in terms of statistical moments. Indeed, differences between means, standard deviations and skewness are on average respectively equal to ±0.43 s, ±0.16 s and ± 0.28.

TABLE 5.15 Statistical characterization of the present wave storm maximum significant wave height for the eight sites along the Italian coast, considering the observed RON data and the modeled HIST data (period 1989-2005).

Location	Data-set	Statistics		
		Mean [m]	STD [m]	Skewness [-]
Alghero	RON	3.46	1.49	1.13
	HIST	3.23	1.37	1.07
La Spezia	RON	2.81	0.95	1.16
	HIST	2.79	1.04	1.39
Monopoli	RON	2.47	0.62	1.20
	HIST	2.38	0.60	1.08
Ortona	RON	2.59	0.81	1.31
	HIST	2.54	0.90	1.79
Catania	RON	2.61	0.83	1.26
	HIST	2.42	0.89	2.30
Crotone	RON	2.56	0.81	1.31
	HIST	2.57	0.87	1.80
Mazara del Vallo	RON	2.70	0.86	1.13
	HIST	2.86	1.14	1.32
Ponza	RON	2.66	0.84	1.49
	HIST	2.77	1.00	1.31

TABLE 5.16 Statistical characterization of the present wave storm duration for the eight sites along the Italian coast, considering the observed RON data and the modeled HIST data (period 1989-2005).

Location	Data-set	Statistics		
		Mean [h]	STD [h]	Skewness [-]
Alghero	RON	58.41	59.85	2.92
	HIST	65.26	74.45	3.42
La Spezia	RON	36.44	38.28	3.33
	HIST	44.96	48.44	2.95
Monopoli	RON	25.30	19.43	1.60
	HIST	23.18	18.70	2.17
Ortona	RON	25.69	21.39	1.77
	HIST	26.83	22.56	1.75
Catania	RON	35.06	33.10	3.41
	HIST	30.02	24.14	1.92
Crotone	RON	31.64	27.20	2.14
	HIST	31.76	25.44	1.53
Mazara del Vallo	RON	44.83	49.29	5.45
	HIST	53.17	51.91	2.10
Ponza	RON	36.63	34.31	2.29
	HIST	39.71	36.56	2.47

TABLE 5.17 Statistical characterization of the present wave storm peak wave period for the eight sites along the Italian coast, considering the observed RON data and the modeled HIST data (period 1989-2005).

Location	Data-set	Statistics		
		Mean [s]	STD [s]	Skewness [-]
Alghero	RON	9.40	1.47	0.29
	HIST	9.23	1.43	0.29
La Spezia	RON	8.18	1.19	0.37
	HIST	8.55	1.35	0.53
Monopoli	RON	7.22	0.89	0.52
	HIST	7.53	0.95	0.86
Ortona	RON	7.20	1.06	0.25
	HIST	7.40	1.13	0.99
Catania	RON	8.47	1.44	0.28
	HIST	8.32	1.40	0.48
Crotone	RON	7.61	1.38	0.69
	HIST	7.71	1.28	0.70
Mazara del Vallo	RON	8.02	1.25	0.55
	HIST	8.49	1.53	0.46
Ponza	RON	7.80	1.20	0.34
	HIST	8.13	1.21	0.49

The results of the comparison between observed and modeled statistics of extreme wave motion descriptors demonstrate that the Copernicus Climate Change Service (2019) data-set is able to give a quite credible statistical representation of the

TABLE 5.18 Statistical characterization of the present wave storm mean wave period for the eight sites along the Italian coast, considering the observed RON data and the modeled HIST data (period 1989-2005).

Location	Data-set	Statistics		
		Mean [s]	STD [s]	Skewness [-]
Alghero	RON	7.53	1.36	0.41
	HIST	6.90	1.11	0.30
La Spezia	RON	6.60	1.09	0.37
	HIST	6.42	1.02	0.47
Monopoli	RON	5.91	0.78	0.35
	HIST	5.58	0.65	0.88
Ortona	RON	5.95	0.98	-0.15
	HIST	5.51	0.75	0.90
Catania	RON	7.00	1.33	0.50
	HIST	6.10	1.05	0.81
Crotone	RON	6.20	1.16	0.78
	HIST	5.67	0.93	0.90
Mazara del Vallo	RON	6.42	1.08	0.52
	HIST	6.24	1.09	0.54
Ponza	RON	6.31	1.01	0.63
	HIST	6.04	0.91	0.61

Italian extreme wave climate. Therefore, the analysis of the effects of climate change on the extreme wave climate statistics under RCP4.5 and RCP8.5 scenarios has been performed.

As regards the wave storm maximum significant wave height under RCP4.5 scenario (see Figure 5.22), no change of the mean is expected, being *FoC* very close to 1.0 for the entire period 2041-2100. The standard deviation shows a similar behavior, with the exception of the sites of Monopoli and Ortona (see Figure 5.22c-d), for which *FoC* oscillates respectively between 1.1 and 1.3, and between 0.8 and 0.9. Finally, important variations of the skewness are observed under RCP4.5 scenario, with *FoC* both greater and smaller than 1.0, in the range 0.6÷1.8, according to different temporal paths. In particular, Alghero is characterized by values of *FoC* around 1.3 until 2070, then a decreasing trend toward the unity is observed. La Spezia, Catania and Crotone present *FoC* around 0.8 for most of the period of analysis, but the unitary value is reached by 2100. *FoC* calculated for Monopoli is always greater than 1.0, assuming values between 1.2 and 1.8, whereas Ortona is characterized by *FoC* always smaller than 1.0, in the range 0.6÷0.9. Finally, Mazara del Vallo and Ponza present *FoC* greater than 1.0 until 2070 with a maximum value around 1.2, then a decreasing tendency towards *FoC* around 0.8 is observed until 2085, followed by an increasing trend towards the unit.

The statistics of the wave storm maximum significant wave height evaluated under RCP.8.5 scenario are very similar to the ones relative to RCP4.5 scenario (see Figure 5.23).Indeed, *Foc* of the mean is about 1.0 for all the eight sites, as well as the *Foc*
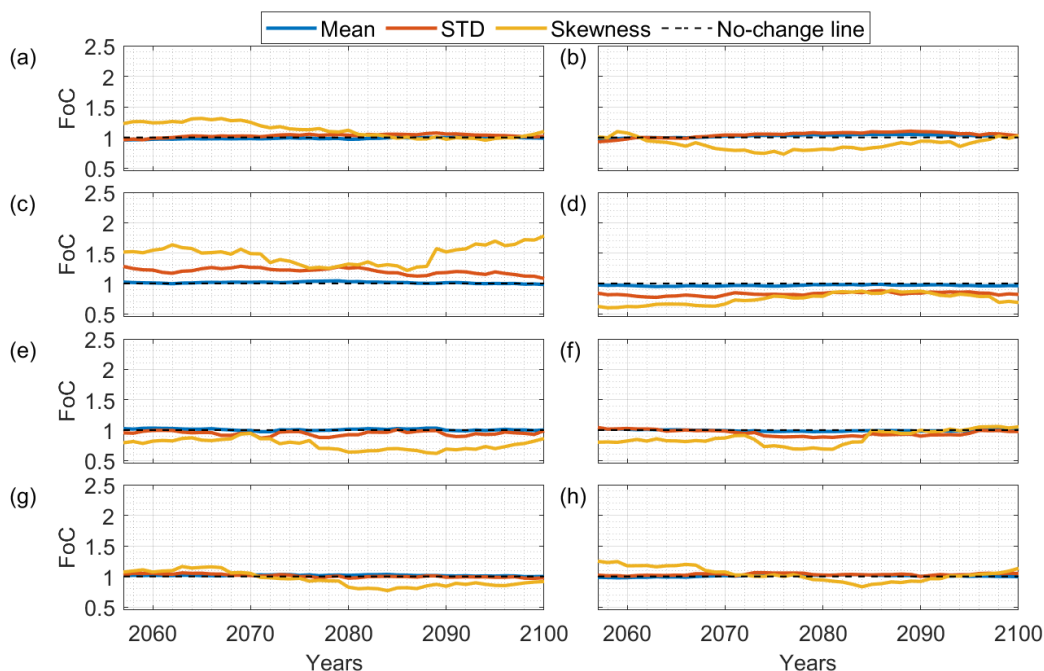
FIGURE 5.22 Factors of change of the statistics of the wave storm maximum significant wave height, evaluated considering the future scenario RCP4.5 for the following sites: (a) Alghero; (b) La Spezia; (c) Monopoli; (d) Ortona; (e) Catania; (f) Crotone; (g) Mazara del Vallo; (h) Ponza.

of the standard deviation, with the exception of Monopoli, Ortona and Catania (see Figure 5.23c-e), for which *FoC* oscillates respectively between 1.2 and 1.9, between 0.7 and 1.1, and between 0.6 and 1.1. A great variability of *FoC* of the skewness is observed for some of the studied sites. In particular, for Alghero and La Spezia *FoC* around 1.2 are observed until 2065, then a decreasing tendency towards a minimum value of 0.9 and 0.8 respectively is registered by 2080, followed by an increasing trend towards values around 1.4 (see Figure 5.23a-b). The site of Monopoli is again characterized by the greater values of *FoC*, which oscillates in the range 1.2÷1.9 (see Figure 5.23c). Finally, for the site of Catania *FoC* presents an initial increasing trend in the range 0.5÷1.0 until 2070, then it remains almost constant until until 2100 (see Figure 5.23e).

To summarize, the wave storm maximum significant wave height for the Italian seas is expected to maintain almost the same mean and standard deviation under both RCP4.5 and RCP8.5 future scenarios. Instead, important increments or reductions of the skewness are likely to occur, thus influencing the symmetry of the statistical distribution of the wave storm maximum significant wave height. In addition, no relevant differences between the results relative to the two future scenarios have been identified.

Concerning the wave storm duration, *FoC* is very close to 1.0 during the considered period under RCP4.5 scenario (see Figure 5.24). The only exceptions are
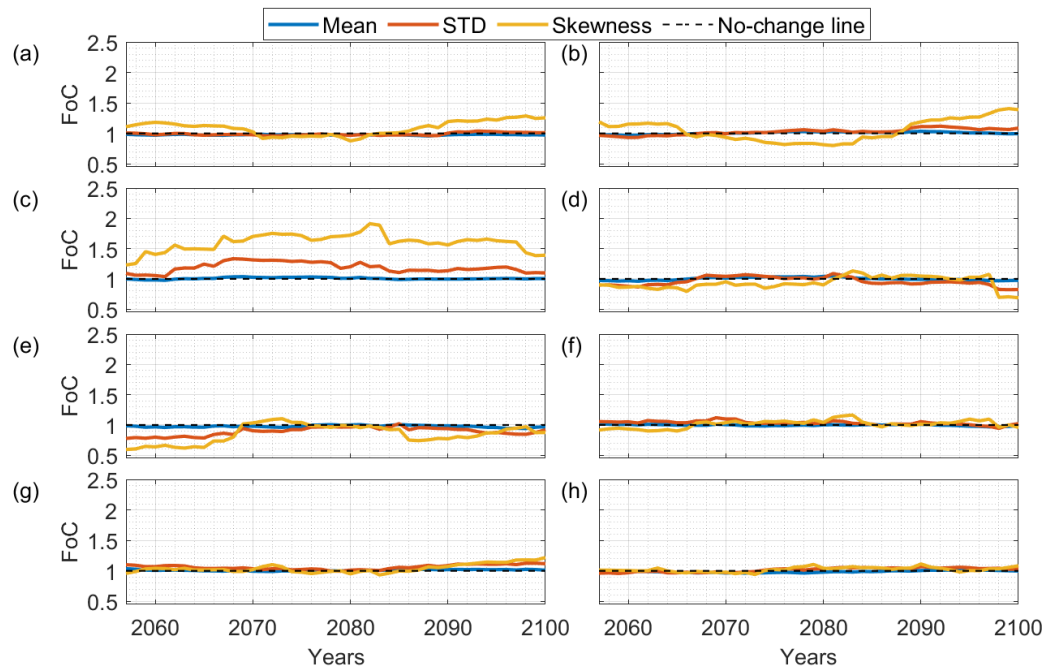
FIGURE 5.23 Factors of change of the statistics of the wave storm maximum significant wave height, evaluated considering the future scenario RCP8.5 for the following sites: (a) Alghero; (b) La Spezia; (c) Monopoli; (d) Ortona; (e) Catania; (f) Crotone; (g) Mazara del Vallo; (h) Ponza.

represented by Monopoli, which is characterized by an almost constant *FoC* equal to 0.9 (see Figure 5.24c), and by Catania, which presents a decreasing *FoC* from 1.3 to 1.0 during the period 2041-2090 (see Figure 5.24e). *FoC* evaluated for the standard deviation shows the same behavior of the one calculated for the mean, with the exception of Alghero (see Figure 5.24a). The skewness is characterized by *FoC* significantly different from the unit. In particular, the site of Alghero presents an initial *FoC* equal to 1.3, which decreases to 0.5 by 2100 (see Figure 5.24a). Figure 5.24b shows that for La Spezia *FoC* is close to 0.8 for the years 2065-2080 and 2095-2100, whereas for the remaining years is equal to 1.0. The variation of *FoC* observed for Monopoli and Ponza is similar (see Figure 5.24c-d): *FoC* is equal to about 1.4 until 2070, then decreases to 1.0 and in 2080 assumes a value close to 1.1. For the site of Catania, *FoC* evaluated for the skewness is almost equal to the ones calculated for the mean and the standard deviation until 2090, then decreases to 0.7 (see Figure 5.24e). Crotone is characterized by *FoC* close to 1.0, with the exception of the period 2070-2090, when it assumes values around 1.5 (see Figure 5.24f). Mazara del Vallo presents *FoC* close to 1.4 until 2065, when a rapid decreasing tendency to 1.0 starts (see Figure 5.24g). Finally, Figure 5.24h shows that *FoC* is equal to 1.1 during the years 2041-2070 and 2090-2100, whereas it assumes values close to 0.7 for the remaining years.

As regards the future scenario RCP8.5 (see Figure 5.25), the *FoC* evaluated for the mean of the wave storm duration is equal to 1.0 for all the sites, with the exception of Alghero, Monopoli and Catania, whose *FoC* assumes values slightly greater
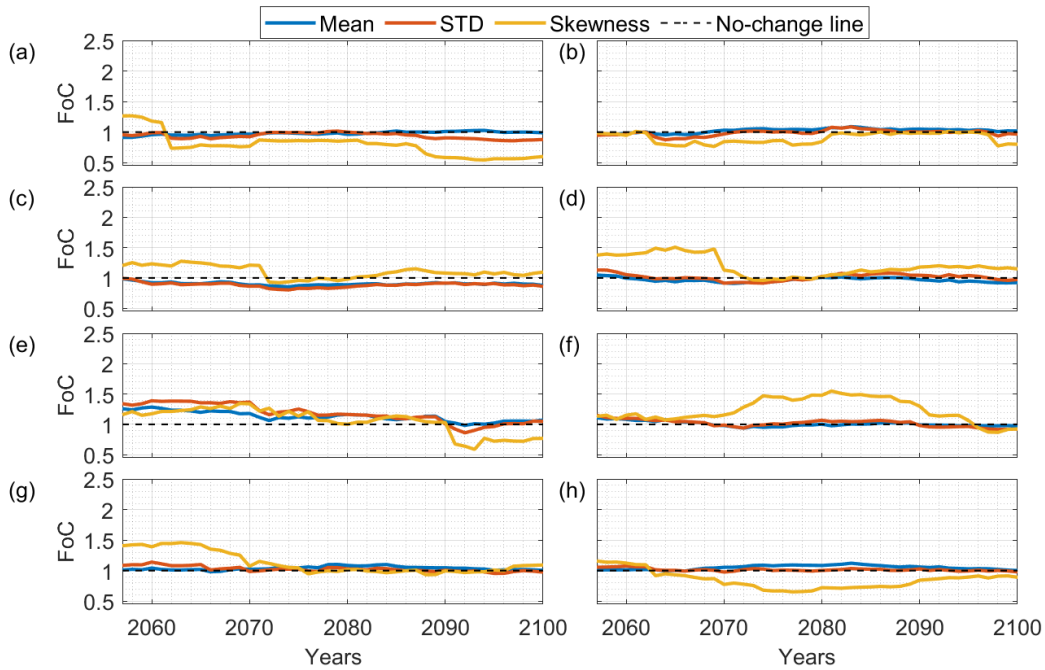
FIGURE 5.24 Factors of change of the statistics of the wave storm duration, evaluated considering the future scenario RCP4.5 for the following sites: (a) Alghero; (b) La Spezia; (c) Monopoli; (d) Ortona; (e) Catania; (f) Crotone; (g) Mazara del Vallo; (h) Ponza.

or smaller than unity (see Figure 5.25a, c and e). *FoC* evaluated for the standard deviation varies in time similarly to the one evaluated for the mean for each of the eight sites. The skewness is always characterized by a greater variability of *FoC*. In particular, for Alghero and La Spezia *FoC* oscillates between 0.9 and 0.6 (see Figure 5.25a-b). For the site of Monopoli *FoC* is about 1.1÷1.3, with the exception of the years between 2080 and 2090, when it assumes values closer to 0.8 (see Figure 5.25c). Ortona presents *FoC* between 1 and 1.2 (see Figure 5.25d), whereas for the sites of Catania, Crotone and Ponza *FoC* oscillates between 0.8 and 1.3 (see Figure 5.25e, f and h). Finally, Mazara del Vallo is characterized by *FoC* close to unity until 2085 with a peak of 1.2 in 2070, which rises up to 1.6 by 2100.

As discussed with reference to the wave storm maximum significant wave height, the *FoC* evaluated under scenarios RCP4.5 and RCP8.5 for the wave storm duration are very similar for the eight considered Italian sites. Indeed, the mean and the standard deviation are expected to suffer slight variations under both RCP4.5 and RCP8.5 scenarios. As regards the skewness, for the two future scenarios *FoC* oscillates between 0.5 and 1.5, but with different temporal patterns. Therefore, also the probability density function of the wave storm duration is likely to vary in terms of symmetry.

Figure 5.26 shows the results of the calculation of *FoC* for the peak wave period of wave storms under RCP4.5 future scenario. The variation of the mean is almost null, being *FoC* very close to unity for each of the studied sites. The standard deviation presents a greater variability during the period of analysis, but *FoC* is always in
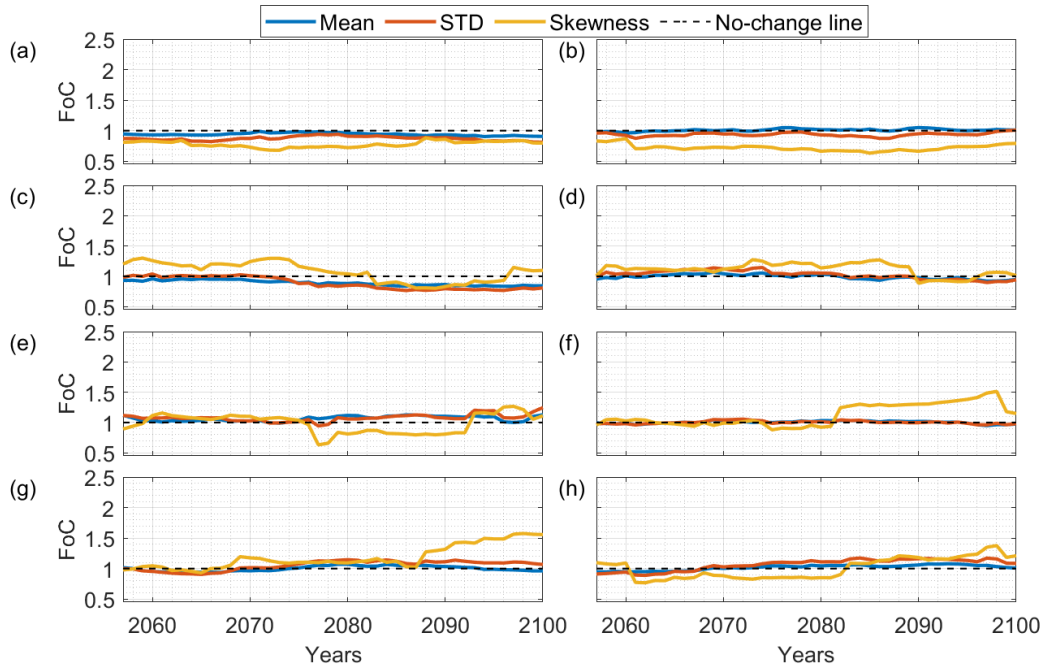
FIGURE 5.25 Factors of change of the statistics of the wave storm duration, evaluated considering the future scenario RCP8.5 for the following sites: (a) Alghero; (b) La Spezia; (c) Monopoli; (d) Ortona; (e) Catania; (f) Crotone; (g) Mazara del Vallo; (h) Ponza.

the range $0.8 \div 1.2$. The skewness is the most variable statistics and the related *FoC* assumes values between 0.5 and 2.0. In particular, Alghero, Mazara del Vallo and Ponza are mainly characterized by *FoC* greater than 1.0, in contrast to Ortona, Catania and Crotone. Instead, for La Spezia and Monopoli *FoC* assumes values closer to 1.00 for great part of the analyzed period, rising up to 1.5 during the last ten years.

The results of the evaluation of *FoC* for the wave storm peak wave period under the future scenario RCP8.5 are presented in Figure 5.27. Since *FoC* evaluated for the mean is always very close to 1.0 for all the eight sites, the mean appears not to suffer substantial variations in time. The standard variation is characterized by a null variation for Alghero, La Spezia, Crotone and Ponza, whereas *FoC* oscillates between 0.8 and 1.1 for the remaining sites. Finally, the skewness is again the most variable statistics, with *FoC* in the range $0.6 \div 1.7$. In particular, Alghero is characterized by *FoC* decreasing from 1.5 to 0.6 in the period 2041-2080, followed by an increasing tendency up to values close to 2.0 (see Figure 5.27a). Similarly, *FoC* evaluated for La Spezia initially decreases from 1.36 to 1.0, but in 2070 a positive trend starts up to values close to 1.7 (see Figure 5.27b). Monopoli, Ortona, Crotone and Ponza present smaller variations, between 0.6 and 1.2 (see Figure 5.27c, d, f and h). For the site of Catania, *FoC* initially oscillates between 0.6 and 1.1, but around 2080 a rapid increase up to $1.4 \div 1.5$ occurs, followed by an instantaneous collapse to 1.00 in 2100 (see Figure 5.27e). Finally, *FoC* evaluated for Mazara del Vallo varies around 1.25 until 2070, when an increasing tendency up 1.8 starts (see Figure 5.27g).

The results on the variation of the wave storm peak wave period demonstrate
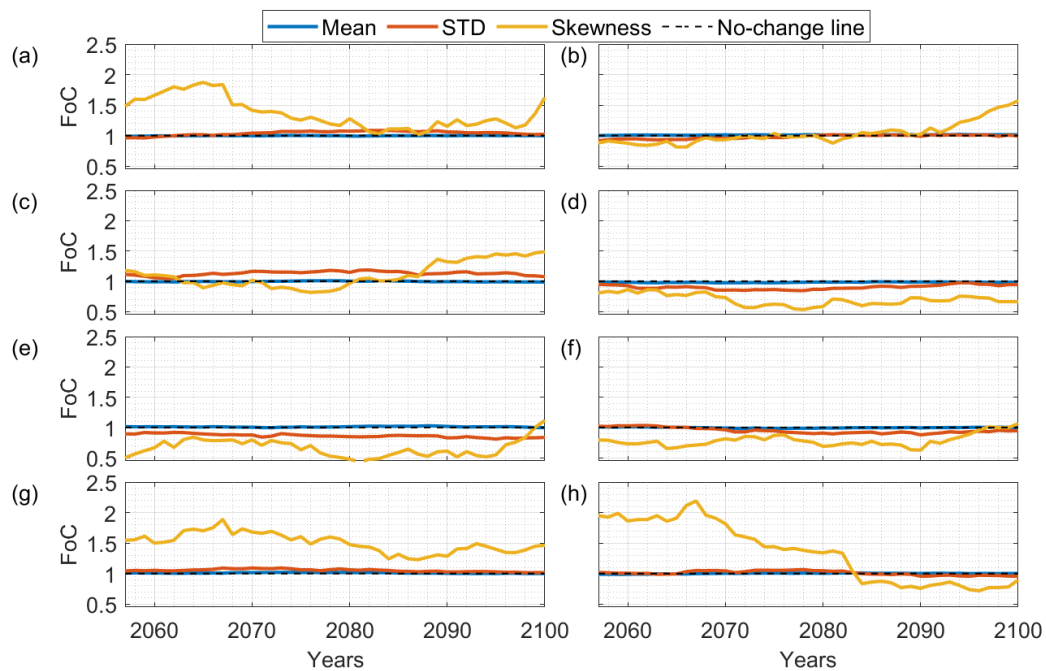
FIGURE 5.26 Factors of change of the statistics of the wave storm peak wave period, evaluated considering the future scenario RCP4.5 for the following sites: (a) Alghero; (b) La Spezia; (c) Monopoli; (d) Ortona; (e) Catania; (f) Crotone; (g) Mazara del Vallo; (h) Ponza.

that there are not relevant differences between the two future scenarios. As in the case of wave storm maximum significant wave height and duration, only the temporal patterns of variation of the skewness are different. Moreover, since the greater *FoC* were found for the skewness, future modifications of the symmetry of the statistical distribution of wave storm peak wave period are expected.

Figure 5.28 and Figure 5.29 show that the results of the analysis of *FoC* for the wave storm mean wave period under RCP4.5 and RCP8.5 scenarios are very similar to the one found for the wave storm peak wave period. In particular, the values of *FoC* calculated for the mean and the standard deviation of the wave storm mean wave period are almost identical to the ones evaluated for the wave storm peak wave period for all the eight considered sites. As regards the skewness, the time variations path of the wave storm mean wave period are very close to the ones of the wave storm peak wave period, but with slightly smaller *FoC* values, with the only exception of Catania under RCP8.5.

In conclusion, the projected variation of the statistics of the extreme Italian wave climate mainly refers to changes in the skewness (i.e. the symmetry) of the probability density functions of the considered variables. However, a coherent behavior among the eight sites has not been found, as well as monotone increasing or decreasing trends for the considered statistics. Therefore, a generalized characterization of the future Italian wave climate is not possible. The modification of the skewness of the extreme wave climate descriptors may cause changes in the frequency of extreme events, whose effects on the response of coastal defense structures could be
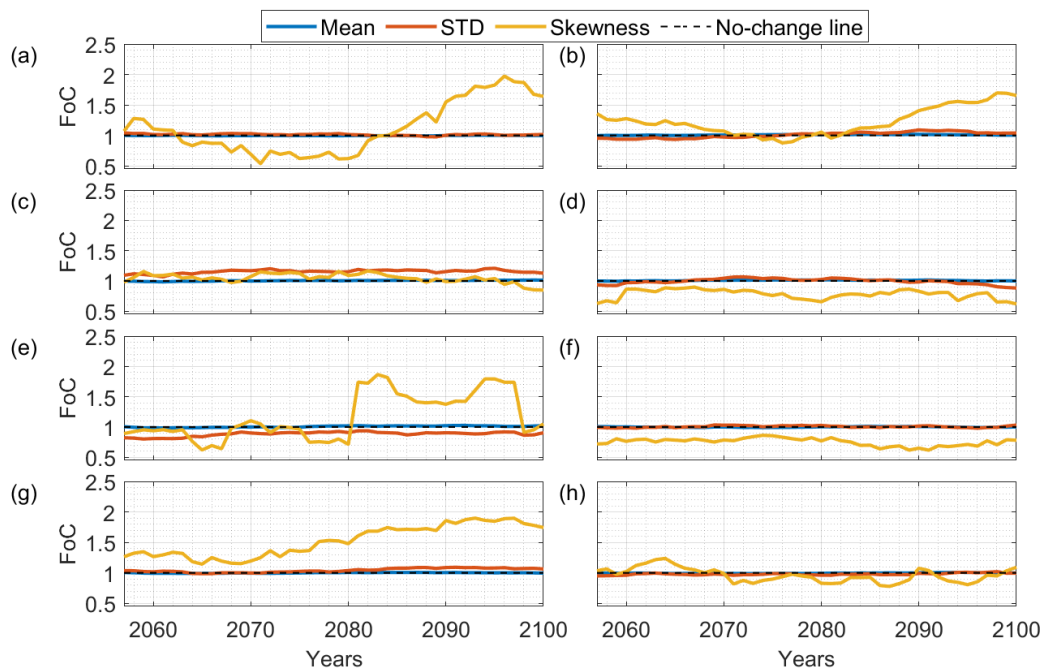
FIGURE 5.27 Factors of change of the statistics of the wave storm peak wave period, evaluated considering the future scenario RCP8.5 for the following sites: (a) Alghero; (b) La Spezia; (c) Monopoli; (d) Ortona; (e) Catania; (f) Crotone; (g) Mazara del Vallo; (h) Ponza.
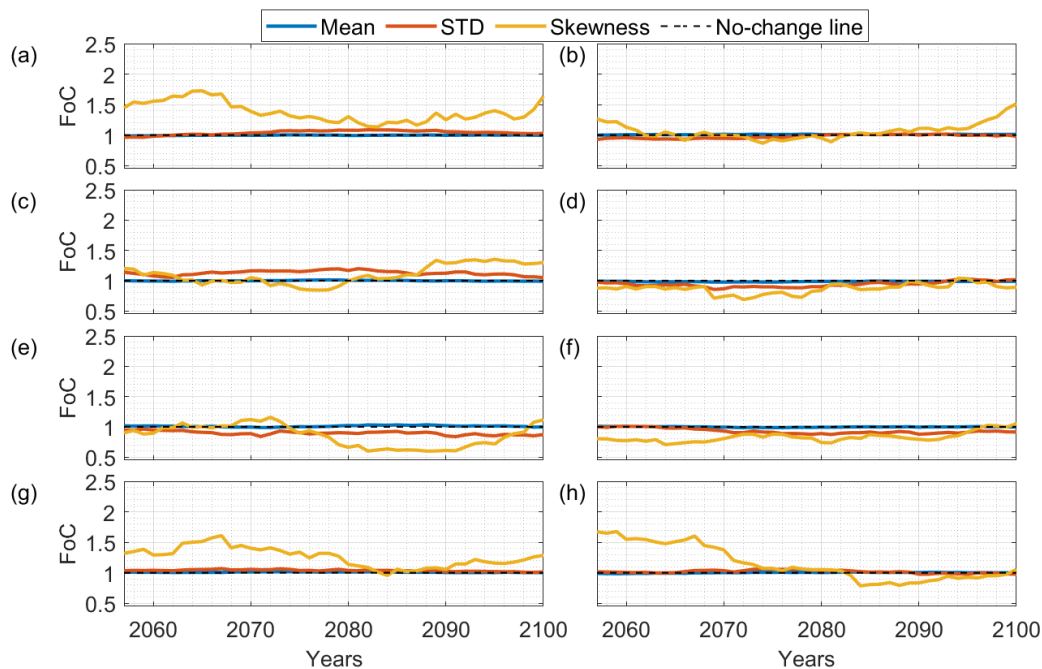
FIGURE 5.28 Factors of change of the statistics of the wave storm mean wave period, evaluated considering the future scenario RCP4.5 for the following sites: (a) Alghero; (b) La Spezia; (c) Monopoli; (d) Ortona; (e) Catania; (f) Crotone; (g) Mazara del Vallo; (h) Ponza.
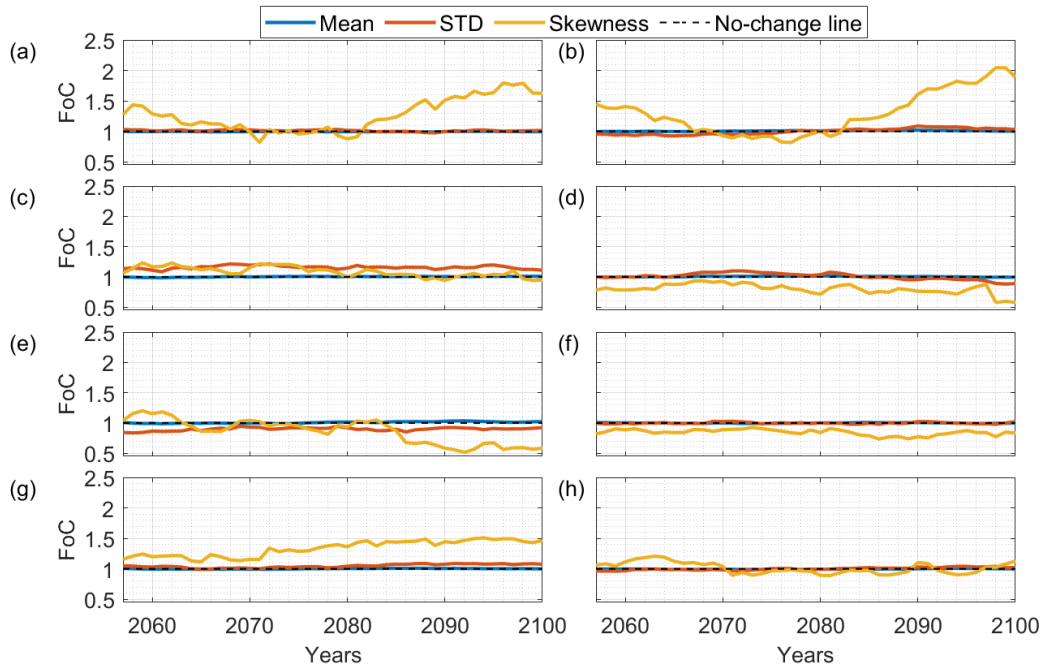
FIGURE 5.29 Factors of change of the statistics of the wave storm mean wave period, evaluated considering the future scenario RCP8.5 for the following sites: (a) Alghero; (b) La Spezia; (c) Monopoli; (d) Ortona; (e) Catania; (f) Crotone; (g) Mazara del Vallo; (h) Ponza.

investigated in terms of variation of their probability of failure, as will be further discussed in Chapter 7.

Chapter 6

Composite modeling of upgraded rubble mound breakwaters

6.1 Overview

The current state of art on the design of rubble mound breakwaters only refers to newly built structures. Indeed, there is a lack of data on the behavior of upgraded rubble mound breakwaters, and there are not specific models or formulations for their design.

The composite (or hybrid) modeling of rubble mound structures, which consists in the combination of physical and numerical modeling, allows one to take advantage of the best features of the two approaches and to reduce their intrinsic limitations. Such a methodology is even more favorable if non-conventional structures such as upgraded rubble mound breakwaters are considered. Indeed, experimental results are essential for the analysis of the behavior of structures which do not necessarily follow state of art formulations for newly built breakwaters. In addition, the use of a properly calibrated numerical models allows to extend and integrate the experimental data-set containing the technical and economical costs, also working at prototype scale. Both experimental and numerical data should be compared with state of art formulas that describes the damage dynamics or the overtopping phenomenon, to verify their applicability for the case of upgraded structures. If necessary, the traditional design equations can be adapted to reliably describe the response to the wave action of the tested upgrading configurations.

In the present work, the composite modeling of upgraded rubble mound breakwaters is described, considering the emblematic case study of the Catania harbor breakwater. First, the experimental set-up and techniques are described and the performed tests are presented. Experimental results on damage dynamic have been obtained from the count of the displaced armor units and from the evaluation of the armor layer erosion through a SfM based technique. In addition, the SfM based technique has been employed to carry out a novel investigation on the damage modes experienced by the different tested upgrading options, which was based on the analysis of the armor layer surface roughness. The mean overtopping discharge has been measured using an on-purpose designed system. In addition, the IH2VOF model

has been employed to extend the experimental data-set on mean overtopping discharge. The outcomes of the composite modeling have been compared with state of art formulas to verify their applicability to the studied case and to propose specific empirical formulas.

6.2 Methodology for modeling rubble mound structures

The acquisition of data on the behavior of upgraded rubble mound breakwaters under wave attack is fundamental for the assessment of the adequacy of the state of art formulas for the evaluation of the hydraulic performances of such non-conventional structures, or for the definitions of new specific experimental design equations. The composite (or hybrid) modeling represents the best tool for the analysis of the complex processes of interaction between upgraded rubble mound breakwaters and waves. Indeed, the combined use of physical and numerical modeling allows one to take advantage of the strengths and limiting the weaknesses of each individual approach (Oumeraci, 1999; Guanche et al., 2015; Di Lauro et al., 2019; Kamphuis, 2020). In particular, in the present work the experimental results on damage dynamics and overtopping discharge of the upgraded Catania harbor breakwater have been extended by numerical analyses regarding the overtopping phenomenon.

Two-dimensional experiments have been carried out at the Hydraulic Laboratory of the University of Catania, considering two representative sections of the Catania harbor breakwater in six upgrading configurations, which involve the addition of different type of extra armor units and/or the heightening of the wave wall. The construction of the model and the choice of the test input parameters have been performed following the indications of Frostick et al. (2011). The wave tank has been equipped with resistance gauges for the measurement of the simulated incident wave motion using the four gauges method of Faraci et al. (2015). Two video cameras have been employed to monitor the area of the model, thus enabling the quantification of the damage suffered by the external armor layer through the traditional parameter N_{od} (Hedar, 1960). Moreover, the development of a SfM based technique has permitted an in-depth analysis of the damage mechanisms, based on the study of the modifications of the armor layer surface roughness. The possibility to use such a technique at the prototype scale has been also verified. Finally, the mean overtopping discharge has been measured, in order to assess and compare the performances of the tested upgrading solutions to protect the harbor basin.

The experimental results on the overtopping phenomenon have been completed by the outcomes of 2D numerical simulations performed by using the IH2VOF model (Lara et al., 2011b; Lara et al., 2011a), which is able to solve the VARANS equations. The set-up of the numerical model has required the construction of the calculus domain, in terms of height, width and grid, so as to balance computational costs and reliability of the results. Then, the calibration of the porosity parameters

characteristic of each layer of the tested breakwater has been performed, employing the measured reflection coefficients and mean overtopping rates as reference data. The calibrated model allowed to obtain a quite large data-set, useful for the evaluation of specific empirical-numerical formulas for the prediction of mean overtopping discharge for the Catania harbor breakwater. Moreover, the possibility to scale up the numerical model has been verified, thus laboratory and prototype scale results have been compared.

The outcomes of the composite modeling of the Catania harbor breakwater represent a contribution to the development of a data-set regarding armor stability and overtopping pehnomenon of upgraded rubble mound structures. In addition, the empirical formulas calculated for the studied case have been employed for the probabilistic assessment of the Catania harbor breakwater performances, as described in Chapter 7.

6.3 Physical modeling of the Catania harbor breakwater

6.3.1 Experimental set-up

Wave tank

The experimental campaign on the upgraded Catania harbor breakwater has been carried out in Hydraulic Laboratory of the University of Catania. The wave tank is 18.00 m long, 1.20 m high and 3.60 m wide, two thirds of which have been used to perform the 2D experiments (see Figure 6.1). The initial and final walls are made up of reinforced concrete, whereas the two side walls are made up of transparent glass panels about 0.01 m thick, fixed on a metallic frame. The final part of the tank houses a gravel beach profile about 2.00 m long, which was used as working area during the experimental campaign.

The waves have been generated by a flap-type wavemaker placed on the initial part of the tank (see Figure 6.1 and Figure 6.2). The wave maker is activated by an electronically controlled oleo-dynamic system, whose components are slotted into an external control panel (see Figure 6.3a). Such a panel allows the generation of sinusoidal, triangular and square waves of specified frequency and amplitude. In addition, the system provides the possibility be controlled by external inputs thanks to a coaxial cable (type RG-59) connected to a National Instruments I/O board and a laptop equipped with an on-purpose developed software for the generation of random waves using JONSWAP spectra (see Figure 6.3b).

Acquisition of the waves characteristics

The wave motion characteristics have been measured by means of five resistance gauges (see Figure 6.4a-b), whose location in the wave tank is showed in Figure 6.1. Gauges n. 1, 2, 3 and 4 are properly spaced (see Table 6.1) in order to measure the incident and reflected wave motion following the four-gauge method of Faraci et
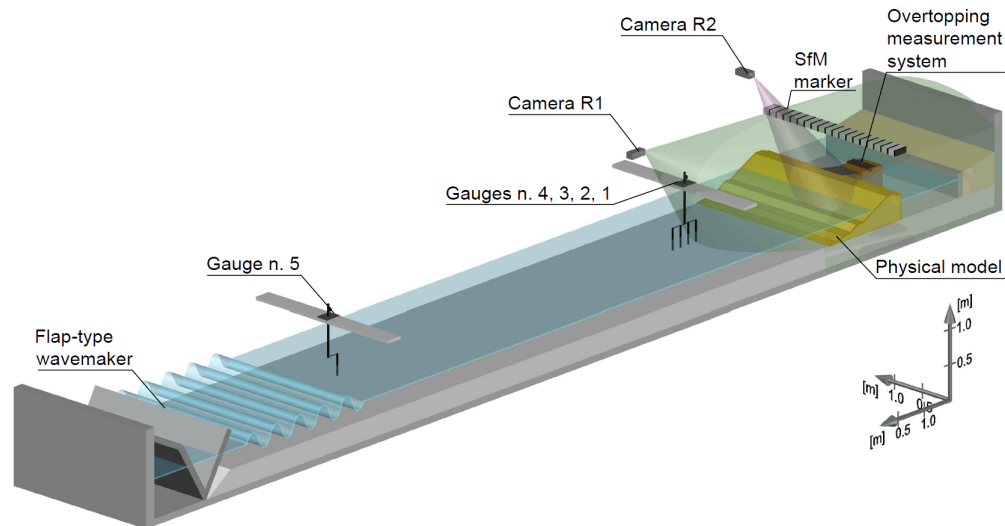
FIGURE 6.1 3D sketch of the section of the wave tank (18.00 × 2.40 × 1.20 m) of the Hydraulic Laboratory of the University of Catania used for the experimental campaign on the upgraded Catania harbor breakwater, and location of the measuring instruments.

al. (2015). In addition, gauge n. 5 is placed 5.0 m from the wave-maker to further monitor the hydrodynamic conditions in the wave generation zone.

Each gauge consisted of two stainless steel wires 0.30 m long, placed in parallel at a distance of 0.012 m. A high frequency voltage passes through the wires and, whose conductance changes proportionally to the immersion depth of the gauge. The changes in conductance due to the variation of free surface elevations (i.e.to the wave motion) corresponds to an analogical voltage output, which is controlled through a wave monitor, converted into a digital signal by an acquisition board (National Instruments NIUSB 6008) and then recorded and visualized through a laptop, thanks to a specially developed *LabView* code (see Figure 6.5). Such a code has allowed us the synchronization between all the measurement instruments (i.e. resistance gauges, video cameras and the acoustic gauge described in the following subsections).

The conversion of the resistance gauges output from voltage to free surface elevation in meters has been performed through a static calibration. Since the voltage output is linearly dependent on the free surface elevation, before each set of tests with constant water level the calibration has been performed by vertically raising and lowering the wave gauges at known distances. For each wave gauge the mean voltage outputs correspondent to three heights were recorded: -0.08 m, 0.00 m and

TABLE 6.1 Distance from the toe of the model of the four resistance gauges placed for the application of the four-gauge method of Faraci et al. (2015).

Gauge 1	Gauge 2	Gauge 3	Gauge 4
1.15 m	1.25 m	1.75 m	1.86 m

FIGURE 6.2 Paddle of the flap-type wave-maker of the wave tank of the Hydraulic Laboratory of the University of Catania.
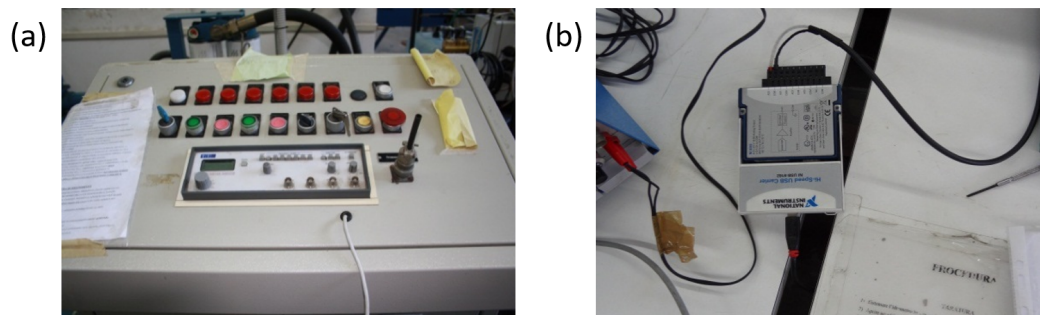
FIGURE 6.3 (a) Control panel for the generation of regular waves; (b) coaxial cable (type RG-59) and National Instruments I/O board used for the connection to a common laptop equipped with a specially developed software for the generation of random waves by means of JONSWAP spectra.

+0.08 m, being the second one the properly fixed working position. Then, the conversion law from Volts to meters has been calculated through the least-squares linear regressions method.

Monitoring of the armor blocks displacements

The video camera R1 (Sony FDR-AX53, see Figure 6.6a) has been placed on a scaffolding at 2.40 m from the toe of the structure (see Figure 6.1), so as to frontally frame
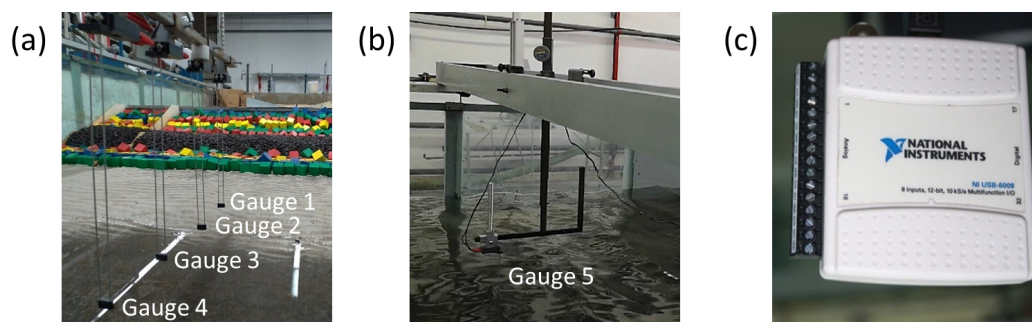
FIGURE 6.4 (a) Resistance gauges placed in front of the model for the application of the four-gauge method of Faraci et al. (2015); (b) resistance gauge placed in front of the wave-maker to monitor the wave generation zone; (c) acquisition board National Instruments (NIUSB 6008).

the whole model. As mentioned in subsection 6.3.1, an on-purpose developed *Lab-View* code has allowed the synchronization between video camera R1 and all the other measurement instruments. In this way, records of the movements of the armor units during wave attack have been acquired. The calculation of the traditional damage parameter N_{od} could be performed by using the following equation (Hedar, 1960):

$$N_{od} = \frac{N_{moved}}{B_s D_{n50}} \tag{6.1}$$

where N_{moved} is the number of displaced units, B_s is the width of the tested section and D_{n50} is the median nominal diameter of the armor units. The cumulative N_{od} has been calculated at the end of each sea state.

Monitoring of the armor layer surface modifications

A Structure from Motion (SfM) technique (Torres et al., 2012; Hofland et al., n.d.; van Gent and van der Werf, 2014) has been used to recover the 3D point cloud of the structure at the beginning and at the end of each sea state from a set of 2D images acquired from the dry model by a camera Sony Cyber-shot DSC-HX9V 16.2 MP G Lens (see Figure 6.6c). Image overlapping was about 80%. The software *Agisoft Metashape* has been employed for the calculation of the point clouds. First, the alignment of each set of 2D images has been performed, setting high accuracy. Then, the resulting point clouds have been converted into dense point clouds, setting the parameter quality to high. The very dense 3D point clouds (density of about 50 points per cm^2) have been scaled using a reference marker, which is a graduated metallic bar placed above the model to be always visible in the 2D shoots (see Figure 6.7). Then, the scaled 3D point clouds have been converted into meshes using
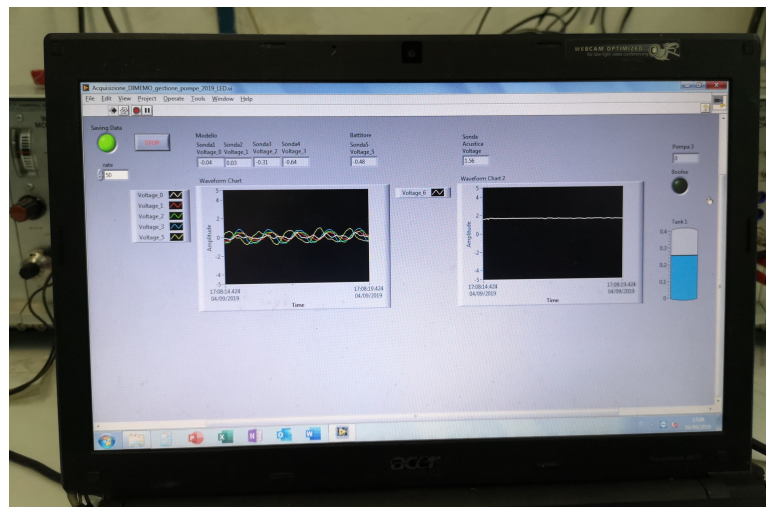
FIGURE 6.5 Interface of the *LabView* code specially developed for the synchronized acquisition of the output coming from the employed resistance gauges, video cameras and acoustic gauge.

FIGURE 6.6 Optical devices employed during the experimental campaign: (a) Sony FDR-AX53; (b) Sony HDR-CX410VE; (c) Sony Cyber-shot DSC-HX9V 16.2 MP G Lens.

FIGURE 6.7 Marker used to scale the 3D point clouds of the model recovered by means of the SfM technique.

a calculation grid 0.001×0.001 m. Such meshes have been employed to monitor the progression of the armor layer erosion under increasing wave load, using both traditional and novel techniques.

The evaluation of the traditional armor layer damage parameter $S_{d,m}$ defined by Broderick and Ahrens (1982) has been performed at end of each sea state with reference to the entire width of the model B (Campos et al., 2014):

$$S_{d,m} = \frac{1}{n_{cs}} \sum_{i=1}^{n_{cs}} \frac{A_{e,i}}{D_{n50}^2} \tag{6.2}$$

where n_{cs} is the number of cross sections of 3D reconstruction of the armor layer (spatial step of 0.001 m), $A_{e,i}$ is the eroded area of the $i - th$ cross section with respect to the zero-damage condition and D_{n50} is the median nominal diameter of the armor units.

Damage maps have been calculated as the difference between the armor layer mesh recovered at the end of each sea state and the initial one. Negative values of the height difference indicate the presence of excavations due to the displacements of one or more armor units, which can deposit in other zones of the armor layer or near the structure toe, generating positive height differences.

The study of the modifications of the armor layer surface roughness can give useful information concerning the damage or simple settling modes experienced by the structure, even if significant damage levels are not reached. In addition, information about the roughness of the existing armor layer is of great interest if damaged rubble

mound breakwaters are considered, since their section could be very different from the design one. Therefore, a novel analysis of the armor layer dynamics has been carried out, considering the surface macro-roughness and micro-roughness. Figure 6.8 shows a simplified sketch of the armor layer macro and micro-roughness: the first one represents the blocks laying surface (wavelength is of the order of $4 \div 5$ times D_{n50}), whereas the latter one gives a measure of the surface porosity of the armor layer (wavelength is of the order of D_{n50}).

The employed technique for the analysis of the armor layer surface is based on the the 3D reconstructions of the structure recovered using the SfM technique at the beginning and at the end of each sea state. For the first time, the mesh processing procedure described by Blateyron (2014) for the analysis of the surface topography of metal foils used in industry has been employed to study the surface roughness of the armor layer of a rubble mound structure. First, the mesh has been properly rotated referring to a horizontal plane and denoised using a low-pass 2D Gaussian filter with a cut-off frequency equal to 0.01 m^{-1}. It is important to point out that in correspondence of the cut-off frequency of a low-pass 2D Gaussian filter, only the 50% reduction of the signal power occurs, and such a reduction increases towards smaller frequencies (Whitehouse, 2002). Another 2D Gaussian filter, with a cut off frequency equal to the inverse of the median nominal diameter of the armor units (i.e. $1/D_{n50}$), has been applied to the elaborated mesh, in order to distinguish the macro-roughness and micro-roughness.

As regards the macro-roughness, bi-dimensional traditional roughness descriptors have been calculated for the ensemble average of the y profiles of the armor layer surface, such as the mean wavelength λ_M and the maximum wave height HD (Gadelmawla et al., 2002).

A two-dimensional spectral analysis of the micro-roughness has been carried out implementing a 2D Fast Fourier Transform (FFT) of the surface (Sidick, 2009;
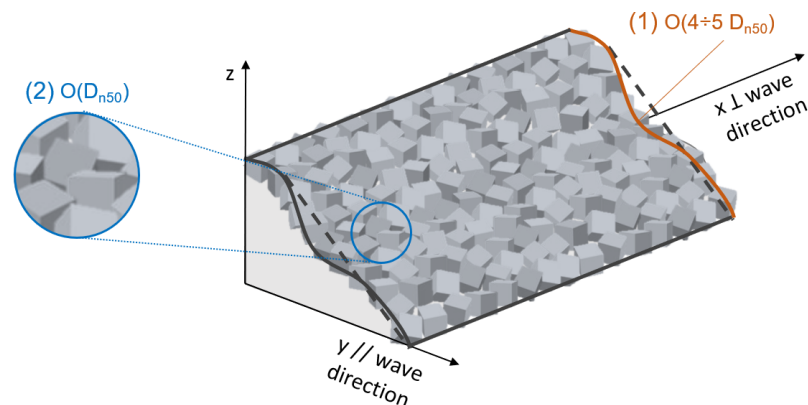
FIGURE 6.8 Sketch of the armor layer surface (1) macro-roughness and (2) micro-roughness analyzed through the SfM-based technique. The dashed and continuous lines respectively represent the generic design and damaged cross section.

Dong and Stout, 1995; Czifra et al., 2011). The micro-roughness surface is not periodic as required for a FFT analysis. Hence, a preliminary removal of the edge artifacts (i.e. several crosses of high-amplitude coefficients in the frequency domain) has been performed by applying the windowing approach, which consists in progressively attenuate the edges of the surface. To this aim, in the present work a radially symmetric Hann window has been applied (Jacobs et al., 2017). Then the micro-roughness spectral wavelength λ_m relative to the spectrum centroid has been calculated using the following equation (Nelson and Voulgaris, 2014; Nelson and Voulgaris, 2015; Voulgaris and Morin, 2008):

$$\lambda_m = \frac{1}{\sqrt{f_{x,c}^2 + f_{y,c}^2}} \tag{6.3}$$

where $f_{x,m}$ and $f_{y,m}$ are the spectral frequencies relative to the spectrum centroid respectively along x and y directions.

Measurement of the overtopping rates

The overtopping phenomenon has been monitored by the video camera R2 (Sony HDR-CX410VE, see Figure 6.6b), which has been placed on a side scaffolding to record the waves going beyond the crest of the structure (see Figure 6.1). It is worth to point out that video camera R2 has been synchronized with the other measurement instruments thanks to a *LabView* code (see subsection 6.3.1).

In addition, the measurement of the mean overtopping discharge rate per linear meter (q) has been performed, by using a specially designed system placed behind the model (see Figure 6.1 and Figure 6.9), as suggested by Iuppa et al. (2019). A collection tank ($0.40 \times 0.40 \times 0.30$ m) has been properly anchored to the ground and equipped with a trapezium-shaped inclined ramp (largest side 0.98 m, smaller side 0.22 m, height 0.60 m) to channel the water that overflow behind the structure.

FIGURE 6.9 System for the measurement of the mean overtopping discharge per meter (q) placed behind the physical model.

An acoustic sensor (Pepperl Fuchs UC500-30GM70-IE2R2-V15) measures the water level inside the reservoir, in sync with the other measurement instruments (see subsection 6.3.1). The continuous measurement of the water volume inside the collection tank has allowed us the calculation of the mean overtopping discharge for a certain time interval, by means of a calibration law which relates levels and volumes inside the collection tank. Such a law has been defined before starting the physical model tests. In particular, the water levels correspondent to subsequent 0.002 m^3 poured water volumes have been measured by the acoustic gauge until a total volume of 0.024 m^3 was collected inside the tank. Then a parabolic volumes-levels law has been calculated through the last-squares method. Three parallel drainage pumps (NEWA JET 6000) connected to the reservoir have ensured its emptying until a minimum threshold (i.e. 0.12 m) when reached the fixed maximum water level (i.e. 0.30 m), thanks to the above mentioned *LabView* code. The tank emptying process lasted about 10 s, and hence it is fast enough to not significantly influence the measurement of the mean overtopping discharge.

6.3.2   Design and construction of the physical model

The upgraded Catania harbor breakwater has been studied through the construction of a 1:70 geometrically undistorted model, according to most current state of art of physical modeling of rubble mound structures (Frostick et al., 2011).

The size of quarry stones and of artificial blocks used for the construction of the physical model has been selected to guarantee the similarity in terms of stability number between model and prototype, according to the methodology proposed by Hudson et al. (1979). Therefore, the weight of each kind of employed unit has been scaled by dividing the prototype weight by the following factor:

$$N_{wa} = \frac{N_{\gamma a} N_L^3}{N_{\gamma a/\gamma w-1}^3} \tag{6.4}$$

where N_{wa} is the stability number, $N_{\gamma a}$ is the ratio between the specific weight of prototype and model unit, N_L is the geometric scale (i.e. 70 in this case) and $N_{\gamma a/\gamma w-1}$ is the ratio between the buoyant density of prototype and model unit.

Table 6.2 reports the densities of the prototype and model units and of water, whereas Table 6.3 shows the results of the application of the method proposed by Hudson et al. (1979) for the calculation of the D_{n50} of both quarry stones and artificial blocks.

It is worth to point out that the used resin for the production of the artificial armor units (see Figure 6.10) has been chosen so that the calculated D_{n50} was sufficiently large to minimize the viscous scale effects, i.e. to ensure Reynolds number of the armor units greater than $1 \div 4 \times 10^4$ (van der Meer, 1988a). In addition, the armor blocks have been painted to both reduce the friction scale effects and facilitate the optical analysis of the armor unit dynamics.

TABLE 6.2 Density of water (ρ_w) and of the employed quarry stones and artificial blocks (respectively ρ_{qs} and ρ_s) at prototype and model scale.

	ρ_w [Kg/m^3]	ρ_{qs} [Kg/m^3]	ρ_s [Kg/m^3]
Prototype	1030	2600	2300
Model	1000	2600	1560

TABLE 6.3 Median nominal diameter (D_{n50}) of the employed quarry stones and artificial blocks at prototype and model scale.

	D_{n50} [m]				
	I category	II category	III category	Cube	Antifer
Prototype	0.268÷0.727	0.727÷1.049	1.049÷1.391	2.998	2.354
Model	0.004÷0.010	0.010÷0.014	0.014÷0.019	0.059	0.046
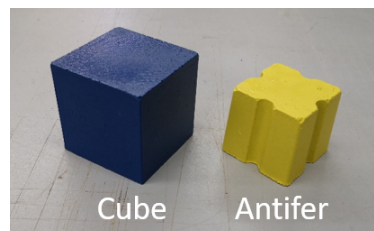
FIGURE 6.10 Artificial cubes (D_{n50}=0.059 m) and Antifer (D_{n50}=0.046 m) employed for the construction of the physical model.

The physical model construction inside the wave tank (see Figure 6.1) consisted of the following steps:

1. building of an impermeable wall as back support of the rubble mound structure (see Figure 6.11a);

2. installation of the specially designed concrete wave wall (see Figure 6.11b);

3. placement of reference side plywood shapes and wires for the correct reproduction of the structures layers (see Figure 6.11a);

4. construction of the structure core by placing I and II category quarry stones, previously selected by means of 1/6″ and 1/2″ sieves, over a plastic squared meshed net of 0.005 m to avoid the removal of the finest bottom material (see Figure 6.12a);

5. construction of the structure core using III category quarry stones, previously selected by means of 1/2″ and 3/4″ sieves (see Figure 6.12b);

6. construction of the existing armor layer by randomly placing the cubic units (see Figure 6.13a);
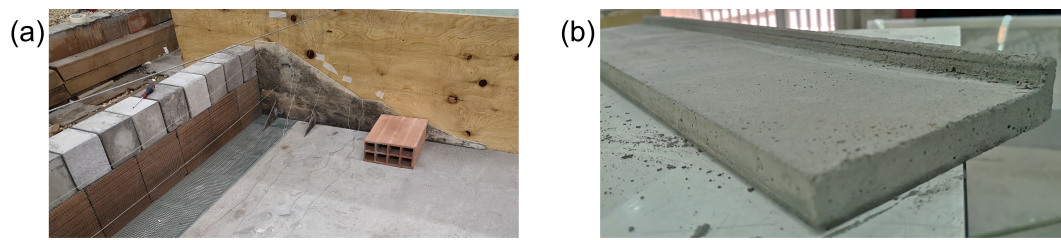
FIGURE 6.11 Construction of the physical model: (a) impermeable wall as back support of the rubble mound structure; (b) specially designed concrete wave wall.
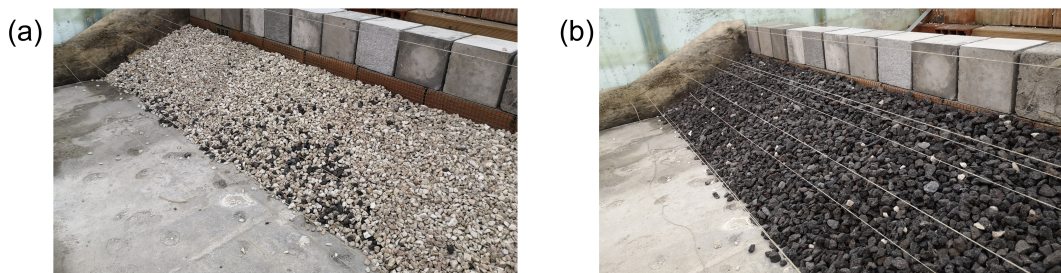
FIGURE 6.12 Construction of the physical model: (a) core of the rubble mound structure made up of I and II category quarry stones; (b) filter layer of the rubble mound structure made up of III category quarry stones.
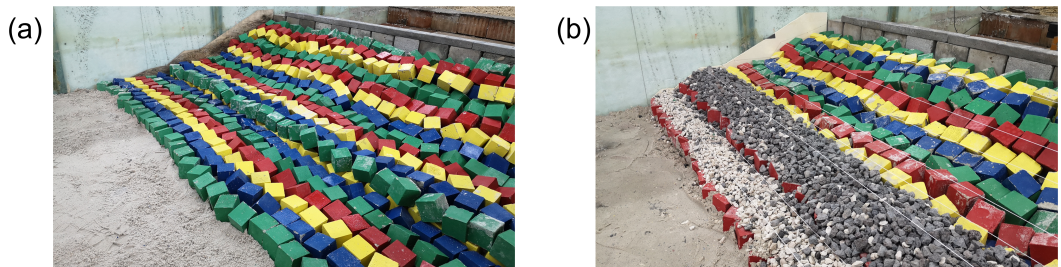
FIGURE 6.13 Construction of the physical model: (a) existing armor layer made up of cubic units; (b) toe berm made up of III category quarry stones.
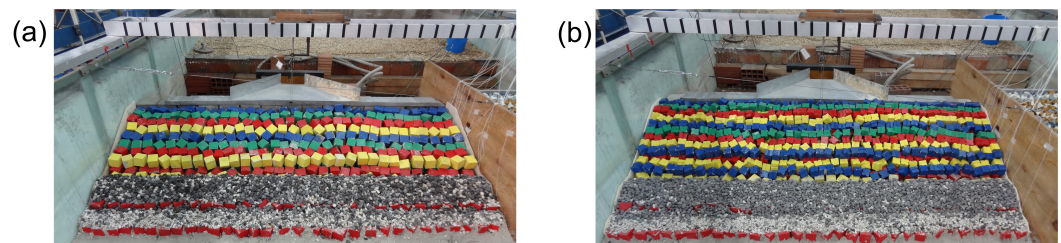
FIGURE 6.14 Construction of the physical model: (a) additional armor layer made up of cubic units; (b) additional armor layer made up of Antifer units.

7. construction of the toe berm using III category quarry stones, previously selected by means of 1/2″ and 3/4″ sieves, to support the additional armor layer (see Figure 6.13b);

8. construction of the additional armor layer by randomly placing the cubic units or the Antifer blocks (see Figure 6.14).

It is worth to point out that the values of armor layer porosity are comparable to the ones of literature experimental campaigns on rubble mound breakwaters made up of cubic (van Gent, 2014) or Antifer (Frens, 2007) armor units (Frens, 2007).

6.3.3 Test conditions and experimental procedure

Two representative sections of the Catania harbor breakwater have been tested, i.e. section n. 10 and n. 40 (see Figure 6.15). Section n. 10, which is showed in Figure 6.16a, has been selected because of its strong geometric irregularities, and it is characterized by a ratio between the design significant wave height and the water depth $H_{s,d}/h = 0.38$ and a product between the design wave number and the water depth (i.e. dispersion parameter) $k_d h = 0.50$. Section n. 40, which is showed in Figure 6.16b, has been chosen because it is representative of the most offshore section, and hence the most exposed part of the breakwater to the wave load, being $H_{s,d}/h = 0.35$ and $k_d h = 0.60$. For both sections, the six upgrading solutions showed in Figure 6.17 and Figure 6.18 and summarized in Table 6.4 have been considered (see section 3.3.3).

TABLE 6.4 Summary of the tested configurations of the Catania Harbor breakwater. Weights and heights are given at prototype scale.

Configuration	Description
E	Existing structure with wave wall crest raised up to +8.50 m above MSL
EM	Existing structure with wave wall crest raised up to +9.50 m above MSL
AS	Originally proposed armor layer restoration with 30 t Antifer units, a quarry stone toe berm and wave wall crest raised up to +8.50 m above MSL
AD	Double layer 30 t Antifer blocks armor layer restoration, a quarry stone toe berm and wave wall crest raised up to +8.50 m above MSL
CM	Single layer 62 t cubic blocks armor layer restoration, a quarry stone toe berm and wave wall crest raised up to +8.50 m above MSL
CS	Armor layer restoration with 62 t cubic blocks laid following the AS section, also moving the existent blocks if necessary, a quarry stone toe berm and wave wall crest raised up to +9.50 m above MSL
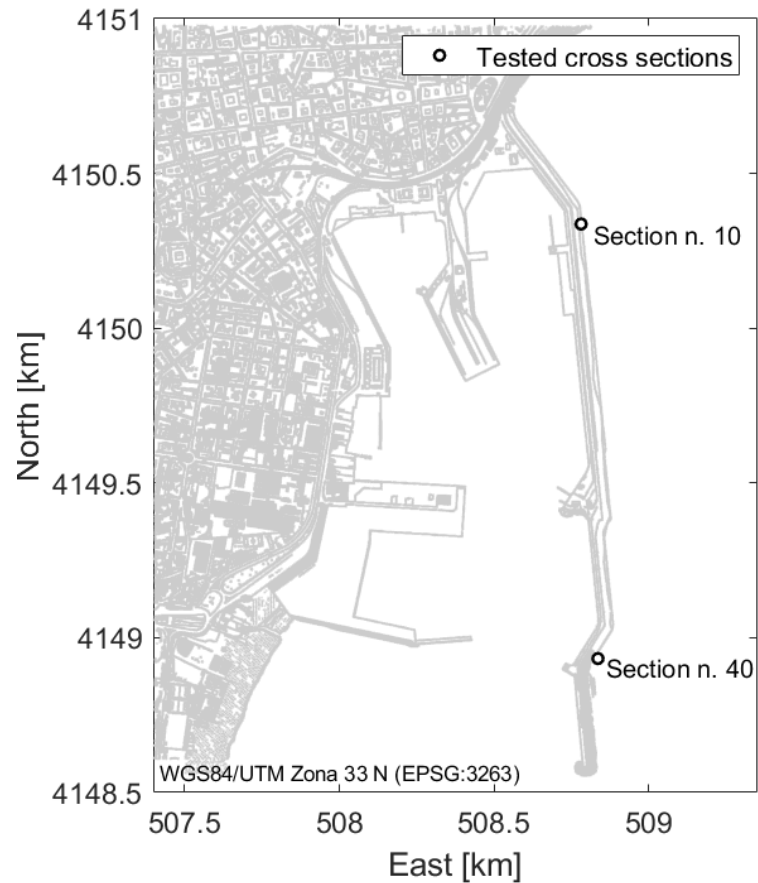
FIGURE 6.15 Layout of the Port of Catania and indication of the outer breakwater representative sections n. 10 ($H_{s,d}/h = 0.38$; $k_d h = 0.50$) and n. 40 ($H_{s,d}/h = 0.36$; $k_d h = 0.60$).
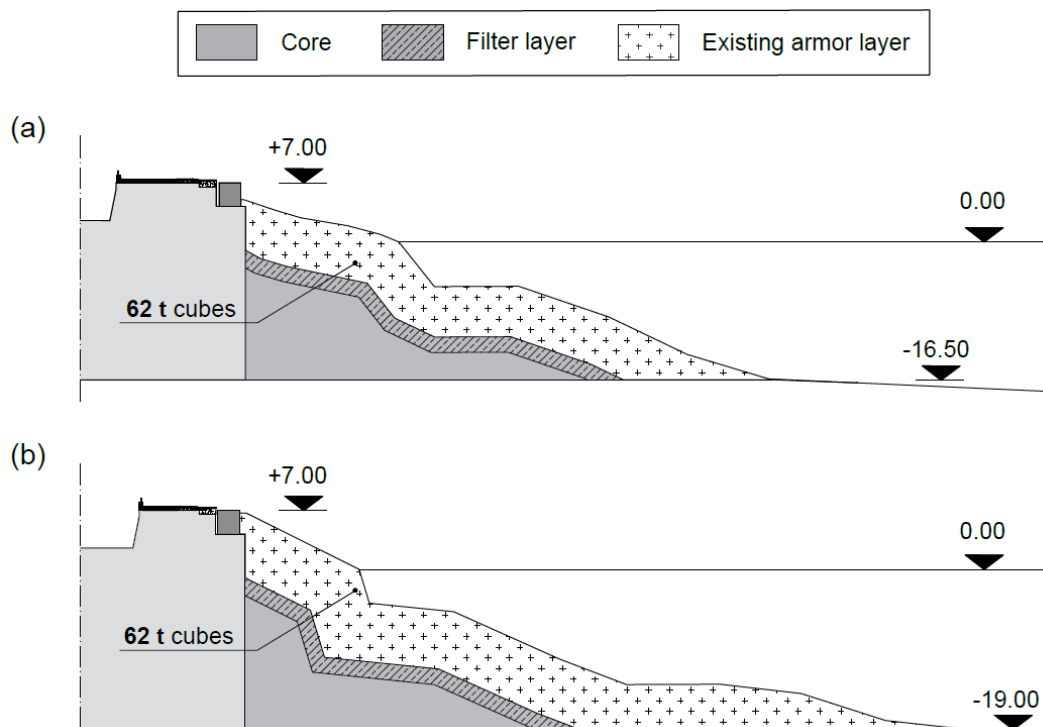
FIGURE 6.16 Sketches of the representative cross-sections of the Catania harbor breakwater: (a) section n. 10 ($H_{s,d}/h = 0.38$; $k_d h = 0.50$); (b) section n. 40 ($H_{s,d}/h = 0.36$; $k_d h = 0.60$).
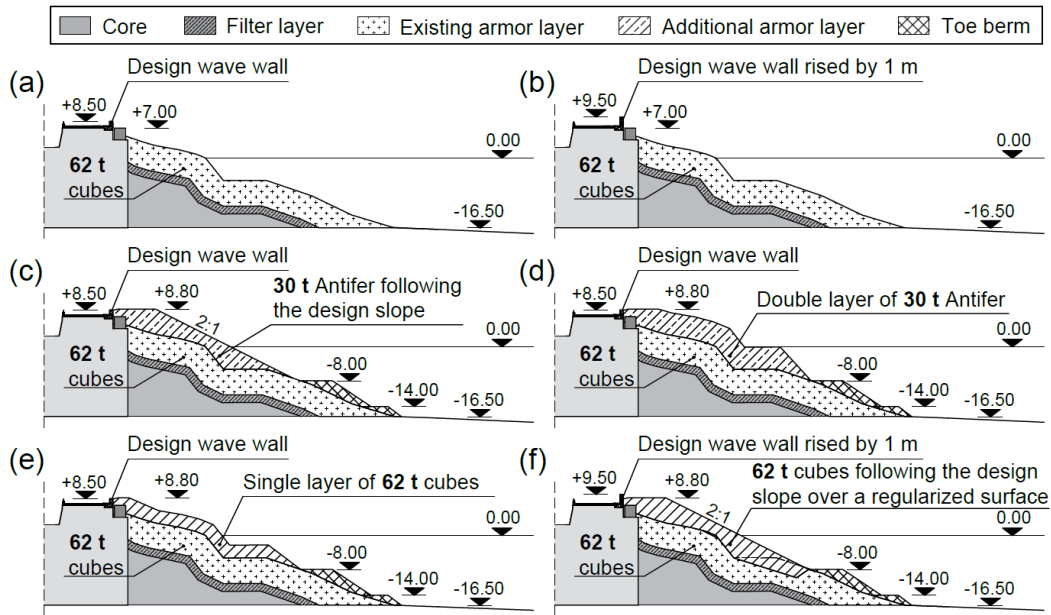
FIGURE 6.17 Sketches of the proposed upgrading solutions for the Catania harbor breakwater, section n. 10: (a) configuration E; (b) configuration EM; (c) configuration AS (originally proposed by the Port Authority); (d) configuration AD; (e) configuration CM; (f) configuration CS. Measures are given at prototype scale.
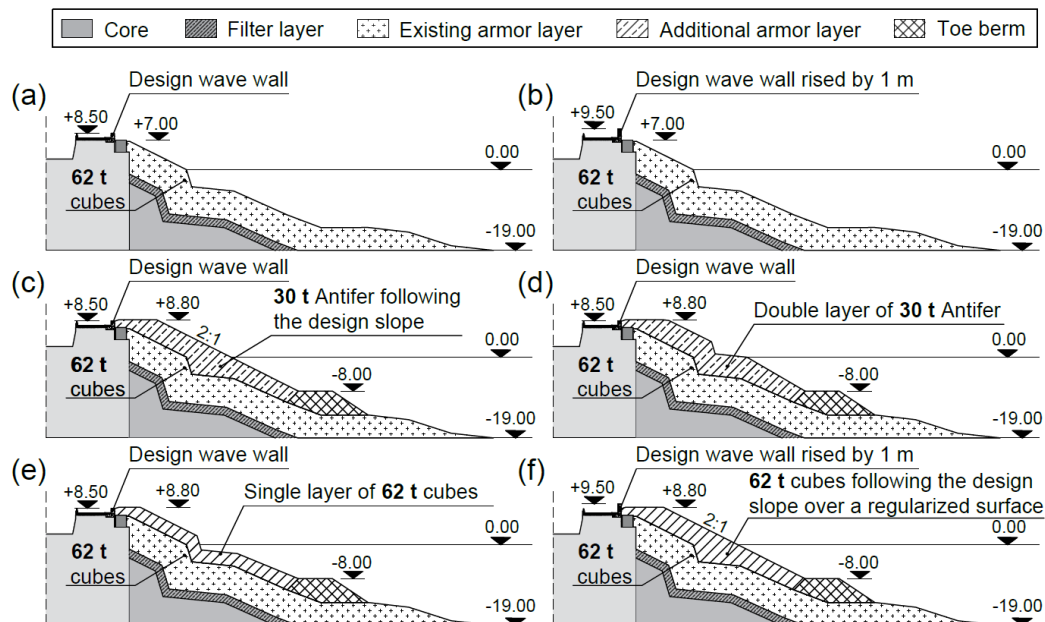
FIGURE 6.18 Sketches of the proposed upgrading solutions for the Catania harbor breakwater, section n. 40: (a) configuration E; (b) configuration EM; (c) configuration AS (originally proposed by the Port Authority); (d) configuration AD; (e) configuration CM; (f) configuration CS. Measures are given at prototype scale.

A precise experimental procedure has been defined to ensure reliability and comparability of the tests outcomes. Moreover, to this aim, 113 preliminary tests have been carried out to properly calibrate the hydrodynamic parameters that govern the wave motion inside the wave tank, and to examine the outputs of the measurement instruments (see Appendix A).

The input hydrodynamics conditions are summarized in Table 6.5 and Table 6.6, in terms of significant wave height H_s and peak wave period T_p of random JON-SWAP wave motion, mean sea level h and number of incident waves N_w. Note that the design h is equal to the water depth at the toe of the structure plus the increase due to meteorological and astronomical tide, which for the site of Catania is equal to 0.50 m. For each configuration (see Table 6.4), first, a shakedown test has been carried out for the settling of the structure with three consecutive sea state of 1500 waves corresponding to 5 years-return period. Then, traditional tests considering sea states of 4500 waves, divided into three equal intervals, corresponding to 10, 50 and 100 years-return period (the latter is the design return period) have been performed. If no damage has been observed, a further sea state of 4500 waves, divided into three identical intervals, characterized by significant wave height equal to 120% of the 100 years-return period one (i.e. $H_{s,d}$) has been reproduced. Finally, the effects of mean sea level rise (SLR) have been investigated, considering the existing structure with wave wall raised up to +8.50 m above MSL (i.e. configuration E, see Figure 6.17a, 6.18a and Table 6.4). Indeed, sea states corresponding to 50 and 100

TABLE 6.5 Input hydrodynamic conditions in terms of significant wave height (H_s), peak wave period (T_p), mean sea level (h) and number of waves (N_w) simulated during the tests on the physical model of section n. 10. The values are given at both prototype and model scale.

| Wave ID | Prototype scale | | | Model scale | | | N_w |
	H_s [m]	T_p [s]	h [m]	H_s [m]	T_p [s]	h [m]	[n. of waves]
I	4.490	9.63	17.00	0.06	1.15	0.24	3×1500
II	4.91	10.06	17.00	0.07	1.20	0.24	3×1500
III	5.81	10.97	17.00 - 18.40	0.08	1.31	0.24 - 0.26	3×1500
IV	6.16	11.34	17.00 - 18.40	0.09	1.36	0.24 - 0.26	3×1500
V	7.39	11.34	17.00	0.11	1.36	0.24	3×1500

TABLE 6.6 Input hydrodynamic conditions in terms of significant wave height (H_s), peak wave period (T_p), mean sea level (h) and number of waves (N_w) simulated during the tests on the physical model of section n. 40. The values are given at both prototype and model scale.

| Wave ID | Prototype scale | | | Model scale | | | N_w |
	H_s [m]	T_p [s]	h [m]	H_s [m]	T_p [s]	h [m]	[n. of waves]
I	4.68	9.65	19.50	0.07	1.15	0.28	3×1500
II	5.14	10.08	19.50	0.07	1.20	0.28	3×1500
III	6.21	11.00	19.50 - 20.90	0.09	1.31	0.28 - 0.30	3×1500
IV	6.65	11.37	19.50 - 20.90	0.10	1.36	0.28 - 0.30	3×1500
V	7.98	11.37	19.50	0.12	1.36	0.28	3×1500

years-return period of 4500 waves, divided into three intervals of 1500, have been simulated in the presence of a 0.02 m (i.e. 1.40 m in the prototype scale, see Table 6.5 and Table 6.6) increase in mean sea level (Lambeck et al., 2011). Therefore, a total of 192 tests have been performed for the six upgrading options of the Catania harbor breakwater (see Appendix A).

6.3.4 Evaluation of the armor layer roughness descriptors

The SfM technique has been used for the 3D reconstruction of the tested configurations of the Catania harbor breakwater, at the beginning and at the end of each sea state. As mentioned in section 6.3.1, such recovered point clouds have been used to perform a novel analysis of the armor layer surface dynamics, in terms of variation of the macro and micro-roughness under increasing wave loads. In the following, the procedure for the evaluation of the macro and micro-roughness descriptors used for the study of the upgraded Catania harbor breakwater is described.

First of all, the mesh of the armor layer surface has been recovered from the 3D point cloud derived from the application of the SfM technique. Figure 6.19 shows the case of configuration AS of section n.10 after the simulation of the 5 years return
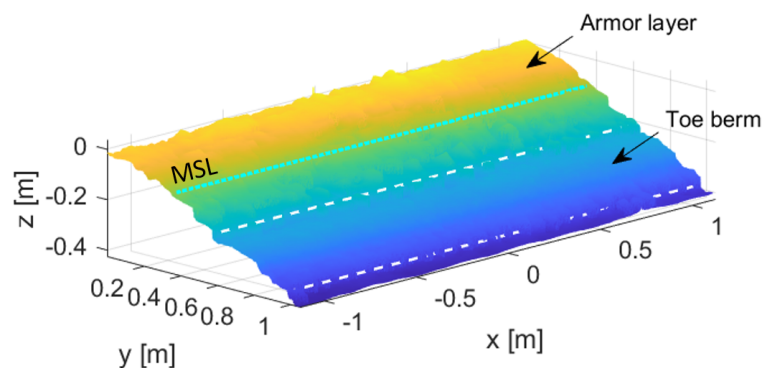
FIGURE 6.19 Example of mesh calculated from the SfM 3D reconstruction of the physical model of the Catania harbor breakwater: configuration AS of section n.10 after the simulation of wave I.
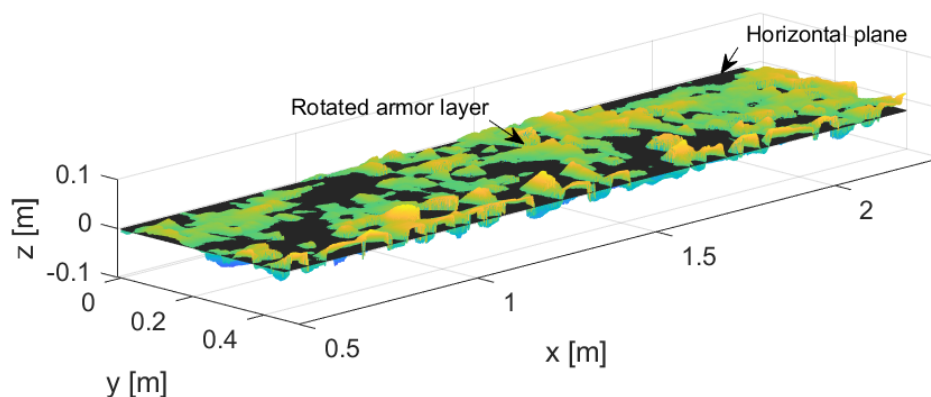
FIGURE 6.20 Example of rotated mesh around the x axis to obtain a null inclination with respect to the $x - y$ plane: configuration AS of section n.10 after the simulation of wave I.

period sea state. The mesh represents both the armor layer and the toe berm, but in the present work the analysis has focused just on the former. Therefore, only mesh of the armor layer has been considered for the analysis of the macro and micro-roughness.

Once the mesh of the armor layer has been isolated, a plane has been adapted to the surface through the least squares method, in order to create a reference for

(a)

(b)
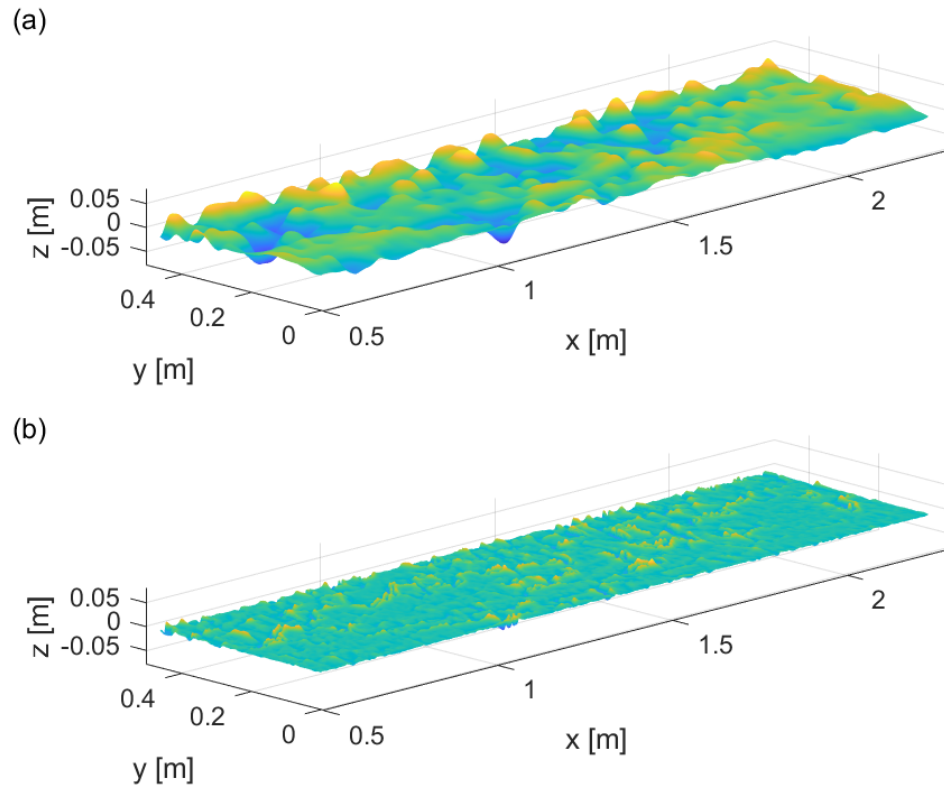
FIGURE 6.21 Example of armor layer (a) macro-roughness and (b) micro-roughness meshes: configuration AS of section n.10 after the simulation of wave I.
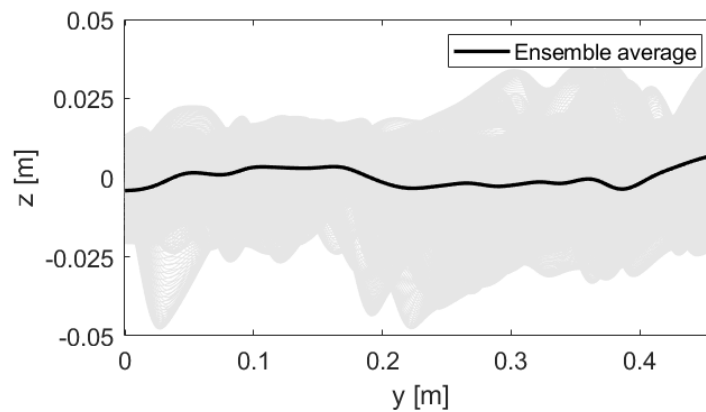
FIGURE 6.22 Example of ensemble average of the *y*-profiles of the armor layer macro-roughness: configuration AS of section n.10 after the simulation of wave I.

the evaluation of the roughness in terms of discrepancy from a smooth plane. Both the plane and the mesh have been rotated around the x axis , so as to obtain a null inclination with respect to the $x - y$ plane (x axis orthogonal to the direction of the wave motion, y axis parallel to the direction of the wave motion, origin in the right upper corner of the mesh) as showed in Figure 6.20. Note that the origin of the z axis corresponds to the the previously fitted plan. Then, the removal of measurement noise from the mesh has been performed using a low-pass 2D Gaussian filter with a cut off frequency equal to 0.01 m $^{-1}$.

The filtered mesh of the armor layer has been further elaborated using another 2D Gaussian filter, with a cut off frequency equal to the inverse of the median nominal diameter of the armor units (i.e. $1/D_{n50}$), for the identification of the macro and micro-roughness (see Figure 6.21). As discussed in section 6.3.1, the macro-roughness represents the waviness of block laying surface (wavelength of the order of $4\div5$ times D_{n50}), whereas the micro-roughness is a measure of the porosity of the armor layer due to the relative position of the units (wavelength of the order of D_{n50}).

The armor layer macro-roughness (see Figure 6.21a) has been analyzed through a bi-dimensional approach along the y direction, in order to characterize the cross-section mean profile. Therefore, the ensemble average of all the y-profiles has been evaluated, as showed in Figure 6.22. The mean wavelength λ_M and the maximum wave height HD have been then calculated for the quantitative description of the ensemble average curve.

As regards the armor layer micro-roughness (see Figure 6.21b), a 2D spectral analysis has been carried out, through the implementation of 2D FFT for the evaluation of the areal power spectral density ($APSD$), after making periodic the considered surface by means of a radially symmetric Hann window. Figure 6.23 shows
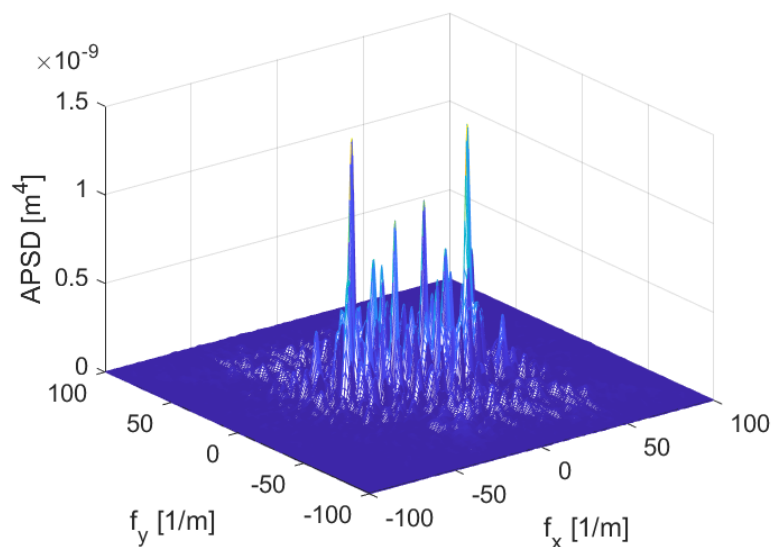
FIGURE 6.23 Example of 2D spectrum of the armor layer micro-roughness: configuration AS of section n.10 after the simulation of wave I.

an example of areal power spectrum, for the case of configuration AS of section n.10 after the simulation of the 5 years return period sea state. Note that the areal power spectra contains many useful information for the characterization of surfaces. In addition, if the input data to the 2D FFT are real numbers, the knowledge of a half of the spectrum is sufficient for the description of the surface (Krogstad, 2004). Under such an assumption, the centroid spectral wavelength λ_m (see equation 6.3) has been identified as the most significant descriptor of the micro-roughness, and its relationship with the damage mechanisms has been investigated.

6.3.5 Analysis of the experimental results

The experimental results on the upgraded Catania harbor breakwater regard both the armor layer damage evolution and the overtopping rates caused by increasing wave load. Therefore, in the following a description of the simulated wave motions is presented, which focuses on the reflection phenomenon. Then, the the armor layer damage dynamic is discussed, referring to both traditional analysis (i.e. counting of displaced units and damage maps) and novel ones (i.e. investigation on macro and micro-roughness of the armor layer surface). Finally, the characterization of the hydraulic performances of each tested configuration is given in terms of mean overtopping discharge. A summary of all the acquired experimental data is provided by Appendix A.

Evaluation of the incident wave motion

The incident wave motion has been evaluated for each test using the four gauge method of Faraci et al. (2015), which allows the calculation of the incident and reflected wave spectra, and of the reflection coefficient.

Figure 6.24 shows the comparison between the input JONSWAP spectrum and the typical experimental incident and reflected wave spectra, smoothed out according to the method proposed by Boccotti (2004). The incident wave spectrum is characterized by some peaks for frequency close to 1.0 Hz, about 2.5 times higher than the JONSWAP spectrum. Instead, at low frequencies the experimental spectrum is quite well approximated by the theoretical one. The discrepancies between measured and theoretical incident wave spectra are likely due to intrinsic characteristics of the input transmission system, and also to the generation procedure typical of the flap type wavemaker. Nevertheless, the simulated waves are sufficiently similar to the JONSWAP ones for the scope of the present work.

As showed in Figure 6.24, wave reflection is quite moderate, considering that an active wave absorption has not been employed. In particular, the reflection coefficient (k_r) measured during the tests is 0.25 on average. Table 6.7 and Table 6.8 report the reflection coefficient evaluated for each tested configuration of sections n. 10 and n. 40, as a function of the Iribarren number ($\xi_{m-1,0}$), which is defined as follows:
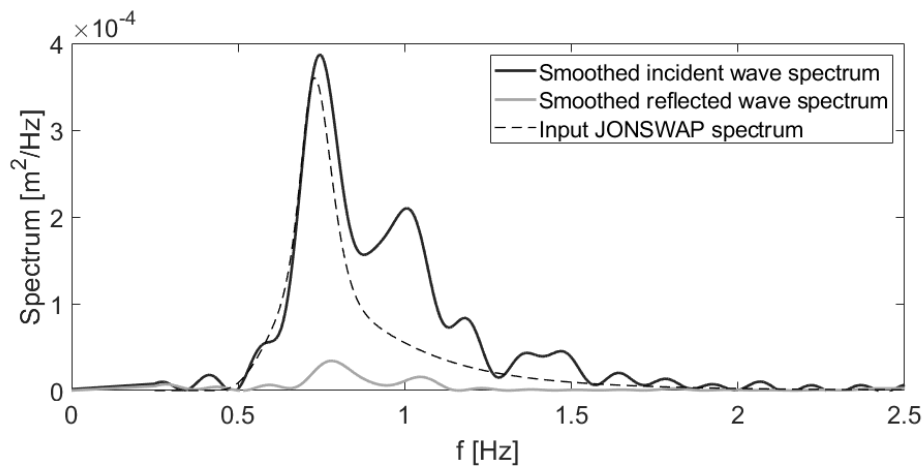
FIGURE 6.24 Example of incident and reflected wave spectra evaluated through the four gauge method of Faraci et al. (2015) and smoothed according to the procedure of Boccotti (2004): configuration AS of section n. 10 under wave IV.

TABLE 6.7 Reflection coefficient and correspondent Iribarren number evaluated for each tested configuration of the upgraded Catania harbor breakwater: section n. 10.

Wave ID	Test	E		EM		AS		AD		CM		CS	
		$\xi_{m-1,0}$	k_r	$\xi_{m-1,0}$	k_r	$\xi_{m-1,0}$	k_r	$\xi_{m-1,0}$	k_r	$\xi_{m-1,0}$	k_r	$\xi_{m-1,0}$	k_r
I	1	2.57	0.20	2.42	0.23	2.48	0.29	2.20	0.23	2.40	0.30	2.47	0.33
	2	2.56	0.20	2.52	0.23	2.61	0.30	2.36	0.22	2.35	0.30	2.55	0.35
	3	2.31	0.19	2.47	0.24	2.39	0.29	2.37	0.22	2.41	0.31	2.53	0.35
II	1	2.35	0.21	2.70	0.26	2.37	0.28	2.45	0.23	2.41	0.30	2.60	0.34
	2	2.32	0.20	2.45	0.24	2.33	0.29	2.30	0.23	2.37	0.29	2.75	0.34
	3	2.36	0.21	2.38	0.23	2.37	0.28	2.39	0.23	2.47	0.29	2.46	0.34
III	1	2.63	0.23	2.50	0.26	2.36	0.27	2.34	0.21	2.46	0.28	2.65	0.32
	2	2.68	0.24	2.64	0.28	2.57	0.27	2.54	0.23	2.45	0.27	2.68	0.32
	3	2.89	0.27	2.66	0.27	2.48	0.26	2.31	0.22	2.54	0.28	2.61	0.33
IV	1	2.66	0.25	2.63	0.26	2.57	0.28	2.81	0.23	2.58	0.26	2.71	0.31
	2	2.54	0.27	2.64	0.28	2.55	0.30	2.57	0.22	2.52	0.27	2.49	0.32
	3	2.66	0.27	2.52	0.26	2.71	0.28	2.31	0.24	2.39	0.26	2.61	0.30
	1 with SLR	2.24	0.24	-	-	-	-	-	-	-	-	-	-
	2 with SLR	2.34	0.24	-	-	-	-	-	-	-	-	-	-
	3 with SLR	2.29	0.24	-	-	-	-	-	-	-	-	-	-
V	1	2.73	0.27	2.57	0.28	2.76	0.26	2.72	0.24	2.66	0.26	2.61	0.32
	2	2.49	0.26	2.67	0.29	2.40	0.26	2.94	0.27	2.71	0.27	2.52	0.32
	3	2.71	0.27	2.37	0.26	2.85	0.27	2.34	0.25	2.55	0.26	2.68	0.31
	1 with SLR	2.16	0.25	-	-	-	-	-	-	-	-	-	-
	2 with SLR	2.18	0.24	-	-	-	-	-	-	-	-	-	-
	3 with SLR	2.34	0.27	-	-	-	-	-	-	-	-	-	-

$$\xi_{m-1,0} = \frac{\tan \alpha}{\sqrt{(2\pi H_s) / \left(g T_{m-1,0}^2 \right)}} \tag{6.5}$$

where α is the armor slope angle (equal to 0.5 for the considered configurations), H_s is the significant wave height and $T_{m-1,0} = m_{-1}/m_0$ is the spectral wave period.

The measured reflection coefficients have been compared with the experimental formulation suggested by Zanuttigh and van der Meer (2008):

$$k_r = tanh \left(a \cdot \xi_{m-1,0}^b \right) \tag{6.6}$$

TABLE 6.8 Reflection coefficient and correspondent Iribarren number evaluated for each tested configuration of the upgraded Catania harbor breakwater: section n. 40.

Wave ID	Test	E		EM		AS		AD		CM		CS	
		$\xi_{m-1,0}$	k_r	$\xi_{m-1,0}$	k_r	$\xi_{m-1,0}$	k_r	$\xi_{m-1,0}$	k_r	$\xi_{m-1,0}$	k_r	$\xi_{m-1,0}$	k_r
I	1	1.99	0.19	2.44	0.21	2.34	0.27	2.15	0.26	2.27	0.23	2.24	0.22
	2	1.92	0.19	2.09	0.19	2.38	0.28	2.27	0.26	2.45	0.24	2.07	0.22
	3	2.00	0.19	2.36	0.21	2.45	0.27	2.20	0.25	2.28	0.26	2.14	0.21
II	1	2.17	0.19	2.35	0.21	2.51	0.27	2.21	0.26	2.31	0.25	2.12	0.23
	2	2.15	0.20	2.40	0.22	2.64	0.28	2.28	0.27	2.41	0.25	2.10	0.23
	3	1.84	0.19	2.48	0.23	2.36	0.26	2.32	0.26	2.45	0.25	2.03	0.22
III	1	2.23	0.21	2.54	0.23	2.44	0.27	2.39	0.27	2.40	0.24	2.25	0.23
	2	2.29	0.21	2.46	0.24	2.31	0.26	2.18	0.25	2.38	0.24	2.58	0.24
	3	2.25	0.22	2.59	0.26	2.12	0.25	2.39	0.25	2.58	0.24	2.32	0.23
IV	1	2.40	0.24	2.33	0.25	2.21	0.26	2.21	0.23	2.43	0.24	2.58	0.25
	2	2.54	0.25	2.84	0.28	2.34	0.23	2.25	0.23	2.32	0.23	2.70	0.25
	3	2.39	0.22	2.77	0.27	2.13	0.24	2.36	0.23	2.39	0.24	2.65	0.25
	1 with SLR	2.43	0.29	-	-	-	-	-	-	-	-	-	-
	2 with SLR	2.49	0.29	-	-	-	-	-	-	-	-	-	-
	3 with SLR	2.20	0.28	-	-	-	-	-	-	-	-	-	-
V	1	2.39	0.24	2.72	0.29	2.10	0.23	2.38	0.21	2.38	0.21	3.02	0.28
	2	2.38	0.25	2.60	0.25	2.49	0.25	2.27	0.22	2.26	0.22	2.28	0.22
	3	2.21	0.23	2.62	0.26	3.57	0.28	2.22	0.22	2.30	0.21	2.58	0.24
	1 with SLR	2.37	0.30	-	-	-	-	-	-	-	-	-	-
	2 with SLR	2.18	0.28	-	-	-	-	-	-	-	-	-	-
	3 with SLR	2.18	0.26	-	-	-	-	-	-	-	-	-	-
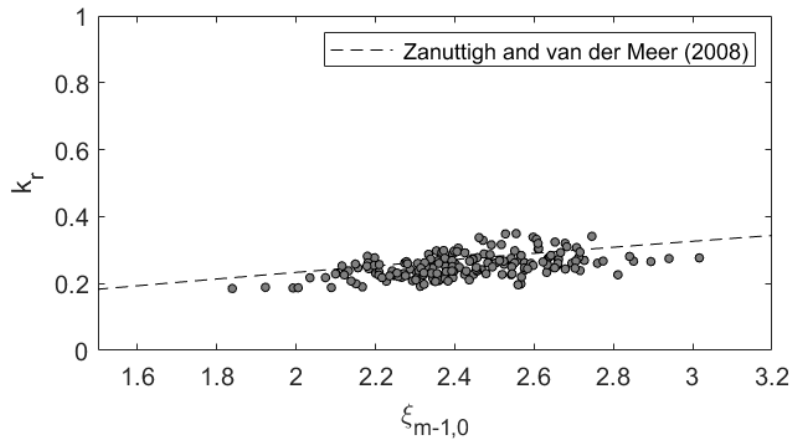
FIGURE 6.25 Comparison between the experimental reflection coefficient k_r expressed as a function of the Iribarren number $\xi_{m-1,0}$ and the equation suggested by Zanuttigh and van der Meer (2008).

$$a_r = 0.167 \cdot \left[1 - exp\left(-3.2\gamma_f \right) \right] \qquad (6.7)$$

$$b_r = 1.49 \cdot \left(\gamma_f - 0.38 \right)^2 + 0.86 \qquad (6.8)$$

where a_r and b_r are two parameters dependent on the friction factor γ_f, which is equal to 0.47 for both double layer of cubes and Antifer blocks (EurOtop, 2018).

Figure 6.25 shows that the experimental points are quite close to the Zanuttigh and van der Meer (2008) curve, despite of a slight tendency to underestimate the theoretical values. Such a results can be due to the fact that equations 6.6-6.8 were calibrated for a homogeneous database on wave reflection referred to newly built breakwaters. Indeed, the smaller slope compared to the design one and irregular

surface of damaged rubble mound structures may likely induce lower reflection than a straight slope. As regards the configurations with additional armor layer, the differences between predicted and experimental reflection coefficient can be due to the influence of a more complex layering on the overall porosity of the structure.

Armor blocks displacements

The evaluation of the damage suffered by the structure under increasing wave load has been performed through the calculation of the parameter N_{od} (see equation 6.1). As stated in section 6.3.3, each simulated sea state has been divided into three wave series, having the same input significant wave height and peak wave period, but different frequencies combinations. The cumulative damage parameter N_{od} has been calculated at end of each wave series, so as to identify possible influences of the sea state duration on the structure response.

Figure 6.26 and Figure 6.27 show the experimental cumulative N_{od} measured during the tests without SLR, as a function of the stability number (i.e. the ratio between the incident significant wave height H_s and the product between the relative buoyant density Δ and the median nominal diameter of the armor units D_{n50}) and of the number of incident waves N_w. The number of incident waves seems to cause a significant increase of the damage level only for N_{od} greater than 2.0, which corresponds to the failure threshold suggested by CIRIA et al. (2007). Only configurations AS and AD of section n. 10 (Figure 6.26c-d) experienced the increment of damage level due to increasing number of incident waves. In particular, for a value of the stability number equal to 3.00, the maximum increase of N_{od} caused by tripling N_w is observed, in the range 15÷20%. For stability numbers greater than 3.00, such an increment is not higher than 10%.

Therefore, the results of the investigation on the effects of sea states duration on damage progression led to the conclusion that the number of incident waves is significant only for severely damaged structures. However, the analysis of damage progression after the failure of the structure has little practical interest in the design process, and hence the effects of N_w on damage dynamic are not further discussed in the following.

The experimental data on armor blocks displacement after 4500 waves are summarized in Figure 6.28, where the cumulative values of damage parameter N_{od} evaluated for each tested configuration are expressed as a function of the stability number. Since there are not state of art damage progression models for upgraded rubble mound breakwaters, the formula proposed by van der Meer (1988c) for double layers of cubes laid on a slope of 1:1.5 with a notional permeability equal to 0.4 (hereinafter vdM formula) has been compared with the experimental results. Such a formula can be applied also for Antifer units, whose geometry is very similar to the cubic ones.

The results showed in Figure 6.28a demonstrate that the already damaged existing armor layer of configurations E and EM (see Figure 6.17a-b, Figure 6.18a-b and
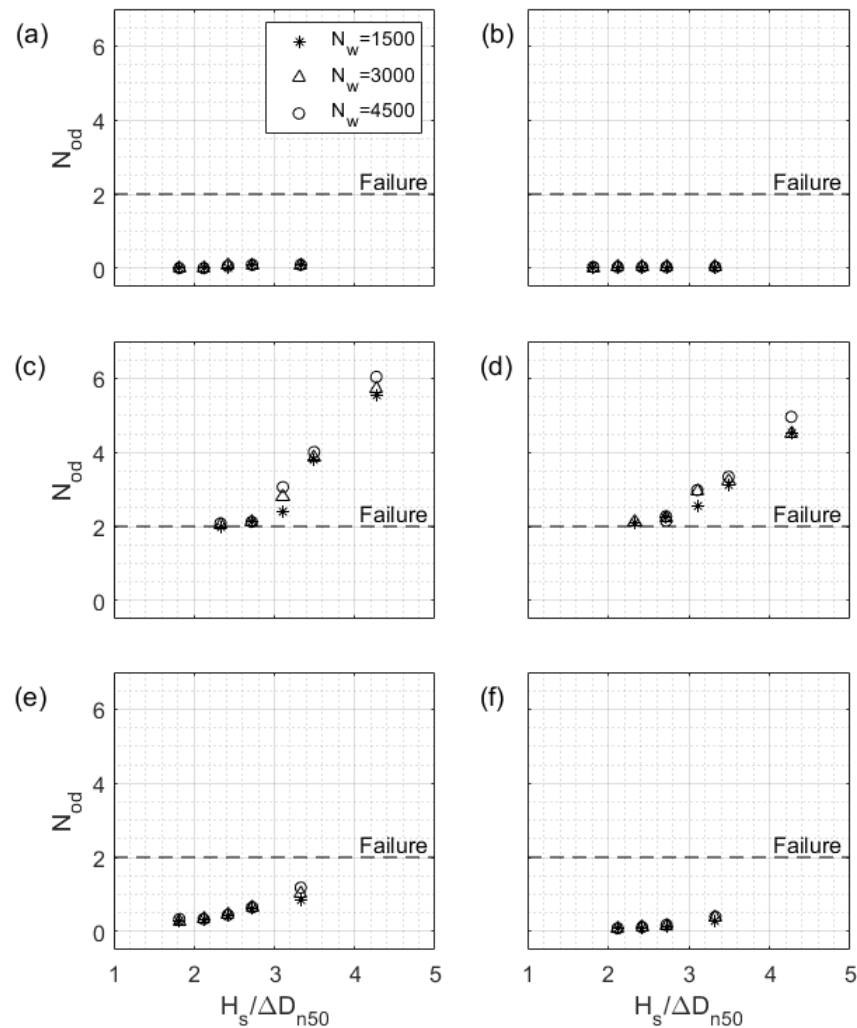
FIGURE 6.26 Damage parameter N_{od} evaluated for section n. 10 as a function of the stability number and of the number of incident waves N_w: (a) configuration E; (b) configuration EM; (c) configuration AS; (d) configuration AD; (e) configuration CM; (f) configuration CS. The failure threshold is suggested by (CIRIA et al., 2007).

Table 6.4) is quite stable and that its behavior is not adequately represented by vdM formula. In particular, the damage suffered by section n. 10 is less than the threshold of initial damage (i.e. 0.50), whereas for section n. 40 the intermediate damage level (i.e. 1.00) is slightly exceeded (CIRIA et al., 2007). Such a result is likely caused by the blocks settlement of the actual armor layer, due to the action of past storms. The different response of the two sections demonstrates that the deterioration processes suffered by the present armor layer of the Catania harbor breakwater led to the creation of voids of different shape and size along the structure, causing a geometric and thus structural non-uniformity, as already discussed in Chapter 4.

As regards the impacts of climate change, Figure 6.28a shows that SLR causes a negligible increase of the damage level reached by the existing armor layer. Indeed, the damage suffered by section n. 10 still remains under the initial damage level, whereas for section n. 40 N_{od} is still close to the intermediate damage level (CIRIA
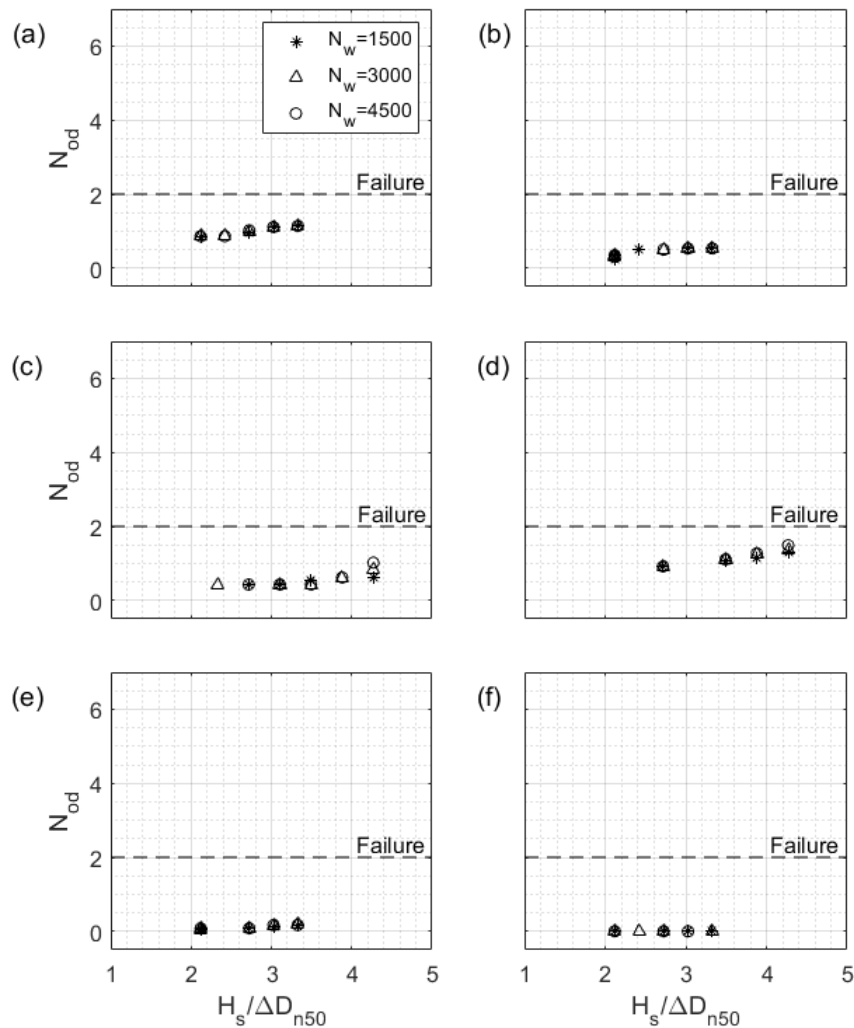
FIGURE 6.27 Damage parameter N_{od} evaluated for section n. 40 as a function of the stability number and of the number of incident waves N_w: (a) configuration E; (b) configuration EM; (c) configuration AS; (d) configuration AD; (e) configuration CM; (f) configuration CS. The failure threshold is suggested by (CIRIA et al., 2007).

et al., 2007).

The results on damage dynamics of the four analyzed upgrading options that consist in rising the wave wall and in adding an extra armor layer over the existing one (i.e. configurations AS, AD, CM and CS, see Figure 6.17c-f and Table 6.4) highlight the existence of two different responses of the structure in the case of presence or absence of a sufficient support at the toe of the additional units. Indeed, as discussed in section 3.3.3, configurations AS, AD and CM present a quarry stone toe berm able to support the extra armor blocks only for section n. 40. Instead, configuration CS always ensure an adequate support to the additional armor layer, thanks to the proper reshaping of the existing structure. Figure 6.28b-c shows that, for the same stability number, the damage parameter N_{od} measured for the configurations with sufficient support (hereinafter SS) at the toe of the extra armor layer reaches values up to 3÷7 times lower than the options which do not provide a proper support
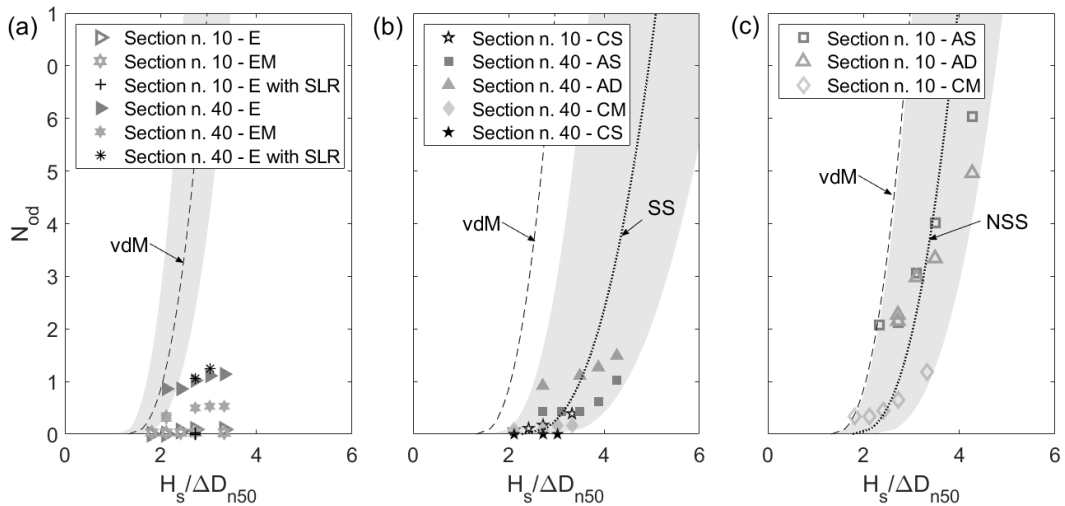
FIGURE 6.28 Damage parameter N_{od} as a function of the stability number: (a) upgrading options which present the simple heightening of the wave wall; (b) upgrading options with a sufficient support at the toe of the additional armor layer (SS); (c) upgrading options without a sufficient support at the toe of the additional armor layer (NSS). The grey areas indicate the 95% confidence bounds of the considered damage formulas.

(hereinafter NSS). Configurations AS, AD and CM present a sufficient support at the toe of the extra armor units only for section n. 40, which is characterized by a more regular laying surface for the additional blocks. Instead, configuration CS is the only one able to guarantee comparable structural responses for both sections n. 10 and n. 40, despite of the extent of irregularity of the existing armor layer. Indeed, the regularization of the existing armor layer before adding the extra blocks ensures a proper support to the armor layer restoration, despite of the geometric irregularities of the existing cross section. The only quarry stone toe berm is not able to provide a sufficient support to the additional armor layer for the most irregular sections, since it is designed to guarantee a certain shape uniformity along the entire breakwater.

Figure 6.28b-c shows that the vdM formula is not able to describe the structural response of the upgraded structure with additional armor layer. Such a result, which in part could be due to the lower wave turbulence caused by the small scale of the physical model (i.e. 1:70), seems to be mainly linked to the non-conventional nature of the considered structure, which is significantly different from the sections tested by van der Meer (1988c) in terms of geometry, layering and porosity. Therefore, the vdM formula has been adapted to the experimental data on the upgraded Catania harbor breakwater, by means of the evaluation of the multiplicative empirical factor f_c, which allows to discriminate between SS and NSS behavior:

$$\frac{H_s}{\Delta D_{n50}} = f_c \times \left(6.7 \frac{N_{od}^{0.4}}{N_w^{0.3}} + 1 \right) \times \left(\frac{2\pi H_s}{g T_m^2} \right)^{-0.1} \tag{6.9}$$

where N_{od} is the damage parameter (see equation 6.1), N_w is the number of incident waves, Δ and D_{n50} are respectively the relative buoyant density and the median nominal diameter of the armor blocks, H_s is the incident significant wave height, T_m

is the mean wave period and g is the gravity acceleration. It is worth to point out that the traditional vdM formula contains an empirical multiplicative factor equal to 1.00 with standard deviation equal to 0.10, which was here substituted by the factor f_c. Table 6.9 presents the estimate of the correction factor f_c and its standard deviation σ_{fc}, for the two cases of sufficient (i.e. SS) and not sufficient support (i.e. NSS) at the toe of the additional armor layer.

Figure 6.28b-c indicates that the vdM formula returns N_{od} greater than the adapted one for the same stability number. In other terms, the vdM formula is more conservative and could led to an expensive over-sizing of the armor blocks, if applied for the design of upgrading solutions where the underlying structure has reached a stable configuration.

Armor layer erosion

The damage dynamics has been further investigated using the the 3D reconstructions of the armor layer surface derived from the application of the SfM technique. The validity of the SfM elaborations has been verified by means of the comparison between the damage parameter $S_{d,m}$ evaluated for all the tested configurations from equation 6.2 and the damage parameter $S_{d,c}$ calculated as a function of N_{od}, using the following empirical relationship (US Army Corps of Engineers, 2002):

$$S_{d,c} = \frac{N_{od}}{G\,(1 - n_V)} \tag{6.10}$$

where G is the armor units gradation factor (equal to 1 for artificial blocks) and n_V is the porosity of the armor layer.

The scatter plot in Figure 6.29 shows that the estimates of $S_{d,m}$ and $S_{d,c}$ agree fairly well, being the data points closely distributed around the bisector, with a root mean square error $RMSE$ equal to 0.13. In addition, the $BIAS$ between the mean values of $S_{d,m}$ and $S_{d,c}$ is equal to -0.07, which means that $S_{d,m}$ evaluated from the SfM technique tends to slightly underestimate $S_{d,c}$. Finally, the correlation coefficient r is equal to 0.87, hence the scatter component of the error between $S_{d,m}$ and $S_{d,c}$ is limited. Therefore, the data acquired through the SfM technique are consistent with the results obtained for N_{od}.

As discussed in section 6.3.1, the meshes of the armor layer surface calculated from the application of the SfM technique at the beginning and at the end of each sea

TABLE 6.9 Coefficient f_c for the vdM formula evaluated from the experimental results on damage dynamics.

	Sufficient support (SS)	Not sufficient support (NSS)
f_c	1.72	1.35
σ_{fc}	0.29	0.20

state have been used for the construction of damage maps for all the tested configurations. The damage maps display the spatial final distribution of the armor layer erosion indicating erosion and deposition, respectively with negative and positive values of Δz.

Considering the upgrading options where an additional armor layer is adopted, Figure 6.30 and Figure 6.31 allow the comparison between the final erosion of configurations AS, AD and CM, whose structural behavior is influenced by the geometry of the existing armor layer, and configuration CS, whose response to the wave load does not depend on the geometry of the existing structure. In any case the toe berm showed a sufficient resistance to the wave load and is subjected only to minimum adjustments. Therefore, the toe berm does not lose its functionality during the tests.

Configuration AS of section n. 10 (see Figure 6.30a) has been subject to a quite uniform erosive process in the region close to the free surface, which has caused the displacement of some Antifer units that the toe berm has not been able to stop. For the same configuration, section n. 40 (see Figure 6.30b) presents greater stability than section n. 10. Indeed, the sliding of the units removed by the wave action has been interrupted by the toe berm, with the exception of the zone in the vicinity of the left side wall of the tank, which is affected by boundary effects.

Configuration AD of section n. 10 (see Figure 6.30c) is characterized by a large excavation uniformly distributed over the entire submerged armor layer. Clearly, the toe berm is not able to avoid the sliding of the armor blocks, which mainly deposit at the toe of the structure. Instead, configuration AD of section n. 40 (see Figure 6.30d) appears significantly more stable. Few units have moved away from the submerged zone and mainly have stopped close to the crest of the toe berm, which has properly supported the armor additional layer.

Also configuration CM shows better stability performances for section n. 40 than
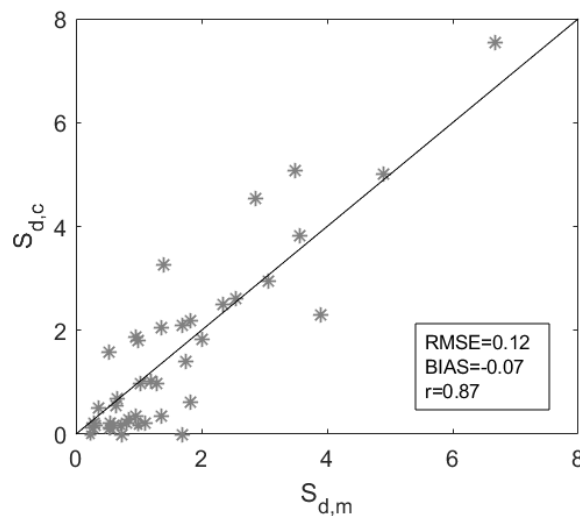
FIGURE 6.29 Comparison between the experimental damage parameter $S_{d,m}$ evaluated by means of the SfM technique and $S_{d,c}$ calculated as a function of the damage parameter N_{od} using the formula proposed by US Army Corps of Engineers (2002).
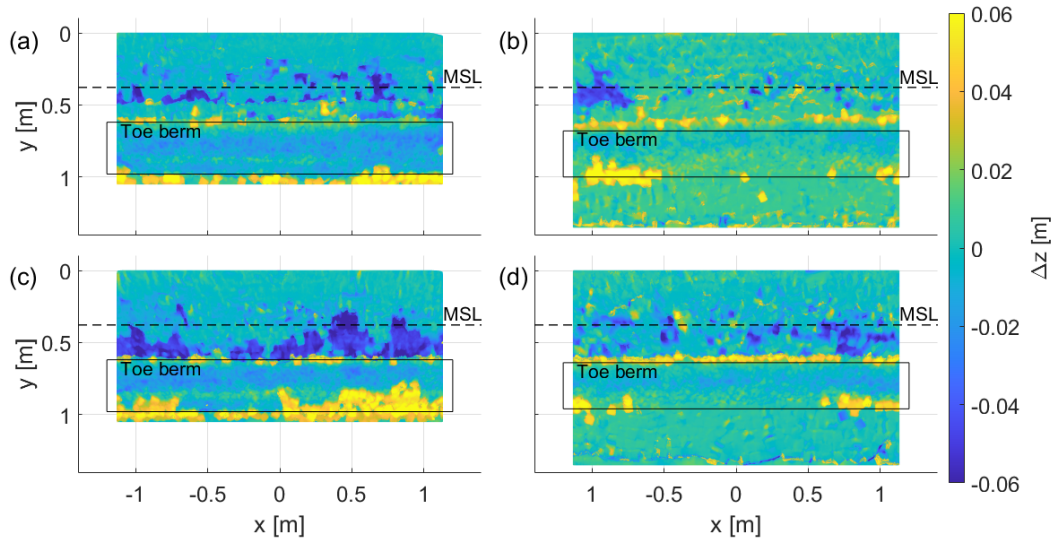
FIGURE 6.30 Final damage maps calculated for: (a) configuration AS of section n. 10; (b) configuration AS of section n. 40; (c) configuration AD of section n. 10; (d) configuration AD of section n. 40. The x and y axes are respectively orthogonal and parallel to the wave attack, whereas Δz is the height difference between the final and initial armor layer meshes.
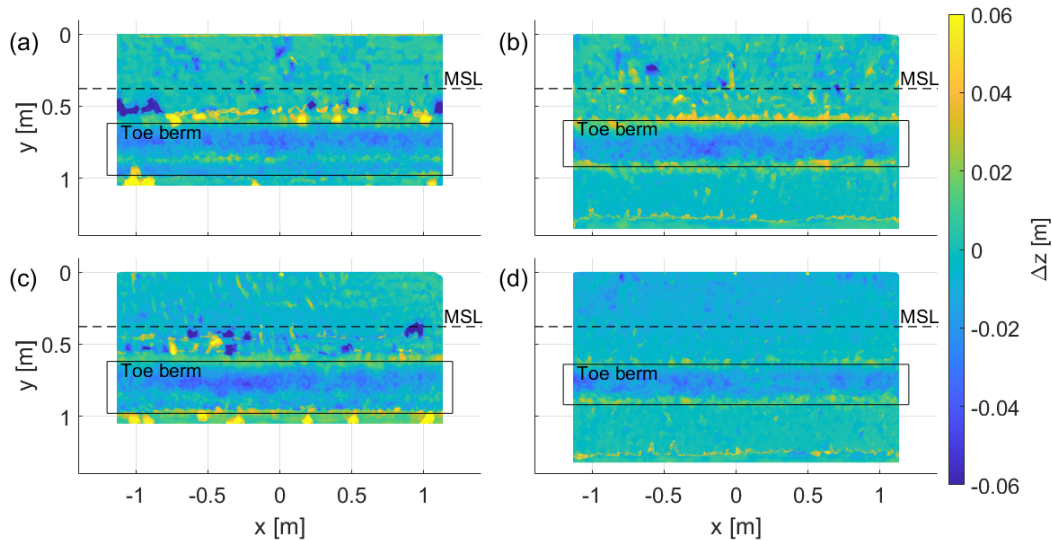
FIGURE 6.31 Final damage maps calculated for: (a) configuration CM of section n. 10; (b) configuration CM of section n. 40; (c) configuration CS of section n. 10; (d) configuration CS of section n. 40. The x and y axes are respectively orthogonal and parallel to the wave attack, whereas Δz is the height difference between the final and initial armor layer meshes.

section n. 10. Indeed, in the former case no significant movements of the armor blocks have been recorded (see Figure 6.31b), whereas in latter one some units (see Figure 6.31a) have overcome the toe berm and have deposited at the base of the structure (note that the wave motion dragged the removed blocks out from the study area), thus causing the excess of the limit of intermediate damage level (CIRIA et al., 2007).

Considering configuration CS (see Figure 6.31c-d), both sections n. 10 and n. 40 show a comparable damage level, thanks to the presence of a sufficient support at the toe of the additional armor layer. Indeed, although in section n. 10 some blocks

have moved from the submerged armor layer towards the toe of the structure, the overall damage level is still close to the initial damage threshold (CIRIA et al., 2007) for both sections.

The analysis of the information given by Figure 6.30 and Figure 6.31 leads to some general conclusions, valid for the upgrading solutions using the additional armor layers (i.e. AS, AD, CM and CS). First, the erosive processes mainly affect the submerged armor layer. Indeed, the emerged structure is subject to simple settlement at best, due to the units local rotations. Secondly, as already stated, the adequacy of the toe berm is fundamental for the overall structure stability. Indeed, only the configuration which provides a proper support at the toe of the additional units through the regularization of the existing armor layer (i.e. CS) ensures the same stability performances regardless of the existing armor layer geometry.

Armor layer surface roughness

The 3D reconstructions of the armor layer surface derived from the application of the SfM technique have been used to perform a novel analysis of the armor layer surface modification due to increasing wave load, based on the characterization of the micro and macro-roughness (see section 6.3.1).

The armor layer macro-roughness represents the blocks laying surface and it is described here by the ratio between its maximum wave height HD and its mean wavelength λ_M, both evaluated referring to the ensemble average of the y-profiles of the surface (see Figure 6.8). Such a ratio represents the mean slope of the macro-roughness, and hence it assumes smaller values if the surface tends to a smooth plane.

Figure 6.32 shows the variation of HD/λ_M at the end of each $j-th$ sea state with respect to the zero-damage condition, as a function of the stability number (i.e. the ratio between the incident significant wave height H_s and the product between the relative buoyant density Δ and the median nominal diameter D_{n50} of the armor blocks). For most of the tested configurations, the greatest deviation from the zero-damage condition occurs during the initial shakedown (i.e. under wave I), which corresponds to stability numbers less than 2.30.

Table 6.10 reports the rate of the variation of HD/λ_M with respect to the zero-damage condition during and after shakedown. During shakedown, configurations without additional armor layer (i.e. E and EM) show different behaviors due to the non-homogeneous geometrical characteristics of the existing structure. Indeed, section n. 10 presents rates of the variation of HD/λ_M one order of magnitude smaller than those of section n. 40, thus confirming that the first section is more stable. However, the settling of the structure minimizes the differences between the two sections, which show similar rates of the variation of HD/λ_M after shakedown.

The upgrading solutions which involve the construction of a proper support at the toe of the additional armor units (SS) suffered minor modifications of the armor layer macro-roughness during the initial shakedown, with rates of the variation

of HD/λ_M between the zero-damage condition and the initial shakedown always smaller than 2% in absolute terms. Also after the shakedown, such a threshold is not overcome, with the exception of configuration CS of section n. 40, whose armor layer macro-roughness seems significantly modified only after sea state corresponding to wave V. During shakedown, upgrading options with extra armor layer but without a proper support at the toe (NSS) present values of the rates of variation of HD/λ_M with respect to the zero damage condition quite larger than 2% in absolute terms, highlighting the poor stability of such configurations. However, the settled structure appears more stable, with rates of variation of HD/λ_M with respect to the zero damage condition similar to the ones measured for SS configurations.
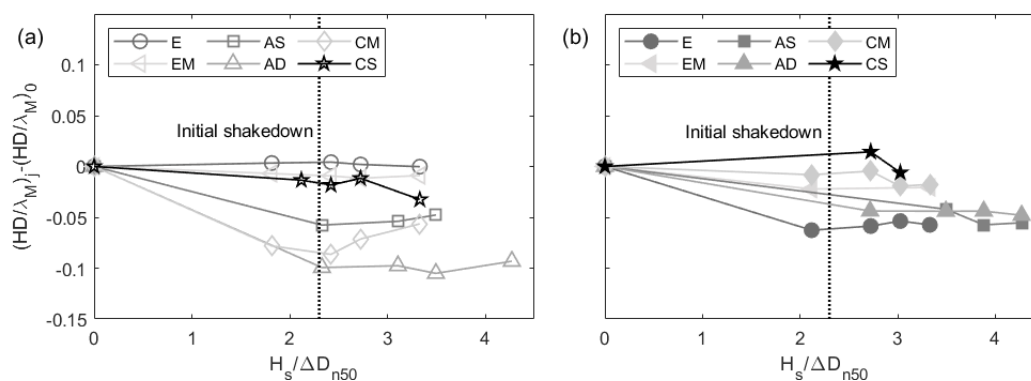
FIGURE 6.32 Variation of the ratio between the maximum wave height (HD) and the mean wavelength (λ_M) of the macro-roughness referred to the zero-damage condition as a function of the stability number: (a) section n. 10; (b) section n. 40. The region on the left of dotted line refers to the initial shakedown of the structure.

TABLE 6.10 Rate of the variation of the ratio between the maximum wave height (HD) and the mean wavelength (λ_M) of the macro-roughness as a function of the stability number ($H_s/\Delta D_{n50}$) with respect to the zero-damage condition during and after the initial shakedown.

Armor layer	Configuration	Rate of $(HD/\lambda_M)_i - (HD/\lambda_M)_0$	
		Pre-shakedown	Post-shakedown
Existing	Section n. 10 - E	0.2%	-0.2%
	Section n. 10 - EM	-0.4%	-0.1%
	Section n. 40 - E	-3.0%	0.4%
	Section n. 40 - EM	-1.0%	0.1%
Additional SS	Section n. 10 - CS	-0.6%	-1.6%
	Section n. 40 - AS	-1.4%	-1.1%
	Section n. 40 - AD	-1.6%	-0.3%
	Section n. 40 - CM	-0.4%	-0.8%
	Section n. 40 - CS	0.5%	-6.7%
Additional NSS	Section n. 10 - AS	-2.5%	0.5%
	Section n. 10 - AD	-4.3%	0.3%
	Section n. 10 - CM	-4.3%	1.4%

The armor layer micro-roughness, which represents the surface porosity, is directly related to the relative distance between the blocks. The mean spectral wavelength of the micro-roughness (λ_m), normalized with respect to the median nominal diameter of the armor units (D_{n50}), was identified as a good proxy of such a surface feature. Figure 6.33 shows the variation of λ_m/D_{n50} at the end of each $j - th$ sea state with respect to the zero-damage condition as a function of the damage parameter N_{od} (see equation 6.1). Four different behaviors can be distinguished.

For structure configurations characterized by small values of the damage parameter N_{od}, small oscillations of the change of λ_m/D_{n50} with respect to the zero-damage condition occur, with $O(10^{-2})$. This means that the armor units are not significantly displaced, neither through local rotations, nor by translation, thus determining the existence of a static equilibrium. Configuration CS of section n. 40 shows the above described behavior (see Figure 6.33b).

The second case corresponds to those configurations characterized by small values of the damage parameter N_{od} but significant oscillation of the variation of λ_m/D_{n50} with respect to the zero-damage condition, $O(10^{-1})$. In this case the armor units locally rotate, but maintaining their original mean position, thus determining the existence of a dynamic equilibrium. Results indicate that configurations E, EM and CS of section n. 10 (see Figure 6.33a) and EM and CM of section n. 40 (see Figure 6.33b) experience a dynamic equilibrium.

In the third case, when the damage parameter N_{od} tends to the intermediate damage level (CIRIA et al., 2007), small oscillations of the variation of λ_m/D_{n50} with respect to the zero-damage condition, $O(10^{-2})$, are recorded. The damage occurs through a bulk sliding of the armor blocks, which does not cause the widening neither the narrowing of the spaces between the units. In the present tests, configuration CM of section n. 10 (see Figure 6.33a) and E of section n. 40 (see Figure 6.33b) approaches the intermediate damage level (CIRIA et al., 2007) through a mass sliding.
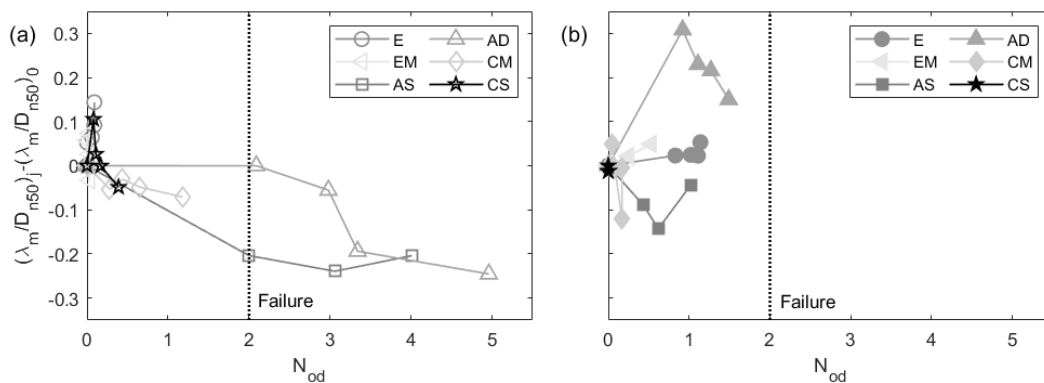
FIGURE 6.33 Variation of the ratio between the spectral wavelength of the micro-roughness (λ_m) and the median nominal diameter of the armor units (D_{n50}) referred to the zero-damage condition as a function of the damage parameter N_{od}: (a) section n. 10; (b) section n. 40. The N_{od} failure threshold is suggested by CIRIA et al. (2007).

TABLE 6.11 Summary of the armor layer damage dynamics derived from the analysis of the armor layer micro-roughness for each tested configuration. Phases 1 and 2 refer to the damage processes respectively during and after the initial shakedown.

Phase 1 \ Phase 2	Static equilibrium	Dynamic equilibrium	Bulk displacement	Differential displacement
Static equilibrium	Section n. 40 - CS	-	-	-
Dynamic equilibrium	-	Section n. 10 - E Section n. 10 - EM Section n. 10 - CS Section n. 40 - EM Section n. 40 - CM	-	-
Bulk displacement	-	-	Section n. 10 - CM Section n. 40 - E	Section n. 10 - AD
Differential displacement	-	-	Section n. 10 - AS	Section n. 40 - AS Section n. 40 - AD

The fourth behavior corresponds to those configurations characterized by values of the damage parameter N_{od} close to the failure level (CIRIA et al., 2007) and also by significant oscillations of the variation of λ_m/D_{n50} with respect to the zero-damage condition, $O(10^{-1})$. Such a case corresponds to differential block displacements, which involve a clear change of the armor layer porosity. The damage progression of configurations AD and AS of section n. 40 follows the above described dynamics (see Figure 6.33b).

It is important to point out that the same configuration could experience more than one behavior during the damage process. For instance, during the initial shakedown configuration AD of section n. 10 (see Figure 6.33a) reaches the failure threshold without variation of λ_m/D_{n50}, i.e. with an overall sliding of the armor blocks. After the initial shakedown, the damage develops with a significantly changing λ_m/D_{n50}, which means that the armor units change their relative position. The damage progression of configuration AS of section n. 10 follows the opposite process.

Table 6.11 summarizes the outcomes of the analysis of the armor layer microroughness for each tested configuration.

Therefore, it seems that the variation of λ_m/D_{n50} with respect to the zero-damage condition may be a useful parameter for the investigation of the way in which the armor layer damage quantified by traditional parameters (e.g. N_{od}) physically develops during increasing wave loads. In addition, the proposed technique allows us the automatic identification of small displacements of the units, and hence a more accurate diagnosis of the initiation of damage.

Overtopping discharge

The validation of the experimental data on mean overtopping discharge has been performed through the comparison with the following empirical relationship, which

is valid for seaside slopes between 1:2 and 1:4/3 and wave attack orthogonal to the breakwater (EurOtop, 2018):

$$q^* = \frac{q}{\sqrt{gH_s^3}} = a_E \times exp\left[-\left(b_E \times \frac{R_c}{H_s \gamma_f} \right)^{1.3} \right] \tag{6.11}$$

where q^* is the mean overtopping discharge per meter, q, normalized with respect to the square root of the product between the gravitational acceleration g and the cube of the incident significant wave height H_s; a_E and b_E are the empirical parameters of the formula, respectively equal to 0.09 with a standard deviation of 0.0135 and 1.50 with a standard deviation of 0.1500; R_c is the maximum value between the crest level and the wave wall height referred to MSL, and γ_f is the roughness factor (0.50 for Antifer blocks, 0.47 for double layer of artificial cubes).

Figure 6.34 shows the comparison between the experimental q^* as a function of H_s / R_c and equation 6.11, distinguishing the upgrading options with simple heightening of the wave wall from the ones that introduce also an additional armor layer made up of Antifer units smaller than the existing cubes or cubes equal to the existing ones. The measured q^* is in good agreement with the prediction of the EurOtop (2018) formula for the configurations with the existing armor layer (see Figure 6.34a) and with additional cubes equal to the existing ones (see Figure 6.34c). On the contrary, Figure 6.34b shows that the values of q^* found for the configurations with additional Antifer units smaller than the existing cubes are in general lower than the prediction of EurOtop (2018). Such a lack of agreement between experimental data and the formula proposed by EurOtop (2018) may be due to the unusual placement
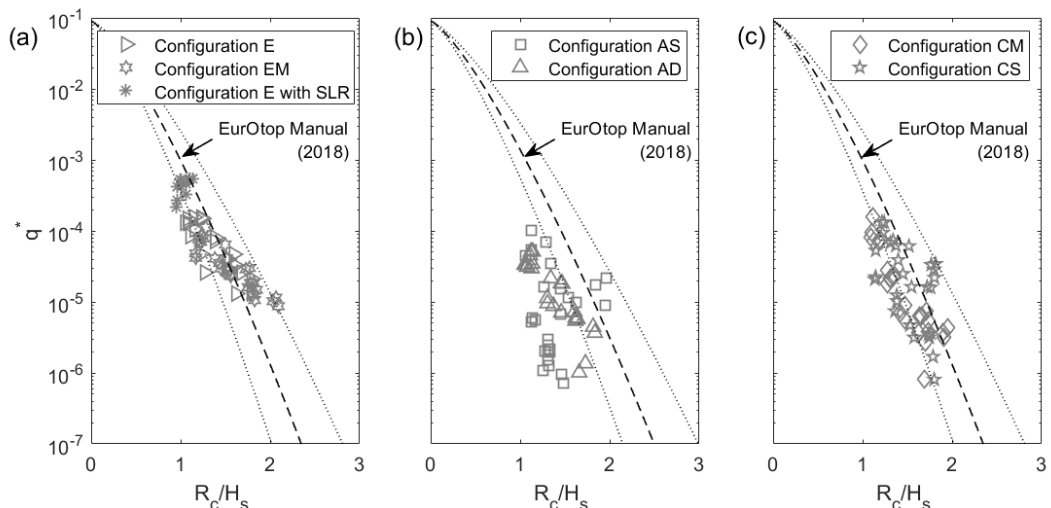
FIGURE 6.34 Comparison between the empirical formula suggested by EurOtop (2018) and the experimental data on dimensionless mean overtopping discharge (q^*), expressed as a function of R_c / H_s: (a) upgrading options with simple raising of the wave wall; (b) upgrading options with raising of the wave wall and additional Antifer units smaller than the existing cubes; (c) upgrading options with raising of the wave wall and additional cubic units equal to the existing ones. The dotted lines indicate the 95% confidence bounds of the EurOtop (2018) formula.

of smaller armor units over the existing ones, whose reciprocal interaction could produce additional dissipation processes and hence reduce overtopping discharges.

As regards the effects of climate change, Figure 6.35a, which shows the increase of the overtopping rate of configuration E caused by SLR (Δq_{SLR}), highlights that SLR induces a significant enhancement of the overtopping phenomenon. Indeed, the mean overtopping discharges of configuration E corresponding to waves III and IV (i.e. to return periods equal to 50 and 100 years) rise by a factor of $7 \div 9$ and $2 \div 4$ respectively. The hydraulic performances of section n. 40 are less affected by the effects of SLR then those of section n. 10. Such a result is due to the fact that section n. 40 is more offshore, i.e. in deeper water than section n. 10 (see Figure 6.15), and hence subject to waves less influenced by mean sea level variations. However, considering the results relative to both sections, the upgrade of the existing armor layer is needed to ensure hydraulic responses able to withstand the future intensification of the overtopping phenomenon.

Figure 6.34 shows that, as expected, configurations E and EM are subject to the higher overtopping rates. Indeed, such options consist only in the heightening of the wave wall. On the contrary, all the other solutions involve the improvement of the hydraulic performances thanks to the addition of an extra armor layer.

Figure 6.35b shows the calculated Δq_{E-}, which is the averaged decrease of the mean overtopping discharge corresponding to wave III and IV (i.e. return period equal to 50 and 100 years) operated by configurations EM, AS, AD, CM and CS with respect to configuration E. The heightening of the wave wall up to +9.50 m above MSL gives significantly different overtopping reductions, i.e. Δq_{E-} respectively equal to 63% and 10% for sections n. 10 and 40. Such a discrepancy leads to the conclusion that the heightening of the wave wall by only one meter for the reduction of the overtopping discharge is less efficient for the most offshore section n. 40, which is subject to higher waves. With reference to those configurations which improve option E only thanks to the addition of an extra armor layer (i.e. AS, AD
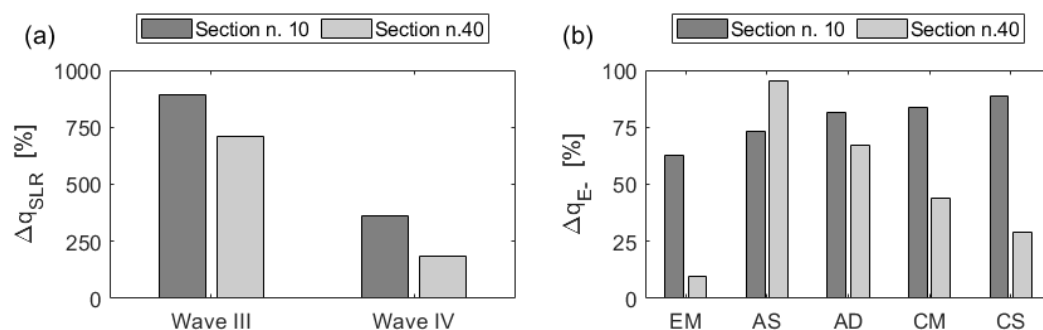
FIGURE 6.35 Experimental results on mean overtopping discharge: (a) increase of the 50 and 100-years return period (respectively wave III and wave IV) overtopping rate of configuration E caused by SLR (Δq_{SLR}); (b) averaged reduction of the 100-years return period (i.e. wave IV) mean overtopping discharge with respect to configuration E (Δq_{E-}) performed by configurations EM, AS, AD, CM and CS.

and CM), Δq_{E-} between $75 \div 85\%$ and $45 \div 95\%$ is observed, for sections n. 10 and n. 40 respectively. Finally, solution CS improves configuration E thanks to the heightening of the wave wall by one meter and the addition of extra armor blocks, giving Δq_{E-} equal to 88% and 30% for sections n. 10 and n. 40 respectively.

The choice of the best upgrading solutions with the additional armor layer cannot be based only on the analysis of the overtopping phenomena. Indeed, all the tested configurations with additional armor units (i.e. AS and AD; CM and CS) guarantee sufficiently high Δq_{E-}, i.e. not lower than 30%, regardless of the type of employed blocks (i.e Antifer units smaller than the existing cubes or cubic units equal to the existing ones) and of the considered cross section geometry and position. As a consequence, the structural behavior of the upgrading solutions should be considered as the main factor for the selection of the overall most performing ones. Therefore, for the case of the Catania harbor breakwater, the most appropriate configuration seems the one that is designed using additional 62 t cubes placed following a 1:2 slope over the regularized existing armor, with a quarry stone toe berm a wave wall raised up to +9.50 m above MSL (i.e. configuration CS).

6.3.6   Comparison between model and prototype armor roughness

The SfM-based technique developed for the analysis of the armor layer roughness at laboratory scale has been employed for the characterization of armor layer of the full-scale Catania harbor breakwater. The scope of the analysis was the verification of the applicability of the proposed the SfM-based technique at prototype scale, which could be employed for the validation of physical models and for the assessment of the damage suffered by existing structures. As stated in Chapter 4, the 3D point cloud recovered from the UAV survey performed in February 2020 has been used for the calculation of the mesh of the emerged armor layer of the entire structure. Sections n. 10 and n. 40 of the breakwater (see Figure 6.15) have been chosen for the armor surface analysis, in order to enable the comparison of the results with experimental data.

For each considered cross section of the full-scale Catania harbor breakwater, a portion of the emerged armor layer has been isolated, which contained a number of armor units similar to the laboratory structure, i.e. about 30 blocks along the direction orthogonal to the wave attack. Such a portion is about 100.00 m long, centered on the studied cross section. Since only the mesh of the emerged full-scale breakwater is available, also at the laboratory scale the emerged armor layer has been isolated, which corresponds to about 6 units along the wave direction. Due to the impossibility to analyze the whole cross-section, the study of the block laying surface (i.e. armor layer macro-roughness) has not been carried out. Instead, the armor layer porosity has been investigated,considering the spectral centroid wavelength of the micro-roughness (see equation 6.3).

Therefore, the procedure presented in section 6.3.1 and examined in detail in section 6.3.4 has been employed for the full-scale structure and for the emerged part of

TABLE 6.12 Assessment of the armor layer micro-roughness in terms of λ_m/D_{n50} in prototype and laboratory scale for sections n. 10 and n. 40.

Section	λ_m/D_{n50}		
	Prototype	Configuration E	Configuration EM
n. 10	0.81	0.82	0.92
n. 40	0.70	0.64	0.77

configurations E and EM (see Figure 6.17a-b, Figure 6.18a-b and Table 6.4) after the shake-down tests. The micro-roughness descriptor λ_m/D_{n50} has been evaluated for sections n. 10 and n. 40, at both prototype and laboratory scale. Table 6.12 shows that for the same section, the prototype and model scale λ_m/D_{n50} are very similar, with absolute differences in the range 0.01÷0.11. In addition, the comparison between section n. 10 and section n. 40 highlights that the prototype armor layer surface porosity is quite similar. As regards the model scale, the small discrepancies between configurations E and EM of the same section are due to the influence of the construction modes, which can not be exactly replicated.

Besides the specific results regarding the Catania harbor breakwater, the general outcome of the performed investigation is that the novel SfM-based technique for the analysis armor layer roughness can be employed at both laboratory and prototype scale. Therefore, the proposed technique could be used for the validation of physical models of existing structures based on the external armor layer porosity. Moreover, the armor layer roughness descriptors could be employed for the evaluation and monitoring of the state of degradation of existing rubble mound breakwaters.

6.4 Numerical modeling of the Catania harbor breakwater

6.4.1 Description of IH2VOF model

The hydraulic behavior of the upgraded Catania breakwater has been investigated by using the IH2VOF numerical model. Such a model has been selected among other numerical models existing in literature because it has been extensively validated for wave–structure interaction in conventional and non-conventional coastal structure typologies (Lara et al., 2008; Guanche et al., 2009; Di Lauro et al., 2019). IH2VOF is able to solve the 2D Reynolds averaged Navier–Stokes (RANS) equations, based on the decomposition of the instantaneous velocity and pressure fields into their mean and turbulent components (Lara et al., 2011b; Lara et al., 2011a). Under this assumption, the RANS equations can be written as follows:

$$\frac{\partial \bar{u}_i}{\partial x_i} = 0 \tag{6.12}$$

$$\frac{\partial \bar{u}_i}{\partial t} + \bar{u}_j \frac{\partial \bar{u}_i}{\partial x_j} = -\frac{1}{\rho}\frac{\partial \bar{p}}{\partial x_i} + g_i + \frac{1}{\rho}\frac{\partial \bar{\tau}_{ij}}{\partial x_j} - \frac{\partial (\overline{u_i' u_j'})}{\partial x_j} \tag{6.13}$$

where $u_i = \bar{u}_i + u_i'$ and $p = \bar{p} + p'$ are respectively the Reynolds-decomposed velocity and pressure fields, ρ is the density of the fluid, g_i is the $i-th$ component of the gravitational acceleration and τ_{ij} is the mean viscous stress tensor. The mean flow characteristics for turbulent conditions are calculated by solving the $k - \epsilon$ model, in which the coefficients proposed by Lin (1998) and Rodi (1993)are employed.

The flow inside the porous media is modeled by means of the Volume-Averaged Reynolds Averaged Navier–Stokes equations (VARANS), which are obtained by applying the intrinsic volume average to the RANS equations and combined with the Forchheimer's relationship (Liu et al., 1999):

$$\frac{\partial \langle \bar{u}_i \rangle}{\partial x_i} = 0 \tag{6.14}$$

$$\frac{\partial \langle \bar{u}_i \rangle}{\partial t} + \frac{\partial \langle \bar{u}_i \rangle \langle \bar{u}_j \rangle}{\partial x_j} = -\frac{1}{\rho}\frac{\partial \langle \bar{p} \rangle}{\partial x_i} + g_i + \frac{1}{\rho}\frac{\partial \langle \bar{\tau}_{ij} \rangle}{\partial x_j} - \frac{\partial \langle \overline{u_i' u_j'} \rangle}{\partial x_j} +$$
$$- \left[\frac{\alpha_F \nu (1-n)^2}{n^2 D_{n50}^2} \langle \bar{u}_i \rangle + \frac{\beta_F (1-n)}{n D_{n50}} \sqrt{\langle \bar{u}_1 \rangle \langle^2 + \bar{u}_2{}^2 \rangle} \langle \bar{u}_i \rangle + c_F \frac{1-n}{n}\frac{\partial \langle \bar{u}_i \rangle}{\partial t} \right] \tag{6.15}$$

where ν is the kinematic viscosity of the fluid, D_{n50} and n_V are respectively the median nominal diameter and the porosity of the porous media, α_F and β_F are two empirical coefficients associated with the linear and nonlinear drag force respectively, and c_F is the empirical parameter of the added mass coefficient, equal to 0.34. The coefficients α_F and β_F depend on several parameters, linked to both flow and structure characteristics. However, an accurate description of such dependencies is still not available for oscillatory flows, and hence the best-fit values for α_F and β_F should be evaluated by comparing experimental data and numerical results (Losada et al., 2008).

The RANS, VARANS and $k - \epsilon$ equations are all solved using the finite differences two-steps projection method (Chorin, 1968; Chorin, 1969). The computational domain is discretized in rectangular cells, whose dimensions can be uniform or different for each sub-region of the numerical channel. The movement of free surface is tracked by the Volume of fluid (VOF) method, which consists in identifying the free surface location recording the density change in each cell of the calculation grid. In addition, the insertion of solid boundaries of arbitrary shape in the computational domain can be performed through a partial cell treatment, which consists in modeling the solid objects as a special case of fluid with an infinite density through the introduction of openness functions. All the scalar quantities (i.e. p, k, ϵ, VOF function and openness function) are defined in the center of the cells, whereas the vector-related quantities (i.e. the components of $\bar{u}$ and the additional openness functions) are referred to the cell faces.

Still water with no wave or current motion is the model initial condition for the mean flow in the whole domain, although specific form for the free surface displacement or mean velocity field can be introduced. As regards the turbulence, non-zero initial values are generated using a chosen seed.

The boundary conditions for solid walls can be the no slip or free slip ones, whereas at the free surface the stress, pressure and gradient of turbulent energy (k) and dissipation (ϵ) are set equal to zero. Moreover, the open boundary condition can be employed to allow two-way flow with free pressure and velocity definition. As regards the wave generation, three procedures are included in the model, i.e. internal wavemaker, static wave paddle (Direchlet boundary condition) and dynamics wave paddle (moving boundary condition). Finally, wave absorption boundary conditions are available, which allow to run longer simulations, avoiding most of the effects of reflected waves inside the numerical flume. In particular, the active wave absorption can be applied to both the Dirichlet and the moving boundary conditions, whereas a sponge layer can be placed on the opposite side of the flume for the passive absorption.

6.4.2 Numerical model set-up

The set-up of the numerical model includes the construction of the domain, in terms of width, height and grid, and the calibration of the porosity parameters based on experimental data. Such a procedure has been employed for the upgraded Catania harbor breakwater, considering the most significant configurations among the ones studied through physical modeling. First, section n. 40 has been selected because it represents the most exposed part of the breakwater to the wave motion, and hence subject to the higher mean overtopping rates. As regards the upgrading options, the less performing upgrading solution and the one which seems the most appropriate options according to the combined results of stability and overtopping analysis have been chosen, i.e. the simple heightening of the wave wall up to +8.50 m above MSL (configuration E, see Figure 6.18a), and the upgrading solution with additional 62 t cubic blocks placed over the regularized existing structure and rise of the wave wall up to +9.50 m above MSL (configuration CS, see Figure 6.18f).

In the following, the detailed description of the 91 preliminary simulations for the set-up of the numerical model is presented, together with the analysis of the results. In each numerical test, the static wave paddle (Direchlet boundary condition) has been employed for the wave generation, and the active wave absorption has been used.

Construction of the numerical domain

The construction of the domain for the numerical modeling of the upgraded Catania harbor breakwater has included the following steps: i) analysis of the wave dissipation along numerical channels of different widths without structure, to select the configuration which guarantees the complete development of wave motion with acceptable decrease of wave height; ii) analysis of the wave dissipation along numerical channels of different widths containing the rubble mound structure, to verify the effect of the latter on the characteristics of incident waves; iii) comparison of

the wave characteristics measured in numerical flumes with same dimensions, but meshed with different uniform grids, to identify the optimal solution in terms of both accuracy of the results and computational time.

The geometry of the numerical domain has been chosen considering the dimension of the structure to test, which is about 1.60 m wide and 0.40 m high, and also the hydrodynamic conditions to simulate. In particular, the characteristics of the laboratory 100-years return period sea state (i.e. wave IV) reproduced in a water depth equal to 0.280 m (see Table 6.6) have been chosen as reference for the preliminary definition of the total width of the channel and of the calculation grid. Therefore, significant wave height equal to 0.100 m, peak wave period equal to 1.27 s and deep-water wavelength equal to 2.52 m have been considered.

On the basis of the above described structure and wave characteristics, the height of the domain has been fixed equal to 0.65 m (i.e. the height of the structure plus 0.25 m), in order to allow the study of overtopping events without interaction with the top boundary. As regards the width of the numerical channel, two different options have been considered (see Figure 6.36), which are the structure width plus two times the deep-water wavelength (i.e. 7.00 m), and the structure width plus one time the deep-water wavelength (i.e. 4.50 m). Figure 6.36 shows the location of seven free-surface and velocity gauges along the two numerical flumes: i) gauge 1 has been placed one meter behind the origin of the domain to monitor the waves close to generation area; ii) gauges 2, 3, 4 and 5 have been located following the arrangement of the laboratory resistance gauges used for the evaluation of the reflection coefficient, and hence of the incident wave motion; iii) gauge 6 has been positioned so as to monitor the waves at the toe of the structure; iv) gauge 7 has been placed in correspondence of the wave wall, in order to measure the overtopping discharge.
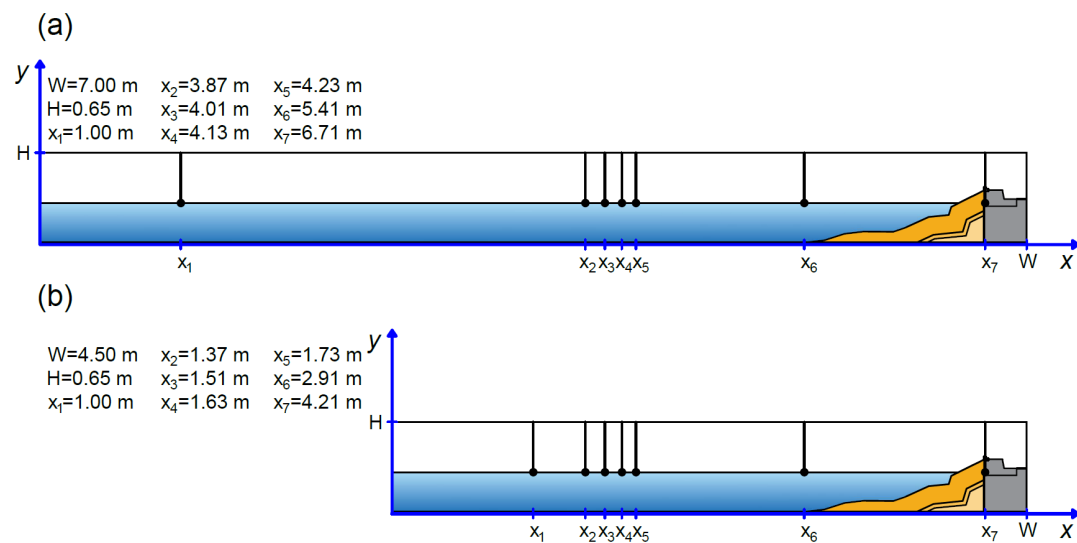
FIGURE 6.36 Dimensions of the domain and location of the free-surface and velocity gauges for the numerical modeling of the upgraded Catania harbor breakwater: (a) channel length equal to 7.00 m; (b) channel length equal to 4.50 m.

Finally, two different uniform grids have been chosen to mesh the domain, whose steps Δx and Δy have been defined in order to ensure respectively at least 10 and 20 cells along the vertical direction per wave height, and also an aspect ratio (i.e. $\Delta x / \Delta y$) equal to 2.

Table 6.13 summarizes the simulations run for the construction of the numerical domain. For each simulation, about 200 waves have been generated (i.e. duration of the sea state equal to 250 s), with calculation time of the employed processor Intel Xeon Silver 4214 2.20 GHz in the following ranges: i) $20 \div 30$ minutes for the 7.00 m long channel meshed with the coarser grid; ii) $12 \div 25$ minutes for the 4.50 m long channel meshed with the coarser grid; iii) $170 \div 240$ minutes for the 4.50 m long channel meshed with the finer grid. The input H_s and T_p for the simulation of the sea states (see Table 6.14) correspond to the experimental incident wave motion measured during the physical model tests carried out considering wave I, II, III, IV and V (see Table 6.6).

The length of the numerical channel which guarantees the complete development of wave motion with acceptable wave dissipation has been chosen on the basis of the results of the simulations without structure (i.e. with empty flume), meshed with the coarser grid. In particular, the percentage difference between input (i.e. experimental) and output (i.e. numerical) significant wave height H_s and peak wave

TABLE 6.13 Summary of the simulations run for the construction of the numerical domain. For each simulation, about 200 waves have been generated (i.e. duration of the sea state equal to 250 s).

Simulations	Width [m]	Height [m]	$\Delta x \times \Delta y$ [m$\times$m]	Configuration	Sea state ID
C01-05	7.00	0.65	0.020×0.010	E	$1 \div 5$
C06-10	4.50	0.65	0.020×0.010	E	$1 \div 5$
C11-15	7.00	0.65	0.020×0.010	no structure	$1 \div 5$
C16-20	4.50	0.65	0.020×0.010	no structure	$1 \div 5$
C21-25	7.00	0.65	0.020×0.010	E	$1 \div 5$
C41-42	4.50	0.65	0.010×0.005	E	1 and 4

TABLE 6.14 Input data of the sea states simulated for the calibration of the numerical model of the upgraded Catania harbor breakwater.

Sea state ID	H_s [m]	T_p [s]	h [m]
1	0.071	1.24	0.280
2	0.075	1.18	0.280
3	0.093	1.27	0.280
4	0.100	1.27	0.280
5	0.109	1.43	0.280

period T_p has been evaluated, according to the following formulas:

$$e_{Hs} = 100 \times \frac{H_{s,num} - H_{s,exp}}{H_{s,exp}} \tag{6.16}$$

$$e_{Tp} = 100 \times \frac{T_{p,num} - T_{p,exp}}{T_{p,exp}} \tag{6.17}$$

where the subscripts *num* and *exp* respectively refer to numerical and experimental values.

Figure 6.37 shows e_{Hs} evaluated for each wave gauges placed in the longer channel and in the shorter one. Most of the numerical dissipation occurs in the first meter of the channel, regardless of its total length, causing the reduction of the significant wave height in the range 9÷18% and 2÷11%, respectively in the case of width of the domain equal to 7.00 m and 4.50 m. The significant wave height remains almost constant in the stretch of the channel between the first and the third gauge, and then e_{Hs} slightly decreases until the section monitored by the fifth gauge. Finally, another increase of e_{Hs} occurs, in the range 11÷19% in the case of width of the domain equal to 7.00 m, and between 6÷16% for the channel 4.50 m long.

As regards the percentage difference between input and output T_p, Figure 6.38 shows e_{Tp} calculated for each wave gauges placed in the longer flume and in the shorter one. The percentage difference between input and output T_p ranges between -8÷+2% and -5÷+9%, respectively in the case of width of the domain equal to 7.00 m and 4.50 m. Therefore, in the shorter channel there is a greater variation of T_p, probably due to the larger effects of reflected waves. For the same reason, the pathways of variation of e_{Tp} along the longer channel are more regular than along the shorter one for each simulated sea state.

On the basis of the results on e_{Hs}, the shorter flume should be selected for the numerical model of the upgraded Catania harbor breakwater, in order to reduce the numerical dissipation which causes the reduction of the significant wave height along the channel. Moreover, the two tested domains give similar outcomes in terms of e_{Tp}.

Further analysis on numerical dissipation and variation of the peak wave period along the channel have been conducted in the presence of the structure. First, the effects of the structure on the characteristic of the simulated wave motion into the two numerical channels have been investigated, considering tentative porosity parameters for the three layers of configuration E (see Figure 6.18a). The results have showed that the presence of the structure seems to have a moderate influence on the characteristics of the incident wave motion, regardless of the width of the domain. Indeed, the incident wave spectra, evaluated using the four gauge method (Faraci et al., 2015), in the presence and in the absence of the breakwater are almost perfectly overlapped in both numerical channels.

Figure 6.39a and Figure 6.39b show e_{Hs} and e_{Tp} evaluated considering the incident wave motion in the presence of the structure. The results confirm that the
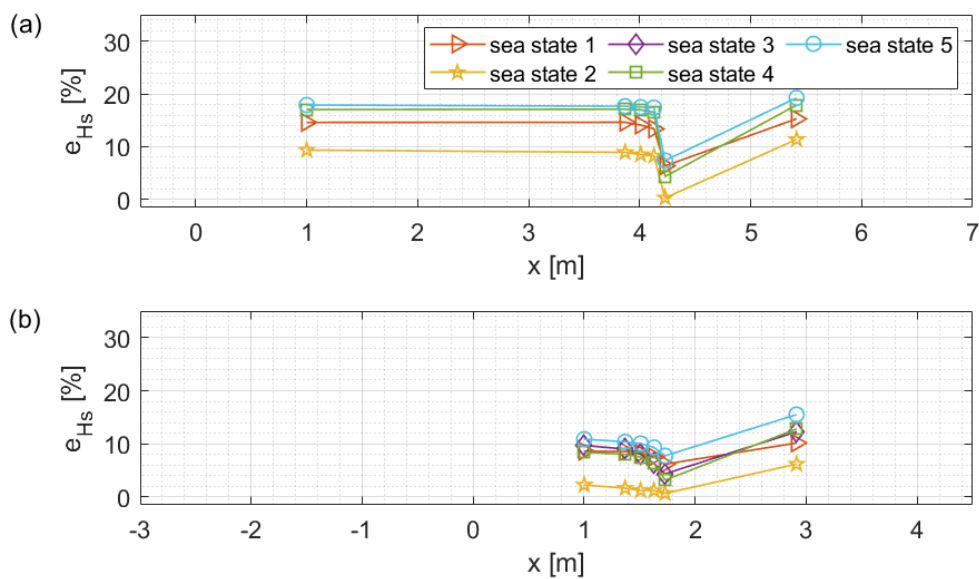
FIGURE 6.37 Percentage error between input and output significant wave height measured by the free-surface gauges placed along the numerical channel with respect to the input value: (a) width of the numerical channel equal to 7.00 m; (b) width of the numerical channel equal to 4.50 m.
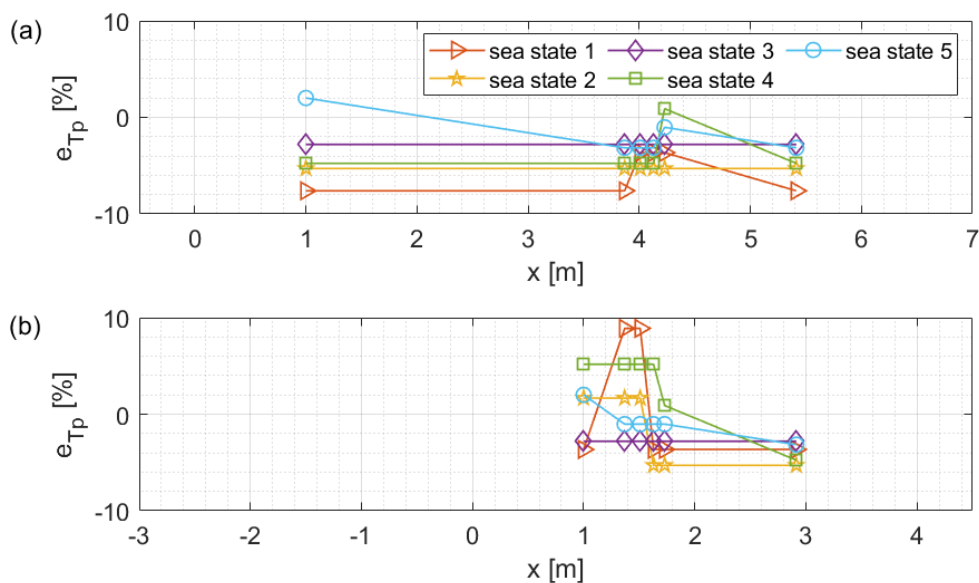
FIGURE 6.38 Percentage error between input and output peak wave period measured by the free-surface gauges placed along the numerical channel with respect to the input value: (a) width of the numerical channel equal to 7.00 m; (b) width of the numerical channel equal to 4.50 m.

differences between input and output peak wave periods are similar for both channel, thus making equivalent the choice of the longer or of the shorter flume.

In light of the above described results, the 4.50 m long numerical channel has been selected for the numerical modeling of the upgraded Catania harbor breakwater. Indeed, the shorter domain seems to be sufficient for the simulation of the
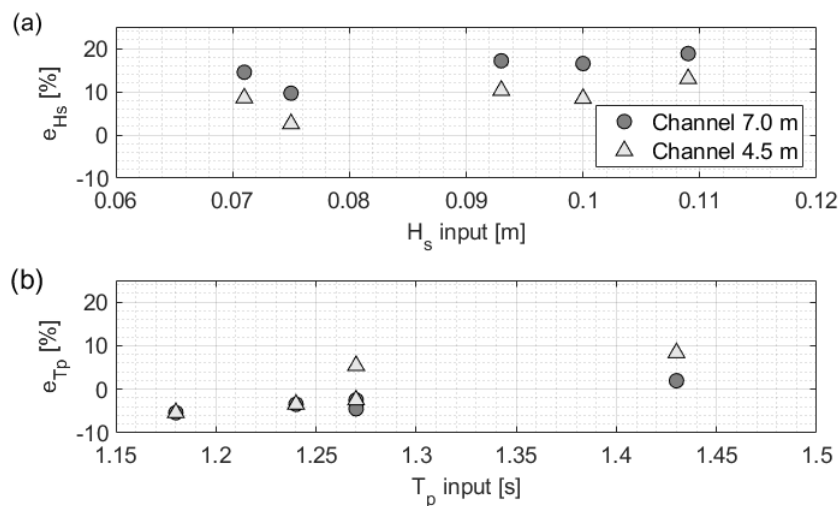
FIGURE 6.39 Percentage error between numerical and experimental (a) significant wave height H_s and (b) peak wave period T_p for the cases of 7.00 m and 4.50 m long numerical channel in the presence of the structure.
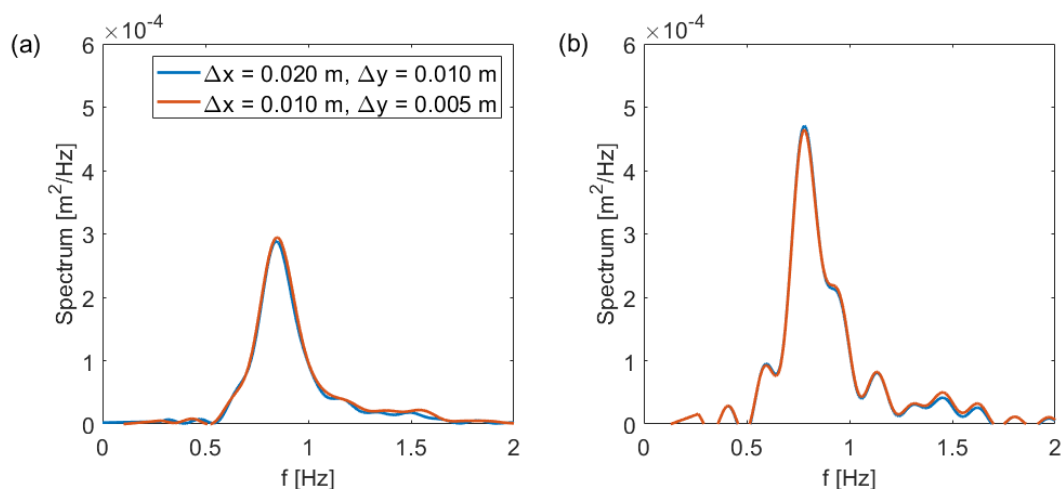
FIGURE 6.40 Comparison between the incident wave spectra evaluated following the four-gauge method of Faraci et al. (2015) using two different grid sizes, in the case of presence of the breakwater: (a) sea state 1; (b) sea state 5.

waves, also ensuring a contained numerical dissipation and lower calculation times.

Further simulations have been run in the presence of the structure for the selection of the horizontal and vertical steps of the grid, considering two possible solutions: i) the coarser grid, with Δx equal to 0.020 m and Δy equal to 0.010 m; ii) the finer grid, with Δx equal to 0.010 m and Δy equal to 0.005 m. Figure 6.40 shows that the incident wave spectra, evaluated using the four gauge method (Faraci et al., 2015), are practically the same for the two considered grids, thus demostrating that the coarser one is able to ensure a good simulation of the wave conditions. Since the calculation times of the coarser grid are one order of magnitude smaller than the ones of the finer grid, the former has been chosen for the numerical modeling of the upgraded Catania harbor breakwater. The adequacy of the selected grid in

reproducing the wave overtopping phenomenon, which is the goal of the present numerical modeling, is demonstrated in the next section.

Calibration of the numerical model

A set of simulations has been run for the calibration of the porosity parameters of the numerical model of the upgraded Catania harbor breakwater, based on the experimental results described in section 6.3. Table 6.15 summarizes the characteristics of such simulations, which have been performed inside a numerical channel 4.50 m wide and 0.65 m high, meshed with a grid 0.020 m (H) $\times$ 0.010 m (V), and considering the input sea states presented in Table 6.14. Parameters α_F and c_F of equation 6.15 have been fixed and respectively equal to 200 and 0.34, according to state of art suggestions (Lara et al., 2008). As regards parameters n_V and β_F of equation 6.15, different reasonable combinations have been tested, which are showed in Table 6.16. The parameter b_F generally ranges between 0.80 and 3.00 for rubble mound breakwaters under wave attack, but values up to 11.0 can characterize variety of rock materials (Losada et al., 2016). The porosity n_V generally varies in a wide range for the core and the filter layer, whereas is usually close to 0.47 for cubic or Antifer armor units (Massie, 1976). Values of n_V of the armor layer equal or lower than 0.30 indicate a very regular and paved placements of the blocks (Vieira et al., 2021). Finally, the values of D_{n50} were deduced from Table 6.3.

The analysis of the characteristics of the wave motion, which have been measured for all the considered combinations of n_V and β_F, has highlighted that the porosity of the structure does not influence the shape of the incident wave spectra. Therefore, the comparison between experimental and modeled incident wave motion could be performed regardless of the porosity of the structure.

TABLE 6.15 Summary of the simulations for the calibration of the numerical model. Each simulation has been performed inside a numerical channel 4.50 m wide and 0.65 m high, meshed with a grid 0.020 m (H) $\times$ 0.010 m (V).

Simulations	Configuration	Porosity ID	Sea state ID	N_w
C06-10	E	1-0	1÷5	200
C26-40	E	2÷4-0	1÷5	200
C43-46	E	5÷6-0	1 and 4	200
C47-50	CS	4-1÷4	4	200
C51-56	CS	4-2	1÷5	1500
C57-61	E	4-0	1÷5	1500
C62-66	CS	8-1	1÷5	1500
C67-71	E	7-0	1÷5	1500
C72-76	E	8-0	1÷5	1500
C77-81	CS	8-1	1÷5	1500
C82-86	CS	8-2	1÷5	1500
C87-91	CS	8-3	1÷5	1500

TABLE 6.16 Combinations of porosity indexes tested for the calibration of the numerical model. Note that the parameters α_F and c_F are fixed and respectively equal to 200 and 0.34.

Porosity ID	Core		Filter		Existing armor		Additional armor		Toe berm	
	n_V	β_F	n_V	β_F	n_V	β_F	n_V	β_F	n_V	β_F
1-0	0.32	1.20	0.35	2.00	0.47	0.60	-	-	-	-
2-0	0.32	1.20	0.35	2.00	0.47	1.20	-	-	-	-
3-0	0.32	1.20	0.35	2.00	0.40	0.60	-	-	-	-
4-0	0.32	1.20	0.35	2.00	0.40	1.20	-	-	-	-
5-0	0.40	1.20	0.40	2.00	0.45	0.60	-	-	-	-
6-0	0.40	1.20	0.40	2.00	0.45	1.20	-	-	-	-
7-0	0.32	1.20	0.35	2.00	0.30	3.00	-	-	-	-
8-0	0.32	1.20	0.35	2.00	0.30	1.50	-	-	-	-
4-1	0.32	1.20	0.35	2.00	0.40	1.20	0.30	1.20	0.35	2.00
4-2	0.32	1.20	0.35	2.00	0.40	1.20	0.30	2.00	0.35	2.00
4-3	0.32	1.20	0.35	2.00	0.40	1.20	0.30	2.00	0.40	1.20
4-4	0.32	1.20	0.35	2.00	0.40	1.20	0.30	3.00	0.35	2.00
7-1	0.32	1.20	0.35	2.00	0.30	3.00	0.30	3.00	0.35	2.00
8-1	0.32	1.20	0.35	2.00	0.30	1.50	0.30	3.00	0.35	2.00
8-2	0.32	1.20	0.35	2.00	0.30	1.50	0.30	3.00	0.35	3.00
8-3	0.32	1.20	0.35	2.00	0.30	1.50	0.25	5.00	0.35	3.00

Figure 6.41 shows that the numerical model is not able to capture the energy which corresponds to frequencies higher than 1 Hz of the experimental spectra. Three main factors can influence the performance of the numerical model in reproducing the experimental waves: i) differences between the laboratory signal and the numerical one, and also between the wave generation procedures; ii) the model does not simulate the interactions between waves and the structure armor units, which generates small and high frequency waves; iii) the laboratory tests were carried out without active wave absorption, contrary to the numerical simulations. However, the higher waves, which represents the main contribution to overtopping volumes, corresponds to frequencies lower than 1 Hz, and also the energy content of laboratory and numerical spectra are almost the same (see Table 6.17). Therefore, the latter have been used for the calibration of the porosity parameters based on the experimental reflection coefficients and overtopping discharge.

The employed procedure for the calibration of the porosity parameters is made up of two steps. First, short simulations (i.e. sea states of about 200 waves) have been run in order to identify the best combinations of n_V and β_F as the ones which provide the greatest accordance between numerical and experimental reflection coefficients. Then, longer simulations (i.e. sea states of about 1500 waves like the experimental ones, see Table 6.6) have been performed considering the chosen porosity parameters, in order to verify the adequacy of the numerical model in reproducing the overtopping phenomena. The evaluation of the mean overtopping discharge has been performed considering more than the 500÷1000 waves suggested by EurOtop, 2018, in order to ensure a sufficient accuracy of the results also for the lower input
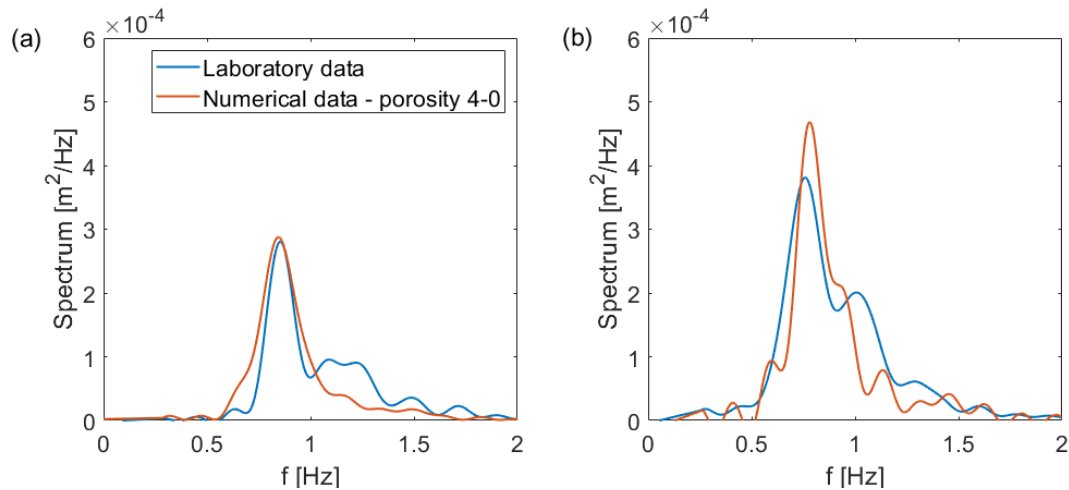
FIGURE 6.41 Comparison between the experimental and numerical incident wave spectra evaluated following the four-gauge method of Faraci et al. (2015): (a) sea state 1; (b) sea state 4.

TABLE 6.17 Wave energy calculated from the incident wave spectra evaluated following the four-gauge method of Faraci et al. (2015).

Incident wave energy $[m^2]$	Sea state 1	Sea state 2	Sea state 3	Sea state 4	Sea state 5
Experimental	7.94E-05	8.88E-05	1.37E-04	1.57E-04	1.89E-04
Numerical	6.63E-05	8.45E-05	1.10E-04	1.30E-04	1.40E-04

waves. Instead, the calculation of the reflection coefficient has been performed considering only 200 waves, because it has been preliminary verified that the resulting k_r was almost identical to the one evaluated with 1500 waves.

The calibration of n_V and β_F of core, filter layer and existing armor layer has been carried out, considering configuration E. Figure 6.42a shows the comparison between the experimental reflection coefficients and the numerical ones, corresponding to the tested combinations of n_V and β_F, as a function of the Iribarren parameter (see equation 6.5). As already discussed in section 6.3.5, the predictions of equations 6.6-6.8 (Zanuttigh and van der Meer, 2008) slightly overestimate the experimental data, probably due to the fact that such equations were not calibrated for irregular slopes like the existing armor layer of the Catania harbor breakwater. The reflection coefficients measured for porosity 4-0 and porosity 8-0 seem to follow the experimental pattern better than the other options. Therefore, the mean overtopping discharge recorded for porosity 4-0 and porosity 8-0 has been compared with the laboratory data. Figure 6.43a shows that both porosity combinations produce non-dimensional mean overtopping rates similar to the experimental ones. However, the solution porosity 8-0 seems the most suitable choice, because it is the only one able to properly simulate the overtopping phenomenon generated by the lower waves. It is worth to point out that the use of n_V equal to 0.30 is justified by the almost regular placement pattern of the cubic armor units (see Figure 6.14a), as suggested by Vieira
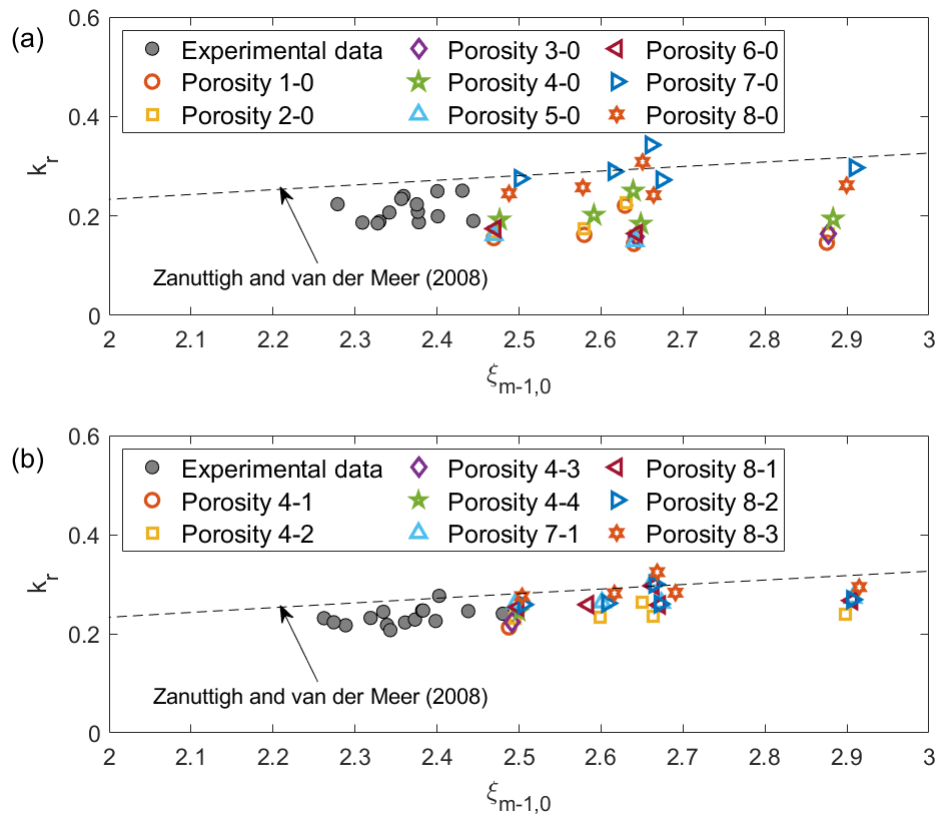
FIGURE 6.42 Comparison between experimental and numerical reflection coefficient (k_r), expressed as a function of the Iribarren number ($\xi_{m-1,0}$) and the equation suggested by Zanuttigh and van der Meer (2008): (a) configuration E; (b) configuration CS.

et al. (2021).

The calibration of the porosity parameters of the additional armor layer and toe berm has been performed for configuration CS. Figure 6.42b shows that the experimental reflection coefficients, expressed as function of the Iribarren parameter (see equation 6.5), are slightly lower than the predicted ones, probably because equations 6.6-6.8 (Zanuttigh and van der Meer, 2008) were not calibrated for upgraded structures (see section 6.3.5). In addition, all the tested combinations of n_V and β_F give similar reflection coefficients. However, since porosity 8-0 seemed the best solution for the existing structure, the adequacy of porosity 8-1, 8-2 and 8-3 has been verified through the comparison between experimental and numerical non-dimensional mean overtopping discharge. Figure 6.43b shows that the numerical results are all acceptable for the higher waves, i.e. lower R_c/H_s, for the three combinations of porosity parameters. The impossibility to capture the overtopping rates produced by the lower waves may be due to the limits of the numerical model, whose results are too sensitive to the characteristics of individual waves when q^* close to 10^{-5} are simulated. The outcomes corresponding to the three considered porosity combinations seems quite similar, but porosity 8-3 is the only one that does not underestimate the experimental q^* measured for the higher waves. Therefore, porosity 8-3 has been identified as the best solution.
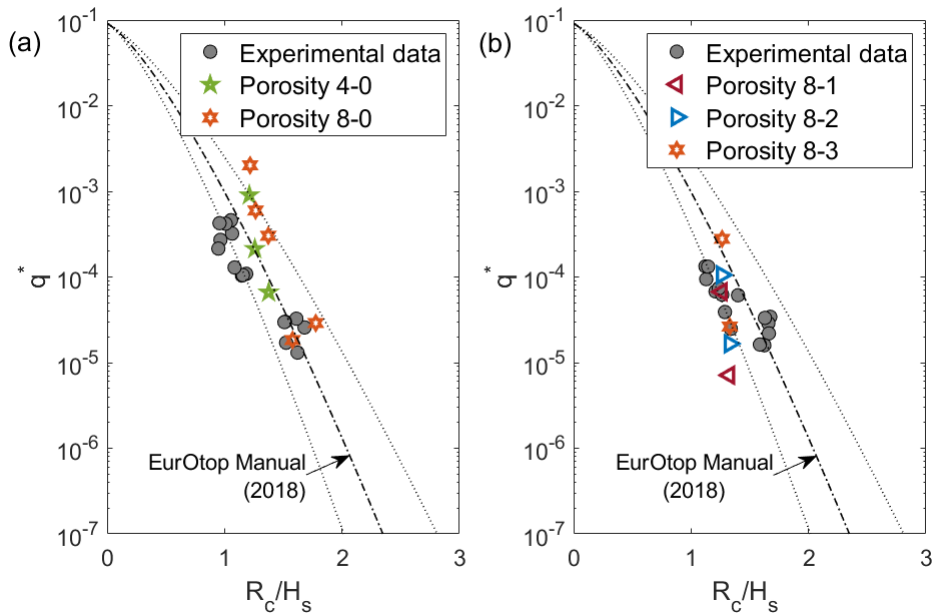
FIGURE 6.43 Comparison between experimental and numerical dimensionless mean overtopping discharge (q^*) and the empirical formula suggested by EurOtop (2018): (a) configuration E; (b) configuration CS. The dotted lines indicate the 95% confidence bounds of the EurOtop (2018) formula.

Summary of the numerical model set-up

The set-up of the numerical model of the upgraded Catania harbor breakwater has included the definition of the dimensions of the domain, the choice of the calculation grid, and the calibration of the porosity parameters. As regards the wave generation, the Direchlet boundary condition has been employed and the active wave absorption has been used.

The selected numerical channel is 4.50 m wide and 0.65 m high (see Figure 6.36b), and it has beens meshed using a grid with Δx equal to 0.020 m and Δy equal to 0.010 m. As regards the porosity parameters, α_F and c_F have been set respectively equal to 200 and 0.34 for all the porous media, whereas the values of D_{n50} have been deduced from Table 6.3. Instead n_V and β_F have been calibrated against experimental results on reflection and overtopping discharge. In particular, combinations 8-0 and 8-3 of Table 6.16 have been selected, respectively for the upgrading solution which consists in the simple heightening of the wave wall (configuration E, see Figure 6.18a) and for the option which provides the rise of the wave wall combined with the addition of an extra armor layer of 62 t cubic blocks (configuration CS, see Figure 6.18f). Therefore, the following n_V and β_F have been selected for the different layers of the structure: i) n_V=0.32 and β_F=1.20 for the core; ii) n_V=0.35 and β_F=2.00 for the filter; iii) n_V=0.30 and β_F=1.50 for the existing armor layer; iv) n_V=0.25 and β_F=5.00 for the additional armor layer; v) n_V=0.35 and β_F=3.00 for the berm at the toe of the additional armor layer.

6.4.3   Scale-up of the numerical model

The possibility to evaluate the overtopping phenomenon at full scale is of great interest, because of the shortcomings of physical modeling due to scale effects could be overcome. Therefore, the numerical model of the Catania harbor breakwater has been scaled up, in order to evaluate the differences between model and prototype results due to scale effects.

Table 6.18 summarizes the numerical tests carried out for the scale-up of the numerical model of the Catania harbor breakwater. The input data of the simulated sea states for the scale-up of the numerical model are presented in Table 6.19, at both prototype and model scale. It is worth to point out that the full scale simulations have been performed inside a numerical channel which is exactly 70 times the laboratory scale one (see Figure 6.36b), i.e. 315.00 m wide and 45.55 m high, meshed with a grid 1.40 m (H) × 0.70 m (V). As regards the porosity parameters (i.e. α_F, β_F, c_F and n_V), the same values have been employed for both model and real scale.

Figure 6.44 shows the dimensionless mean overtopping discharge as a function of the dimensionless structure freeboard, evaluated at model and prototype scale for configurations E and CS. The empirical formula proposed by EurOtop (2018) is also plotted as reference. Figure 6.44a highlights that for configuration E there is a fair agreement between model and full scale data. In particular, for q^* greater than 10^{-4}, the model scale values differ from the real scale ones by no more than 22%. The greater difference that characterizes the lower q^* is in agreement with the higher uncertainty of the numerical model in simulating small overtopping rates, which

TABLE 6.18 Summary of the simulations for the scale-up of the numerical model.

Simulations	Configuration	Scale	Porosity ID	Sea state ID	N_w
C72-76	E	model	8-0	1÷5	1500
SP01-05		prototype			
C90-94	CS	model	8-3	4÷8	1500
SP06-13		prototype			

TABLE 6.19 Input data of the simulated sea states at prototype and model scale.

Sea state ID	Prototype scale			Model scale		
	H_s [m]	T_p [s]	h [m]	H_s [m]	T_p [s]	h [m]
1	4.970	10.37	19.600	0.071	1.24	0.280
2	5.250	9.87	19.600	0.075	1.18	0.280
3	6.510	10.63	19.600	0.093	1.27	0.280
4	7.000	10.63	19.600	0.100	1.27	0.280
5	7.630	11.96	19.600	0.109	1.43	0.280
6	6.650	10.88	19.600	0.095	1.30	0.280
7	7.350	10.88	19.600	0.105	1.30	0.280
8	8.400	10.88	19.600	0.120	1.30	0.280
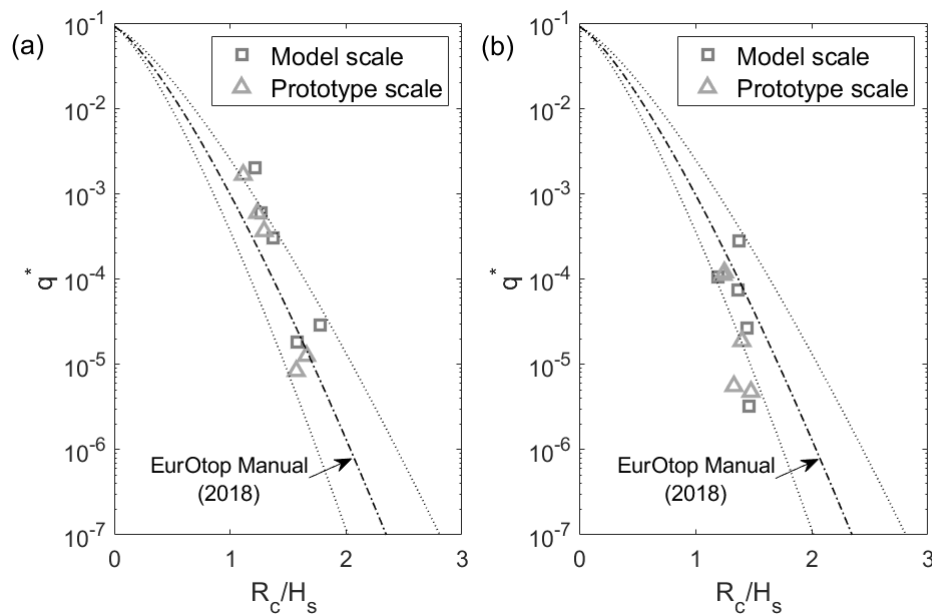
FIGURE 6.44 Comparison between numerical dimensionless mean overtopping discharge (q^*) evaluated at model and prototype scale and the empirical formula suggested by EurOtop (2018): (a) configuration E; (b) configuration CS. The dotted lines indicate the 95% confidence bounds of the EurOtop (2018) formula.

is due to the stronger influence of the individual waves characteristics. Figure 6.44b shows that for configuration CS the two data series seems to follow a similar pattern, even if the discrepancies between model and prototype scale data are greater than the one evaluated for configuration E. Such a result is due to the fact that in general configuration CS is subject to lower overtopping discharges than configuration E, and hence the estimation of q^* is affected by more uncertainty.

Considering the discussed limits of the numerical model in simulating the lower overtopping rates, it is possible to asses that the differences between laboratory and prototype scale mean overtopping discharges are quite limited.

6.4.4 Evaluation of site-specific overtopping prediction formulas

The results described in section 6.4.2 showed that the properly calibrated IH2VOF model is a good prediction tool for mean overtopping discharge, which allows to perform a huge number of simulations considering new hydrodynamic conditions and modifications to the structure geometry in an economically and technically effective way. In addition, as discussed in section 6.4.3, such a numerical model enables to easily go from the laboratory scale to the prototype scale, by simply scaling the geometry of the domain and hydrodynamic conditions. In the present work, the numerical model of the upgraded Catania harbor breakwater has been employed for the definition of site-specific empirical-numerical formulas, considering configurations E and CS of section n. 40. Such formulas can be useful for a more reliable prediction of mean overtopping discharge for the Catania harbor breakwater, which

can also be employed for the probabilistic assessment of port operability and functionality.

To this aim, for each considered configuration six realizations of the same input sea state have been carried out, using different seedings for the random generation of the waves time series. The simulation of different realizations for the same sea state has allowed to analyze the overtopping phenomena including: i) the wave-wave interaction effect; ii) the effects of wave sequence; iii) the effects of the ratio H_{max}/H_s, which is significant for low overtopping events. Such simulations have been performed at both model and prototype scale, for five different input sea states selected among the ones summarized in 6.19. Table 6.20 presents a synthesis of the characteristics of the simulations. Instead, Table 6.21 and Table 6.22 report the characteristics of the generated wave series in terms of significant wave height, mean and peak wave period and H_{max}/H_s, at both model and prototype scale.

The resulting q^* have been employed to calculate new empirical-numerical formulas for the mean overtopping discharge, specific for configurations E and CS at both laboratory and real scale. In particular, equation 6.11, which was proposed by EurOtop (2018), has been fitted to the numerical data through the calculation of the best fit values of the coefficients a_E and b_E. Starting from the values of a_E and b_E suggested by EurOtop (2018), i.e. 0.09 and 1.50 respectively, the new values of a_E and then of b_E have been evaluated using the least squares method.

The results of the curve fitting calculations are graphically showed in Figure 6.45 and Figure 6.46. Each point of the numerical data-set is synthetically represented in terms of mean q^* and R_c/H_s for each reproduced sea state. Horizontal error bars indicate the uncertainty due to the impossibility to perfectly replicate the same incident significant wave height when the seeding for random generation of waves time series varies. However, such an uncertainty is very contained. Instead, vertical error bars are used to represent the uncertainty in the evaluation of q^* for the same sea state. As discussed in section 6.4.2, there is a greater uncertainty for the lowest q^*, i.e. longer vertical error bars. It is worth to point out that the absence of the lower error bar indicates that it has a negative value, which does not have a physical meaning and cannot be plotted in log-scale . Such a condition can occur when null values

TABLE 6.20 Summary of the simulations for the evaluation of site-specific overtopping prediction formulas for the upgraded Catania harbor breakwater.

Simulations	Configuration	Scale	Porosity ID	Sea state ID	N_w
C72-76		model			
C95-119	E		8-0	1÷5	1500
SP01-05		prototype			
SP39-63					
C90-94		model			
C120-144	CS		8-3	4÷8	1500
SP09-38		prototype			

TABLE 6.21 Characteristics of the generated wave series for each sea state (N_w=1500): part I.

Sea state	Generation at model scale				Generation at prototype scale			
	H_s [m]	T_m [s]	T_p [s]	H_{max}/H_s	H_s [m]	T_m [s]	T_p [s]	H_{max}/H_s
1	5.099	8.15	10.85	1.766	0.072	0.99	1.30	1.859
	5.054	8.07	10.77	1.783	0.073	0.98	1.29	1.834
	5.079	8.02	10.73	1.795	0.073	0.98	1.30	1.821
	5.083	8.14	10.77	1.772	0.073	0.97	1.29	1.823
	5.083	8.12	10.81	1.902	0.072	0.99	1.30	1.808
	5.083	8.12	10.81	1.902	0.073	1.00	1.30	1.866
2	5.363	7.72	10.27	1.721	0.078	0.94	1.24	1.802
	5.342	7.73	10.25	1.779	0.076	0.94	1.23	1.845
	5.380	7.74	10.32	1.752	0.077	0.94	1.24	1.833
	5.408	7.82	10.33	1.746	0.076	0.94	1.24	1.685
	5.419	7.69	10.28	1.826	0.076	0.94	1.24	1.848
	5.392	7.67	10.25	1.816	0.076	0.94	1.23	1.847
3	6.712	8.28	11.06	1.767	0.095	1.00	1.33	1.812
	6.655	8.27	11.01	1.828	0.095	1.00	1.32	1.893
	6.624	8.40	11.17	1.828	0.095	1.01	1.33	1.791
	6.606	8.26	11.06	1.778	0.096	1.00	1.32	1.838
	6.672	8.16	10.94	1.801	0.095	1.01	1.33	1.860
	6.643	8.38	11.13	1.712	0.095	1.03	1.34	1.806
4	7.192	8.46	11.22	1.830	0.103	1.02	1.34	1.826
	7.177	9.42	12.52	1.770	0.102	1.01	1.33	1.866
	7.174	8.51	11.14	1.755	0.102	1.02	1.34	1.838
	7.204	8.35	11.10	1.780	0.102	1.00	1.32	1.926
	7.176	8.33	11.10	1.749	0.102	1.00	1.33	1.860
	7.143	8.37	11.12	1.797	0.102	1.00	1.32	1.756

q^* are recorded for some of the six realizations of a certain sea state, as happened for configuration CS at prototype scale (see Figure 6.46b).

Figure 6.45 and Figure 6.46 show that the empirical-numerical formulas for the mean overtopping discharge evaluated at laboratory and prototype scale from the numerical data are very similar to the formula originally proposed by EurOtop (2018), above all the ones calculated for configuration CS. In addition, slight differences between the model and prototype scale formulas are observed, in accordance with the results described in section 6.4.3.

The above discussed outcomes can be deduced also from the analysis of the results of the curve fitting calculations, which are synthesized in Table 6.23. The coefficient a_E assumes values quite different from the value of 0.09 proposed by EurOtop (2018), above all for configuration E. On the contrary, the coefficient b_E is always very close to the value of 1.50 proposed by EurOtop (2018). The differences between the formulas at laboratory and prototype scale are limited, as expected from the results presented in section 6.4.3.

TABLE 6.22 Characteristics of the generated wave series for each sea state (N_w=1500): part II.

Sea state	Generation at model scale				Generation at prototype scale			
	H_s [m]	T_m [s]	T_p [s]	H_{max}/H_s	H_s [m]	T_m [s]	T_p [s]	H_{max}/H_s
	7.801	9.44	12.56	1.724	0.112	1.14	1.50	1.853
	7.799	9.37	12.43	1.833	0.110	1.14	1.50	1.805
5	7.841	9.32	12.42	1.788	0.111	1.15	1.50	1.829
	7.815	9.44	12.49	1.834	0.110	1.12	1.49	1.814
	7.800	9.31	12.43	1.832	0.111	1.13	1.49	1.850
	7.836	9.31	12.43	1.775	0.111	1.15	1.51	1.858
	6.778	8.46	11.29	1.796	0.097	1.03	1.36	1.808
	6.833	8.53	11.36	1.823	0.096	1.03	1.35	1.812
6	6.839	8.50	11.35	1.836	0.097	1.02	1.35	1.853
	6.761	8.45	11.26	1.830	0.097	1.03	1.36	1.878
	6.807	8.59	11.34	1.792	0.097	1.03	1.36	1.897
	6.833	8.61	11.46	1.812	0.096	1.03	1.36	1.781
	7.532	8.48	11.30	1.747	0.108	1.04	1.36	1.853
	7.498	8.54	11.33	1.788	0.107	1.03	1.36	1.836
7	7.564	8.42	11.27	1.787	0.107	1.04	1.36	1.829
	7.547	8.56	11.40	1.779	0.107	1.05	1.37	1.731
	7.544	8.52	11.35	1.828	0.107	1.03	1.36	1.909
	7.559	8.50	11.35	1.836	0.107	1.02	1.35	1.880
	8.603	8.34	11.23	1.806	0.122	1.02	1.36	1.808
	8.576	8.49	11.25	1.841	0.124	1.03	1.36	1.801
8	8.594	8.49	11.27	1.752	0.122	1.03	1.36	1.773
	8.638	8.57	11.37	1.791	0.123	1.04	1.36	1.772
	8.580	8.41	11.24	1.839	0.123	1.03	1.36	1.779
	8.669	8.62	11.39	1.822	0.123	1.04	1.38	1.771

TABLE 6.23 Coefficients of the empirical-numerical formula for the mean overtopping discharge evaluated for configurations E and CS at both model and prototype scale.

Configuration	Scale	a_E		b_E	
		Mean	STD	Mean	STD
E	model	0.3015	0.1433	1.4993	0.0990
	prototype	0.4187	0.1578	1.5022	0.0790
CS	model	0.0616	0.0478	1.4980	0.1452
	prototype	0.0421	0.0200	1.5001	0.0896
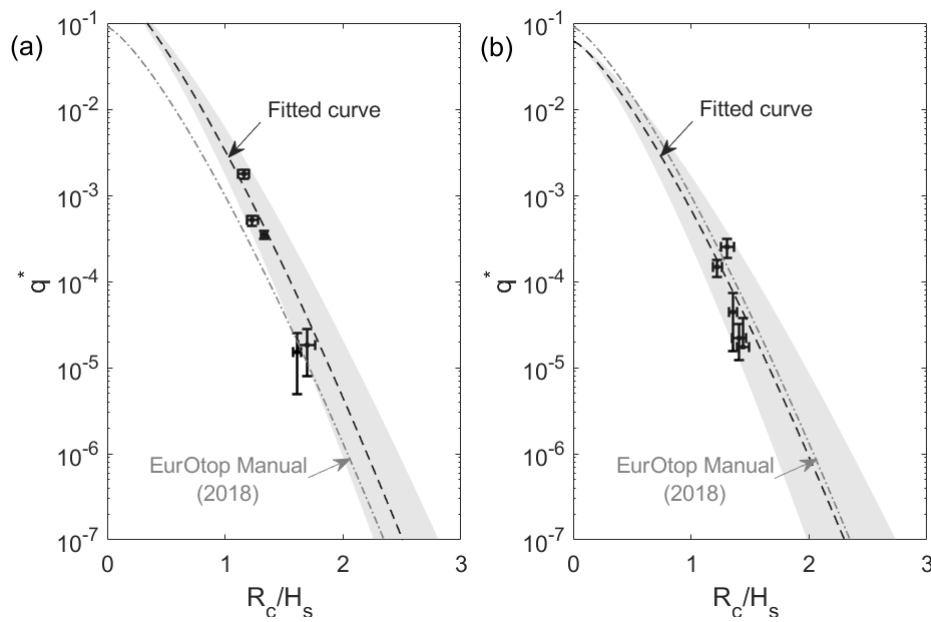
FIGURE 6.45 Comparison between the empirical-numerical formula for the mean overtopping discharge evaluated at laboratory scale and the EurOtop (2018) formula: (a) configuration E; (b) configuration CS. The grey area indicate the 90% confidence bounds of the fitted formula.
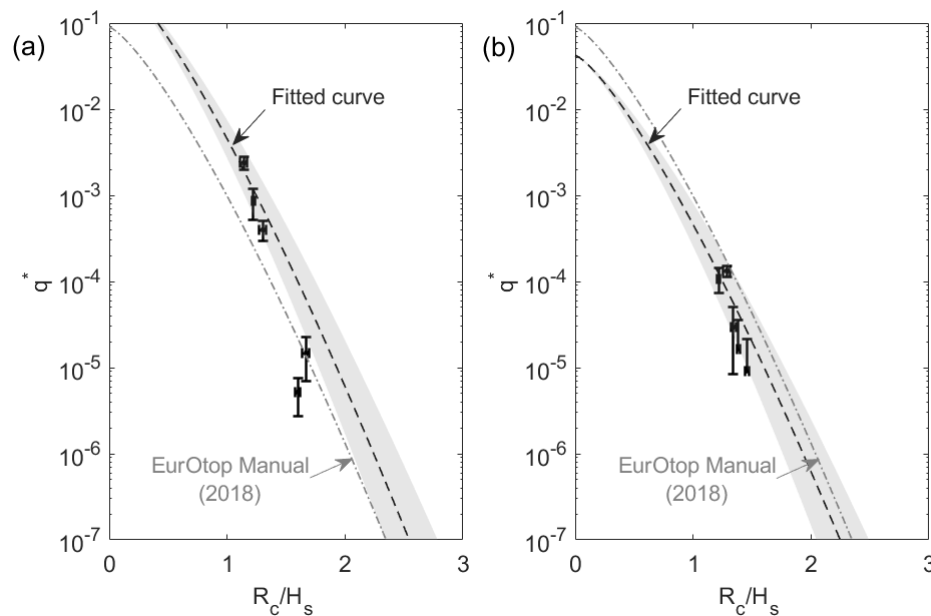
FIGURE 6.46 Comparison between the empirical-numerical formula for the mean overtopping discharge evaluated at prototype scale and the EurOtop (2018) formula: (a) configuration E; (b) configuration CS. The grey area indicate the 90% confidence bounds of the fitted formula.

Chapter 7

Probabilistic assessment of the performances of upgraded structures

7.1 Overview

The design of harbor rubble mound breakwaters should be performed using a probabilistic approach, in order to take into account the uncertainty related to the geometry and the materials of the structure, to the climate conditions and to the employed design formulas. This is even more true if the upgrade of existing structure in the context of climate change is considered. Indeed, there is an absence of validated formulations for the design of upgrading solutions, and the effects of global warming are expected to modify the actual wave climate and sea levels.

The methodology for the probabilistic design of upgrading solutions for harbor rubble mound breakwater followed in the present work consists in five main phases: i) assessment of the current state of the existing structure, in order to identify the most adequate upgrading concepts; ii) definition of the climate condition in the site of interest, also considering the effects of climate change; iii) preliminary design of the selected upgrading options, considering a deterministic approach; iv) composite modeling of the upgrading solutions, to verify their capability to satisfy the design requirements, and the applicability of state of art equations for the description of the behavior of the upgraded structure; v) probabilistic assessment of the performances of the upgrading solutions under present and future climate, considering the ULS and the SLS related to the possible failure mechanisms, whose description can be performed through traditional or adapted formulas. The first four steps of the described methodology have been already discussed in Chapter 4, Chapter 5 and Chapter 6. In the present chapter, the procedure for the assessment of the probability of failure, i.e. of reaching a certain ultimate or serviceability limit state, during the structure lifetime is described.

Such a procedure is based on the performance of Monte Carlo simulations, which consist in the generation of a huge number of realizations of the structure life cycle and in the calculation of the value assumed by the reliability function that describes

the selected failure mode at each iteration. In particular, for each realization, random wave conditions, sea levels, geometry and material characteristics and coefficients of the reliability function are drawn from the correspondent probability distributions. Then, the probability of failure is calculated as the ratio between the number of life cycles with at least one failure (i.e. negative value of the reliability function) and the total number of realizations.

The case study of the Catania harbor breakwater has been selected for the application of the above described procedure. For different upgrading configuration of the structure, the failure due to the collapse of the outer armor layer (ULS) and the one related to excessive mean overtopping discharge (SLS) have been analyzed, assuming that they are part of a series system. Besides the specific results regarding the performances of the Catania harbor breakwater, some generally valid outcomes have been found.

7.2   Probabilistic design of upgraded structures

The applied methodology for the probabilistic design of upgrading solutions for existing harbor rubble mound breakwaters is summarized in Figure 7.1. First, the most suitable upgrading concepts are identified on the basis of the current state of the existing structure, which can be assessed following the approach described in Chapter 4. Then, the deterministic preliminary design of the selected upgrading options is performed using the state of art formulas for conventional structures (US Army Corps of Engineers, 2002; CIRIA et al., 2007), considering the required hydraulic performances and the local hydrodynamic conditions. Due to the relevant effects of climate change on coastal areas, the significance of long-term variations of mean sea level and wave climate should be evaluated, as described in Chapter 5.

The combined physical and numerical modeling (i.e. composite modeling, see Chapter 6) are employed for testing the preliminary design of the upgrading solutions, thus allowing the analysis of their response to increasing wave load, in terms of both stability of the armor layer and overtopping. Moreover, the adaptation of the traditional design formulas for the considered structures is performed if necessary. Indeed, the traditional formulas may not be able to properly describe the response of non-conventional structures, such as upgraded rubble mound breakwaters (Lara et al., 2019).

As described in section 2.2, the probabilistic design of coastal defense structures requires the selection of the main failure modes refereed to a certain limit state. The present work focuses only on ultimate and serviceability limit states (ULS and SLS, respectively), even if the operational limit state (OLS) should be considered for a more complete probabilistic assessment. Therefore, the following described methodology for the probabilistic assessment of the structure performances is valid only for ULS and SLS.
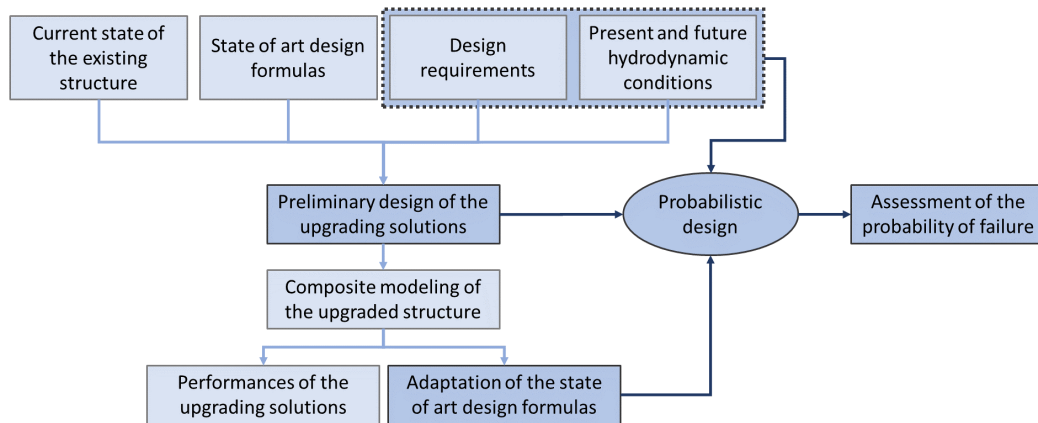
FIGURE 7.1 Block diagram of the proposed methodology for the design of upgrading solutions for existing rubble mound breakwaters.

The governing equation of each of the selected failure modes, correspondent to ULS or SLS, is defined, which represents the reliability function. For the case of upgraded structures, such governing equations are the experimental and numerical formulas derived from the results of the composite modeling. The reliability function can be written as the difference between resistance of the structure and acting load (see equation 2.5). The resistance and solicitation terms depend on several stochastic variables, according to not always well known relationships. In particular, the resistance term is usually linked to the geometry of the structure and to the characteristics of the component materials. Instead, the solicitation term usually contains the water density and the hydrodynamic parameters.

For a given reliability function, the level III probability of failure during lifetime can be evaluated through the implementation of a Monte Carlo simulation. In general, the Monte Carlo simulation is a mathematical technique that generates random scenarios to model the uncertainty of a certain process. Different iterations are run to generate a great number of possible paths for the evaluation of the probability of obtaining negative values of the reliability function Z, i.e. failures of the breakwater. Following the indications of Puertos del Estado (2010), the useful life of the structure is an experiment of the Monte Carlo simulation, which consists of a known number of meteorological years. During each meteorological year a certain number of sea storms occurs, which could cause or not the failure of the breakwater, i.e. the reaching of the considered limit state. A certain number of random life cycles is generated during the Monte Carlo simulation, using as input the probability distributions of the involved variables (i.e. hydrodynamic conditions, materials and geometry). Then, the probability that the structure reaches the selected limit state during lifetime ($P_{f,L}$) and its standard deviation ($\sigma_{Pf,L}$) are evaluated as follows (Lucio et al., 2021):

$$P_{f,L} = \frac{N_f}{N_r} \tag{7.1}$$

$$\sigma_{Pf,L} = \sqrt{\frac{P_{f,L} \times (1 - P_{f,L})}{N_r}} \tag{7.2}$$

where N_f is the number of life cycles with at least one failure (i.e. Z assumes negative values at least one time during lifetime) and N_r is the number of simulated life cycles. It is worth to point out that $P_{f,L}$ can be calculated also as the final cumulative annual probability of failure P_f during the life cycle.

The performance of the above described Monte Carlo simulation implies the following steps:

1. Selection of the length of the life cycle (L). The duration of the useful life for a permanent structure can be fixed considering the index ERI, which quantifies the economic repercussion of the possible failure of the structure itself (Puertos del Estado, 2010).

2. Selection of the number of life cycles (i.e. realizations) to simulate (N_r). N_r can be fixed assuming that the probability of failure P_f follows a binomial distribution and fixing a relative error CV for its estimation, according to the following formula (Jonkman et al., 2015):

$$N_r = \frac{1 - P_{f,Lmax}}{CV^2 P_{f,Lmax}} \tag{7.3}$$

where $P_{f,Lmax}$ is the maximum acceptable probability of failure during life time, whose value depends on the characteristics of the harbor basin (Puertos del Estado, 2010).

3. Random generation of a set of sea storms for each life cycle. The number of sea storms (n_{ss}) to generate for each life cycle is evaluated as follows:

$$n_{ss} = L \times \lambda \tag{7.4}$$

where L is the duration of the useful life of the structure and λ is the mean annual frequency of sea storms, which can be derived from the extreme value analysis of the significant wave height time series.

4. Selection of the ULS and SLS to be verified, and of the reliability functions which correspond to the chosen failure modes.

5. For each simulated life cycle, generation of random values of the variables describing the materials and the geometry of the structure (e.g. density of water and of blocks, slope pf the armor layer, height of the wave wall), which are contained in the selected reliability functions. Under the hypothesis of no changes in the structure composition and geometry during lifetime, such values remain the same during the single life cycle (i.e the single experiment).

6. For each simulated life cycle, generation of random values of the coefficients of the selected reliability functions. Under the hypothesis of no changes in the

structure response to the external loads during lifetime, such values remain the same during the single life cycle (i.e the single experiment).

7. Evaluation of the probability of failure during the lifetime using equation 7.1.

The procedure for the generation of random sea storms deserves further clarifications. In general, the joint probability distributions of the interdependent hydrodynamic variables should be calculated, through more or less sophisticated techniques. For instance, if the time series of the correlated variables are available, copulas can be used for the creation of the multivariate distributions that describe their dependencies. However, such an approach cannot be used when the future projections of wave climate and sea levels are included in the probabilistic calculations through the factor of change method (see 5.4). Indeed, in this case only the statistics of the considered dependent variables are available, which are not sufficient to fit a copula. In order enable the description of interdependent variables even if only their statistics are known, another approach can be considered, which is based on the following three steps: i) identification of the interdependent variables (e.g. significant wave height, mean and peak wave period, sea storm duration and storm surge); ii) identification of the primary variable, which is strongly related to each of the other variables, and calculation of its univariate probability distribution; iii) definition of site-specific empirical relationships between the primary variable and the secondary ones.

The significant wave height is often the primary variable, whose probability density function is obtained through the performance of extreme value analysis in deep water. In this case, the simulation of a generic random sea storm is performed according to the following steps:

1. an initial random H_{s0} is drawn from the central fit of the probability density function of extreme significant wave height;

2. a final random H_{s0} is drawn from the normal distribution having mean equal to H_{s0} previously generated from the central fit, and standard deviation corresponding to the width of the confidence bounds of the distribution (see Figure 7.2);

3. an initial random value of each H_{s0}-dependent variable (i.e. mean and peak wave period, duration of sea storm, storm surge) is generated form the central fit of the site specific empirical law considering the last drawn H_{s0};

4. a final random value of each H_{s0}-dependent variable is generated form the normal distribution having mean equal to the value previously generated from the central fit of the site specific empirical law and standard deviation corresponding to the width of the confidence bounds (see Figure 7.3);

5. a random mean water depth is drawn from a normal distribution, whose standard deviation takes into accounts the oscillations due to the astronomical tide;
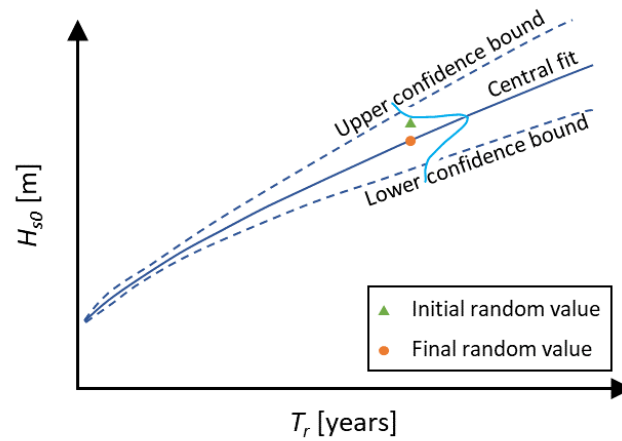
FIGURE 7.2 Sketch of the procedure for the generation of a random H_{s0} from the extreme value distribution of the significant wave height.
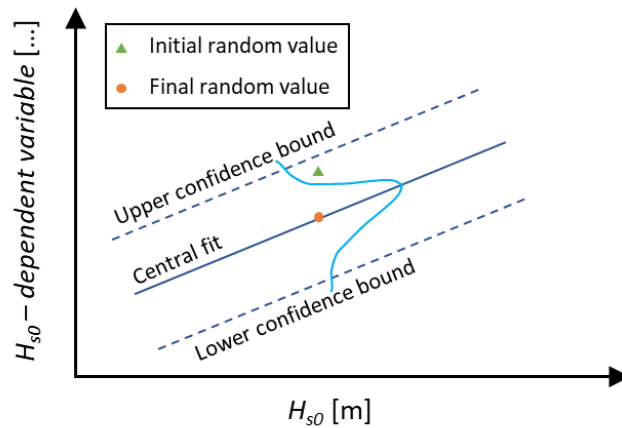
FIGURE 7.3 Sketch of the procedure for the generation of a random H_{s0}-dependent variable from the site specific empirical law.

6. the wave propagation is performed through numerical models or site specific empirical formulas in the case of mild slopes;

7. breaking criteria are applied to identify depth limited (Goda, 2009) or steepness limited (Miche, 1951) waves.

The above described procedure is employed for the generation of the sea storms during each simulated life cycle, thus obtaining a total of $n_{ss} \times N_r$ different sea storms.

The steps for the weather generation can be performed also for the projected future climate. The future period is analyzed using a moving time window of fixed length, as described in section 5.4. Then, the factor of change method is employed for the estimation of the parameters of the extreme value distribution of the deepwater significant wave height. In addition, for each time window, new coefficients

of the site-specific empirical relationships between H_{s0} and the other climate descriptors are estimated. Such an approach is valid under the hypothesis of formal maintenance of the relationships between the considered hydrodynamic variables. As regards the mean water depth, its future normal distribution is defined by adding the contribute of the projected SLR to the mean value. Finally, the wave propagation and breaking are solved using the same formulations employed for the present climate.

7.3 Probabilistic design of the upgraded Catania breakwater

7.3.1 Set-up of the Monte Carlo simulations

The probabilistic calculations described in section 7.2 have been performed for section n. 40 of the upgraded Catania harbor breakwater, i.e. the most section exposed to the wave motion (see Figure 6.15 and Figure 6.18), considering the simplified fault tree represented in Figure 7.4. For the ULS, the collapse of the armor layer has been analyzed, considering the case of addition of an extra armor layer over the existing one (i.e. configurations AS, AD, CM and CS). Instead, for the SLS, the excessive mean overtopping discharge has been studied, considering one of the upgrading options with simple heightening of the wave wall (i.e. configuration E) and one of the solutions with both rise of the wave wall and addition of extra armor unit (i.e. configuration CS). It is worth to point out that the two considered failure mechanisms are related to each other in terms of a series system.

Monte Carlo simulations have been performed for the assessment of the probability of collapse of the outer armor layer and of excessive overtopping during the Catania harbor breakwater lifetime, which has been fixed equal to 50 years according the indications of Puertos del Estado (2010). The number of life cycle to generate for each Monte Carlo simulation has been calculated through equation 7.3, considering $P_{f,Lmax}$ equal to 10^{-1} for both ULS and SLS (Puertos del Estado, 2010) and CV equal to 0.03, thus obtaining N_r equal to 10^4. The assessment of the probability to reach the selected limit states have been evaluated considering both the state of art formulas and the ones adapted to the experimental and numerical data on the upgraded Catania harbor breakwater, in order to compare the results and asses the effect of using specific design formulation.

For each considered limit state and for each correspondent reliability function, three Monte Carlo simulations with the above described characteristics have been performed, considering the following input hydrodynamic conditions:

- present climate derived from the RON measured wave data (APAT, 2004) and from the reanalysis ERA5 time series of storm surge (Hersbach et al., 2019) relative to the site of Catania for the period 1989-2005;
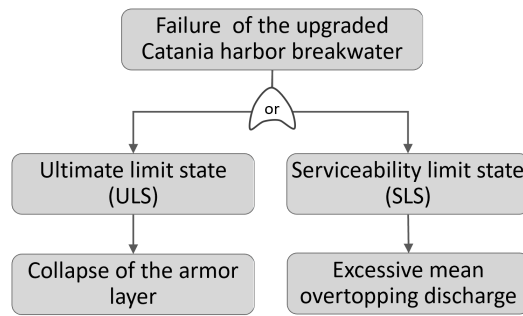
FIGURE 7.4 Fault tree for the upgraded Catania harbor breakwater.

- future climate derived from the ocean surface wave and sea level projections under RCP4.5 scenario provided by Copernicus Climate Change Service (2019) relative to the site of Catania for the period 2071-2100;

- future climate derived from the ocean surface wave and sea level projections under RCP8.5 scenario provided by Copernicus Climate Change Service (2019) relative to the site of Catania for the period 2041-2070.

It is worth to point out that the whole RON data-set covers the period 1989-2014. However, in the present study, only the years 1989-2005 have been considered, because the application of the factor of change method (see section 5.4) requires the comparison with the modeled present data provided by Copernicus Climate Change Service (2019), which covers the above mentioned years. As regards the time series of present storm surge, the reanalysis data have been preferred to the measured one for the sake of simplicity. Indeed, the total water level data-set provided by the Italian observational system should have been pre-processed to distinguish the contributions of astronomical tide and storm surge. Finally, it should be highlighted that the future projections of wave climate and sea level provided by Copernicus Climate Change Service (2019) represent the only freely-available data-set for the European coastal zones.

7.3.2 Generation of the hydrodynamic conditions

The input hydrodynamic conditions for the Monte Carlo simulations have been generated following the methodology described in section 7.2. For the present climate, a Weibull distribution has been adapted using the method of maximum likelihood estimation to the deep-water significant wave height data, whose extreme values have been identified through the application of the peak over thresholds (POT) method and the definition of sea storm proposed by Boccotti (2004). The goodness of fit of the selected probability distribution has been verified through the traditional Kolmogorov-Smirnov and Chi-square tests. Table 7.1 reports the calculated scale, shape and location parameters (respectively α_{sc}, κ_{sh} and ζ_{lc}) of the Weibull distribution, together with the mean number of sea storm per year(λ).

Since the mean number of sea storm per year is equal to about 13, according to equation 7.4, 650 random H_{s0} have been generated for each simulated life cycle, thus obtaining a total of 6.5×10^6 values. Figure 7.5 shows the simulated H_{s0}, together with measured data and the central fit with 95% confidence bounds of the adapted Weibull distribution.

The calculation of the significant wave height at the breakwater site (H_s) has been performed using the following empirical linear relationship, whose coefficient c_{Hs} has been estimated through the least square method, applied to the available data-set of deep-water and correspondent shallow water significant wave heights produced by the the numerical model SWAN (Booij et al., 1999) for the site of Catania:

$$H_s = c_{Hs} H_{s0} \qquad (7.5)$$

Table 7.2 reports the estimate and the 95% confidence bounds of c_{Hs}. The above-described simplified approach is justified by the very mild slope of the bathymetry of the site of interest, and also by the quite high depth at the toe of the structure (i.e. between -16.50 and -19.00 m under MSL, with 100-year return period dispersion parameter $k_d h$ between 0.50 and 0.60). In the case of sites characterized by steeper

TABLE 7.1 Statistical characterization of the deep-water significant wave height H_{s0}, performed using the data provided by RON for the period 1989-2005 for the site of Catania.

Variable	Distribution	α_{sc}	κ_{sh}	ζ_{lc}	λ
H_{s0}	Weibull	1.21	1.36	1.49	12.69
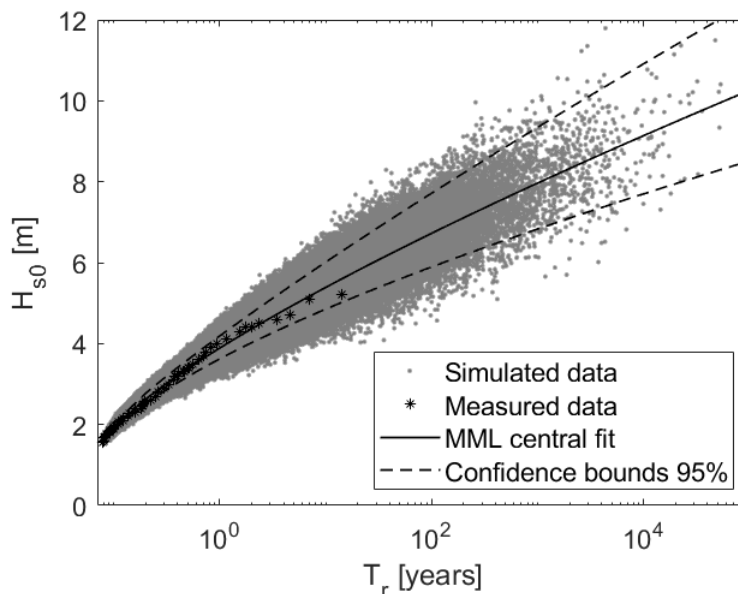
FIGURE 7.5 Central fit and 95% confidence bounds of the Weibull distribution adapted to the measured H_{s0} for the site of Catania (1989-2005). Both the measured and the 6.5×10^6 simulated H_{s0} are displayed.

TABLE 7.2 Estimate and 95% confidence bounds of the coefficient of the site specific empirical law employed for the propagation of the deep-water significant wave height towards the structure.

Coefficient	Estimate	95% CB_{lo}	95% CB_{up}
c_{Hs} [-]	0.7015	0.6865	0.7165
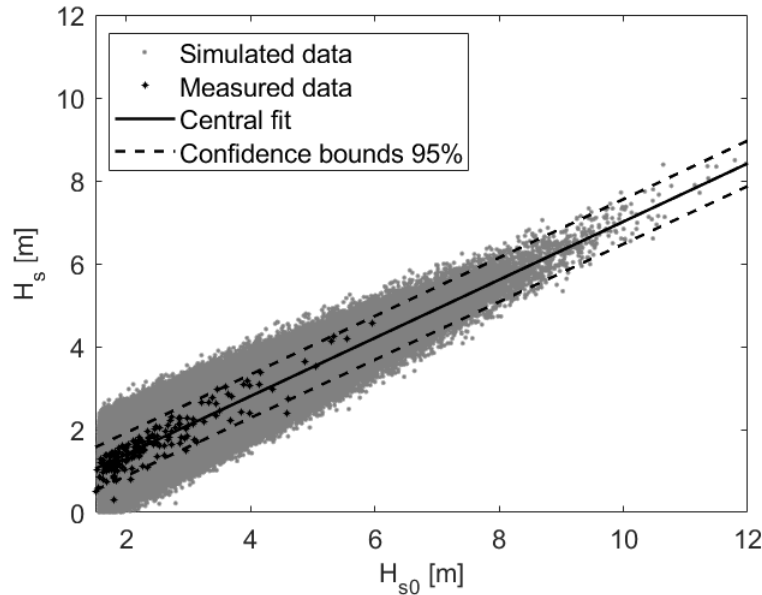
FIGURE 7.6 Central fit and 95% confidence bounds of the site specific empirical law for the wave height propagation. Both the measured and the 6.5×10^6 simulated H_s are displayed. The data refers to the present climate (1989-2005).

slope, more sophisticated approach based on the use of specific numerical models or artificial neural networks should be employed. Figure 7.6 shows the calculated H_s, together with measured data and the central fit with the 95% confidence bounds of the employed empirical relationship.

Once the random values of H_{s0} have been generated, the calculation of the correspondent values of the dependent hydrodynamic parameters has been performed. The deep-water peak and mean wave period (T_p and T_m respectively) have been calculated as functions of the deep-water significant wave height H_{s0}, by adapting the formula proposed by Boccotti (2004) to the site of Catania:

$$T_p = b_{Tp}\pi\sqrt{\frac{H_{s0}}{4g}} \tag{7.6}$$

$$T_m = b_{Tm}\pi\sqrt{\frac{H_{s0}}{4g}} \tag{7.7}$$

where b_{Tp} and b_{Tm} are empirical coefficients evaluated through the least square method. Table 7.3 reports the estimate and the 95% confidence bounds of b_{Tp} and b_{Tm} under present climate. For the site of Catania, whose bathymetry is characterized by

a contained slope, the elaboration of available results on wave propagation in the site of Catania from the numerical model SWAN (Booij et al., 1999) has showed that both the peak and mean wave period at the breakwater site can be assumed equal to the deep-water one. Figure 7.7 and Figure 7.8 respectively show the calculated T_p and T_m, together with measured data and the central fit with the 95% confidence bounds of the employed empirical relationships.

The sea storms duration (d_s) has been calculated using the following linear relationship between d_s and H_{s0}, which is similar to the one proposed by Laface and Arena (2016) for the equivalent exponential storm model (EES):

$$d_s = b_{ds} H_{s0} \tag{7.8}$$

where b_{ds} is an empirical coefficient dependent on the site characteristics which has been evaluated through the least square method. The estimate and the 95% confidence bounds of b_{ds} under present climate are reported in Table 7.3. Figure 7.9 shows the calculated d_s, together with measured data and the central fit with the

TABLE 7.3 Estimate and 95% confidence bounds of the coefficients of the site specific empirical laws employed for the calculation of the variables depending on H_{s0} under the present climate (1989-2005).

Coefficient	Estimate	95% CB_{lo}	95% CB_{up}
b_{Tp} [-]	10.5083	10.2848	10.7318
b_{Tm} [-]	8.6928	8.4910	8.8947
b_{ds} [h/m]	14.7976	13.3794	16.2157
b_{SS} [-]	0.0108	0.0064	0.0152
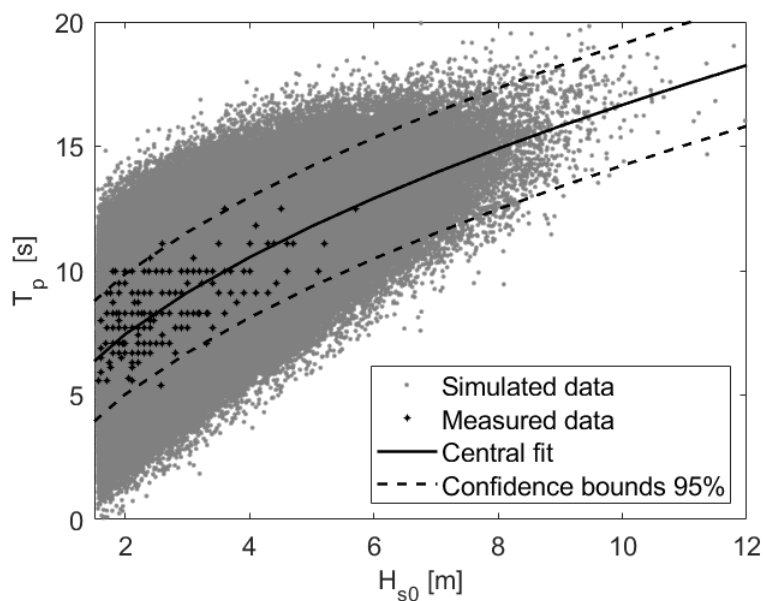
FIGURE 7.7 Central fit and 95% confidence bounds of the site specific empirical law which links the peak wave period to H_{s0}. Both the measured and the 6.5×10^6 simulated T_p are displayed. The data refers to the present climate (1989-2005).
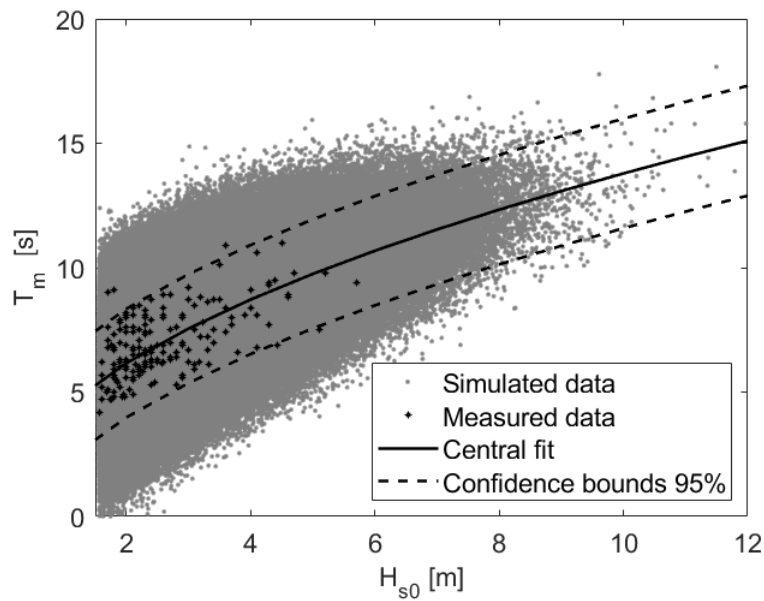
FIGURE 7.8 Central fit and 95% confidence bounds of the site specific empirical law which links the mean wave period to H_{s0}. Both the measured and the 6.5×10^6 simulated T_m are displayed. The data refers to the present climate (1989-2005).
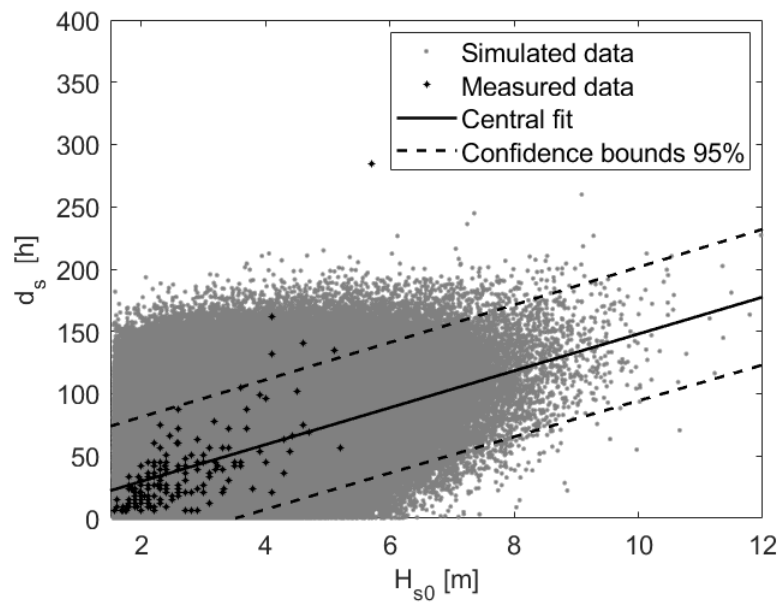
FIGURE 7.9 Central fit and 95% confidence bounds of the site specific empirical law which links the sea storm duration to H_{s0}. Both the measured and the 6.5×10^6 simulated d_s are displayed. The data refers to the present climate. The data refers to the present climate (1989-2005).

95% confidence bounds of the employed empirical relationship.

The storm surge height (h_{SS}) has been calculated using the following linear relationship between h_{SS} and H_{s0}, which is similar to the one proposed by Salmun et al. (2011):

$$h_{SS} = b_{SS} H_{s0} \qquad (7.9)$$

where b_{SS} is an empirical coefficient dependent on the site characteristics which has been evaluated through the least square method. The estimation and the 95% confidence bounds of b_{SS} under present climate are reported in Table 7.3. Figure 7.10 shows the calculated s_{SS}, together with measured data and the central fit with the 95% confidence bounds of the employed empirical relationship.

The mean water depth (h) has been assumed to follow a normal distribution. The mean has been fixed equal to the design water depth of section n. 40. The standard deviation has been calculated according to the simple rule that two standard deviations account for the difference between the maximum (minimum) and the mean value (Castillo et al., 2006), according to the following formula:

$$\sigma = \frac{(h + h_{at}) - (h - h_{at})}{4} \qquad (7.10)$$

where h_{at} is the astronomical tide, equal to about 0.20 m for the site of Catania. Table 7.4 reports the statistical characterization of mean water depth for section n. 40 of the Catania harbor breakwater under present climate.

The last step of the hydrodynamic conditions generation phase is the identification of possible breaking waves. In the present work, the breaking model proposed by Goda (2009) has been employed, in order to calculate the gradual evolution of the shape of the probability density function of the wave heights throughout the surf zone.
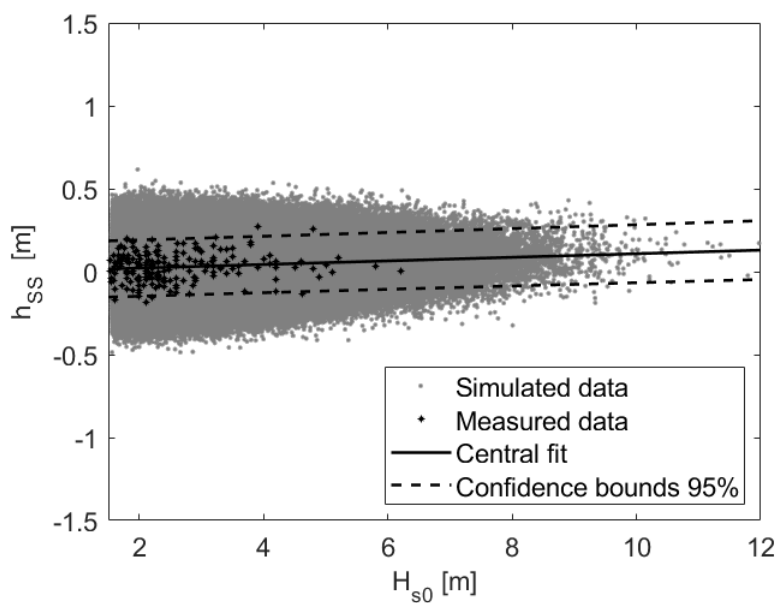
FIGURE 7.10 Central fit and 95% confidence bounds of the site specific empirical law which links the storm surge height to H_{s0}. Both the measured and the 6.5×10^6 simulated h_{SS} are displayed. The data refers to the present climate.

As regards the future hydrodynamic conditions, the periods 2071-2100 under RCP4.5 and 2041-2070 under RCP8.5 have been studied. For a certain variable, the factor of change method requires that the present measured and modeled time series cover the same period, which in the present case is 17 years long (i.e. 1989-2005). Then, the comparison between the statistics of the present and future time series must be carried out considering a moving time window whose length is the same of the control period, as described in section 7.2. For this reason, a 17-years moving window has been employed, thus identifying 14 sub-periods for each considered future scenario. For each sub-period, the generation of random sea storms and sea levels has been performed, following the same procedure employed for the present climate. The parameters of the future extreme value distributions of H_{s0} together with the mean number of sea storms per year have been derived from the present one, using the factor of change method (see section 5.4). Table 7.5 and Table 7.6 show the statistical characterization of the future deep-water significant wave height.

In general, the Weibull distributions of the future H_{s0} are characterized by higher values of α_{sc} and κ_{sh} than the present one, but by lower ζ_{lc}. The only exceptions are represented by the last three RCP8.5 windows: the twelfth window has lower α_{sc} and ζ_{lc}, and a higher κ_{sh}; the thirteenth and fourteenth windows have lower α_{sc} and κ_{sh}, and a higher ζ_{lc}. Figure 7.11 gives useful indications to qualitatively

TABLE 7.4 Statistical characterization of the present mean water depth for section n. 40 of the Catania harbor breakwater.

Variable	Distribution	Mean [m]	Standard deviation [m]
h	Normal	19.00	0.10

TABLE 7.5 Statistical characterization of the future deep-water significant wave height H_{s0} in the site of Catania under RCP4.5 using a 17-years moving window.

Variable	Distribution	Period	α_{sc}	κ_{sh}	ζ_{lc}	λ
		2071-2087	1.53	1.73	1.29	13.12
		2072-2088	1.59	1.78	1.27	12.90
		2073-2089	1.61	1.80	1.26	12.98
		2074-2090	1.40	1.70	1.35	12.33
		2075-2091	1.38	1.71	1.35	12.69
		2076-2092	1.37	1.69	1.35	12.33
		2077-2093	1.44	1.70	1.32	11.98
H_{s0}	Weibull	2078-2094	1.38	1.64	1.36	11.98
		2079-2095	1.42	1.69	1.34	12.33
		2080-2096	1.44	1.65	1.36	12.48
		2081-2097	1.38	1.60	1.38	12.83
		2082-2098	1.35	1.58	1.40	12.90
		2083-2099	1.29	1.53	1.43	12.48
		2084-2100	1.33	1.49	1.41	12.12

TABLE 7.6 Statistical characterization of the future deep-water significant wave height H_{s0} in the site of Catania under RCP8.5 using a 17-years moving window.

Variable	Distribution	Period	α_{sc}	κ_{sh}	ζ_{lc}	λ
H_{s0}	Weibull	2041-2057	1.29	1.84	1.43	13.12
		2042-2058	1.30	1.82	1.40	13.33
		2043-2059	1.24	1.76	1.41	13.83
		2044-2060	1.27	1.77	1.39	14.19
		2045-2061	1.22	1.73	1.41	13.97
		2046-2062	1.28	1.78	1.39	13.83
		2047-2063	1.32	1.80	1.36	13.90
		2048-2064	1.26	1.76	1.39	13.90
		2049-2065	1.26	1.78	1.39	13.55
		2050-2066	1.24	1.63	1.45	13.33
		2051-2067	1.27	1.64	1.43	12.98
		2052-2068	1.18	1.56	1.46	13.19
		2053-2069	1.13	1.34	1.52	13.47
		2054-2070	1.07	1.33	1.56	13.69
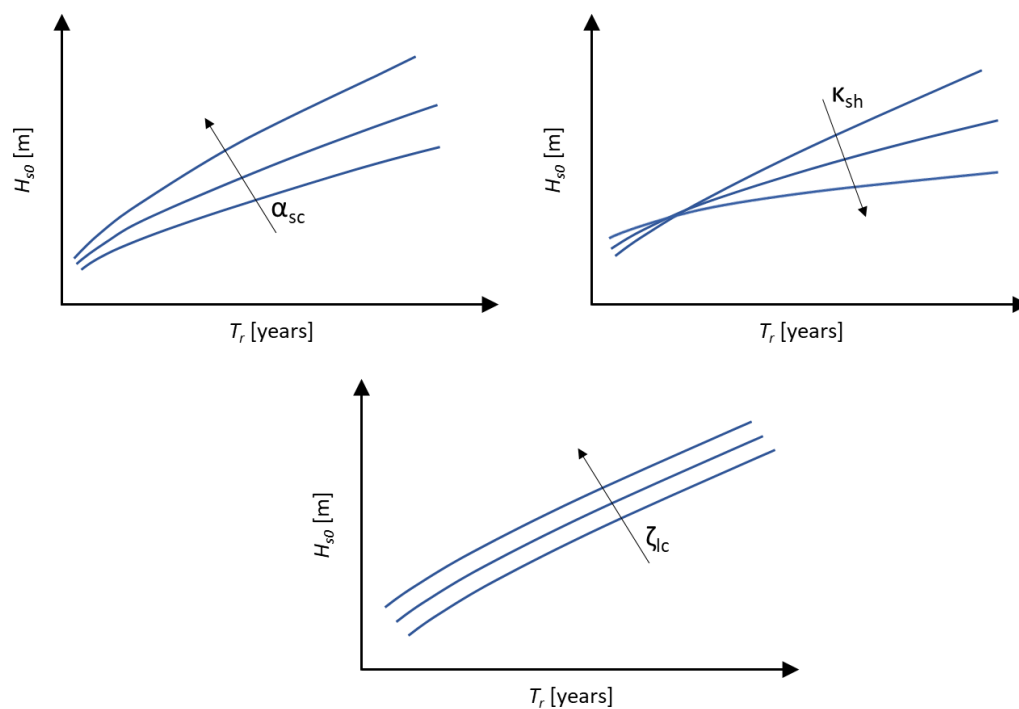
FIGURE 7.11 Effects of the variation of the Weibull scale, shape and location parameters (α_{sc}, κ_{sh} and ζ_{lc} respectively).

understand the effects of the variation of the Weibull parameters on the shape of the distribution: i) the increase of α_{sc} produces an upward rotation of the T_r-H_{s0} curve; ii) the increase of κ_{sh} produces a downward rotation of the T_r-H_{s0} curve; iii) the increase of ζ_{lc} produces an upward translation of the T_r-H_{s0} curve. In addition, considering a fixed return period, the effect of the variation of ζ_{lc} on the corresponding H_{s0} is independent from selected T_r. On the contrary, the effects of the variation of α_{sc}

and κ_{sh} on H_{s0} corresponding to a certain T_r are stronger for higher return periods. According to such indications and to the results of the numerical comparison of the calculated Weibull distributions, in general, the future Weibull of H_{s0} in the site of Catania is under the present one, because of the increase of both α_{sc} and κ_{sh}. The T_r-H_{s0} curve of the twelfth sub-period is also under the present one, because of the decrease of α_{sc} and ζ_{lc} and the increase of κ_{sh}. Finally, also for the thirteenth and fourteenth windows of RCP8.5, the T_r-H_{s0} curve is lower than the present Weibull, being the influence of the decreased α_{sc} greater than the one of the smaller κ_{sh} and the higher ζ_{lc}. Therefore, for all the considered future windows, H_{s0} lower than the present ones are expected. Such a result is in agreement with the results presented by Morim et al. (2019) and with the study of Lionello et al. (2008).

Since the rounded mean number of sea storm per year measured for the sub-periods ranges between 11÷14, according to equation 7.4 600÷700 random H_{s0} have

TABLE 7.7 Estimation and 95% confidence bounds of the coefficients of the site specific empirical laws employed for the calculation of T_p and T_m under the RCP4.5 scenario, evaluated using a 17-years moving window.

Coefficient	Period	Estimation	95% CB_{lo}	95% CB_{up}
b_{Tp} [-]	2071-2087	10.7884	10.5630	11.0139
	2072-2088	10.8049	10.5791	11.0306
	2073-2089	10.7520	10.5257	10.9783
	2074-2090	10.8602	10.6239	11.0966
	2075-2091	10.8521	10.6232	11.0810
	2076-2092	10.8266	10.5950	11.0582
	2077-2093	10.7805	10.5458	11.0153
	2078-2094	10.8096	10.5745	11.0448
	2079-2095	10.7781	10.5462	11.0100
	2080-2096	10.7440	10.5174	10.9707
	2081-2097	10.7704	10.5449	10.9960
	2082-2098	10.7160	10.4984	10.9337
	2083-2099	10.7067	10.4898	10.9236
	2084-2100	10.6421	10.4230	10.8613
b_{Tm} [-]	2071-2087	7.9564	7.8001	8.1127
	2072-2088	7.9785	7.8202	8.1368
	2073-2089	7.9301	7.7776	8.0826
	2074-2090	7.9968	7.8368	8.1569
	2075-2091	7.9817	7.8303	8.1332
	2076-2092	7.9762	7.8202	8.1321
	2077-2093	7.9672	7.8045	8.1298
	2078-2094	7.9550	7.7970	8.1130
	2079-2095	7.9372	7.7788	8.0957
	2080-2096	7.9059	7.7542	8.0576
	2081-2097	7.9018	7.7536	8.0500
	2082-2098	7.8854	7.7395	8.0314
	2083-2099	7.8454	7.7095	7.9813
	2084-2100	7.8312	7.6908	7.9716

been generated for each simulated life cycle, thus obtaining a total of $6.0 \div 7.0 \times 10^6$ values.

The wave propagation towards the breakwater site has been solved using the site-specific formula defined by equation 7.5 and Table 7.2, under the assumption of no future modification of the local bathimetry.

The calculation of the future T_p and T_m correspondent to the generated H_{s0} have been performed using equations 7.6 and 7.7, under the hypothesis of formal mainte-nance of the relationships between the considered hydrodynamic variables. More-over, assuming no modification of the local bathimetry, the peak and mean wave period at the breakwater site have been assumed equal to the deep-water one, as for the present climate. Table 7.7 and Table 7.8 report the results of the estimation of the coefficients of the site specific empirical formulations for each sub-part of the two considered future periods. The estimated future b_{Tp} are slightly higher than

TABLE 7.8 Estimation and 95% confidence bounds of the coefficients of the site specific em-pirical laws employed for the calculation of T_p and T_m under RCP8.5 scenario, evaluated using a 17-years moving window.

Coefficient	Period	Estimation	95% CB_{lo}	95% CB_{up}
b_{Tp} [-]	2041-2057	10.7922	10.5854	10.9990
	2042-2058	10.7410	10.5383	10.9437
	2043-2059	10.7326	10.5367	10.9285
	2044-2060	10.7187	10.5272	10.9103
	2045-2061	10.7293	10.5331	10.9256
	2046-2062	10.7047	10.5078	10.9015
	2047-2063	10.7132	10.5172	10.9092
	2048-2064	10.7364	10.5364	10.9364
	2049-2065	10.7714	10.5671	10.9758
	2050-2066	10.7177	10.5112	10.9242
	2051-2067	10.6967	10.4834	10.9101
	2052-2068	10.7711	10.5519	10.9904
	2053-2069	10.7790	10.5542	11.0038
	2054-2070	10.7834	10.5650	11.0018
b_{Tm} [-]	2041-2057	7.9576	7.8126	8.1027
	2042-2058	7.9065	7.7683	8.0446
	2043-2059	7.9220	7.7798	8.0642
	2044-2060	7.9171	7.7769	8.0574
	2045-2061	7.9108	7.7694	8.0522
	2046-2062	7.9029	7.7604	8.0454
	2047-2063	7.9190	7.7752	8.0629
	2048-2064	7.9524	7.8037	8.1012
	2049-2065	7.9457	7.7986	8.0929
	2050-2066	7.9089	7.7623	8.0555
	2051-2067	7.8871	7.7379	8.0363
	2052-2068	7.9176	7.7681	8.0672
	2053-2069	7.9151	7.7648	8.0653
	2054-2070	7.9260	7.7778	8.0741

the present one, by 0.02 times on average, thus determining higher future T_p for the same H_{s0}. Instead, the estimated future b_{Tm} are slightly lower than the present one, by 0.09 times on average, thus involving a reduction of the future T_m for the same H_{s0}.

As regards d_s and h_{SS}, equations 7.8 and 7.9 have been employed for the calculation of the correspondent values to the generated H_{s0}, under the hypothesis of formal maintenance of the relationships between the considered hydrodynamic variables. Table 7.9 and Table 7.10 show the results of the estimation of the coefficients of the site specific empirical formulations for each of the 14 sub-parts of the two considered future periods. The estimated future b_{ds} are lower then the present one, by 0.07 times on average, thus determining lower future d_s for the same H_{s0}. Also the estimated future b_{SS} are lower than the present one, by 1.09 times on average, thus involving a reduction of the future h_{SS} for the same H_{s0}.

TABLE 7.9 Estimate and 95% confidence bounds of the coefficients of the site specific empirical laws employed for the calculation of d_s and h_{SS} under RCP4.5, evaluated using a 17-years moving window.

Coefficient	Period	Estimate	95% CB_{lo}	95% CB_{up}
b_{ds} [h/m]	2071-2087	14.2861	13.1414	15.4309
	2072-2088	14.4704	13.3254	15.6154
	2073-2089	14.4812	13.3365	15.6258
	2074-2090	13.7357	12.6266	14.8448
	2075-2091	13.2858	12.2494	14.3221
	2076-2092	12.7650	11.7846	13.7453
	2077-2093	12.9244	11.9009	13.9479
	2078-2094	12.9517	11.8291	14.0742
	2079-2095	13.0763	11.9594	14.1932
	2080-2096	13.3915	12.2662	14.5168
	2081-2097	13.5551	12.4288	14.6813
	2082-2098	13.5392	12.4147	14.6637
	2083-2099	13.8623	12.6782	15.0464
	2084-2100	13.7989	12.6122	14.9856
b_{SS} [-]	2071-2087	-0.0055	-0.0113	0.0003
	2072-2088	-0.0049	-0.0106	0.0009
	2073-2089	-0.0049	-0.0109	0.0010
	2074-2090	-0.0044	-0.0105	0.0017
	2075-2091	-0.0025	-0.0085	0.0036
	2076-2092	0.0007	-0.0053	0.0066
	2077-2093	0.0012	-0.0048	0.0072
	2078-2094	0.0023	-0.0038	0.0084
	2079-2095	0.0049	-0.0012	0.0110
	2080-2096	0.0012	-0.0047	0.0070
	2081-2097	-0.0019	-0.0076	0.0039
	2082-2098	-0.0019	-0.0076	0.0038
	2083-2099	-0.0035	-0.0097	0.0026
	2084-2100	-0.0035	-0.0096	0.0025

TABLE 7.10 Estimate and 95% confidence bounds of the coefficients of the site specific empirical laws employed for the calculation of d_s and h_{SS} under RCP8.5, evaluated using a 17-years moving window.

Coefficient	Period	Estimate	95% CB_{lo}	95% CB_{up}
b_{ds} [h/m]	2041-2057	14.6464	13.3002	15.9927
	2042-2058	14.2424	12.9192	15.5655
	2043-2059	13.8703	12.5954	15.1453
	2044-2060	13.9752	12.7523	15.1982
	2045-2061	13.8709	12.6207	15.1211
	2046-2062	13.9759	12.7286	15.2232
	2047-2063	13.8809	12.6811	15.0806
	2048-2064	14.0413	12.8208	15.2619
	2049-2065	14.2032	12.9519	15.4544
	2050-2066	14.0662	12.8266	15.3057
	2051-2067	13.8186	12.5587	15.0785
	2052-2068	13.5947	12.3739	14.8154
	2053-2069	13.4416	12.2703	14.6129
	2054-2070	13.5356	12.3768	14.6943
b_{SS} [-]	2041-2057	0.0013	-0.0050	0.0076
	2042-2058	0.0014	-0.0049	0.0077
	2043-2059	0.0007	-0.0057	0.0070
	2044-2060	-0.0012	-0.0074	0.0051
	2045-2061	-0.0033	-0.0096	0.0031
	2046-2062	-0.0018	-0.0081	0.0045
	2047-2063	0.0003	-0.0057	0.0064
	2048-2064	0.0001	-0.0060	0.0063
	2049-2065	-0.0024	-0.0086	0.0038
	2050-2066	-0.0012	-0.0074	0.0049
	2051-2067	-0.0001	-0.0062	0.0060
	2052-2068	0.0007	-0.0053	0.0067
	2053-2069	0.0012	-0.0045	0.0069
	2054-2070	0.0001	-0.0057	0.0058

The future mean water depth at the breakwater site has been assumed normally distributed. The mean has been calculated by adding the projected SLR to the design water depth of section n. 40. The standard deviation has been calculated according to equation 7.10, considering that for the site of Catania the astronomical tide h_{at} is of about 0.20 m. Table 7.11 and Table 7.12 show the statistical characterization of mean water depth for section n. 40 of the Catania harbor breakwater under future climate.

Finally, the identification of possible breaking waves has been performed applying the breaking model proposed by Goda (2009).

TABLE 7.11 Statistical characterization of the future mean water depth for section n. 40 of the Catania harbor breakwater under RCP4.5 using a 17-years moving window.

Variable	Distribution	Period	Mean [m]	Standard deviation [m]
		2071-2087	19.36	0.10
		2072-2088	19.36	0.10
		2073-2089	19.37	0.10
		2074-2090	19.38	0.10
		2075-2091	19.38	0.10
		2076-2092	19.38	0.10
		2077-2093	19.39	0.10
h	Normal	2078-2094	19.39	0.10
		2079-2095	19.40	0.10
		2080-2096	19.40	0.10
		2081-2097	19.41	0.10
		2082-2098	19.41	0.10
		2083-2099	19.42	0.10
		2084-2100	19.42	0.10

TABLE 7.12 Statistical characterization of the future mean water depth for section n. 40 of the Catania harbor breakwater under RCP8.5 using a 17-years moving window.

Variable	Distribution	Period	Mean [m]	Standard deviation [m]
		2041-2057	19.24	0.10
		2042-2058	19.25	0.10
		2043-2059	19.26	0.10
		2044-2060	19.27	0.10
		2045-2061	19.27	0.10
		2046-2062	19.28	0.10
		2047-2063	19.29	0.10
h	Normal	2048-2064	19.29	0.10
		2049-2065	19.30	0.10
		2050-2066	19.31	0.10
		2051-2067	19.31	0.10
		2052-2068	19.32	0.10
		2053-2069	19.33	0.10
		2054-2070	19.31	0.10

7.3.3 Probabilistic assessment of the armor layer stability

Definition of the reliability function

The reliability function which describes the stability of the additional armor layer of the upgraded structure has been derived from the vdM formula (see equation 6.9), which can be rewritten in accordance with the format of equation 2.5:

TABLE 7.13 Statistical characterization of the coefficient f_c of the vdM formula, which describes the stability of the additional armor layer.

Variable	Version	Distribution	Mean	Standard deviation
f_c	experimental vdM		1.0000	0.1000
	experimental SS	Normal	1.7112	0.2870
	experimental NSS		1.3335	0.1931

$$Z = f_c \times \left(6.7 \frac{N_{od}^{0.4}}{N_w^{0.3}} + 1 \right) \times \Delta D_{n50} - H_s \times \left(\frac{2\pi H_s}{g T_m^2} \right)^{0.1} \qquad (7.11)$$

where f_c is an experimental factor, N_{od} is the damage parameter, N_w is the number of incident waves, Δ and D_{n50} are respectively the relative buoyant density and the median nominal diameter of the armor blocks, H_s is the incident significant wave height, T_m is the mean wave period and g is the gravity acceleration.

Table 7.13 shows the statistical characterization of the coefficient f_c, which is normally distributed. Besides the value of f_c originally proposed by van der Meer (1988c), the results of the experimental estimation performed for the two cases of sufficient (i.e. SS) and not sufficient support (i.e. NSS) at the toe of the additional armor layer of the Catania harbor breakwater are considered (see section 6.3.5).

The probability distributions described in Table 7.13 have been employed for the generation of one random value of the coefficient f_c for each of the 10^4 simulated life cycle, assuming that the structure behavior does not change during lifetime.

The damage parameter N_{od} have been considered as deterministically known and equal to 2.00, which is the damage limit correspondent to the selected ULS, i.e. the collapse of the outer armor layer (CIRIA et al., 2007).

Generation of the geometry and materials characteristics

The reliability function presented in equation 7.11 contains the following parameters related to the geometry and the materials of the structure: i) the relative buoyant density of the armor blocks (Δ); ii) median nominal diameter of the artificial armor units (D_{n50}).

The statistical characterization of Δ and D_{n50} has been performed based on existing literature, according to which such variables are normally distributed (Burcharth, 1992; van der Meer, 1988b). Table 7.14 shows the statistics of Δ and D_{n50} employed for the probabilistic design of the upgraded Catania harbor breakwater. The values of the standard deviations have been deduced from van der Meer (1988b).

The probability distributions described in Table 7.14 have been employed for the generation of one random value of Δ and D_{n50} for each of the 10^4 simulated life cycle, assuming that the structure composition and geometry do not change during the during lifetime.

TABLE 7.14 Statistical characterization of the relative buoyant density of the armor blocks (Δ) and the median nominal diameter of the artificial armor units (D_{n50}).

Variable	Distribution	Mean	Standard deviation
Δ [-]		1.2330	0.0500
D_{n50} Antifer [m]	Normal	2.3540	0.0300
D_{n50} Cube [m]		2.9980	0.0300

Evaluation of the probability of failure

Monte Carlo simulations have been performed for the evaluation of the probability that the upgraded Catania harbor breakwater reaches the ULS due to the collapse of the outer armor layer, considering the reliability function defined by equation 7.11, the previously defined geometry and materials characteristics and the hydrodynamic conditions presented in section 7.3.2. Then, the cumulative annual probability of failure has been calculated for the entire lifetime of the structure, considering the present climate and the future climate under RCP4.5 and RCP8.5 scenarios.

Figure 7.12 shows the results obtained using the present wave climate and sea level and the original (i.e. vdM) and adapted (i.e. SS and NSS) coefficients of the reliability function, in terms of cumulative annual probability of failure and 95% confidence bounds linked to the intrinsic uncertainty of the Monte Carlo simulation. Year 0 represents the end of the construction works, whereas year 50 is the end of the useful life of the structure. First, the evaluated probability of failure is always lower than the acceptance limit for the ULS equal 10^{-1} (Puertos del Estado, 2010), despite of the used formulation and the weight of the employed additional armor units. In this regard, it is worth to highlight that P_f evaluated for the upgrading solution which consists in the addition of 30 t Antifer blocks (see Figure 7.12a) is one order of magnitude greater than P_f calculated for the upgrading option which consists in the addition of 62 t cubic units (see Figure 7.12b), despite of the employed coefficients of the reliability function (i.e. vdM, SS or NSS). Therefore, as expected, the doubling of the weight of the extra armor blocks involves a significant reduction of the probability of collapse of the outer armor layer.

Furthermore, the use of the vdM or SS and NSS coefficients produces substantial differences between the resulting probabilities of failure. Indeed, the vdM formula is far more conservative than the adapted one, giving P_f greater by one order of magnitude, for both 30 t Antifer and 62 t cubic armor units. Such a result indicates that the use of the traditional vdM formula instead of the adapted one for the design of the additional armor layer of the Catania harbor breakwater would lead to a solution that errs on the side of safety. Therefore, in this case the lack of specific formulation does not imply the design of a not sufficiently stable structure, but at most excessive construction costs. Indeed, according to the the results of the adapted formulation (i.e. SS and NSS), lighter and hence less expensive armor blocks could be employed for the upgrade of the Catania harbor breakwater. Reasonably, the probability of
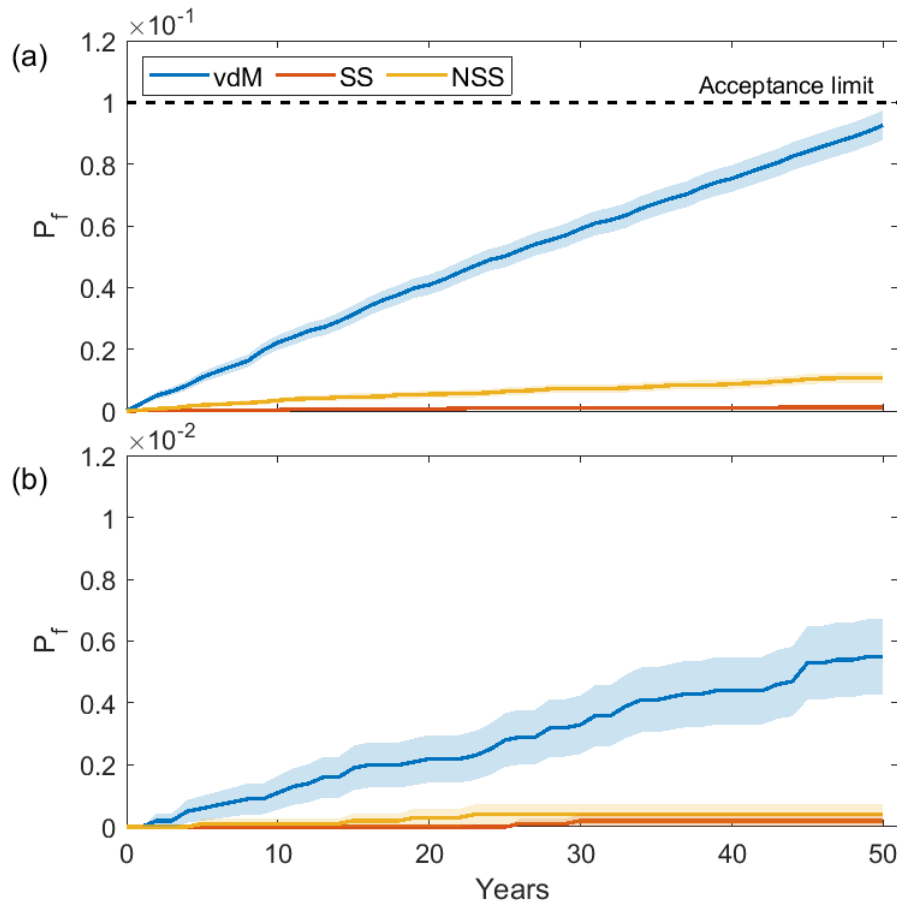
FIGURE 7.12 Cumulative annual probability of failure due to the collapse of the outer armor layer of the upgraded Catania harbor breakwater during its lifetime, evaluated using the present wave climate and sea level: (a) structure with additional Antifer blocks smaller than the existing cubes; (b) structure with additional cubic blocks equal to the existing ones. The shaded areas represent the 95% confidence bounds of the estimated P_f.

failure calculated for the case of presence of adequate support at the toe of the additional armor layer (i.e. SS) is always smaller than the one evaluated in the case of absence of such support (i.e. NSS), although the order of magnitude remains the same.

The cumulative annual probability of failure under RCP4.5 and RCP8.5 future scenarios has been calculated considering the vdM, SS and NSS coefficients for each 17-year moving window, respectively for the periods 2071-2100 and 2041-2070. Figure 7.13 and Figure 7.14 show the mean cumulative annual probability of failure, respectively under RCP4.5 and RCP8.5. The displayed 95% confidence bounds corresponds to the standard deviation of the samples of P_f calculated for the different time windows of the same scenario, thus allowing a visualization of the influence of the climate uncertainty in the results. The evaluated probability of failure is again always lower than the acceptance limit for the ULS equal 10^{-1} (Puertos del Estado, 2010), despite of the used formulation and the weight of the employed additional armor units. As already stated, P_f evaluated for the upgrading solution which consists in the addition of 30 t Antifer units (see Figure 7.13a and Figure 7.14a) is one order of
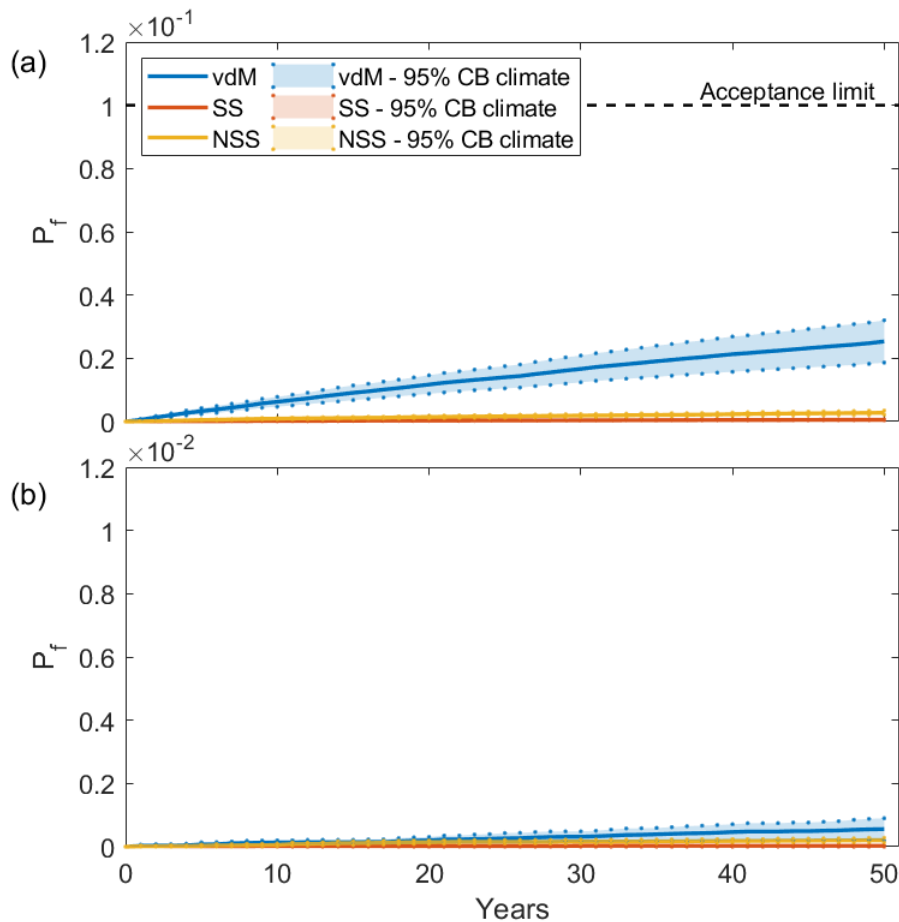
FIGURE 7.13 Mean cumulative annual probability of failure due to the collapse of the outer armor layer of the upgraded Catania harbor breakwater during its lifetime, evaluated using the RCP4.5 wave climate and sea level (2071-2100): (a) structure with additional Antifer blocks smaller than the existing cubes; (b) structure with additional cubic blocks equal to the existing ones. The shaded areas represent the 95% confidence bounds of the estimated P_f due to uncertainty of climate conditions.

magnitude greater than P_f calculated for the upgrading option which consists in the addition of 62 t cubes (see Figure 7.13b and Figure 7.14b), for all the considered formulations (i.e. vdM, SS and NSS). Moreover, the differences between the resulting P_f of the vdM, SS and NSS formulations that have been highlighted for the present climate, are obviously observed also for the future scenarios.

The comparison between the mean cumulative P_f under the two considered future scenarios shows that the highest probabilities of failure have been calculated for the end of the century (i.e. 2071-2100) under RCP4.5 scenario. However, the uncertainty of the results due to the climate conditions is higher for the mid of the century (i.e. 2041-2070) under RCP8.5 scenario, thus indicating that it is affected by a greater variability of the wave characteristics and sea levels than RCP4.5 scenario.

In order to assess the differences in terms of probability of failure between the present and the projected future, the most severe wave climate and sea level under RCP4.5 and RCP8.5 scenarios have been considered, which correspond to the periods 2084-2100 and 2053-2069 respectively. Figure 7.15 and Figure 7.16 show that
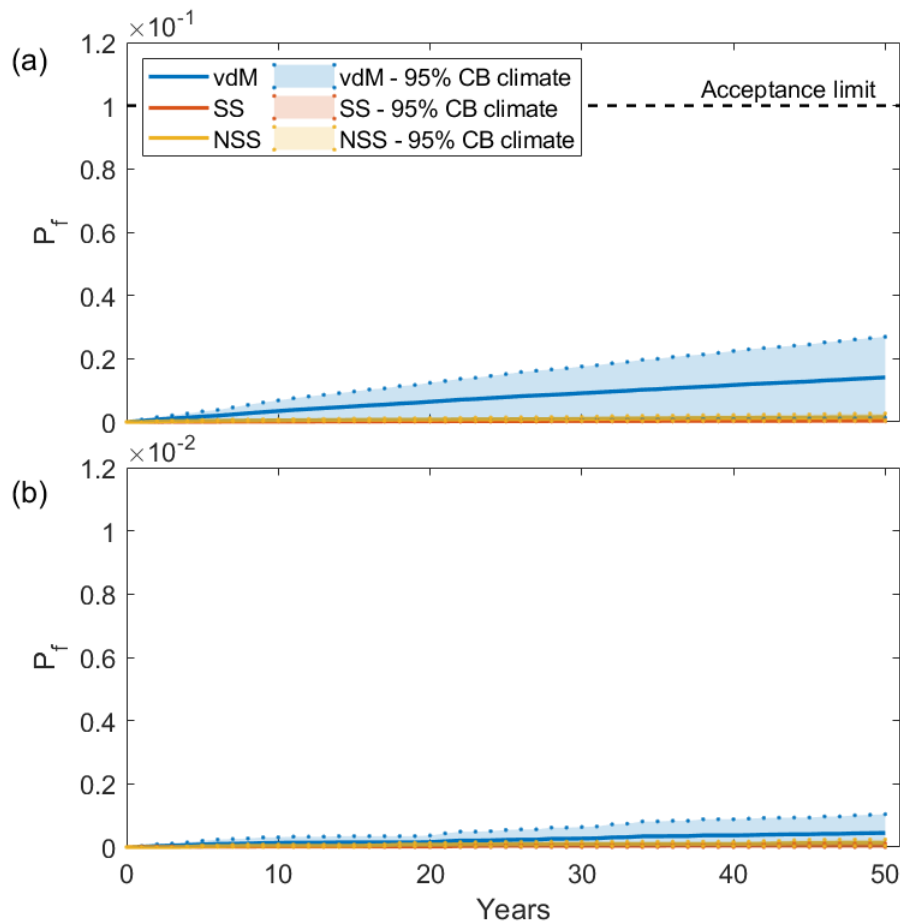
FIGURE 7.14 Mean cumulative annual probability of failure due to the collapse of the outer armor layer of the upgraded Catania harbor breakwater during its lifetime, evaluated using the RCP8.5 wave climate and sea level (2041-2070): (a) structure with additional Antifer blocks smaller than the existing cubes; (b) structure with additional cubic blocks equal to the existing ones. The shaded areas represent the 95% confidence bounds of the estimated P_f due to uncertainty of climate conditions.

the maximum future P_f is in general lower than the present one, despite of the considered scenario. Such a result is consistent with the outcomes presented in section 7.3.2, and in particular with the fact that lower H_s and d_s, which is directly proportional to H_s, are expected for the site of Catania. Indeed, the reliability function for the outer armor layer stability (see equation 7.11) increases as H_s and d_s decrease.

However, the differences between present and future probability of failure are quite contained. Indeed, the order of magnitude of P_f does not change between present and future, as showed in Figure 7.12, Figure 7.15 and Figure 7.16. Such an outcome can be deduced also from Table 7.15, which reports the probability of failure of the structure in a life cycle, considering the wave climate and sea levels of the periods 1989-2005 (i.e. present), 2084-2100 under RCP4.5 and 2053-2069 under RCP8.5. Also the rate of growth of the probability of failure, which is the slope of the curve years-P_f, maintains the same order of magnitude under the present and future climate, as showed in Table 7.16.

In conclusion, the probability of failure of the Catania harbor breakwater is not
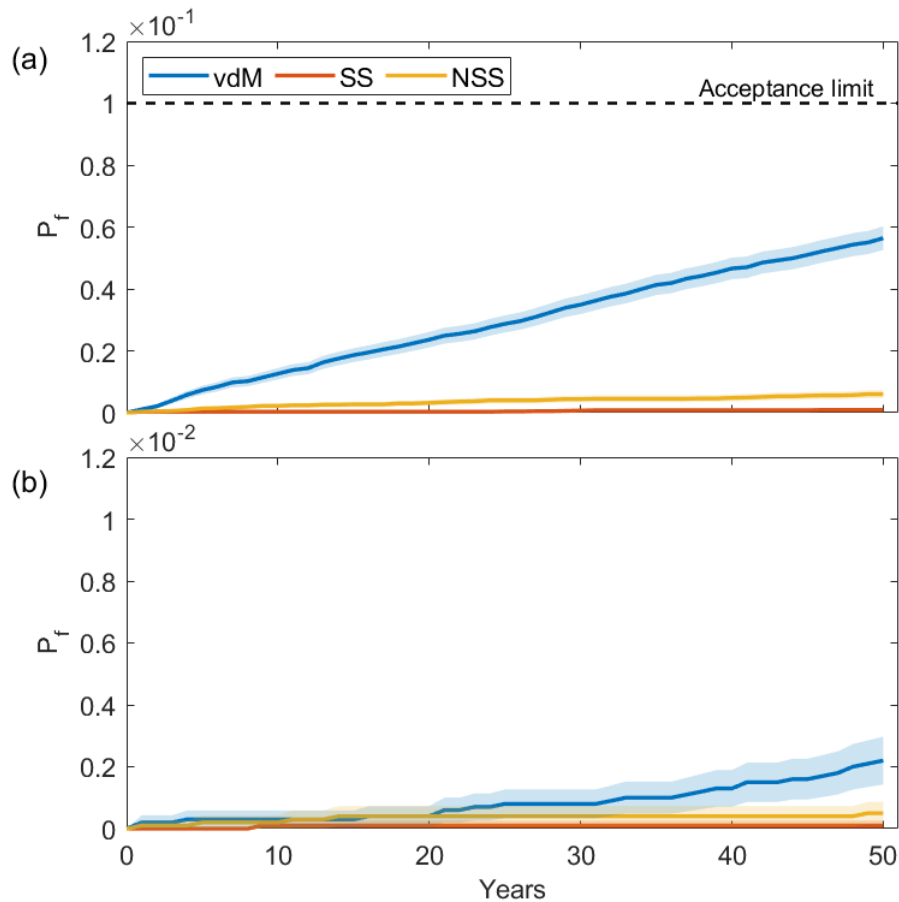
FIGURE 7.15 Cumulative annual probability of failure due to the collapse of the outer armor layer of the upgraded Catania harbor breakwater during its lifetime, evaluated using the most severe wave climate and sea levels under RCP4.5 scenario (2084-2100): (a) structure with additional Antifer blocks smaller than the existing cubes; (b) structure with additional cubic blocks equal to the existing ones. The shaded areas represent the 95% confidence bounds of the estimated P_f.

expected to increase because of the effects of climate change. However, the aging of the structure must be taken into account, and upgrade and maintenance interventions must be planned to ensure the same performances over time.
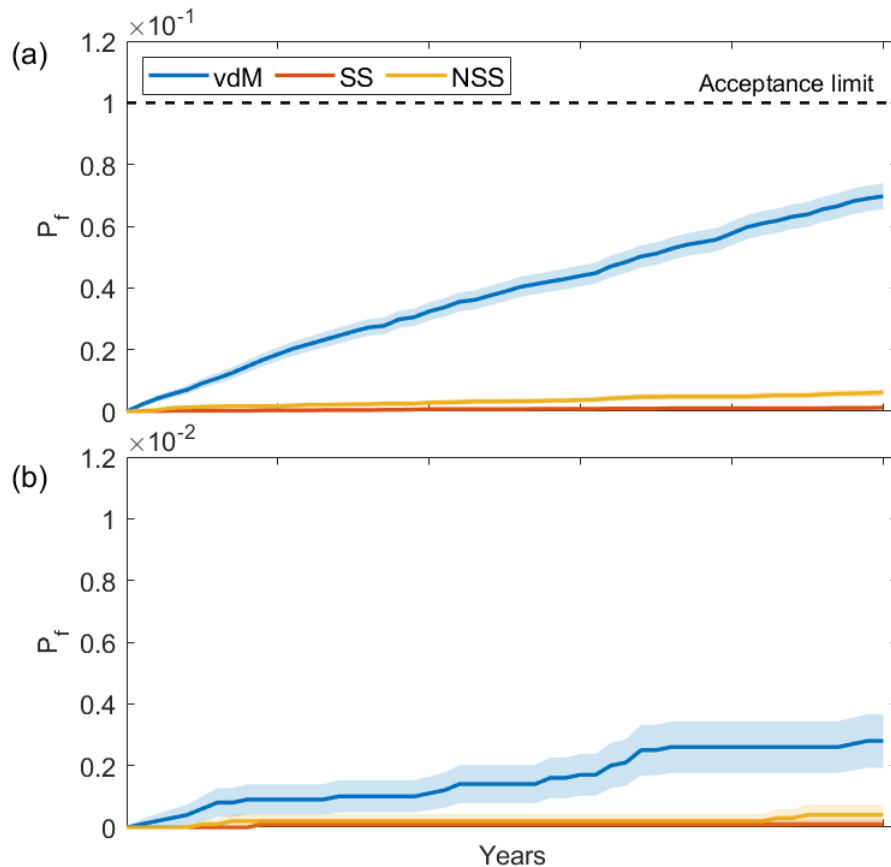
FIGURE 7.16 Cumulative annual probability of failure due to the collapse of the outer armor layer of the upgraded Catania harbor breakwater during its lifetime, evaluated using the most severe wave climate and sea levels under RCP8.5 scenario (2053-2069): (a) structure with additional Antifer blocks smaller than the existing cubes; (b) structure with additional cubic blocks equal to the existing ones. The shaded areas represent the 95% confidence bounds of the estimated P_f.

TABLE 7.15 Probability of failure due to the collapse of the outer armor layer of the upgraded Catania harbor breakwater during its lifetime.

Armor unit	Formula	$P_{f,L}$		
		Present (1989-2005)	RCP4.5 (2084-2100)	RCP8.5 (2053-2069)
Antifer	vdM	9.260×10^{-2}	5.640×10^{-2}	6.970×10^{-2}
	SS	1.200×10^{-3}	9.000×10^{-4}	1.200×10^{-3}
	NSS	1.080×10^{-2}	6.000×10^{-3}	6.100×10^{-3}
Cube	vdM	5.500×10^{-3}	2.200×10^{-3}	2.900×10^{-3}
	SS	2.000×10^{-4}	1.000×10^{-4}	1.000×10^{-4}
	NSS	4.000×10^{-4}	5.000×10^{-4}	4.000×10^{-4}

TABLE 7.16 Growth of probability of failure due to the collapse of the outer armor layer of the upgraded Catania harbor breakwater during its lifetime.

Armor unit	Formula	Growth of P_f [1/year]		
		Present (1989-2005)	RCP4.5 (2084-2100)	RCP8.5 (2053-2069)
Antifer	vdM	1.815×10^{-3}	1.116×10^{-3}	1.347×10^{-3}
	SS	2.227×10^{-5}	1.584×10^{-5}	2.194×10^{-5}
	NSS	1.995×10^{-4}	1.019×10^{-4}	1.058×10^{-4}
Cube	vdM	1.122×10^{-4}	3.673×10^{-5}	5.519×10^{-5}
	SS	5.926×10^{-6}	1.613×10^{-6}	1.613×10^{-6}
	NSS	9.028×10^{-6}	5.575×10^{-6}	5.032×10^{-6}

7.3.4 Probabilistic assessment of excessive mean overtopping discharge

Definition of the reliability function

The reliability function which describes the overtopping phenomenon for the upgraded structure has been derived from the the empirical formula proposed by EurOtop (2018) (see equation 6.11), which can be rewritten in accordance with the format of equation 2.5:

$$Z = q - \sqrt{gH_s^3} \times a_E \times exp\left[-\left(b_E \times \frac{R_c}{H_s \gamma_f}\right)^{1.3}\right] \qquad (7.12)$$

where q is the mean overtopping discharge per meter, g is the gravity acceleration, H_s is the incident significant wave height, R_c is the crest freeboard, a_E and b_E are empirical coefficients and γ_f is the roughness factor (0.47 for double layer of artificial cubes).

Table 7.17 shows the statistical characterization of the coefficients a_E and b_E, which are normally distributed. Besides the values of a_E and b_E originally proposed by EurOtop (2018), the results of the estimation performed on the basis of the numerical data acquired for configurations E and CS at laboratory scale of section n. 40 of the Catania harbor breakwater have been considered (see section 6.4.4).

The probability distributions described in Table 7.17 have been employed for the generation of one random value of the coefficient a_E and of the coefficient b_E for each

TABLE 7.17 Statistical characterization of the coefficients a_E and b_E of the formula proposed by EurOtop (2018), which describes the mean overtopping discharge.

Variable	Version	Distribution	Mean	Standard deviation
	experimental EurOtop (2018)		0.0900	0.0135
a_E	numerical E	Normal	0.3015	0.1433
	numerical CS		0.0616	0.0478
	experimental EurOtop (2018)		1.5000	0.0150
b_E	numerical E	Normal	1.4993	0.0990
	numerical CS		1.4980	0.1452

of the 10^4 simulated life cycle, assuming that the structure behavior does not change during lifetime.

The mean overtopping discharge per meter q have been considered as deterministically known and equal to 0.005 m^3/s per meter, which is the the acceptable mean overtopping discharge to ensure safety for larger yachts, according to EurOtop (2018).

Generation of the geometry and materials characteristics

The reliability function presented in equation 7.12 contains a single parameter related to the structure geometry, which is the height of the wave wall h_{wall} contained in R_c. Indeed, as showed in Figure 7.17, the crest freeboard is calculated as follows:

$$R_c = h_{wall} - (h + h_{SS}) \tag{7.13}$$

The height of the wave wall h_{wall} has been considered as a normally distributed variable, whose statistics are showed in Table 7.18. The mean of h_{wall} depends on the chosen configuration of the upgraded Catania harbor breakwater. Indeed, configuration CS presents a wave wall one meter higher than configuration E. As regards the standard deviation, it has been deduced from Lara et al. (2019).

The probability distributions described in Table 7.18 have been employed for the generation of one random value of h_{wall} and for each of the 10^4 simulated life cycle, assuming that the structure geometry does not change during lifetime.
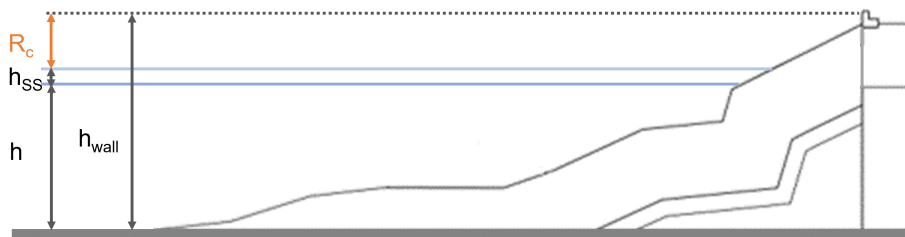
FIGURE 7.17 Sketch of the components for the calculation of the freeboard R_c.

TABLE 7.18 Statistical characterization of height of the wave wall (h_{wall}).

Variable	Distribution	Mean	Standard deviation
h_{wall} E [m]	Normal	27.5000	0.0300
h_{wall} CS [m]		28.5000	0.0300

Evaluation of the probability of failure

Monte Carlo simulations have been performed for the evaluation of the probability that the upgraded Catania harbor breakwater reaches the SLS due to excessive mean overtopping discharge, considering the reliability function defined by equation 7.12, the previously defined geometry and materials characteristics and the hydrodynamic conditions presented in section 7.3.2. Then, the cumulative annual probability of failure has been calculated for the entire lifetime of the structure, considering the present climate and the future climate under RCP4.5 and RCP8.5 scenarios.

Figure 7.18 shows the results obtained using the present wave climate and sea level and the coefficients of the reliability function proposed by EurOtop (2018) and evaluated from the numerical data-set generated for the upgraded Catania harbor breakwater. The cumulative annual probability of failure is displayed with the 95% confidence bounds linked to the intrinsic uncertainty of the Monte Carlo simulation. Year 0 represents the end of the construction works, whereas year 50 is the end of the useful life of the structure. The first result is that the evaluated probability of
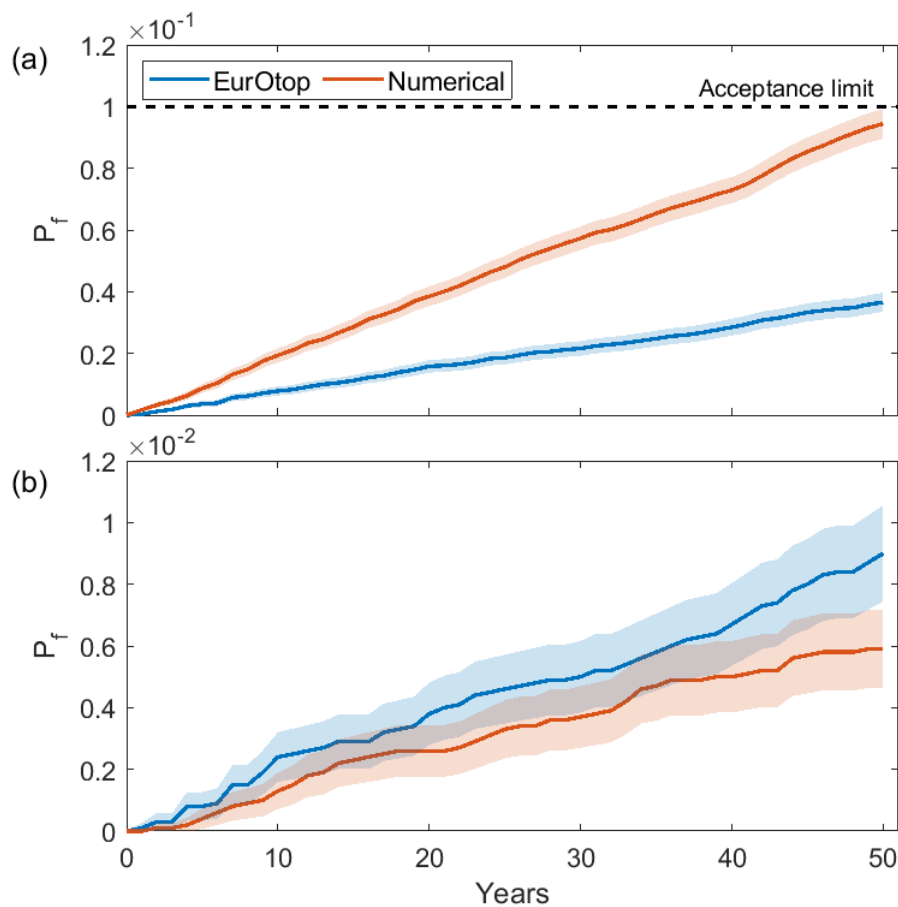
FIGURE 7.18 Cumulative annual probability of failure due to excessive overtopping for the upgraded Catania harbor breakwater during its lifetime, evaluated using the present wave climate and sea level: (a) configuration E; (b) configuration CS. The shaded areas represent the 95% confidence bounds of the estimated P_f.

failure is always lower than the acceptance limit for the SLS equal 10^{-1} (Puertos del Estado, 2010), despite of the used formulation and the considered upgrading solution. In this regard, it is worth to highlight that P_f evaluated for the upgrading solution which consists in the simple heightening of the wave wall up to +8.50 m above MSL (configuration E, see Figure 7.18a) is one order of magnitude greater than P_f calculated for the upgrading option which consists in the addition of 62 t cubic units over the regularized laying surface with the rising of the wave wall up to +9.50 m above MSL (configuration CS, see Figure 7.18b), despite of the employed coefficients of the reliability function. Therefore, as expected, the addition of extra units over the existing armor layer and the heightening of the wave wall involves a significant reduction of the probability of occurrence of excessive mean overtopping discharges.

Moreover, the use of the original formula proposed by EurOtop (2018) or of its adaptation to the numerical data produces evident differences between the resulting probabilities of failure. In particular, the empirical-numerical formula is more conservative for configuration E, giving P_f greater by 1.60 times than the traditional one.
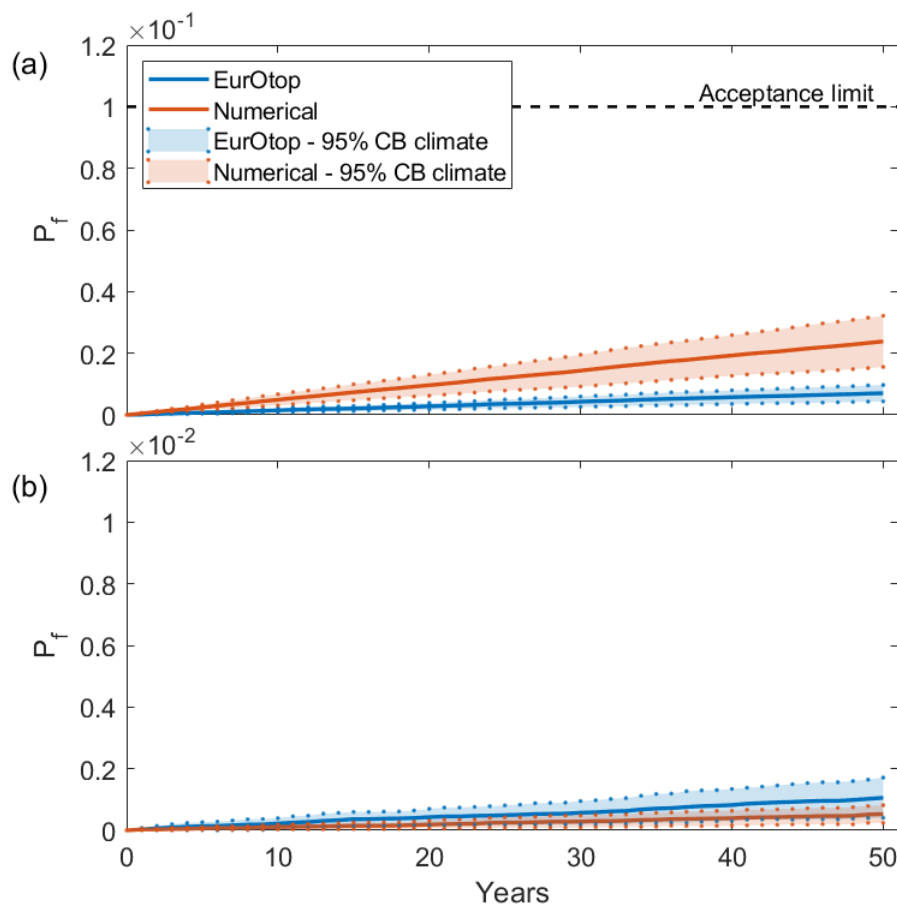
FIGURE 7.19 Mean cumulative annual probability of failure due to excessive overtopping for the upgraded Catania harbor breakwater during its lifetime, evaluated using the mean wave climate and sea level under RCP4.5 scenario (2071-2100): (a) configuration E; (b) configuration CS. The shaded areas represent the 95% confidence bounds of the estimated P_f due to uncertainty of climate conditions.

Such a result indicates that the use of the traditional formula proposed by EurOtop (2018) instead of the adapted one for the design of the simple rising of the wave wall of the Catania harbor breakwater would lead to a solution that does not err on the side of safety. Therefore, in this case the lack of specific formulation implies the design of a structure whose real hydraulic performances are lower than the expected ones, even if in the present case the fixed acceptance limit is not overcome. On the contrary, the empirical-numerical formula proposed by EurOtop (2018) is less conservative for configuration CS, giving P_f smaller by 0.34 times than the traditional one. Hence, in this case the lack of specific formulation does not imply the design of a not sufficiently performing structure, but at most excessive construction costs. It is worth to point out that the differences between the evaluated P_f through the traditional and adapted formula for mean overtopping discharge are modest with respect to the discrepancies observed between the evaluated P_f through the traditional and adapted formula for the outer armor layer stability (see section 7.3.3).

The cumulative annual probability of failure under RCP4.5 and RCP8.5 future
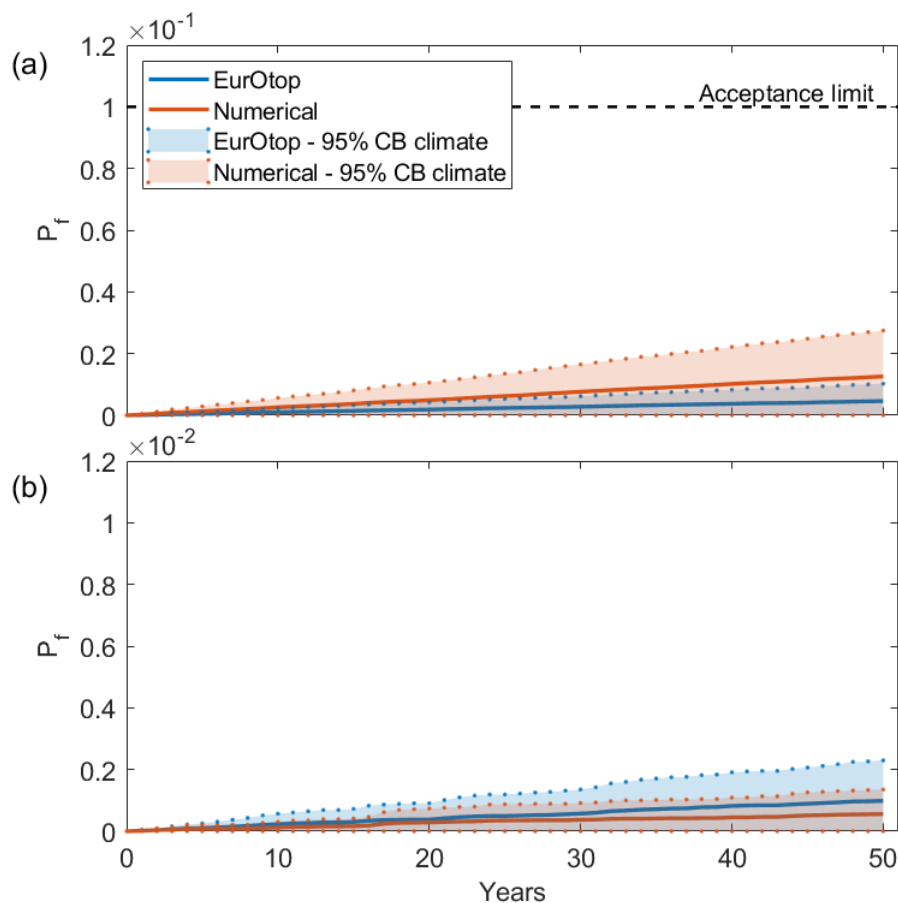
FIGURE 7.20 Mean cumulative annual probability of failure due to excessive overtopping for the upgraded Catania harbor breakwater during its lifetime, evaluated using the mean wave climate and sea level under RCP8.5 scenario (2041-2070): (a) configuration E; (b) configuration CS. The shaded areas represent the 95% confidence bounds of the estimated P_f due to uncertainty of climate conditions.

scenarios has been calculated considering the original formula proposed by EurO-top (2018) and the empirical-numerical one for each 17-year moving window, respectively for the periods 2071-2100 and 2041-2070. Figure 7.19 and Figure 7.20 show the mean cumulative annual probability of failure, respectively under RCP4.5 and RCP8.5. The displayed 95% confidence bounds corresponds to the standard deviation of the samples of P_f calculated for the different time windows of the same scenario, thus allowing a visualization of the influence of the climate uncertainty in the results. The evaluated probability of failure is again always lower than the acceptance limit for the SLS equal 10^{-1} (Puertos del Estado, 2010), despite of the used formulation and the considered upgrading solution. As already stated, P_f evaluated for configuration E (see Figure 7.19a and Figure 7.20a) is one order of magnitude greater than P_f calculated for configuration CS (see Figure 7.19b and Figure 7.20b), for both the considered formulations. In addition, the differences between the resulting P_f of the traditional formula proposed by EurOtop (2018) and of the adapted one that have been highlighted for the present climate, are obviously observed also for the future scenarios.
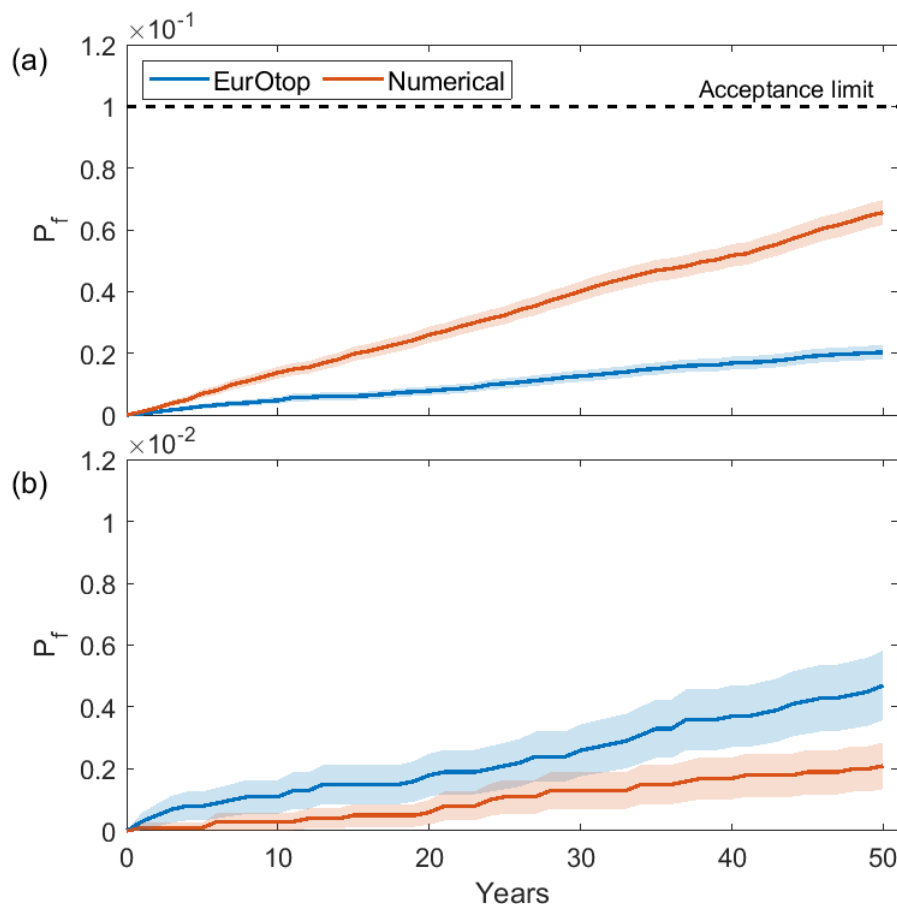
FIGURE 7.21 Cumulative annual probability of failure due to excessive overtopping for the upgraded Catania harbor breakwater during its lifetime, evaluated using the most severe wave climate and sea level under RCP4.5 scenario (2084-2100): (a) configuration E; (b) configuration CS. The shaded areas represent the 95% confidence bounds of the estimated P_f.

The result of the comparison between the mean cumulative P_f under the two considered future scenarios are in accordance with the findings of section 7.3.3 for the stability of the armor layer. Indeed, the highest probabilities of failure have been calculated for the end of the century (i.e. 2071-2100) under RCP4.5 scenario. Moreover, the uncertainty of the results due to the climate conditions is higher for the mid of the century (i.e. 2041-2070) under RCP8.5 scenario, thus indicating that it is affected by a greater variability of the wave characteristics and sea levels than RCP4.5 scenario.

The assessment of the differences in terms of probability of failure between the present and the projected future has been performed considering the most severe wave climate and sea levels under RCP4.5 and RCP8.5 scenarios, which correspond to the periods 2084-2100 and 2053-2069 respectively. Figure 7.21 and Figure 7.22 show that the maximum future P_f is in general lower than the present one, despite of the considered scenario. Such a result is consistent with the fact that slightly lower H_s and h_{SS}, which is directly proportional to H_s, are expected for the site of Catania (see section 7.3.2), but it may appear in contrast with the projected mean
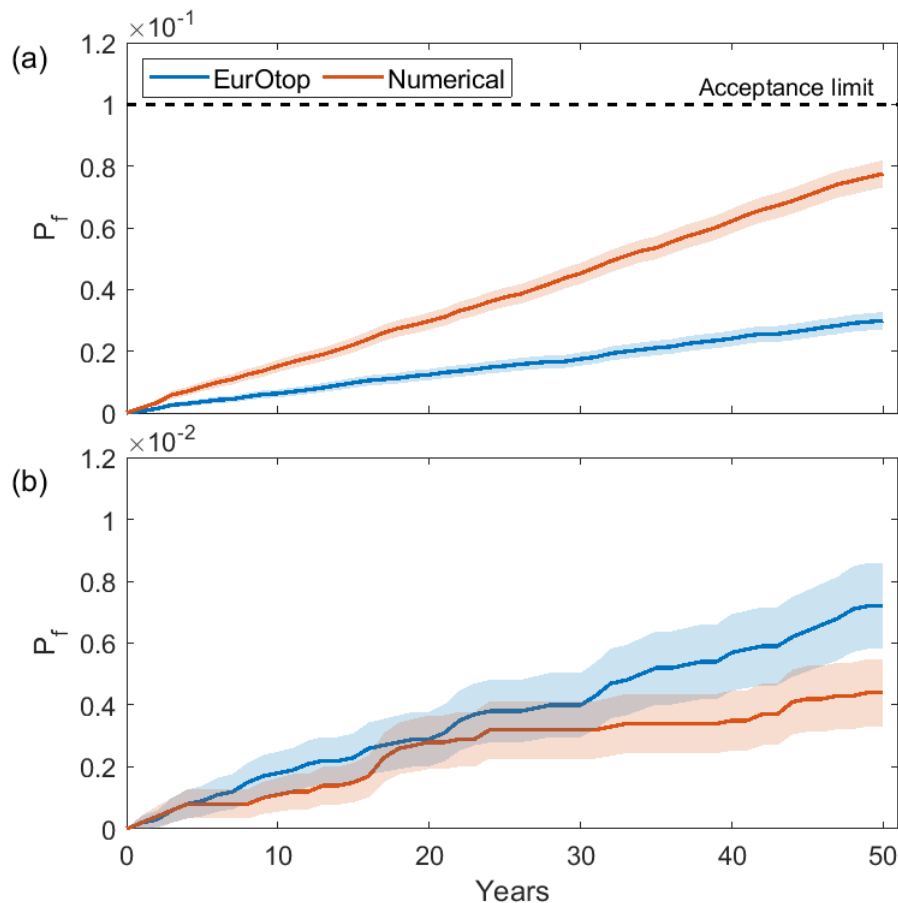
FIGURE 7.22 Cumulative annual probability of failure due to excessive overtopping for the upgraded Catania harbor breakwater during its lifetime, evaluated using the most severe wave climate and sea level under RCP8.5 scenario (2084-2100): (a) configuration E; (b) configuration CS. The shaded areas represent the 95% confidence bounds of the estimated P_f.
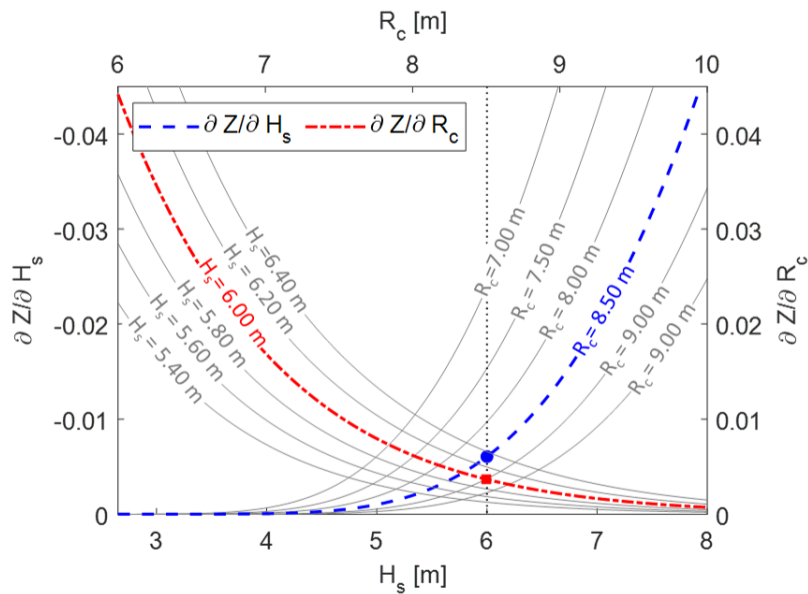
FIGURE 7.23 Comparison between the first-order partial derivatives of the reliability function Z for excessive overtopping discharge, evaluated considering a_E and b_E suggested by (EurOtop, 2018) and a set of H_s and R_c. The circle and the square indicate the first-order partial derivatives of Z in the case of $H_s = 6.00$ m and $R_c = 8.50$ m.

sea level rise of about $0.25 \div 0.40$ m. Therefore, a thorough analysis of the influence of each climate descriptor contained in the reliability function of mean overtopping discharge (see equation 7.12) has been performed. The first partial derivatives of Z with respect to H_s and R_c are used for the quantification of the rate of variation of Z induced by the increase or decrease of H_s and R_c. Figure 7.23 shows the comparison between the first partial derivatives of Z with respect to H_s and R_c, evaluated for a set of possible significant wave heights and structure freeboards. It can be observed that the first partial derivative of Z with respect to H_s is negative and higher, in absolute terms, than the positive first partial derivative of Z with respect to R_c, for each couple H_s-R_c. Therefore, the increase of Z due to decreasing H_s occurs at a greater rate than the decrease of Z due to decreasing R_c, and vice versa. In order to make clear such a finding, the case of H_s equal to 6.00 m and R_c equal to 8.50 m above MSL is highlighted in Figure 7.23. Following the above explanation, the fact that future P_f is lower than the present one is reasonable. Indeed, the reliability function Z suffers most the effect of slightly lower H_s than the influence of higher R_c caused by mean sea level rise.

Anyway, the differences between present and future probability of failure are modest. Indeed, the order of magnitude of P_f does not change between present and future, as showed in Figure 7.18, Figure 7.21 and Figure 7.22. The analysis of the probability of failure of the structure in a life cycle, considering the wave climate and sea levels of the periods 1989-2005 (i.e. present), 2084-2100 under RCP4.5 and 2053-2069 under RCP8.5, which are showed in Table 7.19, leads to the same result. Also the rate of growth of the probability of failure, which is the slope of the curve years-P_f, maintains the same order of magnitude under the present and future climate, as

TABLE 7.19 Probability of failure due to excessive overtopping for the upgraded Catania harbor breakwater during its lifetime.

Configuration	Formula	$P_{f,L}$		
		Present (1989-2005)	RCP4.5 (2084-2100)	RCP8.5 (2053-2069)
E	EurOtop	3.660×10^{-2}	2.030×10^{-2}	2.990×10^{-2}
	Numerical	9.440×10^{-2}	6.560×10^{-2}	7.750×10^{-2}
CS	EurOtop	9.000×10^{-3}	4.700×10^{-3}	7.200×10^{-3}
	Numerical	5.900×10^{-3}	2.100×10^{-3}	4.400×10^{-3}

TABLE 7.20 Growth of the probability of failure due to excessive overtopping for the upgraded Catania harbor breakwater during its lifetime.

Configuration	Formula	Growth of P_f [1/year]		
		Present (1989-2005)	RCP4.5 (2084-2100)	RCP8.5 (2053-2069)
E	EurOtop	7.190×10^{-4}	4.059×10^{-4}	5.875×10^{-4}
	Numerical	1.879×10^{-3}	1.306×10^{-3}	1.561×10^{-3}
CS	EurOtop	1.684×10^{-4}	8.485×10^{-5}	1.365×10^{-4}
	Numerical	1.247×10^{-4}	4.437×10^{-5}	8.232×10^{-5}

showed in Table 7.20.

As observed for the stability of the outer armor layer (see section 7.3.3), the probability of failure of the Catania harbor breakwater due to excessive overtopping is not expected to increase because of the effects of climate change. However, upgrade and maintenance interventions must be planned to withstand aging of the structure and the consequent loss of functionality.

Chapter 8

Conclusions

The maintenance and upgrade of aging harbor breakwaters is a global problem, to be taken into account when developing long-term strategies for the sustainable development of ports under the effects of climate change. Despite of the need to upgrade existing harbor breakwaters, and in particular rubble mound structures, there is a lack of systematic research on the behavior of upgraded structures. Specific design formulas and models have not been defined, and the possibility to use existing formulations for newly built structures has not been tested. Moreover, a methodology able to consider the uncertainties due to the lack of information about existing structures, to the stochastic nature of the external forcing and to the effects of climate change has not been proposed yet.

In this context, the present work aims to give a contribution to the development of a methodology for the design of upgrading solutions for harbor rubble mound harbor breakwaters, which could deal with the above mentioned uncertainties. The following specific objectives have been pursued: i) contributing to the development of a methodology for the assessment of the actual state of deterioration of harbor rubble mound breakwaters; ii) providing a general framework of the variation of the past and future sea conditions due to climate change along the Italian coasts; iii) acquiring experimental and numerical data on the behavior of upgraded rubble mound structures and develop interpretative models and design tools; iv) defining a detailed procedure for the evaluation of the probability of failure of upgraded structure, also considering the effects of climate change.

The methods developed for the achievements of the above mentioned objectives have been applied to the emblematic case study of the Catania harbor breakwater. Such an infrastructure appears severely damaged by past sea storms and it is no more able to ensure a sufficient protection to the harbor basin. Therefore, the upgrade of the the Catania harbor breakwater is necessary for the development of the port potentialities.

Assessment of the current state of rubble mound breakwaters

A novel easy-to-use methodology for the evaluation of the modifications suffered by existing breakwaters during lifetime has been defined, which is based on the quantification of armor layer evolution by measuring erosion and deposition as "shoreline" movements and armor slope modification. To this aim, georeferenced field data (i.e. orthophotos and UAV-recovered 3D point clouds) have been used here.

The assessment of the current state of the Catania harbor breakwater has allowed to observe that during the period 2000-2020 the structure was subjected to a reshaping process, which in some cross sections implied the removal of the 62 t armor blocks. In particular, at present the structure shows an averaged reduction of the mean armor layer slope of about 28%, with respect to the design subsequent to the failure occurred in 1933 (Takahashi, 2002). The analysis has showed also the existence of different damage modes along the structure. Such outcomes highlight the importance of considering the peculiarities of each segment of the breakwater during the design of the upgrading solution, to ensure homogeneous performances in terms of stability and overtopping along the entire structure.

It should be noted that if periodic UAV surveys are planned, the proposed technique for the assessment of the current state of rubble mound breakwaters could be employed to monitor the time evolution of the structure, which is useful for planning maintenance interventions. Such a monitoring technique could be further improved when bathymetric LIDAR technologies (Irish and White, 1998) for both emerged and submerged surveys will become more affordable.

Long-term variation of hydrodynamic conditions in the Italian seas

The design of both new and upgraded harbor defense structures needs information regarding sea level and wave climate of the site of interest. Moreover, the effects of climate change should be considered, since the typical useful lifetime of harbor breakwaters is long enough to experience them. In the present work, an overall framework of the occurred and expected modifications of the wave climate and sea level in the Italian Seas has been presented, by means of the review of existing literature and the analysis of historical and projected time series.

As regards sea level, trend analysis of tidal gauge data has showed that SLR in the range 0.030÷0.278 cm/year has interested most of the Italian coastal sites during the past century (Cazenave et al., 2002; Vecchio et al., 2019). The results of future climate projections are affected by several uncertainties (Morim et al., 2018). However, a general increase of sea level is expected in the Italian Seas, of at least 20.0 cm by 2100 for the less severe scenario (Lambeck et al., 2011; Galassi and Spada, 2014; Vecchio et al., 2019).

The long-term trend analysis of the annual mean and extreme wave climate in the Italian Seas has been carried out, considering eight representative sites belonging to the homogeneous climatic marine macro-regions 1M and 2M defined by CMCC

(2017). The preliminary analysis between the measured RON data (APAT, 2004) and the modelled NOAA (Tolman, 2009) and ERA5 (Hersbach et al., 2019) ones, in terms of single events and detected trends for the overlapping period 1990-2000, has demonstrated that both NOAA and ERA5 data-sets seems able to satisfactorily reproduce the past Italian wave climate. Such a result justify the use of the longer modeled time series for the long-term trend analysis. In particular, the ERA5 data-set has been selected because of the longer covered time period, which spans from 1979 to 2019 (i.e 41 years).

The results of the long-term trend analysis highlight the absence of a clear coherent behavior of all the wave climate descriptors within the same macro-region (i.e. 1M or 2M). The only exceptions are represented by the annual mean significant wave height and peak wave period. The first shows a general increasing trend with values in the range between +0.01%/year and +0.15%/year with respect to the mean value for all the eight studied sites, although with different statistical significance, which is in accordance with the outcomes of Caloiero et al. (2019) for the Calabrian coastal zone and Pomaro et al. (2017) for the Adriatic Sea. Instead, the annual mean peak wave period is characterized by a significant positive tendency between +0.04%/year and +0.09%/year with respect to the mean value for all the considered sites, which is in agreement with the results of Caloiero et al. (2019) for the Calabrian coastal zone.

For each studied site, a strong positive correlation between the long-term trends of the annual mean values of significant wave height, wave power, wave storm duration and storm power index has been detected. Moreover, the long-term trends of annual wave storm frequency are logically inversely proportional to the long-term trend of the annual mean and 99th percentile of interarrival time of wave storms. Finally, a positive correlation between the long-term trends of significant wave height and wave power has been found. As regards the correspondence between the long-term trends of analogue annual mean and 99th percentile of wave climate parameters, it turned out that to an increasing trend of the annual mean value of a certain wave descriptor does not necessarily correspond a similar tendency for the extreme one and vice versa, in accordance with the findings of Pomaro et al. (2017)

The analysis of the Italian future wave climate has been also carried out, considering the projections under the scenarios RCP4.5 and RCP8.5 (2041-2100), and the correspondent modeled present (1989-2005) time series of wave climate descriptors produced by Copernicus Climate Change Service (2019), in combination with the measured RON data. The same eight representative sites of the Italian coastal region selected for the long-term trend analysis have been studied. The characterization of future wave climate has been performed through the application of the factor of change method (Kilsby et al., 2007; Fatichi et al., 2011; Peres and Cancelliere, 2018). Such a method enables to improve the reliability of the analysis on future wave climate, reducing the effects of the sources of uncertainty that typically affect future climate projections. The outcomes of the application of the factor of change method

are used for the calculation of the expected future probability distributions of wave climate descriptors (e.g. extreme significant wave height) through the method of moments estimation (MME), to be employed as input for the probabilistic assessment of the performances of harbor breakwaters.

In the present work, the expected future modifications of the wave climate in the Italian Seas have been analyzed through the calculation of the factors of change of the mean, the standard deviation and the skewness of the following extreme wave parameters: the maximum significant wave height of sea storms, the duration of wave storms, the peak and mean wave period correspondent to the maximum significant wave height of sea storms. First, the adequacy of the data-set provided by Copernicus Climate Change Service (2019) has been verified through the comparison between the mean, standard deviation and skewness of the modeled and measured present time series considering the overlapping 17-years long period 1989-2005, which appear quite similar for all the studied coastal sites. Then, a moving time window of 17 years has been employed to draw the temporal variation of the factors of change during the future period 2041-2100, considering RCP4.5 and RCP8.5 scenarios. The results found for all the considered sites show that the projected variation of the statistics of the extreme Italian wave climate mainly refers to changes in the skewness (i.e. the symmetry) of the considered wave climate descriptors, both positive and negative, which could imply changes in the frequency of extreme events.

Composite modeling of upgraded rubble mound breakwaters

In the absence of specific formulas and data on upgraded rubble mound structures, the composite modeling appears as the most appropriate tool for the investigation on the behavior of upgrading options, which can be carried out combining the advantages of physical and numerical modeling (Oumeraci, 1999; Guanche et al., 2015; Di Lauro et al., 2019; Kamphuis, 2020). The acquired experimental and numerical data can be compared with state of art design formulas to verify their validity for upgraded breakwaters and, if necessary, new specific formulations can be defined. In the present work, the case study of the Catania harbor breakwater has been selected to obtain an experimental and numerical data-set on upgraded rubble mound structures.

First, a systematic experimental campaign has been carried out, considering two representative sections of the Catania harbor breakwater and six different upgrading solutions, which consisted in the rise of the wave wall with or without addition of extra armor units equal or smaller than the existing ones. The aim of the experimental investigation was to acquire useful information to deal with the following issues regarding the design of upgrading solutions: i) the choice of the height of the wave wall, which is linked to the needed overtopping reduction; ii) the choice of the size and shape of the additional armor units, which depends on the possible failure mechanisms which had interested the structure and on its deterioration state;

iii) the possible necessity to regularize the existing armor layer before adding the extra units, in order to ensure their the homogeneous and regular placement; iv) the need for an adequate support at the toe of the additional armor units, which can be guaranteed by a toe berm or the proper reshaping of the existing structure.

A total of 192 two-dimensional experiments have been performed at the Laboratory of Hydraulics of the University of Catania. For each configuration, increasing wave load have been simulated, through the generation of sea states of 4500 waves, divided into three equal intervals. In addition, the effects of mean sea level rise have been investigated, considering the configurations with the simple heightening of the wave wall.

The experimental data on incident and reflected wave motion show that the formulation of Zanuttigh and van der Meer (2008) for the calculation of the reflection coefficient describes quite well behavior of the upgraded structure, despite of a general tendency to slightly overestimate the experimental values. Such modest discrepancies may be due to the fact that the formula has been calibrated for a newly built breakwaters, with a regular armor layer slope and a standard layering, and hence porosity of the structure.

As regards the damage dynamics, it has been found that the number of incident waves seems to cause a significant increase of the damage level only for N_{od} greater than 2.0, which corresponds to the failure threshold suggested by CIRIA et al. (2007). In any case, the maximum increase of N_{od} caused by tripling the number of the incident waves ranges between 10÷20%. Since the damage progression after the failure of the structure has little practical interest in the design process, further analysis have been carried out considering the cumulative damage produced at the end of each sea state.

Due to the lack of state of art damage progression models for upgraded rubble mound breakwaters, the formula proposed by van der Meer (1988c) for double layers of cubes laid on a slope of 1:1.5 with a notional permeability equal to 0.4 (hereinafter vdM formula) has been compared with the experimental results. Concerning the configurations with the simple rising of the wave wall, the results show that the existing armor layer is more stable than the prediction of the vdM formula, probably thanks to the settlement of the existing armor blocks caused by the action of past sea storms. In addition, the differences between the final damage levels reached by the two tested sections demonstrate the lack of geometric and structural uniformity along the Catania harbor breakwater, in accordance with the findings of the assessment of the current state based on field data. As regards the SLR, its influence on damage dynamics of the existing armor layer appears negligible. Concerning the upgrading options that consist in rising the wave wall and adding an extra armor layer over the existing one, two different responses of the structure have been identified, in the case of presence or absence of a sufficient support at the toe of the additional units (SS and NSS, respectively). As already discussed, such a support is not always ensured by the toe berm, thus requiring the regularization of the existing

structure. Indeed, only the configuration that involves the reshaping of the existing armor layer before adding the extra blocks presents a homogeneous response for both tested sections. The experimental values of N_{od} measured for the SS configurations are 3÷7 times lower than the NSS ones. The two groups of data have been compared with the vdM formula, which significantly overestimates the experimental damage, probably because of the non-conventionality of the tested configurations, and to some extent because of scale effects. The vdM formula has been adapted to experimental data on the upgraded Catania harbor breakwater, by means of the evaluation of a multiplicative empirical factor separately estimated for the SS and NSS configurations. The obtained specific damage formulas are useful for the probabilistic evaluation of the stability performances of the upgraded Catania harbor breakwater.

More detailed analysis of the damage dynamics of the additional armor layer have been carried out, using the 3D point clouds of the tested structure recovered at the beginning and at the end of each sea state through the Structure from Motion (SfM) technique. The damage maps, which have been elaborated for each studied configuration, show that the displacement of the armor units mainly regards the submerged zone of the armor layer, in the vicinity of the free surface, despite of the considered configuration. Moreover, the importance of an adequate support at the toe of the armor layer is further highlighted, confirming the necessity to regularize the existing armor layer if the simple toe berm is not sufficient.

Further analysis on damage dynamics have been conducted using a novel technique based on the characterization of the micro and macro-roughness of the armor layer surface, which represent the blocks laying surface and the armor layer porosity respectively. The armor layer macro-roughness has been described by the ratio between its maximum wave height HD and its mean wavelength λ_M, both evaluated referring to the ensemble average of the y-profiles of the surface (i.e. parallel to the wave direction). The analysis of the variation of such a parameter at the end of each $j - th$ sea state with respect to the zero-damage condition as a function of the stability number is useful for the quantification of the modifications of the armor slope irregularities under increasing wave load, thus allowing the identification of those sea states that caused the greatest reshaping of the armor layer, which in some cases produces the increase of the structure stability. For the tested configurations, it was found that the greatest deviation from the zero-damage condition usually occurs during the initial shakedown. The lack of geometric and structural uniformity along the breakwater is confirmed. In addition, the SS configurations present variation of HD/λ_M during shakedown always smaller than the less stable NSS structures. The armor layer micro-roughness has been described by the ratio between the mean spectral wavelength of the micro-roughness λ_m and the median nominal diameter of the armor units D_{n50}. The analysis of the variation of such a parameter with respect to the zero-damage condition is useful for the investigation of the way in which the

armor layer damage quantified by traditional parameters (e.g. N_{od}) physically develops during increasing wave loads. For the studied configurations, four different structural response to the wave load have been distinguished, depending on the pattern of variation with respect to the zero-damage condition of λ_m/D_{n50} as a function of N_{od}: i) static equilibrium; ii) dynamic equilibrium; iii) bulk displacement; iv) differential displacement. It should be noted that the same configuration may experience more than one behavior during the whole damage process.

The possibility to apply the technique for the evaluation of the armor layer surface roughness at prototype scale has been successfully verified. In particular, the micro-roughness of the emerged part of the Catania harbor breakwater has been calculated, using the 3D point cloud recovered from the UAV survey performed in February 2020, and then compared with the experimental data on configurations E and EM. The good agreement between the model and prototype λ_m/D_{n50} demonstrates that the novel SfM-based technique for the analysis armor layer roughness can be employed at both laboratory and prototype scale, thus representing a useful tool for the validation of physical models of existing structures. Moreover, the armor layer roughness descriptors could be employed for the evaluation and monitoring of the state of degradation of existing rubble mound breakwaters.

The upgrading solutions for the Catania harbor breakwater have been studied also in terms of mean overtopping discharge. The experimental data are in good agreement with the predictions of the EurOtop (2018) formula for the configurations with the existing armor layer and with additional cubes equal to the existing ones, but not for the less usual configurations with additional units smaller than the existing ones. Indeed, the reciprocal interaction between the existing armor units and the smaller new ones may produce additional dissipation processes, and hence lower overtopping discharges with respect to the theoretical values. As regards the effects of climate change, the experimental results show that sea level rise causes significant increase of the mean overstepping discharge, also by $7 \div 9$ times. Finally, the comparative analysis of the performances of the six upgrading solutions demonstrates that all the configurations with additional armor layer guarantee reduction of the mean overtopping discharge not lower than 30% with respect to configuration with the simple heightening of the wave wall, regardless of the type of blocks employed and of the geometry and position of the cross section. Therefore, the structural behavior of the upgrading solutions should be considered as the main factor for the selection of the most adequate additional armor layer.

Further investigations on the hydraulic performances of the upgraded Catania harbor breakwater have been carried out through the numerical model IH2VOF, which has been extensively validated for the study of wave–structure interaction in conventional and non-conventional coastal structure typologies (Lara et al., 2008; Guanche et al., 2009; Di Lauro et al., 2019).

The most exposed section of the Catania harbor breakwater has been studied considering two different upgrading solutions: i) heightening of the wave wall; ii)

heightening of the wave wall and addition of extra armor units equal to the existing ones after the regularization of the laying surface. The set-up of the numerical model has been performed on the basis of the results of 91 preliminary simulations. In particular, a numerical channel 4.50 m wide and 0.65 m high has been selected, and meshed with a grid 0.020 m (H) $\times$ 0.010 m (V), which is able to ensure a good simulation of the wave conditions with reasonable calculation times. The adequacy of the selected grid in reproducing the wave overtopping phenomenon has been demonstrated during the calibration of the porosity parameters of the various layers of the breakwater. In particular, α_F and c_F have been set respectively equal to 200 and 0.34 for all the porous media. Instead, n_V and β_F have been calibrated through the comparison of the experimental reflection coefficients and mean overtopping discharge with the ones resulting from numerical simulations, which have been run considering different combinations of such parameters. The following n_V and β_F have been selected for the different layers of the structure: i) n_V=0.32 and β_F=1.20 for the core; ii) n_V=0.35 and β_F=2.00 for the filter; iii) n_V=0.30 and β_F=1.50 for the existing armor layer; iv) n_V=0.25 and β_F=5.00 for the additional armor layer; v) n_V=0.35 and β_F=3.00 for berm the toe of the additional armor layer.

The calibrated model have been scaled-up, in order to compare the mean overtopping discharge at model and prototype scale. The full scale simulations have been performed inside a numerical channel which is exactly 70 times the laboratory scale one. As regards the porosity parameters, the same values have been employed for both model and real scale. Five different sea states of 1500 waves have been simulated. The results have showed that there is a fair agreement between model and full scale data for non-dimensional mean overtopping discharge (q^*) greater than 10^{-4}. The greater differences that characterize the lower q^* is due to the higher uncertainty of the numerical model in reproducing small overtopping rates, which are strongly influenced by the characteristics of individual waves. In any case, the differences between laboratory and prototype scale mean overtopping discharges are quite contained.

The analysis of the numerical results has demonstrated that the properly calibrated IH2VOF model is a good prediction tool for mean overtopping discharge, able to simulate new hydrodynamic conditions and modifications to the structure geometry in a economically and technical effective way, at both model and prototype scale. Therefore, the numerical model of the Catania harbor breakwater has been employed for the definition of site-specific empirical-numerical formulas for the considered upgrading solutions, based on the analysis of the output mean overtopping discharge of 60 simulations at model scale and 60 simulations at prototype scale. In particular, for each considered upgrading option, six realizations of five different sea state have been performed, using different seedings for the random generation of series of 1500 waves. The analysis of the overtopping phenomenon produced by different realizations of the same sea states has allowed to take into

account the wave-wave interaction effect, the effects of wave sequence and the effects of the ratio H_{max}/H_s, which is significant for low overtopping events. The site-specific empirical-numerical formulas have been evaluated by adaptation of the formula proposed by EurOtop (2018) to the numerical data, at both prototype and model scale. The analysis of the empirical-numerical coefficients highlighted that they are very similar to the one proposed by EurOtop (2018). Moreover, slight differences between the model and prototype scale formulas are observed. The empirical-numerical formulas defined for the upgraded Catania harbor breakwater are useful for the probabilistic assessment of the probability of reaching the SLS due to excessive mean overtopping discharge.

Probabilistic assessment of the performances of upgraded structures

The proposed probabilistic assessment of the performances of upgrading solutions for harbor rubble mound breakwaters during their lifetime is based on the results of the previous phases of evaluation of the current state of the existing structure, analysis of the long-term variation of local sea level and wave climate, and composite modeling of the considered upgrading options.

First, the possible failure modes of the structure are identified for the construction of a fault tree, considering ULS and SLS. The acceptable probability of reaching a certain ULS or SLS is set on the basis of the indications of guidelines and codes. For each failure mode, the correspondent reliability function is defined, on the basis of state of art or site-specific equations. Such a function, which contains empirical coefficients and variables describing the external load, the structure geometry and materials, assumes negative values if the failure occurs. A Monte Carlo simulation is run, with a sufficient number of realizations (i.e. life cycles of the structures), selected on the basis of the acceptable probability of failure. For each simulated life cycle, a certain number of random mean water depth and wave storms is generated, based on the probability density functions of mean sea level and extreme significant wave height, whose influence on mean and peak wave period, wave storm duration and storm surge is modeled through site-specific empirical relationships. The wave propagation is performed through numerical models or site specific empirical formulas, and the wave breaking is checked using common breaking criteria. Moreover, for each life cycle random values of the empirical coefficients of the reliability function and of the variables describing the structure geometry and materials are drawn. Finally, the probability of failure during lifetime associated to the considered failure mode is calculated as the ratio between the number of life cycles with at least one failure and total number of realizations, and compared with the acceptance limit.

The probabilistic assessment of the upgraded Catania harbor breakwater has been performed, considering two failure modes related in a series system: i) collapse of the outer armor layer (ULS); ii) excessive mean overtopping discharge (SLS). The acceptable probability of failure during lifetime has been set equal to 0.1 for

both ULS and SLS, according to the suggestions of Puertos del Estado (2010). For each failure mode, Monte Carlo simulations have been run, using reliability functions based on both state of art design formulas and site-specific equations derived from the outcomes of the composite modeling. Furthermore, random sea levels and storms have been generated considering three scenarios: i) present climate (1989-2005), from RON measured wave data (APAT, 2004) and ERA5 reanalysis storm surge data (Hersbach et al., 2019); ii) future wave climate and sea level under RCP4.5 (2071-2100) provided by Copernicus Climate Change Service (2019) ; iii) future wave climate and sea level under RCP8.5 (2041-2070) provided by Copernicus Climate Change Service (2019). As regards the future climate, the factor of change method has been employed for the calculation of the probability density function of extreme wave height, referred to a moving time window 17 years long. For each Monte Carlo simulations, $6.0 \div 7.0 \times 10^6$ realizations have been generated, on the basis of the mean annual number of sea storm characteristic of the considered period.

The results of the Monte Carlo simulations showed that the acceptable probability of failure is never overcome for the considered ULS and SLS, despite of the employed reliability function and the considered climate scenario. Moreover, two generally valid outcomes have been found: i) in some cases, the use of state of art equations not calibrated for the considered upgrading solution could produce a design that does not err in the side of safety; ii) even if climate change does not necessarily imply the increase of external loading, existing harbor breakwaters need maintenance interventions to ensure the design performances during the whole lifetime.

Final remarks

The present work proposes a methodology for the design of upgrading solutions for harbor rubble mound breakwaters, which is able to take into account the current state of existing structure, the effects of climate change on coastal areas and the peculiarities of upgraded structure, using a probabilistic approach. The application of the proposed methodology to the case study of the Catania harbor breakwater provides some general findings concerning the behavior of upgraded structures, with reference to configurations with heightened wave wall and additional armor blocks having shape similar to the existing ones and weight equal or smaller. In addition, the importance of using specific design formulations for upgraded structures have been highlighted. Finally, it has been found that the need for maintaining and upgrading existing harbor rubble mound breakwater is independent from the effects of climate change on coastal areas.

Further research is needed to perform a deeper investigation on the influence of the state of deterioration and of the component materials of the existing structure on the response of the upgrading solutions. Moreover, the experimental and numerical study of the performances of upgrading options which consists in the addition of armor blocks completely different from the existing ones should be carried out,

in order to establish more general and easy-to-use formulations for the design of upgraded structures, which would reduce the time and economic costs due to the physical modeling phase. Finally, it is worth to point out that the proposed methodology for the probabilistic assessment of the performances of upgrading solutions could be further improved to include the operational limit state (OLS) into the probabilistic calculations, which must be considered for a complete assessment of the harbor breakwater performances. In addition, besides the collapse of the armor layer and the excessive mean overtopping discharge, other failure modes should be investigated, such as berm and toe erosion, slip failure, breakage or sliding of the wave wall, excessive maximum overtopping volume, considering both physical interactions and the presence of common parameters in the correspondent limit state equations.

Bibliography

Allsop, N. W. H., McKenna, J. E., Vicinanza, D., and Whittaker, T. T. J. (1997). "New design methods for wave impact loadings on vertical breakwaters and seawalls". In: *Coastal Engineering 1996*, pp. 2508–2521.

Andrade, J. M. and Estévez-Pérez, M. G. (2014). "Statistical comparison of the slopes of two regression lines: A tutorial". In: *Analytica chimica acta* 838, pp. 1–12.

APAT (2004). *Italian Wave Atlas*. APAT.

Arkhipkin, V. S., Gippius, F. N., Koltermann, K. P., and Surkova, G. V. (2014). "Wind waves in the Black Sea: results of a hindcast study". In: *Natural Hazards and Earth System Sciences* 14.11, p. 2883.

Arns, A, Dangendorf, S, Jensen, J, Talke, S, Bender, J, and Pattiaratchi, C (2017). "Sea-level rise induced amplification of coastal protection design heights". In: *Scientific reports* 7, p. 40171.

Bender, M. A., Knutson, T. R., Tuleya, R. E., Sirutis, J. J., Vecchi, G. A., Garner, S., and Held, I. M. (2010). "Modeled impact of anthropogenic warming on the frequency of intense Atlantic hurricanes". In: *Science* 327.5964, pp. 454–458.

Blateyron, F (2014). "Good practices for the use of areal filters". In: *Proc. 3rd Seminar on Surface Metrology of the Americas*, pp. 1–12.

Boccotti, P (2004). *Idraulica marittima*. UTET Università. ISBN: 9788877508744.

Booij, N. R. R. C., Ris, R. C., and Holthuijsen, L. H. (1999). "A third-generation wave model for coastal regions: 1. Model description and validation". In: *Journal of geophysical research: Oceans* 104.C4, pp. 7649–7666.

British Standards Institution (BSI) (1991). *Maritime structures—Part 7: Guide to the design and construction of breakwaters. Law BS 6349. Vol. 6349*.

Broderick, L. L. and Ahrens, J. P. (1982). *Riprap Stability Scale Effects.* Tech. rep. Coastal Engineering Research Center, Fort Belvoir Va.

Bromirski, P. D., Cayan, D. R., Helly, J, and Wittmann, P (2013). "Wave power variability and trends across the North Pacific". In: *Journal of Geophysical Research: Oceans* 118.12, pp. 6329–6348.

Burcharth, H. F. (1987). "The lessons from recent breakwater failures". In: *Developments in breakwater design, Invited Speech Presented at World Federation of Engineering Organizations Technical Congress, Vancouver*.

Burcharth, H. F. (1992). "Introduction of partial coefficients in the design of rubble mound breakwaters". In: *Coastal structures and breakwaters*. Thomas Telford, pp. 543–566.

Burcharth, H. F. (1993a). "Reliability evaluation and probabilistic design of coastal structures". In: *International Seminar on Hydro-Technical Engineering for Futute Development of Ports and Harbors*. Un'yusho- Ko-wan Gijutsu Kenkyu-jo.

Burcharth, H. F. (1993b). "The design of breakwaters". In: *Coastal, estuarial and harbour engineer's reference book*. Ed. by M. B. Abbott and W. A. Price. London: E& FN Spon., pp. 381–424.

Burcharth, H. F., Andersen, T. L., and Lara, J. L. (2014). "Upgrade of coastal defence structures against increased loadings caused by climate change: A first methodological approach". In: *Coastal Engineering* 87, pp. 112–121.

Burcharth, H. F. and Liu, Z (1995). "Rubble mound breakwater failure modes". In: *Proceedings of the Final (MAS2-CT92-0042) Workshop: Rubble mound failure modes, Sorrento, Italy, November 1995*.

Burcharth, H. F. and Sørensen, J. D. (1999). "Design of vertical wall caisson breakwaters using partial safety factors". In: *Coastal Engineering 1998*, pp. 2138–2151.

Caires, S and Swail, V (2004). "Global wave climate trend and variability analysis". In: *Preprints of 8th international workshop on wave hindcasting and forecasting*.

Caloiero, T, Aristodemo, F, and Ferraro, D. A. (2019). "Trend analysis of significant wave height and energy period in southern Italy". In: *Theoretical and Applied Climatology* 138.1-2, pp. 917–930.

Campos, A, Castillo, C, and Molina, R (2014). "Analysis of the influence of the different variables involved in a damage progression probability model". In: *Coastal Engineering*, p. 2.

Camus, P, Losada, I. J., Izaguirre, C, Espejo, A, Menéndez, M, and Pérez, J (2017). "Statistical wave climate projections for coastal impact assessments". In: *Earth's Future* 5.9, pp. 918–933.

Camus, P, Tomás, A, Díaz-Hernández, G, Rodríguez, B, Izaguirre, C, and Losada, I. J. (2019). "Probabilistic assessment of port operation downtimes under climate change". In: *Coastal Engineering* 147, pp. 12–24.

Carver, R. D. (1989). *Technical Report REMR-CO-2. Prototype Experience with the Use of Dissimilar Armor for Repair and Rehabilitation of Rubble-mound Coastal Structures*. US Army Engineer Waterways Experiment Station.

Castillo, C, Mínguez, R, Castillo, E, and Losada, M. A. (2006). "An optimal engineering design method with failure rate constraints and sensitivity analysis. Application to composite breakwaters". In: *Coastal Engineering* 53.1, pp. 1–25.

Castillo, E, Losada, M. A., Mínguez, R, Castillo, C, and Baquerizo, A (2004). "Optimal engineering design method that combines safety factors and failure probabilities: application to rubble-mound breakwaters". In: *Journal of waterway, port, coastal, and ocean engineering* 130.2, pp. 77–88.

Cazenave, A, Bonnefond, P, Mercier, F, Dominh, K, and Toumazou, V (2002). "Sea level variations in the Mediterranean Sea and Black Sea from satellite altimetry and tide gauges". In: *Global and Planetary Change* 34.1-2, pp. 59–86.

Chawla, A, Spindler, D, and Tolman, H (2012). *30 Year Wave Hindcasts using WAVE-WATCH III with CFSR winds Phase*. Tech. rep. NOAA/NWS/NCEP/ MMAB, Maryland USA.

Chini, N, Stansby, P, Leake, J, Wolf, J, Roberts-Jones, J, and Lowe, J (2010). "The impact of sea level rise and climate change on inshore wave climate: A case study for East Anglia (UK)". In: *Coastal Engineering* 57.11-12, pp. 973–984.

Chini, N and Stansby, P. K. (2012). "Extreme values of coastal wave overtopping accounting for climate change and sea level rise". In: *Coastal Engineering* 65, pp. 27–37.

Cho, Y. J. (2021). "Level III Reliability Design of an Armor Block of Rubble Mound Breakwater Using Probabilistic Model of Wave Height Optimized for the Korean Sea Wave Conditions and Non-Gaussian Wave Slope Distribution". In: *Journal of Marine Science and Engineering* 9.2, p. 223.

Chorin, A. J. (1968). "Numerical solution of the Navier-Stokes equations". In: *Mathematics of computation* 22.104, pp. 745–762.

Chorin, A. J. (1969). "On the convergence of discrete approximations to the Navier-Stokes equations". In: *Mathematics of computation* 23.106, pp. 341–353.

Christidis, N, Stott, P. A., and Brown, S. J. (2011). "The role of human activity in the recent warming of extremely warm daytime temperatures". In: *Journal of Climate* 24.7, pp. 1922–1930.

Church, J. A., Clark, P. U., Cazenave, A, Gregory, J. M., Jevrejeva, S, Levermann, A, Merrifield, M. A., Milne, G. A., Nerem, R. S., and Nunn, P. D. e. a. (2013). "Sea level change". In: *Climate change* 1137, p. 1216.

CIAD project group (1985). *Final Report CIAD project group. Breakwaters. Computer aided evaluation of the reliability of a breakwater design*. Tech. rep. isbn 9068180193. CIAD Association, Zoetermeer, the Netherlands.

Cid, A, Menéndez, M, Castanedo, S, Abascal, A., Méndez, F. J., and Medina, R (2016). "Long-term changes in the frequency, intensity and duration of extreme storm surge events in southern Europe". In: *Climate dynamics* 46.5-6, pp. 1503–1516.

CIRIA, CUR, and CETMEF (2007). *The rock manual: the use of rock in hydraulic engineering (2nd edition)*. Vol. c683. Ciria, London.

CMCC (2017). *Piano Nazionale di Adattamento ai cambiamenti climatici (PNACC)*.

Coastal Engineering Research Center (US) (1984). *Shore protection manual*. Vol. 1. US Army Coastal Engineering Research Center.

Consiglio Superiore dei Lavori Pubblici (1996). *Istruzioni Tecniche per La Progettazione Delle Dighe Marittime.* Italy.

Copernicus Climate Change Service (2019). *ECMWF Copernicus Report. Product user guide for sea level and ocean wave products - time series and indicators*.

Croeneveld, R. L., Mol, A, and Nieuwenhuys, E. H. (1985). "Rehabilitation methods for damaged breakwaters". In: *Coastal Engineering 1984*, pp. 2467–2486.

Czifra, A, Goda, T, and Garbayo, E (2011). "Surface characterisation by parameter-based technique, slicing method and PSD analysis". In: *Measurement* 44.5, pp. 906–916.

Davies, G, Callaghan, D. P., Gravois, U, Jiang, W, Hanslow, D, Nichol, S, and Baldock, T (2017). "Improved treatment of non-stationary conditions and uncertainties in probabilistic models of storm wave climate". In: *Coastal Engineering* 127, pp. 1–19.

Di Lauro, E, Lara, J. L., Maza, M, Losada, I. J., Contestabile, P, and Vicinanza, D (2019). "Stability analysis of a non-conventional breakwater for wave energy conversion". In: *Coastal engineering* 145, pp. 36–52.

Dissanayake, P, Brown, J, Wisse, P, and Karunarathna, H (2015). "Effects of storm clustering on beach/dune evolution". In: *Marine Geology* 370, pp. 63–75.

Divinsky, B. V. and Kosyan, R. D. (2020). "Climatic trends in the fluctuations of wind waves power in the Black Sea". In: *Estuarine, Coastal and Shelf Science* 235, p. 106577.

Dong, W. P. and Stout, K. J. (1995). "Two-dimensional fast Fourier transform and power spectrum for surface roughness in three dimensions". In: *Proceedings of the Institution of Mechanical Engineers, Part B: Journal of Engineering Manufacture* 209.5, pp. 381–391.

Drummond, C. D., Harley, M. D., Turner, I. L., A Matheen, A. N., Glamore, W. C., et al. (2015). "UAV applications to coastal engineering". In: *Australasian Coasts & Ports Conference 2015: 22nd Australasian Coastal and Ocean Engineering Conference and the 15th Australasian Port and Harbour Conference*. Engineers Australia and IPENZ, p. 267.

Duffy, P. B. and Tebaldi, C (2012). "Increasing prevalence of extreme summer temperatures in the US". In: *Climatic Change* 111.2, pp. 487–495.

European Environment Agency (2015). *State of Europe's seas. EEA Report No 2/2015*. Tech. rep.

EurOtop (2018). *Manual on wave overtopping of sea defences and related structures. An overtopping manual largely based on European research, but for worldwide application*. Van der Meer, J. W., Allsop, N. W. H., Bruce, T., De Rouck, J., Kortenhaus, A., Pullen, T., Schüttrumpf, H., Troch, P. and Zanuttigh, B.

Faraci, C, Scandura, P, and Foti, E (2015). "Reflection of sea waves by combined caissons". In: *Journal of Waterway, Port, Coastal, and Ocean Engineering* 141.2, p. 04014036.

Fatichi, S, Ivanov, V. Y., and Caporali, E (2011). "Simulation of future climate scenarios with a weather generator". In: *Advances in Water Resources* 34.4, pp. 448–467.

Flato, G, Marotzke, J, Abiodun, B, Braconnot, P, Chou, S. C., Collins, W, Cox, P, Driouech, F, Emori, S, and Eyring, V. w. a. (2014). "Evaluation of climate models". In: *Climate change 2013: the physical science basis. Contribution of Working Group*

I to the Fifth Assessment Report of the Intergovernmental Panel on Climate Change. Cambridge University Press, pp. 741–866.

Fortes, C. J. E. M., Capitão, R, Lemos, R, Neves, M. G., Silva, L. G., Henriques, M. J., and Martins, T (2020). "Sines breakwater harbour: The OSOM+ monitoring program". In: *Italian Journal of Engineering Geology and Environment* 20.1, pp. 49–57.

Foti, E, Musumeci, R. E., and Stagnitti, M (2020). "Coastal defence techniques and climate change: a review". In: *Rendiconti Lincei. Scienze Fisiche e Naturali* 31.1, pp. 123–138.

Franco, L (1994). "Vertical breakwaters: the Italian experience". In: *Coastal Engineering* 22.1-2, pp. 31–55.

Frens, A. B. (2007). "The impact of placement method on Antifer-block stability". MA thesis. TU Delft, Civil Engineering and Geosciences, Hydraulic Engineering.

Frostick, L. E., McLelland, S. J., and Mercer, T. G. (2011). *Users guide to physical modelling and experimentation: Experience of the HYDRALAB network*. CRC Press.

Gadelmawla, E. S., Koura, M. M., Maksoud, T. M. A., Elewa, I. M., and Soliman, H. H. (2002). "Roughness parameters". In: *Journal of materials processing Technology* 123.1, pp. 133–145.

Galassi, G and Spada, G (2014). "Sea-level rise in the Mediterranean Sea by 2050: Roles of terrestrial ice melt, steric effects and glacial isostatic adjustment". In: *Global and Planetary Change* 123, pp. 55–66.

Galiatsatou, P and Prinos, P (2012). "Reliability-based design optimization of a rubble mound breakwater in a changing climate". In: *Comprehensive Flood Risk Management: Research for Policy and Practice*, p. 106.

Gent, M. R. A. van, Smale, A. J., and Kuiper, C (2004). "Stability of rock slopes with shallow foreshores". In: *Coastal Structures 2003*, pp. 100–112.

Goda, Y (2009). "A performance test of nearshore wave height prediction with CLASH datasets". In: *Coastal Engineering* 56.3, pp. 220–229.

González-Alemán, J. J., Pascale, S, Gutierrez-Fernandez, J, Murakami, H, Gaertner, M. A., and Vecchi, G. A. (2019). "Potential increase in hazard from Mediterranean hurricane activity with global warming". In: *Geophysical Research Letters* 46.3, pp. 1754–1764.

González-Jorge, H, Puente, I, Roca, D, Martínez-Sánchez, J, Conde, B., and Arias, P (2016). "UAV photogrammetry application to the monitoring of rubble mound breakwaters". In: *Journal of Performance of Constructed Facilities* 30.1, p. 04014194.

Guanche, R, Iturrioz, A, and Losada, I. J. (2015). "Hybrid modeling of pore pressure damping in rubble mound breakwaters". In: *Coastal Engineering* 99, pp. 82–95.

Guanche, R, Losada, I. J., and Lara, J. L. (2009). "Numerical analysis of wave loads for coastal structure stability". In: *Coastal Engineering* 56.5-6, pp. 543–558.

Gupta, N, Bhaskaran, P. K., and Dash, M. (2015). "Recent trends in wind-wave climate for the Indian Ocean". In: *Current Science*, pp. 2191–2201.

Hanna, S. R. and Heinold, D. W. (1985). *Development and application of a simple method for evaluating air quality models*. 4409. American Petroleum Institute.

Hedar, P. A. (1960). *Stability of rock-fill breakwaters*. Akademiförlaget-Gumperts, Göteborg, Sweden.

Hemer, M. A., Fan, Y, Mori, N, Semedo, A, and Wang, X. L. (2013a). "Projected changes in wave climate from a multi-model ensemble". In: *Nature climate change* 3.5, pp. 471–476.

Hemer, M. A., Katzfey, J, and Trenham, C. E. (2013b). "Global dynamical projections of surface ocean wave climate for a future high greenhouse gas emission scenario". In: *Ocean Modelling* 70, pp. 221–245.

Henriques, M. J., Lemos, R, Capitão, R, and Fortes, C. J. (2017). "The monitoring of rubble mound breakwaters. An assessment of UAV technology". In: *Proceedings of INGEO2017, Lisbon, Portugal*.

Hersbach, H, Bell, B, Berrisford, P, Horányi, A, Sabater, J. M., Nicolas, J, Radu, R, Schepers, D, Simmons, A, and Soci, C. e. a. (2019). "Global reanalysis: goodbye ERA-Interim, hello ERA5". In: *ECMWF Newsl* 159, pp. 17–24.

Hithin, N. K., Kumar, V. S., and Shanas, P. R. (2015). "Trends of wave height and period in the Central Arabian Sea from 1996 to 2012: a study based on satellite altimeter data". In: *Ocean Engineering* 108, pp. 416–425.

Hoegh-Guldberg, O, Poloczanska, E. S., Skirving, W, and Dove, S (2017). "Coral reef ecosystems under climate change and ocean acidification". In: *Frontiers in Marine Science* 4, p. 158.

Hofland, B, Rosa-Santos, P, Taveira-Pinto, F, Almeida, E de, Lemos, R, Mendonça, A, and Juana Fortes, C. J. (n.d.). "Measuring damage in physical model tests of rubble mounds". In.

Hudson, R. Y. (1958). *Design of quarry-stone cover layers for rubble-mound breakwaters*. Tech. rep.

Hudson, R. Y. (1959). "Laboratory investigation of rubble-mound breakwaters". In: *Reprint of the original paper as published in the Journal of the Waterways and Harbors Division of ASCE, proceedings paper 2171*.

Hudson, R. Y., Herrmann, F. A., and Sager, R. A. (1979). *Coastal hydraulic models. Special Report 5*. Tech. rep. Vicksburg, Mississipi: US Army Engineer Waterways Experiment Station.

Hughes, S. A. (2014). "Coastal engineering challenges in a changing world". In: *Journal of Applied Water Engineering and Research* 2.2, pp. 72–80.

IPCC (2007). *Report of the 26th Session of the IPCC. Bangkok. April 30–May 4 2007*. Geneva, Switzerland: Intergovernmental Panel on Climate Change.

IPCC (2010). "Guidance note for lead authors of the IPCC fifth assessment report on consistent treatment of uncertainties". In.

IPCC (2014). *Climate change 2014: synthesis report. Contribution of Working Groups I, II and III to the fifth assessment report of the Intergovernmental Panel on Climate Change*. Intergovernmental Panel on Climate Change.

IPCC (2019). *The Ocean and Cryosphere in a Changing Climate. A special Report of the Intergovernmental Panel on Climate Change. Working Group II Technical Support Unit.* Intergovernmental Panel on Climate Change.

IPCC (2021). *Climate Change 2021: The Physical Science Basis. Contribution of Working Group I to the Sixth Assessment Report of the Intergovernmental Panel on Climate Change.* Intergovernmental Panel on Climate Change.

Irish, J. L. and White, T. E. (1998). "Coastal engineering applications of high-resolution lidar bathymetry". In: *Coastal engineering* 35.1-2, pp. 47–71.

Isobe, M (2013). "Impact of global warming on coastal structures in shallow water". In: *Ocean engineering* 71, pp. 51–57.

Iuppa, C, Cavallaro, L, Musumeci, R. E., Vicinanza, D, and Foti, E (2019). "Empirical overtopping volume statistics at an OBREC". In: *Coastal Engineering* 152, p. 103524.

Izaguirre, C, Losada, I. J., Camus, P, Vigh, J. L., and Stenek, V (2021). "Climate change risk to global port operations". In: *Nature Climate Change* 11.1, pp. 14–20.

Jacobs, T. D. B., Junge, T, and Pastewka, L (2017). "Quantitative characterization of surface topography using spectral analysis". In: *Surface Topography: Metrology and Properties* 5.1, p. 013001.

Jevrejeva, S, Moore, J. C., Grinsted, A, Matthews, A. P., and Spada, G (2014). "Trends and acceleration in global and regional sea levels since 1807". In: *Global and Planetary Change* 113, pp. 11–22.

Jonkman, S. N., Steenbergen, R. D. J. M., Morales-Nápoles, O, Vrouwenvelder, A. C. W. M., and Vrijling, J. K. (2015). "Probabilistic design: risk and reliability analysis in civil engineering". In: *Collegedictaat CIE4130*.

Kamphuis, J. W. (2020). *Introduction to coastal engineering and management*. Vol. 48. World Scientific.

Kilsby, C. G., Jones, P. D., Burton, A, Ford, A. C., Fowler, H. J., Harpham, C, James, P, Smith, A, and Wilby, R. L. (2007). "A daily weather generator for use in climate change studies". In: *Environmental Modelling & Software* 22.12, pp. 1705–1719.

Kim, S.-W. and Suh, K.-D. (2006). "Application of reliability design methods to Donghae harbor breakwater". In: *Coastal engineering journal* 48.1, pp. 31–57.

Kim, S.-W. and Suh, K.-D. (2010). "Reliability analysis of breakwater armor blocks: Case study in Korea". In: *Coastal engineering journal* 52.04, pp. 331–350.

Krogstad, H. E. (2004). "How to use the MATLAB FFT2-routines". In: *Unpublished Report, http://www. mathworks. com/matlabcentral/files/11639*.

Kumar, V. S., Joseph, J, Amrutha, M. M., Jena, B. K., Sivakholundu, K. M., and Dubhashi, K. K. (2018). "Seasonal and interannual changes of significant wave height in shelf seas around India during 1998–2012 based on wave hindcast". In: *Ocean Engineering* 151, pp. 127–140.

Kundzewicz, Z and Robson, A (2000). *Detecting trend and other changes in hydrological data*. World Meteorological Organization.

Laface, V and Arena, F (2016). "A new equivalent exponential storm model for long-term statistics of ocean waves". In: *Coastal Engineering* 116, pp. 133–151.

Lambeck, K, Antonioli, F, Anzidei, M, Ferranti, L, Leoni, G, Scicchitano, G, and Silenzi, S (2011). "Sea level change along the Italian coast during the Holocene and projections for the future". In: *Quaternary International* 232.1-2, pp. 250–257.

Lara, J. L., Losada, I. J., and Guanche, R (2008). "Wave interaction with low-mound breakwaters using a RANS model". In: *Ocean engineering* 35.13, pp. 1388–1400.

Lara, J. L., Losada, I. J., Maza, M, and Guanche, R (2011a). "Breaking solitary wave evolution over a porous underwater step". In: *Coastal Engineering* 58.9, pp. 837–850.

Lara, J. L., Lucio, D, Tomas, A, Di Paolo, B, and Losada, I. J. (2019). "High-resolution time-dependent probabilistic assessment of the hydraulic performance for historic coastal structures: application to Luarca Breakwater". In: *Philosophical Transactions of the Royal Society A* 377.2155, p. 20190016.

Lara, J. L., Ruju, A, and Losada, I. J. (2011b). "Reynolds averaged Navier–Stokes modelling of long waves induced by a transient wave group on a beach". In: *Proceedings of the Royal Society A: Mathematical, Physical and Engineering Sciences* 467.2129, pp. 1215–1242.

Lin, N, Emanuel, K, Oppenheimer, M, and Vanmarcke, E (2012). "Physically based assessment of hurricane surge threat under climate change". In: *Nature Climate Change* 2.6, pp. 462–467.

Lin, P (1998). *Numerical modeling of breaking waves*. Cornell University.

Lionello, P, Cogo, S, Galati, M. B., and Sanna, A (2008). "The Mediterranean surface wave climate inferred from future scenario simulations". In: *Global and Planetary Change* 63.2-3, pp. 152–162.

Lionello, P and Sanna, A (2005). "Mediterranean wave climate variability and its links with NAO and Indian Monsoon". In: *Climate Dynamics* 25.6, pp. 611–623.

Lira-Loarca, A, Cobos, M, Losada, M. A., and Baquerizo, A (2020). "Storm characterization and simulation for damage evolution models of maritime structures". In: *Coastal Engineering* 156, p. 103620.

Liu, P. L.-F., Lin, P, Chang, K.-A., and Sakakiyama, T (1999). "Numerical modeling of wave interaction with porous structures". In: *Journal of waterway, port, coastal, and ocean engineering* 125.6, pp. 322–330.

Losada, I. J., Lara, J. L., Guanche, R, and Gonzalez-Ondina, J. M. (2008). "Numerical analysis of wave overtopping of rubble mound breakwaters". In: *Coastal engineering* 55.1, pp. 47–62.

Losada, I. J., Lara, J. L., and Jesus, M del (2016). "Modeling the interaction of water waves with porous coastal structures". In: *Journal of Waterway, Port, Coastal, and Ocean Engineering* 142.6, p. 03116003.

Lowe, J. A. and Gregory, J. M. (2005). "The effects of climate change on storm surges around the United Kingdom". In: *Philosophical Transactions of the Royal Society A: Mathematical, Physical and Engineering Sciences* 363.1831, pp. 1313–1328.

Lucio, D, Lara, J. L., Tomas, A, and Losada, I. J. (2021). "Climate-related port risk assessment: A methodological approach through a probabilistic analysis". In: *Coastal Engineering*. Under review.

Maciñeira, E, Peña, E, Bajo, V, Sande, J, and Noya, F (2017). "Probabilistic Design of a Secondary Breakwater in the New Harbour Basin of the Port of La Coruña". In: *Coastal Structures and Solutions to Coastal Disasters 2015: Resilient Coastal Communities*. American Society of Civil Engineers Reston, VA, pp. 482–490.

Main, R, Hartley, A, Dengate, C, Rowe, E, and Blacka, M (2016). "Coffs Harbour Northen Breakwater–Not Your Average Upgrade". In: *25th NSW Coastal Conference*.

Malanotte-Rizzoli, P (2018). *Projections of sea level rise in oceans and in the Mediterranean sea: what MoSE can do for Venice.*

Malliouri, D. I. (2020). "Probabilistic design of coastal structures". In: *National Technical University of Athens*.

Malliouri, D. I., Memos, C. D., Soukissian, T. H., and Tsoukala, V. K. (2021). "Assessing failure probability of coastal structures based on probabilistic representation of sea conditions at the structures' location". In: *Applied Mathematical Modelling* 89, pp. 710–730.

Marcos, M and Tsimplis, M. N. (2007). "Forcing of coastal sea level rise patterns in the North Atlantic and the Mediterranean Sea". In: *Geophysical Research Letters* 34.18.

Marsooli, R, Lin, N, Emanuel, K, and Feng, K (2019). "Climate change exacerbates hurricane flood hazards along US Atlantic and Gulf Coasts in spatially varying patterns". In: *Nature communications* 10.1, pp. 1–9.

Martucci, G, Carniel, S, Chiggiato, J, Sclavo, M, Lionello, P, and Galati, M. B. (2010). "Statistical trend analysis and extreme distribution of significant wave height from 1958 to 1999-an application to the Italian Seas." In: *Ocean Science Discussions* 7.2.

Massie, W. W. (1976). *Coastal engineering. Volume III: Breakwater design*. TU Delft, Section Hydraulic Engineering.

Mentaschi, L, Besio, G, Cassola, F, and Mazzino, A (2013). "Problems in RMSE-based wave model validations". In: *Ocean Modelling* 72, pp. 53–58.

Mentaschi, L, Besio, G, Cassola, F, and Mazzino, A (2015). "Performance evaluation of Wavewatch III in the Mediterranean Sea". In: *Ocean Modelling* 90, pp. 82–94.

Miche, M (1951). "Le pouvoir réfléchissant des ouvrages maritimes exposés à l'action de la houle". In: *Annales de Ponts et Chaussées, 121 (285-319)*.

Milly, P. C. D., Betancourt, J, Falkenmark, M, Hirsch, R. M., Kundzewicz, Z. W., Lettenmaier, D. P., and Stouffer, R. J. (2008). "Stationarity is dead: Whither water management?" In: *Earth* 4, p. 20.

Morim, J, Hemer, M, Cartwright, N, Strauss, D, and Andutta, F (2018). "On the concordance of 21st century wind-wave climate projections". In: *Global and planetary change* 167, pp. 160–171.

Morim, J, Hemer, M. A., Wang, X. L., Cartwright, N, Trenham, C, Semedo, A, Young, I, Bricheno, L, Camus, P, and Casas-Prat, M. e. a. (2019). "Robustness and uncertainties in global multivariate wind-wave climate projections". In: *Nature Climate Change* 9.9, pp. 711–718.

Mudersbach, C and Jensen, J (2010). "Nonstationary extreme value analysis of annual maximum water levels for designing coastal structures on the German North Sea coastline". In: *Journal of Flood Risk Management* 3.1, pp. 52–62.

Nakicenovic, N, Alcamo, J, Davis, G, Vries, B. d., Fenhann, J, Gaffin, S, Gregory, K, Grubler, A, Jung, T. Y., and Kram, T. e. a. (2000). "Special report on emissions scenarios". In.

Naseef, T. M. and Kumar, V. S. (2020). "Climatology and trends of the Indian Ocean surface waves based on 39-year long ERA5 reanalysis data". In: *International Journal of Climatology* 40.2, pp. 979–1006.

Nelson, T. R. and Voulgaris, G (2014). "Temporal and spatial evolution of wave-induced ripple geometry: Regular versus irregular ripples". In: *Journal of Geophysical Research: Oceans* 119.2, pp. 664–688.

Nelson, T. R. and Voulgaris, G (2015). "A spectral model for estimating temporal and spatial evolution of rippled seabeds". In: *Ocean Dynamics* 65.2, pp. 155–171.

Nicholls, R. J., Wong, P. P., Burkett, V. R., Codignotto, J. O., Hay, J. E., McLean, R. F., Ragoonaden, S, and Woodroffe, C. D. (2007). *Coastal systems and low-lying areas. Climate Change 2007: Impacts, Adaptation and Vulnerability. Contribution of Working Group II to the Fourth Assessment Report of the Intergovernmental Panel on Climate Change, M. L. Parry, O. F. Canziani, J. P. Palutikof, P. J. van der Linden and C. E. Hanson, Eds*.

Osinowo, A, Lin, X, Zhao, D, and Wang, Z (2016). "Long-term variability of extreme significant wave height in the South China Sea". In: *Advances in Meteorology* 2016.

Oumeraci, H (1994). "Review and analysis of vertical breakwater failures - lessons learned". In: *Coastal engineering* 22.1-2, pp. 3–29.

Oumeraci, H (1999). "Strengths and limitations of physical Modelling in coastal Engineering–synergy effect with numerical modelling and field measurement". In: *Proceedings of HYDRALAB-workshop in Hannover, Germany*, pp. 7–38.

Patra, A and Bhaskaran, P. K. (2016). "Trends in wind-wave climate over the head Bay of Bengal region". In: *International Journal of Climatology* 36.13, pp. 4222–4240.

Pavlic, B, Cepak, F, Sucic, B, Peckaj, M, and Kandus, B (2014). "Sustainable port infrastructure, practical implementation of the green port concept". In: *Thermal Science* 18.3, pp. 935–948.

Peres, D. J. and Cancelliere, A (2018). "Modeling impacts of climate change on return period of landslide triggering". In: *Journal of Hydrology* 567, pp. 420–434.

PIANC (1992). *Analysis of rubble mound breakwaters. Report of WG12 of the Permanent Technical Committee II*. Vol. 78. Brussels: Permanent International Association of Navigation Congresses.

PIANC (2003). *Breakwaters with vertical and inclined concrete walls. Report of WG28 of the Maritime Navigation Commission*. Brussels: Permanent International Association of Navigation Congresses.

Plate, S (1995). "Probabilistic design of breakwaters, the Ennore breakawater project: Failure mechanisms of a crested rubble mound breakwater". MA thesis. Hydraulic Engineering Department, Faculty of Civil Engineering, Delft University of Technology.

Pomaro, A, Cavaleri, L, and Lionello, P (2017). "Climatology and trends of the Adriatic Sea wind waves: analysis of a 37-year long instrumental data set". In: *International Journal of Climatology* 37.12, pp. 4237–4250.

Pomaro, A, Cavaleri, L, Papa, A, and Lionello, P (2018). "39 years of directional wave recorded data and relative problems, climatological implications and use". In: *Scientific data* 5, p. 180139.

Ports and Harbours Bureau, Ministry of Land, Infrastructure, Transport and Tourism, and andPort and Airport Research Institute, N. (2009). *Technical Standards and commentaries on Port and Harbour Facilities in Japan*. Tokyo, Japan: The Overseas Coastal Area and Development Institute of Japan.

Puertos del Estado (2002). *ROM 0.0. General procedure and requirements in the design of harbor and maritime structures. Part I*.

Puertos del Estado (2010). *ROM-1.0-09. Recommendation for the Project Design and Construction of Breakwater. Part I: Calculation and Project Factors. Climate Agents.*

Rahmstorf, S (2007). "A semi-empirical approach to projecting future sea-level rise". In: *Science* 315.5810, pp. 368–370.

Reguero, B. G., Losada, I. J., and Méndez, F. J. (2015). "A global wave power resource and its seasonal, interannual and long-term variability". In: *Applied Energy* 148, pp. 366–380.

Reguero, B. G., Losada, I. J., and Méndez, F. J. (2019). "A recent increase in global wave power as a consequence of oceanic warming". In: *Nature communications* 10.1, pp. 1–14.

Reis, M. T., Neves, M. G., Lopes, M. R., Hu, K, and Silva, L. G. (2011). "Rehabilitation of Sines West Breakwater: wave overtopping study". In: *Proceedings of the Institution of Civil Engineers-Maritime Engineering*. Vol. 164. 1. Thomas Telford Ltd, pp. 15–32.

Rodi, W (1993). *Turbulence models and their application in hydraulics*. CRC Press.

Romero, R and Emanuel, K (2013). "Medicane risk in a changing climate". In: *Journal of Geophysical Research: Atmospheres* 118.12, pp. 5992–6001.

Rueda, A, Camus, P, Tomás, A, Vitousek, S, and Méndez, F. J. (2016). "A multivariate extreme wave and storm surge climate emulator based on weather patterns". In: *Ocean Modelling* 104, pp. 242–251.

Salmun, H, Molod, A, Wisniewska, K, and Buonaiuto, F. S. (2011). "Statistical prediction of the storm surge associated with cool-weather storms at the Battery, New York". In: *Journal of applied meteorology and climatology* 50.2, pp. 273–282.

Sanchez-Arcilla, A, Sierra, J. P., Brown, S, Casas-Prat, M, Nicholls, R. J., Lionello, P, and Conte, D (2016). "A review of potential physical impacts on harbours in the Mediterranean Sea under climate change". In: *Regional environmental change* 16.8, pp. 2471–2484.

Santos-Ferreira, A, Cabral, M, and Santos, C (2015). "The rehabilitation of north breakwater of Nazaré harbor, Portugal". In: *Procedia Engineering* 116, pp. 755–762.

Schüttrumpf, H, Kortenhaus, A, Peters, K, and Fröhle, P (2007). "Expert judgement of uncertainties in coastal structure design". In: *Coastal Engineering 2006: (In 5 Volumes)*. World Scientific, pp. 5267–5278.

Scicchitano, G, Scardino, G, Monaco, C, Piscitelli, A, Milella, M, De Giosa, F, and Mastronuzzi, G (2021). "Comparing impact effects of common storms and Medicanes along the coast of south-eastern Sicily". In: *Marine Geology* 439, p. 106556.

Shanas, P. R. and Kumar, V. S. (2015). "Trends in surface wind speed and significant wave height as revealed by ERA-Interim wind wave hindcast in the Central Bay of Bengal". In: *International Journal of Climatology* 35.9, pp. 2654–2663.

Sheffield, J, Wood, E. F., and Roderick, M. L. (2012). "Little change in global drought over the past 60 years". In: *Nature* 491.7424, pp. 435–438.

Sheng, W and Li, H (2017). "A Method for Energy and Resource Assessment of Waves in Finite Water Depths". In: *Energies* 10.4, p. 460.

Sidick, E (2009). "Power spectral density specification and analysis of large optical surfaces". In: *Modeling Aspects in Optical Metrology II*. Vol. 7390. International Society for Optics and Photonics, p. 73900L.

Simmons, A. J., Willett, K. M., Jones, P. D., Thorne, P. W., and Dee, D. P. (2010). "Low-frequency variations in surface atmospheric humidity, temperature, and precipitation: Inferences from reanalyses and monthly gridded observational data sets". In: *Journal of Geophysical Research: Atmospheres* 115.D1.

Spada, G and Galassi, G (2012). "New estimates of secular sea level rise from tide gauge data and GIA modelling". In: *Geophysical Journal International* 191.3, pp. 1067–1094.

Stopa, J. E., Cheung, K. F., Tolman, H. L., and Chawla, A (2013). "Patterns and cycles in the climate forecast system reanalysis wind and wave data". In: *Ocean Modelling* 70, pp. 207–220.

Sunday, J. M., Fabricius, K. E., Kroeker, K. J., Anderson, K. M., Brown, N. E., Barry, J. P., Connell, S. D., Dupont, S, Gaylord, B, and Hall-Spencer, J. M. e. a. (2017). "Ocean acidification can mediate biodiversity shifts by changing biogenic habitat". In: *Nature Climate Change* 7.1, pp. 81–85.

Tabarestani, M. K., Feizi, A, and Bali, M (2020). "Reliability-based design and sensitivity analysis of rock armors for rubble-mound breakwater". In: *Journal of the Brazilian Society of Mechanical Sciences and Engineering* 42.3, pp. 1–13.

Takagi, H, Kashihara, H, Esteban, M, and Shibayama, T (2011). "Assessment of future stability of breakwaters under climate change". In: *Coastal Engineering Journal* 53.01, pp. 21–39.

Takahashi, S (2002). "Design of vertical breakwaters". In: *PHRI reference document nr. 34*.

Timmermans, B. W., Gommenginger, C. P., Dodet, G, and Bidlot, J.-R. (2020). "Global Wave Height Trends and Variability from New Multimission Satellite Altimeter Products, Reanalyses, and Wave Buoys". In: *Geophysical Research Letters* 47.9, e2019GL086880.

Toimil, A, Losada, I. J., Nicholls, R. J., Dalrymple, R. A., and Stive, M. J. F. (2020). "Addressing the challenges of climate change risks and adaptation in coastal areas: A review". In: *Coastal Engineering* 156, p. 103611.

Tolman, H. L. e. a. (2009). "User manual and system documentation of WAVE-WATCH III TM version 3.14". In: *Technical note, MMAB Contribution* 276, p. 220.

Torres, J. C., Arroyo, G, Romo, C, and De Haro, J (2012). "3D Digitization using structure from motion". In: *CEIG-Spanish Computer Graphics Conference*, pp. 1–10.

US Army Corps of Engineers (2002). *Coastal engineering manual*. US Army Engineering Research and Development Center Vicksburg, Mississippi.

van der Meer, J and Bruce, T (2014). "New physical insights and design formulas on wave overtopping at sloping and vertical structures". In: *Journal of Waterway, Port, Coastal, and Ocean Engineering* 140.6, p. 04014025.

van der Meer, J. W. (1988a). "Rock Slopes and Gravel Beaches under Wave Attack". In: *PhD thesis, Delft University of Technology*.

van der Meer, J. W. (1988b). "Deterministic and probabilistic design of breakwater armor layers". In: *Journal of waterway, port, coastal, and ocean engineering* 114.1, pp. 66–80.

van der Meer, J. W. (1988c). "Stability of Cubes, Tetrapods and Accropode". In: *Breakwaters '88*. American Society of Civil Engineers, pp. 59–68.

van der Meer, J. W. (1995). "Wave run-up and wave overtopping at dikes". In: *Wave forces on inclined and vertical structures, ASCE*.

van Gent, M. R. A. (2014). "Oblique wave attack on rubble mound breakwaters". In: *Coastal engineering* 88, pp. 43–54.

van Gent, M. R. A. and van der Werf, I. M. (2014). "Rock toe stability of rubble mound breakwaters". In: *Coastal Engineering* 83, pp. 166–176.

Van Vuuren, D. P., Edmonds, J, Kainuma, M, Riahi, K, Thomson, A, Hibbard, K, Hurtt, G. C., Kram, T, Krey, V, and Lamarque, J.-F. e. a. (2011). "The representative concentration pathways: an overview". In: *Climatic change* 109.1, pp. 5–31.

Vecchio, A, Anzidei, M, Serpelloni, E, and Florindo, F (2019). "Natural Variability and Vertical Land Motion Contributions in the Mediterranean Sea-Level Records over the Last Two Centuries and Projections for 2100". In: *Water* 11.7, p. 1480.

Vellinga, P, Marinova, N. A., Lionello, P, Gualdi, S, Artale, V, and Jorda, G (2011). *Sea level scenarios for Venice for 2100: an International assessment*. Wageningen UR.

Vicinanza, D, Di Lauro, E, Contestabile, P, Gisonni, C, Lara, J. L., and Losada, I. J. (2019). "Review of innovative harbor breakwaters for wave-energy conversion". In: *Journal of Waterway, Port, Coastal, and Ocean Engineering* 145.4, p. 03119001.

Vieira, F, Taveira-Pinto, F, and Rosa-Santos, P (2021). "New developments in assessment of wave overtopping on single-layer cube armoured breakwaters based on laboratory experiments". In: *Coastal Engineering* 166, p. 103883.

Voulgaris, G and Morin, J. P. (2008). "A long-term real time sea bed morphology evolution system in the South Atlantic Bight". In: *2008 IEEE/OES 9th Working Conference on Current Measurement Technology*. IEEE, pp. 71–79.

Vousdoukas, M. I., Mentaschi, L, Voukouvalas, E, Verlaan, M, Jevrejeva, S, Jackson, L. P., and Feyen, L (2018). "Global probabilistic projections of extreme sea levels show intensification of coastal flood hazard". In: *Nature communications* 9.1, pp. 1–12.

Vousdoukas, M. I., Voukouvalas, E, Annunziato, A, Giardino, A, and Feyen, L (2016). "Projections of extreme storm surge levels along Europe". In: *Climate Dynamics* 47.9, pp. 3171–3190.

Wang, J, Dong, C, and He, Y (2016). "Wave climatological analysis in the East China Sea". In: *Continental Shelf Research* 120, pp. 26–40.

Westra, S, Varley, I, Sharma, A, Hill, P, Jordan, P, Nathan, R, and Ladson, A (2010). "Addressing climatic non-stationarity in the assessment of flood risk". In: *Australian Journal of Water Resources* 14.1, pp. 1–16.

Whitehouse, D. J. (2002). *Handbook of surface and nanometrology*. Taylor & Francis.

Yamaguchi, M and Hatada, Y (2002). "51-year wave hindcast and analysis of wave height climate trend of the Northwestern Pacific ocean". In: *Proc. 7th Int. Workshop on Wave Hindcasting and Forecasting*, pp. 60–69.

Young, I. R. and Ribal, A (2019). "Multiplatform evaluation of global trends in wind speed and wave height". In: *Science* 364.6440, pp. 548–552.

Zanuttigh, B and van der Meer, J. W. (2008). "Wave reflection from coastal structures in design conditions". In: *Coastal engineering* 55.10, pp. 771–779.

Appendix A

Summary of the experimental and numerical tests

A.1 Experimental tests

In the present section, a summary of the two-dimensional physical model tests performed at the Hydraulic Laboratory of the University of Catania is provided. The tested configurations are showed in Figure 6.17 and Figure 6.18 and summarized in Table 6.4.

Figure A.1 schematically describes the parameters of the structure geometry and materials employed for the analysis of the experimental results, whose values are reported in Table A.1. Table A.2 and Table A.3 show the scope of each performed
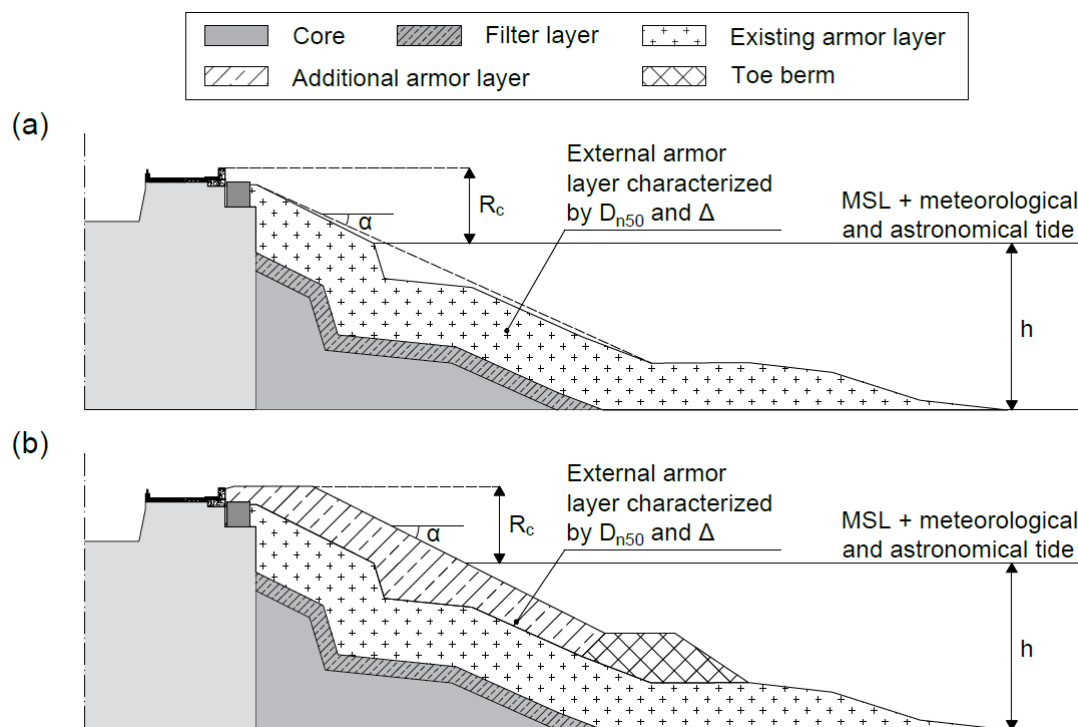
FIGURE A.1 Characteristics of geometry and materials of the tested structures employed for the analysis of the experimental data: (a) upgrading solution with heightened wave wall; (b) upgrading solution with heightened wave wall and additional armor layer.

test, and the correspondent input hydrodynamic conditions, for sections n. 10 and n. 40 respectively. It should be noted that the name of each test consists of three parts: i) "S10_" or "S40_", to indicate the considered cross-section; ii) "E", "ESLR", "EM", "AS", "AD", "CM" or "CS" to indicate configurations E, E with SLR, EM, AS, AD, CM and CS respectively; iii) the progressive number of the test, with reference to a certain cross-section and a certain configuration. Table A.4 and Table A.5 report the characteristics of the simulated wave motion and the reflection coefficient (Faraci et al., 2015) measured during the experiments, for sections n. 10 and n. 40 respectively. Finally, the experimental data on damage of the external armor layer and mean overtopping discharge are presented in Table A.6 and Table A.7, for sections n. 10 and n. 40 respectively.

TABLE A.1 Characteristics of geometry and materials of the tested structures employed for the analysis of the experimental data.

Parameter	Configurations of section n. 10					
	E	EM	AS	AD	CM	CS
R_c [m]	0.114-0.094	0.129	0.119	0.119	0.119	0.129
h [m]	0.240-0.260	0.240	0.240	0.240	0.240	0.240
D_{n50} [m]	0.059	0.059	0.046	0.046	0.046	0.059
Δ	0.56	0.56	0.56	0.56	0.56	0.56
$tan\alpha$	0.50	0.50	0.50	0.50	0.50	0.50

Parameter	Configurations of section n. 40					
	E	EM	AS	AD	CM	CS
R_c [m]	0.114-0.094	0.129	0.119	0.119	0.119	0.129
h [m]	0.280-0.300	0.280	0.280	0.280	0.280	0.280
D_{n50} [m]	0.059	0.059	0.046	0.046	0.046	0.059
Δ	0.56	0.56	0.56	0.56	0.56	0.56
$tan\alpha$	0.50	0.50	0.50	0.50	0.50	0.50

TABLE A.2 Scope of the tests on the physical model of the upgraded Catania harbor breakwater and input hydrodynamic conditions: section n. 10.

Test	Scope of the test	Wave ID	Target H_s [m]	Target T_p [s]	N_w [n. of waves]	h [m]
S10_E001	calibration	I	0.060	1.15	200	0.240
S10_E002	damage - overtopping	I	0.060	1.15	1500	0.240
S10_E003	damage - overtopping	I	0.060	1.15	1500	0.240
S10_E004	damage - overtopping	I	0.060	1.15	1500	0.240
S10_E005	calibration	II	0.070	1.20	200	0.240
S10_E006	damage - overtopping	II	0.070	1.20	1500	0.240
S10_E007	damage - overtopping	II	0.070	1.20	1500	0.240
S10_E008	damage - overtopping	II	0.070	1.20	1500	0.240
S10_E009	calibration	III	0.080	1.31	200	0.240
S10_E010	damage - overtopping	III	0.080	1.31	1500	0.240
S10_E011	damage - overtopping	III	0.080	1.31	1500	0.240

TABLE A.2 Scope of the tests on the physical model of the upgraded Catania harbor break-water and input hydrodynamic conditions: section n. 10 (continued).

Test	Scope of the test	Wave ID	Target H_s [m]	Target T_p [s]	N_w [n. of waves]	h [m]
S10_E012	damage - overtopping	III	0.080	1.31	1500	0.240
S10_E013	calibration	IV	0.090	1.36	200	0.240
S10_E014	calibration	IV	0.090	1.36	200	0.240
S10_E015	damage - overtopping	IV	0.090	1.36	1500	0.240
S10_E016	damage - overtopping	IV	0.090	1.36	1500	0.240
S10_E017	damage - overtopping	IV	0.090	1.36	1500	0.240
S10_E018	calibration	V	0.011	1.36	200	0.240
S10_E019	damage - overtopping	V	0.011	1.36	1500	0.240
S10_E020	damage - overtopping	V	0.011	1.36	1500	0.240
S10_E021	damage - overtopping	V	0.011	1.36	1500	0.240
S10_ESLR001	calibration	III	0.080	1.31	200	0.260
S10_ESLR002	damage - overtopping	III	0.080	1.31	1500	0.260
S10_ESLR003	damage - overtopping	III	0.080	1.31	1500	0.260
S10_ESLR004	damage - overtopping	III	0.080	1.31	1500	0.260
S10_ESLR005	calibration	IV	0.090	1.36	200	0.260
S10_ESLR006	calibration	IV	0.090	1.36	200	0.260
S10_ESLR007	calibration	IV	0.090	1.36	200	0.260
S10_ESLR008	damage - overtopping	IV	0.090	1.36	1500	0.260
S10_ESLR009	damage - overtopping	IV	0.090	1.36	1500	0.260
S10_ESLR010	damage - overtopping	IV	0.090	1.36	1500	0.260
S10_EM001	calibration	I	0.060	1.15	200	0.240
S10_EM002	damage - overtopping	I	0.060	1.15	1500	0.240
S10_EM003	damage - overtopping	I	0.060	1.15	1500	0.240
S10_EM004	damage - overtopping	I	0.060	1.15	1500	0.240
S10_EM005	calibration	II	0.070	1.20	200	0.240
S10_EM006	damage - overtopping	II	0.070	1.20	1500	0.240
S10_EM007	damage - overtopping	II	0.070	1.20	1500	0.240
S10_EM008	damage - overtopping	II	0.070	1.20	1500	0.240
S10_EM009	calibration	III	0.080	1.31	200	0.240
S10_EM010	damage - overtopping	III	0.080	1.31	1500	0.240
S10_EM011	damage - overtopping	III	0.080	1.31	1500	0.240
S10_EM012	damage - overtopping	III	0.080	1.31	1500	0.240
S10_EM013	calibration	IV	0.090	1.36	200	0.240
S10_EM014	damage - overtopping	IV	0.090	1.36	1500	0.240
S10_EM015	damage - overtopping	IV	0.090	1.36	1500	0.240
S10_EM016	damage - overtopping	IV	0.090	1.36	1500	0.240
S10_EM017	calibration	V	0.110	1.36	200	0.240
S10_EM018	damage - overtopping	V	0.110	1.36	1500	0.240
S10_EM019	damage - overtopping	V	0.110	1.36	1500	0.240
S10_EM020	damage - overtopping	V	0.110	1.36	1500	0.240
S10_AS001	calibration	I	0.06	1.15	200	0.240
S10_AS002	calibration	I	0.06	1.15	200	0.240
S10_AS003	damage - overtopping	I	0.06	1.15	1500	0.240

TABLE A.2 Scope of the tests on the physical model of the upgraded Catania harbor breakwater and input hydrodynamic conditions: section n. 10 (continued).

Test	Scope of the test	Wave ID	Target H_s [m]	Target T_p [s]	N_w [n. of waves]	h [m]
S10_AS004	damage - overtopping	I	0.06	1.15	1500	0.240
S10_AS005	damage - overtopping	I	0.06	1.15	1500	0.240
S10_AS006	calibration	II	0.07	1.20	200	0.240
S10_AS007	calibration	II	0.07	1.20	200	0.240
S10_AS008	damage - overtopping	II	0.07	1.20	1500	0.240
S10_AS009	damage - overtopping	II	0.07	1.20	1500	0.240
S10_AS010	damage - overtopping	II	0.07	1.20	1500	0.240
S10_AS011	calibration	III	0.08	1.31	200	0.240
S10_AS012	calibration	III	0.08	1.31	200	0.240
S10_AS013	damage - overtopping	III	0.08	1.31	1500	0.240
S10_AS014	damage - overtopping	III	0.08	1.31	1500	0.240
S10_AS015	damage - overtopping	III	0.08	1.31	1500	0.240
S10_AS016	calibration	IV	0.09	1.36	200	0.240
S10_AS017	calibration	IV	0.09	1.36	200	0.240
S10_AS018	calibration	IV	0.09	1.36	200	0.240
S10_AS019	calibration	IV	0.09	1.36	200	0.240
S10_AS020	damage - overtopping	IV	0.09	1.36	1500	0.240
S10_AS021	damage - overtopping	IV	0.09	1.36	1500	0.240
S10_AS022	damage - overtopping	IV	0.09	1.36	1500	0.240
S10_AS023	calibration	V	0.011	1.36	200	0.240
S10_AS024	calibration	V	0.011	1.36	200	0.240
S10_AS025	calibration	V	0.011	1.36	200	0.240
S10_AS026	calibration	V	0.011	1.36	200	0.240
S10_AS027	damage - overtopping	V	0.011	1.36	1500	0.240
S10_AS028	damage - overtopping	V	0.011	1.36	1500	0.240
S10_AS029	damage - overtopping	V	0.011	1.36	1500	0.240
S10_AD001	calibration	I	0.060	1.15	200	0.240
S10_AD002	calibration	I	0.060	1.15	200	0.240
S10_AD003	damage - overtopping	I	0.060	1.15	1500	0.240
S10_AD004	damage - overtopping	I	0.060	1.15	1500	0.240
S10_AD005	damage - overtopping	I	0.060	1.15	1500	0.240
S10_AD006	calibration	II	0.070	1.20	200	0.240
S10_AD007	damage - overtopping	II	0.070	1.20	1500	0.240
S10_AD008	damage - overtopping	II	0.070	1.20	1500	0.240
S10_AD009	damage - overtopping	II	0.070	1.20	1500	0.240
S10_AD010	calibration	III	0.080	1.31	200	0.240
S10_AD011	damage - overtopping	III	0.080	1.31	1500	0.240
S10_AD012	damage - overtopping	III	0.080	1.31	1500	0.240
S10_AD013	damage - overtopping	III	0.080	1.31	1500	0.240
S10_AD014	calibration	IV	0.090	1.36	200	0.240
S10_AD015	calibration	IV	0.090	1.36	200	0.240
S10_AD016	damage - overtopping	IV	0.090	1.36	1500	0.240
S10_AD017	damage - overtopping	IV	0.090	1.36	1500	0.240

TABLE A.2 Scope of the tests on the physical model of the upgraded Catania harbor breakwater and input hydrodynamic conditions: section n. 10 (continued).

Test	Scope of the test	Wave ID	Target H_s [m]	Target T_p [s]	N_w [n. of waves]	h [m]
S10_AD018	damage - overtopping	IV	0.090	1.36	1500	0.240
S10_AD019	calibration	V	0.011	1.36	200	0.240
S10_AD020	damage - overtopping	V	0.011	1.36	1500	0.240
S10_AD021	damage - overtopping	V	0.011	1.36	1500	0.240
S10_AD022	damage - overtopping	V	0.011	1.36	1500	0.240
S10_CM001	calibration	I	0.060	1.15	200	0.240
S10_CM002	calibration	I	0.060	1.15	200	0.240
S10_CM003	damage - overtopping	I	0.060	1.15	1500	0.240
S10_CM004	damage - overtopping	I	0.060	1.15	1500	0.240
S10_CM005	damage - overtopping	I	0.060	1.15	1500	0.240
S10_CM006	calibration	II	0.070	1.20	200	0.240
S10_CM007	damage - overtopping	II	0.070	1.20	1500	0.240
S10_CM008	damage - overtopping	II	0.070	1.20	1500	0.240
S10_CM009	damage - overtopping	II	0.070	1.20	1500	0.240
S10_CM010	calibration	III	0.080	1.31	200	0.240
S10_CM011	damage - overtopping	III	0.080	1.31	1500	0.240
S10_CM012	damage - overtopping	III	0.080	1.31	1500	0.240
S10_CM013	damage - overtopping	III	0.080	1.31	1500	0.240
S10_CM014	calibration	IV	0.090	1.36	200	0.240
S10_CM015	damage - overtopping	IV	0.090	1.36	1500	0.240
S10_CM016	damage - overtopping	IV	0.090	1.36	1500	0.240
S10_CM017	damage - overtopping	IV	0.090	1.36	1500	0.240
S10_CM018	calibration	V	0.110	1.36	200	0.240
S10_CM019	damage - overtopping	V	0.110	1.36	1500	0.240
S10_CM020	damage - overtopping	V	0.110	1.36	1500	0.240
S10_CM021	damage - overtopping	V	0.110	1.36	1500	0.240
S10_CS001	calibration	I	0.060	1.15	200	0.240
S10_CS002	damage - overtopping	I	0.060	1.15	1500	0.240
S10_CS003	damage - overtopping	I	0.060	1.15	1500	0.240
S10_CS004	damage - overtopping	I	0.060	1.15	1500	0.240
S10_CS005	calibration	II	0.070	1.20	200	0.240
S10_CS006	damage - overtopping	II	0.070	1.20	1500	0.240
S10_CS007	damage - overtopping	II	0.070	1.20	1500	0.240
S10_CS008	damage - overtopping	II	0.070	1.20	1500	0.240
S10_CS009	calibration	III	0.080	1.31	200	0.240
S10_CS010	damage - overtopping	III	0.080	1.31	1500	0.240
S10_CS011	damage - overtopping	III	0.080	1.31	1500	0.240
S10_CS012	damage - overtopping	III	0.080	1.31	1500	0.240
S10_CS013	calibration	IV	0.090	1.36	200	0.240
S10_CS014	damage - overtopping	IV	0.090	1.36	1500	0.240
S10_CS015	damage - overtopping	IV	0.090	1.36	1500	0.240
S10_CS016	damage - overtopping	IV	0.090	1.36	1500	0.240
S10_CS017	calibration	V	0.110	1.36	200	0.240

TABLE A.2 Scope of the tests on the physical model of the upgraded Catania harbor breakwater and input hydrodynamic conditions: section n. 10 (continued).

Test	Scope of the test	Wave ID	Target H_s [m]	Target T_p [s]	N_w [n. of waves]	h [m]
S10_CS018	damage - overtopping	V	0.110	1.36	1500	0.240
S10_CS019	damage - overtopping	V	0.110	1.36	1500	0.240
S10_CS020	damage - overtopping	V	0.110	1.36	1500	0.240

TABLE A.3 Scope of the tests on the physical model of the upgraded Catania harbor breakwater and input hydrodynamic conditions: section n. 40.

Test	Scope of the test	Wave ID	Target H_s [m]	Target T_p [s]	N_w [n. of waves]	h [m]
S40_E001	calibration	I	0.070	1.15	200	0.280
S40_E002	calibration	I	0.070	1.15	200	0.280
S40_E003	damage - overtopping	I	0.070	1.15	1500	0.280
S40_E004	damage - overtopping	I	0.070	1.15	1500	0.280
S40_E005	damage - overtopping	I	0.070	1.15	1500	0.280
S40_E006	calibration	II	0.070	1.20	200	0.280
S40_E007	damage - overtopping	II	0.070	1.20	1500	0.280
S40_E008	damage - overtopping	II	0.070	1.20	1500	0.280
S40_E009	damage - overtopping	II	0.070	1.20	1500	0.280
S40_E010	calibration	III	0.090	1.31	200	0.280
S40_E011	calibration	III	0.090	1.31	200	0.280
S40_E012	damage - overtopping	III	0.090	1.31	1500	0.280
S40_E013	damage - overtopping	III	0.090	1.31	1500	0.280
S40_E014	damage - overtopping	III	0.090	1.31	1500	0.280
S40_E015	calibration	IV	0.100	1.36	200	0.280
S40_E016	calibration	IV	0.100	1.36	200	0.280
S40_E017	calibration	IV	0.100	1.36	200	0.280
S40_E018	damage - overtopping	IV	0.100	1.36	1500	0.280
S40_E019	damage - overtopping	IV	0.100	1.36	1500	0.280
S40_E020	damage - overtopping	IV	0.100	1.36	1500	0.280
S40_E021	calibration	V	0.120	1.36	200	0.280
S40_E022	calibration	V	0.120	1.36	200	0.280
S40_E023	calibration	V	0.120	1.36	200	0.280
S40_E024	damage	V	0.120	1.36	1500	0.280
S40_E025	damage - overtopping	V	0.120	1.36	1500	0.280
S40_E026	damage	V	0.120	1.36	1500	0.280
S40_ESLR001	calibration	III	0.090	1.31	200	0.300
S40_ESLR002	calibration	III	0.090	1.31	200	0.300
S40_ESLR003	calibration	III	0.090	1.31	200	0.300
S40_ESLR004	calibration	III	0.090	1.31	200	0.300
S40_ESLR005	calibration	III	0.090	1.31	200	0.300
S40_ESLR006	calibration	III	0.090	1.31	200	0.300
S40_ESLR007	damage - overtopping	III	0.090	1.31	1500	0.300
S40_ESLR008	damage - overtopping	III	0.090	1.31	1500	0.300

TABLE A.3 Scope of the tests on the physical model of the upgraded Catania harbor breakwater and input hydrodynamic conditions: section n. 40 (continued).

Test	Scope of the test	Wave ID	Target H_s [m]	Target T_p [s]	N_w [n. of waves]	h [m]
S40_ESLR009	damage - overtopping	III	0.090	1.31	1500	0.300
S40_ESLR010	calibration	IV	0.100	1.36	200	0.300
S40_ESLR011	calibration	IV	0.100	1.36	200	0.300
S40_ESLR012	damage - overtopping	IV	0.100	1.36	1500	0.300
S40_ESLR013	damage - overtopping	IV	0.100	1.36	1500	0.300
S40_ESLR014	damage - overtopping	IV	0.100	1.36	1500	0.300
S40_EM001	calibration	I	0.070	1.15	200	0.280
S40_EM002	calibration	I	0.070	1.15	200	0.280
S40_EM003	damage - overtopping	I	0.070	1.15	1500	0.280
S40_EM004	damage - overtopping	I	0.070	1.15	1500	0.280
S40_EM005	damage - overtopping	I	0.070	1.15	1500	0.280
S40_EM006	calibration	II	0.070	1.20	200	0.280
S40_EM007	damage - overtopping	II	0.070	1.20	1500	0.280
S40_EM008	damage - overtopping	II	0.070	1.20	1500	0.280
S40_EM009	damage - overtopping	II	0.070	1.20	1500	0.280
S40_EM010	calibration	III	0.090	1.31	200	0.280
S40_EM011	calibration	III	0.090	1.31	200	0.280
S40_EM012	damage - overtopping	III	0.090	1.31	1500	0.280
S40_EM013	damage - overtopping	III	0.090	1.31	1500	0.280
S40_EM014	damage - overtopping	III	0.090	1.31	1500	0.280
S40_EM015	calibration	IV	0.100	1.36	200	0.280
S40_EM016	damage - overtopping	IV	0.100	1.36	1500	0.280
S40_EM017	damage - overtopping	IV	0.100	1.36	1500	0.280
S40_EM018	damage - overtopping	IV	0.100	1.36	1500	0.280
S40_EM019	calibration	V	0.120	1.36	200	0.280
S40_EM020	damage - overtopping	V	0.120	1.36	1500	0.280
S40_EM021	damage - overtopping	V	0.120	1.36	1500	0.280
S40_EM022	damage - overtopping	V	0.120	1.36	1500	0.280
S40_AS007	calibration	I	0.070	1.15	200	0.280
S40_AS010	damage - overtopping	I	0.070	1.15	1500	0.280
S40_AS011	damage - overtopping	I	0.070	1.15	1500	0.280
S40_AS012	damage - overtopping	I	0.070	1.15	1500	0.280
S40_AS015	calibration	II	0.070	1.20	200	0.280
S40_AS013	damage - overtopping	II	0.070	1.20	1500	0.280
S40_AS014	damage - overtopping	II	0.070	1.20	1500	0.280
S40_AS016	damage - overtopping	II	0.070	1.20	1500	0.280
S40_AS022	calibration	III	0.090	1.31	200	0.280
S40_AS017	damage - overtopping	III	0.090	1.31	1500	0.280
S40_AS023	damage - overtopping	III	0.090	1.31	1500	0.280
S40_AS028	damage - overtopping	III	0.090	1.31	1500	0.280
S40_AS037	calibration	IV	0.100	1.36	200	0.280
S40_AS029	damage - overtopping	IV	0.100	1.36	1500	0.280
S40_AS036	damage - overtopping	IV	0.100	1.36	1500	0.280

TABLE A.3 Scope of the tests on the physical model of the upgraded Catania harbor breakwater and input hydrodynamic conditions: section n. 40 (continued).

Test	Scope of the test	Wave ID	Target H_s [m]	Target T_p [s]	N_w [n. of waves]	h [m]
S40_AS038	damage - overtopping	IV	0.100	1.36	1500	0.280
S40_AS040	calibration	V	0.120	1.36	200	0.280
S40_AS039	damage - overtopping	V	0.120	1.36	1500	0.280
S40_AS051	damage - overtopping	V	0.120	1.36	1500	0.280
S40_AS060	damage - overtopping	V	0.120	1.36	1500	0.280
S40_AD001	calibration	I	0.070	1.15	200	0.280
S40_AD002	calibration	I	0.070	1.15	200	0.280
S40_AD003	calibration	I	0.070	1.15	200	0.280
S40_AD004	calibration	I	0.070	1.15	200	0.280
S40_AD005	damage - overtopping	I	0.070	1.15	1500	0.280
S40_AD006	damage - overtopping	I	0.070	1.15	1500	0.280
S40_AD007	damage - overtopping	I	0.070	1.15	1500	0.280
S40_AD008	calibration	II	0.070	1.20	200	0.280
S40_AD009	calibration	II	0.070	1.20	200	0.280
S40_AD010	damage - overtopping	II	0.070	1.20	1500	0.280
S40_AD011	damage - overtopping	II	0.070	1.20	1500	0.280
S40_AD012	damage - overtopping	II	0.070	1.20	1500	0.280
S40_AD013	calibration	III	0.090	1.31	200	0.280
S40_AD014	calibration	III	0.090	1.31	200	0.280
S40_AD015	damage - overtopping	III	0.090	1.31	1500	0.280
S40_AD016	damage - overtopping	III	0.090	1.31	1500	0.280
S40_AD017	damage - overtopping	III	0.090	1.31	1500	0.280
S40_AD018	calibration	IV	0.100	1.36	200	0.280
S40_AD019	calibration	IV	0.100	1.36	200	0.280
S40_AD020	damage - overtopping	IV	0.100	1.36	1500	0.280
S40_AD021	damage - overtopping	IV	0.100	1.36	1500	0.280
S40_AD022	damage - overtopping	IV	0.100	1.36	1500	0.280
S40_AD023	calibration	V	0.120	1.36	200	0.280
S40_AD024	calibration	V	0.120	1.36	200	0.280
S40_AD025	damage - overtopping	V	0.120	1.36	1500	0.280
S40_AD026	damage - overtopping	V	0.120	1.36	1500	0.280
S40_AD027	damage - overtopping	V	0.120	1.36	1500	0.280
S40_CM001	calibration	I	0.070	1.15	200	0.280
S40_CM002	damage - overtopping	I	0.070	1.15	1500	0.280
S40_CM003	damage - overtopping	I	0.070	1.15	1500	0.280
S40_CM004	damage - overtopping	I	0.070	1.15	1500	0.280
S40_CM005	calibration	II	0.070	1.20	200	0.280
S40_CM006	damage - overtopping	II	0.070	1.20	1500	0.280
S40_CM007	damage - overtopping	II	0.070	1.20	1500	0.280
S40_CM008	damage - overtopping	II	0.070	1.20	1500	0.280
S40_CM009	calibration	III	0.090	1.31	200	0.280
S40_CM010	calibration	III	0.090	1.31	200	0.280
S40_CM011	calibration	III	0.090	1.31	200	0.280

TABLE A.3 Scope of the tests on the physical model of the upgraded Catania harbor break-water and input hydrodynamic conditions: section n. 40 (continued).

Test	Scope of the test	Wave ID	Target H_s [m]	Target T_p [s]	N_w [n. of waves]	h [m]
S40_CM012	damage - overtopping	III	0.090	1.31	1500	0.280
S40_CM013	damage - overtopping	III	0.090	1.31	1500	0.280
S40_CM014	damage - overtopping	III	0.090	1.31	1500	0.280
S40_CM015	calibration	IV	0.100	1.36	200	0.280
S40_CM016	calibration	IV	0.100	1.36	200	0.280
S40_CM017	damage - overtopping	IV	0.100	1.36	1500	0.280
S40_CM018	damage - overtopping	IV	0.100	1.36	1500	0.280
S40_CM019	damage - overtopping	IV	0.100	1.36	1500	0.280
S40_CM020	calibration	V	0.120	1.36	200	0.280
S40_CM021	calibration	V	0.120	1.36	200	0.280
S40_CM022	calibration	V	0.120	1.36	200	0.280
S40_CM023	calibration	V	0.120	1.36	200	0.280
S40_CM024	calibration	V	0.120	1.36	200	0.280
S40_CM025	calibration	V	0.120	1.36	200	0.280
S40_CM026	calibration	V	0.120	1.36	200	0.280
S40_CM027	calibration	V	0.120	1.36	200	0.280
S40_CM028	damage - overtopping	V	0.120	1.36	1500	0.280
S40_CM029	damage	V	0.120	1.36	1500	0.280
S40_CM030	damage	V	0.120	1.36	1500	0.280
S40_CS001	calibration	I	0.070	1.15	200	0.280
S40_CS002	damage - overtopping	I	0.070	1.15	1500	0.280
S40_CS003	damage - overtopping	I	0.070	1.15	1500	0.280
S40_CS004	damage - overtopping	I	0.070	1.15	1500	0.280
S40_CS005	calibration	II	0.070	1.20	200	0.280
S40_CS006	calibration	II	0.070	1.20	200	0.280
S40_CS007	calibration	II	0.070	1.20	200	0.280
S40_CS008	damage - overtopping	II	0.070	1.20	1500	0.280
S40_CS009	damage - overtopping	II	0.070	1.20	1500	0.280
S40_CS010	damage - overtopping	II	0.070	1.20	1500	0.280
S40_CS011	calibration	III	0.090	1.31	200	0.280
S40_CS012	damage - overtopping	III	0.090	1.31	1500	0.280
S40_CS013	damage - overtopping	III	0.090	1.31	1500	0.280
S40_CS014	damage - overtopping	III	0.090	1.31	1500	0.280
S40_CS015	calibration	IV	0.100	1.36	200	0.280
S40_CS016	damage - overtopping	IV	0.100	1.36	1500	0.280
S40_CS017	damage - overtopping	IV	0.100	1.36	1500	0.280
S40_CS018	damage - overtopping	IV	0.100	1.36	1500	0.280
S40_CS019	calibration	V	0.120	1.36	200	0.280
S40_CS020	calibration	V	0.120	1.36	200	0.280
S40_CS021	damage - overtopping	V	0.120	1.36	1500	0.280
S40_CS022	damage - overtopping	V	0.120	1.36	1500	0.280
S40_CS023	damage - overtopping	V	0.120	1.36	1500	0.280

TABLE A.4 Output wave characteristics of the tests on the physical model of the upgraded Catania harbor breakwater: section n. 10.

Test	H_s [m]	T_p [s]	$T_{m-1,0}$ [s]	T_m [s]	$\xi_{m-1,0}$	k_r
S10_E001	0.062	1.15	0.95	0.85	2.37	0.18
S10_E002	0.064	1.13	0.99	0.88	2.44	0.20
S10_E003	0.064	1.16	0.99	0.88	2.45	0.20
S10_E004	0.063	1.19	0.99	0.89	2.45	0.19
S10_E005	0.069	1.18	1.01	0.90	2.41	0.19
S10_E006	0.070	1.20	1.03	0.92	2.44	0.21
S10_E007	0.075	1.24	1.02	0.91	2.33	0.20
S10_E008	0.072	1.21	1.02	0.91	2.39	0.21
S10_E009	0.079	1.12	1.10	0.95	2.44	0.24
S10_E010	0.082	1.32	1.08	0.95	2.36	0.23
S10_E011	0.083	1.36	1.08	0.95	2.36	0.24
S10_E012	0.076	1.39	1.14	0.96	2.59	0.27
S10_E013	0.091	1.25	1.15	1.01	2.38	0.24
S10_E014	0.091	0.97	1.15	0.99	2.38	0.26
S10_E015	0.092	1.25	1.17	1.02	2.41	0.25
S10_E016	0.093	1.46	1.16	1.00	2.38	0.27
S10_E017	0.092	1.33	1.20	1.01	2.46	0.27
S10_E018	0.099	1.24	1.20	1.05	2.37	0.26
S10_E019	0.106	1.33	1.21	1.04	2.32	0.27
S10_E020	0.109	1.33	1.23	1.07	2.32	0.26
S10_E021	0.105	1.67	1.29	1.09	2.48	0.27
S10_ESLR001	0.084	1.33	1.11	0.97	2.39	0.22
S10_ESLR002	0.086	1.26	1.09	0.96	2.32	0.24
S10_ESLR003	0.083	1.26	1.13	0.98	2.45	0.24
S10_ESLR004	0.086	1.30	1.09	0.95	2.32	0.24
S10_ESLR005	0.100	1.36	1.17	1.01	2.32	0.24
S10_ESLR006	0.094	1.23	1.13	0.98	2.31	0.24
S10_ESLR007	0.088	1.41	1.12	0.98	2.36	0.26
S10_ESLR008	0.093	1.33	1.12	0.97	2.30	0.25
S10_ESLR009	0.095	1.24	1.14	0.99	2.31	0.24
S10_ESLR010	0.092	1.40	1.17	1.01	2.40	0.27
S10_EM001	0.060	1.12	0.99	0.90	2.51	0.21
S10_EM002	0.061	1.15	0.98	0.87	2.48	0.23
S10_EM003	0.063	1.18	0.99	0.87	2.46	0.23
S10_EM004	0.062	1.22	1.00	0.87	2.50	0.24
S10_EM005	0.070	1.26	1.05	0.92	2.49	0.25
S10_EM006	0.070	1.29	1.06	0.93	2.51	0.26
S10_EM007	0.071	1.22	1.04	0.91	2.42	0.24
S10_EM008	0.073	1.22	1.04	0.93	2.41	0.23
S10_EM009	0.083	1.22	1.11	0.96	2.42	0.27
S10_EM010	0.082	1.37	1.11	0.96	2.42	0.26
S10_EM011	0.082	1.37	1.15	0.98	2.49	0.28
S10_EM012	0.083	1.32	1.13	0.98	2.45	0.27

TABLE A.4 Output wave characteristics of the tests on the physical model of the upgraded Catania harbor breakwater: section n. 10 (continued).

Test	H_s [m]	T_p [s]	$T_{m-1,0}$ [s]	T_m [s]	$\zeta_{m-1,0}$	k_r
S10_EM013	0.090	1.46	1.19	1.02	2.48	0.27
S10_EM014	0.089	1.47	1.20	1.02	2.52	0.26
S10_EM015	0.093	1.40	1.16	1.01	2.38	0.28
S10_EM016	0.089	1.41	1.19	1.03	2.48	0.26
S10_EM017	0.107	1.49	1.26	1.06	2.41	0.29
S10_EM018	0.110	1.40	1.25	1.08	2.35	0.28
S10_EM019	0.110	1.35	1.33	1.11	2.50	0.29
S10_EM020	0.106	1.47	1.21	1.02	2.33	0.26
S10_AS001	0.068	1.18	0.99	0.89	2.38	0.26
S10_AS002	0.060	1.18	1.00	0.87	2.54	0.28
S10_AS003	0.060	1.20	0.98	0.86	2.49	0.29
S10_AS004	0.061	1.22	1.03	0.89	2.62	0.30
S10_AS005	0.064	1.17	0.98	0.87	2.40	0.29
S10_AS006	0.068	1.18	1.02	0.91	2.45	0.29
S10_AS007	0.069	1.12	1.06	0.94	2.53	0.28
S10_AS008	0.073	1.29	1.04	0.93	2.41	0.28
S10_AS009	0.072	1.24	1.03	0.93	2.39	0.29
S10_AS010	0.072	1.25	1.04	0.92	2.41	0.28
S10_AS011	0.078	1.31	1.11	0.96	2.47	0.28
S10_AS012	0.080	1.36	1.13	0.98	2.49	0.28
S10_AS013	0.081	1.29	1.09	0.95	2.39	0.27
S10_AS014	0.077	1.31	1.15	0.99	2.60	0.27
S10_AS015	0.082	1.39	1.10	0.95	2.40	0.26
S10_AS016	0.087	1.39	1.13	0.99	2.40	0.27
S10_AS017	0.088	1.07	1.15	0.99	2.42	0.27
S10_AS018	0.102	1.32	1.21	1.03	2.37	0.28
S10_AS019	0.092	1.15	1.14	1.00	2.34	0.28
S10_AS020	0.092	1.37	1.16	1.01	2.38	0.28
S10_AS021	0.093	1.26	1.17	1.02	2.40	0.30
S10_AS022	0.088	1.36	1.18	1.02	2.47	0.28
S10_AS023	0.102	1.39	1.20	1.03	2.35	0.26
S10_AS024	0.110	1.17	1.23	1.06	2.32	0.26
S10_AS025	0.104	1.44	1.24	1.06	2.40	0.30
S10_AS026	0.105	1.40	1.25	1.07	2.41	0.27
S10_AS027	0.106	1.40	1.28	1.07	2.46	0.26
S10_AS028	0.105	1.35	1.19	1.03	2.29	0.26
S10_AS029	0.105	1.30	1.25	1.06	2.40	0.27
S10_AD001	0.058	1.18	0.97	0.87	2.52	0.18
S10_AD002	0.063	1.18	1.01	0.89	2.52	0.20
S10_AD003	0.065	1.12	0.97	0.87	2.39	0.23
S10_AD004	0.065	1.22	0.98	0.87	2.41	0.22
S10_AD005	0.065	1.07	1.00	0.89	2.44	0.22
S10_AD006	0.072	1.13	1.02	0.91	2.37	0.22

TABLE A.4 Output wave characteristics of the tests on the physical model of the upgraded Catania harbor breakwater: section n. 10 (continued).

Test	H_s [m]	T_p [s]	$T_{m-1,0}$ [s]	T_m [s]	$\xi_{m-1,0}$	k_r
S10_AD007	0.068	1.24	1.04	0.92	2.50	0.23
S10_AD008	0.071	1.24	1.05	0.93	2.45	0.23
S10_AD009	0.069	1.22	1.02	0.89	2.43	0.23
S10_AD010	0.081	1.39	1.10	0.96	2.42	0.22
S10_AD011	0.081	1.31	1.10	0.97	2.43	0.21
S10_AD012	0.081	1.46	1.14	0.97	2.49	0.23
S10_AD013	0.081	1.33	1.09	0.95	2.38	0.22
S10_AD014	0.085	1.31	1.18	1.03	2.53	0.22
S10_AD015	0.090	1.37	1.16	1.01	2.41	0.22
S10_AD016	0.086	1.21	1.17	1.02	2.48	0.23
S10_AD017	0.093	1.31	1.16	1.01	2.38	0.22
S10_AD018	0.088	1.44	1.15	0.99	2.42	0.24
S10_AD019	0.105	1.59	1.29	1.06	2.49	0.26
S10_AD020	0.106	1.46	1.25	1.07	2.40	0.24
S10_AD021	0.107	1.30	1.27	1.08	2.42	0.27
S10_AD022	0.105	1.29	1.22	1.06	2.35	0.25
S10_CM001	0.066	1.18	0.97	0.86	2.35	0.28
S10_CM002	0.063	1.12	0.99	0.88	2.47	0.29
S10_CM003	0.062	1.24	0.99	0.88	2.47	0.30
S10_CM004	0.063	1.19	0.97	0.86	2.42	0.30
S10_CM005	0.061	1.18	0.98	0.87	2.49	0.31
S10_CM006	0.068	1.18	1.05	0.94	2.53	0.29
S10_CM007	0.070	1.21	1.03	0.90	2.43	0.30
S10_CM008	0.070	1.19	1.03	0.90	2.42	0.29
S10_CM009	0.073	1.25	1.04	0.92	2.41	0.29
S10_CM010	0.086	1.29	1.09	0.95	2.32	0.27
S10_CM011	0.080	1.32	1.13	0.99	2.49	0.28
S10_CM012	0.083	1.29	1.08	0.95	2.35	0.27
S10_CM013	0.080	1.34	1.10	0.96	2.42	0.28
S10_CM014	0.090	1.40	1.21	1.03	2.51	0.26
S10_CM015	0.091	1.33	1.14	0.99	2.37	0.26
S10_CM016	0.091	1.37	1.17	1.03	2.43	0.27
S10_CM017	0.093	1.33	1.15	1.00	2.35	0.26
S10_CM018	0.109	1.23	1.23	1.06	2.33	0.26
S10_CM019	0.109	1.41	1.24	1.06	2.34	0.26
S10_CM020	0.107	1.46	1.27	1.07	2.42	0.27
S10_CM021	0.106	1.41	1.21	1.06	2.31	0.26
S10_CS001	0.068	1.18	1.01	0.90	2.43	0.34
S10_CS002	0.072	1.17	1.01	0.90	2.35	0.33
S10_CS003	0.071	1.17	1.05	0.94	2.46	0.35
S10_CS004	0.072	1.18	1.04	0.92	2.42	0.35
S10_CS005	0.071	1.29	1.07	0.94	2.52	0.34
S10_CS006	0.073	1.23	1.06	0.94	2.45	0.34

TABLE A.4 Output wave characteristics of the tests on the physical model of the upgraded Catania harbor breakwater: section n. 10 (continued).

Test	H_s [m]	T_p [s]	$T_{m-1,0}$ [s]	T_m [s]	$\zeta_{m-1,0}$	k_r
S10_CS007	0.074	1.30	1.08	0.93	2.47	0.34
S10_CS008	0.074	1.15	1.05	0.93	2.42	0.34
S10_CS009	0.078	1.32	1.15	0.98	2.56	0.32
S10_CS010	0.082	1.30	1.12	0.97	2.44	0.32
S10_CS011	0.083	1.36	1.15	0.99	2.50	0.32
S10_CS012	0.084	1.31	1.13	0.98	2.44	0.33
S10_CS013	0.090	1.40	1.18	1.03	2.46	0.30
S10_CS014	0.093	1.46	1.22	1.04	2.49	0.31
S10_CS015	0.094	1.30	1.16	1.01	2.36	0.32
S10_CS016	0.093	1.51	1.19	1.03	2.44	0.30
S10_CS017	0.105	1.31	1.22	1.06	2.34	0.32
S10_CS018	0.112	1.32	1.22	1.04	2.27	0.32
S10_CS019	0.113	1.37	1.20	1.05	2.24	0.32
S10_CS020	0.112	1.31	1.28	1.08	2.40	0.31

TABLE A.5 Output wave characteristics of the tests on the physical model of the upgraded Catania harbor breakwater: section n. 40.

Test	H_s [m]	T_p [s]	$T_{m-1,0}$ [s]	T_m [s]	$\zeta_{m-1,0}$	k_r
S40_E001	0.070	1.15	1.01	0.90	2.39	0.20
S40_E002	0.072	1.14	1.01	0.90	2.35	0.19
S40_E003	0.075	1.18	1.01	0.91	2.31	0.19
S40_E004	0.070	1.20	0.99	0.88	2.33	0.19
S40_E005	0.068	1.12	0.99	0.88	2.38	0.19
S40_E006	0.070	1.25	1.04	0.93	2.45	0.20
S40_E007	0.071	1.24	1.04	0.93	2.44	0.19
S40_E008	0.075	1.25	1.06	0.93	2.40	0.20
S40_E009	0.076	1.22	1.02	0.91	2.33	0.19
S40_E010	0.087	1.10	1.12	0.96	2.36	0.22
S40_E011	0.092	1.35	1.14	0.99	2.34	0.21
S40_E012	0.093	1.27	1.14	0.99	2.34	0.21
S40_E013	0.090	1.35	1.14	0.99	2.38	0.21
S40_E014	0.090	1.42	1.14	0.98	2.38	0.22
S40_E015	0.102	1.05	1.23	1.05	2.40	0.25
S40_E016	0.102	1.05	1.23	1.05	2.40	0.25
S40_E017	0.102	1.05	1.23	1.05	2.40	0.25
S40_E018	0.100	1.27	1.19	1.02	2.36	0.24
S40_E019	0.097	1.41	1.19	1.04	2.40	0.25
S40_E020	0.099	1.24	1.15	1.02	2.28	0.22
S40_E021	0.102	1.33	1.18	1.03	2.30	0.24
S40_E022	0.099	1.33	1.19	1.03	2.37	0.25
S40_E023	0.106	1.41	1.28	1.08	2.45	0.26

TABLE A.5 Output wave characteristics of the tests on the physical model of the upgraded Catania harbor breakwater: section n. 40 (continued).

Test	H_s [m]	T_p [s]	$T_{m-1,0}$ [s]	T_m [s]	$\xi_{m-1,0}$	k_r
S40_E024	0.109	1.43	1.25	1.07	2.36	0.24
S40_E025	0.105	1.40	1.26	1.07	2.43	0.25
S40_E026	0.107	1.41	1.23	1.07	2.36	0.23
S40_ESLR001	0.107	1.38	1.20	1.07	2.30	0.27
S40_ESLR002	0.094	1.32	1.16	1.01	2.36	0.29
S40_ESLR003	0.083	1.31	1.09	0.96	2.37	0.28
S40_ESLR004	0.081	1.32	1.10	0.96	2.40	0.29
S40_ESLR005	0.094	1.26	1.13	0.99	2.30	0.27
S40_ESLR006	0.092	1.35	1.14	0.99	2.36	0.29
S40_ESLR007	0.089	1.42	1.16	1.00	2.43	0.29
S40_ESLR008	0.089	1.32	1.19	1.03	2.50	0.29
S40_ESLR009	0.093	1.32	1.12	0.99	2.30	0.28
S40_ESLR010	0.091	1.41	1.20	1.02	2.47	0.30
S40_ESLR011	0.102	1.36	1.17	1.02	2.29	0.29
S40_ESLR012	0.099	1.41	1.18	1.01	2.35	0.30
S40_ESLR013	0.098	1.32	1.14	1.00	2.29	0.28
S40_ESLR014	0.100	1.44	1.17	1.01	2.31	0.26
S40_EM001	0.063	1.15	0.97	0.87	2.41	0.21
S40_EM002	0.069	1.20	1.01	0.90	2.39	0.20
S40_EM003	0.072	1.19	1.02	0.91	2.37	0.21
S40_EM004	0.074	1.12	1.00	0.91	2.29	0.19
S40_EM005	0.073	1.20	1.05	0.92	2.43	0.21
S40_EM006	0.068	1.15	0.99	0.89	2.38	0.20
S40_EM007	0.071	1.25	1.03	0.91	2.42	0.21
S40_EM008	0.071	1.24	1.03	0.91	2.42	0.22
S40_EM009	0.070	1.24	1.02	0.89	2.39	0.23
S40_EM010	0.077	1.31	1.09	0.95	2.46	0.24
S40_EM011	0.089	1.19	1.12	0.98	2.36	0.23
S40_EM012	0.085	1.27	1.12	0.97	2.41	0.23
S40_EM013	0.090	1.35	1.12	0.98	2.34	0.24
S40_EM014	0.086	1.35	1.13	0.99	2.42	0.26
S40_EM015	0.100	1.40	1.21	1.04	2.40	0.26
S40_EM016	0.102	1.33	1.18	1.02	2.31	0.25
S40_EM017	0.101	1.35	1.21	1.03	2.38	0.28
S40_EM018	0.104	1.49	1.22	1.04	2.36	0.27
S40_EM019	0.111	1.54	1.19	1.01	2.22	0.26
S40_EM020	0.106	1.32	1.24	1.06	2.38	0.29
S40_EM021	0.105	1.30	1.22	1.05	2.36	0.25
S40_EM022	0.107	1.40	1.23	1.06	2.34	0.26
S40_AS007	0.091	1.33	1.14	0.99	2.37	0.29
S40_AS010	0.078	1.33	1.04	0.91	2.33	0.27
S40_AS011	0.080	1.33	1.06	0.92	2.35	0.28
S40_AS012	0.081	1.33	1.05	0.92	2.31	0.27

TABLE A.5 Output wave characteristics of the tests on the physical model of the upgraded Catania harbor breakwater: section n. 40 (continued).

Test	H_s [m]	T_p [s]	$T_{m-1,0}$ [s]	T_m [s]	$\zeta_{m-1,0}$	k_r
S40_AS015	0.086	1.27	1.13	0.98	2.40	0.26
S40_AS013	0.071	1.35	1.08	0.93	2.54	0.27
S40_AS014	0.063	1.43	1.11	0.91	2.76	0.28
S40_AS016	0.069	1.37	1.03	0.88	2.46	0.28
S40_AS022	0.089	1.32	1.10	0.96	2.31	0.26
S40_AS017	0.076	1.33	1.07	0.93	2.44	0.27
S40_AS023	0.090	1.40	1.11	0.96	2.31	0.26
S40_AS028	0.092	1.20	1.06	0.95	2.18	0.25
S40_AS037	0.102	1.32	1.16	1.00	2.27	0.24
S40_AS029	0.087	1.19	1.07	0.95	2.27	0.26
S40_AS036	0.101	1.44	1.22	1.04	2.40	0.23
S40_AS038	0.104	1.31	1.14	0.99	2.20	0.24
S40_AS040	0.109	1.41	1.14	0.99	2.15	0.23
S40_AS039	0.105	1.35	1.13	0.98	2.18	0.23
S40_AS051	0.108	1.34	1.23	1.04	2.33	0.25
S40_AS060	0.110	1.82	1.42	1.13	2.66	0.28
S40_AD001	0.078	1.19	1.06	0.93	2.37	0.26
S40_AD002	0.082	1.16	1.02	0.91	2.22	0.26
S40_AD003	0.076	1.19	1.03	0.92	2.33	0.27
S40_AD004	0.075	1.18	0.99	0.88	2.25	0.25
S40_AD005	0.074	1.13	0.98	0.88	2.26	0.26
S40_AD006	0.073	1.17	0.98	0.88	2.27	0.26
S40_AD007	0.073	1.11	0.98	0.88	2.25	0.25
S40_AD008	0.067	1.12	1.00	0.90	2.42	0.27
S40_AD009	0.073	1.15	1.02	0.91	2.37	0.26
S40_AD010	0.072	1.26	1.01	0.90	2.34	0.26
S40_AD011	0.074	1.24	1.02	0.91	2.35	0.27
S40_AD012	0.074	1.21	1.02	0.91	2.36	0.26
S40_AD013	0.084	1.42	1.10	0.94	2.38	0.29
S40_AD014	0.091	1.27	1.11	0.95	2.30	0.26
S40_AD015	0.091	1.27	1.12	0.97	2.33	0.27
S40_AD016	0.091	1.27	1.10	0.95	2.28	0.25
S40_AD017	0.091	1.33	1.12	0.97	2.32	0.25
S40_AD018	0.099	1.33	1.13	1.00	2.25	0.24
S40_AD019	0.109	1.36	1.22	1.06	2.30	0.22
S40_AD020	0.105	1.31	1.18	1.02	2.28	0.23
S40_AD021	0.105	1.31	1.17	1.03	2.27	0.23
S40_AD022	0.104	1.37	1.18	1.02	2.29	0.23
S40_AD023	0.108	1.33	1.21	1.06	2.29	0.21
S40_AD024	0.109	1.39	1.22	1.06	2.32	0.22
S40_AD025	0.111	1.44	1.21	1.05	2.28	0.21
S40_AD026	0.110	1.41	1.23	1.06	2.31	0.22
S40_AD027	0.113	1.22	1.22	1.06	2.28	0.22

TABLE A.5 Output wave characteristics of the tests on the physical model of the upgraded Catania harbor breakwater: section n. 40 (continued).

Test	H_s [m]	T_p [s]	$T_{m-1,0}$ [s]	T_m [s]	$\xi_{m-1,0}$	k_r
S40_CM001	0.072	1.12	1.01	0.91	2.35	0.23
S40_CM002	0.069	1.18	1.01	0.91	2.41	0.23
S40_CM003	0.070	1.19	1.06	0.94	2.51	0.24
S40_CM004	0.071	1.17	1.05	0.92	2.46	0.26
S40_CM005	0.075	1.28	1.07	0.95	2.44	0.24
S40_CM006	0.073	1.24	1.05	0.92	2.42	0.25
S40_CM007	0.069	1.30	1.02	0.90	2.44	0.25
S40_CM008	0.068	1.19	1.03	0.90	2.47	0.25
S40_CM009	0.080	1.33	1.12	0.98	2.48	0.25
S40_CM010	0.090	1.30	1.14	0.99	2.36	0.24
S40_CM011	0.090	1.33	1.13	0.98	2.34	0.24
S40_CM012	0.088	1.33	1.12	0.98	2.37	0.24
S40_CM013	0.093	1.33	1.15	1.01	2.36	0.24
S40_CM014	0.088	1.33	1.13	0.97	2.39	0.24
S40_CM015	0.100	1.33	1.20	1.03	2.37	0.24
S40_CM016	0.097	1.14	1.19	1.02	2.38	0.23
S40_CM017	0.099	1.39	1.19	1.02	2.37	0.24
S40_CM018	0.101	1.39	1.20	1.03	2.36	0.23
S40_CM019	0.101	1.39	1.20	1.01	2.36	0.24
S40_CM020	0.105	1.31	1.21	1.05	2.34	0.23
S40_CM021	0.103	1.32	1.20	1.03	2.33	0.23
S40_CM022	0.101	1.07	1.20	1.03	2.35	0.24
S40_CM023	0.088	1.25	1.18	1.03	2.50	0.24
S40_CM024	0.079	1.43	1.10	0.95	2.45	0.23
S40_CM025	0.077	1.52	1.13	0.96	2.55	0.22
S40_CM026	0.079	1.26	1.11	0.97	2.48	0.25
S40_CM027	0.105	1.43	1.19	1.04	2.30	0.22
S40_CM028	0.105	1.52	1.22	1.06	2.35	0.21
S40_CM029	0.106	1.32	1.19	1.04	2.29	0.22
S40_CM030	0.105	1.40	1.21	1.06	2.34	0.21
S40_CS001	0.069	1.15	0.97	0.87	2.31	0.23
S40_CS002	0.071	1.16	1.01	0.89	2.36	0.22
S40_CS003	0.072	1.18	1.00	0.90	2.34	0.22
S40_CS004	0.073	1.18	1.01	0.91	2.34	0.21
S40_CS005	0.077	1.12	1.00	0.90	2.24	0.21
S40_CS006	0.075	1.13	0.99	0.88	2.26	0.22
S40_CS007	0.073	1.13	1.00	0.88	2.30	0.23
S40_CS008	0.071	1.20	1.03	0.90	2.40	0.23
S40_CS009	0.073	1.24	1.03	0.90	2.37	0.23
S40_CS010	0.075	1.18	1.00	0.89	2.29	0.22
S40_CS011	0.085	1.37	1.10	0.95	2.34	0.25
S40_CS012	0.092	1.24	1.10	0.96	2.26	0.23
S40_CS013	0.085	1.24	1.16	0.99	2.48	0.24

TABLE A.5 Output wave characteristics of the tests on the physical model of the upgraded Catania harbor breakwater: section n. 40 (continued).

Test	H_s [m]	T_p [s]	$T_{m-1,0}$ [s]	T_m [s]	$\zeta_{m-1,0}$	k_r
S40_CS014	0.089	1.27	1.10	0.97	2.32	0.23
S40_CS015	0.098	1.44	1.20	1.01	2.40	0.25
S40_CS016	0.098	1.39	1.19	1.04	2.38	0.25
S40_CS017	0.094	1.39	1.19	1.03	2.44	0.25
S40_CS018	0.096	1.32	1.18	1.01	2.38	0.25
S40_CS019	0.094	1.43	1.22	1.01	2.49	0.27
S40_CS020	0.105	1.11	1.18	1.01	2.27	0.25
S40_CS021	0.105	1.32	1.25	1.05	2.40	0.28
S40_CS022	0.106	1.35	1.18	1.02	2.27	0.22
S40_CS023	0.104	1.35	1.20	1.02	2.33	0.24

TABLE A.6 Experimental data on damage of the armor layer and mean overtopping discharge derived from the tests on the physical model of the upgraded Catania harbor breakwater: section n. 10. The bold values, which have been recorded before starting the experiments, refers to the zero-damage condition.

Test	Cumulative damage of the armor layer					Mean overtopping		
	$H_s/\Delta D_{n50}$	N_{od}	$S_{d,m}$	HD/λ_M	λ_m/D_{n50}	R_c/H_s	q [m³/s · m]	q^*
S10_E001	1.88	0.00	-	**0.091**	**0.882**	1.84	-	-
S10_E002	1.93	0.00	-	-	-	1.79	1.06×10^{-6}	2.11×10^{-5}
S10_E003	1.93	0.00	-	-	-	1.79	6.63×10^{-7}	1.32×10^{-5}
S10_E004	1.92	0.00	0.23	0.095	0.935	1.80	8.62×10^{-7}	1.72×10^{-5}
S10_E005	2.08	0.00	-	-	-	1.66	-	-
S10_E006	2.13	0.00	-	-	-	1.63	2.29×10^{-6}	3.93×10^{-5}
S10_E007	2.26	0.00	-	-	-	1.53	1.76×10^{-6}	2.76×10^{-5}
S10_E008	2.17	0.00	-	-	-	1.59	2.81×10^{-6}	4.68×10^{-5}
S10_E009	2.39	0.00	-	-	-	1.45	-	-
S10_E010	2.49	0.03	-	-	-	1.39	5.95×10^{-6}	8.02×10^{-5}
S10_E011	2.50	0.06	-	-	-	1.38	5.34×10^{-6}	7.17×10^{-5}
S10_E012	2.30	0.06	0.53	0.095	0.946	1.51	5.64×10^{-6}	8.61×10^{-5}
S10_E013	2.75	0.06	-	-	-	1.26	-	-
S10_E014	2.76	0.06	-	-	-	1.25	-	-
S10_E015	2.79	0.09	-	-	-	1.24	1.29×10^{-5}	1.47×10^{-4}
S10_E016	2.81	0.09	-	-	-	1.23	1.37×10^{-5}	1.54×10^{-4}
S10_E017	2.80	0.09	0.72	0.093	0.974	1.24	1.33×10^{-5}	1.51×10^{-4}
S10_E018	3.01	0.09	-	-	-	1.15	-	-
S10_E019	3.21	0.09	-	-	-	1.08	1.60×10^{-5}	1.48×10^{-4}
S10_E020	3.29	0.09	-	-	-	1.05	1.46×10^{-5}	1.30×10^{-4}
S10_E021	3.18	0.09	0.99	0.091	1.026	1.09	8.74×10^{-6}	8.18×10^{-5}
S10_ESLR001	2.55	0.00	-	-	-	1.12	-	-
S10_ESLR002	2.59	0.00	-	-	-	1.10	4.26×10^{-5}	5.44×10^{-4}
S10_ESLR003	2.51	0.00	-	-	-	1.14	4.09×10^{-5}	5.49×10^{-4}

TABLE A.6 Experimental data on damage of the armor layer and mean overtopping discharge derived from the tests on the physical model of the upgraded Catania harbor breakwater: section n. 10. The bold values, which have been recorded before starting the experiments, refers to the zero-damage condition (continued).

Test	Cumulative damage of the armor layer					Mean overtopping		
	$H_s/\Delta D_{n50}$	N_{od}	$S_{d,m}$	HD/λ_M	λ_m/D_{n50}	R_c/H_s	q $[\text{m}^3/\text{s}\cdot\text{m}]$	q^*
S10_ESLR004	2.61	0.00	-	-	-	1.09	4.20×10^{-5}	5.28×10^{-4}
S10_ESLR005	3.04	0.00	-	-	-	0.94	-	-
S10_ESLR006	2.83	0.00	-	-	-	1.01	-	-
S10_ESLR007	2.67	0.00	-	-	-	1.07	-	-
S10_ESLR008	2.83	0.03	-	-	-	1.01	4.68×10^{-5}	5.24×10^{-4}
S10_ESLR009	2.87	0.03	-	-	-	1.00	4.77×10^{-5}	5.23×10^{-4}
S10_ESLR010	2.79	0.03	-	-	-	1.02	4.73×10^{-5}	5.41×10^{-4}
S10_EM001	1.82	0.00	-	**0.085**	**0.784**	2.13	-	-
S10_EM002	1.86	0.00	-	-	-	2.09	4.15×10^{-7}	8.69×10^{-6}
S10_EM003	1.92	0.00	-	-	-	2.03	5.11×10^{-7}	1.02×10^{-5}
S10_EM004	1.88	0.03	0.29	0.078	0.841	2.06	5.57×10^{-7}	1.14×10^{-5}
S10_EM005	2.11	0.03	-	-	-	1.84	-	-
S10_EM006	2.11	0.03	-	-	-	1.85	8.49×10^{-7}	1.48×10^{-5}
S10_EM007	2.16	0.03	-	-	-	1.80	9.37×10^{-7}	1.57×10^{-5}
S10_EM008	2.22	0.03	-	-	-	1.75	1.00×10^{-6}	1.61×10^{-5}
S10_EM009	2.50	0.03	-	-	-	1.55	-	-
S10_EM010	2.49	0.03	-	**-**	**-**	1.56	1.71×10^{-6}	2.31×10^{-5}
S10_EM011	2.50	0.03	-	-	-	1.56	1.82×10^{-6}	2.45×10^{-5}
S10_EM012	2.50	0.03	0.55	0.076	0.858	1.55	2.08×10^{-6}	2.79×10^{-5}
S10_EM013	2.72	0.03	-	-	-	1.43	-	-
S10_EM014	2.69	0.03	-	-	-	1.45	2.45×10^{-6}	2.96×10^{-5}
S10_EM015	2.82	0.03	-	-	-	1.38	3.63×10^{-6}	4.09×10^{-5}
S10_EM016	2.71	0.03	0.80	0.073	0.810	1.44	3.04×10^{-6}	3.63×10^{-5}
S10_EM017	3.24	0.03	-	-	-	1.20	-	-
S10_EM018	3.33	0.03	-	-	-	1.17	4.78×10^{-6}	4.19×10^{-5}
S10_EM019	3.34	0.03	-	-	-	1.17	5.52×10^{-6}	4.82×10^{-5}
S10_EM020	3.20	0.03	1.11	0.076	0.751	1.22	5.15×10^{-6}	4.78×10^{-5}
S10_AS001	2.64	1.36	-	**0.115**	**0.976**	1.75	-	-
S10_AS002	2.33	1.48	-	-	-	1.98	-	-
S10_AS003	2.34	2.00	-	-	-	1.97	9.92×10^{-7}	2.14×10^{-5}
S10_AS004	2.35	2.06	-	-	-	1.96	4.15×10^{-7}	8.88×10^{-6}
S10_AS005	2.50	2.08	2.55	0.057	0.772	1.84	8.96×10^{-7}	1.75×10^{-5}
S10_AS006	2.64	2.08	-	-	-	1.74	-	-
S10_AS007	2.67	2.08	-	-	-	1.72	-	-
S10_AS008	2.83	2.12	-	-	-	1.63	6.07×10^{-7}	9.87×10^{-6}
S10_AS009	2.81	2.12	-	-	-	1.64	2.56×10^{-7}	4.18×10^{-6}
S10_AS010	2.79	2.12	-	-	-	1.65	4.32×10^{-7}	7.15×10^{-6}
S10_AS011	3.02	2.12	-	-	-	1.52	-	-
S10_AS012	3.09	2.16	-	**-**	**-**	1.49	-	-
S10_AS013	3.16	2.41	-	-	-	1.46	4.98×10^{-7}	6.84×10^{-6}
S10_AS014	2.99	2.79	-	-	-	1.54	7.83×10^{-7}	1.17×10^{-5}

TABLE A.6 Experimental data on damage of the armor layer and mean overtopping discharge derived from the tests on the physical model of the upgraded Catania harbor breakwater: section n. 10. The bold values, which have been recorded before starting the experiments, refers to the zero-damage condition (continued).

Test	Cumulative damage of the armor layer						Mean overtopping	
	$H_s/\Delta D_{n50}$	N_{od}	$S_{d,m}$	HD/λ_M	λ_m/D_{n50}	R_c/H_s	q $[\text{m}^3/\text{s}\cdot\text{m}]$	q^*
S10_AS015	3.18	3.06	3.57	0.061	0.737	1.45	1.12×10^{-6}	1.52×10^{-5}
S10_AS016	3.37	3.08	-	-	-	1.36	-	-
S10_AS017	3.42	3.14	-	-	-	1.34	-	-
S10_AS018	3.95	3.22	-	-	-	1.17	-	-
S10_AS019	3.58	3.49	-	-	-	1.28	-	-
S10_AS020	3.58	3.80	-	-	-	1.29	6.19×10^{-6}	7.06×10^{-5}
S10_AS021	3.62	3.88	-	-	-	1.27	1.43×10^{-6}	1.61×10^{-5}
S10_AS022	3.43	4.01	4.90	0.067	0.772	1.34	2.85×10^{-6}	3.47×10^{-5}
S10_AS023	3.94	4.36	-	-	-	1.17	-	-
S10_AS024	4.28	4.44	-	-	-	1.08	-	-
S10_AS025	4.03	4.50	-	-	-	1.14	-	-
S10_AS026	4.07	4.62	-	-	-	1.13	-	-
S10_AS027	4.10	5.54	-	-	-	1.12	4.28×10^{-6}	3.99×10^{-5}
S10_AS028	4.09	5.71	-	-	-	1.13	5.78×10^{-6}	5.40×10^{-5}
S10_AS029	4.09	6.04	-	-	-	1.13	1.10×10^{-5}	1.03×10^{-4}
S10_AD001	2.25	1.40	-	**0.153**	**1.006**	2.05	-	-
S10_AD002	2.43	1.99	-	-	-	1.89	-	-
S10_AD003	2.52	2.09	-	-	-	1.83	2.11×10^{-7}	4.08×10^{-6}
S10_AD004	2.51	2.13	-	-	-	1.83	1.89×10^{-7}	3.67×10^{-6}
S10_AD005	2.54	2.15	1.40	0.054	1.006	1.82	2.33×10^{-7}	4.45×10^{-6}
S10_AD006	2.79	2.15	-	-	-	1.65	-	-
S10_AD007	2.64	2.23	-	-	-	1.74	6.85×10^{-8}	1.23×10^{-6}
S10_AD008	2.77	2.25	-	-	-	1.66	6.04×10^{-8}	1.01×10^{-6}
S10_AD009	2.66	2.27	-	-	-	1.73	7.65×10^{-8}	1.36×10^{-6}
S10_AD010	3.14	2.27	-	-	-	1.47	-	-
S10_AD011	3.13	2.54	-	-	-	1.47	1.29×10^{-6}	1.80×10^{-5}
S10_AD012	3.16	2.94	-	-	-	1.46	1.34×10^{-6}	1.83×10^{-5}
S10_AD013	3.16	2.98	2.86	0.056	0.951	1.46	5.15×10^{-7}	7.10×10^{-6}
S10_AD014	3.32	3.02	-	-	-	1.39	-	-
S10_AD015	3.49	3.08	-	-	-	1.32	-	-
S10_AD016	3.36	3.10	-	-	-	1.37	6.98×10^{-7}	8.76×10^{-6}
S10_AD017	3.59	3.22	-	-	-	1.28	1.23×10^{-6}	1.40×10^{-5}
S10_AD018	3.43	3.34	3.49	0.048	0.812	1.34	1.76×10^{-6}	2.14×10^{-5}
S10_AD019	4.07	3.47	-	-	-	1.13	-	-
S10_AD020	4.11	4.52	-	-	-	1.12	5.51×10^{-6}	5.11×10^{-5}
S10_AD021	4.15	4.52	-	-	-	1.11	4.95×10^{-6}	4.52×10^{-5}
S10_AD022	4.09	4.96	6.68	0.060	0.760	1.13	3.17×10^{-6}	2.96×10^{-5}
S10_CM001	2.00	0.25	-	**0.154**	**0.750**	1.80	-	-
S10_CM002	1.90	0.25	-	-	-	1.89	-	-
S10_CM003	1.88	0.28	-	-	-	1.91	1.54×10^{-7}	3.16×10^{-6}
S10_CM004	1.89	0.28	-	-	-	1.89	1.80×10^{-7}	3.67×10^{-6}

TABLE A.6 Experimental data on damage of the armor layer and mean overtopping discharge derived from the tests on the physical model of the upgraded Catania harbor breakwater: section n. 10. The bold values, which have been recorded before starting the experiments, refers to the zero-damage condition (continued).

Test	Cumulative damage of the armor layer					Mean overtopping		
	$H_s/\Delta D_{n50}$	N_{od}	$S_{d,m}$	HD/λ_M	λ_m/D_{n50}	R_c/H_s	q $[\mathrm{m^3/s \cdot m}]$	q^*
S10_CM005	1.84	0.33	0.36	0.076	0.697	1.95	2.03×10^{-7}	4.33×10^{-6}
S10_CM006	2.05	0.33	-	-	-	1.75	-	-
S10_CM007	2.11	0.33	-	-	-	1.70	1.54×10^{-7}	2.67×10^{-6}
S10_CM008	2.13	0.33	-	**-**	**-**	1.68	1.92×10^{-7}	3.27×10^{-6}
S10_CM009	2.21	0.33	-	-	-	1.63	2.29×10^{-7}	3.72×10^{-6}
S10_CM010	2.59	0.33	-	-	-	1.38	-	-
S10_CM011	2.43	0.41	-	-	-	1.48	6.36×10^{-7}	8.92×10^{-6}
S10_CM012	2.52	0.44	-	-	-	1.42	5.32×10^{-7}	7.06×10^{-6}
S10_CM013	2.44	0.44	0.66	0.067	0.720	1.47	3.94×10^{-7}	5.51×10^{-6}
S10_CM014	2.72	0.47	-	-	-	1.32	-	-
S10_CM015	2.75	0.62	-	-	-	1.31	1.82×10^{-6}	2.13×10^{-5}
S10_CM016	2.74	0.65	-	-	-	1.31	1.87×10^{-6}	2.20×10^{-5}
S10_CM017	2.81	0.65	1.19	0.083	0.702	1.28	2.46×10^{-6}	2.78×10^{-5}
S10_CM018	3.29	0.75	-	-	-	1.09	-	-
S10_CM019	3.28	0.83	-	-	-	1.09	9.00×10^{-6}	8.04×10^{-5}
S10_CM020	3.24	1.03	-	-	-	1.11	1.04×10^{-5}	9.47×10^{-5}
S10_CM021	3.22	1.18	2.00	0.097	0.680	1.11	1.75×10^{-5}	1.60×10^{-4}
S10_CS001	2.05	0.03	-	**0.150**	**0.708**	1.90	-	-
S10_CS002	2.18	0.08	-	-	-	1.79	2.22×10^{-7}	3.67×10^{-6}
S10_CS003	2.16	0.08	-	-	-	1.80	2.23×10^{-7}	3.73×10^{-6}
S10_CS004	2.18	0.08	0.27	0.136	0.813	1.79	2.22×10^{-7}	3.67×10^{-6}
S10_CS005	2.14	0.08	-	-	-	1.82	-	-
S10_CS006	2.21	0.08	-	-	-	1.76	4.81×10^{-8}	7.80×10^{-7}
S10_CS007	2.24	0.08	-	-	-	1.74	1.02×10^{-7}	1.62×10^{-6}
S10_CS008	2.23	0.08	-	-	-	1.74	1.98×10^{-7}	3.16×10^{-6}
S10_CS009	2.36	0.08	-	-	-	1.65	-	-
S10_CS010	2.47	0.08	-	-	-	1.58	2.30×10^{-7}	3.15×10^{-6}
S10_CS011	2.52	0.11	-	-	-	1.55	1.22×10^{-6}	1.63×10^{-5}
S10_CS012	2.54	0.11	0.54	0.131	0.734	1.53	3.60×10^{-7}	4.71×10^{-6}
S10_CS013	2.73	0.11	-	-	-	1.42	-	-
S10_CS014	2.81	0.11	-	-	-	1.38	9.14×10^{-7}	1.03×10^{-5}
S10_CS015	2.86	0.14	-	-	-	1.36	6.74×10^{-7}	7.41×10^{-6}
S10_CS016	2.82	0.17	0.84	0.138	0.707	1.38	1.10×10^{-6}	1.24×10^{-5}
S10_CS017	3.19	0.20	-	**-**	**-**	1.22	-	-
S10_CS018	3.40	0.28	-	-	-	1.15	6.24×10^{-6}	5.30×10^{-5}
S10_CS019	3.43	0.36	-	-	-	1.14	2.49×10^{-6}	2.09×10^{-5}
S10_CS020	3.39	0.39	1.82	0.117	0.659	1.15	2.62×10^{-6}	2.23×10^{-5}

TABLE A.7 Experimental data on damage of the armor layer and mean overtopping discharge derived from the tests on the physical model of the upgraded Catania harbor breakwater: section n. 40. The bold values, which have been recorded before starting the experiments, refers to the zero-damage condition.

Test	Cumulative damage of the armor layer						Mean overtopping	
	$H_s/\Delta D_{n50}$	N_{od}	$S_{d,m}$	HD/λ_M	λ_m/D_{n50}	R_c/H_s	q [m³/s · m]	q^*
S40_E001	2.11	0.78	-	**0.167**	**0.692**	1.64	-	-
S40_E002	2.19	0.78	-	-	-	1.58	-	-
S40_E003	2.27	0.83	-	-	-	1.52	2.57×10^{-6}	4.00×10^{-5}
S40_E004	2.13	0.86	-	-	-	1.62	7.67×10^{-7}	1.31×10^{-5}
S40_E005	2.06	0.86	0.52	0.105	0.715	1.68	1.43×10^{-6}	2.57×10^{-5}
S40_E006	2.13	0.86	-	-	-	1.62	-	-
S40_E007	2.15	0.86	-	-	-	1.61	1.93×10^{-6}	3.26×10^{-5}
S40_E008	2.28	0.86	-	-	-	1.51	1.95×10^{-6}	3.00×10^{-5}
S40_E009	2.29	0.86	-	-	-	1.51	1.90×10^{-6}	2.92×10^{-5}
S40_E010	2.64	0.86	-	-	-	1.31	-	-
S40_E011	2.80	0.86	-	-	-	1.24	-	-
S40_E012	2.82	0.94	-	-	-	1.23	4.21×10^{-6}	4.73×10^{-5}
S40_E013	2.72	0.99	-	-	-	1.27	2.19×10^{-6}	2.60×10^{-5}
S40_E014	2.72	1.02	0.95	0.109	0.716	1.27	3.20×10^{-6}	3.78×10^{-5}
S40_E015	3.08	1.05	-	-	-	1.12	-	-
S40_E016	3.08	1.08	-	-	-	1.12	-	-
S40_E017	3.08	1.08	-	-	-	1.12	-	-
S40_E018	3.01	1.11	-	-	-	1.15	1.53×10^{-5}	1.56×10^{-4}
S40_E019	2.92	1.11	-	-	-	1.18	1.28×10^{-5}	1.36×10^{-4}
S40_E020	2.99	1.11	1.36	0.114	0.715	1.16	1.02×10^{-5}	1.05×10^{-4}
S40_E021	3.08	1.11	-	-	-	1.12	-	-
S40_E022	2.99	1.11	-	-	-	1.16	-	-
S40_E023	3.20	1.11	-	-	-	1.08	-	-
S40_E024	3.29	1.14	-	-	-	1.05	-	-
S40_E025	3.19	1.14	-	-	-	1.09	1.38×10^{-5}	1.29×10^{-4}
S40_E026	3.23	1.14	1.70	0.110	0.745	1.07	-	-
S40_ESLR001	3.23	0.93	-	-	-	0.88	-	-
S40_ESLR002	2.85	0.96	-	-	-	1.00	-	-
S40_ESLR003	2.50	0.96	-	-	-	1.14	-	-
S40_ESLR004	2.47	0.96	-	-	-	1.16	-	-
S40_ESLR005	2.85	1.01	-	-	-	1.00	-	-
S40_ESLR006	2.78	1.01	-	-	-	1.03	-	-
S40_ESLR007	2.70	1.06	-	-	-	1.06	3.85×10^{-5}	4.60×10^{-4}
S40_ESLR008	2.68	1.06	-	-	-	1.06	2.65×10^{-5}	3.21×10^{-4}
S40_ESLR009	2.83	1.06	-	-	-	1.01	3.74×10^{-5}	4.19×10^{-4}
S40_ESLR010	2.76	1.06	-	-	-	1.04	-	-
S40_ESLR011	3.09	1.06	-	-	-	0.92	-	-
S40_ESLR012	2.98	1.19	-	-	-	0.96	4.12×10^{-5}	4.25×10^{-4}
S40_ESLR013	2.96	1.19	-	-	-	0.97	2.59×10^{-5}	2.71×10^{-4}
S40_ESLR014	3.01	1.24	-	-	-	0.95	2.11×10^{-5}	2.14×10^{-4}

TABLE A.7 Experimental data on damage of the armor layer and mean overtopping discharge derived from the tests on the physical model of the upgraded Catania harbor breakwater: section n. 40. The bold values, which have been recorded before starting the experiments, refers to the zero-damage condition (continued).

Test	Cumulative damage of the armor layer					Mean overtopping		
	$H_s/\Delta D_{n50}$	N_{od}	$S_{d,m}$	HD/λ_M	λ_m/D_{n50}	R_c/H_s	q [m³/s · m]	q^*
S40_EM001	1.92	0.18	-	**0.100**	**0.726**	2.03	-	-
S40_EM002	2.10	0.23	-	-	-	1.86	-	-
S40_EM003	2.19	0.25	-	-	-	1.78	1.12×10^{-6}	1.85×10^{-5}
S40_EM004	2.25	0.30	-	-	-	1.73	1.83×10^{-6}	2.88×10^{-5}
S40_EM005	2.20	0.30	0.63	0.078	0.748	1.77	1.84×10^{-6}	3.00×10^{-5}
S40_EM006	2.06	0.30	-	-	-	1.89	-	-
S40_EM007	2.14	0.35	-	-	-	1.82	1.09×10^{-6}	1.85×10^{-5}
S40_EM008	2.16	0.35	-	-	-	1.80	7.41×10^{-7}	1.24×10^{-5}
S40_EM009	2.13	0.35	-	-	-	1.83	6.21×10^{-7}	1.06×10^{-5}
S40_EM010	2.34	0.38	-	-	-	1.66	-	-
S40_EM011	2.68	0.45	-	-	-	1.45	-	-
S40_EM012	2.57	0.50	-	-	-	1.52	3.18×10^{-6}	4.11×10^{-5}
S40_EM013	2.71	0.50	-	-	-	1.43	2.97×10^{-6}	3.53×10^{-5}
S40_EM014	2.60	0.50	-	-	-	1.50	5.06×10^{-6}	6.43×10^{-5}
S40_EM015	3.03	0.53	-	-	-	1.28	-	-
S40_EM016	3.10	0.53	-	-	-	1.25	8.09×10^{-6}	7.88×10^{-5}
S40_EM017	3.04	0.53	-	-	-	1.28	1.11×10^{-5}	1.11×10^{-4}
S40_EM018	3.15	0.53	-	-	-	1.24	8.94×10^{-6}	8.52×10^{-5}
S40_EM019	3.36	0.53	-	-	-	1.16	-	-
S40_EM020	3.20	0.53	-	-	-	1.22	7.52×10^{-6}	6.99×10^{-5}
S40_EM021	3.18	0.53	-	-	-	1.22	7.58×10^{-6}	7.11×10^{-5}
S40_EM022	3.24	0.53	1.28	0.080	0.775	1.20	8.38×10^{-6}	7.63×10^{-5}
S40_AS007	3.52	0.33	-	**0.168**	**1.021**	1.31	-	-
S40_AS010	3.03	0.43	-	-	-	1.52	2.55×10^{-7}	3.73×10^{-6}
S40_AS011	3.10	0.43	-	-	-	1.49	1.82×10^{-7}	2.59×10^{-6}
S40_AS012	3.15	0.43	-	-	-	1.46	1.08×10^{-7}	1.48×10^{-6}
S40_AS015	3.33	0.43	-	-	-	1.38	-	-
S40_AS013	2.75	0.43	-	-	-	1.67	1.66×10^{-7}	2.80×10^{-6}
S40_AS014	2.44	0.43	-	-	-	1.89	1.61×10^{-7}	3.27×10^{-6}
S40_AS016	2.67	0.43	-	-	-	1.73	2.08×10^{-7}	3.69×10^{-6}
S40_AS022	3.46	0.43	-	-	-	1.33	-	-
S40_AS017	2.94	0.43	-	-	-	1.57	1.31×10^{-7}	2.01×10^{-6}
S40_AS023	3.48	0.43	-	-	-	1.32	9.75×10^{-8}	1.16×10^{-6}
S40_AS028	3.57	0.43	1.02	0.126	0.932	1.29	1.79×10^{-7}	2.05×10^{-6}
S40_AS037	3.95	0.43	-	-	-	1.17	-	-
S40_AS029	3.37	0.56	-	-	-	1.37	1.19×10^{-8}	1.48×10^{-7}
S40_AS036	3.91	0.60	-	-	-	1.18	5.02×10^{-8}	5.02×10^{-7}
S40_AS038	4.05	0.62	1.75	0.110	0.878	1.14	7.00×10^{-8}	6.62×10^{-7}
S40_AS040	4.24	0.62	-	-	-	1.08	-	-
S40_AS039	4.08	0.62	-	-	-	1.13	5.75×10^{-7}	5.39×10^{-6}
S40_AS051	4.21	0.84	-	-	-	1.09	6.34×10^{-7}	5.68×10^{-6}

TABLE A.7 Experimental data on damage of the armor layer and mean overtopping discharge derived from the tests on the physical model of the upgraded Catania harbor breakwater: section n. 40. The bold values, which have been recorded before starting the experiments, refers to the zero-damage condition (continued).

Test	Cumulative damage of the armor layer						Mean overtopping	
	$H_s/\Delta D_{n50}$	N_{od}	$S_{d,m}$	HD/λ_M	λ_m/D_{n50}	R_c/H_s	q $[\mathrm{m}^3/\mathrm{s} \cdot \mathrm{m}]$	q^*
S40_AS060	4.28	1.02	3.90	0.112	0.977	1.07	5.51×10^{-7}	4.80×10^{-6}
S40_AD001	3.03	0.92	-	**0.109**	**0.785**	1.52	-	-
S40_AD002	3.17	0.92	-	-	-	1.45	-	-
S40_AD003	2.95	0.92	-	-	-	1.56	-	-
S40_AD004	2.91	0.92	-	-	-	1.58	-	-
S40_AD005	2.86	0.92	-	-	-	1.61	3.54×10^{-7}	5.65×10^{-6}
S40_AD006	2.84	0.92	-	-	-	1.62	3.71×10^{-7}	5.99×10^{-6}
S40_AD007	2.84	0.92	0.99	0.066	1.092	1.62	3.36×10^{-7}	5.42×10^{-6}
S40_AD008	2.61	0.92	-	-	-	1.76	-	-
S40_AD009	2.81	0.92	-	-	-	1.64	-	-
S40_AD010	2.81	0.92	-	-	-	1.64	3.50×10^{-7}	5.75×10^{-6}
S40_AD011	2.86	0.92	-	-	-	1.61	4.03×10^{-7}	6.42×10^{-6}
S40_AD012	2.86	0.92	-	-	-	1.61	4.55×10^{-7}	7.25×10^{-6}
S40_AD013	3.24	0.92	-	-	-	1.42	-	-
S40_AD014	3.53	0.92	-	-	-	1.31	-	-
S40_AD015	3.53	1.07	-	-	-	1.30	9.73×10^{-7}	1.13×10^{-5}
S40_AD016	3.52	1.11	-	-	-	1.31	8.95×10^{-7}	1.05×10^{-5}
S40_AD017	3.53	1.11	1.82	0.065	1.014	1.31	8.17×10^{-7}	9.53×10^{-6}
S40_AD018	3.84	1.11	-	-	-	1.20	-	-
S40_AD019	4.23	1.11	-	-	-	1.09	-	-
S40_AD020	4.07	1.15	-	-	-	1.13	4.51×10^{-6}	4.24×10^{-5}
S40_AD021	4.06	1.25	-	-	-	1.13	3.68×10^{-6}	3.47×10^{-5}
S40_AD022	4.03	1.27	2.35	0.065	1.000	1.14	5.35×10^{-6}	5.10×10^{-5}
S40_AD023	4.20	1.27	-	-	-	1.09	-	-
S40_AD024	4.21	1.27	-	-	-	1.09	-	-
S40_AD025	4.30	1.31	-	-	-	1.07	3.85×10^{-6}	3.33×10^{-5}
S40_AD026	4.28	1.37	-	-	-	1.08	3.57×10^{-6}	3.12×10^{-5}
S40_AD027	4.39	1.49	3.07	0.061	0.935	1.05	3.95×10^{-6}	3.32×10^{-5}
S40_CM001	2.17	0.05	-	**0.067**	**0.693**	1.65	-	-
S40_CM002	2.09	0.05	-	-	-	1.71	4.27×10^{-7}	7.49×10^{-6}
S40_CM003	2.12	0.05	-	-	-	1.69	4.69×10^{-8}	8.08×10^{-7}
S40_CM004	2.16	0.08	0.31	0.059	0.742	1.66	3.74×10^{-7}	6.26×10^{-6}
S40_CM005	2.28	0.08	-	-	-	1.58	-	-
S40_CM006	2.20	0.08	-	-	-	1.63	3.87×10^{-7}	6.30×10^{-6}
S40_CM007	2.08	0.08	-	-	-	1.73	3.01×10^{-7}	5.35×10^{-6}
S40_CM008	2.07	0.08	-	-	-	1.74	2.16×10^{-7}	3.86×10^{-6}
S40_CM009	2.41	0.08	-	-	-	1.49	-	-
S40_CM010	2.74	0.08	-	-	-	1.31	-	-
S40_CM011	2.73	0.08	-	-	-	1.31	-	-
S40_CM012	2.66	0.08	-	-	-	1.35	1.96×10^{-6}	2.41×10^{-5}
S40_CM013	2.81	0.08	-	-	-	1.28	1.59×10^{-6}	1.79×10^{-5}

TABLE A.7 Experimental data on damage of the armor layer and mean overtopping discharge derived from the tests on the physical model of the upgraded Catania harbor breakwater: section n. 40. The bold values, which have been recorded before starting the experiments, refers to the zero-damage condition (continued).

Test	Cumulative damage of the armor layer						Mean overtopping	
	$H_s/\Delta D_{n50}$	N_{od}	$S_{d,m}$	HD/λ_M	λ_m/D_{n50}	R_c/H_s	q $[\text{m}^3/\text{s} \cdot \text{m}]$	q^*
S40_CM014	2.66	0.08	0.60	0.063	0.688	1.35	1.80×10^{-6}	2.21×10^{-5}
S40_CM015	3.01	0.08	-	-	-	1.19	-	-
S40_CM016	2.95	0.11	-	-	-	1.22	-	-
S40_CM017	2.99	0.14	-	-	-	1.20	7.15×10^{-6}	7.34×10^{-5}
S40_CM018	3.05	0.14	-	-	-	1.18	7.15×10^{-6}	7.13×10^{-5}
S40_CM019	3.05	0.17	0.96	0.048	0.573	1.18	7.15×10^{-6}	7.12×10^{-5}
S40_CM020	3.18	0.17	-	-	-	1.13	-	-
S40_CM021	3.12	0.17	-	-	-	1.15	-	-
S40_CM022	3.06	0.17	-	-	-	1.17	-	-
S40_CM023	2.66	0.17	-	-	-	1.35	-	-
S40_CM024	2.40	0.17	-	-	-	1.50	-	-
S40_CM025	2.34	0.17	-	-	-	1.53	-	-
S40_CM026	2.38	0.17	-	-	-	1.51	-	-
S40_CM027	3.18	0.17	-	-	-	1.13	-	-
S40_CM028	3.18	0.17	-	-	-	1.13	7.78×10^{-6}	7.28×10^{-5}
S40_CM029	3.22	0.17	-	-	-	1.12	-	-
S40_CM030	3.19	0.17	1.37	0.050	0.688	1.13	-	-
S40_CS001	2.09	0.00	-	**0.028**	**0.797**	1.86	-	-
S40_CS002	2.14	0.00	-	-	-	1.82	2.02×10^{-6}	3.43×10^{-5}
S40_CS003	2.16	0.00	-	-	-	1.80	1.72×10^{-6}	2.88×10^{-5}
S40_CS004	2.20	0.00	-	-	-	1.77	2.05×10^{-6}	3.33×10^{-5}
S40_CS005	2.33	0.00	-	-	-	1.67	-	-
S40_CS006	2.28	0.00	-	-	-	1.71	-	-
S40_CS007	2.22	0.00	-	-	-	1.75	-	-
S40_CS008	2.16	0.00	-	-	-	1.80	1.31×10^{-6}	2.19×10^{-5}
S40_CS009	2.21	0.00	-	-	-	1.76	9.85×10^{-7}	1.59×10^{-5}
S40_CS010	2.26	0.00	-	-	-	1.72	1.04×10^{-6}	1.62×10^{-5}
S40_CS011	2.58	0.00	-	-	-	1.51	-	-
S40_CS012	2.78	0.00	-	-	-	1.40	3.40×10^{-6}	3.89×10^{-5}
S40_CS013	2.56	0.00	-	-	-	1.52	4.72×10^{-6}	6.11×10^{-5}
S40_CS014	2.68	0.00	0.73	0.043	0.784	1.45	2.05×10^{-6}	2.48×10^{-5}
S40_CS015	2.96	0.00	-	-	-	1.31	-	-
S40_CS016	2.97	0.00	-	-	-	1.31	6.53×10^{-6}	6.78×10^{-5}
S40_CS017	2.84	0.00	-	-	-	1.37	5.58×10^{-6}	6.21×10^{-5}
S40_CS018	2.90	0.00	-	-	-	1.34	6.88×10^{-6}	7.39×10^{-5}
S40_CS019	2.84	0.00	-	-	-	1.37	-	-
S40_CS020	3.17	0.00	-	-	-	1.23	-	-
S40_CS021	3.18	0.00	-	-	-	1.22	1.01×10^{-5}	9.44×10^{-5}
S40_CS022	3.20	0.00	-	-	-	1.22	1.43×10^{-5}	1.33×10^{-4}
S40_CS023	3.13	0.00	1.69	0.022	0.785	1.24	1.38×10^{-5}	1.32×10^{-4}

A.2 Numerical tests

In the present section, a summary of the two-dimensional numerical simulations performed with the software IH2VOF (Lara et al., 2011b; Lara et al., 2011a) is provided. The Direchlet boundary condition for wave generation and the active wave absorption have been employed for testing configurations E and CS of section n. 40 of the Catania harbor breakwater. Figure 6.36 shows a sketch of the considered numerical domains and the location of the free-surface and velocity gauges, whereas Table 6.16 presents the tested combinations of porosity parameters.

Figure A.1 schematically describes the parameters of the structure geometry employed for the analysis of the experimental results, whose values are reported in Table A.8, both at model and prototype scale. Table A.9 and Table A.10show the scope of each performed simulation, and the correspondent set-up parameters and calculation time, at model and prototype scale respectively. It should be noted that the name of each simulation consists of two parts: i) "IH_C" or "IH_SP", to indicate the model and prototype scale, respectively; ii) the progressive number of the test, with reference to a certain scale. Table A.11 and Table A.12 report the input hydrodynamic conditions, at model and prototype scale respectively. Finally, Table A.13 and Table A.14 summarize the characteristics of the incident wave motion and the reflection coefficient (Faraci et al., 2015) measured during the simulations, and the numerical data on mean overtopping discharge, at model and prototype scale respectively.

TABLE A.8 Geometric characteristics of the tested structures employed for the analysis of the numerical data.

Parameter	Model scale		Prototype scale	
	E	CS	E	CS
R_c [m]	0.114-0.094	0.129	8.00-6.60	9.00
h [m]	0.280-0.300	0.280	19.60-21.00	19.60
$tan\alpha$	0.50	0.50	0.50	0.50

TABLE A.9 Scope, set-up parameters and calculation time of the numerical simulations performed for the upgraded Catania breakwater: model scale.

Simulation	Scope of the simulation	W [m]	H [m]	$\Delta x \times \Delta y$ [m × m]	Configuration	Porosity ID	Calculation time [h]
IH_C01	domain	7.00	0.65	0.020 × 0.010	E	1-0	0.48
IH_C02	domain	7.00	0.65	0.020 × 0.010	E	1-0	0.37
IH_C03	domain	7.00	0.65	0.020 × 0.010	E	1-0	0.34
IH_C04	domain	7.00	0.65	0.020 × 0.010	E	1-0	0.45
IH_C05	domain	7.00	0.65	0.020 × 0.010	E	1-0	0.51
IH_C06	domain, calibration	4.50	0.65	0.020 × 0.010	E	1-0	0.32

TABLE A.9 Scope, set-up parameters and calculation time of the numerical simulations performed for the upgraded Catania breakwater: model scale (continued).

Simulation	Scope of the simulation	W [m]	H [m]	$\Delta x \times \Delta y$ [m $\times$ m]	Configuration	Porosity ID	Calculation time [h]
IH_C07	domain, calibration	4.50	0.65	0.020×0.010	E	1-0	0.25
IH_C08	domain, calibration	4.50	0.65	0.020×0.010	E	1-0	0.22
IH_C09	domain, calibration	4.50	0.65	0.020×0.010	E	1-0	0.29
IH_C10	domain, calibration	4.50	0.65	0.020×0.010	E	1-0	0.33
IH_C11	domain	7.00	0.65	0.020×0.010	no structure	-	0.45
IH_C12	domain	7.00	0.65	0.020×0.010	no structure	-	0.36
IH_C13	domain	7.00	0.65	0.020×0.010	no structure	-	0.32
IH_C14	domain	7.00	0.65	0.020×0.010	no structure	-	0.42
IH_C15	domain	7.00	0.65	0.020×0.010	no structure	-	0.47
IH_C16	domain	4.50	0.65	0.020×0.010	no structure	-	0.29
IH_C17	domain	4.50	0.65	0.020×0.010	no structure	-	0.23
IH_C18	domain	4.50	0.65	0.020×0.010	no structure	-	0.21
IH_C19	domain	4.50	0.65	0.020×0.010	no structure	-	0.00
IH_C20	domain	4.50	0.65	0.020×0.010	no structure	-	0.30
IH_C21	domain	7.00	0.65	0.020×0.010	E	2-0	0.53
IH_C22	domain	7.00	0.65	0.020×0.010	E	2-0	0.41
IH_C23	domain	7.00	0.65	0.020×0.010	E	2-0	0.38
IH_C24	domain	7.00	0.65	0.020×0.010	E	2-0	0.49
IH_C25	domain	7.00	0.65	0.020×0.010	E	2-0	0.55
IH_C26	calibration	4.50	0.65	0.020×0.010	E	2-0	0.35
IH_C27	calibration	4.50	0.65	0.020×0.010	E	2-0	0.28
IH_C28	calibration	4.50	0.65	0.020×0.010	E	2-0	0.25
IH_C29	calibration	4.50	0.65	0.020×0.010	E	2-0	0.31
IH_C30	calibration	4.50	0.65	0.020×0.010	E	2-0	0.35
IH_C31	calibration	4.50	0.65	0.020×0.010	E	3-0	0.35
IH_C32	calibration	4.50	0.65	0.020×0.010	E	3-0	0.27
IH_C33	calibration	4.50	0.65	0.020×0.010	E	3-0	0.25
IH_C34	calibration	4.50	0.65	0.020×0.010	E	3-0	0.32
IH_C35	calibration	4.50	0.65	0.020×0.010	E	3-0	0.39
IH_C36	calibration	4.50	0.65	0.020×0.010	E	4-0	0.36
IH_C37	calibration	4.50	0.65	0.020×0.010	E	4-0	0.29
IH_C38	calibration	4.50	0.65	0.020×0.010	E	4-0	0.26
IH_C39	calibration	4.50	0.65	0.020×0.010	E	4-0	0.33
IH_C40	calibration	4.50	0.65	0.020×0.010	E	4-0	0.38
IH_C41	domain	4.50	0.65	0.010×0.005	E	1-0	3.97
IH_C42	domain	4.50	0.65	0.010×0.005	E	1-0	2.84
IH_C43	calibration	4.50	0.65	0.020×0.010	E	5-0	0.45
IH_C44	calibration	4.50	0.65	0.020×0.010	E	5-0	0.35
IH_C45	calibration	4.50	0.65	0.020×0.010	E	6-0	0.33

TABLE A.9 Scope, set-up parameters and calculation time of the numerical simulations performed for the upgraded Catania breakwater: model scale (continued).

Simulation	Scope of the simulation	W [m]	H [m]	$\Delta x \times \Delta y$ [m $\times$ m]	Configuration	Porosity ID	Calculation time [h]
IH_C46	calibration	4.50	0.65	0.020×0.010	E	6-0	0.25
IH_C47	calibration	4.50	0.65	0.020×0.010	CS	4-1	0.36
IH_C48	calibration	4.50	0.65	0.020×0.010	CS	4-2	0.38
IH_C49	calibration	4.50	0.65	0.020×0.010	CS	4-3	0.38
IH_C50	calibration	4.50	0.65	0.020×0.010	CS	4-4	0.43
IH_C51	calibration	4.50	0.65	0.020×0.010	CS	4-1	2.81
IH_C52	calibration	4.50	0.65	0.020×0.010	CS	4-2	2.12
IH_C53	calibration	4.50	0.65	0.020×0.010	CS	4-2	2.48
IH_C54	calibration	4.50	0.65	0.020×0.010	CS	4-2	4.18
IH_C55	calibration	4.50	0.65	0.020×0.010	CS	4-2	2.87
IH_C56	calibration	4.50	0.65	0.020×0.010	CS	4-2	3.10
IH_C57	calibration	4.50	0.65	0.020×0.010	E	4-0	2.52
IH_C58	calibration	4.50	0.65	0.020×0.010	E	4-0	1.97
IH_C59	calibration	4.50	0.65	0.020×0.010	E	4-0	1.89
IH_C60	calibration	4.50	0.65	0.020×0.010	E	4-0	2.39
IH_C61	calibration	4.50	0.65	0.020×0.010	E	4-0	0.04
IH_C62	calibration	4.50	0.65	0.020×0.010	CS	8-1	2.99
IH_C63	calibration	4.50	0.65	0.020×0.010	CS	8-1	3.36
IH_C64	calibration	4.50	0.65	0.020×0.010	CS	8-1	2.48
IH_C65	calibration	4.50	0.65	0.020×0.010	CS	8-1	2.41
IH_C66	calibration	4.50	0.65	0.020×0.010	CS	8-1	3.02
IH_C67	calibration	4.50	0.65	0.020×0.010	E	7-0	3.06
IH_C68	calibration	4.50	0.65	0.020×0.010	E	7-0	3.35
IH_C69	calibration	4.50	0.65	0.020×0.010	E	7-0	2.60
IH_C70	calibration	4.50	0.65	0.020×0.010	E	7-0	2.54
IH_C71	calibration	4.50	0.65	0.020×0.010	E	7-0	3.09
IH_C72	calibration, overtopping, scale-up	4.50	0.65	0.020×0.010	E	8-0	2.95
IH_C73	calibration, overtopping, scale-up	4.50	0.65	0.020×0.010	E	8-0	3.16
IH_C74	calibration, overtopping, scale-up	4.50	0.65	0.020×0.010	E	8-0	2.36
IH_C75	calibration, overtopping, scale-up	4.50	0.65	0.020×0.010	E	8-0	2.27
IH_C76	calibration, overtopping, scale-up	4.50	0.65	0.020×0.010	E	8-0	2.81
IH_C77	calibration	4.50	0.65	0.020×0.010	CS	8-1	3.19
IH_C78	calibration	4.50	0.65	0.020×0.010	CS	8-1	2.61

TABLE A.9 Scope, set-up parameters and calculation time of the numerical simulations performed for the upgraded Catania breakwater: model scale (continued).

Simulation	Scope of the simulation	W [m]	H [m]	$\Delta x \times \Delta y$ [m $\times$ m]	Configuration	Porosity ID	Calculation time [h]
IH_C79	calibration	4.50	0.65	0.020 × 0.010	CS	8-1	2.50
IH_C80	calibration	4.50	0.65	0.020 × 0.010	CS	8-1	3.06
IH_C81	calibration	4.50	0.65	0.020 × 0.010	CS	8-1	3.39
IH_C82	calibration	4.50	0.65	0.020 × 0.010	CS	8-2	2.82
IH_C83	calibration	4.50	0.65	0.020 × 0.010	CS	8-2	2.31
IH_C84	calibration	4.50	0.65	0.020 × 0.010	CS	8-2	2.21
IH_C85	calibration	4.50	0.65	0.020 × 0.010	CS	8-2	2.71
IH_C86	calibration	4.50	0.65	0.020 × 0.010	CS	8-2	2.99
IH_C87	calibration	4.50	0.65	0.020 × 0.010	CS	8-3	3.05
IH_C88	calibration	4.50	0.65	0.020 × 0.010	CS	8-3	2.46
IH_C89	calibration	4.50	0.65	0.020 × 0.010	CS	8-3	2.40
IH_C90	calibration, overtopping, scale-up	4.50	0.65	0.020 × 0.010	CS	8-3	2.84
IH_C91	calibration, overtopping, scale-up	4.50	0.65	0.020 × 0.010	CS	8-3	3.14
IH_C92	overtopping, scale-up	4.50	0.65	0.020 × 0.010	CS	8-3	2.85
IH_C93	overtopping, scale-up	4.50	0.65	0.020 × 0.010	CS	8-3	3.08
IH_C94	overtopping, scale-up	4.50	0.65	0.020 × 0.010	CS	8-3	3.50
IH_C95	overtopping	4.50	0.65	0.020 × 0.010	E	8-0	2.66
IH_C96	overtopping	4.50	0.65	0.020 × 0.010	E	8-0	2.09
IH_C97	overtopping	4.50	0.65	0.020 × 0.010	E	8-0	2.00
IH_C98	overtopping	4.50	0.65	0.020 × 0.010	E	8-0	2.50
IH_C99	overtopping	4.50	0.65	0.020 × 0.010	E	8-0	2.85
IH_C100	overtopping	4.50	0.65	0.020 × 0.010	E	8-0	2.65
IH_C101	overtopping	4.50	0.65	0.020 × 0.010	E	8-0	2.09
IH_C102	overtopping	4.50	0.65	0.020 × 0.010	E	8-0	2.01
IH_C103	overtopping	4.50	0.65	0.020 × 0.010	E	8-0	2.48
IH_C104	overtopping	4.50	0.65	0.020 × 0.010	E	8-0	2.83
IH_C105	overtopping	4.50	0.65	0.020 × 0.010	E	8-0	2.65
IH_C106	overtopping	4.50	0.65	0.020 × 0.010	E	8-0	2.09
IH_C107	overtopping	4.50	0.65	0.020 × 0.010	E	8-0	1.99
IH_C108	overtopping	4.50	0.65	0.020 × 0.010	E	8-0	2.49
IH_C109	overtopping	4.50	0.65	0.020 × 0.010	E	8-0	2.81
IH_C110	overtopping	4.50	0.65	0.020 × 0.010	E	8-0	2.64
IH_C111	overtopping	4.50	0.65	0.020 × 0.010	E	8-0	2.09
IH_C112	overtopping	4.50	0.65	0.020 × 0.010	E	8-0	1.98
IH_C113	overtopping	4.50	0.65	0.020 × 0.010	E	8-0	2.50
IH_C114	overtopping	4.50	0.65	0.020 × 0.010	E	8-0	2.84

TABLE A.9 Scope, set-up parameters and calculation time of the numerical simulations performed for the upgraded Catania breakwater: model scale (continued).

Simulation	Scope of the simulation	W [m]	H [m]	$\Delta x \times \Delta y$ [m $\times$ m]	Configuration	Porosity ID	Calculation time [h]
IH_C115	overtopping	4.50	0.65	0.020×0.010	E	8-0	2.62
IH_C116	overtopping	4.50	0.65	0.020×0.010	E	8-0	2.04
IH_C117	overtopping	4.50	0.65	0.020×0.010	E	8-0	1.97
IH_C118	overtopping	4.50	0.65	0.020×0.010	E	8-0	2.45
IH_C119	overtopping	4.50	0.65	0.020×0.010	E	8-0	2.77
IH_C120	overtopping	4.50	0.65	0.020×0.010	CS	8-3	3.04
IH_C121	overtopping	4.50	0.65	0.020×0.010	CS	8-3	3.13
IH_C122	overtopping	4.50	0.65	0.020×0.010	CS	8-3	2.88
IH_C123	overtopping	4.50	0.65	0.020×0.010	CS	8-3	3.06
IH_C124	overtopping	4.50	0.65	0.020×0.010	CS	8-3	3.39
IH_C125	overtopping	4.50	0.65	0.020×0.010	CS	8-3	2.86
IH_C126	overtopping	4.50	0.65	0.020×0.010	CS	8-3	3.10
IH_C127	overtopping	4.50	0.65	0.020×0.010	CS	8-3	3.03
IH_C128	overtopping	4.50	0.65	0.020×0.010	CS	8-3	3.06
IH_C129	overtopping	4.50	0.65	0.020×0.010	CS	8-3	3.47
IH_C130	overtopping	4.50	0.65	0.020×0.010	CS	8-3	2.97
IH_C131	overtopping	4.50	0.65	0.020×0.010	CS	8-3	3.12
IH_C132	overtopping	4.50	0.65	0.020×0.010	CS	8-3	2.85
IH_C133	overtopping	4.50	0.65	0.020×0.010	CS	8-3	3.05
IH_C134	overtopping	4.50	0.65	0.020×0.010	CS	8-3	3.56
IH_C135	overtopping	4.50	0.65	0.020×0.010	CS	8-3	2.96
IH_C136	overtopping	4.50	0.65	0.020×0.010	CS	8-3	3.09
IH_C137	overtopping	4.50	0.65	0.020×0.010	CS	8-3	2.87
IH_C138	overtopping	4.50	0.65	0.020×0.010	CS	8-3	3.05
IH_C139	overtopping	4.50	0.65	0.020×0.010	CS	8-3	3.40
IH_C140	overtopping	4.50	0.65	0.020×0.010	CS	8-3	2.95
IH_C141	overtopping	4.50	0.65	0.020×0.010	CS	8-3	3.10
IH_C142	overtopping	4.50	0.65	0.020×0.010	CS	8-3	2.79
IH_C143	overtopping	4.50	0.65	0.020×0.010	CS	8-3	3.05
IH_C144	overtopping	4.50	0.65	0.020×0.010	CS	8-3	3.42

TABLE A.10 Scope, set-up parameters and calculation time of the numerical simulations performed for the upgraded Catania breakwater: prototype scale.

Simulation	Scope of the simulation	W [m]	H [m]	$\Delta x \times \Delta y$ [m $\times$ m]	Configuration	Porosity ID	Calculation time [h]
IH_SP01	scale-up, overtopping	315.00	45.55	1.40×0.70	E	8-0	3.89
IH_SP02	scale-up, overtopping	315.00	45.55	1.40×0.71	E	8-0	3.45
IH_SP03	scale-up, overtopping	315.00	45.55	1.40×0.72	E	8-0	3.33

TABLE A.10 Scope, set-up parameters and calculation time of the numerical simulations performed for the upgraded Catania breakwater: prototype scale (continued).

Simulation	Scope of the simulation	W [m]	H [m]	$\Delta x \times \Delta y$ [m × m]	Configuration	Porosity ID	Calculation time [h]
IH_SP04	scale-up, overtopping	315.00	45.55	1.40 × 0.73	E	8-0	4.03
IH_SP05	scale-up, overtopping	315.00	45.55	1.40 × 0.74	E	8-0	4.22
IH_SP06	scale-up	315.00	45.55	1.40 × 0.75	CS	8-3	4.39
IH_SP07	scale-up	315.00	45.55	1.40 × 0.76	CS	8-3	3.79
IH_SP08	scale-up	315.00	45.55	1.40 × 0.77	CS	8-3	3.74
IH_SP09	scale-up, overtopping	315.00	45.55	1.40 × 0.78	CS	8-3	4.17
IH_SP10	scale-up, overtopping	315.00	45.55	1.40 × 0.79	CS	8-3	4.48
IH_SP11	scale-up, overtopping	315.00	45.55	1.40 × 0.80	CS	8-3	8.84
IH_SP12	scale-up, overtopping	315.00	45.55	1.40 × 0.81	CS	8-3	4.43
IH_SP13	scale-up, overtopping	315.00	45.55	1.40 × 0.82	CS	8-3	4.69
IH_SP14	overtopping	315.00	45.55	1.40 × 0.83	CS	8-3	4.24
IH_SP15	overtopping	315.00	45.55	1.40 × 0.84	CS	8-3	4.42
IH_SP16	overtopping	315.00	45.55	1.40 × 0.85	CS	8-3	4.19
IH_SP17	overtopping	315.00	45.55	1.40 × 0.86	CS	8-3	4.40
IH_SP18	overtopping	315.00	45.55	1.40 × 0.87	CS	8-3	4.68
IH_SP19	overtopping	315.00	45.55	1.40 × 0.88	CS	8-3	4.33
IH_SP20	overtopping	315.00	45.55	1.40 × 0.89	CS	8-3	4.44
IH_SP21	overtopping	315.00	45.55	1.40 × 0.90	CS	8-3	4.19
IH_SP22	overtopping	315.00	45.55	1.40 × 0.91	CS	8-3	4.43
IH_SP23	overtopping	315.00	45.55	1.40 × 0.92	CS	8-3	4.73
IH_SP24	overtopping	315.00	45.55	1.40 × 0.93	CS	8-3	4.33
IH_SP25	overtopping	315.00	45.55	1.40 × 0.94	CS	8-3	4.47
IH_SP26	overtopping	315.00	45.55	1.40 × 0.95	CS	8-3	4.19
IH_SP27	overtopping	315.00	45.55	1.40 × 0.96	CS	8-3	4.71
IH_SP28	overtopping	315.00	45.55	1.40 × 0.97	CS	8-3	4.40
IH_SP29	overtopping	315.00	45.55	1.40 × 0.98	CS	8-3	4.31
IH_SP30	overtopping	315.00	45.55	1.40 × 0.99	CS	8-3	4.42
IH_SP31	overtopping	315.00	45.55	1.40 × 0.100	CS	8-3	4.39
IH_SP32	overtopping	315.00	45.55	1.40 × 0.101	CS	8-3	4.54
IH_SP33	overtopping	315.00	45.55	1.40 × 0.102	CS	8-3	4.88
IH_SP34	overtopping	315.00	45.55	1.40 × 0.103	CS	8-3	4.43
IH_SP35	overtopping	315.00	45.55	1.40 × 0.104	CS	8-3	4.55
IH_SP36	overtopping	315.00	45.55	1.40 × 0.105	CS	8-3	4.32
IH_SP37	overtopping	315.00	45.55	1.40 × 0.106	CS	8-3	4.53
IH_SP38	overtopping	315.00	45.55	1.40 × 0.107	CS	8-3	4.85
IH_SP39	overtopping	315.00	45.55	1.40 × 0.108	E	8-0	3.99

TABLE A.10 Scope, set-up parameters and calculation time of the numerical simulations performed for the upgraded Catania breakwater: prototype scale (continued).

Simulation	Scope of the simulation	W [m]	H [m]	$\Delta x \times \Delta y$ [m $\times$ m]	Configuration	Porosity ID	Calculation time [h]
IH_SP40	overtopping	315.00	45.55	1.40 × 0.109	E	8-0	3.45
IH_SP41	overtopping	315.00	45.55	1.40 × 0.110	E	8-0	3.31
IH_SP42	overtopping	315.00	45.55	1.40 × 0.111	E	8-0	3.87
IH_SP43	overtopping	315.00	45.55	1.40 × 0.112	E	8-0	4.17
IH_SP44	overtopping	315.00	45.55	1.40 × 0.113	E	8-0	4.00
IH_SP45	overtopping	315.00	45.55	1.40 × 0.114	E	8-0	3.43
IH_SP46	overtopping	315.00	45.55	1.40 × 0.115	E	8-0	3.32
IH_SP47	overtopping	315.00	45.55	1.40 × 0.116	E	8-0	3.89
IH_SP48	overtopping	315.00	45.55	1.40 × 0.117	E	8-0	4.23
IH_SP49	overtopping	315.00	45.55	1.40 × 0.118	E	8-0	4.11
IH_SP50	overtopping	315.00	45.55	1.40 × 0.119	E	8-0	3.47
IH_SP51	overtopping	315.00	45.55	1.40 × 0.120	E	8-0	3.33
IH_SP52	overtopping	315.00	45.55	1.40 × 0.121	E	8-0	3.91
IH_SP53	overtopping	315.00	45.55	1.40 × 0.122	E	8-0	4.23
IH_SP54	overtopping	315.00	45.55	1.40 × 0.123	E	8-0	4.00
IH_SP55	overtopping	315.00	45.55	1.40 × 0.124	E	8-0	3.43
IH_SP56	overtopping	315.00	45.55	1.40 × 0.125	E	8-0	3.32
IH_SP57	overtopping	315.00	45.55	1.40 × 0.126	E	8-0	3.87
IH_SP58	overtopping	315.00	45.55	1.40 × 0.127	E	8-0	4.20
IH_SP59	overtopping	315.00	45.55	1.40 × 0.128	E	8-0	4.01
IH_SP60	overtopping	315.00	45.55	1.40 × 0.129	E	8-0	3.39
IH_SP61	overtopping	315.00	45.55	1.40 × 0.130	E	8-0	3.26
IH_SP62	overtopping	315.00	45.55	1.40 × 0.131	E	8-0	3.83
IH_SP63	overtopping	315.00	45.55	1.40 × 0.132	E	8-0	4.15

TABLE A.11 Input hydrodynamic conditions of the numerical simulations performed for the upgraded Catania breakwater: model scale.

Simulation	Sea state ID	h [m]	Target H_s [m]	Target T_p [s]	N_w [n. of waves]
IH_C01	4	0.280	0.100	1.27	200
IH_C02	2	0.280	0.075	1.18	200
IH_C03	1	0.280	0.071	1.24	200
IH_C04	3	0.280	0.093	1.27	200
IH_C05	5	0.280	0.109	1.43	200
IH_C06	4	0.280	0.100	1.27	200
IH_C07	2	0.280	0.075	1.18	200
IH_C08	1	0.280	0.071	1.24	200
IH_C09	3	0.280	0.093	1.27	200
IH_C10	5	0.280	0.109	1.43	200
IH_C11	4	0.280	0.100	1.27	200
IH_C12	2	0.280	0.075	1.18	200
IH_C13	1	0.280	0.071	1.24	200

TABLE A.11 Input hydrodynamic conditions of the numerical simulations performed for the upgraded Catania breakwater: model scale (continued).

Simulation	Sea state ID	h [m]	Target H_s [m]	Target T_p [s]	N_w [n. of waves]
IH_C14	3	0.280	0.093	1.27	200
IH_C15	5	0.280	0.109	1.43	200
IH_C16	4	0.280	0.100	1.27	200
IH_C17	2	0.280	0.075	1.18	200
IH_C18	1	0.280	0.071	1.24	200
IH_C19	3	0.280	0.093	1.27	200
IH_C20	5	0.280	0.109	1.43	200
IH_C21	4	0.280	0.100	1.27	200
IH_C22	2	0.280	0.075	1.18	200
IH_C23	1	0.280	0.071	1.24	200
IH_C24	3	0.280	0.093	1.27	200
IH_C25	5	0.280	0.109	1.43	200
IH_C26	4	0.280	0.100	1.27	200
IH_C27	2	0.280	0.075	1.18	200
IH_C28	1	0.280	0.071	1.24	200
IH_C29	3	0.280	0.093	1.27	200
IH_C30	5	0.280	0.109	1.43	200
IH_C31	4	0.280	0.100	1.27	200
IH_C32	2	0.280	0.075	1.18	200
IH_C33	1	0.280	0.071	1.24	200
IH_C34	3	0.280	0.093	1.27	200
IH_C35	5	0.280	0.109	1.43	200
IH_C36	4	0.280	0.100	1.27	200
IH_C37	2	0.280	0.075	1.18	200
IH_C38	1	0.280	0.071	1.24	200
IH_C39	3	0.280	0.093	1.27	200
IH_C40	5	0.280	0.109	1.43	200
IH_C41	4	0.280	0.100	1.27	200
IH_C42	2	0.280	0.075	1.18	200
IH_C43	4	0.280	0.100	1.27	200
IH_C44	2	0.280	0.075	1.18	200
IH_C45	4	0.280	0.100	1.27	200
IH_C46	2	0.280	0.075	1.18	200
IH_C47	4	0.280	0.100	1.27	200
IH_C48	4	0.280	0.100	1.27	200
IH_C49	4	0.280	0.100	1.27	200
IH_C50	4	0.280	0.100	1.27	200
IH_C51	4	0.280	0.100	1.27	200
IH_C52	4	0.280	0.100	1.27	1500
IH_C53	2	0.280	0.075	1.18	1500
IH_C54	1	0.280	0.071	1.24	1500
IH_C55	3	0.280	0.093	1.27	1500
IH_C56	5	0.280	0.109	1.43	1500

TABLE A.11 Input hydrodynamic conditions of the numerical simulations performed for the upgraded Catania breakwater: model scale (continued).

Simulation	Sea state ID	h [m]	Target H_s [m]	Target T_p [s]	N_w [n. of waves]
IH_C57	4	0.280	0.100	1.27	1500
IH_C58	2	0.280	0.075	1.18	1500
IH_C59	1	0.280	0.071	1.24	1500
IH_C60	3	0.280	0.093	1.27	1500
IH_C61	5	0.280	0.109	1.43	1500
IH_C62	4	0.280	0.100	1.27	1500
IH_C63	5	0.280	0.109	1.43	1500
IH_C64	2	0.280	0.075	1.18	1500
IH_C65	1	0.280	0.071	1.24	1500
IH_C66	3	0.280	0.093	1.27	1500
IH_C67	4	0.280	0.100	1.27	1500
IH_C68	5	0.280	0.109	1.43	1500
IH_C69	2	0.280	0.075	1.18	1500
IH_C70	1	0.280	0.071	1.24	1500
IH_C71	3	0.280	0.093	1.27	1500
IH_C72	4	0.280	0.100	1.27	1500
IH_C73	4	0.280	0.100	1.27	1500
IH_C74	2	0.280	0.075	1.18	1500
IH_C75	1	0.280	0.071	1.24	1500
IH_C76	3	0.280	0.093	1.27	1500
IH_C77	5	0.280	0.109	1.43	1500
IH_C78	2	0.280	0.075	1.18	1500
IH_C79	1	0.280	0.071	1.24	1500
IH_C80	3	0.280	0.093	1.27	1500
IH_C81	5	0.280	0.109	1.43	1500
IH_C82	4	0.280	0.100	1.27	1500
IH_C83	2	0.280	0.075	1.18	1500
IH_C84	1	0.280	0.071	1.24	1500
IH_C85	3	0.280	0.093	1.27	1500
IH_C86	5	0.280	0.109	1.43	1500
IH_C87	4	0.280	0.100	1.27	1500
IH_C88	2	0.280	0.075	1.18	1500
IH_C89	1	0.280	0.071	1.24	1500
IH_C90	3	0.280	0.093	1.27	1500
IH_C91	5	0.280	0.109	1.43	1500
IH_C92	6	0.280	0.095	1.30	1500
IH_C93	7	0.280	0.105	1.30	1500
IH_C94	8	0.280	0.120	1.30	1500
IH_C95	4	0.280	0.100	1.27	1500
IH_C96	2	0.280	0.075	1.18	1500
IH_C97	1	0.280	0.071	1.24	1500
IH_C98	3	0.280	0.093	1.27	1500
IH_C99	5	0.280	0.109	1.43	1500

TABLE A.11 Input hydrodynamic conditions of the numerical simulations performed for the upgraded Catania breakwater: model scale (continued).

Simulation	Sea state ID	h [m]	Target H_s [m]	Target T_p [s]	N_w [n. of waves]
IH_C100	4	0.280	0.100	1.27	1500
IH_C101	2	0.280	0.075	1.18	1500
IH_C102	1	0.280	0.071	1.24	1500
IH_C103	3	0.280	0.093	1.27	1500
IH_C104	5	0.280	0.109	1.43	1500
IH_C105	4	0.280	0.100	1.27	1500
IH_C106	2	0.280	0.075	1.18	1500
IH_C107	1	0.280	0.071	1.24	1500
IH_C108	3	0.280	0.093	1.27	1500
IH_C109	5	0.280	0.109	1.43	1500
IH_C110	4	0.280	0.100	1.27	1500
IH_C111	2	0.280	0.075	1.18	1500
IH_C112	1	0.280	0.071	1.24	1500
IH_C113	3	0.280	0.093	1.27	1500
IH_C114	5	0.280	0.109	1.43	1500
IH_C115	4	0.280	0.100	1.27	1500
IH_C116	2	0.280	0.075	1.18	1500
IH_C117	1	0.280	0.071	1.24	1500
IH_C118	3	0.280	0.093	1.27	1500
IH_C119	5	0.280	0.109	1.43	1500
IH_C120	4	0.280	0.100	1.27	1500
IH_C121	5	0.280	0.109	1.43	1500
IH_C122	6	0.280	0.095	1.30	1500
IH_C123	7	0.280	0.105	1.30	1500
IH_C124	8	0.280	0.120	1.30	1500
IH_C125	4	0.280	0.100	1.27	1500
IH_C126	5	0.280	0.109	1.43	1500
IH_C127	6	0.280	0.095	1.30	1500
IH_C128	7	0.280	0.105	1.30	1500
IH_C129	8	0.280	0.120	1.30	1500
IH_C130	4	0.280	0.100	1.27	1500
IH_C131	5	0.280	0.109	1.43	1500
IH_C132	6	0.280	0.095	1.30	1500
IH_C133	7	0.280	0.105	1.30	1500
IH_C134	8	0.280	0.120	1.30	1500
IH_C135	4	0.280	0.100	1.27	1500
IH_C136	5	0.280	0.109	1.43	1500
IH_C137	6	0.280	0.095	1.30	1500
IH_C138	7	0.280	0.105	1.30	1500
IH_C139	8	0.280	0.120	1.30	1500
IH_C140	4	0.280	0.100	1.27	1500
IH_C141	5	0.280	0.109	1.43	1500
IH_C142	6	0.280	0.095	1.30	1500

TABLE A.11 Input hydrodynamic conditions of the numerical simulations performed for the upgraded Catania breakwater: model scale (continued).

Simulation	Sea state ID	h [m]	Target H_s [m]	Target T_p [s]	N_w [n. of waves]
IH_C143	7	0.280	0.105	1.30	1500
IH_C144	8	0.280	0.120	1.30	1500

TABLE A.12 Input hydrodynamic conditions of the numerical simulations performed for the upgraded Catania breakwater: prototype scale.

Simulation	Sea state ID	h [m]	Target H_s [m]	Target T_p [s]	N_w [n. of waves]
IH_SP01	4	19.600	7.000	10.63	1500
IH_SP02	2	19.600	5.250	9.87	1500
IH_SP03	1	19.600	4.970	10.37	1500
IH_SP04	3	19.600	6.510	10.63	1500
IH_SP05	5	19.600	7.630	11.96	1500
IH_SP06	4	19.600	7.000	11.96	1500
IH_SP07	2	19.600	5.250	9.87	1500
IH_SP08	1	19.600	4.970	10.37	1500
IH_SP09	3	19.600	6.510	10.63	1500
IH_SP10	5	19.600	7.630	11.96	1500
IH_SP11	6	19.600	6.650	10.88	1500
IH_SP12	7	19.600	7.350	10.88	1500
IH_SP13	8	19.600	8.400	10.88	1500
IH_SP14	4	19.600	7.000	10.63	1500
IH_SP15	5	19.600	7.630	11.96	1500
IH_SP16	6	19.600	6.650	10.88	1500
IH_SP17	7	19.600	7.350	10.88	1500
IH_SP18	8	19.600	8.400	10.88	1500
IH_SP19	4	19.600	7.000	10.63	1500
IH_SP20	5	19.600	7.630	11.96	1500
IH_SP21	6	19.600	6.650	10.88	1500
IH_SP22	7	19.600	7.350	10.88	1500
IH_SP23	8	19.600	8.400	10.88	1500
IH_SP24	4	19.600	7.000	10.63	1500
IH_SP25	5	19.600	7.630	11.96	1500
IH_SP26	6	19.600	6.650	10.88	1500
IH_SP27	7	19.600	7.350	10.88	1500
IH_SP28	8	19.600	8.400	10.88	1500
IH_SP29	4	19.600	7.000	10.63	1500
IH_SP30	5	19.600	7.630	11.96	1500
IH_SP31	6	19.600	6.650	10.88	1500
IH_SP32	7	19.600	7.350	10.88	1500
IH_SP33	8	19.600	8.400	10.88	1500
IH_SP34	4	19.600	7.000	10.63	1500
IH_SP35	5	19.600	7.630	11.96	1500

TABLE A.12 Input hydrodynamic conditions of the numerical simulations performed for the upgraded Catania breakwater: prototype (continued).

Simulation	Sea state ID	h [m]	Target H_s [m]	Target T_p [s]	N_w [n. of waves]
IH_SP36	6	19.600	6.650	10.88	1500
IH_SP37	7	19.600	7.350	10.88	1500
IH_SP38	8	19.600	8.400	10.88	1500
IH_SP39	4	19.600	7.000	10.63	1500
IH_SP40	2	19.600	5.250	9.87	1500
IH_SP41	1	19.600	4.970	10.37	1500
IH_SP42	3	19.600	6.510	10.63	1500
IH_SP43	5	19.600	7.630	11.96	1500
IH_SP44	4	19.600	7.000	10.63	1500
IH_SP45	2	19.600	5.250	9.87	1500
IH_SP46	1	19.600	4.970	10.37	1500
IH_SP47	3	19.600	6.510	10.63	1500
IH_SP48	5	19.600	7.630	11.96	1500
IH_SP49	4	19.600	7.000	10.63	1500
IH_SP50	2	19.600	5.250	9.87	1500
IH_SP51	1	19.600	4.970	10.37	1500
IH_SP52	3	19.600	6.510	10.63	1500
IH_SP53	5	19.600	7.630	11.96	1500
IH_SP54	4	19.600	7.000	10.63	1500
IH_SP55	2	19.600	5.250	9.87	1500
IH_SP56	1	19.600	4.970	10.37	1500
IH_SP57	3	19.600	6.510	10.63	1500
IH_SP58	5	19.600	7.630	11.96	1500
IH_SP59	4	19.600	7.000	10.63	1500
IH_SP60	2	19.600	5.250	9.87	1500
IH_SP61	1	19.600	4.970	10.37	1500
IH_SP62	3	19.600	6.510	10.63	1500
IH_SP63	5	19.600	7.630	11.96	1500

TABLE A.13 Output wave characteristics of the simulations performed for the upgraded Catania harbor breakwater and correspondent numerical data on mean overtopping discharge: model scale.

Simulation	Output wave characteristics								Mean overtopping	
	H_s [m]	T_p [s]	$T_{m-1,0}$ [s]	T_m [s]	H_{max}/H_s	$\xi_{m-1,0}$	k_r	R_c/H_s	q [m³/s · m]	q^*
IH_C01	0.083	1.33	1.24	1.13	1.83	2.69	0.16	1.37	1.04×10^{-5}	1.39×10^{-4}
IH_C02	0.068	1.24	1.19	1.11	1.80	2.85	0.13	1.68	0.00	0.00
IH_C03	0.061	1.29	1.22	1.13	1.86	3.09	0.14	1.88	0.00	0.00
IH_C04	0.077	1.31	1.25	1.15	1.81	2.82	0.16	1.48	2.47×10^{-6}	3.67×10^{-5}
IH_C05	0.088	1.40	1.41	1.26	1.85	2.97	0.22	1.29	3.01×10^{-5}	3.66×10^{-4}
IH_C06	0.091	1.20	1.19	1.08	1.83	2.47	0.16	1.25	2.52×10^{-5}	2.93×10^{-4}
IH_C07	0.073	1.24	1.14	1.04	1.80	2.64	0.14	1.56	1.27×10^{-6}	2.06×10^{-5}

TABLE A.13 Output wave characteristics of the simulations performed for the upgraded Catania harbor breakwater and correspondent numerical data on mean overtopping discharge: model scale (continued).

Simulation	Output wave characteristics								Mean overtopping	
	H_s [m]	T_p [s]	$T_{m-1,0}$ [s]	T_m [s]	H_{max}/H_s	$\xi_{m-1,0}$	k_r	R_c/H_s	q [m^3/s·m]	q^*
IH_C08	0.065	1.29	1.17	1.07	1.86	2.88	0.15	1.76	0.00	0.00
IH_C09	0.084	1.31	1.19	1.07	1.81	2.58	0.16	1.36	5.78×10^{-6}	7.64×10^{-5}
IH_C10	0.095	1.31	1.29	1.13	1.85	2.63	0.22	1.20	7.56×10^{-5}	8.29×10^{-4}
IH_C11	0.083	1.33	1.24	1.13	1.83	2.69	0.09	-	-	-
IH_C12	0.068	1.24	1.18	1.10	1.80	2.82	0.09	-	-	-
IH_C13	0.061	1.33	1.21	1.12	1.86	3.07	0.07	-	-	-
IH_C14	0.077	1.31	1.24	1.13	1.81	2.79	0.08	-	-	-
IH_C15	0.089	1.40	1.40	1.24	1.85	2.94	0.09	-	-	-
IH_C16	0.091	1.20	1.18	1.06	1.83	2.44	0.11	-	-	-
IH_C17	0.073	1.16	1.13	1.03	1.80	2.62	0.11	-	-	-
IH_C18	0.065	1.29	1.17	1.07	1.86	2.86	0.09	-	-	-
IH_C19	0.084	1.31	1.18	1.06	1.81	2.54	0.10	-	-	-
IH_C20	0.096	1.31	1.28	1.11	1.85	2.59	0.11	-	-	-
IH_C21	0.083	1.33	1.24	1.14	1.83	2.70	0.17	1.38	4.86×10^{-6}	6.53×10^{-5}
IH_C22	0.068	1.24	1.19	1.11	1.80	2.85	0.15	1.69	0.00	0.00
IH_C23	0.060	1.33	1.22	1.13	1.86	3.09	0.16	1.89	0.00	0.00
IH_C24	0.077	1.31	1.25	1.15	1.81	2.82	0.17	1.48	0.00	0.00
IH_C25	0.088	1.40	1.41	1.25	1.85	2.97	0.22	1.29	1.73×10^{-5}	2.11×10^{-4}
IH_C26	0.091	1.20	1.19	1.08	1.83	2.47	0.17	1.25	1.07×10^{-5}	1.23×10^{-4}
IH_C27	0.073	1.24	1.14	1.04	1.80	2.64	0.16	1.56	0.00	0.00
IH_C28	0.065	1.29	1.17	1.07	1.86	2.88	0.16	1.76	0.00	0.00
IH_C29	0.084	1.31	1.19	1.08	1.81	2.58	0.17	1.36	2.17×10^{-6}	2.86×10^{-5}
IH_C30	0.095	1.31	1.30	1.13	1.85	2.63	0.23	1.20	6.48×10^{-5}	7.10×10^{-4}
IH_C31	0.091	1.20	1.19	1.08	1.83	2.47	0.17	1.25	1.97×10^{-5}	2.29×10^{-4}
IH_C32	0.073	1.24	1.14	1.05	1.80	2.64	0.16	1.56	7.67×10^{-7}	1.24×10^{-5}
IH_C33	0.065	1.29	1.17	1.07	1.86	2.88	0.17	1.76	0.00	0.00
IH_C34	0.083	1.31	1.20	1.08	1.81	2.59	0.18	1.37	2.91×10^{-5}	3.88×10^{-4}
IH_C35	0.095	1.31	1.30	1.13	1.85	2.63	0.23	1.21	9.30×10^{-5}	1.02×10^{-3}
IH_C36	0.091	1.20	1.19	1.08	1.83	2.48	0.19	1.25	1.83×10^{-5}	2.13×10^{-4}
IH_C37	0.073	1.24	1.14	1.05	1.80	2.65	0.18	1.56	0.00	0.00
IH_C38	0.065	1.29	1.17	1.08	1.86	2.88	0.19	1.76	0.00	0.00
IH_C39	0.083	1.31	1.20	1.08	1.81	2.59	0.20	1.37	4.95×10^{-6}	6.60×10^{-5}
IH_C40	0.094	1.31	1.30	1.13	1.85	2.64	0.25	1.21	8.20×10^{-5}	9.02×10^{-4}
IH_C41	0.092	1.20	1.18	1.05	1.83	2.43	0.20	1.23	1.23×10^{-4}	1.40×10^{-3}
IH_C42	0.076	1.16	1.13	1.02	1.80	2.56	0.17	1.51	1.00×10^{-5}	1.54×10^{-4}
IH_C43	0.091	1.20	1.19	1.08	1.83	2.47	0.16	1.25	1.81×10^{-5}	2.10×10^{-4}
IH_C44	0.073	1.24	1.14	1.04	1.80	2.64	0.15	1.56	1.16×10^{-6}	1.88×10^{-5}
IH_C45	0.091	1.20	1.19	1.08	1.83	2.47	0.17	1.25	1.26×10^{-5}	1.47×10^{-4}
IH_C46	0.073	1.24	1.14	1.05	1.80	2.64	0.16	1.56	0.00	0.00
IH_C47	0.090	1.26	1.20	1.08	1.83	2.49	0.21	1.43	0.00	0.00
IH_C48	0.090	1.26	1.20	1.08	1.83	2.49	0.23	1.44	0.00	0.00

TABLE A.13 Output wave characteristics of the simulations performed for the upgraded Catania harbor breakwater and correspondent numerical data on mean overtopping discharge: model scale (continued).

Simulation	Output wave characteristics								Mean overtopping	
	H_s [m]	T_p [s]	$T_{m-1,0}$ [s]	T_m [s]	H_{max}/H_s	$\zeta_{m-1,0}$	k_r	R_c/H_s	q [m³/s·m]	q^*
IH_C49	0.090	1.26	1.20	1.08	1.83	2.49	0.22	1.43	0.00	0.00
IH_C50	0.089	1.26	1.20	1.08	1.83	2.50	0.24	1.44	0.00	0.00
IH_C51	0.090	1.26	1.20	1.08	1.83	2.49	0.21	1.43	0.00	0.00
IH_C52	0.090	1.26	1.20	1.08	1.83	2.49	0.23	1.44	1.06×10^{-6}	1.26×10^{-5}
IH_C53	0.072	1.24	1.15	1.05	1.80	2.66	0.23	1.78	0.00	0.00
IH_C54	0.064	1.29	1.18	1.08	1.86	2.90	0.24	2.00	0.00	0.00
IH_C55	0.083	1.31	1.20	1.08	1.81	2.60	0.23	1.56	0.00	0.00
IH_C56	0.094	1.31	1.30	1.14	1.85	2.65	0.26	1.37	1.72×10^{-6}	1.90×10^{-5}
IH_C57	0.091	1.20	1.19	1.08	1.83	2.48	0.19	1.25	2.32×10^{-5}	2.70×10^{-4}
IH_C58	0.073	1.24	1.14	1.05	1.80	2.65	0.18	1.56	3.13×10^{-7}	5.08×10^{-6}
IH_C59	0.065	1.29	1.17	1.08	1.86	2.88	0.19	1.76	7.08×10^{-7}	1.37×10^{-5}
IH_C60	0.083	1.31	1.20	1.08	1.81	2.59	0.20	1.37	1.12×10^{-5}	1.49×10^{-4}
IH_C61	0.094	1.31	1.30	1.13	1.85	2.64	0.25	1.21	1.04×10^{-4}	1.14×10^{-3}
IH_C62	0.090	1.20	1.20	1.08	1.83	2.50	0.28	1.43	7.64×10^{-5}	9.05×10^{-4}
IH_C63	0.093	1.31	1.30	1.13	1.85	2.66	0.34	1.38	2.35×10^{-4}	2.63×10^{-3}
IH_C64	0.072	1.16	1.15	1.05	1.80	2.67	0.27	1.79	1.51×10^{-6}	2.49×10^{-5}
IH_C65	0.064	1.29	1.18	1.08	1.86	2.91	0.30	2.01	2.03×10^{-6}	3.99×10^{-5}
IH_C66	0.082	1.31	1.20	1.08	1.81	2.62	0.29	1.57	3.56×10^{-5}	4.80×10^{-4}
IH_C67	0.090	1.26	1.20	1.08	1.83	2.50	0.26	1.27	9.12×10^{-7}	1.09×10^{-5}
IH_C68	0.094	1.31	1.31	1.14	1.85	2.66	0.31	1.21	7.03×10^{-6}	7.79×10^{-5}
IH_C69	0.072	1.24	1.15	1.05	1.80	2.67	0.26	1.58	0.00	0.00
IH_C70	0.064	1.29	1.18	1.08	1.86	2.91	0.27	1.78	0.00	0.00
IH_C71	0.082	1.31	1.20	1.08	1.81	2.60	0.26	1.38	0.00	0.00
IH_C72	0.090	1.20	1.20	1.08	1.83	2.49	0.25	1.26	5.09×10^{-5}	5.98×10^{-4}
IH_C73	0.090	1.26	1.20	1.08	1.83	2.50	0.25	1.27	5.98×10^{-7}	7.13×10^{-6}
IH_C74	0.072	1.16	1.15	1.05	1.80	2.66	0.24	1.58	1.12×10^{-6}	1.83×10^{-5}
IH_C75	0.064	1.29	1.18	1.08	1.86	2.90	0.26	1.77	1.48×10^{-6}	2.90×10^{-5}
IH_C76	0.083	1.25	1.19	1.07	1.81	2.58	0.26	1.37	2.28×10^{-5}	3.03×10^{-4}
IH_C77	0.094	1.31	1.30	1.13	1.85	2.65	0.31	1.37	1.82×10^{-4}	2.01×10^{-3}
IH_C78	0.072	1.24	1.15	1.05	1.80	2.67	0.26	1.79	0.00	0.00
IH_C79	0.064	1.29	1.18	1.08	1.86	2.91	0.27	2.01	0.00	0.00
IH_C80	0.083	1.25	1.19	1.08	1.81	2.58	0.26	1.56	0.00	0.00
IH_C81	0.094	1.31	1.31	1.14	1.85	2.66	0.30	1.37	6.07×10^{-6}	6.72×10^{-5}
IH_C82	0.089	1.26	1.20	1.08	1.83	2.51	0.26	1.45	1.38×10^{-6}	1.66×10^{-5}
IH_C83	0.072	1.24	1.15	1.05	1.80	2.67	0.26	1.79	0.00	0.00
IH_C84	0.064	1.29	1.18	1.08	1.86	2.91	0.27	2.01	0.00	0.00
IH_C85	0.082	1.31	1.20	1.08	1.81	2.61	0.26	1.57	0.00	0.00
IH_C86	0.094	1.31	1.31	1.14	1.85	2.67	0.30	1.37	9.52×10^{-6}	1.06×10^{-4}
IH_C87	0.089	1.26	1.20	1.08	1.83	2.50	0.28	1.45	2.20×10^{-6}	2.64×10^{-5}
IH_C88	0.072	1.24	1.15	1.06	1.80	2.69	0.28	1.80	0.00	0.00
IH_C89	0.064	1.29	1.18	1.09	1.86	2.91	0.29	2.02	0.00	0.00

TABLE A.13 Output wave characteristics of the simulations performed for the upgraded Catania harbor breakwater and correspondent numerical data on mean overtopping discharge: model scale (continued).

| Simulation | Output wave characteristics | | | | | | | | Mean overtopping | |
	H_s [m]	T_p [s]	$T_{m-1,0}$ [s]	T_m [s]	H_{max}/H_s	$\xi_{m-1,0}$	k_r	R_c/H_s	q [m^3/s·m]	q^*
IH_C90	0.082	1.31	1.20	1.08	1.81	2.62	0.28	1.57	0.00	0.00
IH_C91	0.094	1.31	1.31	1.14	1.85	2.67	0.32	1.38	2.51×10^{-5}	2.79×10^{-4}
IH_C92	0.088	1.26	1.22	1.08	1.80	2.56	0.28	1.47	2.60×10^{-7}	3.19×10^{-6}
IH_C93	0.094	1.36	1.21	1.09	1.83	2.47	0.29	1.37	6.70×10^{-6}	7.44×10^{-5}
IH_C94	0.108	1.26	1.23	1.10	1.81	2.33	0.27	1.19	1.17×10^{-5}	1.05×10^{-4}
IH_C95	0.091	1.33	1.22	1.10	1.87	2.52	0.26	1.25	4.48×10^{-5}	5.20×10^{-4}
IH_C96	0.073	1.08	1.13	1.05	1.85	2.62	0.23	1.57	1.78×10^{-6}	2.89×10^{-5}
IH_C97	0.067	1.25	1.17	1.08	1.83	2.83	0.25	1.70	7.20×10^{-8}	1.32×10^{-6}
IH_C98	0.087	1.26	1.20	1.08	1.82	2.53	0.25	1.30	2.54×10^{-5}	3.14×10^{-4}
IH_C99	0.099	1.34	1.29	1.12	1.84	2.56	0.29	1.15	1.59×10^{-4}	1.63×10^{-3}
IH_C100	0.090	1.28	1.20	1.08	1.83	2.50	0.26	1.27	3.90×10^{-5}	4.61×10^{-4}
IH_C101	0.070	1.13	1.14	1.06	1.83	2.68	0.22	1.62	1.34×10^{-6}	2.29×10^{-5}
IH_C102	0.071	1.25	1.18	1.10	1.80	2.78	0.25	1.61	1.67×10^{-6}	2.82×10^{-5}
IH_C103	0.085	1.16	1.19	1.08	1.84	2.55	0.25	1.34	2.94×10^{-5}	3.79×10^{-4}
IH_C104	0.106	1.46	1.30	1.12	1.80	2.49	0.30	1.07	1.86×10^{-4}	1.72×10^{-3}
IH_C105	0.100	1.21	1.18	1.07	1.82	2.33	0.25	1.15	4.97×10^{-5}	5.06×10^{-4}
IH_C106	0.069	1.16	1.13	1.04	1.68	2.69	0.24	1.65	1.93×10^{-7}	3.39×10^{-6}
IH_C107	0.071	1.35	1.19	1.10	1.83	2.79	0.25	1.62	1.09×10^{-6}	1.86×10^{-5}
IH_C108	0.085	1.19	1.19	1.08	1.83	2.54	0.25	1.34	3.10×10^{-5}	3.99×10^{-4}
IH_C109	0.096	1.46	1.28	1.12	1.79	2.59	0.30	1.19	1.90×10^{-4}	2.04×10^{-3}
IH_C110	0.095	1.25	1.19	1.07	1.82	2.42	0.26	1.20	5.33×10^{-5}	5.84×10^{-4}
IH_C111	0.072	1.23	1.13	1.05	1.85	2.64	0.23	1.59	7.60×10^{-7}	1.26×10^{-5}
IH_C112	0.064	1.20	1.16	1.07	1.82	2.86	0.25	1.78	8.83×10^{-7}	1.74×10^{-5}
IH_C113	0.087	1.23	1.18	1.06	1.82	2.51	0.25	1.32	2.91×10^{-5}	3.65×10^{-4}
IH_C114	0.102	1.36	1.28	1.12	1.78	2.51	0.29	1.12	1.65×10^{-4}	1.62×10^{-3}
IH_C115	0.092	1.17	1.18	1.06	1.81	2.42	0.26	1.24	3.71×10^{-5}	4.24×10^{-4}
IH_C116	0.070	1.15	1.13	1.05	1.85	2.66	0.22	1.62	2.59×10^{-7}	4.42×10^{-6}
IH_C117	0.069	1.20	1.18	1.09	1.83	2.82	0.24	1.66	8.34×10^{-7}	1.47×10^{-5}
IH_C118	0.088	1.28	1.21	1.09	1.80	2.55	0.26	1.30	2.83×10^{-5}	3.46×10^{-4}
IH_C119	0.097	1.40	1.31	1.12	1.84	2.62	0.31	1.17	1.48×10^{-4}	1.55×10^{-3}
IH_C120	0.089	1.28	1.20	1.08	1.87	2.52	0.29	1.45	1.42×10^{-6}	1.72×10^{-5}
IH_C121	0.098	1.32	1.29	1.12	1.84	2.56	0.31	1.31	2.18×10^{-5}	2.26×10^{-4}
IH_C122	0.090	1.30	1.22	1.09	1.83	2.53	0.29	1.43	1.26×10^{-6}	1.48×10^{-5}
IH_C123	0.092	1.26	1.22	1.09	1.83	2.52	0.29	1.41	1.85×10^{-6}	2.13×10^{-5}
IH_C124	0.101	1.40	1.21	1.07	1.75	2.38	0.28	1.27	1.98×10^{-5}	1.97×10^{-4}
IH_C125	0.089	1.28	1.20	1.08	1.83	2.52	0.29	1.45	1.42×10^{-6}	1.72×10^{-5}
IH_C126	0.106	1.46	1.30	1.13	1.80	2.50	0.31	1.22	2.84×10^{-5}	2.64×10^{-4}
IH_C127	0.090	1.32	1.22	1.10	1.80	2.54	0.28	1.43	1.51×10^{-6}	1.79×10^{-5}
IH_C128	0.098	1.26	1.23	1.11	1.82	2.46	0.29	1.32	5.32×10^{-6}	5.56×10^{-5}
IH_C129	0.105	1.24	1.21	1.08	1.78	2.33	0.28	1.22	1.48×10^{-5}	1.38×10^{-4}
IH_C130	0.099	1.21	1.18	1.07	1.82	2.34	0.28	1.30	3.60×10^{-6}	3.68×10^{-5}

TABLE A.13 Output wave characteristics of the simulations performed for the upgraded Catania harbor breakwater and correspondent numerical data on mean overtopping discharge: model scale (continued).

Simulation	Output wave characteristics								Mean overtopping	
	H_s [m]	T_p [s]	$T_{m-1,0}$ [s]	T_m [s]	H_{max}/H_s	$\zeta_{m-1,0}$	k_r	R_c/H_s	q [m³/s · m]	q^*
IH_C131	0.095	1.46	1.28	1.12	1.79	2.60	0.31	1.35	2.84×10^{-5}	3.09×10^{-4}
IH_C132	0.094	1.31	1.22	1.10	1.85	2.50	0.29	1.38	5.11×10^{-6}	5.68×10^{-5}
IH_C133	0.094	1.21	1.22	1.09	1.81	2.49	0.30	1.37	7.77×10^{-7}	8.62×10^{-6}
IH_C134	0.103	1.35	1.23	1.09	1.79	2.39	0.28	1.26	1.76×10^{-5}	1.71×10^{-4}
IH_C135	0.094	1.25	1.20	1.08	1.82	2.44	0.28	1.37	7.68×10^{-7}	8.52×10^{-6}
IH_C136	0.101	1.36	1.29	1.13	1.78	2.53	0.30	1.27	2.87×10^{-5}	2.85×10^{-4}
IH_C137	0.091	1.40	1.23	1.12	1.84	2.55	0.30	1.42	8.90×10^{-7}	1.04×10^{-5}
IH_C138	0.096	1.31	1.21	1.08	1.84	2.44	0.29	1.34	7.43×10^{-6}	7.93×10^{-5}
IH_C139	0.104	1.21	1.22	1.11	1.77	2.37	0.27	1.24	1.44×10^{-5}	1.37×10^{-4}
IH_C140	0.091	1.23	1.18	1.06	1.81	2.44	0.29	1.42	2.15×10^{-6}	2.51×10^{-5}
IH_C141	0.097	1.40	1.31	1.12	1.84	2.62	0.33	1.33	1.31×10^{-5}	1.38×10^{-4}
IH_C142	0.084	1.28	1.22	1.10	1.84	2.63	0.29	1.53	1.24×10^{-7}	1.62×10^{-6}
IH_C143	0.097	1.32	1.23	1.09	1.80	2.46	0.28	1.33	2.76×10^{-6}	2.91×10^{-5}
IH_C144	0.109	1.30	1.23	1.10	1.77	2.33	0.28	1.18	1.45×10^{-5}	1.28×10^{-4}

TABLE A.14 Output wave characteristics of the simulations performed for the upgraded Catania harbor breakwater and correspondent numerical data on mean overtopping discharge: prototype scale.

Simulation	Output wave characteristics								Mean overtopping	
	H_s [m]	T_p [s]	$T_{m-1,0}$ [s]	T_m [s]	H_{max}/H_s	$\zeta_{m-1,0}$	k_r	R_c/H_s	q [m³/s · m]	q^*
IH_SP01	6.467	10.81	9.87	8.87	1.83	2.43	0.24	1.23	3.07×10^{-2}	5.95×10^{-4}
IH_SP02	5.094	10.07	9.40	8.67	1.72	2.60	0.23	1.57	3.00×10^{-4}	8.34×10^{-6}
IH_SP03	4.822	10.52	9.78	9.05	1.77	2.78	0.25	1.65	4.16×10^{-4}	1.25×10^{-5}
IH_SP04	6.189	10.55	10.14	9.17	1.77	2.55	0.26	1.29	1.76×10^{-2}	3.64×10^{-4}
IH_SP05	7.188	12.37	10.90	9.37	1.72	2.54	0.30	1.11	1.00×10^{-1}	1.66×10^{-3}
IH_SP06	6.430	10.81	9.89	8.91	1.83	2.44	0.29	1.40	9.55×10^{-4}	1.87×10^{-5}
IH_SP07	5.053	10.07	9.41	8.71	1.72	2.61	0.27	1.79	0.00	0.00
IH_SP08	4.789	10.52	9.81	9.10	1.77	2.80	0.30	1.89	0.00	0.00
IH_SP09	6.131	10.55	10.14	9.19	1.77	2.56	0.31	1.47	0.00	0.00
IH_SP10	7.203	12.37	10.92	9.41	1.72	2.54	0.33	1.25	7.24×10^{-3}	1.20×10^{-4}
IH_SP11	6.090	10.49	10.16	9.17	1.78	2.57	0.30	1.48	2.24×10^{-4}	4.75×10^{-6}
IH_SP12	6.760	11.66	10.00	8.96	1.76	2.40	0.29	1.34	3.05×10^{-4}	5.55×10^{-6}
IH_SP13	7.270	10.27	10.19	8.95	1.81	2.36	0.31	1.24	6.86×10^{-3}	1.12×10^{-4}
IH_SP14	6.619	12.06	10.77	9.38	1.76	2.61	0.33	1.36	2.76×10^{-3}	5.18×10^{-5}
IH_SP15	7.027	11.86	10.82	9.42	1.84	2.55	0.32	1.29	8.41×10^{-3}	1.44×10^{-4}
IH_SP16	6.290	10.88	10.16	9.11	1.82	2.53	0.31	1.44	0.00	0.00
IH_SP17	6.575	11.13	10.20	9.04	1.79	2.48	0.30	1.37	1.16×10^{-3}	2.20×10^{-5}
IH_SP18	7.469	10.88	10.16	8.95	1.84	2.32	0.29	1.21	6.43×10^{-3}	1.01×10^{-4}
IH_SP19	6.467	10.35	10.00	9.04	1.76	2.46	0.29	1.40	0.00	0.00

TABLE A.14 Output wave characteristics of the simulations performed for the upgraded Catania harbor breakwater and correspondent numerical data on mean overtopping discharge: prototype scale (continued).

Simulation	Output wave characteristics							Mean overtopping		
	H_s [m]	T_p [s]	$T_{m-1,0}$ [s]	T_m [s]	H_{max}/H_s	$\xi_{m-1,0}$	k_r	R_c/H_s	q [m³/s·m]	q^*
IH_SP20	7.095	11.22	10.85	9.45	1.79	2.55	0.32	1.27	9.27×10^{-3}	1.57×10^{-4}
IH_SP21	6.137	11.13	10.14	9.03	1.81	2.56	0.30	1.47	1.43×10^{-3}	2.99×10^{-5}
IH_SP22	6.802	10.27	10.20	8.99	1.79	2.44	0.30	1.33	1.00×10^{-3}	1.81×10^{-5}
IH_SP23	7.332	10.42	10.08	8.90	1.76	2.33	0.30	1.23	4.12×10^{-3}	6.62×10^{-5}
IH_SP24	6.542	10.65	10.03	9.08	1.78	2.45	0.29	1.38	5.79×10^{-4}	1.10×10^{-5}
IH_SP25	7.019	12.06	10.83	9.35	1.83	2.55	0.33	1.29	8.13×10^{-3}	1.40×10^{-4}
IH_SP26	6.217	10.49	10.00	8.90	1.79	2.51	0.30	1.45	0.00	0.00
IH_SP27	6.705	10.64	10.29	9.23	1.78	2.48	0.30	1.35	3.65×10^{-3}	6.72×10^{-5}
IH_SP28	7.453	11.57	10.18	8.99	1.80	2.33	0.30	1.21	5.03×10^{-3}	7.90×10^{-5}
IH_SP29	6.513	11.14	9.92	8.98	1.76	2.43	0.29	1.39	0.00	0.00
IH_SP30	6.981	12.58	10.82	9.36	1.83	2.56	0.33	1.29	7.59×10^{-3}	1.31×10^{-4}
IH_SP31	6.162	10.42	10.13	9.11	1.79	2.55	0.30	1.47	0.00	0.00
IH_SP32	6.865	11.66	10.25	9.08	1.81	2.44	0.30	1.32	1.88×10^{-3}	3.34×10^{-5}
IH_SP33	7.354	10.64	10.18	8.97	1.75	2.35	0.31	1.23	1.00×10^{-2}	1.60×10^{-4}
IH_SP34	6.435	10.50	10.28	9.31	1.75	2.53	0.30	1.40	8.85×10^{-4}	1.73×10^{-5}
IH_SP35	6.724	12.37	10.91	9.37	1.77	2.63	0.33	1.34	5.62×10^{-3}	1.03×10^{-4}
IH_SP36	6.239	10.80	10.23	9.16	1.81	2.56	0.31	1.45	9.43×10^{-4}	1.93×10^{-5}
IH_SP37	6.610	11.13	10.12	8.92	1.81	2.46	0.30	1.37	1.59×10^{-3}	2.99×10^{-5}
IH_SP38	7.441	10.34	10.30	9.12	1.83	2.36	0.29	1.21	8.38×10^{-3}	1.32×10^{-4}
IH_SP39	6.649	11.46	10.73	9.29	1.76	2.60	0.31	1.20	8.06×10^{-2}	1.50×10^{-3}
IH_SP40	5.021	9.74	9.49	8.78	1.78	2.64	0.23	1.59	1.97×10^{-4}	5.59×10^{-6}
IH_SP41	4.645	10.23	9.72	8.93	1.79	2.82	0.24	1.72	2.78×10^{-4}	8.86×10^{-6}
IH_SP42	5.933	11.20	10.08	9.01	1.83	2.58	0.25	1.35	9.74×10^{-3}	2.15×10^{-4}
IH_SP43	7.043	11.86	10.81	9.40	1.84	2.54	0.30	1.13	1.39×10^{-1}	2.38×10^{-3}
IH_SP44	6.514	10.35	9.96	8.98	1.76	2.44	0.25	1.23	4.13×10^{-2}	7.93×10^{-4}
IH_SP45	4.967	10.14	9.48	8.81	1.75	2.66	0.23	1.61	2.23×10^{-4}	6.43×10^{-6}
IH_SP46	4.901	10.37	9.76	9.04	1.80	2.76	0.24	1.63	2.52×10^{-4}	7.43×10^{-6}
IH_SP47	6.281	10.87	10.06	9.13	1.82	2.51	0.25	1.27	2.15×10^{-2}	4.35×10^{-4}
IH_SP48	7.120	11.22	10.82	9.42	1.79	2.53	0.30	1.12	1.60×10^{-1}	2.70×10^{-3}
IH_SP49	6.598	10.65	10.02	9.02	1.78	2.44	0.25	1.21	3.24×10^{-2}	6.11×10^{-4}
IH_SP50	5.007	10.14	9.48	8.80	1.74	2.65	0.22	1.59	1.56×10^{-4}	4.44×10^{-6}
IH_SP51	4.795	10.30	9.74	8.96	1.77	2.78	0.25	1.66	3.39×10^{-4}	1.03×10^{-5}
IH_SP52	6.035	10.87	9.93	8.98	1.76	2.53	0.26	1.32	1.86×10^{-2}	4.00×10^{-4}
IH_SP53	7.053	12.06	10.79	9.29	1.83	2.54	0.31	1.13	1.28×10^{-1}	2.18×10^{-3}
IH_SP54	6.555	11.14	9.89	8.93	1.76	2.41	0.24	1.22	3.71×10^{-2}	7.06×10^{-4}
IH_SP55	5.067	10.36	9.48	8.76	1.82	2.63	0.23	1.57	1.70×10^{-4}	4.76×10^{-6}
IH_SP56	4.807	10.09	9.83	9.06	1.84	2.80	0.25	1.66	8.14×10^{-4}	2.47×10^{-5}
IH_SP57	6.227	10.33	9.99	9.04	1.80	2.50	0.25	1.28	2.27×10^{-2}	4.66×10^{-4}
IH_SP58	7.002	12.58	10.79	9.31	1.83	2.55	0.31	1.14	1.48×10^{-1}	2.55×10^{-3}
IH_SP59	6.473	10.28	10.27	9.27	1.75	2.52	0.26	1.23	4.74×10^{-2}	9.19×10^{-4}
IH_SP60	4.884	9.49	9.34	8.63	1.81	2.64	0.23	1.63	3.98×10^{-5}	1.18×10^{-6}

TABLE A.14 Output wave characteristics of the simulations performed for the upgraded Catania harbor breakwater and correspondent numerical data on mean overtopping discharge: prototype scale (continued).

Simulation	Output wave characteristics							Mean overtopping		
	H_s [m]	T_p [s]	$T_{m-1,0}$ [s]	T_m [s]	H_{max}/H_s	$\xi_{m-1,0}$	k_r	R_c/H_s	q [m³/s · m]	q^*
IH_SP61	4.807	10.09	9.83	9.06	1.84	2.80	0.25	1.66	8.14×10^{-4}	2.47×10^{-5}
IH_SP62	6.204	9.59	9.99	9.01	1.72	2.51	0.25	1.29	2.57×10^{-2}	5.32×10^{-4}
IH_SP63	6.714	12.37	10.91	9.33	1.77	2.63	0.31	1.19	1.53×10^{-1}	2.81×10^{-3}